



*The tear behaviour of some tri-block copolymer elastomers.*

HODGKINSON, John Michael.

Available from the Sheffield Hallam University Research Archive (SHURA) at:

<http://shura.shu.ac.uk/19802/>

## A Sheffield Hallam University thesis

This thesis is protected by copyright which belongs to the author.

The content must not be changed in any way or sold commercially in any format or medium without the formal permission of the author.

When referring to this work, full bibliographic details including the author, title, awarding institution and date of the thesis must be given.

Please visit <http://shura.shu.ac.uk/19802/> and <http://shura.shu.ac.uk/information.html> for further details about copyright and re-use permissions.

SHEFFIELD CITY  
POLYTECHNIC LIBRARY  
POND STREET  
SHEFFIELD S1 1WB

6816

7924519017



**Sheffield City Polytechnic  
Eric Mensforth Library**

**REFERENCE ONLY**

This book must not be taken from the Library

PL/26

R5193

ProQuest Number: 10697104

All rights reserved

INFORMATION TO ALL USERS

The quality of this reproduction is dependent upon the quality of the copy submitted.

In the unlikely event that the author did not send a complete manuscript and there are missing pages, these will be noted. Also, if material had to be removed, a note will indicate the deletion.



ProQuest 10697104

Published by ProQuest LLC (2017). Copyright of the Dissertation is held by the Author.

All rights reserved.

This work is protected against unauthorized copying under Title 17, United States Code  
Microform Edition © ProQuest LLC.

ProQuest LLC.  
789 East Eisenhower Parkway  
P.O. Box 1346  
Ann Arbor, MI 48106 – 1346

THE TEAR BEHAVIOUR OF SOME  
TRI-BLOCK COPOLYMER ELASTOMERS

by

John Michael Hodgkinson, MSc

This Thesis Has Been Submitted in Partial Fulfilment  
of the Requirements for the Award of the  
Degree of Doctor of Philosophy  
of the Council for National Academic Awards

Sponsoring Establishment :-  
Sheffield City Polytechnic

Collaborating Establishment :-  
International Synthetic Rubber Company

June 1980





7924519 -01

# THE TEAR BEHAVIOUR OF SOME TRI-BLOCK COPOLYMER ELASTOMERS

by

John M. Hodgkinson

## ABSTRACT

Four SBS block copolymers were subjected to extensive chemical examination to determine block molecular weights and styrene fractions.

Casting from different solvent systems into sheet form resulted in a range of microstructural formations for the normally dispersed styrene phase. These morphological details were studied using transmission electron microscopy and low angle X-ray scattering.

Dynamic mechanical tests, on sheet material cast from different solvent systems, in both shear and tension over a wide temperature range, and static tensile tests at +20°C, revealed significant differences in viscoelastic properties between the materials. These differences were related to changes in morphological detail by the use of a model for composite materials. The large strain behaviour at +20°C is modelled by the inverse Langevin function and a debonding parameter which is related to void growth in the material.

The conventional analysis of tear behaviour, developed originally for vulcanised rubbers, whilst ranking SBS block copolymers alongside the most tear resistant vulcanised materials over wide ranges of temperature and tearing rate, was found to be suspect for this class of materials. An alternative interpretation, however, succeeds in relating tear strength to tensile properties for the temperatures and tear rates studied, and also relates the tearing behaviour of these elastomers to that of a wide variety of other materials.

Four S-B-S block copolymers were subjected to thorough chemical examination to determine block molecular weight and styrene content. Casting the copolymers from several solvent systems resulted in different microstructured details, which were revealed by transmission electron microscopy and small angle X-ray scattering to be either lamellar or cylindrical formations of styrene in a butadiene matrix. Isotropy in the plane of the cast sheets is conferred by the randomness of the orientation of areas maintaining internal orientation.

Dynamic mechanical tests in both shear and tension were conducted over a wide temperature range encompassing the transition points relating to the styrene and butadiene phases. The high modulus recorded at low temperature falls rapidly to a plateau level between the two transitions; as the styrene glass temperature is approached, the modulus again falls rapidly. The value of the plateau modulus is dependent upon the casting solvent system, solvents favouring the formation of a largely lamellar morphology recording higher moduli than solvents forming the cylindrical type of structure. The relationship between dynamic tensile and shear moduli was found to be described by  $E' = 1.5 G'$ . The loss tangent recorded at the transition points was also found to be a function of casting solvent, lamellae-forming solvents resulting in a low  $\tan \delta$  at the butadiene transition, and a high value at the styrene peak, the opposite being the case for cylinder-forming solvents.

Static tensile tests at +20°C showed that the initial modulus varied with the casting solvent system or microstructure, the lamellar material resulting in an enhanced modulus and yielding accompanied by necking; materials containing a cylindrical structure had a relatively low modulus with no necking. Between 2% and 600% strain, cold drawing occurred, followed by an increase in stress leading to final rupture. The tensile behaviour was found to be described by two analytical functions which, when combined with a debonding parameter, gives expression to an internal cavitation process which is dependent upon the microstructure of the material.

A theory for the composite modulus is described which incorporates a structure factor (Einstein coefficient,  $k$ ) so that the modulus of the product of a particular material/solvent system could be described in terms of the structure factor, the modulus of the individual phases and

the volume proportion of the dispersed phase. Using data from static tensile tests, the relevant structure factors for the materials were determined. The composite theory is further extended to include the prediction of dynamic tensile and shear moduli and loss tangent over a range of  $k$  values. Using the previously determined structure coefficients for each material, the experimentally determined dynamic moduli and  $\tan \delta$  were compared with the predicted values at  $-90^{\circ}\text{C}$  and  $+20^{\circ}\text{C}$ . Although agreement with experimental data was not absolute, the approach shows some promise.

The final set of experiments concerned the tearing behaviour of these materials over wide temperature and tearing rate ranges. The data were analysed according to the conventional method originally proposed by workers at the Natural Rubber Producer's Research Association. It was, however, noted that this analysis is based on a linear relationship between the tearing force and the material thickness, whereas the data here appear to support more nearly a square relationship. Using this premise, a relationship is presented between the tearing force and the product of the elastic modulus, energy to break in tension and material thickness squared. The experimental evidence supports this relationship over the complete temperature and rate ranges investigated, and S-B-S block copolymers are shown to fit a composite curve for a wide range of materials, including metals and other polymers.

# ACKNOWLEDGEMENTS

The author would like to express his thanks for assistance and advice from Director of Studies, Dr N.C. Hilyard, supervisors Dr G. Corfield and Dr D. Quayle of Sheffield City Polytechnic, and Dr I. Bowman of the International Synthetic Rubber Company for his contribution as industrial supervisor.

Parts of the chemical characterisation were carried out at the Universities of Sheffield, Manchester and Akron (USA), for which thanks are due to Dr R.N. Young, Dr C. Price and Dr L.J. Fetters, respectively. The Rubber and Plastics Research Association (RAPRA) also collaborated in respect of characterisation studies.

A special thank you goes to all members of the Sheffield City Polytechnic technical, secretarial and library staff who have helped in a variety of ways, but particularly to Mr R. Codd for his unstinting assistance with the electron microscopy.

The author is indebted to the Sheffield Local Education Authority for financing the project in the form of a Research Assistantship.

Finally, many thanks to Mrs E.A. Hall of the Polymer Engineering Group at Imperial College, London, for typing the manuscript.

	<u>Page</u>
Abstract	1
Summary	2
Acknowledgements	4
Contents	5
List of Figures	10
Nomenclature	18
 <u>CHAPTER 1: INTRODUCTION</u>	 23
 <u>CHAPTER 2: LITERATURE SURVEY</u>	 26
2.1 The Chemistry of Block Copolymers	26
2.1.1 Synthesis	26
2.1.2 Chemical characterisation	27
2.1.3 Polymeric impurities	29
2.1.4 Thermodynamics of microphase separation	30
2.1.5 Summary	33
2.2 The Microstructure of Block Copolymers	34
2.2.1 Introduction	34
2.2.2 Block copolymers under the electron microscope	34
2.2.3 Small angle X-ray scattering (SAXS)	37
2.2.4 Summary	39
2.3 Mechanical Properties	41
2.3.1 Introduction	41
2.3.2 Dynamic viscoelastic properties	41
2.3.3 Swelling	43
2.3.4 Tensile properties	45
2.3.4.1 Stress-strain characteristics	45
2.3.4.2 The effect of structural modification	46
2.3.4.3 Relaxation phenomena	47
2.3.4.4 Models of two-phase systems	47
2.4 Tearing of Rubbers	50
2.4.1 Introduction	50
2.4.2 Choice of test-piece shape and analysis	50
2.4.2.1 Trousers test-piece	51
2.4.2.2 Pure shear test-piece	53

2.4.3	Some problems with the trouser-leg specimen	54
2.4.4	Qualitative information obtained from tearing - two types of tearing	55
2.4.5	The effect of filler reinforcement on tear energy	57
2.4.6	The non-WLF viscosity dependence of SBR (Gum) tear energy	58
2.4.7	Tearing energy from the strain concentration at an incision	58
<u>CHAPTER 3:</u>	<u>POLYMER CHARACTERISATION</u>	67
3.1	Introduction	67
3.1.1	The triblock copolymer elastomers	67
3.1.2	Parameters investigated and experimental methods used	67
3.2	Number Average Molecular Weight by Osmotic Pressure	69
3.3	Gel Permeation Chromatography for Molecular Weight, Polydispersity and Polymeric Impurity	71
3.3.1	The GPC tests	73
3.3.2	Analysis of chromatograms	74
3.3.2.1	$\overline{M}_n$ , $\overline{M}_w$ and polydispersity	74
3.3.2.2	Proportions of triblock, diblock and homopolymer	74
3.3.3	Discussion	77
3.4	Copolymer Composition and Structure by $^1\text{H}$ NMR	80
3.4.1	The NMR phenomenon	80
3.4.2	Analysis of NMR spectra	80
3.4.3	The NMR spectra	81
3.4.4	Data derived from NMR spectra	83
3.4.5	Discussion	86
3.5	Network Parameters by Microswelling	87
3.5.1	The swelling experiment	87
3.5.2	Analysis of swelling data	88
3.5.3	Discussion	91
3.6	The Plasticiser	93
<u>CHAPTER 4:</u>	<u>MATERIAL MORPHOLOGY</u>	115
4.1	Introduction	115

	<u>Page</u>
4.2 Polymer Sheet Preparation	115
4.3 Preparation of Specimens for Electron Microscopy	116
4.4 The Electron Micrographs	117
4.4.1 Analysis of domain parameters	117
4.5 Small Angle X-Ray Scattering Measurements (SAXS)	123
4.5.1 Introduction	123
4.5.2 Experimental	124
4.5.3 Results of SAXS	124
4.6 Discussion	126
 <u>CHAPTER 5: SMALL STRAIN DYNAMIC PROPERTIES</u>	 137
5.1 Introduction	137
5.2 The Torsion Pendulum	137
5.2.1 Description of equipment and testing procedure	137
5.2.2 Analysis	139
5.2.3 Experimental results	141
5.3 The Rheovibron	144
5.3.1 Description of equipment and testing procedure	144
5.3.2 Experimental results for small strain dynamic tensile modulus and loss tangent	145
5.4 Discussion of Dynamic Mechanical Results	146
 <u>CHAPTER 6: LARGE STRAIN TENSILE BEHAVIOUR</u>	 170
6.1 Introduction	170
6.2 Analysis	173
6.2.1 The simple kinetic theory	173
6.2.2 The inverse Langevin function	173
6.2.3 Mathematical model for tensile response	174
6.3 Discussion	180
 <u>CHAPTER 7: THE ELASTIC MODULUS OF BLOCK COPOLYMERS</u>	 204
7.1 Introduction	204
7.2 The Nielsen Equations	207
7.3 The Initial Static Tensile Moduli: Results and Discussion	210
7.3.1 Series-parallel model	210
7.3.2 Use of the structure parameter	212



	<u>Page</u>
7.4 A Theoretical Analysis for the Dynamic Moduli	216
7.5 The Prediction of Dynamic Moduli: Results and Discussion	220
 <u>CHAPTER 8: THE TEARING BEHAVIOUR OF THERMOPLASTIC ELASTOMERS</u>	 233
8.1 The Classical Analysis and Related Experimentation	233
8.1.1 Introduction	233
8.1.2 The modified trousers tear specimen	234
8.1.3 Environmental chamber and temperature control equipment	235
8.1.4 The testing programme	235
8.1.5 Test procedure	236
8.1.6 Testing the tear criterion	237
8.1.7 Tearing energy/rate/temperature surfaces	237
8.1.8 Detailed analysis of tear data	238
8.1.9 The effect of temperature and rate	238
8.1.10 The effect of casting solvent	239
8.1.11 Comparing TR1101 and TR1102	241
8.1.12 A comparison of the tear behaviour of thermoplastic elastomers with other rubbery materials	242
8.1.13 Discussion	243
8.2 An Alternative Correlation	246
8.2.1 Introduction	246
8.2.2 Theoretical	246
8.2.3 Energy density at break, $W_p^*$	247
8.2.4 Elasticity modulus, $E$	248
8.2.5 The relationship between tearing force and thickness	248
8.2.6 The relationship between tearing force and tensile data	250
8.2.7 Discussion	250
 <u>CHAPTER 9: FINAL DISCUSSION AND CONCLUSIONS</u>	 295
 References	 299
 Appendix A Tearing energy/temperature/rate surfaces	 A1
Appendix B Tearing energy/rate curves for TR4122, 4113 and 1102	B1

Appendix C	Tearing energy/rate curves for TR1102	C1
Appendix D	Tearing energy/rate curves comparing TR1101 and 1102	D1
Appendix E	Tearing force as a function of the tensile parameter for TR1102, 4122 and 4113	E1

Chapter 2

Figure 2.1	: ABA copolymer chain molecule	60
Figure 2.2	: Effect of polystyrene content on idealised micro-structure for SBS block copolymers	61
Figure 2.3	: Schematic of stress cycling hysteresis	62
Figure 2.4	: Effect of styrene content on the stress-strain curve	63
Figure 2.5	: Trousers and plane strain tearing specimen	64
Figure 2.6	: Three-dimensional of tearing energy versus temperature and rate for NR and SBR	65
Figure 2.7	: Strain concentration at an incision	66

Chapter 3

Figure 3.1	: Membrane osmometry, $\pi/C$ versus $C$	94
Figure 3.2	: Gel material in a section of GPC column	95
Figure 3.3	: Calibration for GPC	96
Figure 3.4	: Calibration for GPC	97
Figure 3.5	: GPC chromatogram for TR4122	98
Figure 3.6	: GPC chromatogram for TR4122	99
Figure 3.7	: GPC chromatogram for TR4122	100
Figure 3.8	: GPC chromatogram for TR4122	101
Figure 3.9	: NMR spectrum at 60 MHz for TR1101	102
Figure 3.10	: NMR spectrum at 60 MHz for TR1102	103
Figure 3.11	: NMR spectrum at 60 MHz for TR4122	104
Figure 3.12	: NMR spectrum at 60 MHz for TR4113	105
Figure 3.13	: NMR spectrum at 60 MHz for TR4113 deplasticised	106
Figure 3.14	: NMR spectrum at 100 MHz for TR1101	107
Figure 3.15	: NMR spectrum at 300 MHz for TR1101	108
Figure 3.16	: NMR spectrum expanding the 1,4 aliphatic protons for TR1101	109
Figure 3.17	: NMR spectrum expanding the 1,4 olefinic protons for TR1101	110
Figure 3.18	: NMR spectrum spin-decoupled for TR1101	111
Figure 3.19	: The swelling experiment	112
Figure 3.20	: Swelling data for triblocks swelling as a function of time	113
Figure 3.21	: Linear plot of Kraus equation to evaluate $v_{r0}$	114

Chapter 4

Figure 4.1	: The sledge microtome	130
Figure 4.2	: Micrograph TR1101 BEN/HEP	131
Figure 4.3	: Micrograph TR1102 BEN/HEP	131
Figure 4.4	: Micrograph TR4122 BEN/HEP	131
Figure 4.5	: Micrograph TR4113 BEN/HEP	131
Figure 4.6	: Micrograph TR1101 CCl <sub>4</sub>	132
Figure 4.7	: Micrograph TR1102 CCl <sub>4</sub>	132
Figure 4.8	: Micrograph TR4122 CCl <sub>4</sub>	132
Figure 4.9	: Micrograph TR4113 CCl <sub>4</sub>	132
Figure 4.10	: Micrograph TR1101 THF/MEK	133
Figure 4.11	: Micrograph TR1101 THF/MEK	133
Figure 4.12	: Micrograph TR1102 THF/MEK	133
Figure 4.13	: Micrograph TR4122 THF/MEK	133
Figure 4.14	: Micrograph TR4113 THF/MEK	134
Figure 4.15	: Micrograph TR1101 Ethyl acetate	134
Figure 4.16	: Micrograph TR1102 Ethyl acetate	134
Figure 4.17	: The X-ray scattering pin-hole camera	135
Figure 4.18	: SAXS photograph for TR1101 THF/MEK and TR1102 CCl <sub>4</sub>	136

Chapter 5

Figure 5.1	: The torsion pendulum	152
Figure 5.2	: The torsion pendulum	153
Figure 5.3	: $G'$ as a function of temperature at 1 Hz for TR1101	154
Figure 5.4	: $G'$ as a function of temperature at 1 Hz for TR1102	155
Figure 5.5	: Tan $\delta$ at 1 Hz for TR1101	156
Figure 5.6	: Tan $\delta$ at 1 Hz for TR1102	157
Figure 5.7	: The Rheovibron	158
Figure 5.8	: Tan $\delta$ at 11 Hz for TR1101	159
Figure 5.9	: Tan $\delta$ at 11 Hz for TR1102	160
Figure 5.10	: Tan $\delta$ at 11 Hz for TR4122	161
Figure 5.11	: Tan $\delta$ at 11 Hz for TR4113	162
Figure 5.12	: $E'$ at 11 Hz for TR1101	163
Figure 5.13	: $E'$ at 11 Hz for TR1102	164
Figure 5.14	: $E'$ at 11 Hz for TR4122	165
Figure 5.15	: $E'$ at 11 Hz for TR4113	166
Figure 5.16	: Model showing connectivity for SBS	167

Figure 5.17	: The ratio $E'/G'$ as a function of temperature for TR1101	168
Figure 5.18	: The ratio $E'/G'$ as a function of temperature for TR1102	169
 <u>Chapter 6</u>		
Figure 6.1	: The dumbbell tensile specimen	182
Figure 6.2	: Tensile stress-strain curves for TR1101 and TR1102	183
Figure 6.3	: Tensile stress-strain curves for TR1101 and TR1102	184
Figure 6.4	: Tensile stress-strain curves for TR4122 and TR4113	185
Figure 6.5	: Tensile stress-strain curves for TR4122 and TR4113	186
Figure 6.6	: Stress as a function of strain (simple kinetic theory)	187
Figure 6.7	: Stress as a function of strain using Langevin	188
Figure 6.8	: Schematic of stress versus strain	189
Figure 6.9	: True stress as a function of strain for TR1102	190
Figure 6.10	: The debonding factor $B_d$ as a function of strain	191
Figure 6.11	: $\text{Log} (-\log B_d)$ as a function of strain for TR1101	192
Figure 6.12	: $\text{Log} (-\log B_d)$ as a function of strain for TR1102	193
Figure 6.13	: $\text{Log} (-\log B_d)$ as a function of strain for TR4122	194
Figure 6.14	: $\text{Log} (-\log B_d)$ as a function of strain for TR4113	195
Figure 6.15	: Initial modulus as a function of exponent $b_2$	196
Figure 6.16	: Rubbery modulus as a function of exponent $b_2$	197
Figure 6.17	: Initial modulus as a function of the strain intersection of the exponents $b_1$ and $b_2$	198
Figure 6.18	: Equilibrium swelling strain as a function of styrene content	199
Figure 6.19	: $M_c$ as a function of styrene content	200
Figure 6.20	: Maximum extension ratio $\lambda_m$ as a function of $M_c$	201
Figure 6.21	: Styrene content as a function of maximum extension ratio $\lambda_m$	202
Figure 6.22	: Equilibrium swelling strain as a function of predicted maximum tensile strain	203

Chapter 7

Figure 7.1	: The parallel/series model of Takayanagi	222
Figure 7.2	: Arrangement of ribbons in the Halpin-Tsai theory	223
Figure 7.3	: Arrangement of ribbons and their dimensions in the Halpin-Tsai theory	224
Figure 7.4	: Effect of composition on modulus after Nielsen	225
Figure 7.5	: The effect of packing fraction on predicted static tensile modulus	226
Figure 7.6	: The determination of k from predicted modulus	227
and 7.7	curves TR1101 and TR1102	228
Figure 7.8	: Comparison of predicted and experimental dynamic	229
and 7.9	data at $-90^{\circ}\text{C}$	230
Figure 7.10	: Comparison of predicted and experimental dynamic	231
and 7.11	data at $+20^{\circ}\text{C}$	232

Chapter 8

Figure 8.1	: Specimen cutting jig for trousers tear test piece	252
Figure 8.2	: The environmental chamber	253
Figure 8.3	: Instron and ancilliary equipment for tear testing	254
Figure 8.4	: Tear test piece dimensions	255
Figure 8.5	: Instron and tear test specimen	256
Figure 8.6	: Tearing force as a function of crosshead movement	257
Figure 8.7	: Tearing load as a function of specimen thickness for TR1101	258
Figure 8.8	: Three-dimensional tearing surface for TR1101 THF/MEK	259
Figure 8.9	: Three-dimensional tearing surface for TR1101 BEN/HEP	260
Figure 8.10	: Three-dimensional tearing surface for TR1101 $\text{CCl}_4$	261
Figure 8.11	: Tearing energy as a function of rate for TR1101 THF/MEK	262
Figure 8.12	: Tearing energy as a function of rate for TR1101 $\text{CCl}_4$	263
Figure 8.13	: Tearing energy as a function of rate for TR1101 BEN/HEP	264
Figure 8.14	: Tearing energy as a function of rate for TR1101 comparing solvent effects	265
Figure 8.15	: Tearing energy as a function of rate for TR1101 comparing solvent effects	266
Figure 8.16	: Tearing energy as a function of rate for TR1101 comparing solvent effects	267

Figure 8.17	:	Tearing energy as a function of rate for TR1101 comparing solvent effects	268
Figure 8.18	:	Tearing energy as a function of rate comparing TR1101 and TR1102 THF/MEK	269
Figure 8.19	:	Tearing energy as a function of rate comparing TR1101 and TR1102 THF/MEK	270
Figure 8.20	:	Tearing energy as a function of rate comparing TR1101 and TR1102 THF/MEK	271
Figure 8.21	:	Tearing energy as a function of rate comparing TR1101 and TR1102 THF/MEK	272
Figure 8.22	:	Tearing energy versus rate for several rubbery materials	273
Figure 8.23	:	Tearing energy versus rate for several rubbery materials	274
Figure 8.24	:	Tearing energy versus rate for several rubbery materials	275
Figure 8.25	:	Tearing strength as a function of dynamic modulus	276
Figure 8.26	:	Tearing strength as a function of dynamic modulus	277
Figure 8.27	:	Tearing strength as a function of dynamic modulus	278
Figure 8.28	:	Energy density $W_p^*$ as a function of temperature for TR1101	279
Figure 8.29	:	Tearing force as a function of material thickness at +20°C	280
Figure 8.30	:	Tearing force as a function of material thickness at -40°C	281
Figure 8.31	:	Tearing force as a function of material thickness at +40°C	282
Figure 8.32	:	Tearing force as a function of material thickness at -80°C	283
Figure 8.33	:	Tearing force as a function of material thickness at +20°C	284
Figure 8.34	:	Tearing force as a function of tensile properties for TR1101 at 0.1 cm/min	285
Figure 8.35	:	Tearing force as a function of tensile properties for TR1101 at 0.5 cm/min	286
Figure 8.36	:	Tearing force as a function of tensile properties for TR1101 at 10 cm/min	287
Figure 8.37	:	Tearing force as a function of tensile properties for TR1101 at 50 cm/min	288

Figure 8.38	: Histogram of measured force about predicted force	289
Figure 8.39	: Tearing force as a function of tensile properties for a number of materials	290
Figure 8.40	: Tearing force as a function of tensile properties for TR1101 at 0.1 cm/min	291
Figure 8.41	: Tearing force as a function of tensile properties for TR1101 at 0.5 cm/min	292
Figure 8.42	: Tearing force as a function of tensile properties for TR1101 at 10 cm/min	293
Figure 8.43	: Tearing force as a function of tensile properties for TR1101 at 50 cm/min	294

#### Appendix A

Figure A.1	: Tear energy surface for TR1102 THF/MEK	A2
Figure A.2	: Tear energy surface for TR1102 BEN/HEP	A3
Figure A.3	: Tear energy surface for TR1102 $\text{CCl}_4$	A4
Figure A.4	: Tear energy surface for TR4122 THF/MEK	A5
Figure A.5	: Tear energy surface for TR4122 BEN/HEP	A6
Figure A.6	: Tear energy surface for TR4122 $\text{CCl}_4$	A7
Figure A.7	: Tear energy surface for TR4113 THF/MEK	A8
Figure A.8	: Tear energy surface for TR4113 BEN/HEP	A9
Figure A.9	: Tear energy surface for TR4113 $\text{CCl}_4$	A10

#### Appendix B

Figure B.1	: Tearing energy as a function of rate for TR4122 THF/MEK	B2
Figure B.2	: Tearing energy as a function of rate for TR4122 $\text{CCl}_4$	B3
Figure B.3	: Tearing energy as a function of rate for TR4122 BEN/HEP	B4
Figure B.4	: Tearing energy as a function of rate for TR4113 THF/MEK	B5
Figure B.5	: Tearing energy as a function of rate for TR4113 $\text{CCl}_4$	B6
Figure B.6	: Tearing energy as a function of rate for TR4113 BEN/HEP	B7
Figure B.7	: Tearing energy as a function of rate for TR1102 THF/MEK	B8



Figure B.8	: Tearing energy as a function of rate for TR1102 $\text{CCl}_4$	B9
Figure B.9	: Tearing energy as a function of rate for TR1102 BEN/HEP	B10

Appendix C

Figure C.1	: Tearing energy as a function of rate for TR1102, all solvents	C2
Figure C.2	: Tearing energy as a function of rate for TR1102, all solvents	C3
Figure C.3	: Tearing energy as a function of rate for TR1102, all solvents	C4
Figure C.4	: Tearing energy as a function of rate for TR1102, all solvents	C5

Appendix D

Figure D.1	: Tearing energy as a function of rate comparing TR1101 and TR1102 $\text{CCl}_4$	D2
Figure D.2	: Tearing energy as a function of rate comparing TR1101 and TR1102 $\text{CCl}_4$	D3
Figure D.3	: Tearing energy as a function of rate comparing TR1101 and TR1102 $\text{CCl}_4$	D4
Figure D.4	: Tearing energy as a function of rate comparing TR1101 and TR1102 $\text{CCl}_4$	D5
Figure D.5	: Tearing energy as a function of rate comparing TR1101 and TR1102 BEN/HEP	D6
Figure D.6	: Tearing energy as a function of rate comparing TR1101 and TR1102 BEN/HEP	D7
Figure D.7	: Tearing energy as a function of rate comparing TR1101 and TR1102 BEN/HEP	D8
Figure D.8	: Tearing energy as a function of rate comparing TR1101 and TR1102 BEN/HEP	D9

Appendix E

Figure E.1	: Tearing force as a function of tensile properties for TR1102 at 0.1 cm/min	E2
Figure E.2	: Tearing force as a function of tensile properties for TR1102 at 0.5 cm/min	E3

Figure E.3	: Tearing force as a function of tensile properties for TR1102 at 10 cm/min	E4
Figure E.4	: Tearing force as a function of tensile properties for TR1102 at 50 cm/min	E5
Figure E.5	: Tearing force as a function of tensile properties for TR4122 at 0.1 cm/min	E6
Figure E.6	: Tearing force as a function of tensile properties for TR4122 at 0.5 cm/min	E7
Figure E.7	: Tearing force as a function of tensile properties for TR4122 at 10 cm/min	E8
Figure E.8	: Tearing force as a function of tensile properties for TR4122 at 50 cm/min	E9
Figure E.9	: Tearing force as a function of tensile properties for TR4113 at 0.1 cm/min	E10
Figure E.10	: Tearing force as a function of tensile properties for TR4113 at 0.5 cm/min	E11
Figure E.11	: Tearing force as a function of tensile properties for TR4113 at 10 cm/min	E12
Figure E.12	: Tearing force as a function of tensile properties for TR4113 at 50 cm/min	E13

# NOMENCLATURE

$A, A_i$	: constants dependent upon the geometry in composite systems
$A_a$	: area of aromatic protons on NMR curve
$A_o$	: unstrained area of specimen
AB	: diblock copolymer
ABA	: triblock copolymer
$a_r$	: width of reinforcement in composite system
$a_v$	: exponent in Mark-Houwink equation
$B^*, B, B_i, B', B'', B'_i, B''_i$	: constants dependent upon geometry and moduli of component phases in composite system
$B_b$	: area of other than aromatic protons on NMR curve
$B_d$	: debonding parameter
BEN	: benzene
$b$	: width of specimen
$b_r$	: thickness of reinforcement in composite system
$b_t, b_1, b_2$	: exponents describing the dimensionality of crack growth
$C$	: solution concentration
$CCl_4$	: carbon tetrachloride
$c$	: crack length
$c(t)$	: instantaneous crack length
$c_1$	: a constant
$D$	: instantaneous diameter of swollen specimen
$D_o$	: initial diameter of swelling specimen
$(D/D_o)_e$	: equilibrium swelling fraction
$D_i$	: microstructural dimension, e.g. sphere diameter
$d$	: thickness of specimen
$d_t$	: tear tip diameter
$d_{int}$	: interdomain distance
$E$	: tensile modulus
$E_o$	: initial tensile modulus
$E_I$	: tensile modulus of interfacial phase
$E_m$	: terminal modulus (from Kaelble)
$E_L$	: terminal modulus (from Langevin)
$E_1$	: tensile modulus of composite matrix
$E_2$	: tensile modulus of composite reinforcement
$E_{11}$	: tensile modulus in direction of reinforcement orientation
$E'$	: tensile storage modulus
$E''$	: tensile loss modulus

$E^*$	: tensile complex modulus
$E_s$	: energy stored elastically per unit volume at edge of cut at angular distance $\theta$ from the centre of a semi-circular hole
$E_b$	: energy stored to break per unit volume of material
$\Delta E$	: energy absorbed by nuclei in NMR
E/A	: ethyl acetate
$F$	: force on legs of tear specimen
$F(s)$	: cumulative survival function
$f$	: functionality of network crosslinks
$G$	: shear modulus
$G'_c, G'_x$	: dynamic shear modulus
$G^*$	: complex shear modulus of composite
$G_1^*$	: complex shear modulus of butadiene phase
$G_2^*$	: complex shear modulus of styrene phase
$G_U^*$	: complex upper bound shear modulus of composite
$G_L^*$	: complex lower bound shear modulus of composite
$G_1'$	: storage shear modulus of butadiene phase
$G_1''$	: loss shear modulus of butadiene phase
$G_2'$	: storage shear modulus of styrene phase
$G_2''$	: loss shear modulus of styrene phase
$G'$	: storage shear modulus of composite
$G''$	: loss shear modulus of composite
$G_U'$	: upper bound storage modulus of composite
$G_U''$	: upper bound loss modulus of composite
$G_L'$	: lower bound storage modulus of composite
$G_L''$	: lower bound loss modulus of composite
$G_c$	: fracture toughness
$\Delta G$	: Gibbs free energy difference
GPC	: gel permeation chromatography
$G_r$	: generalised flaw growth rate
$G_x, G_y, G_z$	: growth rate of crack in $x, y, z$ directions
$g$	: parameter dependent upon $b/d$ ratio
$\Delta H$	: enthalpy change of mixing
HEP	: heptane
$H_i$	: GPC curve to base line height
$H_o$	: magnetic field in NMR
$h$	: Planck's constant
$I$	: moment of inertia
$I_o$	: moment of inertia of torsion pendulum with no added masses

$I_1, I_2, I_3$	: strain invariants
$K$	: a constant in the Mark-Houwink equation
$K_1$	: a constant
$K_2$	: a constant
$k$	: Einstein coefficient
$L$	: specimen length
$L_y, L_z$	: fixed crack dimensions in $y$ and $z$ directions
$l$	: width of plastic zone at crack tip
$l_0$	: distance ahead of crack tip at which stress reduces to zero
$M$	: modulus of composite
$M_1$	: modulus of butadiene phase
$M_2$	: modulus of styrene phase
$M_1^*$	: complex modulus of butadiene phase
$M_2^*$	: complex modulus of styrene phase
$M_U$	: upper bound modulus of composite
$M_L$	: lower bound modulus of composite
$\overline{M}_n$	: number-average molecular weight
$\overline{M}_w$	: weight-average molecular weight
$\overline{M}_w/\overline{M}_n$	: dispersity ratio of molecular weight
$\overline{M}_v$	: viscosity-average molecular weight
$M_c$	: network molecular weight or molecular weight between entanglements in elastomer homopolymer
$M_i$	: calibrated molecular weight in GPC
MEK	: methyl ethyl ketone
$M_f$	: weight of styrene sample
$M_s/M$	: weight fraction of styrene in block copolymer
$m$	: mass of added weights on torsion bar
$m_l$	: constant with dimensions of length
NR	: natural rubber
NMR	: nuclear magnetic resonance
$n$	: number of links in statistical chain
$n_s$	: order of SAXS maxima
$OsO_4$	: osmium tetroxide
$P_x, P'$	: period of torsion pendulum
$P_s$	: period of torsion pendulum without a sample
$P$	: load
$R$	: tear propagation rate
$R_I$	: ideal gas constant
$r$	: radius
$\Delta S$	: entropy change of mixing

SBS	: triblock copolymer of styrene-butadiene-styrene
SIS	: triblock copolymer of styrene-isoprene-styrene
SBR	: styrene-butadiene rubber
SAXS	: small angle X-ray scattering
$T$	: temperature
$T_c$	: critical tearing energy
$T_B$	: temperature relating to $\tan \delta$ maximum for diene phase
$T_S$	: temperature relating to $\tan \delta$ maximum for styrene phase
$T_R$	: temperature at which a rapid decrease in modulus occurs
$T_g$	: glass transition temperature
THF	: tetra hydrofuran
TMS	: tetra methylsilane
$t$	: material thickness
$\tan \delta$	: loss factor in dynamic measurements
$\tan \delta_x, \tan \delta_c$	: loss tangent relating to torsion pendulum measurements
$\tan \delta_U$	: upper bound loss factor
$\tan \delta_L$	: lower bound loss factor
$V_v$	: total molar volume of block copolymer system
$V_A, V_B$	: molar volumes of homopolymers
$V_R$	: retention volume
$V_S/V$	: volume fraction of styrene in block copolymer
$\nu$	: rate of extension approaching the crack tip
$\nu_o$	: frequency of resonant radio-frequency field in NMR
$\nu_e$	: concentration of elastically effective chains
$\nu_r$	: molar fraction of rubber in swollen network
$\nu_s$	: molar volume of solvent
$\nu_{ro}$	: true volume fraction of rubber in swollen network
$\nu_d$	: defect volume
$\nu_d(t)$	: instantaneous defect volume
$W$	: elastically stored free energy of deformation
$W_o$	: energy stored elastically per unit volume of material
$W_p^*$	: area under stress-strain curve
WLF	: Williams-Landel-Ferry equation for time-temperature superposition
$w$	: width of sheet specimen
$X_2$	: weight fraction of polystyrene

#### Greek Symbols

$\alpha, \beta, \gamma$	: temperature dependent transitions
$\delta$	: solubility parameter

$\delta_A, \delta_B$	: solubility parameters of homopolymers A and B
$\chi$	: polymer-solvent interaction parameter
$\chi_{12}$	: polymer-polymer interaction parameter
$\lambda, \lambda_1, \lambda_2, \lambda_3$	: extension ratios
$\lambda_t$	: extension ratio at crack tip
$\lambda_m$	: theoretical maximum extension ratio
$\lambda_b$	: extension ratio at break
$\lambda_R$	: wavelength of radiation
$\pi$	: osmotic pressure
$[\eta]$	: intrinsic viscosity
$[\eta] M_v$	: hydrodynamic volume
$\mu$	: magnetic moment
$\rho_S$	: density of styrene
$\rho_B$	: density of butadiene
$\Delta$	: logarithmic decrement
$\theta$	: scattering angle
$\sigma$	: stress
$\epsilon$	: strain
$\psi$	: reduced concentration term dependent upon $\phi_m$
$\psi_i$	: as $\psi$ but for inverted composite system
$\nu$	: Poisson's ratio
$\phi_L, \phi_R, \phi_S$	: styrene volume fractions for lamellar, rod-like and spherical structures
$\phi_1$	: volume fraction of butadiene
$\phi_2$	: volume fraction of styrene
$\phi_m$	: volumetric packing fraction in normal system
$\phi'_m$	: volumetric packing fraction in inverted system
$\phi_U$	: fraction of styrene in continuous phase which is actually continuous
$\phi_L$	: fraction of butadiene in continuous phase which is actually continuous

## CHAPTER 1

### INTRODUCTION

In recent years, there has been considerable interest and research effort in the field of heterophase polymer systems possessing improved physical properties in the elastomeric state. With their enhanced properties, these systems comprise an integral and increasingly important section of the engineering materials presently available; and the technology offers the possibility of designing materials to perform given functions under specific conditions.

The search for novel elastomeric solids led to the eventual discovery of the class of materials known as thermolastic elastomers. At ambient temperatures, these materials exhibit properties similar to those of vulcanised rubber, but whereas the product of vulcanisation is a thermosetting rubber, thermolastic elastomers may be remoulded at elevated temperatures as thermoplastic materials. It is quite normal for these materials to have tensile strengths in excess of  $30 \times 10^6 \text{ Nm}^{-2}$  and fracture elongations of greater than 1000 per cent at temperatures of about 20°C.

This unusual combination of properties is a reflection of the chain structure of the block copolymer. A relatively simple block polymer may be defined as a macromolecule composed of alternating segments, or blocks, of two essentially pure homopolymers. If A and B represent the two component homopolymers, then possible configurations include AB, ABA, BAB, ABAB and so on.

The particular class of materials of interest here are those where the component blocks are polystyrene (S) and polybutadiene (B), the limit of use being the softening point of the polystyrene domains, above which they become thermoplastic and flow. In addition, the polybutadiene blocks are unsaturated and must be protected from oxidation. Polybutadiene degrades under oxidation by crosslinking to give a hard, insoluble resinous product, so that degraded SBS block copolymers become hard, more viscous, and eventually insoluble and infusible. Effective antioxidants for these materials are thiodipropionate and hindered phenols. SBS polymers are also subject to degradation by ozone, and various antiozonants have been investigated. The most effective being dibutylthiourea and nickel dibutyldithiocarbamate. Degradation by ultra violet radiation also causes problems, but benzotriazole derivatives are effective stabilisers. If opaque products are acceptable, the addition of either a reflective



material, such as titanium dioxide, or a light absorbing material, such as carbon black, gives improved stability.

The combination of elasticity with solubility and thermoplasticity makes SBS block copolymers useful in the formulation of contact and pressure-sensitive adhesives, joint sealants, strain relief interlaps and solution adhesives. The polymers themselves are tack-free, but may be tackified by the use of appropriate resins. SBS copolymer can also be compounded with other materials, such as inorganic fillers, petroleum oils, asphalts and reactive monomers to develop desirable properties. Absorption of naphthenic oil imparts improved tack to copolymer/resin blends used as pressure-sensitive adhesives, decreases melt viscosity in hot melt formulations, and plasticises the copolymer to reduce its cohesive strength for caulk and sealants. Dispersed in small proportions in hot asphalts, SBS copolymers give low temperature flexibility and resistance to flow at higher temperatures. At increased proportions, blends with asphalt are extremely tacky and make useful cements.

Elastomeric block copolymers may be fabricated in conventional plastics processing equipment, such as extruders, blow moulders, and injection moulders, and have been used to make a wide variety of moulded articles. Elastic bands may be prepared by tumble blending the crumb with antioxidant and anti-blocking agents, followed by tube extrusion and cutting. Various types of shoe soles and heels giving a wide range of hardness and stiffness, coupled with high surface friction, are manufactured, as is microcellular soling using SBS as the base polymer to give a higher stiffness at equivalent hardness than other elastomers. Numerous products such as baby bottle teats, toy tyres, bath mats and pencil erasers are injection moulded, and blow moulding is used in the manufacture of children's toys. The material is used in the form of rubber sheeting for the backing of self-laying carpet tiles, and for sound insulation in automobile interiors. Further outlets include pharmaceutical, medical and food packaging applications.

Although many studies of the mechanical behaviour of these materials have been reported in the literature, and some understanding obtained of the relationships between composition, microstructure and properties, little information is currently available concerning the tear strength and the mechanisms involved in the tearing process. Tear phenomena are of fundamental importance to the mechanical qualities of a material. Even with simple, homogeneous solids, fracture is a complex process, and material strength is governed by a number of factors, some of which are

interrelated. These include the energy required to create new surface, ductile processes, hysteresis and crack propagation mechanisms, all of which may themselves be dependent upon such factors as the environmental conditions and the rate of crack propagation.

The purpose of this work is to characterise as far as possible a number of SBS block copolymers in terms of composition, microstructure, molecular size, small and large strain quasi-static mechanical properties and small strain dynamic behaviour. The aim being to elucidate the mechanisms involved in the tear process, and to help explain the observed tear behaviour.

In the first part of this thesis, literature pertinent to the chemical, microstructural and molecular characterisation of thermoplastic triblock copolymers and their mechanical behaviour is reviewed. The application of these characterisation techniques to the polymers of the present study is then discussed. The techniques employed include nuclear magnetic resonance, gel permeation chromatography and membrane osmometry. Use of these systems allows the determination of overall molecular weight, individual block molecular weights, polymeric diblock and homopolymer impurity, styrene content, and the cis-trans structure of the diene centre-block. This type of analysis is desirable in any work involving the investigation of mechanical behaviour of polymers, but is essential when the morphology of the system depends upon such chemical properties, as may occur with these materials.

Since it is known that the technique used for sample preparation determines to a large extent the morphology, and hence the mechanical properties of the material, it is demonstrated how, by the use of different mixtures of casting solvents, these morphologies are achieved. Electron microscopy and small angle X-ray scattering are vehicles used for the determination of particular microstructural formations.

Later, static tensile, dynamic tensile and shear, and tearing properties are investigated over a wide temperature range, and, where possible, attention is drawn to links between these mechanical properties and the chemical and morphological characteristics of the block polymer systems.

CHAPTER 2  
LITERATURE SURVEY

2.1 THE CHEMISTRY OF BLOCK COPOLYMERS

2.1.1 Synthesis

It is only within the last 15 years that complete characterisation of block copolymers has been possible, primarily due to earlier difficulties in analysis and in the synthesis of pure blocks of uniform molecular weight. A number of books and review papers currently available [1-6] summarise the addition and condensation reactions used in the synthesis of early block copolymer materials of commercial importance. More recently, termination-free homogeneous anionic polymerisation has been developed as a useful technique for the synthesis of block copolymers. It is well documented that this method, which involves initiation by alkyllithium compounds (dubbed 'living' polymerisation), produced block polymers with well defined blocks of nearly uniform molecular weight [7-22].

The preparation of ABA type block polymers possessing precise and predictable structures can be achieved by four methods [23], each using soluble organo-alkali metal initiators:

- (a) a three-stage process using monofunctional initiators;
- (b) using difunctional initiators, for example sodium naphthalene, leading to a two-stage process (that is, polymerisation of monomer B followed by polymerisation of monomer A);
- (c) using monofunctional initiators, a two-stage process to synthesise AB diblock polymer with subsequent coupling to AB-BA polymer;
- (d) again using monofunctional initiators, a two-stage process involving the formation of an initial A block followed by the copolymerisation of A and B in which the latter is preferentially polymerised. Thus, a 'tapered' segment of monomers A and B is formed between the middle block and the final A block.

It is important when dienes are used to prepare the centre segment in a styrene-diene-styrene block polymer that the polymerisation be carried out in a hydrocarbon solvent (benzene, for example), since the polydiene microstructure is influenced by the presence of ether type solvents [23]. Studies [24] of the polyisoprene microstructure have demonstrated that certain solvents such as tetrahydrofuran (THF) alter the

microstructure from the high cis-1,4 structure obtained in hydrocarbon solvents to that of a chain containing significant amounts of the 1,2 and 3,4 forms of addition. A similar effect is seen for polybutadiene which has the high 1,4 content when prepared in hydrocarbon solvents [25], while ether solvents convert the structure to virtually all the 1,2 type [8].

The structure of an individual polymer chain may be represented in the manner of Figure 2.1. The particular example shown is that of the copolymerisation of butadiene and styrene, for which the most commercially successful systems have a relatively long butadiene segment between two shorter polystyrene segments. Polymers of this type exhibit elastomeric properties without vulcanisation.

### 2.1.2 Chemical Characterisation

Although the synthesis of block copolymers is a well-publicised field of research [10,18,21,22], it was not until comparatively recently that most researchers began to include appropriate characterisation data in their published work. It is clear that polymer characterisation is desirable in order to gain an appreciation of the efficiency of the synthesis procedure used, and to give an assessment of the purity of the material. An equally important point is that without full characterisation as an integral part of any research programme, the comparison of inter-laboratory data, whether it be chemical, physical or mechanical, is hindered.

Dependent upon the particular characterisation technique used, information may be gained about block length, overall molecular weights, polydispersity in molecular weight and composition, and estimates of the percentage and type of chains present [7,8,11,14].

Membrane osmometry gives information on the absolute overall molecular weight of a material and involves the use of various concentrations of the polymer in a suitable solvent. These solutions are introduced individually into the sample compartment of the osmometer. Solvent from the instrument side of the membrane diffuses through to the polymer sample, thus creating a pressure. When equilibrium is reached and solvent flow ceases, this osmotic pressure may be related to the number average molecular weight,  $\bar{M}_n$  [26-28].

Gel permeation chromatography (GPC) has been widely used [29-36] to estimate the number ( $\bar{M}_n$ ) and weight average ( $\bar{M}_w$ ) molecular weights of block polymers. GPC is a technique for separating molecules based on

differences in molecular size, and is therefore a potent characterisation tool for commercial block polymers, not only in the measurement of molecular weight, but also for determining the molecular composition in terms of triblock, diblock and homopolymer.

In the GPC separation, a solution of the polymer is passed through columns containing a separating medium or gel consisting of pores ranging in size from 6 nm to  $10^6$  nm average diameter. The gel is completely immersed in the solvent and when a polymer solution is passed through the column, polymer molecules enter those pores capable of accommodating them. Consequently, if the columns are packed with gel having a distribution of pore sizes, a separation of the polymer molecules can be effected. Very large molecules have only a small number of pores available to them, and pass through the columns fairly rapidly. Very small molecules enter most of the gel pores and therefore take longer to pass through. The concentration of the species in the solvent stream emerging from the columns is monitored continuously using a suitable detector.

Since the technique is a comparative one, polymers with a narrow molecular weight distribution are required for calibration purposes. The standards used are anionically prepared polystyrenes with polydispersity ( $\overline{M}_w/\overline{M}_n$ ) ratios of the order 1.06-1.15. Although such standards may be prepared by individual experimenters, the normal source of such materials is the Pressure Chemical Company, which markets a range of sharp molecular weight fractions.

High resolution nuclear magnetic resonance (NMR) spectroscopy [37-42] has become an important tool in the field of compositional and structural analysis of block copolymers. The technique makes use of the magnetic moment possessed by the  $H^+$  proton, and the predictable movement when a magnetic field is applied. It follows that certain types of proton usually appear in the same region of the NMR spectrum and may be identified. Another feature which may be observed is the interaction between protons through the bonds joining them, again allowing the identification of the protons giving rise to the excitation. The intensity of the resonance peak is proportional to the number of protons causing the peak, so that analysis of the relative intensities of observed peaks can give important information on the composition of the material. In addition to providing an accurate estimate of the weight content of styrene in an SBS copolymer, it is possible, with sufficiently high resolution spectrometers, to determine the microstructure of the central diene block in terms of its 1,4-cis, 1,4-trans, and 1,2 content.

### 2.1.3 Polymeric Impurities

Polymeric impurities are the result of either termination during polymerisation or incomplete coupling if this procedure is used. Although small quantities of block polymer may be manufactured under laboratory conditions in order to maintain a narrow distribution of molecular weight and to prevent premature termination or incomplete coupling, commercially it is not normally possible to control the process sufficiently rigidly to obtain a material which is 100% ABA.

Taking the simplest case where termination is rapid in comparison to propagation, any terminating impurities cause the formation of homopolystyrene or a styrene-diene diblock (SB) polymer. The effect of these polymeric species on the properties of SDS block polymers has been studied [43] by blending known quantities of the impurity with the pure triblock. It was found that the addition of homopolystyrene had virtually no effect on the tensile strength of the block polymer, although the stress for a given strain was increased; apparently, the homopolystyrene located itself in the block polystyrene domains, so that the net result was equivalent to having a polymer with a higher styrene content. The addition of free polydiene decreased the tensile strength and decreased the stress for a given strain, the polydiene serving as a diluent for the block polydiene chains in the network. When the homopolystyrene differed greatly in molecular weight ( $\bar{M}_w$ ) from the block polystyrene, significant incompatibility was achieved with consequent deterioration of the tensile properties of the material. Here, the term incompatibility refers to the fact that it may be physically impossible for the styrene of higher molecular weight to fit into the domains formed by the lower molecular weight end blocks. The conclusions to be drawn are that the presence of free styrene homopolymer is not harmful to the tensile properties of these block polymers, provided it is of a similar molecular weight to that of the styrene end block. However, the presence of only a few percent of diblock material has a marked effect on the tensile properties of the triblock copolymer. The diblock material apparently causes network defects by virtue of the fact that the styrene block is absorbed into the glassy domain while the diene block is unattached at one end. It becomes apparent that there are certain points during the polymerisation process where some termination may be tolerated, equally at other times termination will have a deleterious influence on the physical properties of the material.

#### 2.1.4 Thermodynamics of Microphase Separation

The mixing of two components has associated with it a free-energy of mixing given by the equation:

$$\Delta G = \Delta H - T \Delta S \quad (2.1)$$

where  $\Delta H$  and  $\Delta S$  are, respectively, the enthalpy and entropy changes of mixing, and  $T$  is the absolute temperature. If  $\Delta G$  is negative, a true molecular solution will form; if it is positive, however, the two components will segregate into separate phases. Although this thermodynamic analysis is in principle applicable only to reversible or equilibrium processes, and the mixing of two polymer molecules is not an equilibrium process due to restricted large-scale molecular mobility, the analysis is still qualitatively useful. The mixing of any two components is accompanied by an increase in the disorder of the system, and hence, by an increase in entropy (that is,  $\Delta S > 0$ ), with  $\Delta S$  being smaller for two polymer molecules than for the mixing of lower molecular weight materials of equivalent mass [44]. The entropy contribution to the free-energy change is then always favourable to the formation of a molecularly homogeneous system. It follows that the enthalpy,  $\Delta H$ , change can be negative, zero or a small positive number for  $\Delta G$  to remain negative. However, when two homopolymers are mixed,  $\Delta H$  may be expressed:

$$\Delta H_{mix} = V_v (\delta_A - \delta_B)^2 V_A V_B \quad (2.2)$$

where  $V_v$  is the total molar volume of the system, and  $\delta_A$  and  $\delta_B$  are solubility parameters for homopolymers A and B. From equation (2.2),  $\Delta H$  is necessarily positive, and the common result is that the enthalpy term dominates the free-energy expression (equation (2.1)), giving a positive free-energy change for mixing which predicts that it is unlikely that a single homogeneous phase will form when two polymer molecules are mixed.

Fedors [45], Meier [46] and Krause [47,48] have studied some of the aspects of compatibility by deriving criteria for domain formation in block copolymers, starting from thermodynamic principles. Fedors' work is based on the liquid lattice theory as developed by Flory & Huggins for the mixing of two polymer molecules. It is assumed that the chemical potentials of mixing are affected by chemical structure only through the

polymer-polymer interaction parameter,  $\chi_{12}$ , which can be predicted from the properties of the individual homopolymers. By arbitrarily defining that values of  $\chi_{12}$  greater than 10 indicate insolubility, Fedors [45] was able to predict minimum molecular weights required for immiscibility. In an SBS block polymer, he predicts the minimum molecular weights to be about 6000 for the butadiene segment, and 2500 each for the styrene segments. Hence, the lowest molecular weight for the SBS system which would guarantee insolubility would be 11,000. Krause [47] considered the entropy change associated with the decrease in total volume available to each polymer block when separation occurs, assuming that there is no volume change on mixing. Complete phase separation with sharp boundaries between phases was assumed so that the only contacts between the blocks were via the covalent bonds linking the A and B blocks. In a further work [48], Krause included a term to represent the decrease in entropy caused by the immobilisation at the interface of the A-B junctions in each copolymer molecule. Taking  $\Delta G$  to be zero, an expression was derived for the critical interaction parameter,  $(\chi_{12})_{critical}$ , which was used to make predictions about the types of block copolymer that exhibit phase separation. Some interesting conclusions arose from this treatment:

- (a)  $\Delta S$  increases as the number of blocks increases in a copolymer molecule of given length, so that phase separation becomes more difficult.
- (b) For constant copolymer composition and the same number of blocks per molecule, phase separation becomes easier as molecular weight increases.
- (c) For molecules having the same chain length and the same number of blocks, a copolymer with  $V_A = 0.25$  and  $V_B = 0.75$  undergoes phase separation less readily than a copolymer with  $V_A = V_B = 0.5$ .

Meier's [46] argument is similar to that of Krause with the size of the domains fixed by molecular chain dimensions. He predicts that the critical molecular weights for domain formation in the S-B block polymer system would be between 5000 and 10000 for the styrene segment when the polybutadiene block molecular weight is of the order of 50000. Meier cites some observations from Holden et al [49] which tend to verify the prediction. Although insufficient data were available to compute the size of the polystyrene domains, the molecular weight would put an upper limit on the spherical domain radius in that work at about 20 nm.



The arguments of Fedors and Meier have been applied only to spherical domains. However, the phases in block polymers may take shapes other than spheres; for example, layered and cylindrical structures have been observed [16,50,51]. If a similar argument as that used by Meier [46] to compute approximate spherical domain radii is applied to determine the thickness of lamellar domains, or the radius of cylindrical regions, and one assumes that the domains are essentially pure with little or no phase mixing; then for an ABA copolymer, the absolute maximum thickness of the layer A, or the maximum diameter of the cylinder, would be just twice the fully extended length of the A segment. Other assumptions are implicit in this argument, the density of the layers or cylinders is assumed to be uniform, and more importantly perhaps, the effects of shrinkage during solvent evaporation are ignored. Further work by Soen et al [52] on domain structure in block copolymers cast from solution points out that isotropic shrinkage is a reasonable assumption for spherical domain structures, but the same assumption would be unreasonable for rod-like or lamellar formations. They conclude that on solvent evaporation, spherical micelles shrink isotropically to form spherical domains of a diameter proportional to the  $2/3$  power of the molecular weight of the corresponding block segment. Rod-like and lamellar micelles, on the other hand, shrink anisotropically to form rod-like and lamellar domains such that the diameter and thickness of the respective structures are roughly proportional to the  $1/2$  power of the molecular weight of the corresponding block segment.

The incompatibility of two components manifests itself in the aggregation of like segments into separate phases. In a study of rubber blends, Corish [53] presents a practical, if not very sophisticated, definition of compatibility which may be applied to block polymers. Incompatibility being indicated by the presence of two or more transition temperatures,  $T_g$ , approximately equal to the  $T_g$ 's of the component polymers. Compatibility of the components being indicated by a single  $T_g$  intermediate between the values which represent the components. Using this definition, any method which defines glass transition regions could discern whether a block copolymer was phase-separated or not. Differential thermal analysis (DTA), dynamic mechanical experiments, dilatometry and other experiments would all be adequate. However, this definition is not conclusive evidence for the existence of a two-phase system, since some copolymers exhibit several transition regions; for example, the multiple transition regions noted by Clough & Schneider [54] in block polyester-urethanes.

Also, some single-phase systems exhibit multiple transition regions; for example, the  $\alpha$ ,  $\beta$  and  $\gamma$  transitions in polystyrene [55,231]

#### 2.1.5 Summary

The materials under consideration are a combination of polystyrene (S) and a polydiene (B), the polydiene being the inner segment ( $\bar{M}_w$  of the order of  $5 \times 10^4$ ), while the outer segments of styrene have  $\bar{M}_w$  of around  $1 \times 10^4$ . When this type of polymer is moulded at a higher temperature than the glass transition ( $T_g$ ) for polystyrene (a practical lower limit for moulding is  $150^\circ\text{C}$  [56]), the styrene end blocks soften, diffusing to join other end segments and, being incompatible with the polydiene, form discrete aggregates when cooled. Similarly, a three-dimensional lattice structure is formed when the polymer is cast from a solvent. Phase separation occurs since the entropy to be gained by mixing is very small. This is due to the small number of molecules per unit mass involved, simply as a result of their high molecular weight. Therefore, a normally insignificant positive free-energy of interaction is sufficient to overwhelm this small entropy of mixing. It follows that two polymers do not have to be very dissimilar before they are incompatible leading to a two-phase mixture. Taking the example of SBS polymers, a low styrene content will yield styrene as the discrete phase, uniformly distributed in the continuous butadiene phase. However, at intermediate proportions of styrene, either styrene or butadiene may be the discrete phase, and at high proportions of styrene it may be continuous. A good balance of thermoplastic and elastomeric properties is obtained when the styrene phase is discrete and the butadiene phase is continuous. This is normally obtained at between 15% and 40% by weight of styrene [57].

By the use of a combination of testing techniques, the block copolymer may be chemically characterised to determine overall molecular weight, polydispersity, the molecular weight of individual blocks, the magnitude of any polymeric impurities, the composition and chemical structure of the polymer. Used in concert with one another, the techniques available may yield information pertaining not only to the polymer itself, but also to its method of preparation.

Of the three possible polymeric impurities, homopolymer S, homopolymer B, and diblock SB, it is apparent that the triblock polymer can tolerate only homopolymer S without suffering decreased tensile properties, and then only when the polymer is similar in  $\bar{M}_n$  to the end block.

## 2.2 THE MICROSTRUCTURE OF BLOCK COPOLYMERS

### 2.2.1 Introduction

An interesting feature of many block polymers is that they exhibit optical clarity, even though a heterophase structure exists. Normally, light is scattered at the interface between two coexistent phases; one would therefore expect block copolymers to be opaque. However, most block copolymer systems have been reported as either transparent or translucent. There are in this case two possible mechanisms for optical clarity; either the refractive indices of the phases are equal, or a dispersed phase may exist in domains which are small compared with the wavelength of visible light, and the amount of visible radiation scattered in this case would be small, resulting in a nearly transparent material. Although the first possibility cannot be discounted, the phases of many block copolymers are not similar enough chemically to allow equality of their refractive indices. So that, in the general case, block polymers rely for their optical clarity on the existence of a dispersed phase which scatters little visible radiation.

A number of experimental techniques have been developed to facilitate the study of the morphological detail of block copolymers, not least amongst these being electron microscopy, and low angle X-ray scattering; other techniques used to a lesser extent are phase microscopy, birefringence and light scattering. For the purposes of this presentation, it is intended to report on work done using electron microscopy and low angle X-ray scattering.

### 2.2.2 Block Copolymers under the Electron Microscope

Transmission electron microscopy has been applied primarily to block copolymers containing one unsaturated component, allowing staining with osmium tetroxide by addition to the double bond. Kato [58-61] demonstrated this technique in the study of flow patterns in moulded ABS thermoplastics. Principally, results have been reported for copolymers containing either polybutadiene or polyisoprene, both of which react with osmium tetroxide. Other techniques, such as shadowing with carbon, gold or platinum, have been developed for the sub-microscopic study of materials which cannot be treated with osmium tetroxide ( $\text{OsO}_4$ ).

Beecher et al [62] made one of the most significant early contributions to the understanding of block copolymer structure in both the unstrained and strained conditions. Electron micrographs of SBS and SIS led to the conclusion that in both systems, the polystyrene blocks may

tend to aggregate into spherical domains of diameter about 120 Å. The domains were found to be present in solution cast films from different solvents and also in compression moulded samples, with the domain size being dependent upon the method of sample preparation. The spheres were thought to be interconnected by thin paths of polystyrene, and regions of up to 1000 Å square were found to exhibit local order which approximated to a simple cubic lattice. When samples were strained, the spheres first deformed into ellipsoids, but at high strains the ellipsoids began to break apart.

In a similar study, Morton et al [14] observed that an SIS polymer exhibited a highly dispersed polystyrene phase in the continuous polyisoprene matrix. The size of the dispersed phase in this case was found to be around 400 Å.

An interesting phenomenon is that block polymers of polystyrene and butadiene or isoprene may form different two-phase structures dependent upon such variables as the molecular weight, or the molecular weight distribution in the molecule. Bradford & Vanzo [16,19], studying A-B type block polymers of styrene and butadiene using electron and phase microscopy, found that their copolymers formed alternate molecular layers of polystyrene and butadiene in a lamination effect. Good agreement was found between the layer spacings measured from micrographs and the chain lengths calculated on the basis of the molecular weights of the two phases as determined from independent light scattering experiments. The thickness of the laminations varied between 25 - 50 nm, dependent upon the molecular weight of the sample. It was found also that the structure was dependent upon the method of sample preparation; lamellae being observed in samples cast from concentrated solutions, and a proportion of spherical domains resulting from a dilute 1% solution.

Similarly, Inoue et al [50,63,64], in a study of SI block polymers, observed alternate lamellae of styrene and isoprene. As the percentage of polystyrene in the material was increased above 60%, the isoprene phase appeared as discrete spheres.

Matsuo et al [65] report electron microscopic observations of both SB and SBS copolymers with the terminal block being either styrene or butadiene (SBS or BSB). For the SBS polymer, almost spherical butadiene islands, of the order of 20 - 50 nm diameter, in a styrene matrix were reported. The dimensions of the domains decreasing with decreasing butadiene sequence length. On the other hand, the polymers of SB or BSB showed that the butadiene chains linked together to form irregular rod-like

structures. Again, Matsuo [51,66] noted that in the SBS block polymers, as the block fraction of butadiene was increased, the domain structure passed from spherical to rod-like to layered. It was shown that the microstructure was also dependent upon the solvent used to cast the material, with the change in structure resulting in marked differences in physical properties.

Other workers who were early in the field demonstrated that materials other than SBS and SIS had a regular sub-microscopic structure. Molau & Wittbrodt [67,68] studied phase separation and compatibility in blends of compositionally different styrene-acrylonitrile copolymers, and in mixtures of block polymers with their component homopolymers. Blokland & Prins [69], using light scattering and birefringence to support electron microscopy, claimed the existence of rod-like structures of approximate length between 300 nm and 800 nm in cross-linked polyurethane elastomers.

More recent work has tended towards the investigation of new materials or materials of high purity (that is, containing very little low molecular weight species), and also the examination of materials prepared in different ways.

Lewis & Price [70,71] studied the microphase separation of SBS copolymers and also a graft copolymer formed by the grafting of polyisoprene chains onto the polystyrene backbone. The domain structure was found to be a function of the rate of evaporation of the solvent from cast films.

Bi & Fetters [72] were concerned with the microstructure of star block polymers of styrene and isoprene. They demonstrated the coexistence of three styrene domain arrangements, square (100 plane), rectangular (110 plane), and hexagonal (111 plane). These features were rationalised and explained by reference to the body centred cubic lattice. By the rotation of this lattice structure around a prescribed crystallographic axis, it is possible to observe all three morphologies. They discount the possibility of cylindrical domains, suggesting that their observation is caused by the illusion presented when spheres overlap.

Pedemonte & Alfonso [73], working with an SBS copolymer cast from various mixtures of the solvents tetrahydrofuran (THF) and methyl ethyl ketone (MEK), found only what they claim to be a lamellar structure, in contrast to what other workers say should be a cubic array of styrene spheres in the butadiene matrix. However, Pedemonte supports his microstructural evidence with tensile stress-strain curves which indicate the

presence of a continuous polystyrene phase.

An interesting technique has been employed by a number of researchers, including Douy [32] and Mayer [33], when studying the solution structure of ABA polymers of differing composition. Electron microscopy was facilitated by the use of a polymerisable solvent in order that the solution could be transformed into a solid for microtoming and structural determination.

Two groups of workers have concerned themselves with the effects of orientation on the microstructure of block copolymers. Keller et al [74-77] investigated SBS polymers using extrusion techniques to obtain a high degree of orientation. Similarly, Pedemonte et al [78] studied an SIS polymer in both the 'as-received' condition and after extrusion processing. The polymer had a relatively low styrene content (10%), and the structure noted was of polystyrene spheres in the isoprene matrix. Annealing of the extruded sample at 150°C for several days resulted in a sharp increase in phase separation and in the long range order of the microstructure. Later [79,80], Pedemonte and coworkers investigated the microstructure of an SBS copolymer after extrusion processing.

### 2.2.3 Small Angle X-Ray Scattering (SAXS)

Electron microscopical examination of polymers suffers from the disadvantage that only replicated or microtomed thin films may be studied; neither of these techniques necessarily shows the true material structure in the bulk. SAXS has the primary advantage that it permits direct measurement on bulk specimen. For block polymers, the results obtained also give information about the size of domains and the average distance between them.

The earliest work concerning SAXS of ABA block polymers was conducted by Hendus & coworkers [81]. It was reported that diffraction patterns of an SBS polymer showed a discrete diffraction ring corresponding to a domain spacing of the same order as observed by electron microscopy. Other investigators [82,83] also reported that the Bragg spacing of laboratory manufactured and commercial SBS polymers agreed with the inter-domain distances obtained from electron microscopic studies.

As techniques improved, it became possible to assign lattice parameters to the domain structures by the use of SAXS results. Brown, Fulcher & Wetton [84] claimed agreement on the basis of a simple cubic

lattice of spherical domains for a commercial 30 wt% styrene SBS polymer cast from a variety of solvents. On the other hand, McIntyre & Campos-Lopez [85], using a laboratory prepared SBS polymer of 38.5 wt% styrene, cast from 90/10 THF/MEK, and of a similar molecular weight to the polymer studied by Brown et al [84], assigned the face-centred orthorhombic lattice. Later, Campos-Lopez, McIntyre & Fetters [35], in a more ambitious study of laboratory prepared samples of SBS triblocks, held the styrene content at 27 wt% and varied the number average molecular weight ( $\bar{M}_n$ ). The diblock and homopolymer impurity was claimed to be low and the polydispersity factor,  $\bar{M}_w/\bar{M}_n \approx 1.1$ . Casting from 90/10 THF/MEK solution, the domain arrangement was found to be a face-centre cubic array. From the cell dimensions and sphere size, the end-to-end distance of molecular chains, the extent of the interfacial region and molecular weight dependence of the domain size and spacing was deduced, with good agreement with the theory of Meier.

Kim [86] compression moulded specimen of the same commercial SBS material used by Brown et al [84], and he concludes that there is a sharp interface between the styrene domains and the butadiene phase, and that the domains are spherical with a radius of 13.2 nm. Brown had previously deduced that his solvent-cast samples had domains of maximum radius 12 nm.

A study of SI and SIS polymers and mixtures of the two together with the homopolymers was carried out by Inoue et al [87], all samples were found to be consistent with the spherical styrene in isoprene matrix pattern. Experiments were conducted in order to monitor the tensile deformation behaviour using the SAXS technique. When loaded, the domain spacing was found to increase in the direction of loading, although not as a monotonic function of the macroscopic strain. Later, in a similar study, Montiel, Kuo & McIntyre [88] confirmed the structure of their SBS sample cast from 90/10 THF/MEK to be one of spherical domains in a butadiene matrix; they went on to show that at relatively small strains ( $\lambda < 1.3$ ) compared with the study of Inoue et al [87] ( $\lambda < 2.2$ ), the X-ray patterns changed with increasing strain, and again the interdomain strain was not directly proportional to the strain in the bulk material.

On the basis of SAXS measurements, other workers have assigned the hexagonal array of cylindrical domains to their preparations. For instance, Keller et al [74], with their extruded plugs of SBS, found that the diffraction pattern after annealing revealed single 'crystals' with hexagonal symmetry along the extrusion direction. Lewis & Price [70],

using two samples of SBS of differing block lengths, prepared solvent cast and compression moulded specimen. The compression moulded samples were found to give X-ray reflections indicative of hexagonally packed domains. The solvent cast patterns, however, although in a regular array, were indefinite and no conclusions were drawn as to the nature of the packing arrangement. Pillai, Livingston & Strang [89] concur that the commercial SBS material subject to their attention formed rod-like domains of polystyrene when cast from a variety of solvents, in agreement with Meier's theory for preferential solvents to produce these structures in the transition region between low and high styrene content polymers.

The final type of structure to be found in these polymers is the lamellar form. Relatively few examples of workers using such a material are available. However, Dlugosz, Folkes & Keller [76] studied a high styrene content SBS with their usual extrusion technique and found a long range ordering of lamellae. When the specimens were annealed, the extent of the ordering and its perfection were found to increase. Hashimoto et al [90] also discovered a lamellar structure in SI copolymers cast from toluene; the SAXS study indicated that the lamellae were oriented almost parallel to the surface of the cast sheets.

Sadron, Douy & Gallot [32,34,91] studied laboratory prepared SB, BSB and SBS polymers using SAXS techniques. Their work was conducted in order to discover the morphology of the copolymers whilst in solution. Structural parameters were investigated as a function of solution concentration, type of solvent, molecular weight variations of each block type, proportion of styrene, and temperature. A similar study of copolymers in solution and also in the solid form is attributed to Mayer [33], who investigated SI and SIS polymers, looking at variations in structure related to solvent concentration, copolymer composition and heat treatment.

#### 2.2.4 Summary

The morphology of linear polystyrene-polydiene block copolymers has received intensive scrutiny in recent years, mainly by means of electron microscopy and small angle X-ray scattering (SAXS). Electron micrographs of these block copolymers show that there is a pronounced tendency for polystyrene (when the minority component) to form ordered domains in the polydiene matrix. SAXS has also clearly shown the lattice-like arrangements of the polystyrene domains.



The most commonly examined materials have been linear diblock and triblock copolymers in which the polystyrene content has ranged between 10 wt% and 40 wt%. Commercially available copolymers with relatively high polydispersity ratios ( $\bar{M}_w/\bar{M}_n$ ) and significant diblock and homopolymer content have been studied in addition to laboratory prepared samples with reduced polydispersity and little low molecular weight impurity.

Contrasting interpretations have been made as to the structure of the phase-separated polystyrene domains, with spherical, cylindrical and lamellar structures having been reported to exist. More controversy has occurred over attempts to assign structural lattice formations to the domain arrangements.

It is now accepted that varying the ratio of the block lengths determines firstly which is the dispersed and which is the matrix phase; as to be expected, the component which is present in the larger proportion (in terms of block ratio) is always the matrix phase. For the most disparate compositions, the dispersed phase is in the form of spheres as shown in Figure 2.2; for more closely similar but still unequal proportions, it is in the form of cylinders. In both cases, the matrix becomes the dispersed phase as the ratios are reversed. In the case of comparable compositions, the structure is lamellar when there is no distinction between matrix and dispersed phases. This general rule may be complicated by processing variables such as the casting solvent, which may inhibit or promote the formation of one structure or another. Variation of the molecular weight of the copolymer molecule determines the scale of the microphase structure; that is, molecular weight variations affect the dimensions of the domains and their separation.

## 2.3 MECHANICAL PROPERTIES

### 2.3.1 Introduction

The vast potential of block copolymers arises largely from their improved mechanical properties relative to the component homopolymers or to the random copolymer of equivalent composition. It has been proposed that these enhanced properties are due to the hard domains acting as virtual or pseudo-crosslinks for the rubbery segments, similar in effect to an inert filler. Another explanation proposed by Holden et al [49] is that the glassy domains do not themselves lead directly to the enhancement, but act rather as "tie-down" points which prevent disentanglement of the rubbery matrix. Regardless of the actual mechanism of reinforcement, these unfilled, uncrosslinked heterophase elastomers exhibit higher modulus, tensile strength and resilience at small strains than the unfilled rubbery homopolymers.

Since the hard domains in block copolymers apparently give rise to mechanical reinforcement, the distribution of these segments along the copolymer chain should be of considerable importance. If they act as a tie-down point, or quasi-crosslink, a requirement for enhanced strength should be that at least one rubbery block per molecule be surrounded by two glassy blocks [92]. If A represents the hard segment and B the soft segment, then properties of molecules of the type ABA, ABAB and ABABA should show improvement over the component homopolymers, whereas the properties of AB and BAB types should not. This requirement is supported by Morton et al [14], Holden et al [49] and Matsuo et al [65], all working with copolymers of polystyrene and either polybutadiene or polyisoprene. Furthermore, it has been shown that increasing the number of blocks in a molecule above three (e.g. from ABA to ABABA) is not accompanied by appreciable property improvement [14].

### 2.3.2 Dynamic Viscoelastic Properties

The dynamic mechanical properties of block copolymers have been the subject of a number of investigations utilising different types of apparatus in order to vary the mode of stress application. There are primarily three types of dynamic apparatus in general use: the vibrating reed, torsion pendulum and rheovibron viscoelastometer.

Using a torsion pendulum, Kraus et al [93] studied the effect of monomer sequence on dynamic properties. The materials used varied from random copolymers of uniform composition along the polymer chain to ideal block polymers of a specific block sequence. Uniform composition

random copolymers were found to exhibit a single glass transition temperature with a corresponding, very narrow, dynamic loss peak. On the other hand, block copolymers displayed two transitions, one at the  $T_g$  for each type of block. The position and width of the dynamic loss peaks were related to block length and compositional purity of the constituent blocks.

Matsuo et al [65] also investigated the effect of sequence arrangement in a series of SBS block copolymers. Using a Vibron viscoelastometer, they studied the temperature dependence of the dynamic modulus  $E'$  and dynamic loss  $E''$ . Each polymer showed peaks at around  $-80^\circ\text{C}$  and  $+110^\circ\text{C}$ , with the heights of  $E''$  maxima varying with butadiene sequence length.

Performing their experiments on SBS Kraton 101 and also several SIS polymers, Beecher et al [62,94] used a vibrating reed apparatus to study the damping curves. For the SBS polymer, major peaks were discovered at  $-80^\circ\text{C}$  and  $+90^\circ\text{C}$  with a broad intermediate peak near  $+35^\circ\text{C}$  in the case of a sample cast from  $\text{CCl}_4$ . Smaller intermediate peaks were noted for materials cast from 90/10 benzene/heptane (BEN/HEP) and 90/10 tetrahydrofuran/methyl ethyl ketone (THF/MEK). A similar pattern of behaviour was noted when attention was drawn to SIS polymers, with major transitions at  $-50^\circ\text{C}$  and  $+100^\circ\text{C}$ , and intermediate peaks at  $+40^\circ\text{C}$ . Beecher suggests that the intermediate damping peak is due to the degree of mixing between the styrene and the butadiene or isoprene, the greater the degree of mixing the more significant the peak, as in the  $\text{CCl}_4$  cast samples. THF/MEK cast materials showed the largest and best-defined styrene transition and only a small intermediate peak, indicating a lower degree of phase-mixing. Obviously, this phase-mixing is indicative of an interfacial region.

Robinson & White [95] with a Nonius torsion pendulum utilising free torsional oscillations, found damping peaks at  $+10^\circ\text{C}$  and  $+100^\circ\text{C}$  for the SIS triblock copolymers used in their study. The peak at  $+10^\circ\text{C}$  they suggest indicates the onset of rotation of the polyisoprene segments ( $T_g$ ); the transition is shifted in their case to a relatively high temperature owing to a high concentration of 3,4 and 1,2 structure due to sodium initiation in a polar solvent.

Miyamoto et al [96] cast SBS film samples from toluene,  $\text{CCl}_4$ , ethyl acetate and methyl ethyl ketone (MEK). They observed two major peaks on the loss curve at about  $-70^\circ\text{C}$  and  $+100^\circ\text{C}$  which they attributed to glass transitions and the onset of segmental motion. The butadiene peak heights

were found to vary with the degree of solubility in the particular solvent used; however, the styrene peaks varied in the converse order. Additionally, a third peak was observed at +10°C for specimens cast from ethyl acetate and methyl ethyl ketone. A transition corresponding to this peak was also noticed in thermal analysis data. They propose that the aggregation of polystyrene blocks is relatively incomplete in specimens cast from poor polystyrene solvents.

In a follow-up study to that of Miyamoto et al [96], using similar polymers and the same solvents, Kraus et al [97] looked at the dynamic properties in both tensile and shear deformation modes. Between the glass transition regions of the styrene and butadiene, the ratio of storage moduli  $E'/G'$  in tension and shear for the same polymer varied from 3 to more than 30, depending upon the sample preparation and hence the structural anisotropy of the system. For films cast from good solvents, the ratio was near to 3, the larger  $E'/G'$  ratios resulting from deposition from poor polybutadiene solvent systems or from compression moulding. Above the polystyrene glass transition,  $E'/G'$  approached 3 for all samples. The effect observed is ascribed to various degrees of polystyrene domain connectivity. In addition, it was noted that the loss tangent in tension is an effective discriminator for variations in styrene connectivity; whereas, in the shear mode, the loss tangent was only moderately affected by differences in morphology.

Two studies by Cohen & Tschoegl [98,99] are of some interest. They studied blends of SB diblock and SBS triblock networks with controlled amounts of terminal chains of known molecular weight. Mechanical properties of these materials were measured dynamically in free oscillation over a temperature range -150°C to +100°C. The terminal chains were found to act as internal plasticiser, lowering the storage modulus in the transition region. If the molecular weight was sufficiently large, a second broad maximum appeared in the loss modulus curve. However, the appearance of the polybutadiene transition region was unaffected by the amount of terminal chains. The second paper [99] deals with a mathematical model which describes the phenomenon of entanglement slippage in the elastomeric triblock-diblock copolymer blends. The predictions of the model compared well with the previously described measurements of the dynamic properties.

### 2.3.3 Swelling

Owing to the highly disordered state of long chain amorphous

polymers, the presence of entanglements between neighbouring chains is inevitable. The extension of unvulcanised elastomers causes entanglement slippage, resulting in stress relaxation and/or flow. If, however, both ends of each elastomer molecule are held firmly in place, as in the domains of block copolymers, this gradual disentanglement is not longer possible. The entanglements will then serve as effective cross-links. In which case, the network molecular weight,  $M_c$ , for SIS and SBS block polymers might be expected to be of the order of the molecular weight between entanglements in the elastomer homopolymer, rather than the molecular weight of the elastomer segments in the block copolymers. It follows that the elastic moduli of these block polymers at constant styrene content should be substantially unaffected by the molecular weights of the elastomer segments.

The molecular weight between effective cross-links may be calculated from the saturation absorption of a swelling agent by an elastomer network, using a form of the equation developed by Flory & Rehner [100] for conventional vulcanisation (see section 3.5.2, equation (3.5)).

The theory assumes the network contains no imperfections or free chain ends and that the cross-link functionality is 4. Application of this approach has also been made to vulcanisates containing fillers [101].

The treatment may be applied to SBS and SIS [49,102] block copolymers if a swelling agent is used which swells the elastomer phase but does not affect the polystyrene domains, and if the polymer-solvent interaction parameter is known.

Meier [103] argues that the Flory-Rehner treatment of swelling in block polymers (using Gaussian statistics) is not satisfactory. He points out that existing theories [101,104] relating the deformational properties of filled elastomers to network statistics contain a fundamental flaw. That is, the effect of the filler or inclusions is assumed to arise from a perturbation of the local strain field rather than from the change in the network statistics caused by the inclusions. The assumption is incorrect since network statistics are affected by inclusions; certain regions in space are excluded to the network chains so that space is not isotropic and the mere presence of an inclusion near a chain will bias the distribution function of the chain. It is suggested that a proper account of the effect of fillers on the deformation of a network would be based on the evaluation of the probability of finding the network in the deformed or undeformed state. Such an approach is impractical for the general

case of filled elastomers. However, the treatment is possible for ABA block copolymers, since in this case the filler system (A domains) has a high degree of regularity, and the origin of the B chains can be taken as the surface of the domains.

#### 2.3.4 Tensile Properties

##### 2.3.4.1 Stress-strain characteristics

Generally, the tensile strength of the block polymer is superior to that of conventional vulcanizates and similar to that of a vulcanizate containing filler or possessing the ability to crystallise on elongation [49,102].

The stress-strain data for SBS triblock polymers presented by Cooper [106] and Fielding-Russell [107] for Kratons 101 and 1101, respectively, are representative of block copolymer elastomers possessing a structural high-modulus phase. On the first loading, a high modulus is observed at low elongation, further strain leads to yielding followed by a distinct drawing region. Plastic flow continues to higher elongations, where a rapid increase in stress occurs. Smith & Dickie [108] and again Smith [109-111] claim that the higher modulus domains, being small and closely packed, impede crack growth, resulting in the need for a much higher applied stress to produce a crack of a critical size necessary to cause failure.

It should be emphasised that the shape of the stress-strain curve and particularly the yielding phenomenon is sensitive to the block composition [31,43,65,95,112], and to the method of sample preparation, with particular sensitivity to the casting solvent [43,62,80,107,113]. Normally, no yielding is observed if the block polymer contains less than 30 wt% hard block, although when films are cast from a solvent which is preferentially a much better solvent for the hard phase than the soft, a yield point may be observed at a lower hard-segment concentration.

If the test sample is not taken to the break point but is relaxed to zero stress, stress-softening or stress hysteresis is observed, as shown schematically in Figure 2.3. Subsequent stress-strain cycling produces increased stress-softening, but the hysteresis decreases in magnitude after the first cycle and has been reported to attain an equilibrium or steady-state value after several cycles [79,80,107]. When specimens are cast from a preferential solvent for the hard phase, the stress-softening is particularly marked, whereas preferential solvents for the rubbery phase produce a less marked effect [107].

The fact that the stress decreases on repeated straining suggests a disruption of the block polymer structure. However, any breakdown, if it occurs, appears to be reversible and apparently does not involve the cleavage of primary intrachain bonds or permanent viscous flow. Original stress-strain properties may be recovered either by allowing the sample to relax for long periods of time [62,114,115], by annealing at elevated temperatures [62,116], or by hot water treatment [14]. This reversibility of the mechanical breakdown has been further demonstrated by Bailey et al [117], who followed stress-strain experiments by dissolution and recasting or by remoulding. Both methods were found to return the original stress-strain properties.

#### 2.3.4.2 The effect of structural modification

The tensile properties of block polymers are dependent upon the relative proportions and molecular weights of the components, and also upon the block arrangement. It has already been indicated that one requirement for high tensile strength in the styrene-butadiene system is that there should be at least two styrene blocks per molecule. With only one styrene block in the molecule, the tensile strength, modulus and extension at break are drastically reduced. Matsuo et al [65] have also observed that ABA and ABAB type copolymers are extremely tough; on the other hand, AB and BAB types are brittle despite the presence of the rubbery component. There also appears to be no advantage in extending the block sequence beyond ABA to ABABA, etc. [14].

With essentially constant total copolymer molecular weight, increasing hard block content in SBS copolymers is reported to produce a pronounced effect on the stress-strain curve. As shown in Figure 2.4, at low styrene contents, a non-yield maximum develops; at higher styrene concentration, a definite yield point is observed [42,92,107] followed by a draw period. At still higher styrene concentrations, the block copolymer becomes much less extensible. In general, as the styrene fraction increases while the total molecular weight is held constant, the yield strength increases but elongation at break decreases [18,31,43,65].

Caution should be exercised in the interpretation of ultimate property data as a function of hard segment fraction because of changes in other associated parameters. Morton et al [14], in their investigation of SIS, have shown that not only the styrene fraction but also the block molecular weights and the polydispersity of each block significantly affect the ultimate properties.

#### 2.3.4.3 Relaxation phenomena

The dynamic mechanical and tensile properties of this class of materials has been shown to be strongly dependent upon the two-phase structure and also upon the deformation and relaxation of the structure during the experiment. Studies aimed solely at the elucidation of the relaxation phenomena are rare; only in a few instances have sufficient stress-relaxation data been accumulated to allow the construction of master curves by time-temperature superposition [92,94,108,118].

Data for polystyrene and most other non-polar amorphous polymers can usually be transformed fairly easily into a master curve by translation along the time axis using the Williams, Landel & Ferry equation [119]. However, structurally more complicated systems are rheologically complex and do not yield master curves quite so readily. For example, in semi-crystalline systems such as polyethylene, a translation along the abscissa must be accompanied by a translation along the ordinate to create a master curve [120].

Likewise, master curves may be constructed for block polymers, although their construction may be more complicated than for simpler one-phase amorphous elastomers. Such curves have been prepared by several investigators [94,108,121-124] with the conclusion that for SBS block polymers, the shift factors do not follow the WLF equation, especially in the rubbery region. Smith & Dickie [108] also point out that from their experiments, the shift factor,  $\log a_T$ , varied linearly with temperature above  $-30^{\circ}\text{C}$ .

The later works of Lim, Cohen & Tschoegl [125], Fesko & Tschoegl [124], and Fielding-Russell & Fitzhugh [123] indicate that below a characteristic temperature of  $16^{\circ}\text{C}$  [125] or between  $24^{\circ}\text{C}$  and  $37^{\circ}\text{C}$  [123], dependent upon the particular polymer and solvent system used in the preparation of specimens, the shift factors obeyed a WLF type equation. Above the indicated temperatures, the shift factors obeyed an Arrhenius type equation.

#### 2.3.4.4 Models of two-phase systems

In early attempts to describe quantitatively the mechanical behaviour of two-phase systems, elastomeric materials were loaded with spherical inorganic filler particles [104,126] and it was assumed that the modulus of the filled elastomer was equal to that of the unfilled elastomer multiplied by a function of the volume fraction of the



filler. This type of model was also applied by Nielsen & Stockton [127] to crystalline polymers by treating the crystallites as inert filler particles. Only qualitative agreement between experimental results and theoretical predictions was obtained.

These ideas were refined by Smallwood [128] and Schwarzl et al [129], who allowed the multiplying factor between filled and unfilled moduli to be a function not only of filler concentration but also of other filler characteristics, such as filler size and shape. However, when these refined models for filled systems are applied to block copolymers, agreement is still poor.

Although the work of Einstein [130,131] and Smallwood [128], and more recently Kerner and others [132-135], provides a semi-quantitative description of modulus enhancement using representative moduli for the hard and soft segments; none of the models predict a high enough level of modulus improvement [136]. It has been suggested [137] that discrepancies between experimental data and the model of Uemura & Takayanagi [135] arise because the model assumes that the filler particles are spherical (which they may not be); in addition, possible interactions between neighbouring particles are neglected in the model.

Fujino et al [138] and Takayanagi [55] developed series-parallel models for mechanical mixtures and polymer blends, respectively, which take account of the degree of mixing of the separate components as well as the composition. Both models assume series and/or parallel arrangement of components with the further assumptions that perfect adhesion exists between phases and that there are no chemical interactions. The model parameters are evaluated from properties of the homopolymers. Wilkes & Stein [118] attempted to fit dynamic mechanical data on styrene-butadiene block copolymers to the generalised model of Takayanagi and noted that the parameters of the model depend on the solvent system used for film casting. Dickie [139] reviews the work of Kerner [132], Uemura & Takayanagi [135], Hashin & Shtrikman [140], and Halpin & Tsai [141,142]. He concludes that the results of Kerner and Takayanagi are identical, although arrived at by a different approach; and that Kerner's results for inclusions stiffer than the matrix are the same as the lower-bound expressions derived by Hashin. Halpin & Tsai write the same result in a somewhat different form, which displays more clearly the concentration dependence of the composite modulus and is more easily extended to non-spherical inclusions. The Halpin-Tsai equations are based on the self-consistent micromechanics methods developed by Hill [143,144].

Hermans [145] employed the model to obtain a solution in terms of Hill's reduced moduli. Halpin & Tsai reduced Hermans' solution to a simpler analytical form and extended its use to a variety of filament geometries. A review [146] traces the development of the micromechanics relationships which form the operational basis for the composite analogy employed for semi-crystalline polymers. Further reviews of the above mentioned models and theories of the mechanical response of composite media [147-149] examine the utility of predictive methods developed for two-component engineering composites to predict the mechanical properties of macromolecular systems, such as crystalline and oriented thermoplastics, block copolymers, thermosetting resins and particulate-filled systems.

A further attempt to generalise the Halpin-Tsai equations to a wide range of morphologies has been proposed by Nielsen [150]; he extends the theory by using the concept of a generalised Einstein coefficient. This approach is shown to be applicable to a number of systems, including block polymers and polyblends [151].

In a series of papers [122,152-155], Kaelble et al investigated the tensile properties of Kraton 101, strongly promoting the thesis that an interfacial region exists around the domains. The response indicated that cavitation and void formation accompanied initial yielding and cold drawing; a function was proposed which defined the loss of interfacial integrity. Using further data from Holden et al [49] for a range of different block length polymers, the series-parallel model of Takayanagi in a generalised form was tested against the experimental data. The Halpin model for the kinetics of defect growth was applied to the interfacial bonding function defining two stages of cavitation. Initial nucleation followed by propagation and cavity coalescence.

## 2.4 TEARING OF RUBBERS

### 2.4.1 Introduction

The resistance to tearing of a rubber material is usually determined by loading in a specified manner a test-piece of the rubber of a standard shape, into which a notch has been introduced, either in the moulding process or by cutting the test-piece in a standard fashion. A wide variety of shapes of test-piece and notch and of methods of loading have been recommended by various authors [156].

Many of these methods of determining tear resistance give results which are characteristic of the method of test as well as of the particular type of test-piece used, owing to a pronounced direct dependence on modulus. This is not to say that modulus has no effect on tear strength, but that the influence of modulus should be allowed to operate in the immediate tearing zone and not in regions of the specimen remote from the locus of the tear. In other words, a tear test specimen should not be an ill-shaped tensile modulus test specimen.

In 1953, Rivlin & Thomas, at the Natural Rubber Producers' Research Association (NRPRA), began an investigation into the rupture of rubber, with special emphasis on tearing. Specifically, they sought to define and measure a tear strength that was independent of test-piece shape, the parameter measured being a material property and not a combined property of material and specimen. The work done at NRPRA over a period of several years is fully described in a series of papers [157-169].

Firstly, it was found possible to describe the tear performance of a rubber in terms of a characteristic tearing energy. This energy being related to the elastic energy stored in the highly strained zone at the tip of a growing tear. With growth of the tear, most of this energy is dissipated irreversibly as heat, being many times larger than that required to form the new surfaces. A simple method for measuring the tearing energy was employed, and a 'trousers' shaped test-piece, shown in Figure 2.5(a), was adopted as a preferred type. It was found that the value of the tearing energy was greatly influenced by the type of rubber, nature of filler, and temperature of environment.

### 2.4.2 Choice of Test-Piece Shape and Analysis

The original work was based on a criterion originally proposed by Griffith [170] in 1920 for fracture propagation in glass and was based on energetic considerations.

Considering a sheet of rubber of thickness  $t$ , containing a cut of length  $c$ . Assume that for the cut to extend under load by an amount  $dc$ , an amount of work  $T t dc$  must be done, where  $T$  is an energy term characteristic of the material. If  $W$  is the elastically stored free-energy of deformation of the test-piece, then the change in free-energy of deformation due to the cut growth  $dc$  is given by:

$$- \left[ \frac{\partial W}{\partial c} \right]_l = T_c t \quad (2.3)$$

The suffix  $l$  denoting differentiation carried out under constant displacement of the test-piece boundaries over which forces are applied; that is to say, the cut growth occurs under a quasi-static condition; for example, there is no work done on the sample by the forces extending it during the cut growth period.

The criterion (equation (2.3)) was tested by using test-pieces of different size and shape with different lengths of initial cut, with  $(\partial W / \partial c)_l$  being estimated initially by graphical integration. Since the above method was quite laborious and involved a degree of inaccuracy due to the graphical integration, it was demonstrated that by particular choice of specimen shape, a more convenient formula could be derived for the calculation of tear energy.

#### 2.4.2.1 Trousers test-piece

Considering the trouser specimen in Figure 2.5(a). If a force  $F$  is applied to the legs to produce tearing along the central axis, and if the legs are long in comparison to their width  $b$ , there is a region of each leg subjected to simple extension with extension ratio  $\lambda$ . The extension ratio is the ratio of the extended length to the non-extended length. For an increase,  $dc$ , in tear length, a region or volume ahead of the tear, where no tension or extension exists, is transferred to the region of the legs just behind the cut and is put into tension at the extension ratio  $\lambda$ . It can be seen geometrically that the overall distance between the clamps,  $l$ , increases by an amount  $dl$  which is equal to  $2\lambda dc$ , so:

$$dl = 2\lambda dc$$

or:

$$\left[ \frac{\partial \mathcal{L}}{\partial c} \right]_F = 2\lambda \quad (2.4)$$

Rivlin & Thomas [157] state that since the energy stored elastically is a function of cut length  $c$  and overall length  $\mathcal{L}$ , the total differential of  $W$  should be:

$$dW = \left( \frac{\partial W}{\partial c} \right)_{\mathcal{L}} dc + \left( \frac{\partial W}{\partial \mathcal{L}} \right)_c d\mathcal{L}$$

which, for  $F = (\partial W / \partial \mathcal{L})_c$ , gives:

$$dW = \left( \frac{\partial W}{\partial c} \right)_{\mathcal{L}} dc + F d\mathcal{L} \quad (2.5)$$

dividing through by  $dc$  and combining with equation (2.4):

$$\left( \frac{\partial W}{\partial c} \right)_{\mathcal{L}} = \left( \frac{\partial W}{\partial c} \right)_F - 2\lambda F \quad (2.6)$$

Since at constant force  $F$ , an increase in cut length  $dc$  transfers a volume  $A_o dc$  of rubber from the undeformed state to one of simple extension, the change  $dW$  in stored energy is equal to  $W_o A_o dc$  or:

$$\left( \frac{\partial W}{\partial c} \right)_F = W_o A_o \quad (2.7)$$

where  $W_o$  is the energy stored elastically per unit volume of material, and is dependent upon the strain invariants  $I_1$  and  $I_2$ , being defined:

$$I_1 = \lambda_1^2 + \lambda_2^2 + \lambda_3^2$$

$$I_2 = \frac{1}{\lambda_1^2} + \frac{1}{\lambda_2^2} + \frac{1}{\lambda_3^2}$$

$$I_3 = \lambda_1^2 \lambda_2^2 \lambda_3^2 = 1$$

For the case of simple tension, where  $\lambda_1 = \lambda$  and  $\lambda_2 = \lambda_3 = 1/\lambda$ , the force  $F$  necessary to maintain the elongation in a sample of cross-sectional area  $\frac{1}{2}A_0$  becomes:

$$F = A_0 \left( \lambda - \frac{1}{\lambda^2} \right) \left( \frac{\partial W_0}{\partial I_1} + \frac{1}{\lambda} \frac{\partial W_0}{\partial I_2} \right) \quad (2.8)$$

Taking equations (2.6) and (2.7) together yields:

$$\left( \frac{\partial W}{\partial c} \right)_l = W_0 A_0 - 2\lambda F \quad (2.9)$$

If  $\lambda$  is maintained close to one by having wide test-piece legs, it is seen that in equation (2.8)  $F$  will depend on  $(\lambda - 1)$ , while  $W_0$  which is  $\int F d\lambda$  will depend on  $(\lambda - 1)^2$ ; thus making  $2\lambda F$  the dominant term in equation (2.9) for sufficiently small values of  $(\lambda - 1)$ . Hence:

$$\left( \frac{\partial W}{\partial c} \right)_l = -2F \quad (2.10)$$

Combining equations (2.2) and (2.10) yields the simple relationship between tearing energy, tearing force, and thickness:

$$T_c = \frac{2F}{t} \quad (2.11)$$

#### 2.4.2.2 Pure shear test-piece

With the pure shear test-piece (Figure 2.5(b)), the advance of the tear by an amount  $dc$ , referred to the undeformed state, transfers a volume  $L_0 t dc$  of rubber from a state of pure shear to the undeformed state,  $L_0$  and  $t$  being, respectively, the grip separation and test-piece thickness in the undeformed state.

From equation (2.3):

$$T_c t dc = W_0 L_0 t dc$$

$$T_c = W_o L_o \quad (2.12)$$

where  $W_o$  is the stored energy per unit volume in the region of pure shear well removed from the tip of the tear.

#### 2.4.3 Some Problems with the Trouser-Leg Specimen

Relatively recent research in the field of tearing [172,173] has indicated certain deficiencies when the requirement is for regular testing of a wide variety of rubber materials.

Many of the published reports by the NRPRA workers imply that the equation  $T_c = 2E/t$  is satisfactory to use for routine tear measurements. However, tear tests using the simple trousers specimen highlight two serious problems:

- (a) For many compounds, there may be appreciable leg extension ( $\lambda \neq 1$ ), even when  $b$  is chosen to be suitably large, often knotty tearing develops with the tear deviating sideways or even circling around under increasing force until a new tear breaks ahead [160,174], or one of the legs of the specimen tears through.
- (b) The development of the characteristic tearing equation  $T_c = 2E/t$  is based on tear propagation down the central axis of the test-piece.

Leg extension may be allowed for if the strain energy density,  $W$ , is known, but a separate stress-strain curve is required. When one leg of the specimen is torn through, obviously further testing is precluded with that specimen. These problems often mitigate against any quick and meaningful routine tear strength measurements with the simple trousers test-piece.

The specimen may be modified, however, in order to avoid these deficiencies. The obvious method is to reinforce the legs to prevent their elongation and to provide a path of least resistance for tear propagation. Veith [172] used a specially moulded trouser specimen incorporating a longitudinal groove with a particular cross-sectional geometry to provide the path of least resistance. The legs of the specimen were also reinforced with a fabric in order to resist any extension during the test.

Alternatively, Gent & Henry [173], in an attempt to determine the relative importance of tear deviation, employed trouser-shaped specimens with parallel strips of steel foil bonded to the legs, to restrict possible deviation of the tear from a linear path.

#### 2.4.4 Qualitative Information Obtained from Tearing - Two Types of Tearing

A great deal of information on rupture may be obtained from tearing which cannot be achieved by other methods. Inspection of the tips of growing tears, study of the torn surfaces, together with an appreciation of the significance of different types of tearing which occur, yield valuable information.

There are two main types of tearing action [159]:

- (a) Stable or steady tearing, where the tear propagates at a uniform rate; and
- (b) Stick-slip tearing, where the tear propagates in a series of jumps.

Steady tearing implies that the tearing energy/rate of propagation relation has a positive slope. Stick-slip tearing implies, conversely, that the relation has a negative slope; only an approximation to the true relation can be obtained in this case. Provided this limitation is borne in mind, the consequences are not severe so far as a broad survey of tear behaviour is concerned.

A distinctive form of stick-slip behaviour is often observed, particularly in rubbers containing fillers; known as "knotty tearing" [160], it manifests itself as pronounced lateral deviation of the tear tip, resulting in large tip diameters, and consequent high tear initiation energies.

An approximate relationship between the rate of propagation of the tear and the rate of extension at the tip of the tear was derived by Greensmith [164], yielding the following equation:

$$R = [(\ell_o/d)(\lambda_t - 1)] v d_t \quad (2.13)$$

where  $R$  = tear propagation rate

$\ell_o$  = distance ahead of the tear tip at which the stress reduces to zero



$d_t$  = tear tip diameter

$\lambda_t$  = extension ratio at the tear tip

$v$  = rate of extension of rubber approaching the tear tip

However, owing to  $[l/d_t(\lambda_t - 1)]$  values having been calculated from the results of a static test, this approximation turned out to be good only at low rates of propagation.

Thomas [162] noted that at 20°C, SBR(75/25) gum vulcanizate showed a change in tear type at about  $10^{-2}$  cm/sec tear speed. Below this speed, tearing was by a stick-slip process, and above  $10^{-2}$  cm/sec the process was characterised by steady tearing. In fact, the tear energies of both natural rubber and SBR vulcanisates have been found to be temperature and rate sensitive [159,162,164,171,175,176] with SBR showing the more pronounced dependence (Figure 2.6). It has been suggested that the mechanism causing this time-temperature dependence of steady tearing is directly related to viscosity, being described by a pseudo-Williams-Landel-Ferry (WLF) relation of viscosity and free volume [175,176].

On the other hand, the stick-slip process of tearing has been thought to be related to secondary mechanisms occurring as the rubber is stretched to break directly in front of the tear tip. The stick-slip phenomenon has been explained [159,164,175,176] as a hysteretic effect caused by stretching to break immediately ahead of the tear tip. Busse [177] reports that the stress concentration at the tip of an incision, which has grown in a highly hysteretic material, is considerably lower than would otherwise be expected, and cut growth therefore ceases. This is true for elastomers such as natural rubber (NR), where crystallisation occurs on stretching. The stick-slip behaviour of NR caused by crystallisation is reflected in the plot of tear energy versus rate and temperature shown in Figure 2.6. A plateau region is maintained over a wide range of temperatures and tear rates. Above 100°C, tear energy falls owing to increased mobility of chain segments which reduces the crystallisation effect and its associated strengthening effect.

For a non-crystallising rubber such as SBR, elastic recovery takes place continuously [176], and the stress concentration at the growing tip increases accordingly; therefore, the cut continues to grow, giving rise to steady tearing. At particular tear rates and temperatures, however, a high degree of orientation occurs ahead of the tear, causing anisotropy which is almost equal in effect to the crystallisation of NR [165].

#### 2.4.5 The Effect of Filler Reinforcement on Tear Energy

It has been noted by Greensmith [160] and Mullins [178,179] that fillers, mainly carbon blacks, produce large increases in tearing energy over particular tear rates and temperatures. This, they suppose, is caused by an increase in tear-tip diameter attributed to the addition of the carbon black.

Mullins reports that the percentage of carbon black found on the rupture surface is always greater than the actual proportion of black originally mixed into the elastomer. This difference, which appears to be greatest in slow tearing, is said to be due to the tear preferentially picking a path through the interfaces between rubber and filler. In order to obtain the increased tear energy, sufficient time must be allowed for the strengthening effect to develop. When sufficient time is allowed, the tear-tip broadens and the torn surfaces appear rough. Because the filler particles act as stress raisers, the interface between particles and the rubber is relatively weak, the tear path therefore wandering back and forth seeking these weaker areas.

Similarly, Andrews [168] states that since tear energy is high at high tear rates and low temperature for SBR vulcanizates, the energy needed to continue cut growth is largely used up in irreversible viscous processes. He adds that rigid filler particles act as stress raisers in the elastic matrix and the tear-tip, having a high stress field around it, causes rupture of polymer-filler interfaces, which dissipates energy stored elastically around the filler particles. In addition, it is suggested that, ahead of the tear-tip, secondary fractures may start from filler particles. Andrews' theory of frozen stresses [168] suggests that molecular chains remain in their elongated form for a time after the stress has fallen. When a stress pattern has developed around the tear tip, with the locus of maximum stress curving away from the imaginary centre line ahead of the cut, the tear bursts through so quickly that the stress pattern remains virtually frozen. The tear then deviates from its straight ahead path towards the high stress axis. The cut propagates along this locus of maximum stress until a point is reached at which the stress is not high enough to give rise to additional propagation. Evidence of this curving effect from the central axis is found in the form of cusps off the main axis of tearing when filled elastomers or NR are alternately stressed and relaxed during tearing. The reason given for this hysteresis is the effect of filler particles or crystallites formed on stretching; these tend to key the molecules momentarily in their

oriented shape, keeping the deformation the same once the cut bursts through. At lower temperatures and high rates of tear with these materials, the increased viscosity aids the development of the frozen stress pattern ahead of the tear-tip.

#### 2.4.6 The Non-WLF Viscosity Dependence of SBR (Gum) Tear Energy

The effect of tear rate and temperature on the tear energy of a series of butadiene-styrene and butadiene-acrylonitrile copolymers has been studied by Mullins [165]. Using the trousers test-piece, he determined that tear energies could be transformed into one master curve. The experimentally determined shift factors,  $\log a_T$ , did not match those predicted by the WLF equation, but were a factor of 1.4 greater. Observing that the tear energy is a function of the energy to break and the tear-tip diameter, he suggests that since both of these factors are themselves rate and temperature dependent, the more complex dependence of the tear energy than that predicted by WLF is not surprising. Mullins also demonstrated the direct relationship between tear energy and hysteresis. Plotting tear energy versus the imaginary part of the complex shear modulus ( $G''$ ), which were obtained by means of a torsion pendulum, he found that as damping increased so did the hysteresis and the tear energy. This means that the longer the time taken for molecules to reach an unstrained configuration after being stretched almost to break, the higher the tear energy.

#### 2.4.7 Tearing Energy from the Strain Concentration at an Incision

Thomas [158] developed an additional tear energy equation based on the strain concentration around a particular incision, a parallel-sided slit which terminated in a semi-circle (Figure 2.7). The value of  $T_c$ , defined in equation (2.3), may be used to describe any strained specimen containing any type of cut. It is necessary to obtain the change in elastically stored energy  $W$  when the cut propagates a small distance  $dc$ . The strain energy loss arises from the fact that the volume of material, shaded in Figure 2.7, which is initially in a state of simple extension, is removed from the system. The loss of strain energy is given by the equation:

$$-dW = \int_{-\pi/2}^{+\pi/2} E_s dc t r \cos \theta d\theta \quad (2.14)$$

where  $E_s$  is the energy elastically stored per unit volume of rubber at the edge of the cut an angular distance  $\theta$  from the centre of the semi-circular hole,  $t$  is the thickness of the material, and  $r$  is the radius of the semi-circle. From equation (2.3):

$$T_c t = \left( \frac{dW}{dc} \right) l$$

then: 
$$T_c = \frac{1}{t} \left( \frac{dW}{dc} \right) l$$

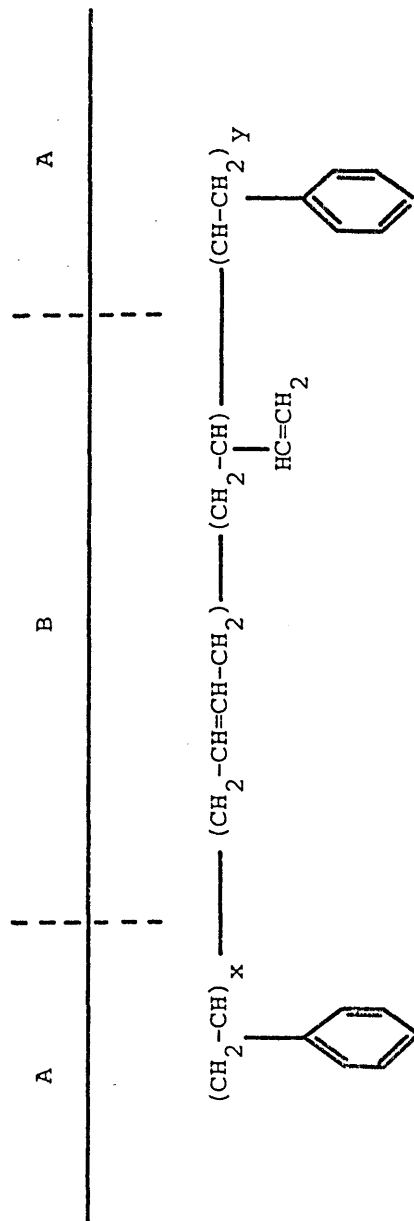
$$= r \int_{-\pi/2}^{+\pi/2} E_s \cos \theta d\theta \quad (2.15)$$

When the tear energy reaches its critical value,  $E_s$  in equation (2.15) becomes the energy stored to break per unit volume of material, and the critical tearing energy may be approximated by the equation:

$$T_c \approx 2r E_b = d_t E_b \quad (2.16)$$

where  $d_t$  is the diameter of the tear tip, and  $E_b$  is the energy stored to break per unit volume of material.

Greensmith [164,171] and Thomas [162] have found that, even though the value of  $T_c/d_t$  is of the order of  $E_b$ , the former is always larger than the latter. The reason given for this occurrence is that, in tearing the tear-tip diameter might be as large as the thickness of the tear sample, whereas in the tensile test measurement, the crack that initiates failure is very much smaller than the thickness of the material. Hence, the tear tip diameters being very different, one would expect the value of  $T_c/d_t$  to be higher than  $E_b$ . Regardless of this difference, Thomas [158,162] has found that the ratio  $T_c/E_b$  gave calculated values of tear-tip diameter equalling the dimensions of irregularities in the torn surfaces of elastomers.



Styrene blocks are denoted by x and y. The butadiene may be present as either in-chain (1,4) or pendant (vinyl) structures of unsaturation. The in-chain unsaturation of butadiene may be of the cis-1,4 or trans-1,4 varieties.

Figure 2.1 ABA block copolymer chain molecule.

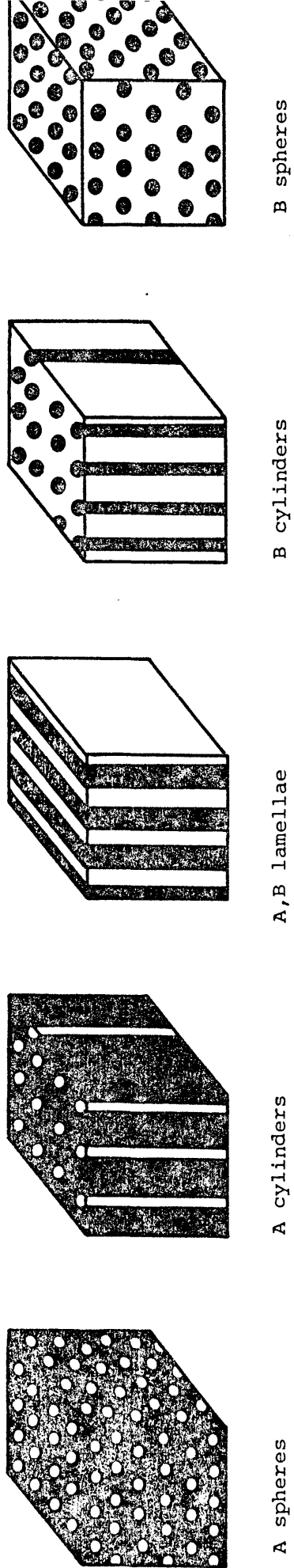


Figure 2.2 Structural variations in tri-block copolymers with changing A and B content giving hexagonally packed spheres and cylinders or a lamellar structure.

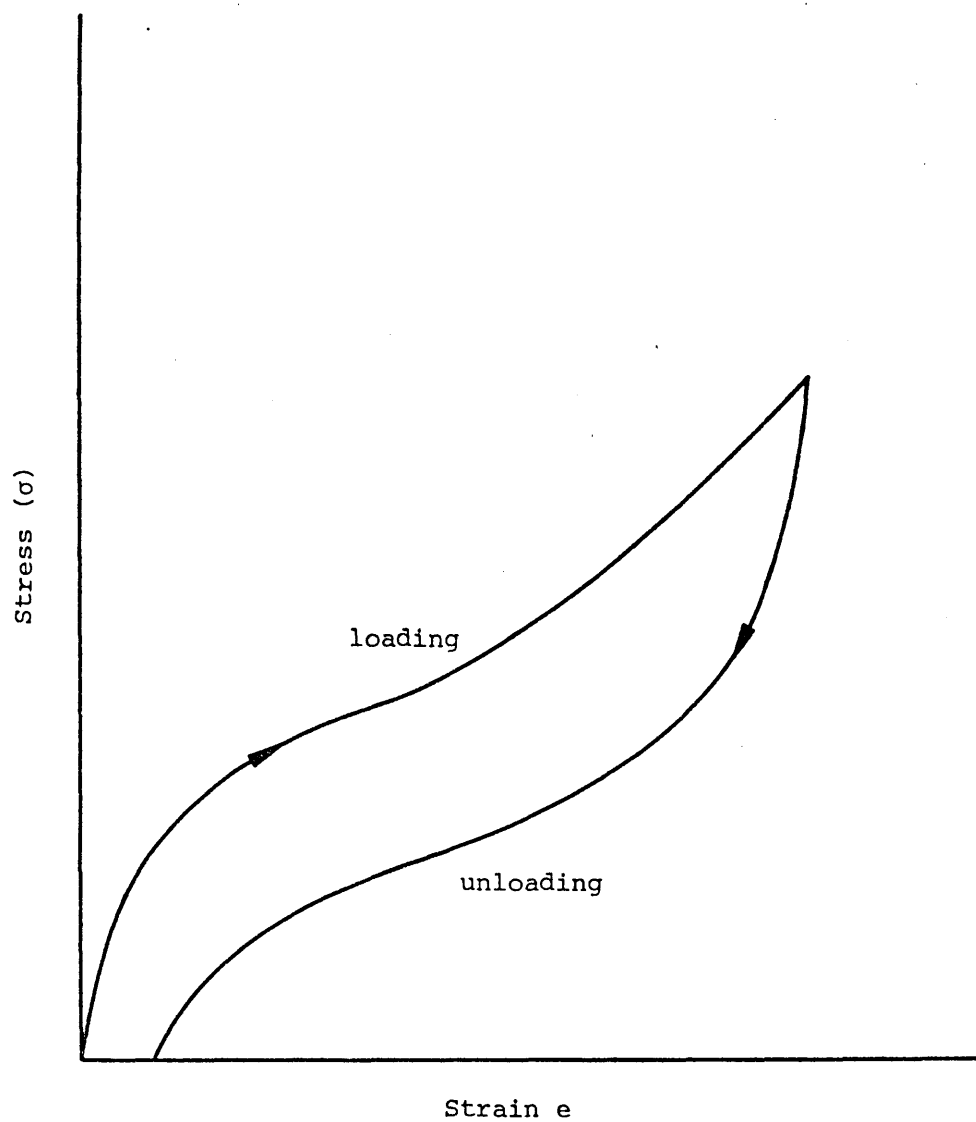


Figure 2.3 Schematic of loading and unloading in SBS block copolymers showing hysteresis effect.

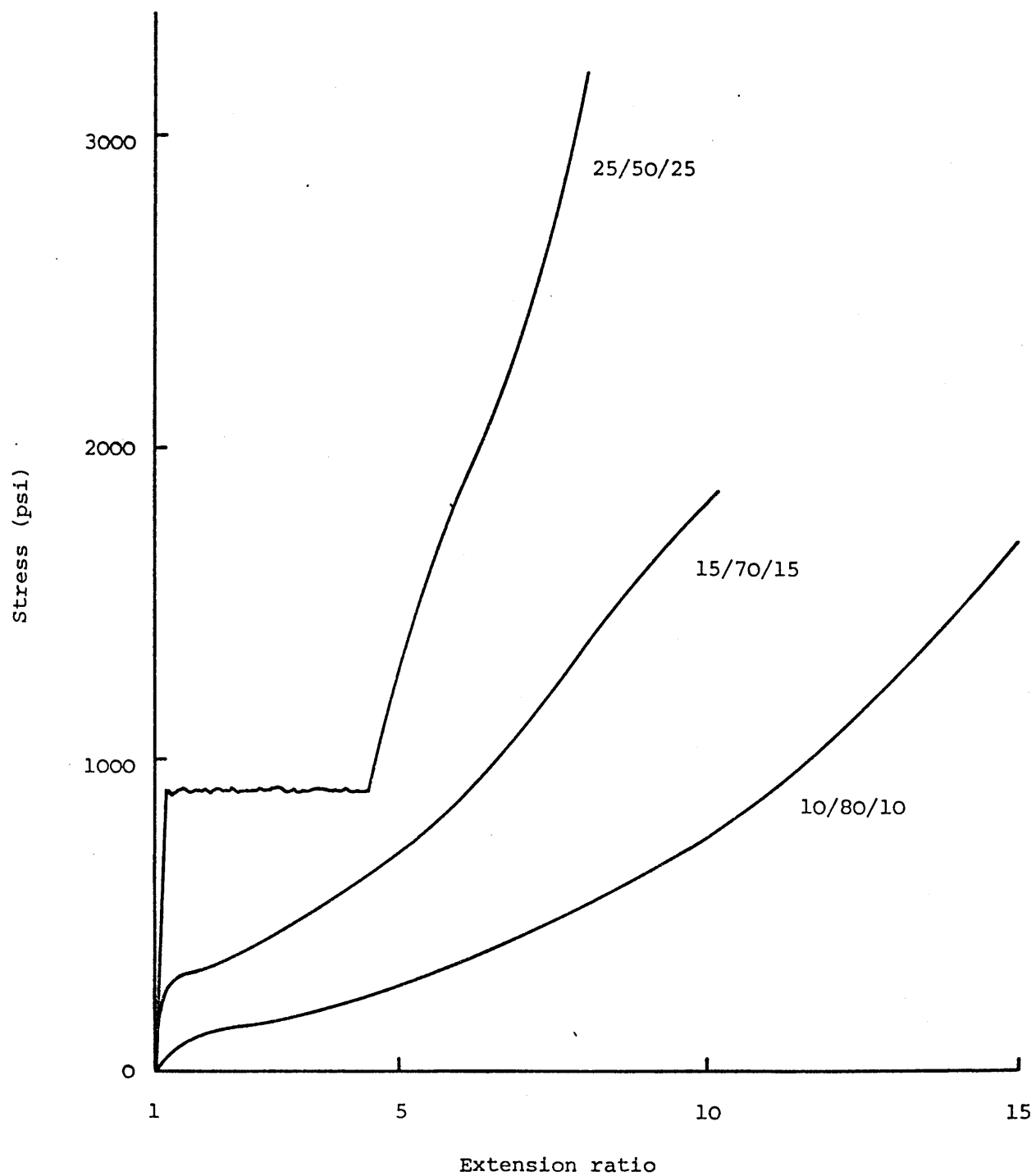


Figure 2.4 The effect of increasing the styrene fraction at constant total molecular weight (taken from Childers and Kraus ref. 92)



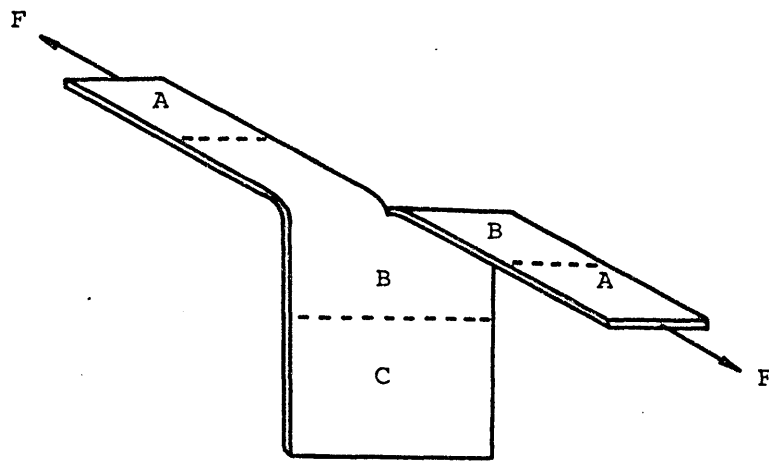


Figure 2.5(a) Trouser leg tear specimen.

Region A is in simple tension.

Region B contains a highly deformed area.

Region C is undeformed.

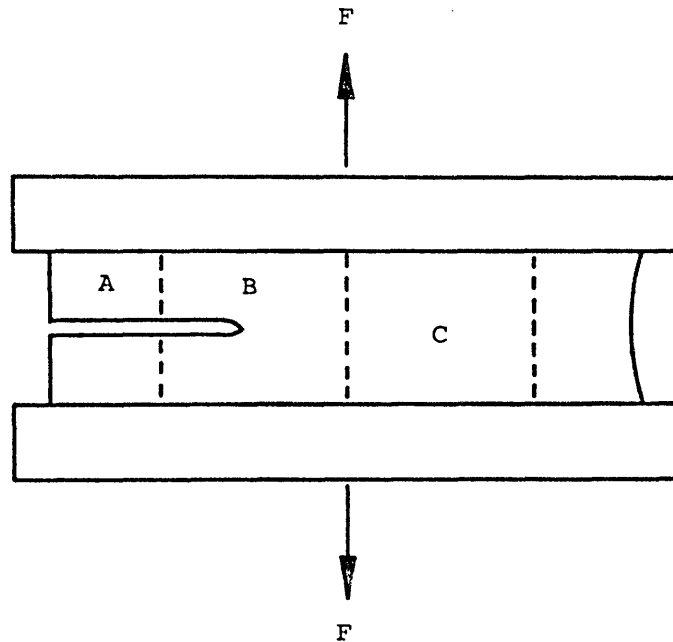


Figure 2.5(b) Pure shear tear specimen.

Region A is undeformed.

Region B contains a highly deformed area.

Region C is in pure shear.

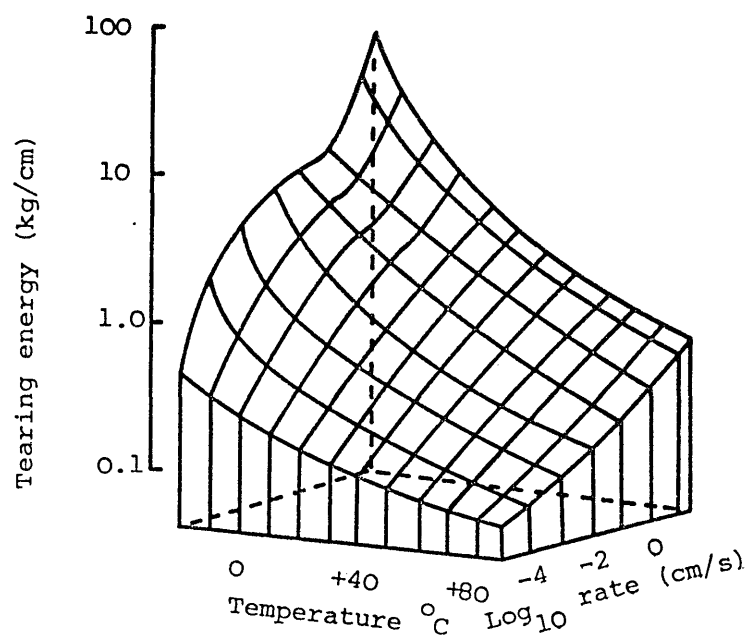


Figure 2.6(a) Tearing energy surface for GR-S vulcanizate.

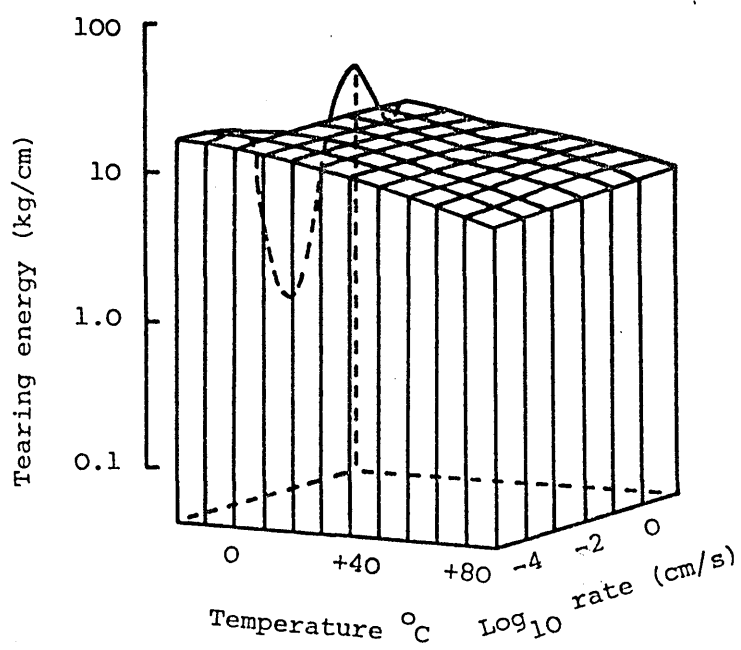


Figure 2.6(b) Tearing energy surface for natural rubber vulcanizate.

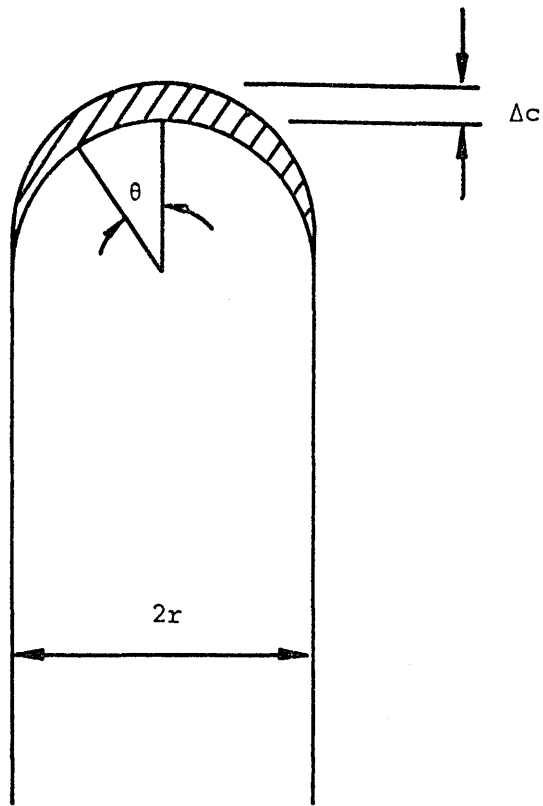


Figure 2.7 Parallel-sided slit terminating in a semi-circle (after Thomas ref. 156).

### 3.1 INTRODUCTION

#### 3.1.1 The Triblock Copolymer Elastomers

Initially, the Shell Chemical Company UK Limited supplied commercial grade thermoplastic elastomers in crumb form for use in this study. The materials were of the Cariflex TR range which are equivalent to the well-known Kraton range of materials manufactured and marketed by Shell in the United States.

The particular polymers involved in this work were:

- A. TR1101, a high molecular weight SBS
- B. TR1102, a low molecular weight SBS
- C. TR4122, a plasticised SBS with high styrene content
- D. TR4113, a plasticised SBS

Although Shell have published some data on the chemical and physical properties of these polymers; and in addition a number of researchers in universities and other establishments throughout the world have added more detailed information on some of the properties of selected Cariflex (or Kraton) materials; it is still not possible to obtain data which fully characterises the chemical, physical or mechanical nature of the range of materials chosen for this project. In any event, it is considered prudent to carry out a programme which will chemically characterise the materials used in any project, since the risk of batch to batch variations is indeed a real one. Not only that, but the results obtained from a chemical characterisation procedure may be compared with other people's work, to give clues to possible discrepancies in physical and mechanical properties data. Without confirming that the polymers being compared are actually the same, it is difficult or impossible, certainly unwise, to make any statement about interlaboratory tests.

It was decided, therefore, that the materials used here be fully characterised. The important chemical parameters concerned were identified and investigated, the results being presented in subsequent sections of this chapter.

#### 3.1.2 Parameters Investigated and Experimental Methods Used

The chemical composition of triblock copolymer elastomers,

particularly commercial polymers, is such that great importance must be attached to the overall molecular weight, block molecular weight, block proportions by weight, the proportions of diblock and homopolymer impurity, the polydispersity or molecular weight distribution, the microstructure (cis, trans) of the polydiene centre block, the plasticiser content, and the type of plasticiser used.

In order that these quantities be determined, it was necessary to adopt a number of discrete experimental procedures. Most of these experiments are well-known, standard techniques in everyday use throughout the industrialised world. Table 3.1 shows the experiments used to gain the information required.

TABLE 3.1  
Techniques Used for Characterisation of Polymers

EXPERIMENTAL TECHNIQUE	MEASURED PROPERTY
Membrane Osmometry	$\bar{M}_n$
Gel Permeation Chromatography	$\bar{M}_n, \bar{M}_w, \bar{M}_w/\bar{M}_n$ . Molecular weight distribution. Composition in terms of triblock, diblock and homopolymer. Individual block molecular weights.
Nuclear Magnetic Resonance	Styrene content. Diene microstructure. Presence of plasticiser.
Infra-Red Spectroscopy	Type of plasticiser
Soxhlet Extraction	Proportion of plasticiser
Swelling in n-Heptane	Network molecular weight, $M_c$

### 3.2 NUMBER AVERAGE MOLECULAR WEIGHT BY OSMOTIC PRESSURE

The determination of molecular weight by osmotic pressure is often termed a colligative method because it arises from the decrease in activity of a solvent upon addition of a soluble sample. Activity is the effective concentration, that is, the product of the molar concentration and the activity coefficient. This coefficient usually has values somewhat less than unity and its magnitude can be calculated when the characteristics of the solvent and solute molecules are known. The osmotic pressure is developed when the solvent diffuses through a semi-permeable membrane to dilute the solution to produce more nearly equal activities. Because of its high sensitivity and membrane limitations, this method is most commonly used for measuring molecular weights between 20,000 and 500,000. Detailed descriptions of the method are given by Wagner & Moore [26], by Bonnar et al [27], and by Doty & Spurlin [28].

Measurements are made of the pressure exerted by solvent molecules diffusing through a semi-permeable membrane into a solution in which the activity of the solvent molecules is lower. If the solution compartment is closed, the pressure builds up until an equilibrium pressure is reached, after which no net solvent flow occurs. This osmotic pressure,  $\pi$ , is related to the number-average molecular weight,  $\bar{M}_n$ , and concentration,  $C$ , of the solute by the relationship:

$$\frac{\pi}{C} = R_I T \left( \frac{1}{\bar{M}_n} \right) \quad (3.1)$$

where  $R_I$  is the ideal gas-law constant, and  $T$  is the absolute temperature.

In order to determine the molecular weight of a sample, values of  $\pi/C$  are found at several concentrations, and plotted against concentration. Such a plot is often linear, and the intercept at the  $\pi/C$  axis gives a value for zero concentration, from which  $\bar{M}_n$  may be calculated using equation (3.1).

The Hewlett-Packard high speed membrane osmometer (Model 501) was used in all these experiments with 0 - 8 non-aqueous membranes. Polymer solutions in toluene were introduced into the equipment at +37°C; four different concentrations of solution being used for each polymer in the range 2.5 to 15 g.litre<sup>-1</sup>. Two readings were taken at each solution concentration once equilibrium was attained, the average being used for calculation purposes.

The results for all the polymers used in this study are shown in Figure 3.1, and the  $\bar{M}_n$  values determined are presented in Table 3.2. Also shown in Table 3.2 are molecular weights for the similar Kraton 1101 and 1102, determined by the osmotic pressure technique, as quoted in the literature by several authors. It is clear that the data obtained in this work compares fairly well with that achieved by other research groups.

TABLE 3.2  
Number-Average Molecular Weight,  $\bar{M}_n$ , by Osmotic Pressure

Polymer	Number-Average Molecular Weight, $\bar{M}_n$ /10 <sup>-4</sup> g.mole <sup>-1</sup>			
	This Study	Reference [80]	Reference [36]	References [94,107]
TR1101	8.2	8.4	9.4	7.6
TR1102	6.7	7.5	7.8	
4122 Deplasticised	9.4			
4113 Deplasticised	10.3			

### 3.3 GEL PERMEATION CHROMATOGRAPHY FOR MOLECULAR WEIGHT, POLYDISPERSITY AND POLYMERIC IMPURITY

The use of gel permeation chromatography (GPC) in the analysis of block copolymer systems is now very widespread. The technique has been shown to be an extremely powerful tool in the determination of molecular weight, and in the analysis of diblock and homopolymer impurities.

GPC is a form of liquid chromatography which sorts polymer molecules, in a gel-packed column, according to their size in solution. A size exclusion, or restricted diffusion principle is used for the size sorting. The longitudinal section of a column packed with a typical "gel" material is shown schematically in Figure 3.2.

The gel is a rigidly structured porous network and may consist of materials such as polystyrene cross-linked with divinyl benzene or a porous glass material. Solvent is continually pumped through the gel and column by means of an external pumping system. A solution of the polymer sample is injected into the top of the column, and the sample is percolated through the system by means of the flowing solvent stream. The size sorting of the polymer molecules takes place in the pores of the gel. As illustrated in Figure 3.2, the very large molecules cannot enter many of the pores and thus travel mostly around the gel beads and come out of the column first. The very small molecules, on the other hand, enter most of the pore volume, have a larger amount of the column at their disposal, and take a more tortuous route through the column. These smallest molecules come out last. Molecules intermediate in size exit at intermediate times depending on the general size relationships. Because of this size sorting process, GPC is an ideal system for measuring the size distribution of polymers.

As the molecules exit from the column, they may be detected by a variety of methods, including ultra-violet photometry or differential refractive index measurements, but many other detection methods exist.

Applied GPC is not an absolute technique; calibration [30,182-186] is required to yield accurate or quantitative expressions of the size distribution and molecular weights. Calibration can be made with standards by relating the logarithm of the molecular weight,  $M_i$ , or the logarithm of the hydrodynamic volume,  $\log [\eta] M_i$ , to the retention volume,  $V_R$ . Molecular weight data are dependent on polymer type, solvent and temperature. Type dependency exists because the size of the polymer molecule coil in solution is not the same per unit molecular weight for all polymers. The viscosity of different polymer molecules of the same



molecular weight varies widely.

In order to define the usefulness of a GPC column packing material, it is necessary to state the range of molecular size over which it will separate, and any special surface property that will lead to separation by properties of the solute other than molecular size. A number of studies have been made of the effect of column packing particle size and its distribution on column separation efficiency [187,188].

An interesting aspect of this present study is that four different laboratories were used for GPC measurements, all using different column combinations, producing widely differing end results. Table 3.3 shows the permeability ranges of the column sets used. It can be seen that while Akron used seven columns, each covering a comparatively narrow permeability range, Manchester, ISR and RAPRA had a wider range of pore size using four-column sets.

TABLE 3.3  
The Permeability Ranges of the Four GPC Column Sets

Manchester (Å)	Akron (Å)	ISR (Å)	RAPRA (Å)
$0.7 - 2 \times 10^3$	$2 - 5 \times 10^3$	-	$0.7 - 2 \times 10^3$
$5 - 15 \times 10^3$	$2 \times 5 - 15 \times 10^3$	$5 - 15 \times 10^3$	-
-	$1.5 - 5 \times 10^4$	$1.5 - 5 \times 10^4$	$1.5 - 5 \times 10^4$
$5 - 15 \times 10^4$	$5 - 15 \times 10^4$	-	-
-	$1.5 - 7 \times 10^5$	$1.5 - 7 \times 10^5$	-
$7 - 50 \times 10^5$	$7 - 50 \times 10^5$	-	$7 - 50 \times 10^5$
-	-	$2 - 10 \times 10^6$	$5 - 10 \times 10^6$

Another effect which deserves consideration is the flow-rate in the column set [189-191]. In practical applications of GPC analysis, close control of the flow-rate is essential for obtaining accurate results, since not only the elution volumes, but also the resolution of GPC peaks are affected by the variation in flow-rate. For the calculation of molecular weight distribution, it is important that both the GPC elution curve and the calibration curve be obtained at the same flow-rate. Since the logarithm of the molecular weight is plotted in the calibration curve, a small difference in the calibration curves obtained at different flow-

rates may cause a significant error in the calculated molecular weight distribution.

The resolution of most column sets is improved by reducing the eluent flow-rate, using only columns that fractionate over the molecular size range of interest, using longer columns, increasing the solvent temperature and reducing the weight of solute injected. Most GPC practitioners use the lowest sample weight and highest solvent temperature compatible with obtaining a useful, noise-free chromatogram; and accept the resolution obtainable at normal flow-rates (1 ml/min through a  $\frac{3}{8}$ " column) through the minimum number of pre-packed columns that separate over the interesting range.

### 3.3.1 The GPC Tests

All four laboratories calibrated their column sets with Pressure Chemical Company standard polystyrenes. The relevant calibration curves are shown in Figures 3.3 and 3.4.

Table 3.4 shows details of the experimental conditions under which the GPC curves were obtained at each laboratory.

TABLE 3.4  
Experimental Operating Parameters of GPC Equipment

	Manchester	R A P R A	I S R	Akron
Solution concentration	0.25%	0.20%	0.50%	0.25%
Solvent	THF*	THF*	Toluene	THF*
Injection volume	2 ml	1 ml	1 ml	1 ml
Flow-rate	1 ml/min	1 ml/min	1 ml/min	1 ml/min
Temperature	25°C	25°C	25-60°C	45°C

\* THF: Tetrahydrofuran

Chromatograms were of course obtained for all the polymers used in this study, but it is intended to present only those graphs concerning TR4122 in order that comparisons may be made. These are shown in Figures 3.5 to 3.8. The quality and resolution of the chromatograms for the other materials are similar for the same laboratory.

### 3.3.2 Analysis of Chromatograms

#### 3.3.2.1 $\bar{M}_n$ , $\bar{M}_w$ and polydispersity

The chromatograms are curves of some detector function, normally refractive index difference versus molecular weight measured as retention volume or peak count. Measuring the height of the curve,  $H_i$ , above the base line at discrete peak counts, and using the calibration curve at the same peak counts,  $M_i$ , the number-average ( $\bar{M}_n$ ) and weight-average ( $\bar{M}_w$ ) molecular weights of the sample may be calculated according to the equations:

$$\bar{M}_n = \frac{\sum_{i=1}^n H_i}{\sum_{i=1}^n \left( \frac{H_i}{M_i} \right)} \quad (3.2)$$

$$\bar{M}_w = \frac{\sum_{i=1}^n H_i M_i}{\sum_{i=1}^n H_i} \quad (3.3)$$

hence, the polydispersity of the sample,  $\bar{M}_w/\bar{M}_n$ .

When the chromatograms are sufficiently well resolved, as is the case for samples run at ISR and Akron, it is possible to calculate the molecular weights of the individual component blocks of the polymer. This is done in a similar manner to that described above. The peaks corresponding to the ABA, AB and homopolymer A are taken separately, so that knowing the molecular weights of A, AB and ABA, the molecular weight of B can be determined; it follows that the molecular weights of the pure triblock, diblock and homopolymer are known. The molecular weight data for the polymers is presented in Tables 3.5 to 3.7.

It should, of course, be borne in mind that the data here are derived from polystyrene calibration curves. Since reliable  $K$  and  $a_p$  values are not available for these polymers for insertion in the Mark-Houwink dilute solution viscosity equation ( $[\eta] = K \bar{M}_v^{a_p}$ ), subsequent use of the universal calibration curve [184] was not possible.

#### 3.3.2.2 Proportions of triblock, diblock and homopolymer

The chromatograms are also of use in determining the amounts of diblock and homopolymer impurity in the commercial materials.

TABLE 3.5

GPC Molecular Weight Data from RAPRA and Manchester University

	Material	$M_n$ (g.mole <sup>-1</sup> × 10 <sup>-4</sup> )	$M_w$ (g.mole <sup>-1</sup> × 10 <sup>-4</sup> )	$M_w/M_n$
RAPRA	TR1101	15.70 13.75	19.73 19.41	1.26 1.41
	TR1102	12.03 10.73	14.60 14.40	1.21 1.34
	TR4113	15.00 14.46	18.55 18.45	1.24 1.28
	TR4122	15.41 13.90	19.26 18.83	1.25 1.35
Manchester	TR1101	9.95	15.20	1.53
	TR1102	8.37	11.70	1.40
	TR4113	-	-	-
	TR4122	10.30	14.60	1.42

TABLE 3.7

GPC Molecular Weight Data Showing Molecular Weights for  
Triblock, Diblock and Homopolymer - Data from Akron

Material	ABA		AB		A	
	$M_n$	$M_w$	$M_n$	$M_w$	$M_n$	$M_w$
TR1101	15.2	18.4	7.80	8.71	1.35	1.42
TR1102	11.9	13.2	5.84	6.10	1.07	1.13
TR4113	13.8	16.5	7.37	7.71	1.36	1.36
TR4122	15.2	16.7	7.33	7.70	2.16	2.25

All values g.mole<sup>-1</sup> × 10<sup>-4</sup>

TABLE 3.6

GPC Molecular Weight Data from ISR and Akron University

Material	$M_n$ (g.mole <sup>-1</sup> × 10 <sup>-4</sup> )	$M_w$ (g.mole <sup>-1</sup> × 10 <sup>-4</sup> )	$\overline{M}_w/\overline{M}_n$	ABA (%)	A(0.5B) (%)	A (%)
ISR	TR1101	9.74	14.50	1.49	70	26
	TR1102	8.34	11.30	1.36	75	22
	TR4113	10.90	14.30	1.31	75	24
	TR4122	10.80	13.90	1.29	72	24
	TR4113 Deplastified	9.80	13.20	1.35	68	28
Akron	TR1101	10.30	16.55	1.61	84.5	12
	TR1102	9.64	12.40	1.29	90	8.5
	TR4113	13.26	16.44	1.24	91.5	8
	TR4122	11.27	15.06	1.34	84.5	12

Since the three resolved peaks correspond to ABA, AB and homopolymer A, as shown in Figure 3.8, by measurement of the area under the curves, the relative proportions are deduced. The areas under the curves were measured accurately by means of a planimeter, and the results for each of the polymers are shown in Table 3.6.

### 3.3.3 Discussion

It is apparent from Tables 3.5 and 3.6 that precise agreement has not been achieved between data determined using different column systems. It should, however, be pointed out that experiments of this nature, where different instruments and operators are involved, invariably yield data with a higher degree of inconsistency than that which would be expected from one operator on a single instrument. Table 3.3 shows the permeability ranges of the four column systems used, and it can be seen that the ranges of pore size covered vary widely from instrument to instrument. When the chromatograms produced by the different instruments are compared (Figures 3.5 to 3.8), it becomes clear that a link exists between good resolution of the chromatogram and the choice of permeability range on the instrument. The chromatograms from Akron gave the best resolution, followed closely by those produced by the instrument at ISR. In both cases, the permeability ranges of the columns were fairly narrow and were chosen so that no large gaps in pore size existed over the range of molecular weights occurring in the materials under study. It follows that very careful judgement is necessary in the choice of columns and permeability range when GPC is to be used for a particular polymer.

Even though precise agreement was not achieved in these experiments, each instrument ranked the materials in the same order, giving a certain qualitative agreement. In fact, the data for number-average molecular weight, produced by Akron, ISR and Manchester, show remarkably close agreement, considering the different column systems used.

Although no data could be found in the literature for the average molecular weight,  $\bar{M}_n$ , determined by GPC, for the complete block polymer, some results have been quoted for the individual block lengths. The data for block molecular weights from this study are compared with the results of other workers in Table 3.8. The data for comparison is limited, but demonstrates the value of high resolution GPC (this work) compared with other (erroneous) determinations of  $\bar{M}_n$  for the pure triblock.

Other data obtained from GPC analysis concerns the polydispersity and polymeric impurity content of the triblocks. The results

TABLE 3.8

Centre and End Block Molecular Weights from Several Sources ( $\bar{M}_n$ )

Polymer	Block Molecular Weight/ $10^{-4}$ g.mole $^{-1}$					
	This Study		References [94,107]		Reference [80]	
	End block	Centre block	End block	Centre block	End block	Centre block
TR1101	1.35	12.90	1.1	5.4	1.7	6.8
TR1102	1.07	9.54	-	-	1.0	5.5

for polydispersity indicate a considerable molecular weight spectrum ( $\bar{M}_w/\bar{M}_n \approx 1.35$ ); the closer this ratio is to unity, the more monodisperse is the molecular weight. It is a simple matter to discover why the ratio is relatively high. Making reference to the GPC elution chromatograms in Figures 3.5 to 3.8 for TR4122 and Table 3.6, where the data for polymeric impurity are shown, the chromatograms indicate that substantial quantities of diblock polymer are present, with traces of low molecular weight styrene homopolymer. The presence of these impurities in commercial polymers is an indication that termination occurs during the sequential copolymerisation. Fetters [36] made a study of the impurity content of several Kratons, including 1101 and 1102, so that it is of interest to compare his results with those of the present work. Table 3.9 shows both sets of data for the 1101 and 1102 series of materials.

TABLE 3.9

Polymeric Impurity Comparison

Polymer	This Study (%)			Fetters et al [36] (%)		
	ABA	A $\frac{1}{2}$ B	A	ABA	A $\frac{1}{2}$ B	A
TR1101	84.5	12.0	3.5	82	18	0
TR1102	90.0	8.5	1.5	84	16	0

Again, good agreement is found between the results of this work and that quoted in the literature. This data is particularly interesting in that the polymers of this present study were actually run on Fetters' own GPC equipment. Since the publication of Fetters' work [36], however, two extra columns were added to the instrument, and this could account for the differences in the results. For instance, Fetters records no styrene homopolymer present but the chromatograms of Figures 3.5 to 3.8 reveal a substantial presence of this low molecular weight material.



### 3.4 COPOLYMER COMPOSITION AND STRUCTURE BY <sup>1</sup>H NMR

High resolution nuclear magnetic resonance (NMR) spectroscopy has become an important tool for the elucidation of copolymer composition and microstructure. Bovey, Tiers & Filipovich [37] first studied high resolution NMR of polymers in solution in 1959. Since that time, numerous articles [38-42] have been published dealing with NMR of various polymer systems. Chen [192,193] developed the technique for a quantitative compositional analysis of polymers by NMR, working on butadiene/isoprene copolymers. Senn [194] extended the method to the determination of structures in styrene, 1,2 butadiene and 1,4 butadiene in butadiene/styrene copolymers. More recently, large strides have been made by Morton et al [38-40] using more powerful equipment, providing higher resolution.

#### 3.4.1 The NMR Phenomenon

When the spin quantum number of a nucleus is  $\frac{1}{2}$  or greater, the nucleus possesses a magnetic moment. The proton is an example of such a nucleus. It has a spin of  $\frac{1}{2}$  and when placed in a magnetic field  $H_0$ , it can occupy either of two energy levels, corresponding to alignment of its magnetic moment,  $\mu$ , with or against the field. The two orientations differ in energy by:

$$\Delta E = h \nu_0 = 2\mu H_0 \quad (3.4)$$

where  $\nu_0$  is the frequency of the resonant radio-frequency field which causes transitions between these energy levels, and is also the rate at which the nuclear magnetic moments precess about the field direction, called the Larmor frequency. The quantity of energy  $\Delta E$  must be absorbed to raise the nuclei in the lower state up to the higher level, and is emitted in the reverse process. As equation (3.4) indicates,  $\nu_0$  is proportional to  $H_0$  and to  $\mu$ . For a field of 14,100 G,  $\nu_0 = 60$  MHz for protons. In a 23,400 G field,  $\nu_0 = 100$  MHz. These are the fields most commonly employed at present; however, instruments capable of 300 MHz are now available, enabling greatly increased resolution.

#### 3.4.2 Analysis of NMR Spectra

For the purpose of this discussion, there are three important features of a high resolution NMR spectrum.

- (a) Chemical shift: This is simply the position of a resonance peak in the NMR spectrum with respect to a reference signal given, for example, by tetramethyl silane (TMS) dissolved in the sample. The chemical shift is directly related to the electronic environment of the nucleus being studied, so that a certain type of proton will usually appear in the same region of the NMR spectrum and can often be identified as such.
- (b) Spin-spin coupling: This feature results from an indirect interaction of two or more protons through the bonds joining them. This is manifested in the spectrum by splitting of the resonances involved into multiplets. These multiplets and their separations can also be used to identify the protons giving rise to them. In polymer NMR spectra, this fine structure is often unobserved because of general broadening of the resonances, hence the requirement for greater resolution.
- (c) Intensities: If the NMR spectrum is obtained under "non-saturation" conditions, the area (intensity) under a resonance peak is directly proportional to the number of protons giving rise to the peak. Therefore, relative intensities of the various peaks can be used qualitatively and quantitatively in the analysis. Extreme care must be taken to assure that resonance signals are not saturated. Experimentally, this involves proper adjustment of  $H_0$ , the field strength, and the rate of sweeping through the spectrum.

These three features of the NMR spectrum supplement each other in the analysis. In the composition and structural analysis of polymers, NMR requires no external calibration. Each spectrum is self-calibrating. This gives a decided advantage over most other methods of analysis, including infra-red.

#### 3.4.3 The NMR Spectra

The data obtained in these laboratories was the result of experiments carried out on equipment with a 60 MHz field width, a Jeol C-60HL NMR spectrometer using carbon tetrachloride ( $\text{CCl}_4$ ) as solvent. However, with spectrometers of this field width, features in both the aliphatic and olefinic regions are not resolved. Therefore, although the 60 MHz results are quite adequate for the calculation of block content, their use in defining the microstructure of the polybutadiene centre block

is strictly limited. For this reason, it was necessary to resort to outside help in order to obtain spectra sufficiently well resolved to allow the butadiene to be analysed.

The 60MHz spectra for each material are shown in Figures 3.9 to 3.13. The spectrum for TR1102 was found to be similar in many respects to that for TR1101, and that for TR4122 was similar to TR4113. Figure 3.13 shows the spectrum for TR4113 after plasticiser removal by Soxhlet extraction.

Ignoring for the moment the complex situation in TR4113, centred at 1.0 ppm, caused by the plasticiser, all the peaks in the SBS polymers occur in the same positions relative to TMS. The assignment of the various peaks is indicated for TR1101 in Figure 3.9.

Figure 3.14 shows the spectrum for TR1101 at 100 MHz and an attempt has been made to resolve the aliphatic protons centred at 2.02 ppm. Even at this frequency, the peak remains unresolved. Other spectra run at 100 MHz showed little improvement over the 60 MHz results.

However, spectra obtained at 300 MHz have been shown capable of the resolution of the various aliphatic and olefinic proton environments in polybutadiene [38-40]. The spectrum for TR1101 is shown in Figure 3.15 and reveals complete resolution of both the aliphatic (2.0 ppm) and olefinic (5.4 ppm) proton peaks into the 1,2 and cis- and trans-1,4 components. The main features of the spectrum are indicated. All of the other materials run on the 300 MHz spectrometer were equally well resolved, making possible the analysis of the diene centre block in each one.

Figure 3.16 shows the expansion of the 1,4 aliphatic protons for TR1101 and, for the same material, Figure 3.17 presents the expanded 1,4 olefinic protons on the 300 MHz spectrometer using a sweep width of 250 Hz, increasing the resolution of the spectrum.

Figure 3.18 shows the spin-decoupled spectrum of the cis and trans resonances on an expanded scale. In this figure, the methylene resonances of the 1,4 units (and the methine resonance) are being irradiated, thus rendering the coupling with these protons unobservable. The vinyl protons are shifted out of the spectrum.

The six major peaks observed in the spectrum are essentially devoid of spin-spin coupling and can be assigned to isomeric triads. The six resonances are assigned as shown in Figure 3.18. The cis units are designated by c and the trans units by t. The peaks are assigned to the

olefinic protons of the central unit of the triads.

#### 3.4.4 Data Derived from NMR Spectra

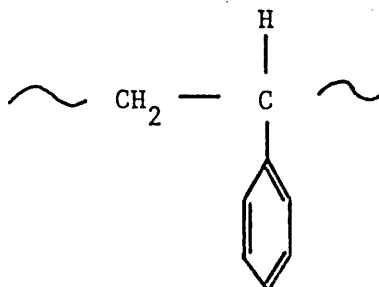
In order to calculate the polystyrene content of block copolymers from NMR spectra, it is necessary to separate the influence of the aromatic protons from that of the olefinic and aliphatic protons. Measurement of areas under the peaks would be necessitated, however, these measurements are supplied by the modern automatic spectrometers which provide an integration curve (Figure 3.10) in addition to the normal spectrum.

If  $A$  = area of aromatic protons, and  $B$  = total area for other protons, then for SBS copolymers:

$$\text{weight \% styrene } (\phi_w)_s = \frac{104(A/5)}{104(A/5) + 54((B - 3/5A)/6)} \times 100$$

The constants 104, 54 and 6 arise from the molecular weights of the styrene and diene units respectively:

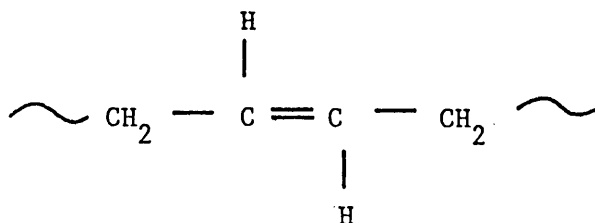
For polystyrene:



there are 8 carbon atoms and 8 hydrogen atoms in the molecule; therefore:

$$\begin{aligned} \text{molecular weight (styrene)} &= (8C + 8H) \\ &= 96 + 8 \\ &= 104 \end{aligned}$$

Similarly, for cis 1,4 polybutadiene there are 4 carbon,



and 6 hydrogen atoms in the molecule; hence, the molecular weight for butadiene is (4C + 6H) or (48 + 6) = 54.

Styrene content data for all the materials analysed are tabulated in Table 3.10. Only the spectra at 300 MHz were sufficiently well resolved to analyse the polydiene centre block structure. The results of this analysis are presented in Table 3.11 for the samples TR1101, TR1102, TR4113 and TR4122.

TABLE 3.10  
NMR Results at Different Frequencies Showing Styrene Content

Sample	Polystyrene Content Wt% ( $\phi_w$ ) <sub>s</sub>		
	60 MHz	100 MHz	300 MHz
TR1101	32	27	31
TR1102	29	26	28
TR1107	15	13	—
TR4113	20	—	22
TR4113 Deplasticised	32	—	31
TR4122	30	—	29
TR4122 Deplasticised	48	49	43

TABLE 3.11  
NMR Data at 300 MHz Showing 1,2 and 1,4 Butadiene (Cis and Trans) Contents

Sample	1,2 Butadiene (%)	1,4 Butadiene (%)	1,4 Trans (%)	1,4 Cis (%)
TR1101	9.8	90.2	47	53
TR1102	8.2	91.8	57	43
TR4113	10.2	89.8	56	44
TR4122	8.7	91.3	52	48

In order to calculate the volume fraction from the weight fraction, using the 300 MHz data, the following calculation was carried out:

$$\frac{V_S}{V} = (\phi_2)_S = \text{the volume fraction of styrene}$$

$$\frac{M_S}{M} = (X_2)_S = \text{the weight fraction of styrene}$$

$$\rho_S = \text{density of styrene (1.055 g cm}^{-3}\text{)}$$

$$\rho_B = \text{density of butadiene (0.90 g cm}^{-3}\text{)}$$

Now:

$$\begin{aligned} \frac{M_S}{M} = (X_2)_S &= \frac{\rho_S V_S}{\rho_S V_S + \rho_B V_B} \\ &= \frac{\rho_S V_S}{\rho_S V_S + \rho_B (V - V_S)} \end{aligned}$$

Rearranging, it can be shown that:

$$(\phi_2)_S = \frac{V_S}{V} = \frac{(X_2)_S \rho_B}{\{\rho_S - (X_2)_S (\rho_S - \rho_B)\}}$$

The results of this calculation for the materials of this study are shown in Table 3.12.

TABLE 3.12

Converting Weight Fraction Styrene to Volume Fraction for the 300 MHz Data

Material	Styrene Weight Fraction % at 300 MHz	Styrene Volume Fraction %
TR1101	31.0	27.7
TR1102	28.0	24.9
TR4122	43.0	39.0
TR4113	31.0	27.7

### 3.4.5 Discussion

Small variations in results obtained at different frequencies are indicated in the NMR data. The 60 MHz and 300 MHz spectrometers gave almost identical results for styrene content; the 100 MHz instrument consistently showed a slightly lower proportion.

Analysis of the data from the 300 MHz spectra reveals differences in the 1,2 and 1,4 cis and trans microstructure of the butadiene in different materials. The most significant being in TR1101, which appears to contain a significantly higher proportion of cis 1,4 rubber than the other materials (Table 3.11).

Comparing the data of this study with that quoted in the literature, it was found that other workers had used infra-red spectroscopy for the determination of centre block microstructure. Table 3.13 shows the results of this study compared with those of other workers. The data for comparison is again limited; however, good agreement is achieved, particularly in view of the fact that two different methods of analysis have been used.

TABLE 3.13  
Comparison of Styrene Content and Centre Block Microstructure Data  
with that of Other Workers

Polymer, Method and Source	Styrene (wt %)	Butadiene Microstructure		
		Trans 1,4	Cis 1,4	1,2
Kraton 1101 Infra-red (reference [80])	33	42	49	9
TR1101 NMR (this study)	31	48	42	10
Kraton 1102 Infra-red (reference [80])	26	48	44	8
TR1102 NMR (this study)	28	52	40	8

### 3.5 NETWORK PARAMETERS BY MICROSWELLING

Thermodynamic incompatibilities of the A and B sequences of block copolymers lead to microphase formation in the bulk polymer. The junction points between the A and B blocks are at or near the domain surface. Both ends of an elastomeric chain may terminate in the same polystyrene domain or in separate domains, and each domain is the terminal point for many elastomer chains. For instance, the average number of chains emanating from a spherical domain in a 15-100-15 block copolymer should be about 200. The domains therefore serve as cross-linking sites of very high functionality and give the elastomeric chain a continuous three-dimensional network character.

Interchain loopings or entanglements are an important feature of the network. Some entanglements do not contribute to the network since they disentangle upon extension of the network. On the other hand, many entanglements are topologically trapped and serve as tetra-functional cross-links for the network. It should be noted, also, that entanglements may render a chain elastically effective even if both ends of the chain terminate in the same domain.

The domains, because they are rigid, securely attached to the rubber network at many points on their surface, and have sizes of the order of a few hundred Ångströms, can serve a function comparable to that of reinforcing filler particles. With the entanglements serving as cross-links, the molecular configuration of the thermoplastic elastomer is then very similar to that of a conventional rubber vulcanizate containing reinforcing fillers.

#### 3.5.1 The Swelling Experiment

The swelling of fibres and films, particularly equilibrium swelling, has been studied extensively by many researchers because of its practical and theoretical importance; the technique has proved fruitful in the investigation of a large number of conventional rubber networks [195-198], and block copolymers have also proved amenable to the swelling approach [102,103,112,199].

Swelling solvents are restricted to those which can adequately swell the rubbery centre block forming the matrix, while leaving the polystyrene domains intact. Isooctane (2,2,4-trimethylpentane) has been found to be such a swelling agent for SBS block copolymers [102,112].

Films of the polymers were cast from several different solvent



systems (see Chapter 4) onto PTFE surfaces; discs approximately 5 mm in diameter were then die-cut from the films which were some 0.2 mm thick.

Swelling took place in small flat-bottomed glass dishes, as shown in Figure 3.19, the discs being immersed in isooctane and viewed using an overhead projection microscope. An image of the sample was obtained by shining light through the bottom of the dish, the image being focused onto the screen of the profile microscope where it could be measured by a moveable stage arrangement fitted to the base of the instrument. Floating and wrinkling of the specimens was prevented by weighting them with a glass microscope coverslip. Measurements were taken of the changing diameter of the specimen at convenient intervals over a 24 hour period, evaporation of the solvent being restricted by covering the dish with a sheet of glass.

This method, which is similar to that employed by Bishop & Davison [102], allows readings to be taken rapidly, and also gives the opportunity to view the magnified specimen ( $\times 20$  magnification) to assess the uniformity of the swelling. Swelling was noticeable immediately the solvent was introduced and increased rapidly for about 20 minutes, after which time changes in diameter generally occurred at a slower rate. Figure 3.20 shows the function  $D/D_0$  (where  $D$  is the instantaneous diameter of the specimen and  $D_0$  is the initial diameter) plotted versus swelling time for the four materials originally cast from a 90:10 solution of tetrahydrofuran:methyl ethyl ketone (THF/MEK). As shown in Figure 3.20, it was necessary to estimate the equilibrium swelling function,  $(D/D_0)_e$ , by the extrapolation of the two straight line portions of the curve, the point of intersection indicating equilibrium swelling [102,112]. Table 3.14 shows the equilibrium swelling data for all the materials used.

### 3.5.2 Analysis of Swelling Data

The concentration of elastically effective chains in the elastomeric block network can be calculated from the swelling ratios based on apparent equilibrium diameter by use of the well-known Flory-Rehner equation [102]:

$$v_e = -\frac{1}{v_s} \frac{\ln(1-v_r) + v_r + \chi v_r^2}{v_r^{1/3} - 2v_r/f} \quad (3.5)$$

where  $v_e$  = the concentration of elastically effective chains

$v_s$  = molar volume of the solvent

TABLE 3.14

Equilibrium Swelling Data for 1101, 1102, 4113 and 4122 in Isooctane

Material	Casting Solvent	$D_o$	$(D)_e$	$(D/D_o)_e$
TR1102	90/10 tetrahydrofuran/ methyl ethyl ketone (THF/MEK)	5.392	7.258	1.346
TR1101		5.321	6.625	1.245
TR4113		5.424	6.482	1.195
TR4122		5.386	5.521	1.025
TR1102	90/10 benzene/heptane (BEN/HEP)	5.280	6.711	1.271
TR1101		5.342	6.517	1.220
TR4113		5.447	6.678	1.226
TR4122		5.337	5.470	1.025
TR1102	carbon tetrachloride ( $CCl_4$ )	5.439	7.016	1.290
TR1101		5.356	6.834	1.276
TR4113		5.336	6.419	1.203
TR4122		5.364	5.439	1.014

$\chi$  = interaction parameter of polymer-solvent system

$f$  = the functionality of cross-links

and  $v_r$  = the volume fraction of rubber in the swollen network

The applicability of the Flory-Rehner equation to thermoplastic elastomers should be examined considering a number of pre-conditions [102]:

- (a) That the swelling of the diene centre block is governed by the interaction parameter of the corresponding homopolymer-solvent system. In fact, the interaction parameter may well differ for the thermoplastic elastomer owing to phase-separation. However, any quantitative error introduced by the assumption should not detract from the conclusions.
- (b) Swelling of the styrene end block is insignificant. Experiments [102] have shown that isooctane does not swell polystyrene to any significant extent.
- (c) The centre block is continuous (the matrix) and the end block is discrete. From evidence provided by electron microscopy, this condition is reasonably satisfied, except perhaps for three-dimensional arrangements of interconnected rods or lamellar structures.
- (d) Effective cross-links are primarily tetrafunctional. This assumption is based on the conjecture that the main source of effective cross-links is the interlooping type of entanglement.

- (e) That there is an insignificant number of free ends. This is patently not met by a commercial block copolymer since a significant amount of diblock and homopolymer is present in the system. However, for the application of the Flory-Rehner equation, this point need not be met. What must be noted is that the Flory-Rehner equation yields the concentration of elastically effective cross-links. If it is required to identify this quantity with the total concentration of cross-links, then some correction factor, which accounts for the non-effective cross-links is necessary [101,112].

$v_r$  is calculated using the equation:

$$v_r = (1 - (\phi_2)_S) D_o^3 / (D^3 - (\phi_2)_S D_o^3) \quad (3.6)$$

where  $v_r$  = the volume fraction of rubber in the swollen centre block

$D_o, D$  = the diameters of the unswollen and swollen samples, respectively

$(\phi_2)_S$  = the volume fraction of end block in the polymer, calculated from NMR and the densities of the corresponding homopolymers (for this calculation, see section 3.4.4)

In the derivation of this equation, it was assumed that the swelling was exclusively in the diene centre block. It should also be pointed out that uniformity of swelling is implicit in the use of the equation.

The value of the relevant polymer-solvent interaction parameter was taken from work by Bishop & Davison [102] and Kraus [200]:

$$\chi = 0.406 + 0.522 v_r \quad (3.7)$$

Having used the Flory-Rehner equation (3.5) to determine  $v_e$ , the concentration of elastically effective cross-links, it was possible to use the relation:

$$M_c = \frac{\rho_B}{v_e} \quad (3.8)$$

to calculate  $M_c$ , the molecular weight between cross-links. In this

equation,  $\rho_B$  is the density of the diene centre block ( $0.90 \text{ g cm}^{-3}$ ), and  $v_e$  for the pure triblock was obtained by dividing the apparent  $v_e$  by the triblock fraction determined from GPC analysis (section 3.3.2.2) [102]. Table 3.15 shows the  $M_c$  values obtained by this analysis for the SBS materials used in this study.

TABLE 3.15  
 $M_c$  Data for the SBS Materials Cast from Different Solvents

Material	Casting Solvent	$M_c$ Corrected For % ABA
TR1101	THF/MEK	7170
	CCl <sub>4</sub>	9230
	BEN/HEP	5620
TR1102	THF/MEK	12900
	CCl <sub>4</sub>	8980
	BEN/HEP	7790
TR4113	THF/MEK	4500
	CCl <sub>4</sub>	4900
	BEN/HEP	6200
TR4122	THF/MEK	150
	CCl <sub>4</sub>	90
	BEN/HEP	150

### 3.5.3 Discussion

The swelling experiments produced some interesting results. Materials TR1101, 1102 and 4113 all showed a considerable propensity to swell in isooctane, but with TR4122 virtually no swelling occurred at all. TR4122 is, of course, the plasticised high styrene polymer, which was expected to show a higher resistance to swelling than the other materials; even so, one might intuitively have expected more reaction than was evident in this case. However, from Uchida et al [112], block polymers with styrene contents of over 44% indicated very low  $M_c$  with little swelling (TR4122 contains some 48% styrene). From the results in Table 3.15, it is obvious that the value of  $M_c$  determined by swelling for each material is far smaller than  $\bar{M}_n$  for the middle block segment (Table 3.7) determined

by GPC. A further correction may be made for the filler effect of the dispersed styrene component, in which the butadiene centre blocks are anchored, although the correction is not large enough to make  $M_c$  and  $\bar{M}_n$  comparable. From the Kraus equation [101]:

$$v_{ro}/v_r = 1 - \{3C (1-v_{ro}^{1/3}) + v_{ro} - 1\} \phi_2/(1-\phi_2) \quad (3.9)$$

where  $C$  is a constant and  $v_{ro}$  is the true volume fraction of rubber in the swollen network. A linear relationship should exist between  $1/v_r$  and  $\phi_2/(1-\phi_2)$ ; this is shown plotted in Figure 3.21 for these polymers, and also for data from Bishop & Davison [102] on SBS polymers of varying block lengths, the SIS data is taken from Uchida et al [112]. In each case, the linear relationship holds fairly well, and, although the slopes of the lines are different, the intercepts on the  $1/v_r$  axis at  $\phi_2/(1-\phi_2) = 0$  is almost precisely the same, and is taken as 3.75. Using the value of  $v_{ro}$ , thus derived, in place of  $v_r$  in equations (3.5) and (3.7), a corrected  $M_c$  of 16000 is calculated which is identical to the value obtained by Bishop & Davison [102]. This value, although lower than  $\bar{M}_n$  for the centre block, is close to values observed for normal entanglement lengths in the homopolymer. If the further refinement of correcting for the proportion of triblock present is made, then  $M_c$  is recalculated to be 23000.

### 3.6 THE PLASTICISER

Two of the materials used in this work (TR4122 and TR4113) were known to contain a plasticising agent, and it was thought worthwhile to attempt to ascertain the proportion of plasticisers in the material, and also to identify the type used.

Plasticiser was removed from the raw polymer by the leaching process known as Soxhlet extraction. The samples were repeatedly soaked in hot methanol which automatically syphoned off at frequent intervals. The process was allowed to run for 96 hours, at the end of which time no trace of plasticiser was indicated by NMR tests on the samples, as shown in Figures 3.12 and 3.13 for TR4113 before and after deplasticisation.

When the methanol had been distilled off, the appearance of the plasticiser residue was of a colourless liquid with oily globules floating on its surface. An infra-red spectrum showed several peaks which were typical of a saturated aliphatic hydrocarbon. A further small peak indicated the presence of a  $C = O$  (ester) group.

The proportion of plasticiser in the original polymer samples was determined by weighing before and after extraction, and by weighing the plasticiser residue. TR4122 was found to contain 35% plasticiser and TR4113 had 31% by weight.

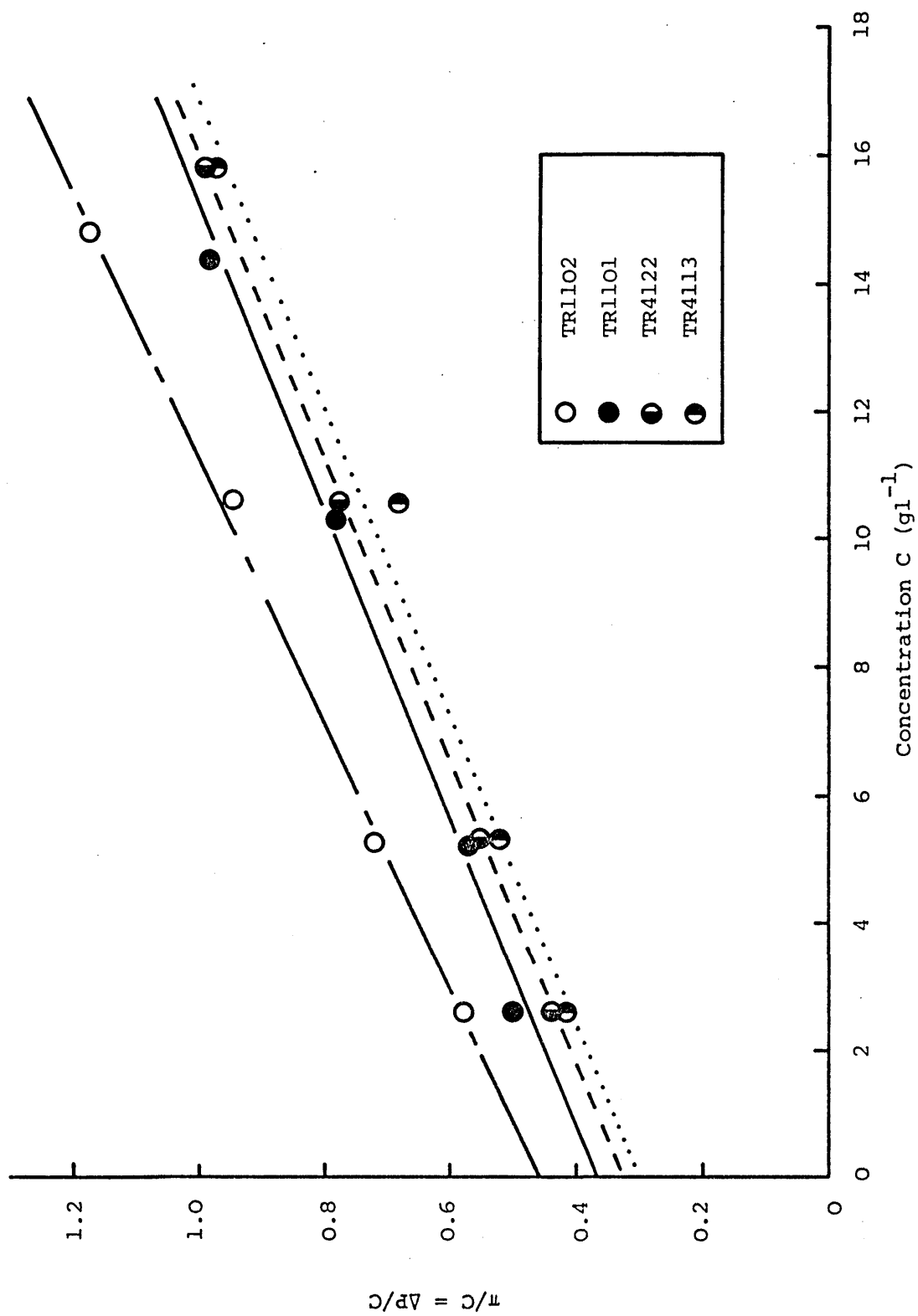


Figure 3.1 Results from membrane osmometer.

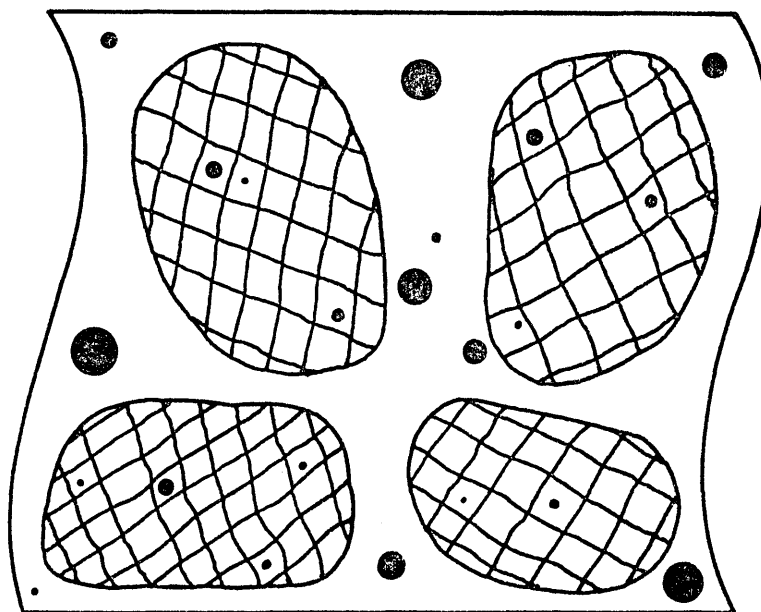


Figure 3.2 Longitudinal section of a chromatographic column containing a porous gel matrix and dissolved polymer molecules (schematic).



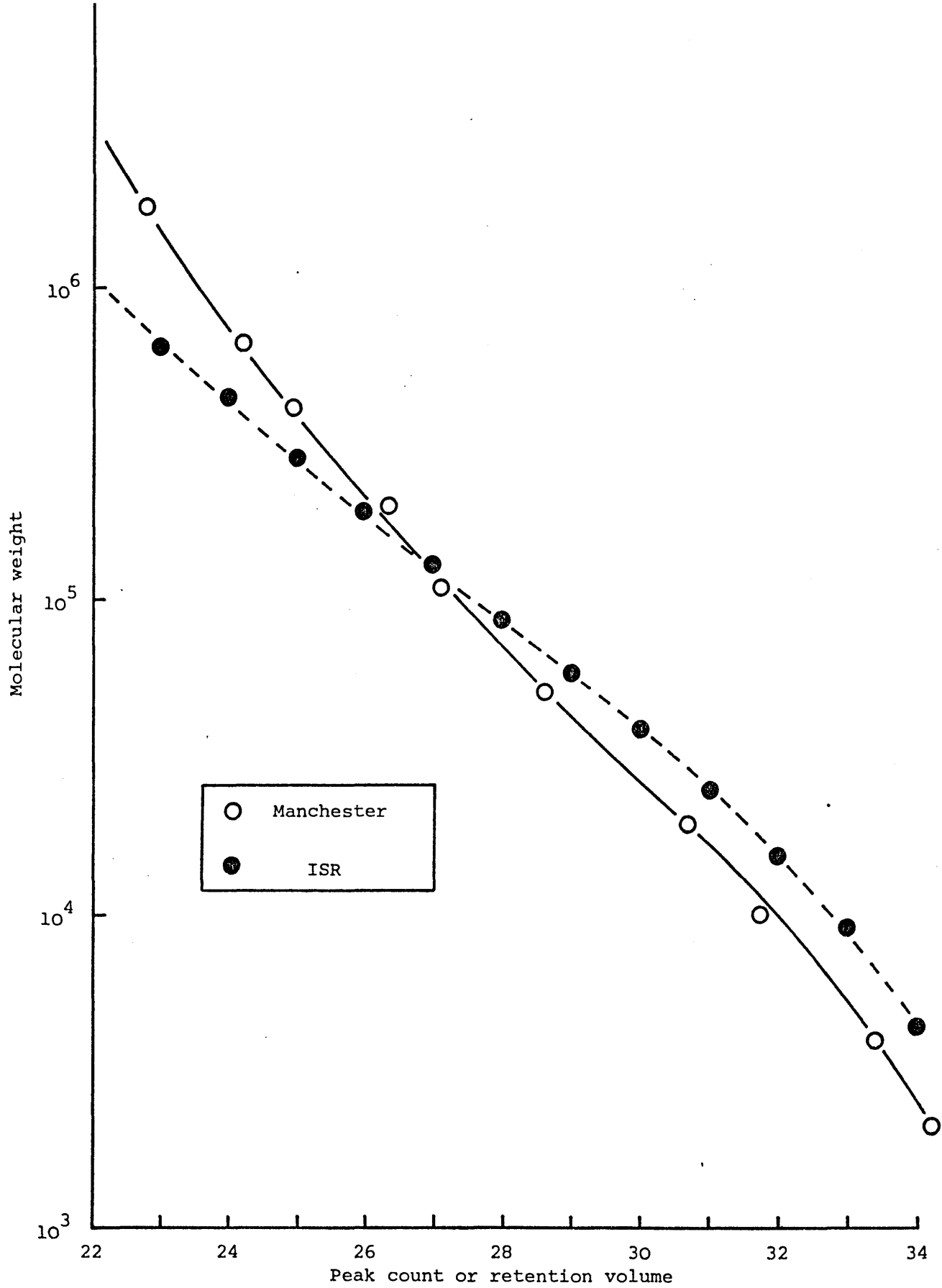


Figure 3.3 GPC polystyrene calibration.

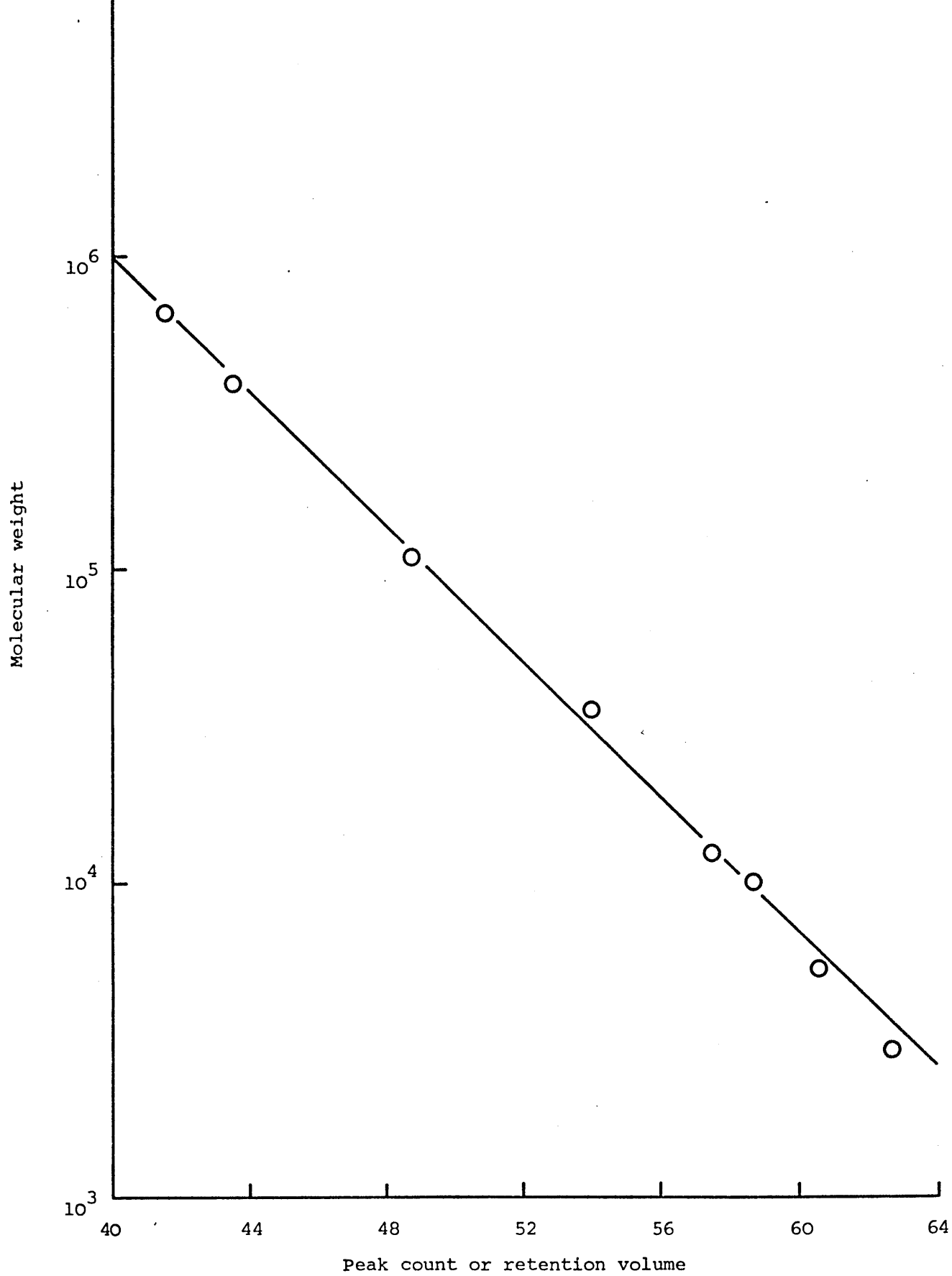


Figure 3.4 GPC calibration curve from Akron.

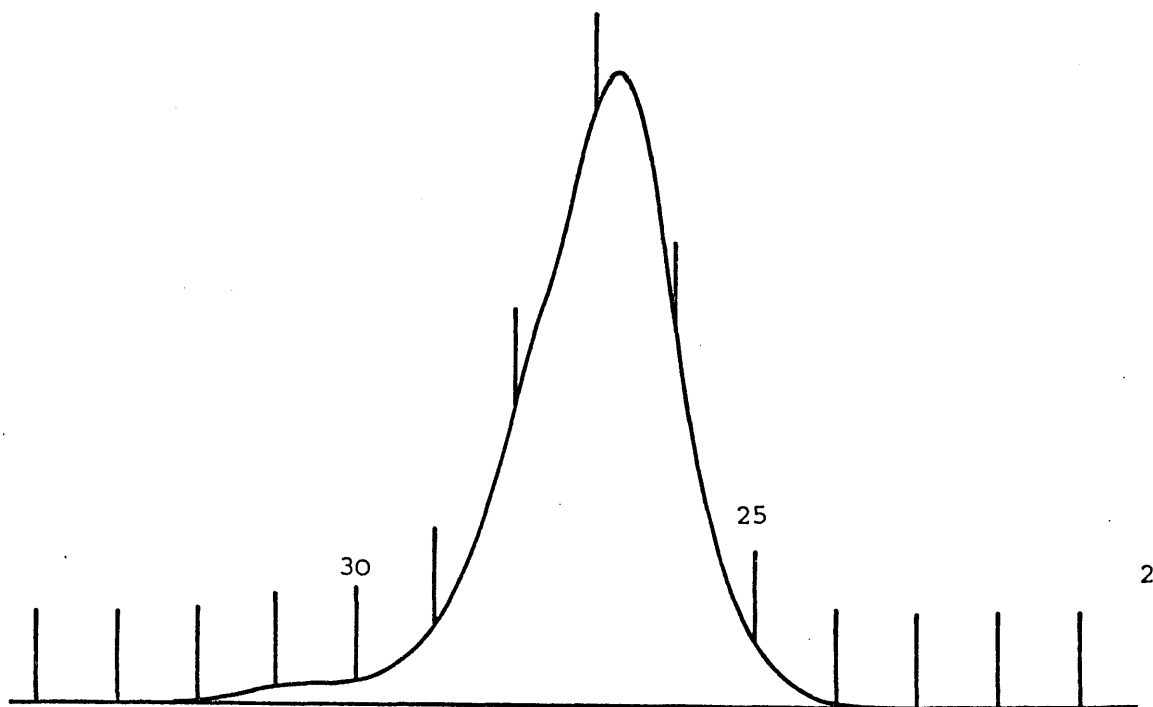


Figure 3.5 GPC curve for TR 4122 - Manchester.

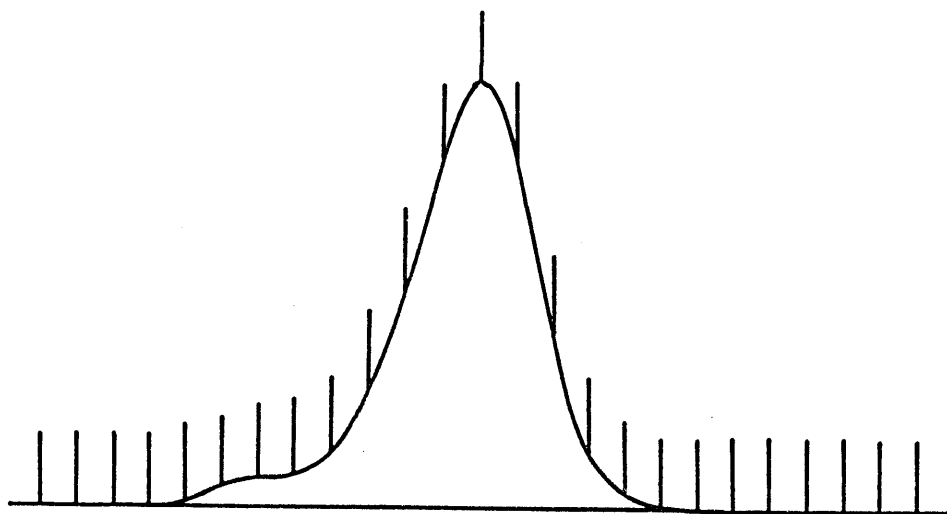


Figure 3.6 GPC curve for TR 4122 - RAPRA.

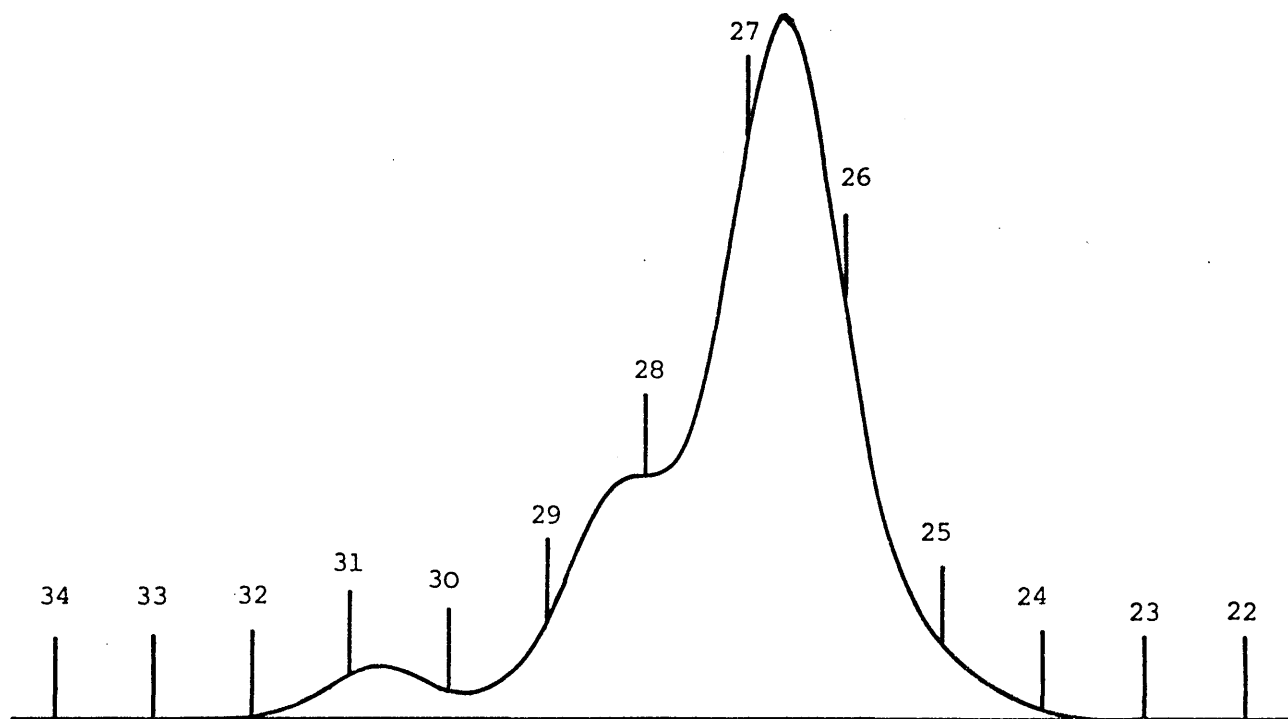


Figure 3.7 GPC curve for TR 4122 - ISR.

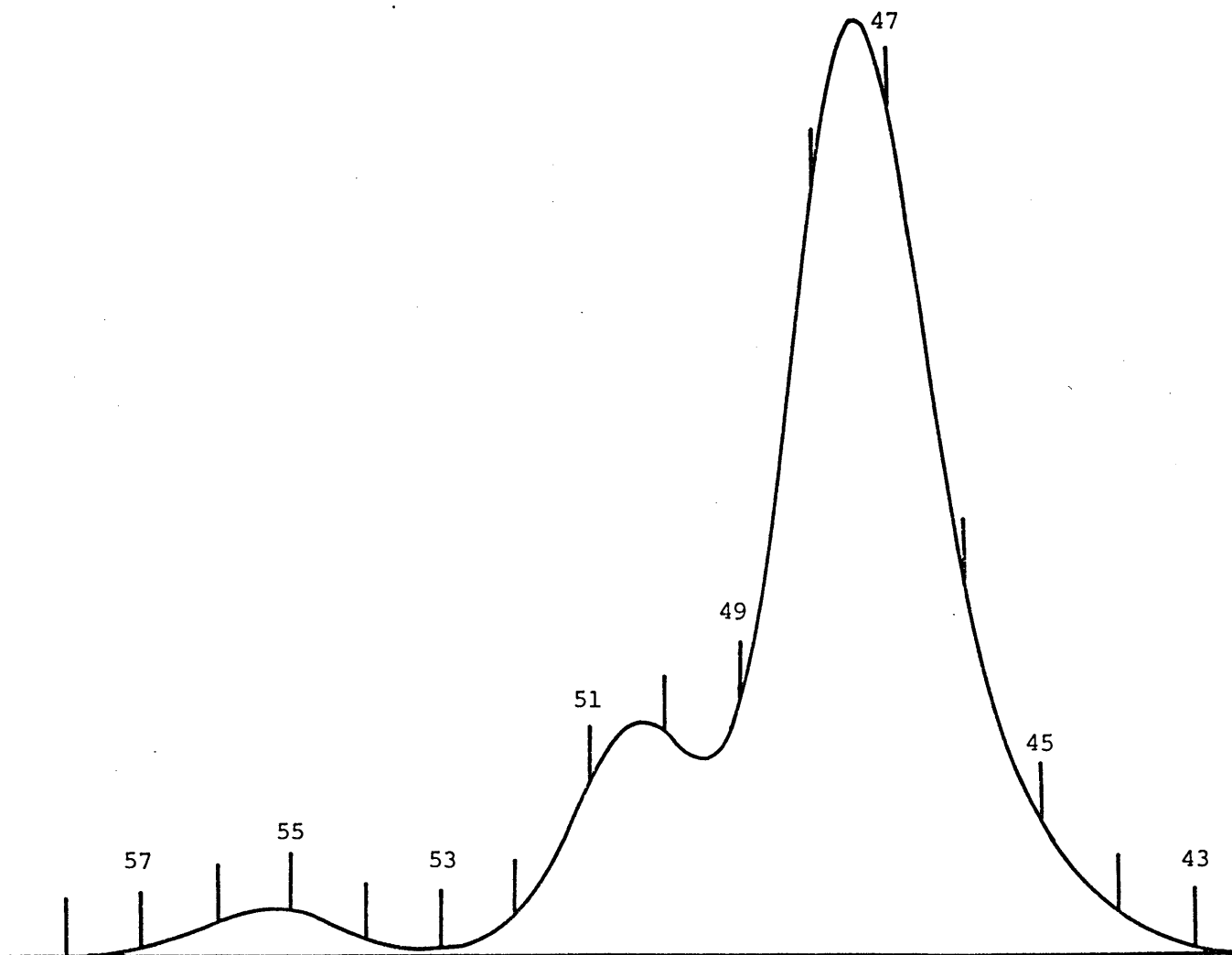


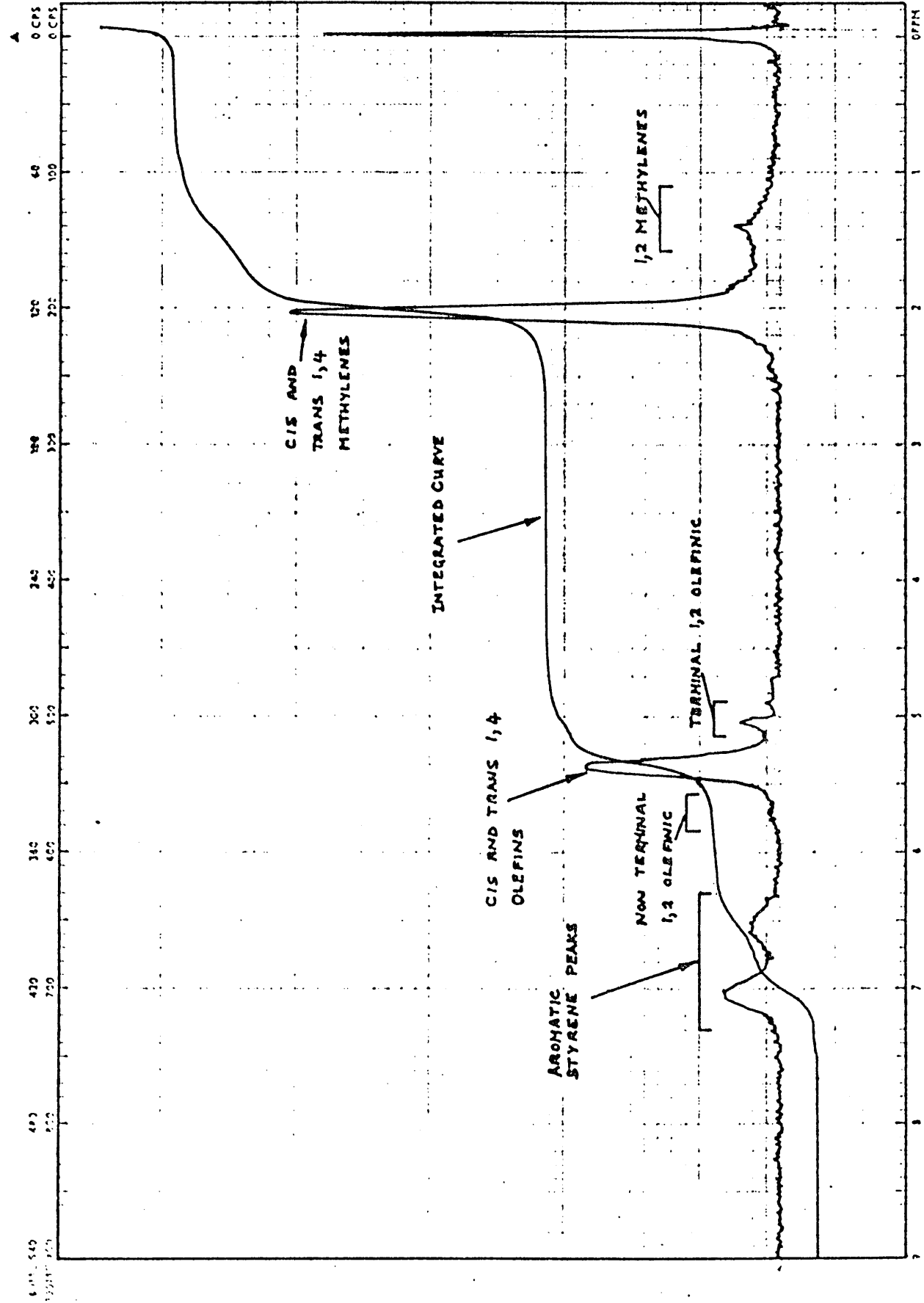
Figure 3.8 GPC curve for TR4122 - Akron.

SPECTRUM NO. 1160  
 DATE 10/11/72  
 FREQ. 60 MHz  
 NUCLEUS <sup>13</sup>C  
 SAMPLE KIEHL  
 RND

SOLVENT CCl<sub>4</sub>  
 CONC. 100%  
 REFERENCE TMS  
 LOCK 100%  
 TEMP. 25°C  
 R.F. LEVEL 100%  
 R.F. GAIN 3  
 A.F. LEVEL 100%  
 A.F. GAIN 10  
 VAR. FREQ. 100%  
 RESPONSE 100%  
 SWEEP 100%  
 WIDTH 100%  
 TIME 2.5  
 OFFSET 0  
 OPERATOR J.E.O.  
 REMARKS

SWEEP WIDTH 100%  
 SCALED BY 1  
 GAIN BY 1  
 OFFSET BY 1  
 SCALED BY 1  
 GAIN BY 1  
 OFFSET BY 1

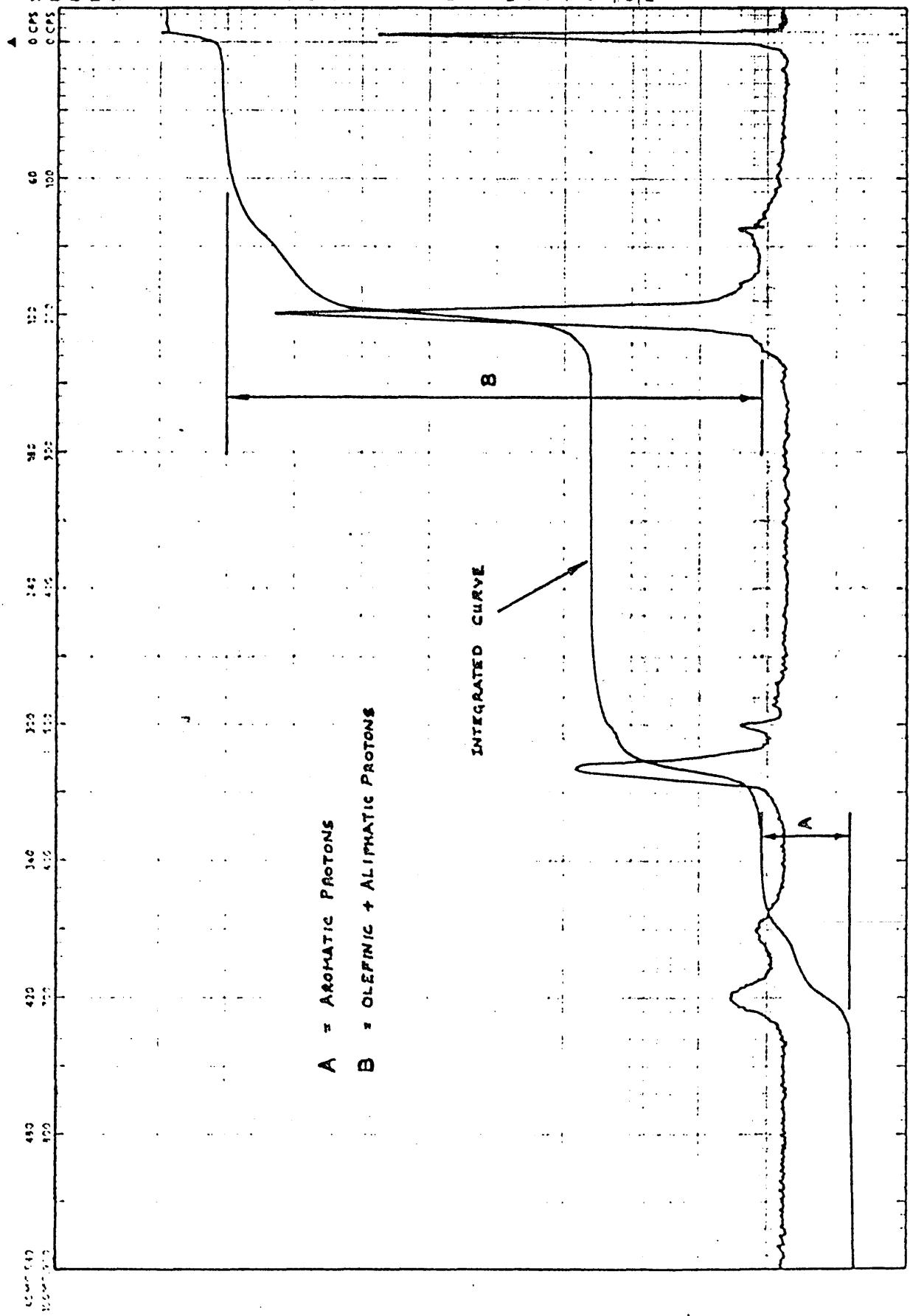
JEOL  
 JNM-FX 100  
 JNM-FX 100



SPECTRUM NO. 168  
DATE 11/17  
FREQ 154.4  
NUCLEUS 117  
SAMPLE ANALYST 11/17

SOLVENT	CCl <sub>4</sub>
CONC.	—
REFERENCE	MS
LOCK	EXT
TEMP.	RT
R.F. LEVEL	20
R.F. GAIN	5-10
A.F. LEVEL	—
IND. FREQ.	—
VARI. FREQ.	—
A.F. GAIN	10-15
RESPONSE	1
SLEEP	—
WIDTH	9x
TIME	3.5
OFFSET	—
REL. SENSITIVITY	100
OPERATOR	PC
REMARKS:	

AND / S&C) ALIQUOT DEPARTS	DATE	TIME	1	2
	1/10/75	11:12		
	1/10/75	11:12		
	1/10/75	11:12		
	1/10/75	11:12		





204W(A) 3810

SPECTRUM No.

DATE

FREQ.

NUCLEUS

SAMPLE K4122

SOLVENT

CONC.

REFERENCE

LOCK

TEMP.

R.F. LEVEL

R.F. GAIN

A.F. LEVEL

FIXED FREQ.

VARI. FREQ.

A.F. GAIN

RESPONSE

SWEEP

WIDTH

TIME

OFFSET

FREQ. FIELD/FREQ. FIELD

OPERATOR

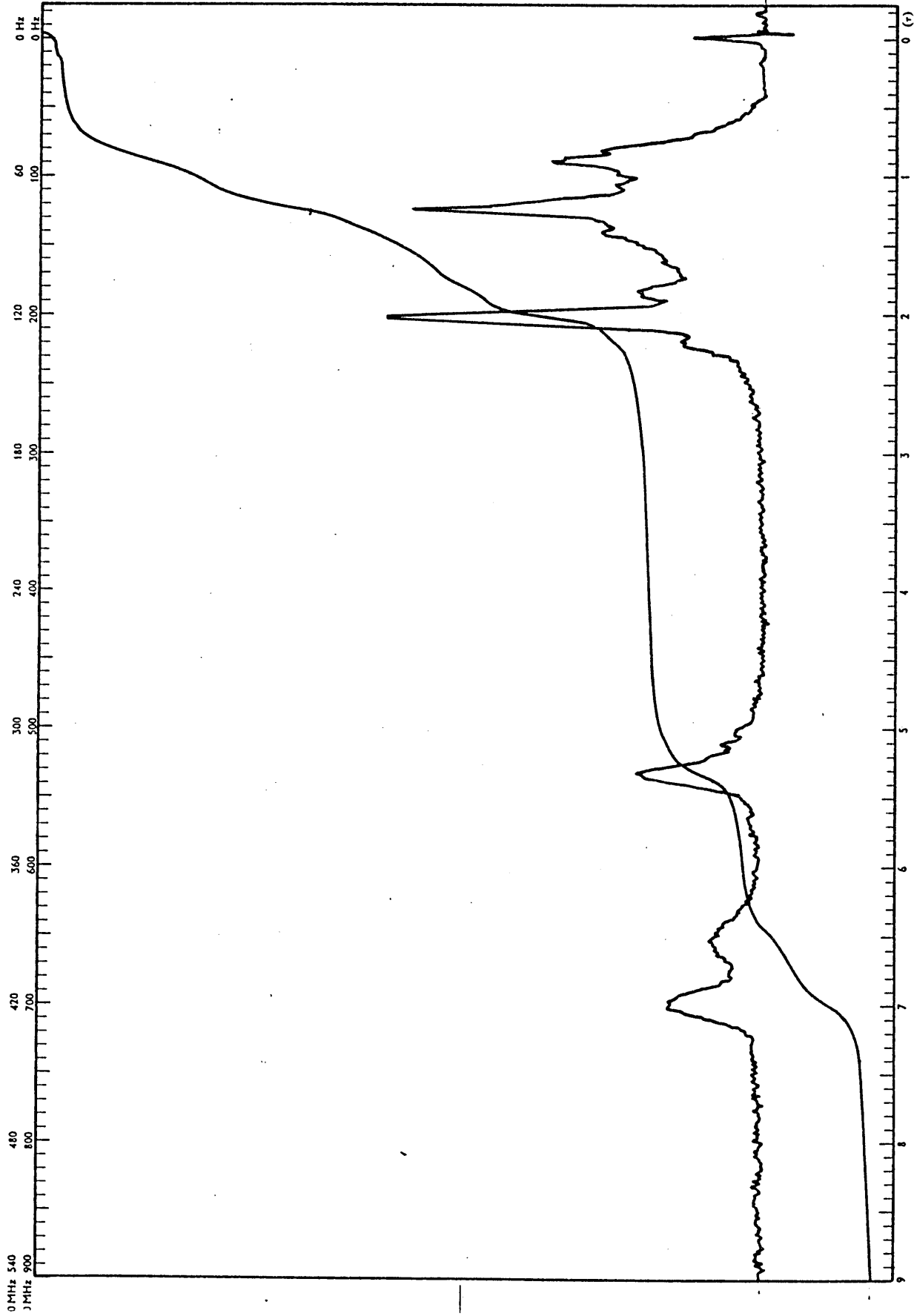
REMARKS

Ref. 41-A

SENSITISED COATINGS LTD.

COULDSOM, SURREY

Prod 346



67

0 CPS SPECTRUM No. 1677  
 0 CPS DATE  
 FREQ

NUCLEUS  
 SAMPLE

DATE

JEOL

4P

JEOL

JEOL

JEOL

JEOL

JEOL

JEOL

JEOL

JEOL

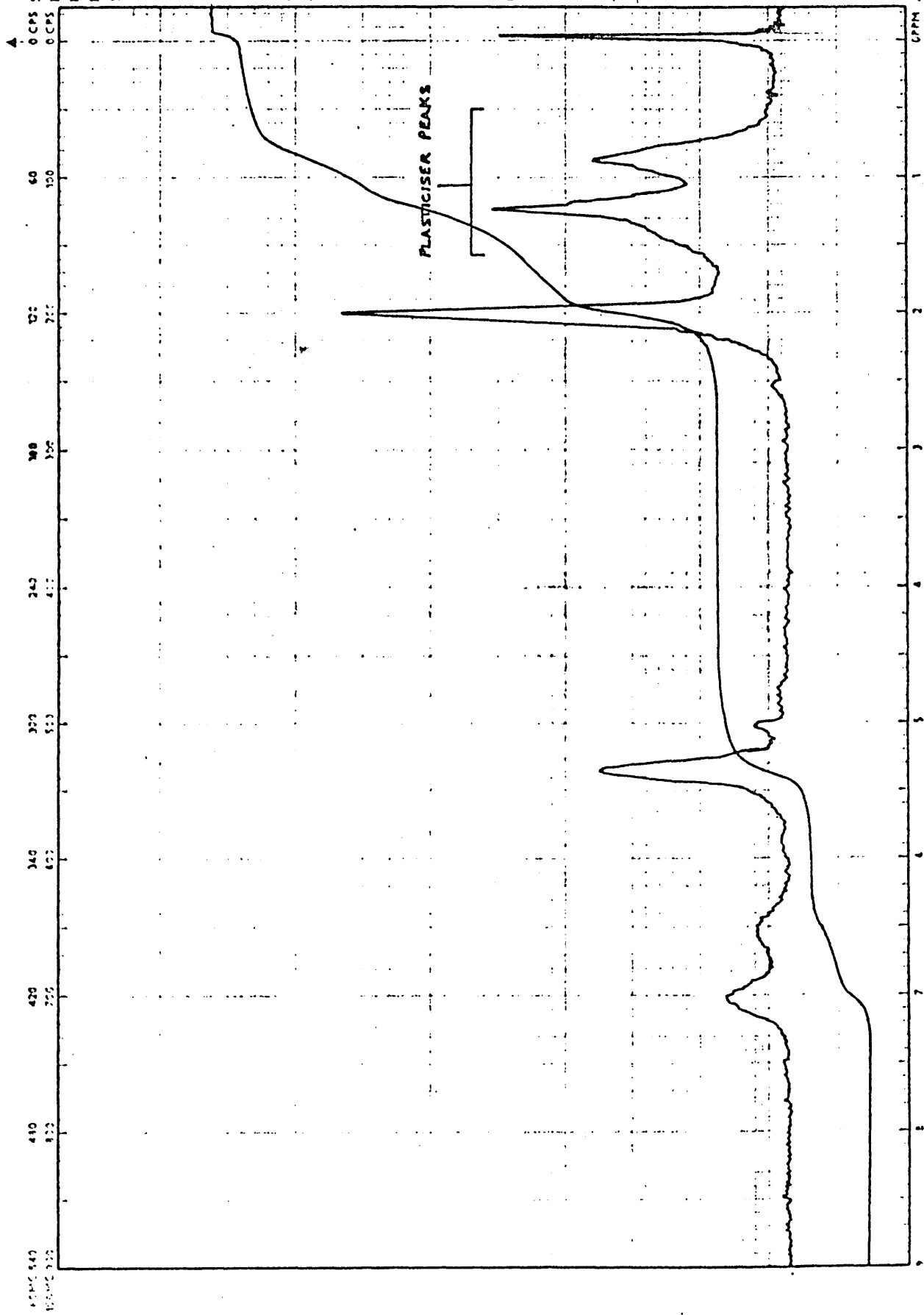
JEOL

JEOL

JEOL

JEOL

JEOL



PLASTICISER PEAKS

0 CPS SPECTRUM NO. 173  
 DATE \_\_\_\_\_

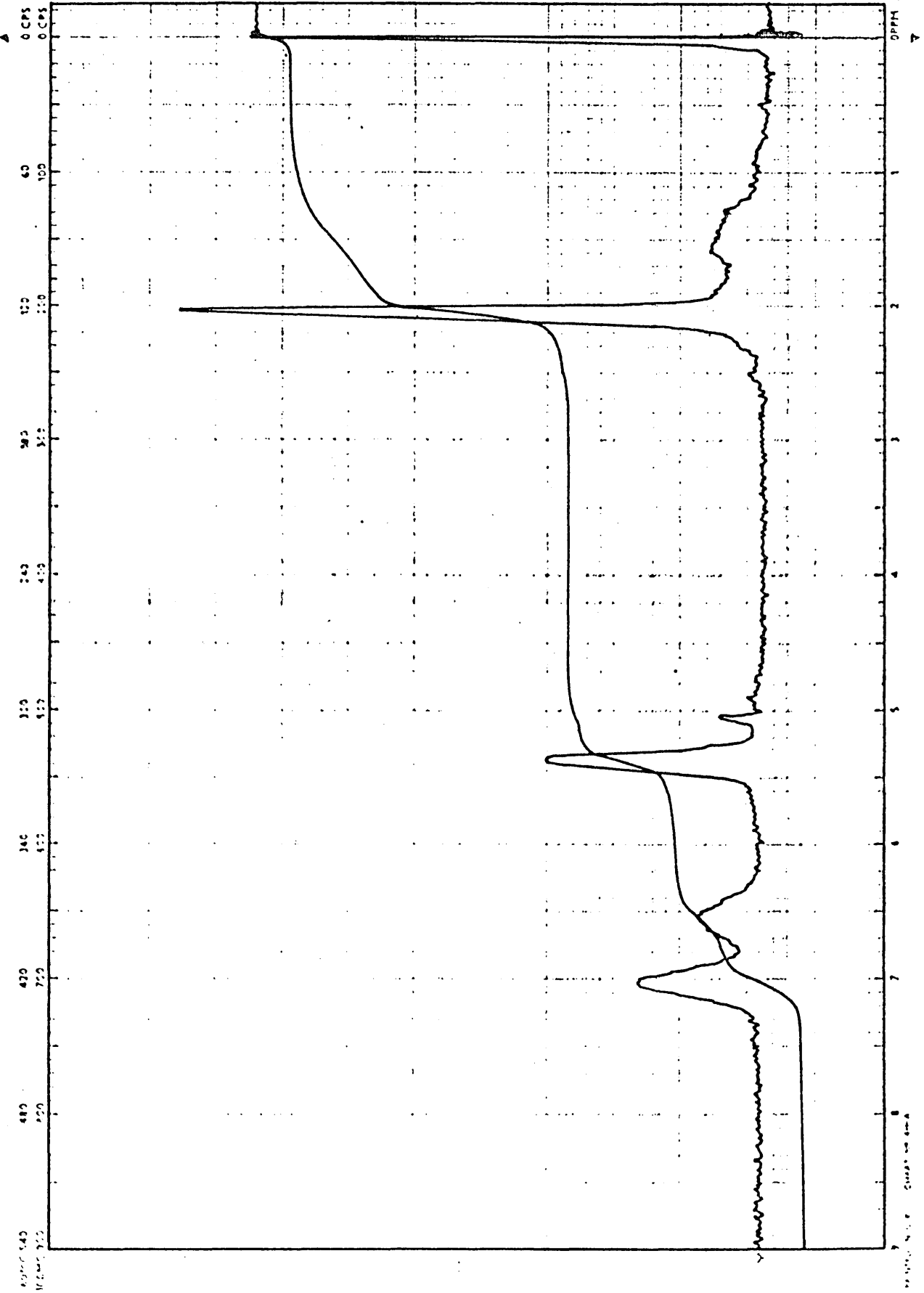
NUCLEUS \_\_\_\_\_  
 SAMPLE 173  
*hydrocarbons*  
*and*  
*isomers*

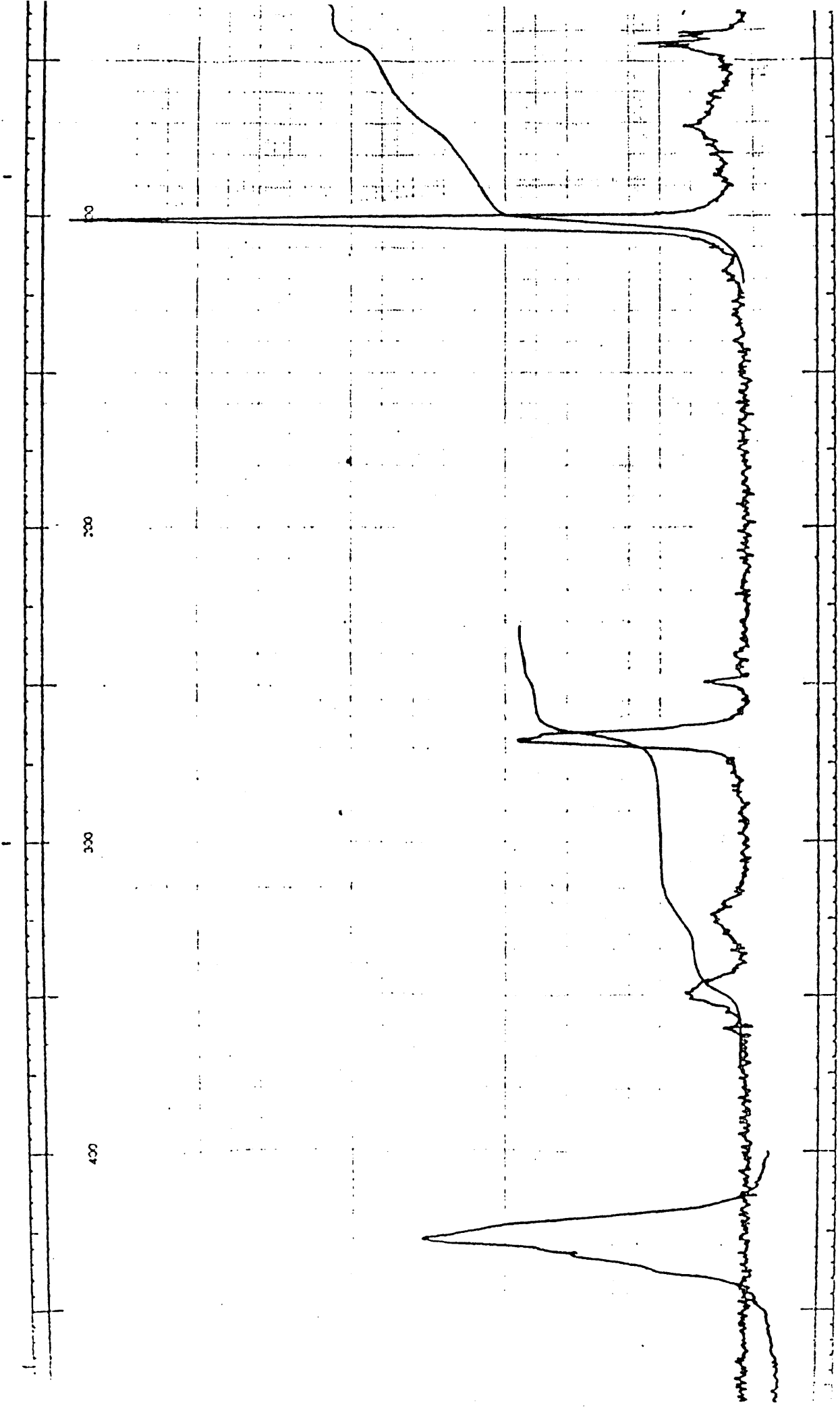
SOLVENT \_\_\_\_\_  
 CONC. \_\_\_\_\_  
 REFERENCE \_\_\_\_\_  
 LOCK \_\_\_\_\_  
 TEMP. \_\_\_\_\_  
 R.F. LEVEL \_\_\_\_\_  
 R.F. GAIN \_\_\_\_\_  
 A.F. LEVEL \_\_\_\_\_  
 FIXED FREQ \_\_\_\_\_  
 VAR FREQ \_\_\_\_\_  
 A.F. GAIN \_\_\_\_\_  
 RESPONSE \_\_\_\_\_  
 SWEEP \_\_\_\_\_  
 WIDTH \_\_\_\_\_  
 TIME \_\_\_\_\_  
 OFFSET \_\_\_\_\_

FREQ. FIELD FREQ. FID  
 OPERATOR LUC  
 REMARKS \_\_\_\_\_

SWEEP WIDTH (KHZ)  
 100 200 300 400 500 600 700 800 900 1000  
 1000 2000 3000 4000 5000 6000 7000 8000 9000 10000

JEOL  
 JNM-FX 100  
 TOKYO JAPAN





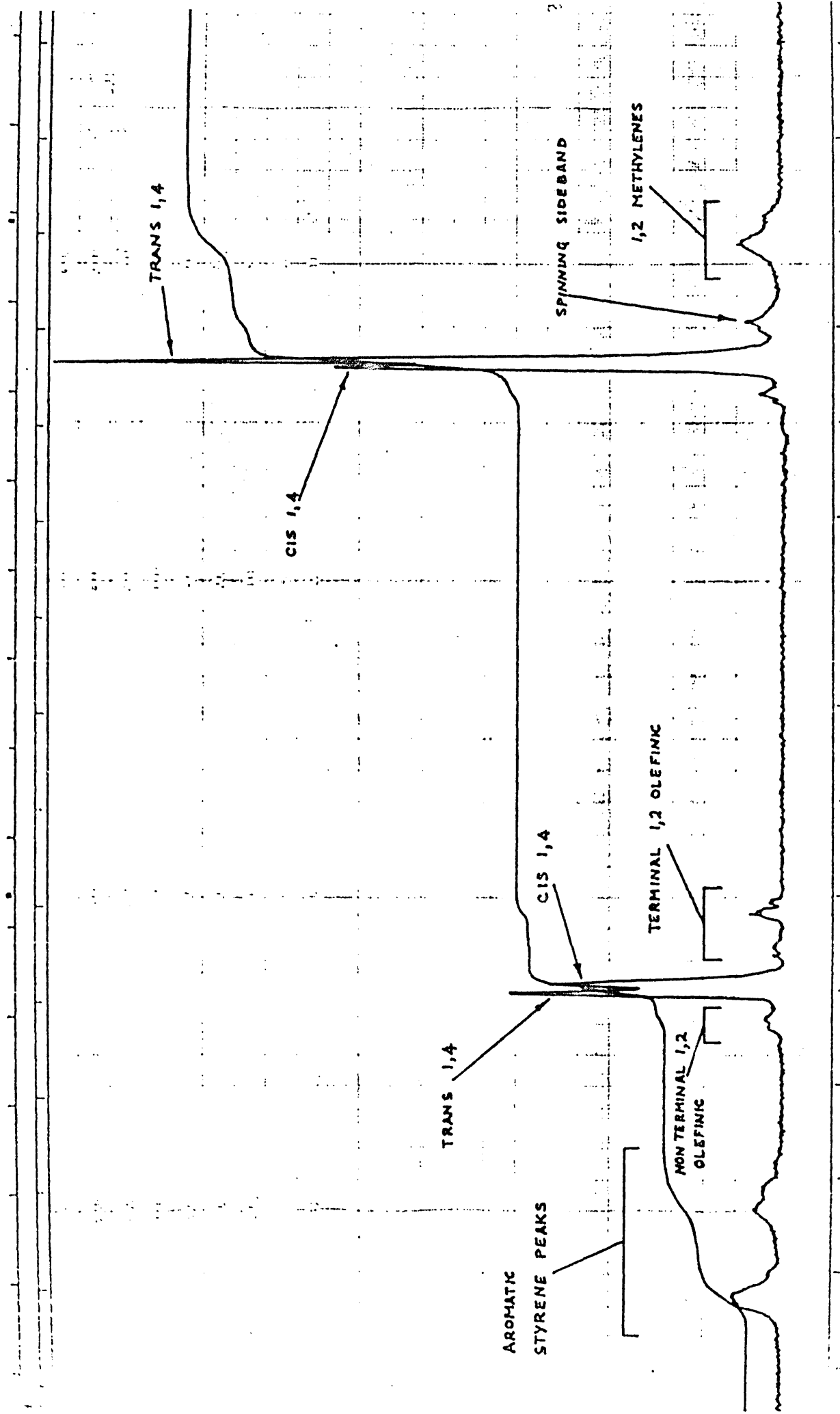
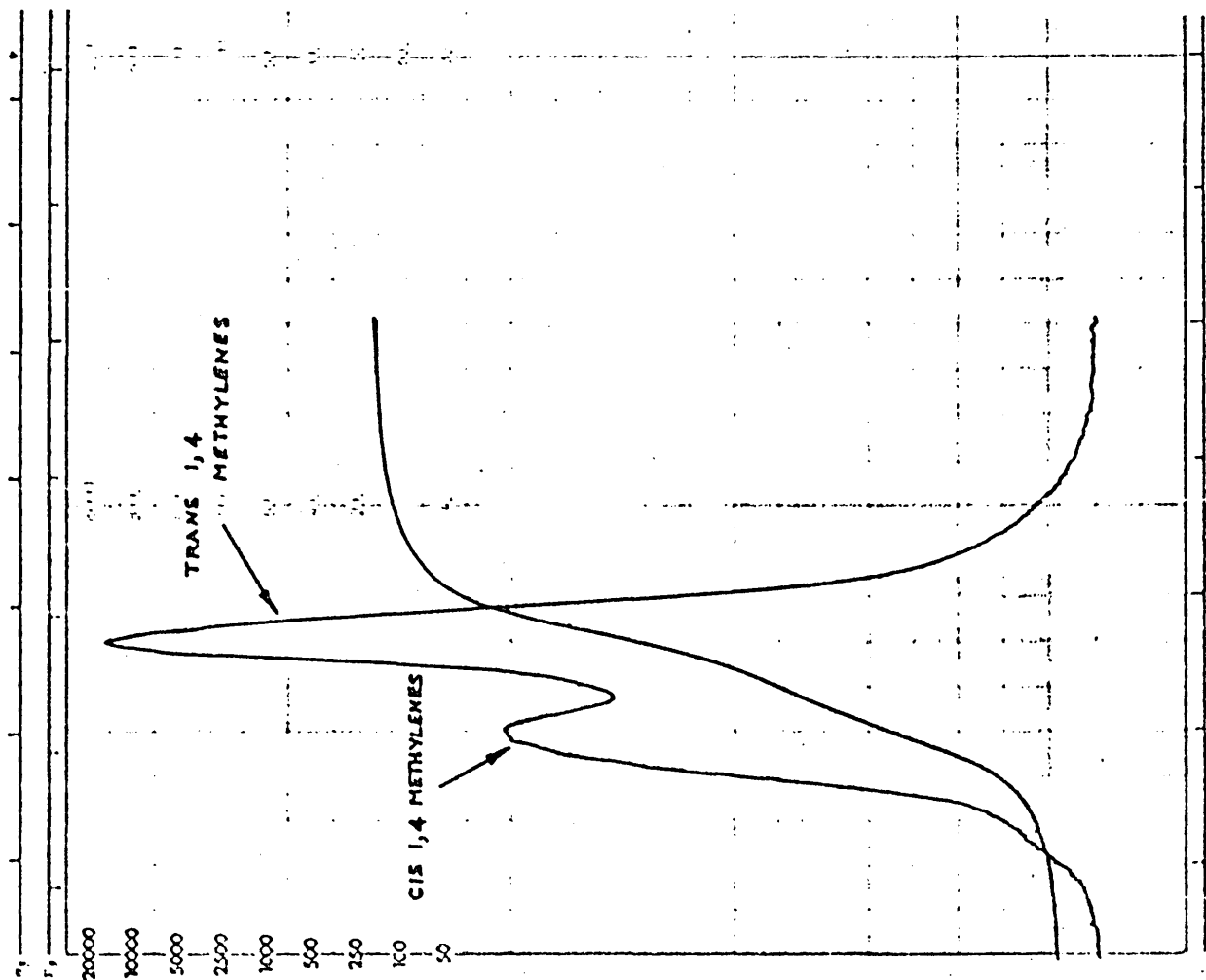
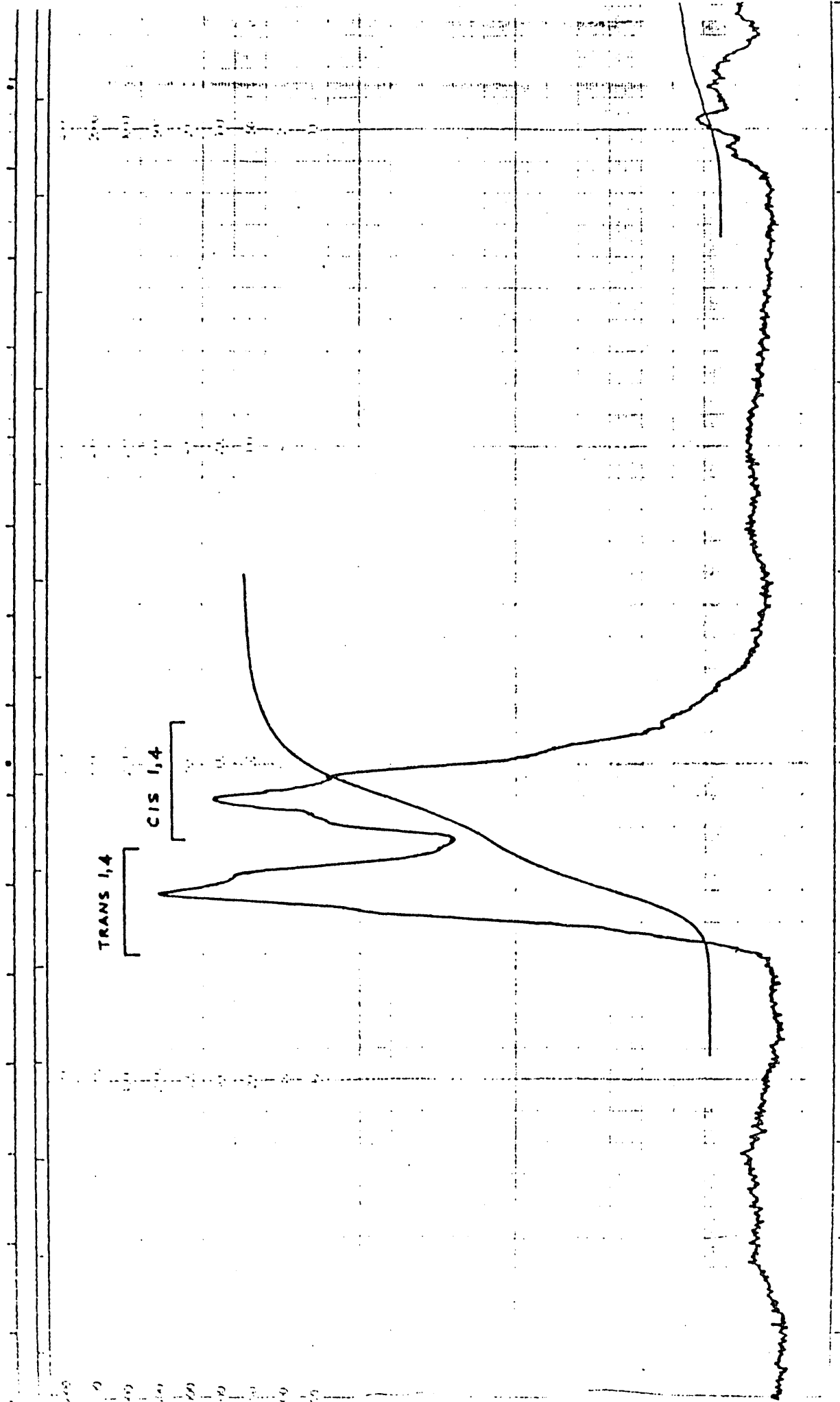
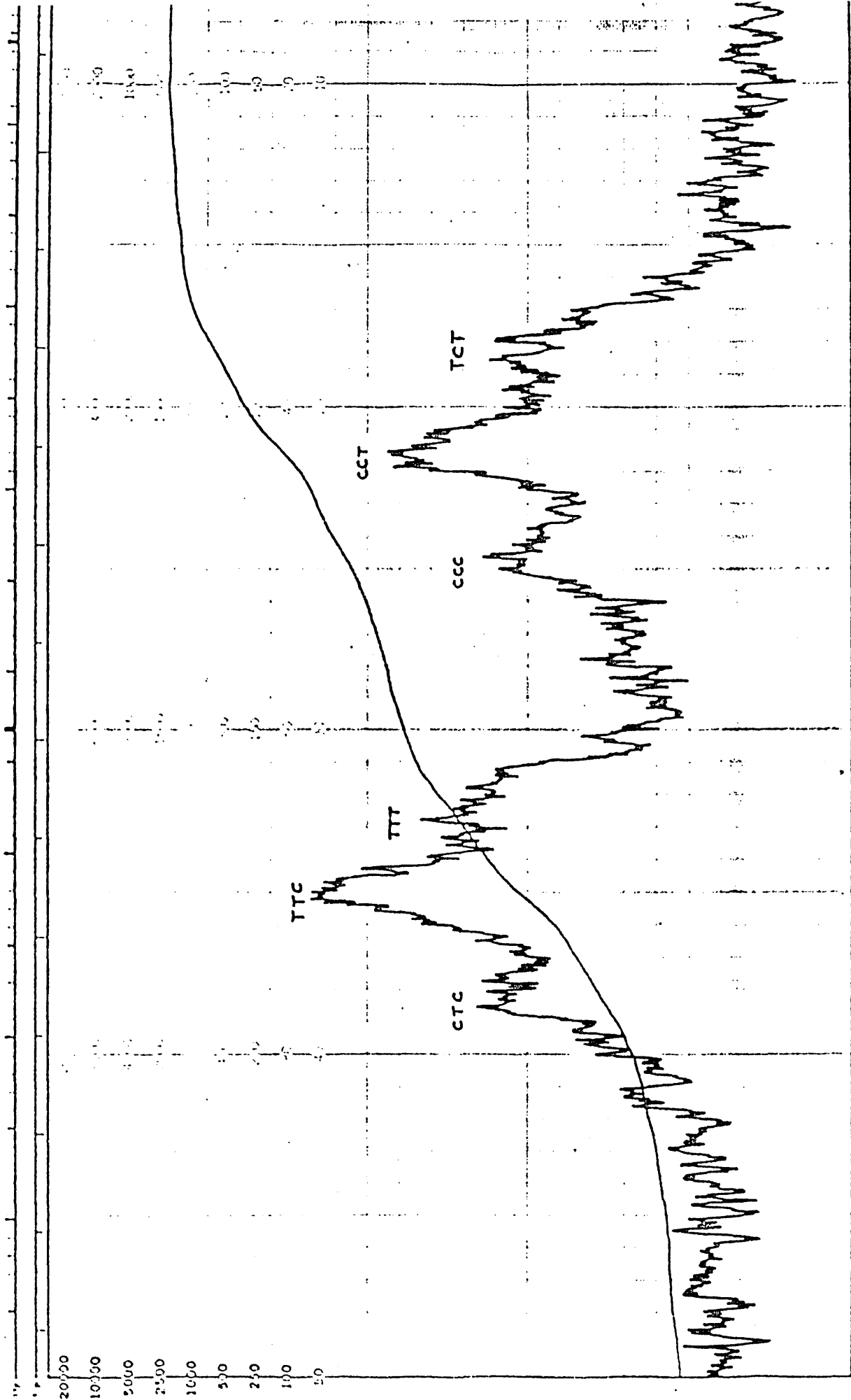


Figure 3.16 TR1101 300 MHz NMR showing the  
expanded aliphatic protons









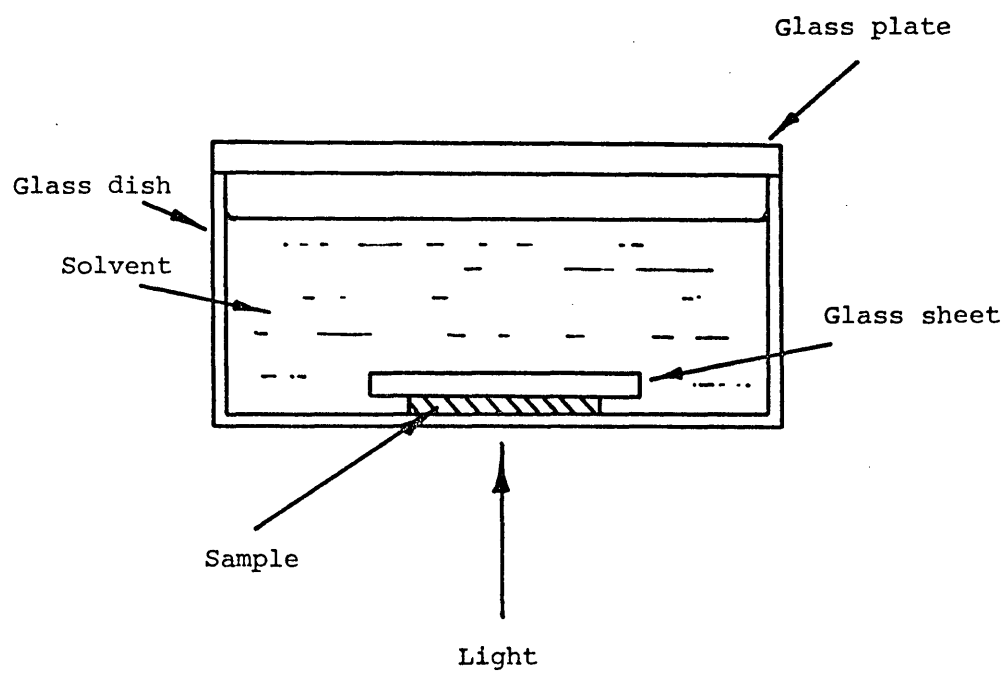
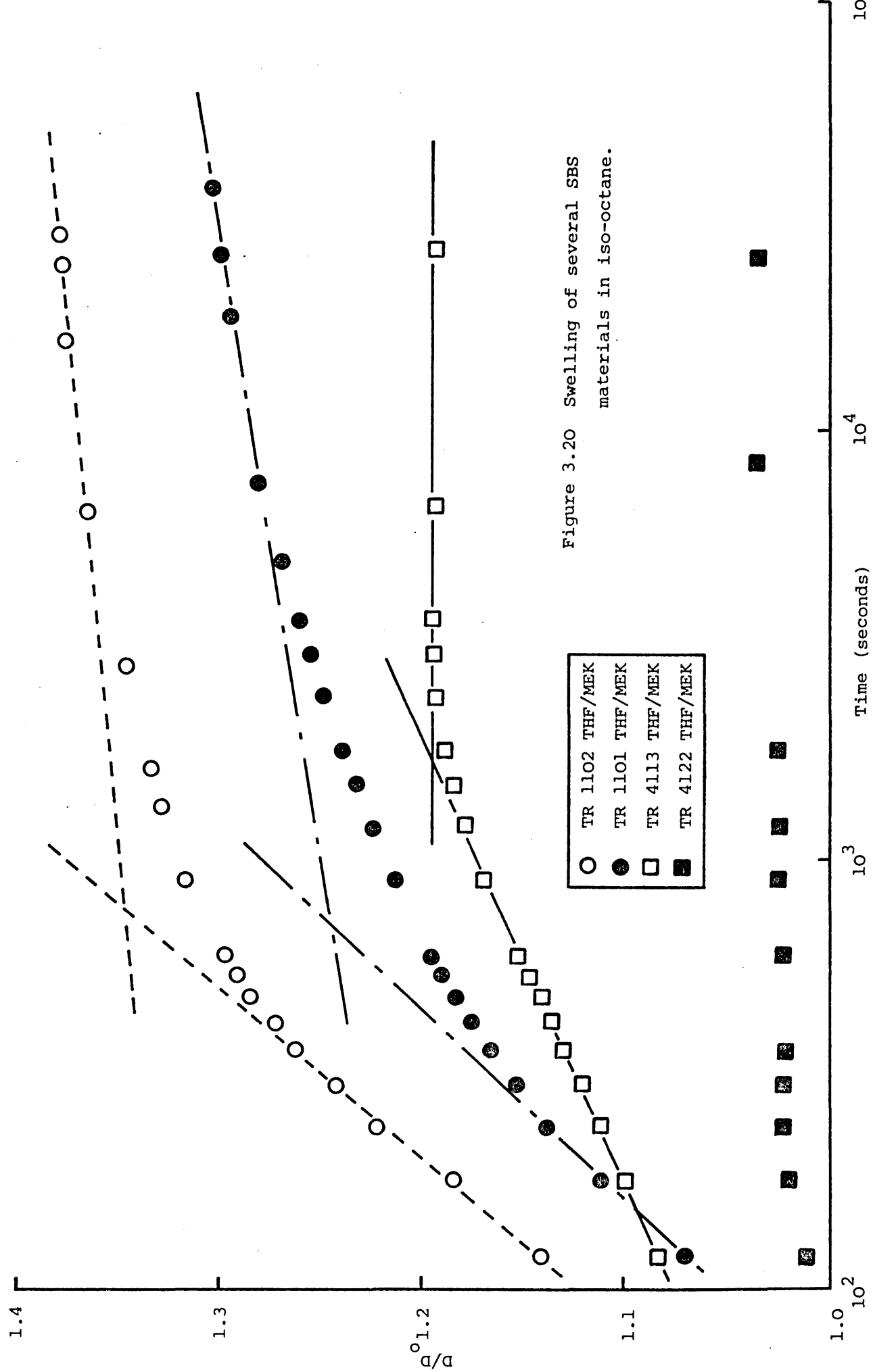


Figure 3.19 Apparatus for swelling experiments.



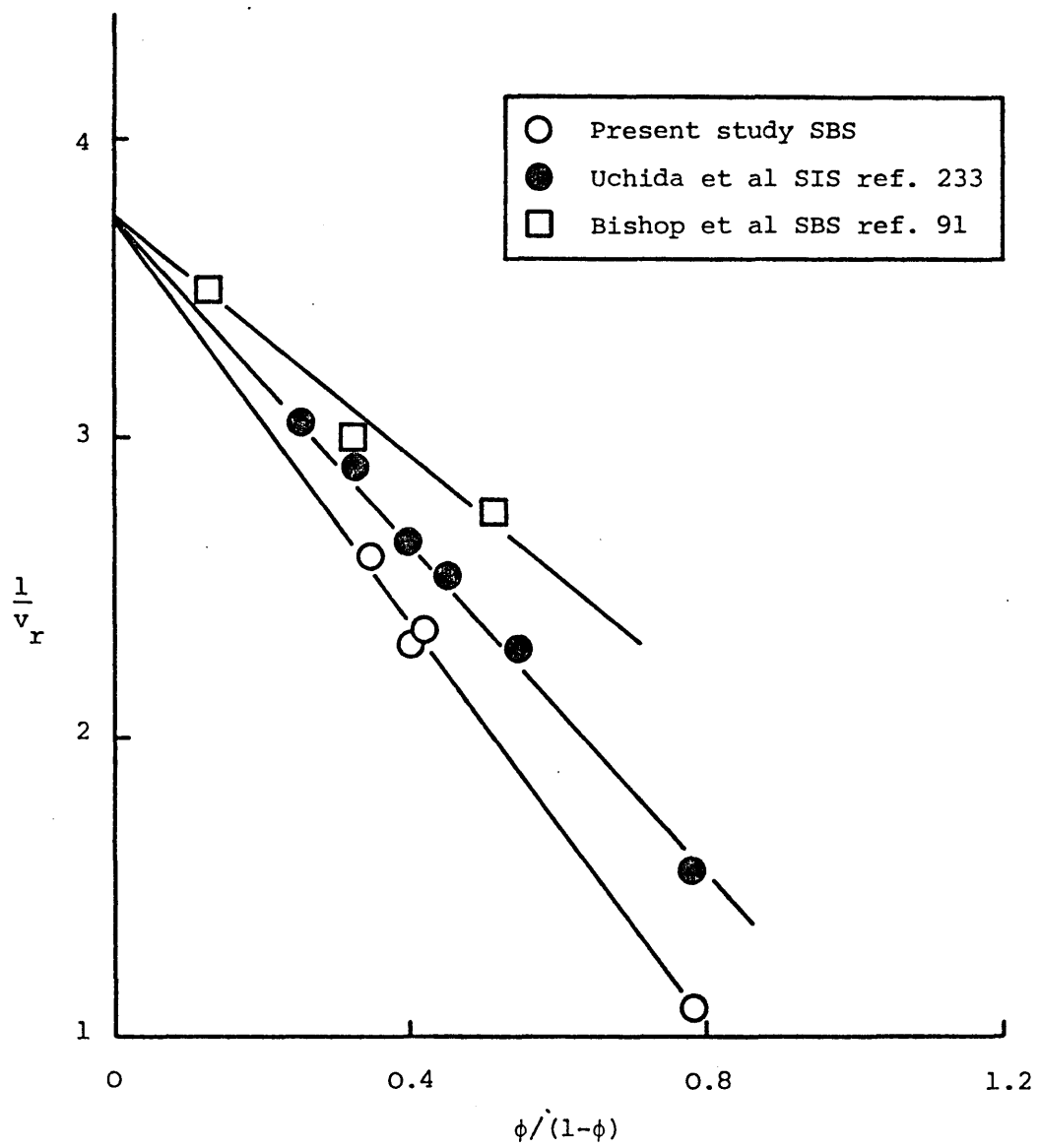


Figure 3.21  $1/v_r$  as a function of  $\phi/(1-\phi)$  to determine  $v_{ro}$ .

CHAPTER 4  
MATERIAL MORPHOLOGY

4.1 INTRODUCTION

The background research work available on the morphology of block polymers is quite extensive and has been discussed in section 2.2. For the purposes of this present study, since the preparation technique of the materials was known to have a profound effect on the morphological and mechanical properties, it was necessary to carry out a detailed analysis of the microstructure of each polymer. To this end, the two major techniques of microstructural examination relevant to this class of materials have been employed in order that statements may be made about the detailed fine structures involved. The two techniques used were electron microscopy (EM) and small angle X-ray scattering (SAXS).

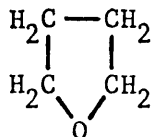
Specimens were prepared by casting the polymers from solutions of different solvent systems, evaporating the solvent to form sheets of material. For electron microscopy, pieces were cut from these sheets and microtomed to produce slivers thin enough for examination. SAXS was applied to the full sheet thickness. Only relatively small amounts of polymer were required for these tests, the remainder of the material being used for mechanical testing, for which several sheets of each polymer were needed cast from the different solvent systems.

4.2 POLYMER SHEET PREPARATION

The raw polymer samples were in the form of crumb and dissolving in suitable solvents was a relatively straightforward procedure using an automatic stainless steel stirrer.

The solvent systems employed were:

- (a) Ethyl acetate,  $C_4H_8O_2$ .
- (b) 90% tetrahydrofuran (THF),  $H_2C-CH_2$ , with



- 10% methyl ethyl ketone (MEK)  $CH_3CO C_2H_5$ .
- (c) 90% benzene (BEN),  $C_6H_6$ , with 10% heptane (HEP),  $C_7H_{16}$ .
- (d) Carbon tetrachloride,  $CCl_4$ .

Having dissolved 30% by weight of polymer into solution, the jar was degassed, sealed and allowed to stand for 24 hours to allow any air to come

out of solution. The polymer solution was then poured onto flat sheets of PTFE which incorporated glass surrounds to restrict the polymer flow. In this way, sheets approximately 1 mm thick and 250 mm square were formed after solvent evaporation at room temperature; this took a further 24 hours. Remaining traces of solvent were removed by annealing each sheet for 6 days in an oven at +50°C. The sheets were then stored in a freezer at -25°C until required for morphological studies or mechanical testing. Films of this thickness were translucent and those cast from ethyl acetate, BEN/HEP and  $\text{CCl}_4$  were milky white in colour, but when the casting solvent was THF/MEK a distinct brown discolouration was observed.

#### 4.3 PREPARATION OF SPECIMENS FOR ELECTRON MICROSCOPY

A 5 mm square piece of polymer was cut from a sheet using a sharp scalpel blade. This piece of material was stuck using Stephens Gum to the copper base of a sledge microtome (Figure 4.1), the bowl of which was filled with liquid nitrogen to cool the polymer to a temperature below the  $T_g$  of its butadiene phase.

The sledge microtome was modified to support a glass blade which was used to cut 5 micron thick slices of the material using alcohol as a lubricant. These slivers were collected and treated for several days by submerging them in osmium tetroxide ( $\text{OsO}_4$ ) in order to fix (or stain) the butadiene phase.

Stained sections were cast in "Durcupan" (an araldite type compound) using "Beem" capsules, and cured for two days in an oven at +50°C. Using a sharp scalpel blade, as much Durcupan as possible was cut from the face of the pyramid formed at the tip of the Beem capsule to facilitate the cutting of ultra thin sections. These ultra thin sections (500 Å to 800 Å thick) were cut using a Reichart ultramicrotome, the sections being collected on grids suitable for use in the Jeol Jem 100B electron microscope.

#### 4.4 THE ELECTRON MICROGRAPHS

Representative electron micrographs of all the materials concerned in this study are shown in Figures 4.2 to 4.16. A general observation is that the structures in each case are of poly aggregates, of uniform microstructure, which are randomly oriented in the material, thus conferring isotropy in the plane of the cast sheets. More detailed study of the micrographs reveals distinct differences in structure, dependent not only on the particular polymer, but also upon the casting solvent.

The easiest structure to identify is that associated with casting from 90/10 BEN/HEP, shown in Figures 4.2 to 4.5, and  $\text{CCl}_4$  (Figures 4.6 to 4.9). In each of these cases, the micrographs show round domains and rods of (white) polystyrene in a matrix of (black) polybutadiene. The round domains cause something of a problem since they could conceivably be spheres of polystyrene; however, it is also possible that they represent an "end-on" view of the sectioned rod-like structures which are evident in neighbouring regions. The domains generally associate together in a regular packing unit which most closely resembles that of hexagonal packing.

The microstructures of materials cast from the other solvents, 90/10 THF/MEK and ethyl acetate, are not so readily identified, although there is little doubt that they are different. The solvent mixture THF/MEK (Figures 4.10 to 4.14) presents the most difficulty since more than one structure appears to occur. A large number of specimens were examined but no evidence of any hexagonally packed structure was observed, although areas with long rod-like polystyrene domains appeared regularly. The other major structure noted was one of short, contorted, interconnected rods. Taken together, these two observations indicate that the short "rods" might be a form of underdeveloped platelet structure which would be evidence of a primary lamellar formation.

When ethyl acetate is used as the casting solvent (in this case, only TR1101 and TR1102 were investigated), the picture is slightly more convincing. These micrographs are shown in Figures 4.15 and 4.16. The short interconnected rods are still to be found, but not in such abundance as with THF/MEK; in addition, when rods appear, they usually give the impression of actually being surfaces sectioned at an angle [97], as would occur with more fully developed lamellar structures.

##### 4.4.1 Analysis of Domain Parameters

An analysis of domain size,  $D_d$ , and interdomain distance,  $d_{int}$ , was carried out for each microstructure. Use was made of the relationships

between styrene volume fraction and domain parameters proposed by Price et al [201] to determine the probable type of structure present, and the resulting styrene volume fraction.

The relationships used are:

Lamellae: 
$$\phi_L = \left[ \frac{D_i}{d_{int}} \right]$$

where  $D_i$  is the thickness of the lamella.

Rods: 
$$\phi_R = 0.91 \left[ \frac{D_i}{d_{int}} \right]^2$$

where  $D_i$  is the rod diameter.

Spheres: 
$$\phi_S = 0.74 \left[ \frac{D_i}{d_{int}} \right]^3$$

where  $D_i$  is the sphere diameter.

The volume fraction determined in this way may then be compared with that obtained by NMR analysis. The results of this comparison are shown in Table 4.1. The measured values of both  $d_{int}$  and  $D_i$  vary quite widely from material to material, and also within the same material when cast from different solvents.

For TR1101 cast from ethyl acetate and THF/MEK, TR1102 cast from ethyl acetate, TR4122 cast from all solvents, and TR4113 cast from THF/MEK, good correlation is found between the volume fractions predicted by the lamellar model and that determined by NMR. For TR1102 cast from THF/MEK, BEN/HEP and  $CCl_4$ , and TR1101 and TR4113 cast from BEN/HEP and  $CCl_4$ , the rod-like or cylinder model appears to be more suitable, when measurements are taken from rod-like domains. If, however, measurements are taken from the disc-like structures, observed more frequently in TR1101 and TR1102 cast from BEN/HEP and  $CCl_4$ , it is found that TR1101 is satisfied by the model for spherical domains, but TR1102 still predicts the likelihood of a rod-like structure. Insufficient circular domains were found in TR4113 cast materials to make an examination worthwhile.

Although this type of analysis is far from foolproof, it does provide additional evidence on which to base a reasoned argument as to what



TABLE 4.1

Domain Parameters and Volume Fraction of Polystyrene

Material	Solvent	$d_{int}$ (nm)	$D$ (nm)	Volume % Polystyrene			% Average Styrene From Microstructure	% Styrene
				Lamellar	Rods	Spheres		
1101	Ethyl Acetate	32.3	9.5	29.4*	7.9	1.9	26.5	27.7
	THF/MEK	25.0	7.1	28.4*	7.3	1.7		
	BEN/HEP	23.8 (24.1)	11.9 (15.8)	50.0 (65.6)	23.0* (39.1)	9.3 (21.0)*		
	CCl <sub>4</sub>	22.6 (20.4)	11.9 (13.8)	52.7 (67.7)	25.0* (41.6)	10.8 (23.0)*		
1102	Ethyl Acetate	21.9	5.7	26.0*	6.2	1.3	24.3	24.9
	THF/MEK	22.9	11.9	52.0	24.6*	10.4		
	BEN/HEP	19.1 (18.0)	9.5 (11.0)	49.7 (61.1)	22.6* (34.0)	9.1 (16.9)		
	CCl <sub>4</sub>	16.7 (18.7)	8.6 (10.1)	51.5 (54.0)	24.0* (26.6)*	10.1 (11.7)		

\* denotes most likely structure

(continued)

TABLE 4.1 (continued)

Material	Solvent	$d_{int}$ (nm)	$D$ (nm)	Volume % Polystyrene			% Average Styrene From Microstructure	% Styrene
				Lamellar	Rods	Spheres		
4122	THF/MEK	27.6	11.4	41.4*	15.5	5.2	41.0	39.0
	BEN/HEP	23.2	9.5	41.0*	15.3	5.1		
	$\text{CCl}_4$	17.6	7.1	40.5*	14.8	4.9		
4113	THF/MEK	16.2	4.76	29.4*	7.9	1.9	28.5	27.7
	BEN/HEP	17.1	9.5	55.6	28.1*	12.7		
	$\text{CCl}_4$	17.1	9.5	55.6	28.1*	12.7		

\* denotes most likely structure

structures are present in a particular material. Since, if the model for spherical domains is used and it predicts a volume fraction of some 10%, and the known volume fraction is nearer 25%, clearly there cannot be a predominantly spherical domain structure present. There may, indeed, be a limited spherical component, but the predominant structure is far more likely to be rod-like. Equally, if the rod-like model predicts a reasonably accurate volume fraction, and some disc-like domains are present, and these, using the spherical model, predict an equally accurate volume fraction, then it is reasonable to argue that both rods and spheres are present, probably in near equal proportions.

With the materials and solvents used in this work, a reasonable picture of the predominant microstructures present has been built-up using electron microscopy. Table 4.2 gives details of the likely domain types determined using this technique; the proposed microstructures are not conclusive, and further evidence from small angle X-ray diffraction could confirm or oppose the structures which are thought to be present at this stage. One disadvantage of the electron microscopical technique being that only very small, possibly unrepresentative, areas can be studied; the back-up of another microstructural analytical technique is almost mandatory.

TABLE 4.2

Proposed Microstructures Revealed by Microscopy

MATERIAL	SOLVENT	MICROSTRUCTURE
TR1101	Ethyl Acetate	Lamellar/interconnected rods or spheres
	THF/MEK	Lamellar/interconnected rods or spheres
	BEN/HEP	Rod-like plus possibly spherical
	CCl <sub>4</sub>	Rod-like plus possibly spherical
TR1102	Ethyl Acetate	Lamellar/interconnected rods or spheres
	THF/MEK	Interconnected rods or spheres/rod-like
	BEN/HEP	Rod-like
	CCl <sub>4</sub>	Rod-like
TR4122	THF/MEK	Lamellar/interconnected rods or spheres
	BEN/HEP	Lamellar/interconnected rods or spheres
	CCl <sub>4</sub>	Lamellar/interconnected rods or spheres
TR4113	THF/MEK	Lamellar/interconnected rods or spheres
	BEN/HEP	Rod-like
	CCl <sub>4</sub>	Interconnected rods or spheres/rod-like

## 4.5 SMALL ANGLE X-RAY SCATTERING MEASUREMENTS (SAXS)

### 4.5.1 Introduction

The nature of the microstructures involved in SBS block polymers clearly points to electron microscopy for detailed study. However, since the structural elements are of the order of several hundred ångströms, and in view of the periodicity involved and its scale, SAXS is an obvious complementary technique which, due to its inherent averaging effect, may be more representative of the bulk material.

SAXS gives rise to intensity maxima indicative of the long range periodic structure of the material, the spacings following directly from Bragg's Law:

$$n_s \lambda_R = 2d_{int} \sin \theta \quad (4.1)$$

where  $n_s$  is the order of the maximum,  $\lambda_R$  the wavelength of the radiation used,  $\theta$  being a measure of the scattering angle, and  $d_{int}$  the inter-particle distance.

In the case of SBS copolymers, since they are amorphous, a series of ring images are obtained. With increasing diffraction angle, the spacings of consecutive orders are found to form systematic sequences:

- (a)  $1 : (\frac{1}{2}) : (\frac{1}{3}) : (\frac{1}{4})$  , which is consistent with regularly periodic parallel lamellae.
- (b)  $1 : (\frac{1}{3})^{\frac{1}{2}} : (\frac{1}{4})^{\frac{1}{2}} : (\frac{1}{7})^{\frac{1}{2}}$  ; this sequence is consistent with a regular hexagonal arrangement of cylinders.
- (c)  $1 : (\frac{3}{4})^{\frac{1}{2}} : (\frac{3}{8})^{\frac{1}{2}} : (\frac{3}{11})^{\frac{1}{2}}$  , corresponding to spacings in a face centred cubic lattice of spheres.

The spacings obtained define only the overall periodicity, and do not give information such as the thickness of lamellae or the diameters of cylinders or spheres. Such information may be obtained, however, if the composition of the system is known independently, assuming that the macroscopic values of the specific volumes hold for the microscopic state.

#### 4.5.2 Experimental

The SAXS experiments were carried out using an evacuated Warhus pinhole camera (shown schematically in Figure 4.17) with extra beam collimation. Chromium  $K_{\alpha}$  radiation was generated by a Philips PW1130 X-ray generator, the tube operating at 40 kV and 35 mA, a vanadium filter being used to absorb  $K_{\beta}$  radiation.

Diffraction patterns were recorded on Kodak Industrex 'D' film with a sample to film distance of 29 cm. A 72-hour exposure time was found to be necessary and all samples were exposed for this time. Specimens were viewed normally to the sheet surface, thickness being of the order of 1 mm. After exposure, the film was developed, washed and air-dried for several hours. Spacings were then measured directly from the negative using a Wooster Mk III recording microdensitometer.

#### 4.5.3 Results of SAXS

A maximum of four detectable diffraction peaks were observed, the first peak being far more intense than those of higher order. Figure 4.18 shows the SAXS patterns for TR1101 THF/MEK and TR1102  $CCl_4$ . The spot in the centre of these photographs is caused by the shadow of a lead disc, supported by a thin wire, which stops the main straight-through X-ray beam. All peaks were rather broad and it is thought that each major observed peak is in fact a convolution of two or possibly more peaks, indicating the presence of a dual morphology. This effect was not as noticeable in materials cast from ethyl acetate and THF/MEK. If, however, the presence of a single, predominant morphology is assumed, since SAXS has an inherent averaging effect, a reasonable estimate of the major microstructure present should be obtainable.

Each detectable peak was taken as an order of Bragg spacing, and it can be seen from Table 4.3 that it is possible to designate two main models for each material dependent upon the casting solvent. Ethyl acetate and THF/MEK giving a predominantly lamellar structure; BEN/HEP and  $CCl_4$  indicating a formation of polystyrene cylinders in the butadiene matrix.

If one attempts to make the assumption that more than one microstructure is present, the analysis becomes extremely tedious, and the conclusions far from certain. So that, as far as the SAXS results are concerned, it is probably as well to stick with the microstructures indicated in Table 4.3, and to use these as a complementary factor in discussion of both SAXS and electron microscopical investigations; bearing

in mind that SAXS also indicates the presence of more than one structure in almost every case.

TABLE 4.3

Comparison of Sequences of the Observed SAXS Maxima with those Predicted for Different Microstructures

Solvent	Order ( <i>n</i> )	<i>d</i> (nm)	$d_1/d_n$ (exp)	$d_1/d_n$ (theoretical)	
				Lamellae	Hexagonally Packed Rods
Ethyl Acetate	1	31	1.0	1.00	
	2	16	2.0	2.00	
	3	11	3.0	3.00	
	4	-	-	4.00	
THF/MEK	1	30	1.0	1.00	
	2	15	2.0	2.00	
	3	10	3.0	3.00	
	4	-	-	4.00	
BEN/HEP	1	28	1.0		1.00
	2	16	1.7		1.73
	3	-	-		2.00
	4	10	2.7		2.65
CCl <sub>4</sub>	1	27	1.0		1.00
	2	16	1.7		1.73
	3	-	-		2.00
	4	10	2.7		2.65

#### 4.6 DISCUSSION

Although neither the electron micrographs or SAXS results are conclusive on their own, both methods have indicated the presence of dual morphologies in these materials when cast from a variety of solvents. When these approaches are considered together, it is possible to deduce a fairly accurate picture of what the structures are, or at least to present a good argument as to what the primary and secondary structures consist of. Although to a certain extent the picture which emerges is a qualitative one, and there is room for other possibilities, the morphologies proposed in Table 4.4 do present a realistic analysis of the available evidence.

In addition, the analysis of domain parameters presented in Table 4.1 indicates some interesting solvent influences. For instance, TR1101 cast from ethyl acetate has the same proposed structure as that cast from THF/MEK, but the spacing of the domains,  $d_{int}$ , shows a substantial increase when ethyl acetate is the casting solvent; the domain size,  $D_i$ , is also somewhat larger for the ethyl acetate cast material. When the materials TR1101 and TR1102 are compared for the same solvent system, it is found that TR1102 cast from ethyl acetate displays both a smaller  $d_{int}$  and domain size than does TR1101. When these materials are cast from THF/MEK, TR1101 produces a predominantly lamellar structure, whilst TR1102 consists mainly of cylinders. BEN/HEP and  $CCl_4$  both produce a cylindrical morphology in TR1101 and TR1102, but the cylinders in the former have a large diameter and are more widely spaced; it is thought that this effect is due to the higher molecular weight of both the styrene and butadiene in TR1101.

TR4122 appears to produce a typically lamellar structure independent of the solvent used; this was anticipated since the styrene content of the material is high at some 39% by volume (at least 43% by weight). This type of structure has been noted by a number of workers [76,80,112, 202,203] when investigating the microstructure of block copolymers containing almost equal block proportions. The dimensions of the lamellae, and their spacing, are, however, a function of the solvent, both  $d_{int}$  and  $D_i$  decreasing in the order THF/MEK > BEN/HEP >  $CCl_4$ .

TR4113 has an identical styrene content to TR1101 and, although similar microstructures are evident when the casting solvent is the same, the domain dimensions for TR4113 are slightly smaller than those for TR1101. This comparison is complicated by the presence of a plasticiser in TR4113, the effect of which on the microstructure is not known. Since the



TABLE 4.4

Proposed Microstructures for the Materials of this Study in the Light of Evidence from Electron Microscopy and SAXS

Material	Solvent	Evidence From Electron Microscopy	Evidence from SAXS	Proposed Microstructure	
				Primary	Secondary
TR1101	Ethyl Acetate	Lamellar with interconnected rods or spheres	Lamellar	Lamellar	Interconnected cylinders or spheres
	THF/MEK	Lamellar with interconnected rods or spheres	Lamellar	Lamellar	Interconnected cylinders or spheres
	BEN/HEP	Rod-like plus possibly spherical	Rod-like	Styrene cylinders	Spheres
	CCl <sub>4</sub>	Rod-like plus possibly spherical	Rod-like	Styrene cylinders	Spheres
TR1102	Ethyl Acetate	Lamellar with interconnected rods or spheres	Lamellar	Lamellar	Interconnected cylinders or spheres
	THF/MEK	Interconnected rods or spheres plus rod-like	Lamellar	Styrene cylinders	Interconnected cylinders or spheres
	BEN/HEP	Rod-like	Rod-like	Styrene cylinders	Spheres
	CCl <sub>4</sub>	Rod-like	Rod-like	Styrene cylinders	Spheres

(continued)

TABLE 4.4 (continued)

Material	Solvent	Evidence From Electron Microscopy	Evidence From SAXS	Proposed Microstructure	
				Primary	Secondary
TR4122	THF/MEK	Lamellar with interconnected rods or spheres	-	Lamellar	Interconnected cylinders or spheres
	BEN/HEP	Lamellar with interconnected rods or spheres	-	Lamellar	Interconnected cylinders or spheres
	CCl <sub>4</sub>	Lamellar with interconnected rods or spheres	-	Lamellar	Interconnected cylinders or spheres
	THF/MEK	Lamellar with interconnected rods or spheres	-	Lamellar	Interconnected cylinders or spheres
TR4113	BEN/HEP	Rod-like	-	Styrene cylinders	Spheres
	CCl <sub>4</sub>	Interconnected rods or spheres plus rod-like	-	Styrene cylinders	Spheres

molecular weight,  $\overline{M}_n$ , of the polystyrene is almost identical (Table 3.7), it might be expected that the domain size for similar microstructures would be more or less the same. Triblock polymerisation is slightly more complete in TR4113 ( $\approx 92\%$  as opposed to  $\approx 85\%$ ) and there is rather more diblock and homopolymer styrene in TR1101 which may give a clue to the different domain sizes. The unattached styrene homopolymer in TR1101 tends to accumulate in the styrene domains [36], thus increasing their otherwise largest possible diameter. Whilst the presence of more free-ended butadiene molecules might well increase the inter-domain distance.

Since some of the physical properties to be investigated must be dependent upon the morphology of the systems tested, the subtle differences observed by electron microscopy and SAXS should play a rôle in explaining such variations in mechanical behaviour.

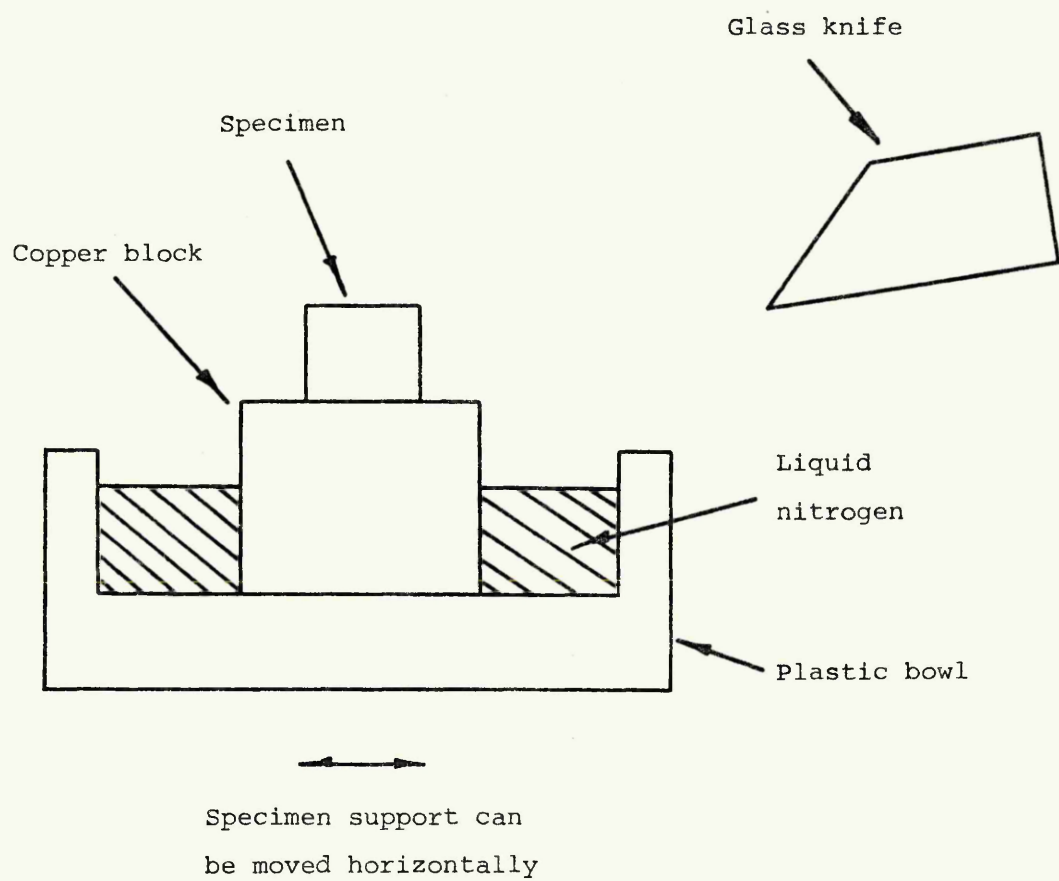


Figure 4.1 The sledge microtome.

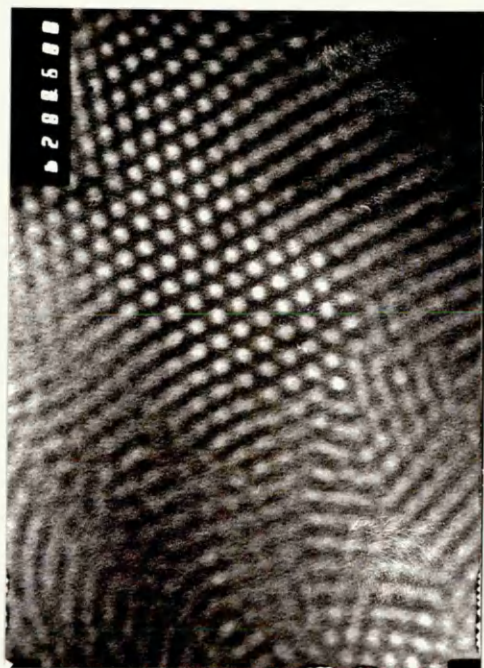


Figure 4.2 Micrograph TR1101 BEN/HEP

100 nm

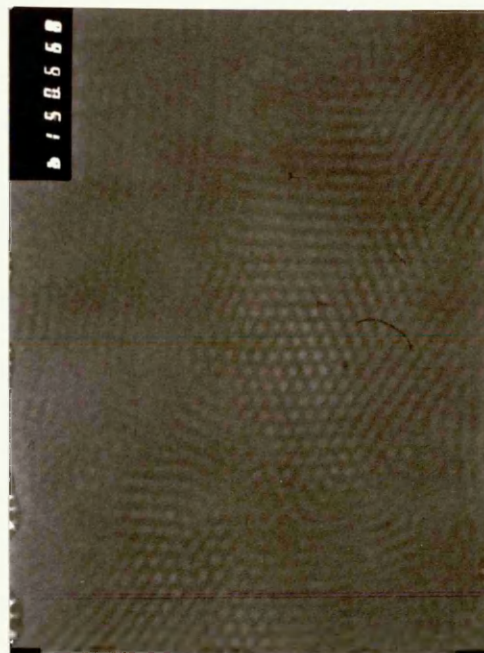


Figure 4.3 Micrograph TR1102 BEN/HEP

100 nm

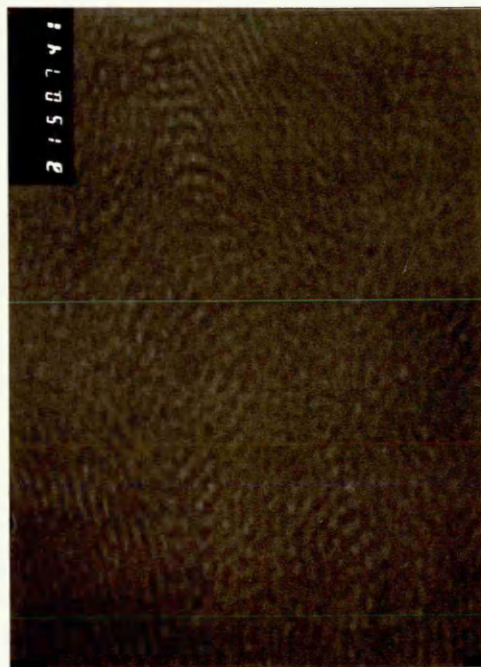


Figure 4.4 Micrograph TR4122 BEN/HEP

100 nm

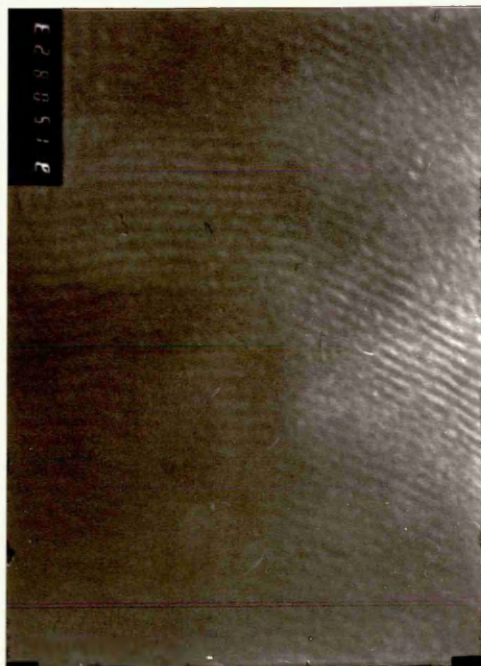


Figure 4.5 Micrograph TR4113 BEN/HEP

100 nm





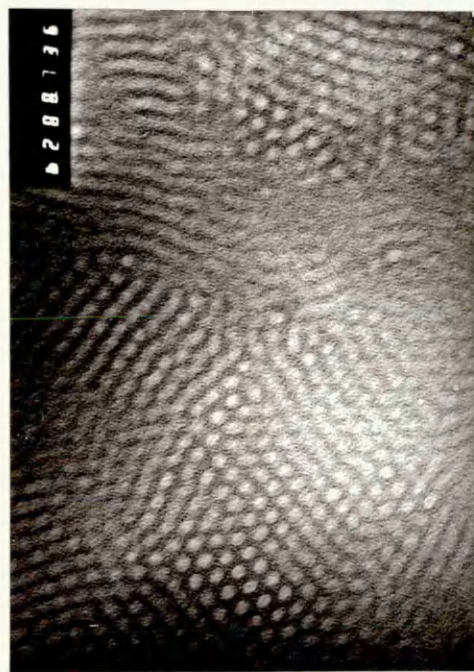


Figure 4.6 Micrograph TR1101  $\text{CCl}_4$

100 nm

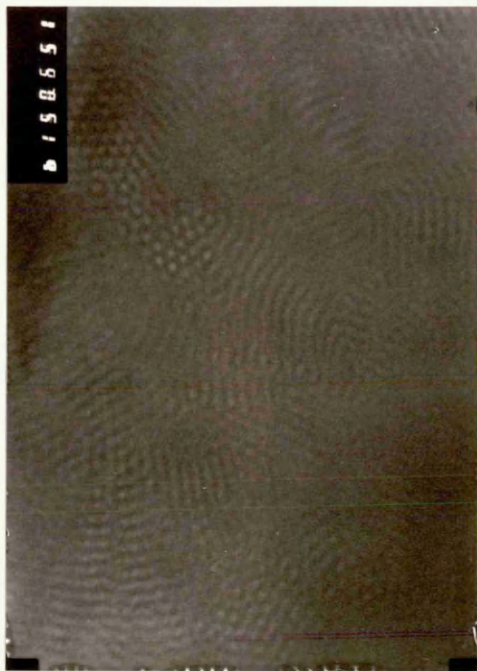


Figure 4.7 Micrograph TR 1102  $\text{CCl}_4$

100 nm

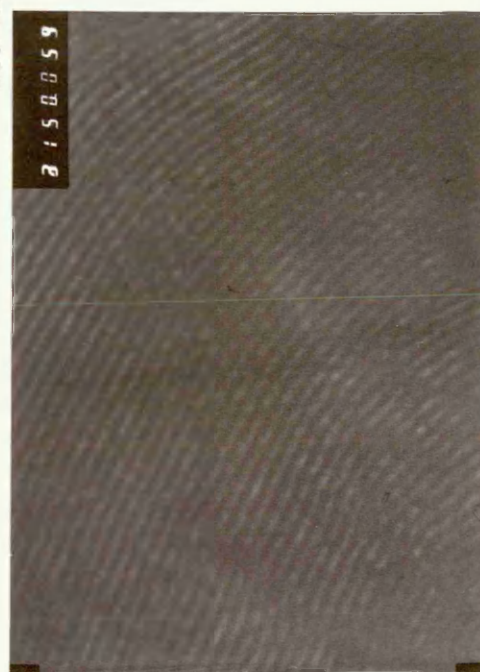


Figure 4.8 Micrograph TR4122  $\text{CCl}_4$

100 nm

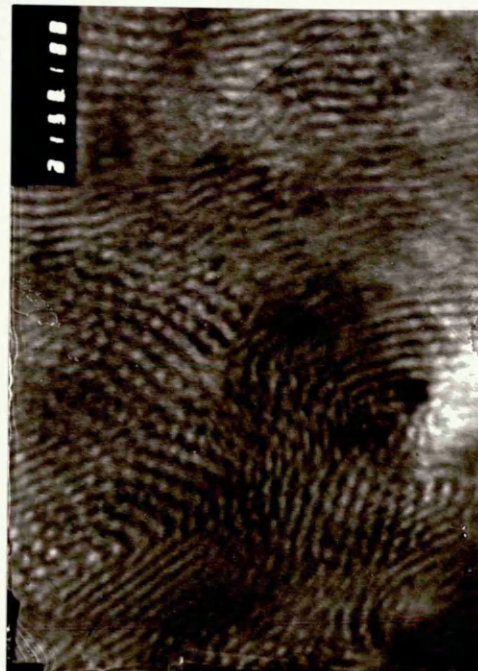
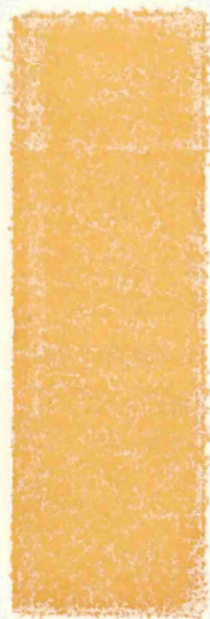


Figure 4.9 Micrograph TR4113  $\text{CCl}_4$

100 nm







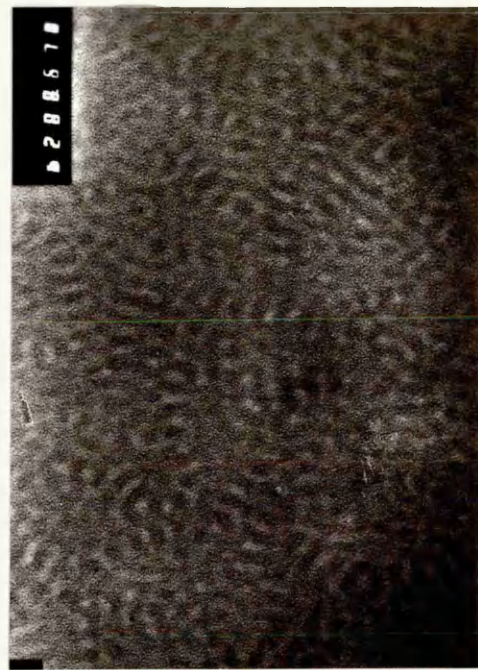


Figure 4.10 Micrograph TR1101 THF/MEK 100 nm

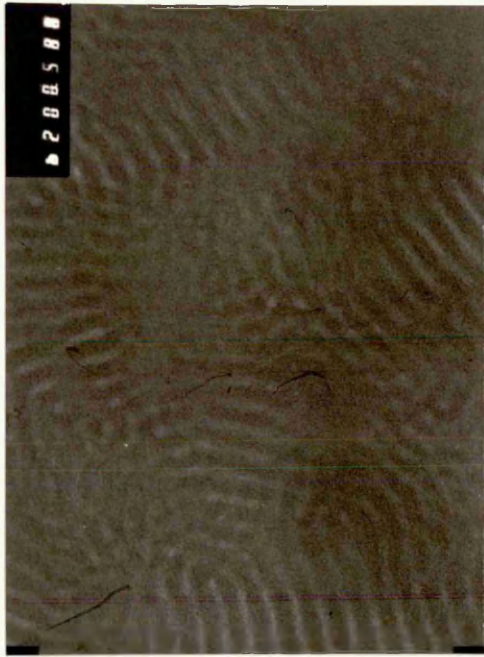


Figure 4.11 Micrograph TR1101 THF/MEK 100 nm

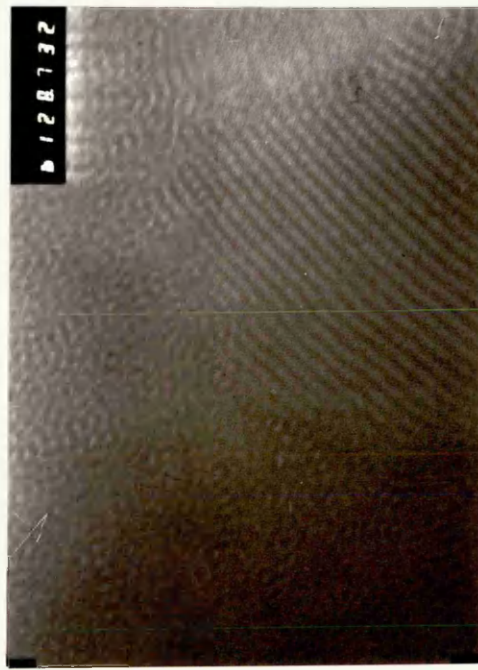


Figure 4.12 Micrograph TR1102 THF/MEK 100 nm

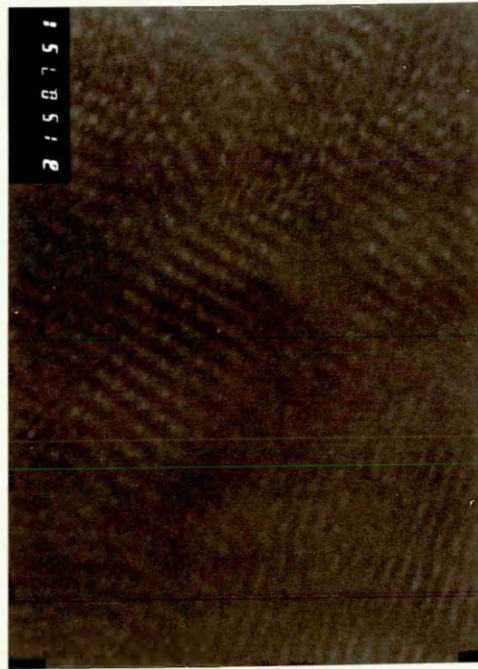
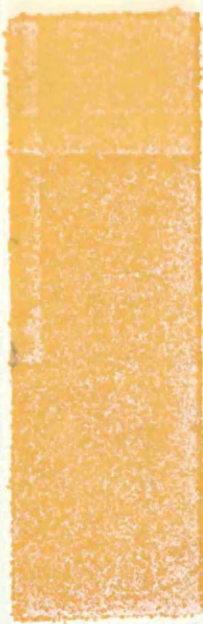


Figure 4.13 Micrograph TR4122 THF/MEK 100 nm





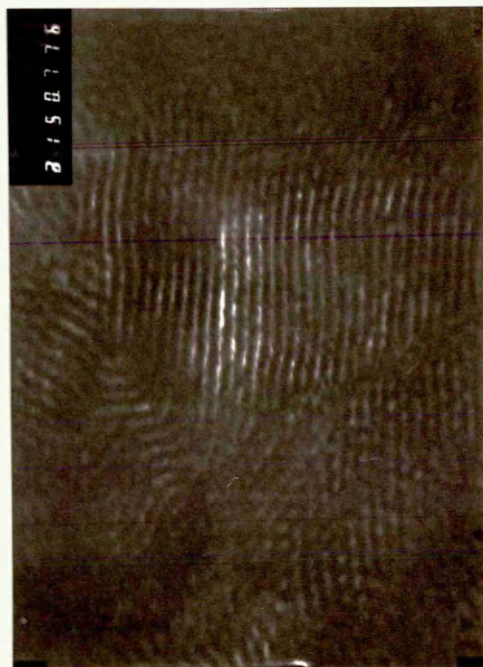



Figure 4.14 Micrograph TR4113 THF/MEK  100 nm

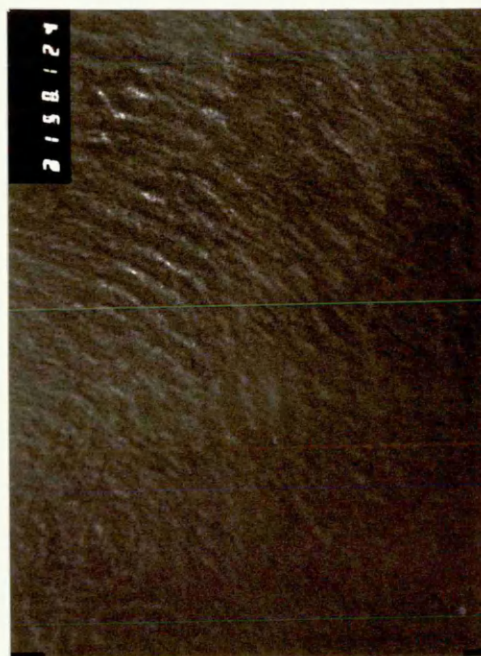



Figure 4.15 Micrograph TR1101 Ethyl acetate  100 nm

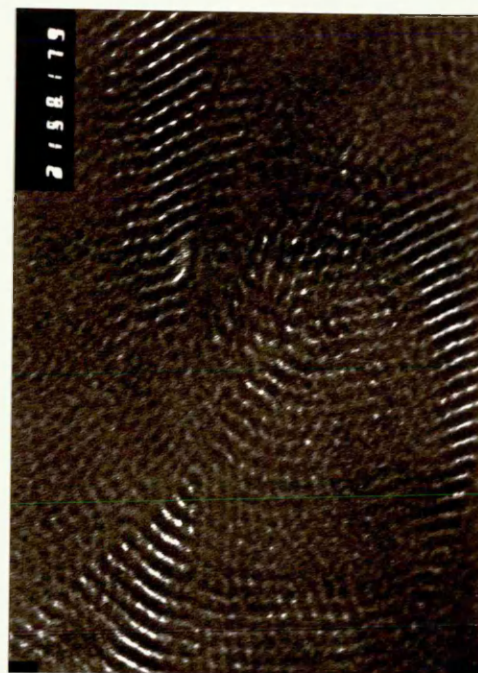

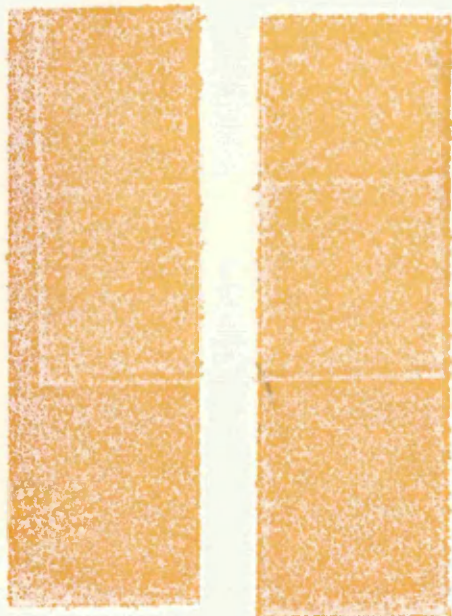
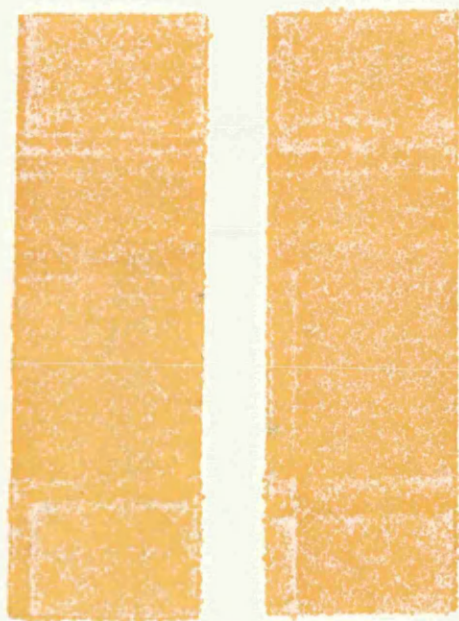
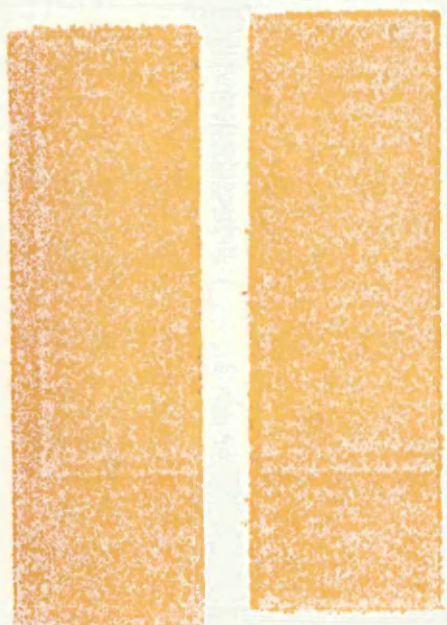


Figure 4.16 Micrograph TR1102 Ethyl acetate  100 nm



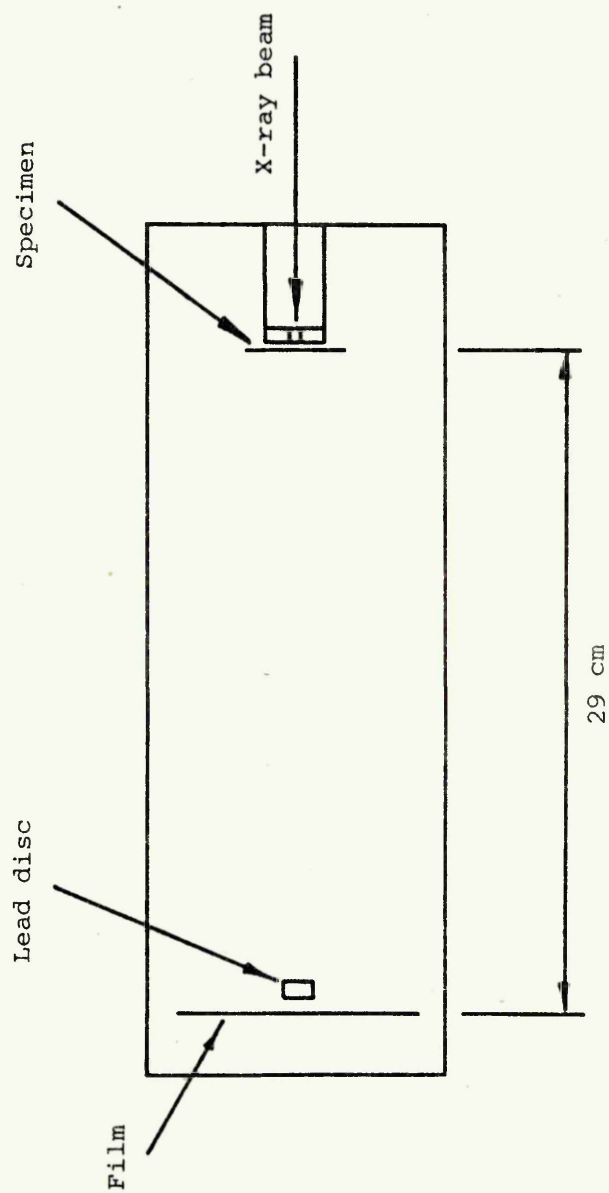


Figure 4.17 The pinhole camera for SAXS experiments.



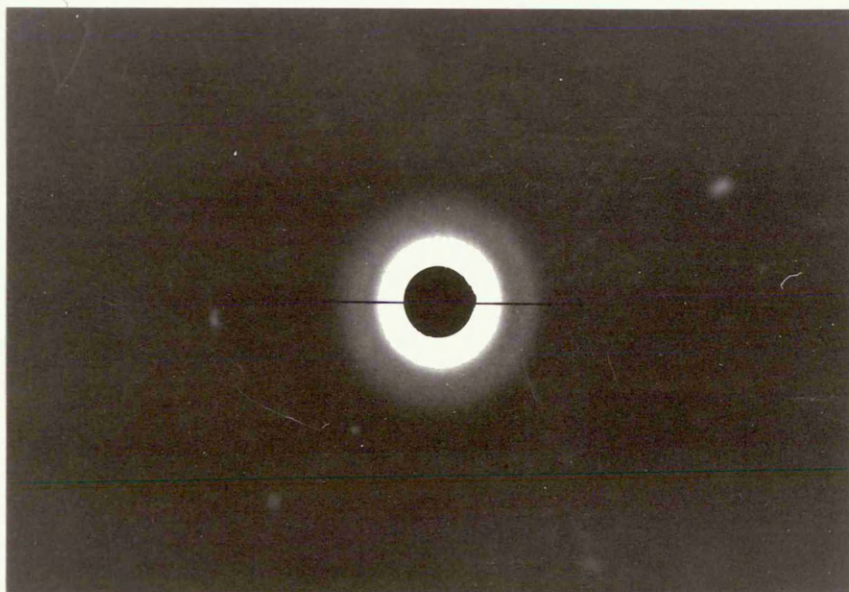


Figure 4.18(a) Low angle x-ray scattering for TR1101 THF/MEK.

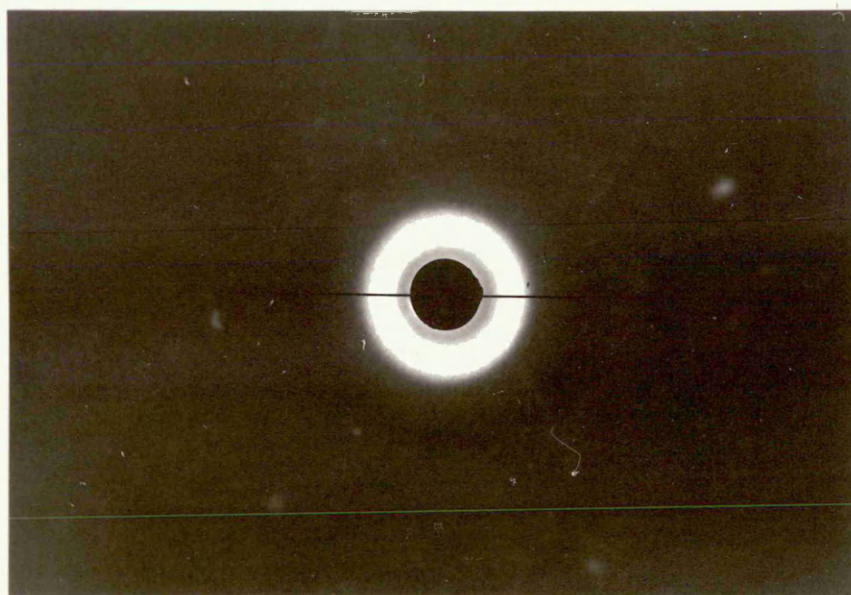
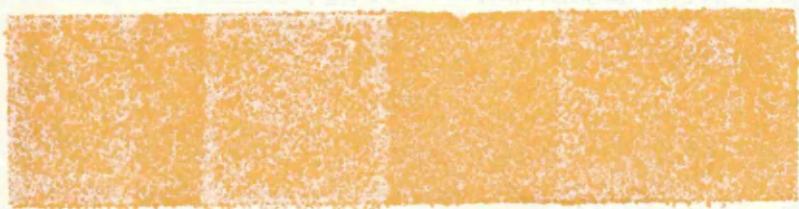
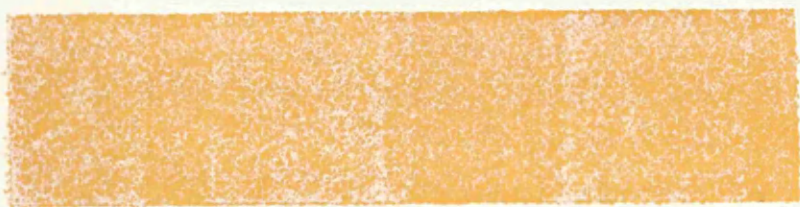
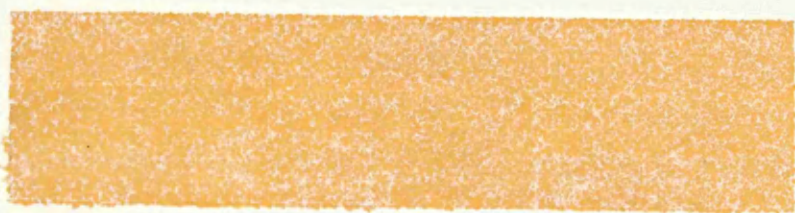


Figure 4.18(b) Low angle x-ray scattering for TR1102 CCl<sub>4</sub>.



CHAPTER 5  
SMALL STRAIN DYNAMIC PROPERTIES

5.1 INTRODUCTION

Several groups of workers [71,73,96,204] have concerned themselves with the physical properties of solvent cast SBS block copolymers. It has been determined that as a consequence of the mutual incompatibility of the blocks, polymers of this type form regular phase-separated domains. The styrene to butadiene ratio has proved to be a major factor in deciding the solid state structure of the material, and thermodynamic arguments [46] have been used to successfully predict the size and shape of these domains. Other factors influencing the morphology, such as the casting solvent [139,204] and its evaporation rate [204], have also been investigated to a limited extent.

In the present work, the effects of four solvent systems on dynamic properties have been investigated; details of solubility parameter and an indication of solvent efficiency for each block are given in Table 5.1. Section 4.2 gives details of solution treatment, casting method and post-casting heat treatment of the materials.

Four materials were involved in the study, TR1101 and TR1102 being cast from all four solvent systems, TR4122 and TR4113 from all except ethyl acetate. Two types of dynamic mechanical experiment were performed, shear modulus and  $\tan \delta$  being investigated using a torsion pendulum, whilst tensile modulus and  $\tan \delta$  measurements were made using a Rheovibron Dynamic Viscoelastometer (model DDV II C). In each case, measurements were made in the temperature range between  $-100^{\circ}\text{C}$  and  $+100^{\circ}\text{C}$ .

5.2 THE TORSION PENDULUM

5.2.1 Description of Equipment and Testing Procedure

The torsion pendulum used for the measurement of small strain dynamic properties in shear was designed, constructed and commissioned in the laboratories of Sheffield City Polytechnic\*. The apparatus is shown schematically in Figures 5.1 and 5.2. Being of the counterbalance type, it was necessary to apply a small weight to the free end of the suspension wire in order to maintain the correct sample configuration. To keep the tensile strain in the sample to a minimum, the mass of this counterweight

---

\* by Dr N.C. Hilyard



TABLE 5.1  
Characteristics of Casting Solvents

	Solvent	Solubility* Parameter $\delta$ (cal.g <sup>-3</sup> ) <sup>1/2</sup>	Comments
	Ethyl acetate	9.1	Moderate hydrogen bonding parameter; good solvent for polystyrene, poor solvent for butadiene
	Tetrahydrofuran	9.1	Moderate hydrogen bonding parameter
9.1	Methyl ethyl ketone	9.3	Moderate hydrogen bonding parameter; good solvent for polystyrene, poor solvent for butadiene
	Benzene	9.2	Poor hydrogen bonding parameter
9.0	Heptane	7.4	Poor hydrogen bonding parameter
	Carbon tetrachloride	8.6	Poor hydrogen bonding parameter; good solvent for both blocks

The solubility parameters of polybutadiene and polystyrene are 8.4 and 9.1 (cal.g<sup>-3</sup>)<sup>1/2</sup>, respectively.

\* From Brandrup, J., & Immergut, E.H., "Polymer Handbook", Wiley (1975).

was made as small as possible, putting a tensile load of some 50 g on the specimen. Transverse stability was controlled by using a thin flexible polyurethane foam pad which made a low pressure contact with the suspension wire. Torsional oscillation of the specimen was measured by means of a coil attached to the suspension wire between the poles of a permanent magnet, the output from the coil being recorded on an ultra violet chart recorder. All measurements were made at about 1 Hz, the frequency being controlled by placing brass masses at different positions along the inertia bar. Initiation of the torsional oscillations was achieved by passing a current pulse through electro magnets placed close to the ends of the stainless steel inertia bars which contained soft iron slugs. Care was taken to ensure that there was no magnetic interaction between these iron slugs and the permanent magnet of the detector system.

Samples were cut from cast sheets using a template and scalpel; specimen width was 8 mm and the mounted length 50 mm. A dewar flask around the sample acted as a temperature cabinet, the temperature being altered by a gas heat exchange system. Low temperatures were achieved by cooling nitrogen gas with liquid nitrogen and controlling the gas flow rate. For above ambient temperatures, an industrial hot air blower fitted with an induction motor was used. Measurements were taken continuously between  $-120^{\circ}\text{C}$  and  $+100^{\circ}\text{C}$ , the rate of temperature change of the sample being approximately  $1^{\circ}\text{C}$  per minute. Thermocouples at the top and bottom of the specimen measured the temperature distribution to be less than  $\pm 1^{\circ}\text{C}$  over most of the temperature range ( $-90^{\circ}\text{C}$  to  $+80^{\circ}\text{C}$ ); however, outside these limits a larger differential existed.

### 5.2.2 Analysis

Shear modulus,  $G'_x$ , and loss tangent,  $\tan \delta_x$ , were calculated using equations (5.1) and (5.2) [205,206]:

$$G'_x = \frac{64 \pi^2 L I}{b d^3 g P_x^2} \quad (5.1)$$

$$\tan \delta_x = \frac{\Delta}{\pi} \quad (5.2)$$

where  $L$ ,  $b$  and  $d$  are the length, width and thickness of the specimen,  $P_x$  the measured period of torsional oscillation, and  $g$  a parameter dependent upon the width/thickness ratio [206].  $\Delta$  is the measured logarithmic decrement.

The moment of inertia,  $I$ , of the system was determined by measuring the period of oscillation,  $P'$ , for a high tensile steel sample with inertia masses,  $m$ , placed at different distances,  $r$ , from the axis of rotation of the inertia bar. Since:

$$P'^2 = K_1 (I_O + I') \quad (5.3)$$

where  $K_1$  is a constant,  $I_O$  the moment of inertia of the system with no added masses, and  $I' = 2mr^2$ . Plotting  $P'^2$  as a function of  $I'$  results in a straight line of slope  $K_1$ , with intercepts  $P_x'^2 = K_1 I_O$  at  $I' = 0$ , and  $I_O = -I'$  at  $P_x'^2 = 0$ . The value of  $I_O$  obtained in this way agreed well with that calculated from the mass and geometry of the components of the system.

The samples used in this work had low stiffness and it was necessary under some conditions to correct for the stiffness of the suspension wire [206,207]. Equations given by Nielsen [206] were used:

$$G'_c = \frac{G'_x (P_s'^2 - P_x'^2)}{P_s'^2} \quad (5.4)$$

$$\tan \delta_c = \frac{\tan \delta_x P_s'^2}{(P_s'^2 - P_x'^2)} \quad (5.5)$$

where  $P_s$  is the period of oscillation of the system without a sample.

At temperatures close to the glass transitions of the two phases, it was also necessary to correct for the influence of damping on the measured value of  $G'$  [208-210] so that:

$$G' = G'_c [1 - \tan^2 \delta_x / 4] \quad (5.6)$$

$$\tan \delta = \tan \delta_c \left[ \frac{1}{1 - \tan^2 \delta_x / 4} \right] \quad (5.7)$$

where  $G'$  and  $\tan \delta$  are the storage shear modulus and loss tangent of the material.

### 5.2.3 Experimental Results

The previously described (section 5.2.1) torsion pendulum was used at approximately 1 Hz to measure the dynamic modulus,  $G'$ , and loss tangent,  $\tan \delta$ , in shear. The materials TR1101 and TR1102 cast from the four different solvent systems were used for this series of tests, and the results are shown in Figures 5.3 to 5.6. As expected, two damping maxima were exhibited in each case (Figures 5.5 and 5.6) at temperatures corresponding closely to the glass transitions of the component phases of the block copolymers.  $T_B$ , the maximum associated with the polybutadiene phase, occurred at approximately  $-90^\circ\text{C}$ , and  $T_g$  for the polystyrene domains at between  $85^\circ\text{C}$  and  $95^\circ\text{C}$  (see Table 5.2). The high temperature,  $T_g$ , loss maximum of the lower stiffness samples (TR1101 and TR1102 cast from BEN/HEP and  $\text{CCl}_4$ ) were not well defined due to measurement difficulties at these temperatures.

At low temperatures,  $-100^\circ\text{C}$ ,  $G'$  approximates to the same value ( $10^9 \text{ Nm}^{-2}$ ) for both series of samples independent of casting solvent system (Figures 5.3 and 5.4). However, at the other end of the temperature range, around  $+90^\circ\text{C}$ , although the moduli of the samples within each series were similar and independent of solvent system, the moduli of the 1101 series were significantly higher than those of the 1102 series. In the plateau region, the modulus depends upon the macromorphology, which in turn is governed by the casting solvent system. The slopes of the  $G'-T$  graphs in the plateau region are very similar, but above  $+60^\circ\text{C}$  the rate of decrease in  $G'$  with increasing temperature is higher for the 1102 materials than for the 1101 series.

Drawing lines through the data points in the plateau regions and tangents to the curves in the temperature range  $+80^\circ\text{C}$  to  $+90^\circ\text{C}$ , at the point of intersection an estimate is achieved of the temperature,  $T_R$ , at which a rapid decrease in modulus begins. Although no systematic variation of  $T_R$  with solvent system is revealed within each series,  $T_R$  for the 1101 materials occurs at a higher temperature,  $+66^\circ\text{C} \pm 3^\circ\text{C}$ , than for the 1102 series,  $+60^\circ\text{C} \pm 3^\circ\text{C}$ .

An interesting point to note is that in the 1101 series, the BEN/HEP cast material is stiffer over the whole temperature range than that cast from  $\text{CCl}_4$ . However, in the case of the 1102 series, the situation is reversed with the  $\text{CCl}_4$  specimen being the stiffer of the two.

At the two glass transitions,  $T_B$  and  $T_g$ , there are systematic variations of the maximum values of loss tangent with solvent system. This data is presented in Table 5.2 in addition to Figures 5.5 and 5.6.

TABLE 5.2

Glass Transition Temperatures and Peak Loss Tangent Data in Shear and Tension

Material	Casting Solvent	Butadiene				Styrene			
		$T_g$ (°C)		$\tan \delta$ (peak)		$T_g$ (°C)		$\tan \delta$ (peak)	
		Shear	Tension	Shear	Tension	Shear	Tension	Shear	Tension
TR1101	Ethyl acetate 90/10 THF/MEK 90/10 BEN/HEP CCl <sub>4</sub>	-92	-78	0.28	0.12	89	109	0.46	1.05
		-91	-82	0.47	0.22	88	105	0.40	0.70
		-91	-76	0.84	0.60	92	110	0.29	0.36
		-91	-75	0.96	0.75	92	110	0.15	0.34
TR1102	Ethyl acetate 90/10 THF/MEK 90/10 BEN/HEP CCl <sub>4</sub>	-90	-79	0.46	0.23	87	98	0.59	0.65
		-91	-79	0.61	0.40	87	95	0.40	0.41
		-90	-76	1.02	0.84	92	105	0.30	0.34
		-90	-76	0.87	0.75	95	105	0.30	0.33
TR4122	90/10 THF/MEK 90/10 BEN/HEP CCl <sub>4</sub>		-62		0.15		95		1.1
			-64		0.21		93		0.9
			-66		0.42		90		0.65
TR4113	90/10 THF/MEK 90/10 BEN/HEP CCl <sub>4</sub>		-65		1.08		94		0.3
			-65		1.12		94.		0.3
			-65		1.13		90		0.26

Samples with the lowest room temperature modulus exhibit the largest loss maxima at  $T_B$  and the smallest maxima at  $T_S$ . This behaviour is in agreement with that predicted by the theory of Dickie for the viscoelastic properties of polymer composites [139], and found experimentally for triblock polymers by Miyamoto et al [96] and Kraus et al [97].

### 5.3 THE RHEOVIBRON

#### 5.3.1 Description of Equipment and Testing Procedure

The Rheovibron dynamic viscoelastometer, shown schematically in Figure 5.7, was used to measure the elastic modulus  $E'$  and loss tangent. Developed by Professor N. Takayanagi and his associates at Kyushu University in Japan, this equipment is marketed commercially throughout the world [211]. The film sample is driven at a predetermined frequency and displacement, the resultant strain and stress being measured simultaneously and independently. The extent to which the stress is out of phase with strain,  $\tan \delta$ , is read directly from a meter, and absolute values of the complex modulus  $|E^*|$  are calculated directly from stress and strain measurements. From the information available, the tensile storage modulus,  $E'$  (the real part of the tensile complex modulus), can be deduced:

$$E' = |E^*| \cos \delta \quad (5.8)$$

and it follows that the loss modulus,  $E''$ , the imaginary part of  $|E^*|$ , is given by:

$$E'' = E' \tan \delta \quad (5.9)$$

It is possible to vary the temperature at a continuous rate while measurements are being taken, and there are facilities for above and below ambient conditions, the full practical temperature range being of the order of  $-150^\circ\text{C}$  to  $+200^\circ\text{C}$ .

Samples were cut from cast sheets using a template and scalpel, the same sample being used for the whole temperature range (approximately  $-100^\circ\text{C}$  to  $+120^\circ\text{C}$ ). The specimen width was 3 mm and the gauge length 20 mm. Measurements of  $\tan \delta$  and the stress and strain on the sample were taken at about  $5^\circ\text{C}$  intervals over most of the temperature range, but more frequently close to the glass transitions of the two phases.

Although the frequency of forced vibrations is adjustable with this equipment, all the experiments here were carried out at a frequency of 11 Hz.

### 5.3.2 Experimental Results for Small Strain Dynamic Tensile Modulus and Loss Tangent

Figures 5.8 to 5.11 show  $\tan \delta$  as a function of temperature for the materials and casting solvents used in this study. Clearly, as with the data obtained in shear, the principal features are the glass transitions of the individual blocks, which occur at the temperatures shown in Table 5.2. This table also shows the influence of solvent on peak height at the transitions, and again systematic variations of the peak values occur with casting solvent.

Of particular interest are the materials containing plasticiser, TR4122 and TR4113, which were not evaluated in shear. Taking first TR4122, in Figure 5.10, a material known to have a relatively high polystyrene content. Here, as expected, at  $T_g$  the damping maximum is high, reflecting the increased styrene content, but in addition, samples cast from THF/MEK and BEN/HEP indicate intermediate broad damping peaks at about  $+20^\circ\text{C}$  and  $-5^\circ\text{C}$ , respectively. However, no intermediate peak is noted with the sample cast from  $\text{CCl}_4$ . Turning to the results for TR4113 in Figure 5.11, this material has a lower styrene content and the peak at  $T_B$  is high and that at  $T_g$  low, but the interesting feature here is that the effect of casting solvent is almost imperceptible, and in no case is there any indication of an intermediate peak.

The dispersion curves for the tensile dynamic modulus are shown in Figures 5.12 to 5.15; in each graph, the modulus is plotted as a function of temperature for one material cast from each of the solvent systems. At  $-100^\circ\text{C}$ , the modulus value is of the order of  $10^9 \text{ Nm}^{-2}$ , although for TR4122 it is slightly lower, and individual solvent effects do vary somewhat at this modulus value.

Over the temperature range, TR1101 cast materials are consistently stiffer than TR1102, as was the case in shear. It is also noted again that the BEN/HEP cast 1101 is stiffer than the  $\text{CCl}_4$  material, but the opposite is true for TR1102. Although ethyl acetate and THF/MEK solvent systems always give a stiffer product, this advantage is less marked for TR4122 for which BEN/HEP and  $\text{CCl}_4$  record a particularly high modulus. There is virtually no difference in modulus values for TR4113 whatever the casting solvent; however, in this case, all the recorded moduli are very low.



#### 5.4 DISCUSSION OF DYNAMIC MECHANICAL RESULTS

The casting solvents used in this study were chosen in order to give a wide variety of elastic response to the block copolymer materials to be tested. It was known [94] that the mechanical behaviour of samples cast from 90/10 THF/MEK differed markedly from that of specimens cast from 90/10 BEN/HEP and  $\text{CCl}_4$ ; ethyl acetate was more of an unknown quantity but, being a good solvent for polystyrene and a non-solvent for polybutadiene, promised some interesting results. Both ethyl acetate and MEK are micellating solvents so that the materials cast from these solvents were expected to have a different microstructure and hence a different dynamic response to materials cast from 90/10 BEN/HEP and  $\text{CCl}_4$ .

This indeed proved to be the case. With one or two exceptions, in both shear and tension, a systematic solvent effect was noted in the  $\tan \delta$  peak heights at  $T_B$  and  $T_S$ , the glass transition temperatures of the component polybutadiene and polystyrene phases. For TR1101 at  $T_B$ , the order was  $\text{CCl}_4 > \text{BEN/HEP} > \text{THF/MEK} > \text{ethyl acetate}$ , the reverse being true at  $T_S$ . A similar picture occurred for TR1102, except that in this case BEN/HEP and  $\text{CCl}_4$  changed places. TR4122 followed the normal pattern set by TR1101, but TR4113 showed virtually no solvent effect whatsoever.

With some relatively minor variations, the transitions for TR1101 and TR1102 occurred at approximately the same temperatures, the major difference here is that the temperatures in shear and tension were not the same. In shear,  $T_B$  occurred consistently at  $-90^\circ\text{C}$  and  $T_S$  at about  $+100^\circ\text{C}$ , whereas in tension  $T_B$  was at  $-78^\circ\text{C}$  and  $T_S$  at  $+110^\circ\text{C}$ . This can be attributed partly to the effect of frequency [96], the tensile data being obtained at a frequency an order of magnitude greater than that of the shear data, and a shift towards a higher temperature would be expected, the temperature difference between the peaks in each case being almost identical.

Elsewhere [96,204] it has been suggested that a mixed phase exists in TR1101 when cast from some solvents, indicated by a  $\tan \delta$  peak at temperatures intermediate between the two major glass transition peaks. Another possible explanation for such minor transitions being observed is the  $\beta$ -mechanism in polystyrene [231]. In this work, no such intermediate transitions were observed in TR1101, TR1102 or TR4113; however, the behaviour of TR4122 cast from THF/MEK and BEN/HEP indicated quite broad peaks centering at  $+20^\circ\text{C}$  and  $-5^\circ\text{C}$ , respectively. Since no effect was noticed when  $\text{CCl}_4$  was the solvent, and TR4113 showed no intermediate transitions, it seems reasonable to discount the plasticiser as the source of this behaviour. Also, any  $\beta$ -transition in polystyrene would be evident

at higher temperatures, and if this were the cause it would be observed when  $\text{CCl}_4$  was used as solvent; it would also be expected to occur at a similar temperature in each case. If the effect is considered to be due to phase mixing, then the difference in temperature at which the peaks occur might well be expected, since the peak temperature would be dependent upon the proportions of styrene and butadiene making up this mixed phase. It is likely that these proportions would be dependent upon the solvent system.  $\text{CCl}_4$  might be expected to show little phase mixing since it is a good solvent for both styrene and butadiene, producing well separated domains. It is thought that TR4122 is affected by this phase mixing owing to its high styrene content.

In addition to the casting solvent causing variations in  $\tan \delta$  peak heights, there are also considerable differences in the dynamic moduli achieved by the same material when cast from different solvents. Ethyl acetate and THF/MEK produced materials with the highest modulus in all cases. This can be associated with the connectivity of the polystyrene phase in these samples (section 4.6). It was noted that for each material, the casting solvents which gave higher  $T_g$  peaks produced stiffer materials throughout the temperature range in both shear and tension. A point of interest is that TR4113 showed virtually no solvent effect in its tensile dynamic modulus curves owing, it is thought, to the plasticising effect on a relatively low styrene content polymer.

Arridge & Folkes [229] examined the dynamic behaviour of annealed "single crystals" of an SBS block polymer formed by an extrusion technique. They showed that for a rubber, reinforced by a hexagonally spaced array of parallel glassy polystyrene cylinders extending completely through the sample, fibre reinforcement theory predicted shear moduli which were dominated by the shear modulus of the rubbery matrix. Their experimental results agreed well with the theory.

Although the far less perfect structures of the present study could not be expected to conform to the fibre reinforcement theory used by Arridge & Folkes, it is possible to make some qualitative comments at this stage. Making reference to the schematic diagram of Figure 5.16(a), no connectivity of the polystyrene domains exists in the  $x$  or  $y$  directions of the rod-like sample, so that the polystyrene cylinders make only a modest contribution to the shear modulus if the shear plane is either the  $yz$  or  $xz$  plane. Also, if the shear plane is the  $xy$  plane, the cylinders are deformed in the bending mode, and since the force to deflect a cylindrical fibre in bending is proportional to  $r^4/L^3$ , and in this case  $r \ll L$ , again

the contribution of the styrene cylinders to the composite shear modulus is small.

In the case of lamellae in Figure 5.16(b), connectivity exists in both the  $x$  and  $z$  directions. Shearing in a plane perpendicular to the  $y$  axis, in the  $x$  or  $z$  directions, results in a low modulus since the rubbery phase absorbs most of the strain. Shearing in planes normal to the  $x$  or  $z$  axes, in the  $y$  direction, gives a slightly increased modulus since the hard thin lamellae are deformed in bending. Finally, shearing normal to the  $x$  axis in the  $z$  direction, or normal to the  $z$  axis in the  $x$  direction, produces high resistance since the lamellae are deformed in their own plane.

It follows that on the macro-scale where bundles of cylinders or lamellae are randomly oriented, the lamellar morphology will exhibit a higher shear modulus than the cylindrical morphology. This proves to be true in the present work. In Chapter 4, it was shown that the effect of ethyl acetate and THF/MEK as casting solvents was to promote a largely lamellar styrene microstructure in TR1101, and ethyl acetate only in TR1102, THF/MEK here giving a structure more intermediate between cylinders of styrene and an incomplete lamellar formation. It was also demonstrated that for the same materials, BEN/HEP and  $\text{CCl}_4$  solvents tended to cause a largely cylindrical styrene morphology. The data presented in Figure 5.3 for TR1101 shows that in shear the modulus exhibited when ethyl acetate is the casting solvent is an order of magnitude higher than when  $\text{CCl}_4$  is the solvent. The difference is almost as great when ethyl acetate is compared with BEN/HEP casting. THF/MEK shows a five-fold increase over  $\text{CCl}_4$  cast TR1101, reflecting the conclusion from morphological data that THF/MEK casting produces an inferior lamellar structure to that given by ethyl acetate.

Examining the data for TR1102 (Figure 5.4) reveals that the modulus for ethyl acetate casting is lower than when TR1101 was used, but that it is still considerably higher than for  $\text{CCl}_4$  and BEN/HEP cast samples. The reason for the difference in modulus between TR1101 and TR1102 when cast from ethyl acetate is the decrease in styrene content in TR1102 (Table 3.10) which leads to more imperfections in the lamellar structure.

THF/MEK cast TR1102 also suffers a reduction in shear modulus when compared with TR1101, but this was anticipated since the morphological data (Table 4.4) suggests a cylindrical styrene microstructure for TR1102 cast from THF/MEK and a predominantly lamellar structure for TR1101.

The differences between BEN/HEP and  $\text{CCl}_4$  as casting solvents for

either material are far less marked. One point of interest does emerge, however, in that the shear modulus for TR1102 cast from  $\text{CCl}_4$  actually increases compared with the TR1101 value, and in fact exceeds the BEN/HEP cast modulus which is almost identical for both materials. This may be due to the reduced styrene content resulting in a favourable combination of length to diameter ratio for the cylinders, coupled with changes in the interdomain distance and the long range order of the particles. Whatever the cause of this unexpected behaviour, it is repeated in the tensile dynamic situation (Figures 5.12 and 5.13). However, in this case, the BEN/HEP cast TR1102 has a reduced tensile modulus compared with TR1101, and the  $\text{CCl}_4$  cast materials exhibit a more or less identical value.

The behaviour in tension follows that of the shear data, with ethyl acetate producing the stiffest material in each case. Again, this pattern of behaviour would be expected when the structure of the samples change from lamellar to cylindrical. A point worth mentioning is that TR1102, using THF/MEK in both shear and tension, is intermediate between the modulus levels set by ethyl acetate and that of the BEN/HEP and  $\text{CCl}_4$  samples, an indication of the dual microstructure bordering on the cylinder/lamellar interchange (Table 4.4).

Turning to the tensile dynamic moduli of the plasticised materials TR4122 and TR4113. The morphology of TR4122 was shown in Chapter 4 to be largely lamellar for all the casting solvent systems investigated. This evidence is supported by the dynamic data for TR4122 shown in Figure 5.14. Here, the tensile modulus recorded at  $0^\circ\text{C}$  when the casting solvent THF/MEK is equivalent to that exhibited at the same temperature by TR1101 cast from THF/MEK. Even the less effective lamellae forming solvents, BEN/HEP and  $\text{CCl}_4$ , record moduli in excess of that shown by TR1102 cast from THF/MEK.

Figure 5.15 shows the tensile dynamic modulus data for TR4113, and reveals no solvent effect at all. The modulus recorded at  $0^\circ\text{C}$  is less than one-half the value of any other material/solvent system at this temperature. The most likely cause of this behaviour is the effect of the plasticiser on what is a relatively low styrene content polymer.

Since both shear and tensile moduli were measured for TR1101 and TR1102, it is of interest to compare these two quantitatively. Some workers [212] have, when necessary for their calculations, used the classical elasticity relationship between shear and tensile modulus:

$$E = 3G \quad (5.10)$$

Figures 5.17 and 5.18 show the function  $E'/G'$  for TR1101 and TR1102 cast from each of the solvent systems and plotted as a function of temperature. Both graphs reflect the offset temperature relationship between  $E'$  and  $G'$ . That is, at high and low temperatures,  $E'/G'$  increases rapidly owing to the transitions in tension and shear occurring at different temperatures, always favouring a higher value of  $E'$ . Between  $-50^{\circ}\text{C}$  and  $+50^{\circ}\text{C}$ , a fairly constant value of  $E'/G'$  is achieved for each material/solvent combination. This intermediate value of  $E'/G'$  is dependent upon the casting solvent system for each material. The order for TR1101 is THF/MEK > ethyl acetate >  $\text{CCl}_4$  > BEN/HEP; however, for TR1102, the order changes to ethyl acetate > THF/MEK > BEN/HEP >  $\text{CCl}_4$ .

Values of  $E'/G'$  at  $0^{\circ}\text{C}$  for the two materials and all the solvent systems investigated are summarised in Table 5.3, and it is immediately obvious that equation (5.10) does not hold for these materials. The average value of the  $E'/G'$  ratio is 1.5 and perhaps this would be a better approximation, so that:

$$E' = 1.5 G'$$

TABLE 5.3  
The Function  $E'/G'$  at  $0^{\circ}\text{C}$  for TR1101 and  
TR1102 Cast from Several Solvent Systems

Material Solvent	TR1101	TR1102
Ethyl Acetate	1.9	1.87
90/10 THF/MEK	2.18	1.44
90/10 BEN/HEP	1.45	0.92
$\text{CCl}_4$	1.56	0.60

Comparing the data here with that recorded by Kraus et al [97]. Values of the tensile modulus  $E'$  are very similar in both pieces of work, even though Kraus et al used a Rheovibron at a frequency of 35 Hz. In

addition, Kraus presents a limited set of data for  $G'$  measured using a Rheovibron; he covers the range  $+20^{\circ}\text{C}$  to  $+120^{\circ}\text{C}$ , but his curves are extremely shallow and the values for  $G'$  very low. So that the  $E'/G'$  function in his case achieves values in excess of 20 for film cast from ethyl acetate.

Whilst it may be advantageous to use the same instrument for the tension and shear experiments, and Kraus [97] has done this, some doubts must be raised about the reliability of the shear results obtained using the Rheovibron, particularly since the data Kraus records are so low. The Rheovibron as originally conceived was designed to perform tests in the tensile mode, and data obtained at most of the instrument's set frequencies are quite satisfactory. However, at 35 Hz, performance is often erratic owing to resonance of the instrument's vibrating parts. It is usually possible to control this effect in the tensile mode, and Kraus appears to have been able to achieve such control in his tensile experiments. In the shear mode, on the other hand, it is likely that at the selected frequency of 35 Hz, considerably more difficulty would be experienced in achieving meaningful results. These doubts are reinforced by Kraus' loss tangent data in shear which shows no maximum corresponding to the styrene block glass transition at a temperature between  $80^{\circ}\text{C}$  and  $100^{\circ}\text{C}$ . Instead, the data form a rising linear plot from  $+20^{\circ}\text{C}$  to  $+120^{\circ}\text{C}$ .

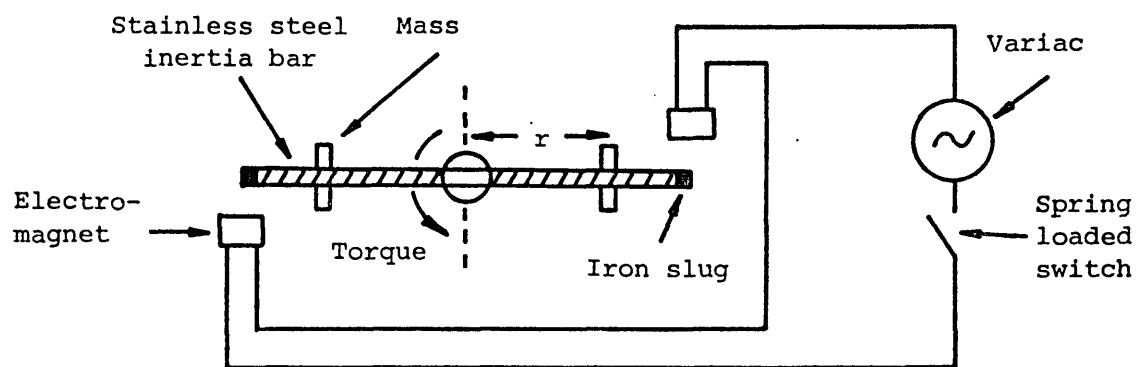
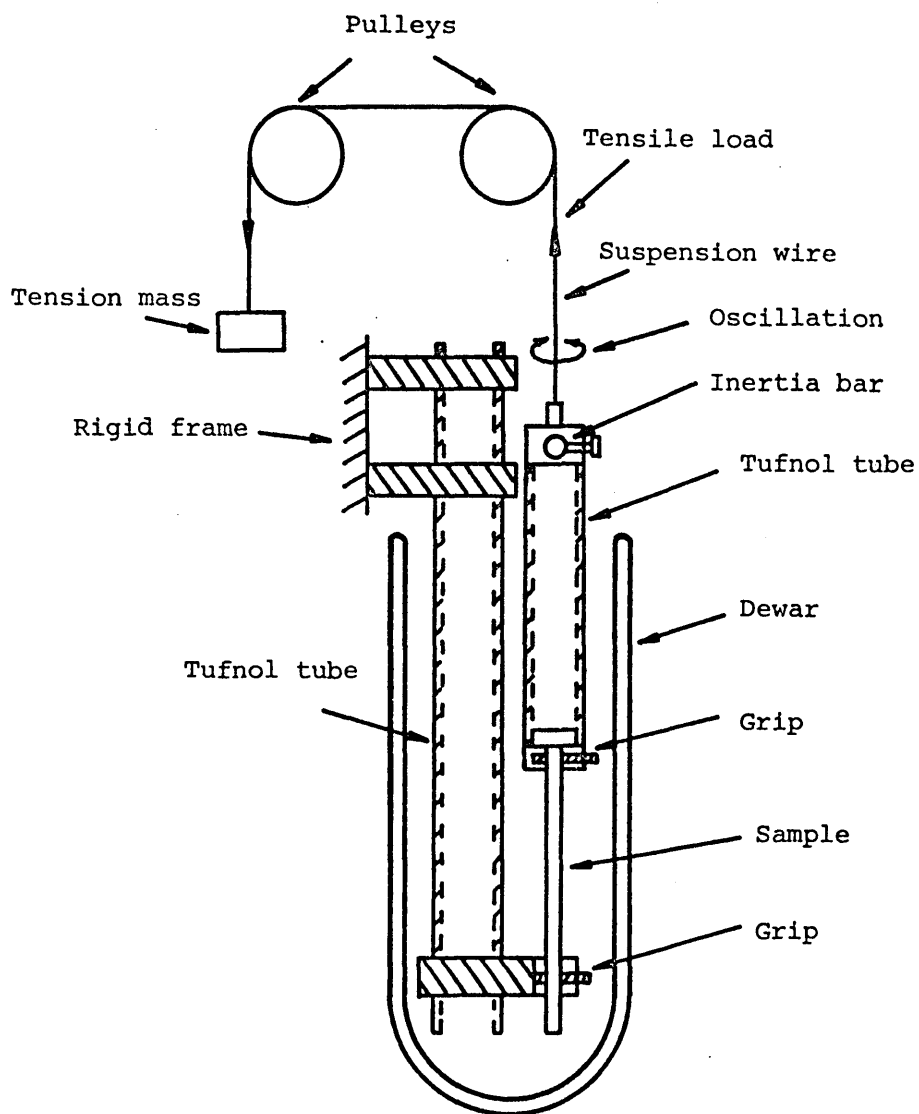


Figure 5.1 The torsion pendulum.

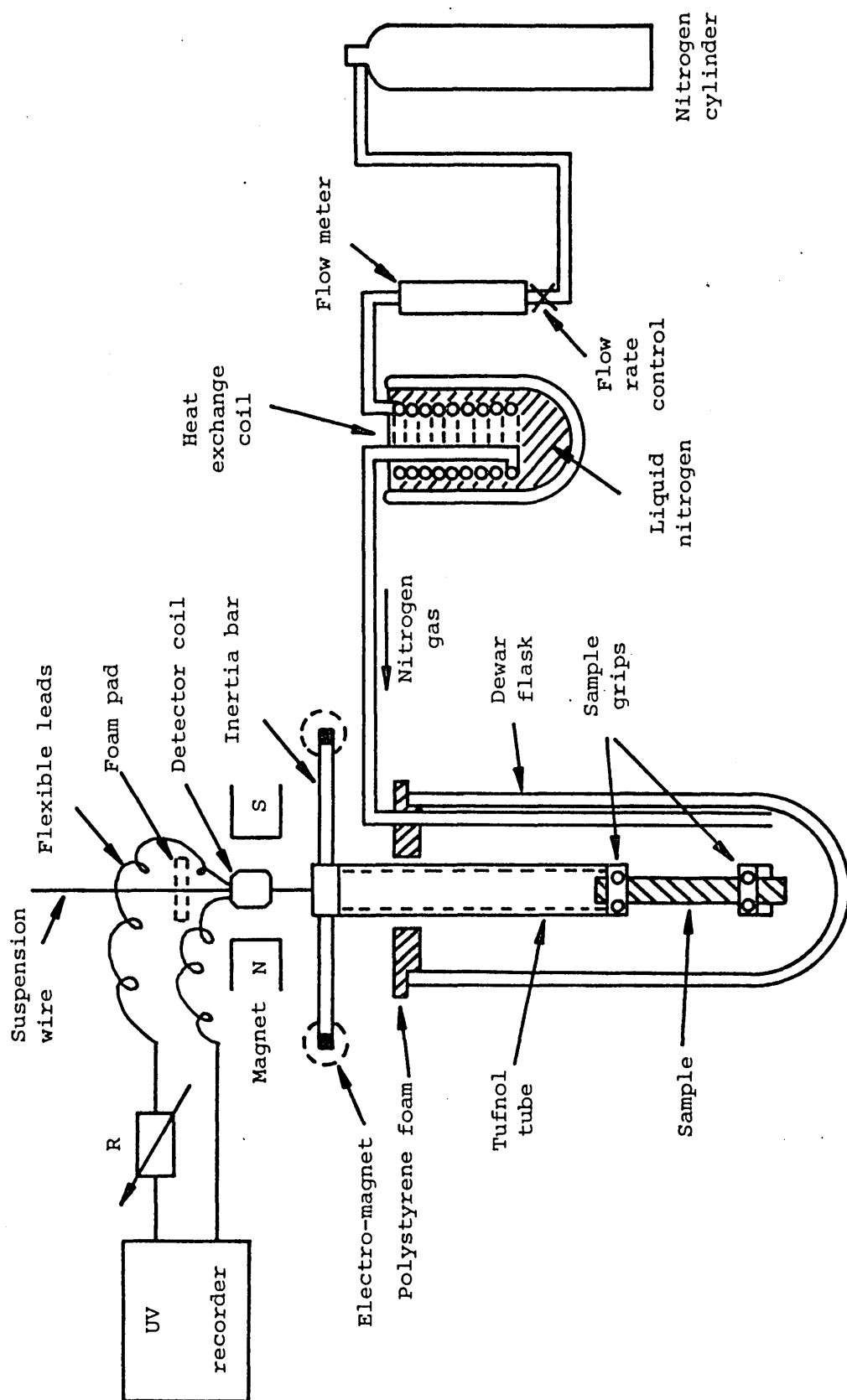


Figure 5.2 The torsion pendulum and ancillary equipment.



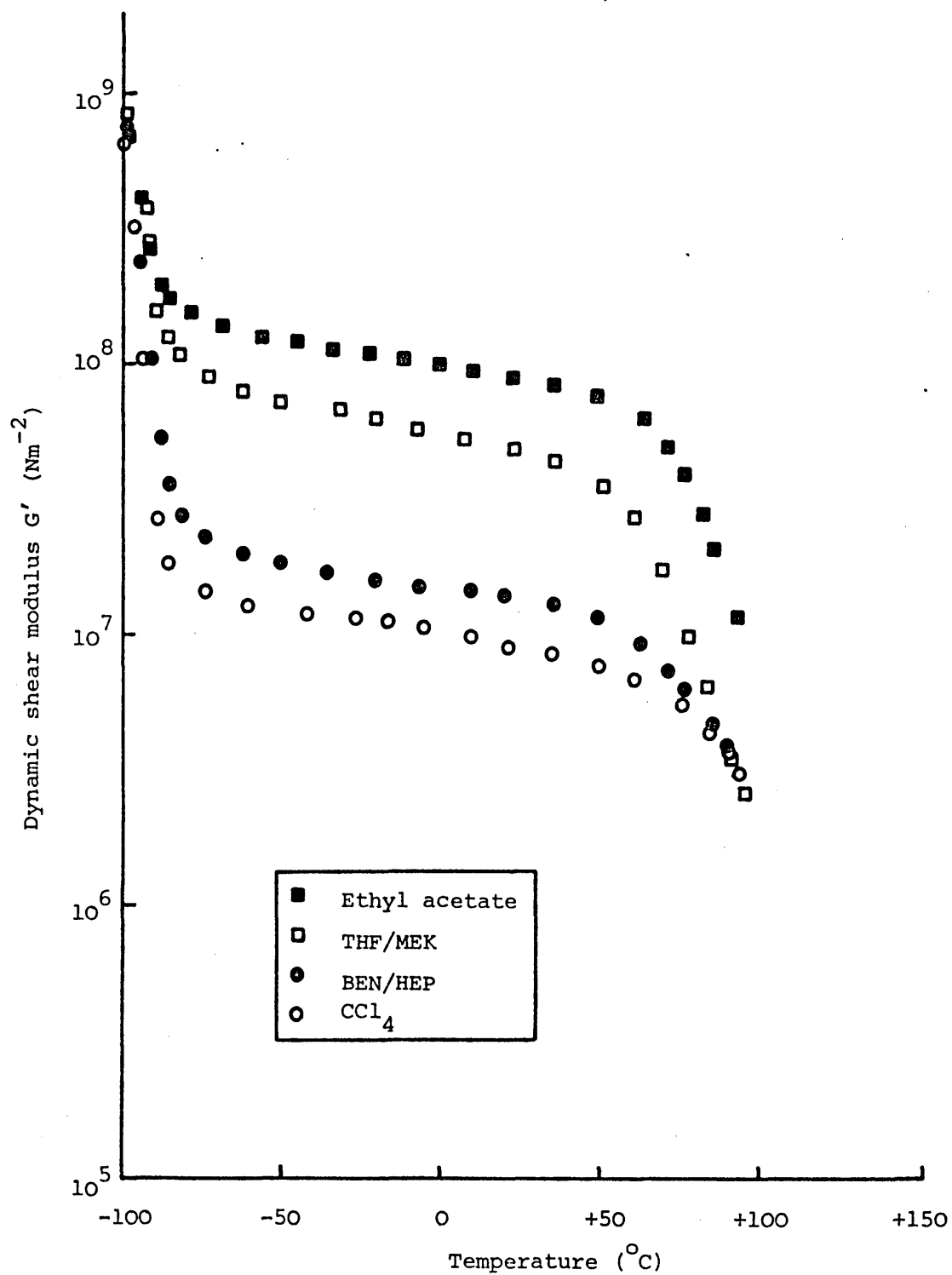


Figure 5.3 Dynamic shear modulus for TR 1101 as a function of temperature.

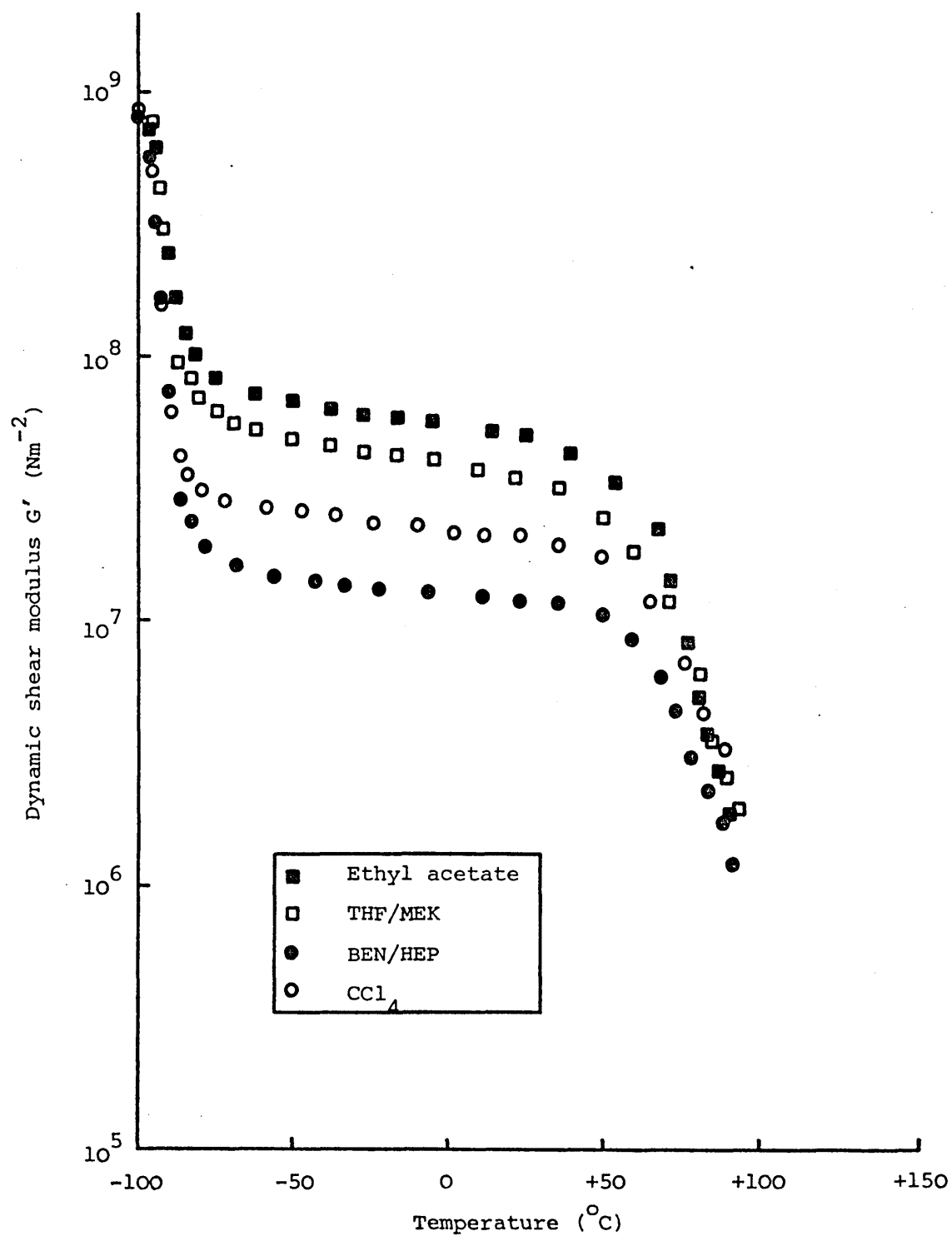


Figure 5.4 Dynamic shear modulus for TR1102 as a function of temperature.

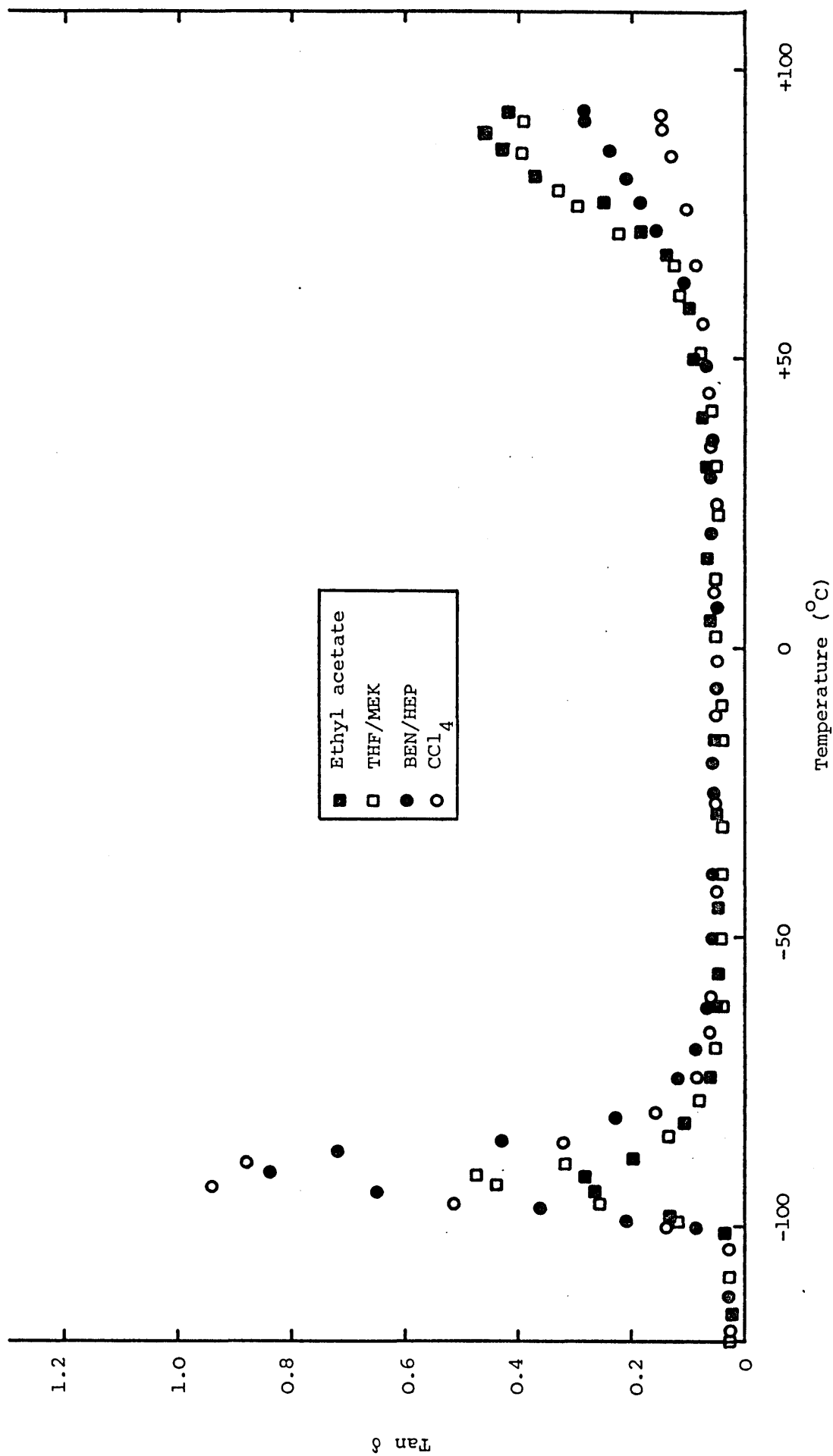


Figure 5.5 Loss tangent as a function of temperature for TR 1101 cast from several solvent systems. Using the torsion pendulum at approximately 1Hz.

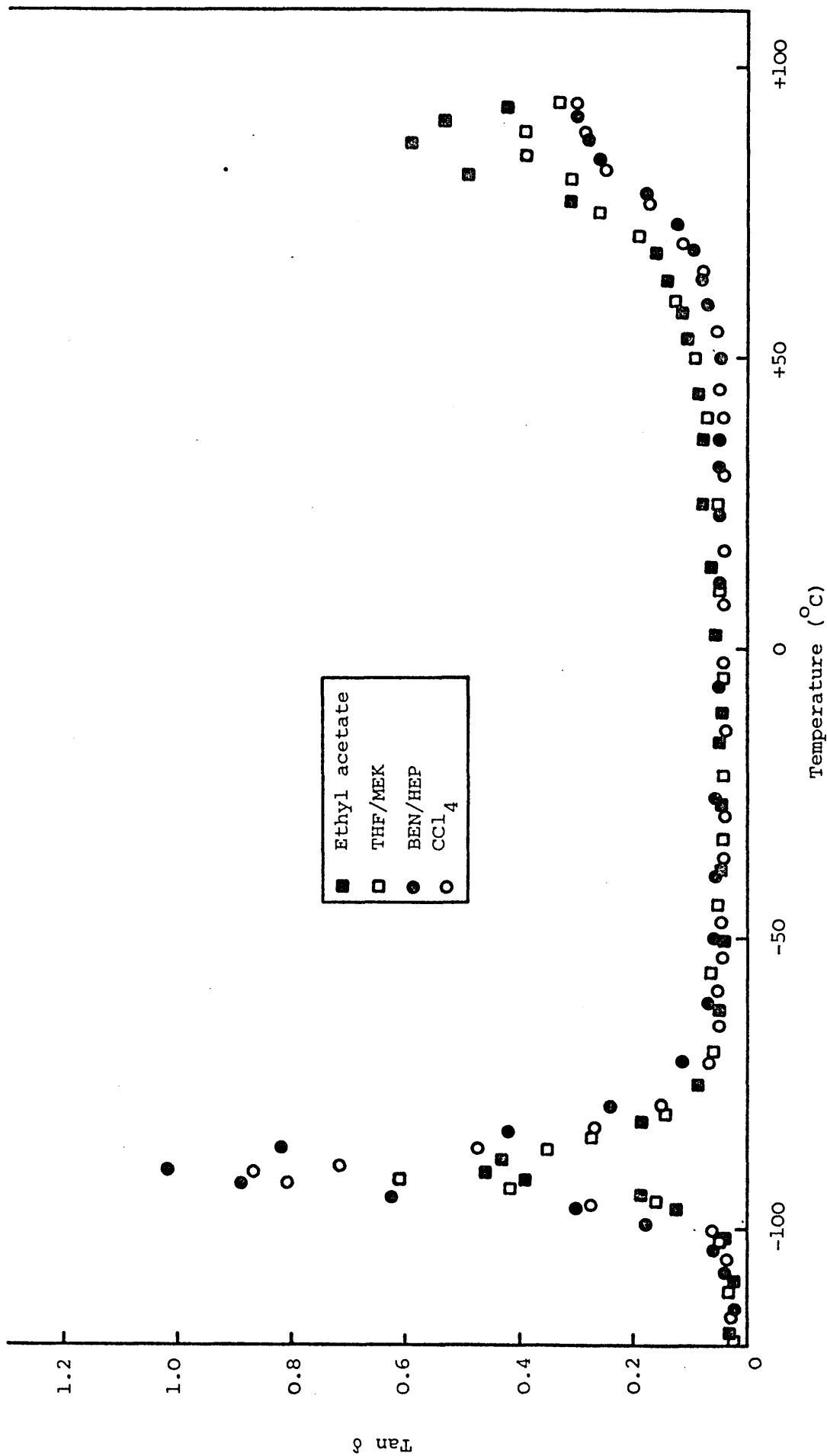


Figure 5.6 Loss tangent as a function of temperature for TR 1102 cast from several solvent systems. Using the torsion pendulum at approximately 1Hz.

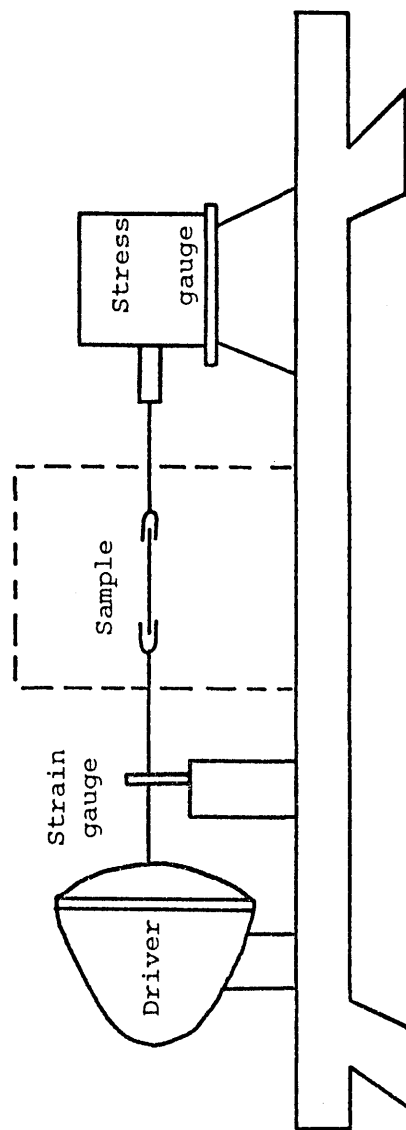


Figure 5.7 Schematic diagram of the Rheovibron instrument for measuring the response of a polymer sample to forced vibrations.

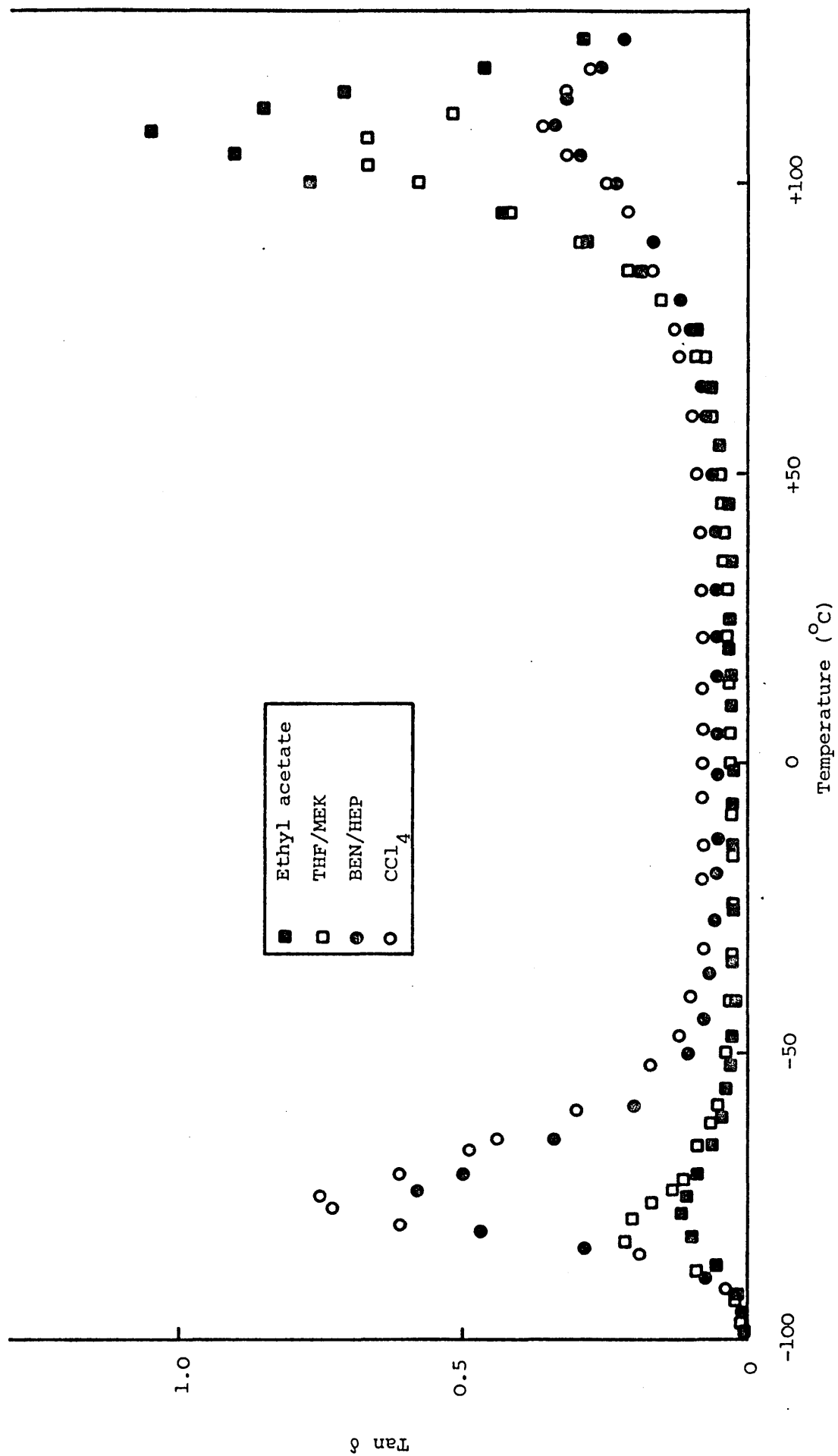


Figure 5.8 Loss tangent as a function of temperature for TR101 cast from several solvent systems. Using the Rheovibron at 11Hz.

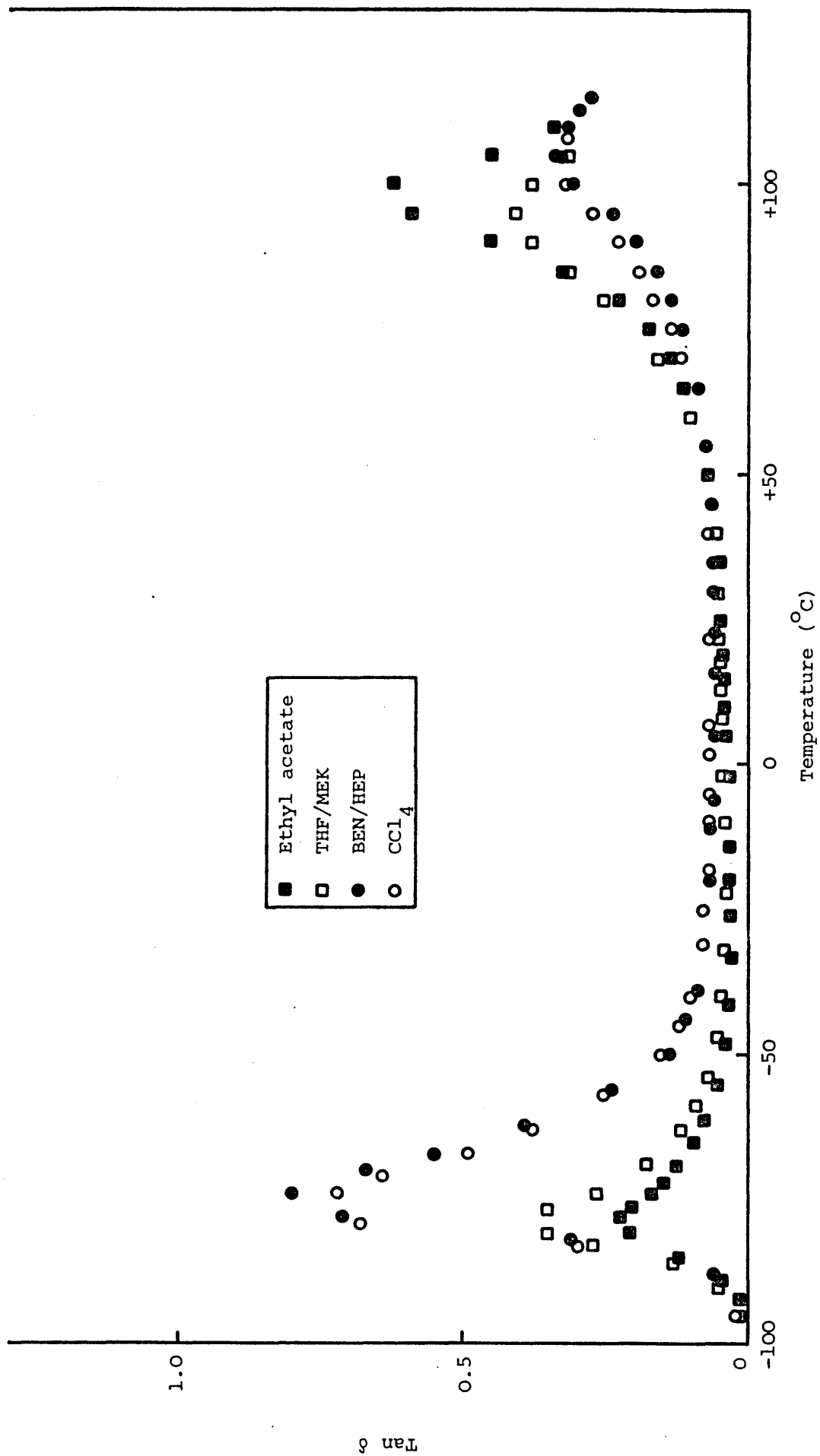


Figure 5.9 Loss tangent as a function of temperature for TR 1102 cast from several solvent systems. Using the Rheovibron at 11Hz.

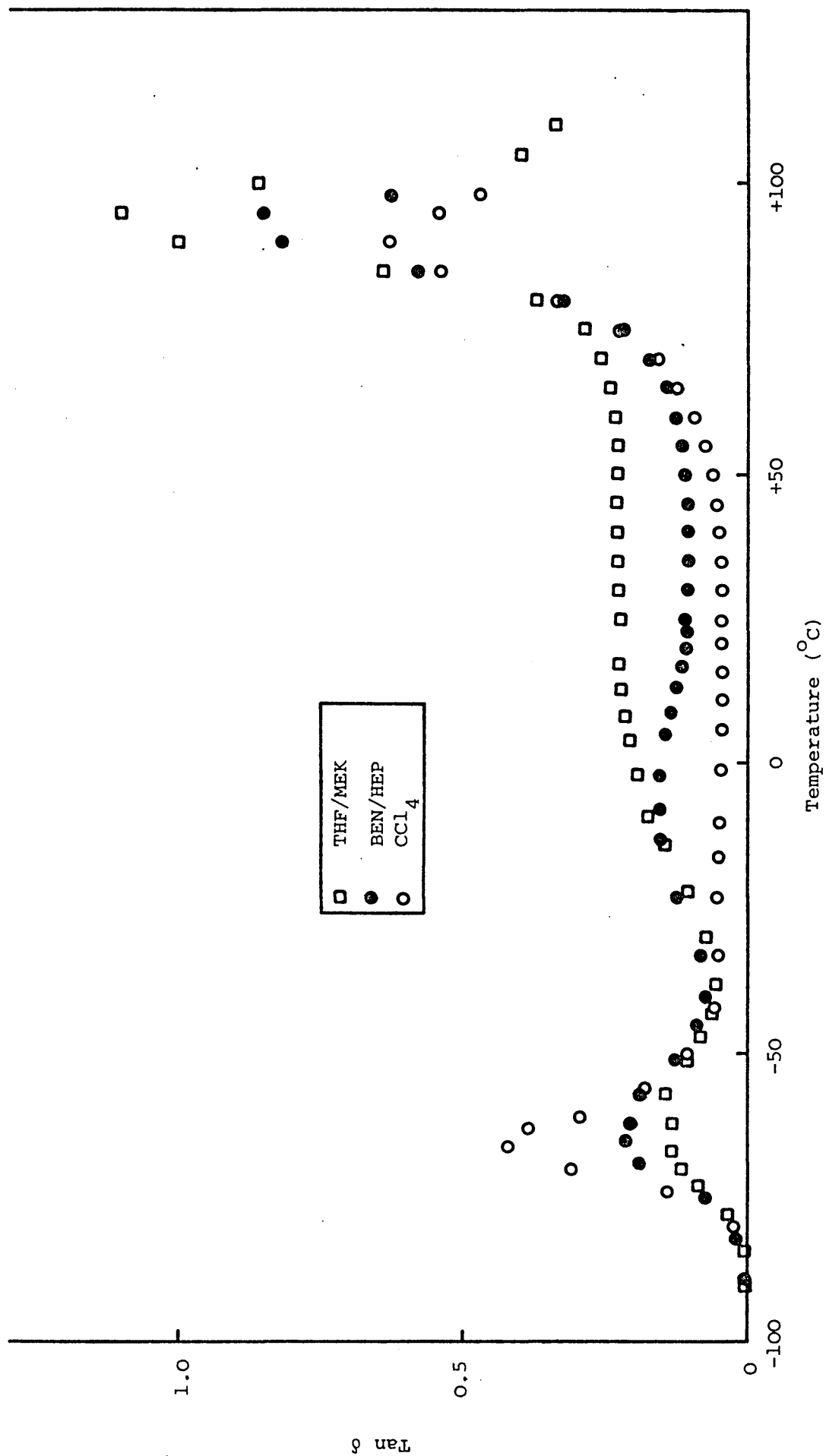


Figure 5.10 Loss tangent as a function of temperature for TR 4l22 cast from several solvent systems. Using the Rheovibron at 11Hz.



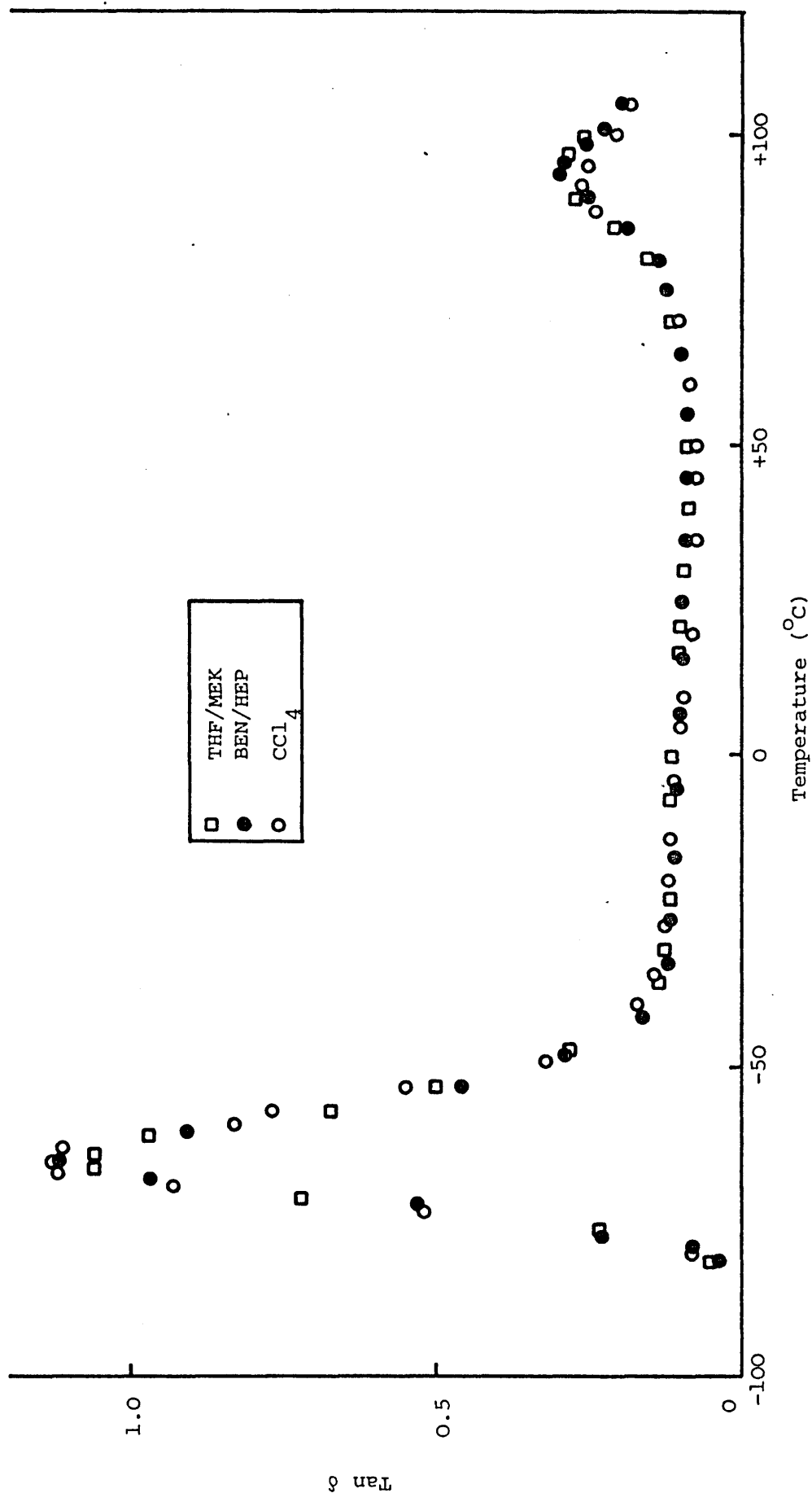


Figure 5.11 Loss tangent as a function of temperature for TR 4113 cast from several solvent systems. Using the Rheovibron at 11Hz.

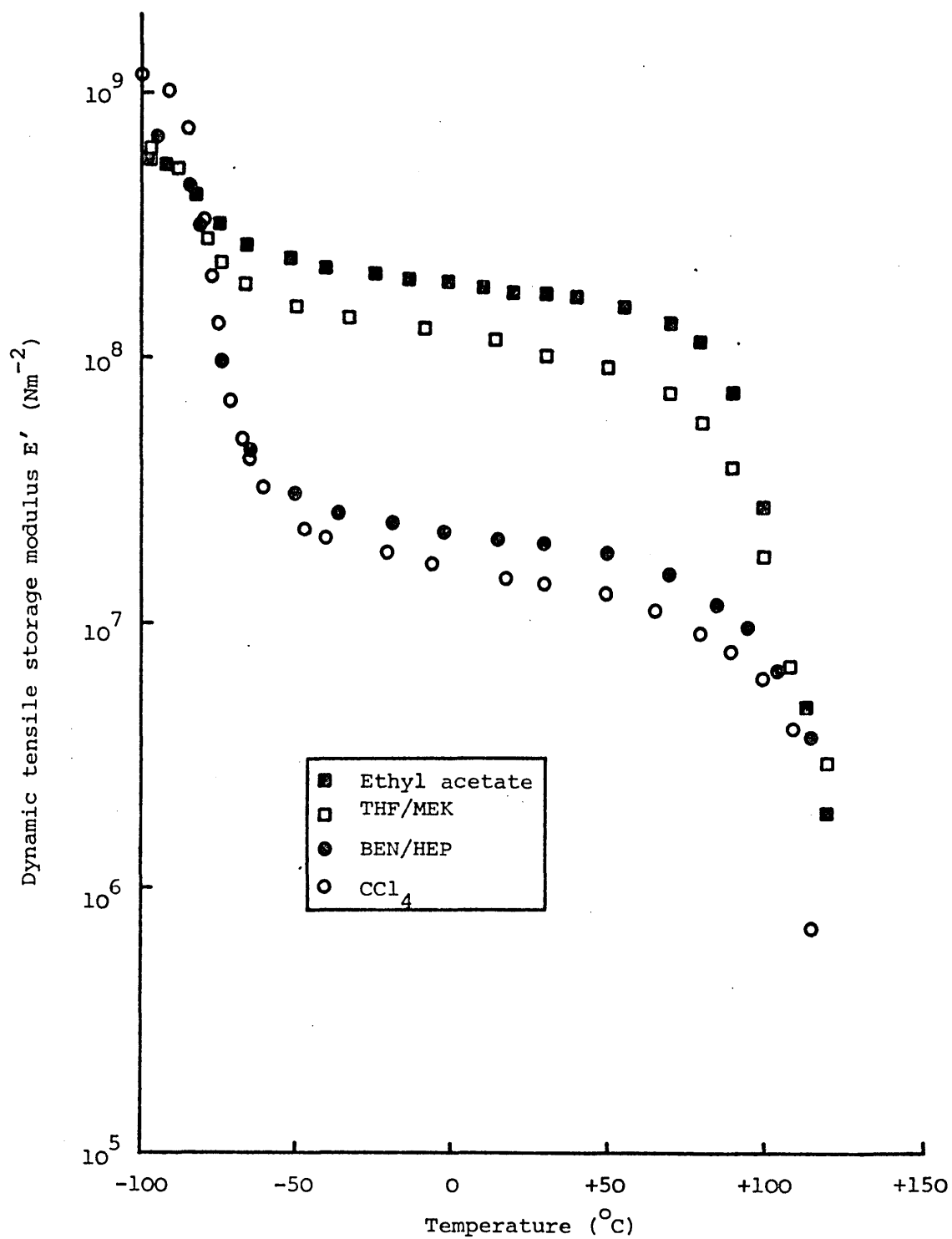


Figure 5.12 Dynamic storage modulus in tension as a function of temperature for TR 1101 cast from several solvent systems ( 11Hz ).

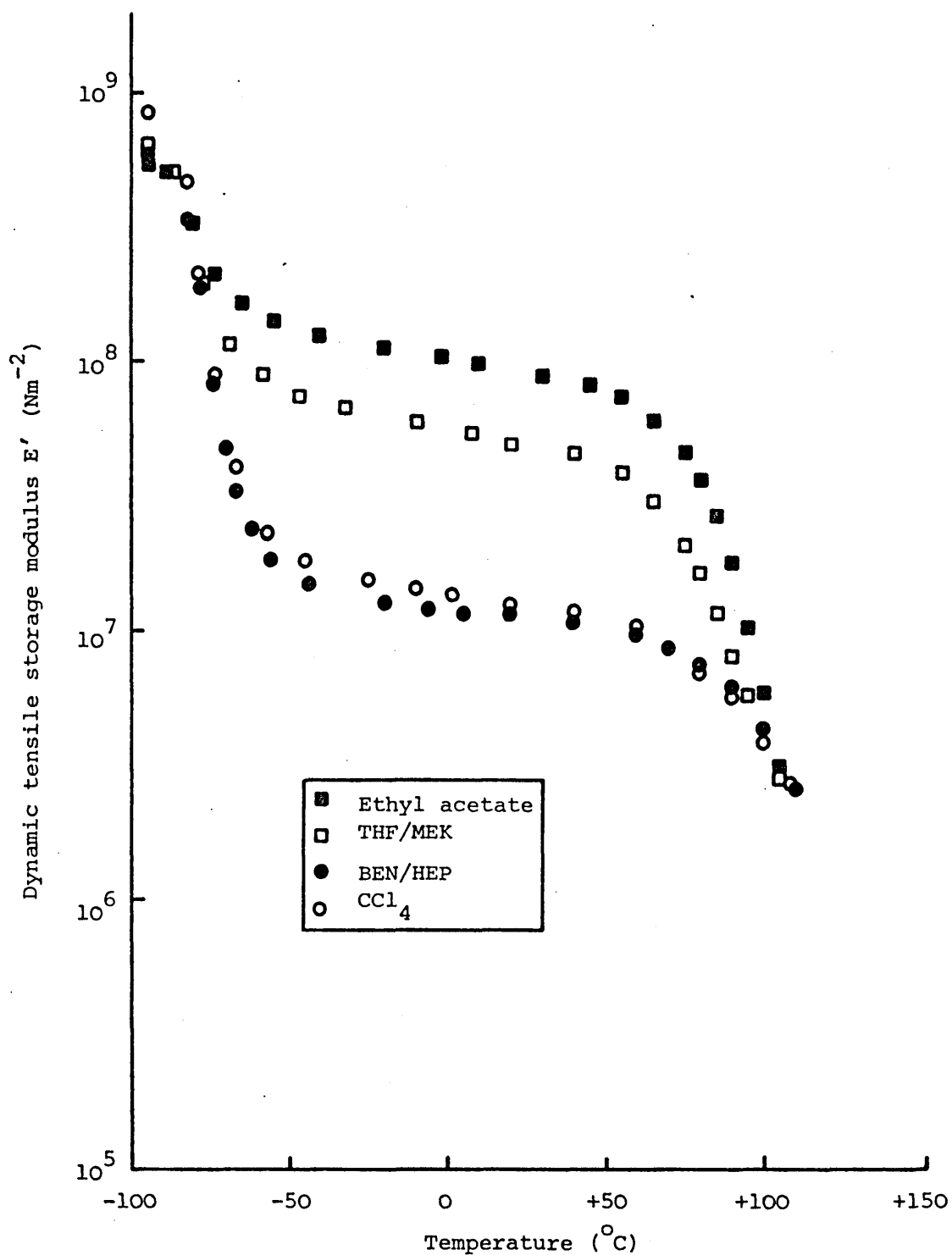


Figure 5.13 Dynamic storage modulus in tension as a function of temperature for TR 1102 cast from several solvent systems ( 11Hz ).

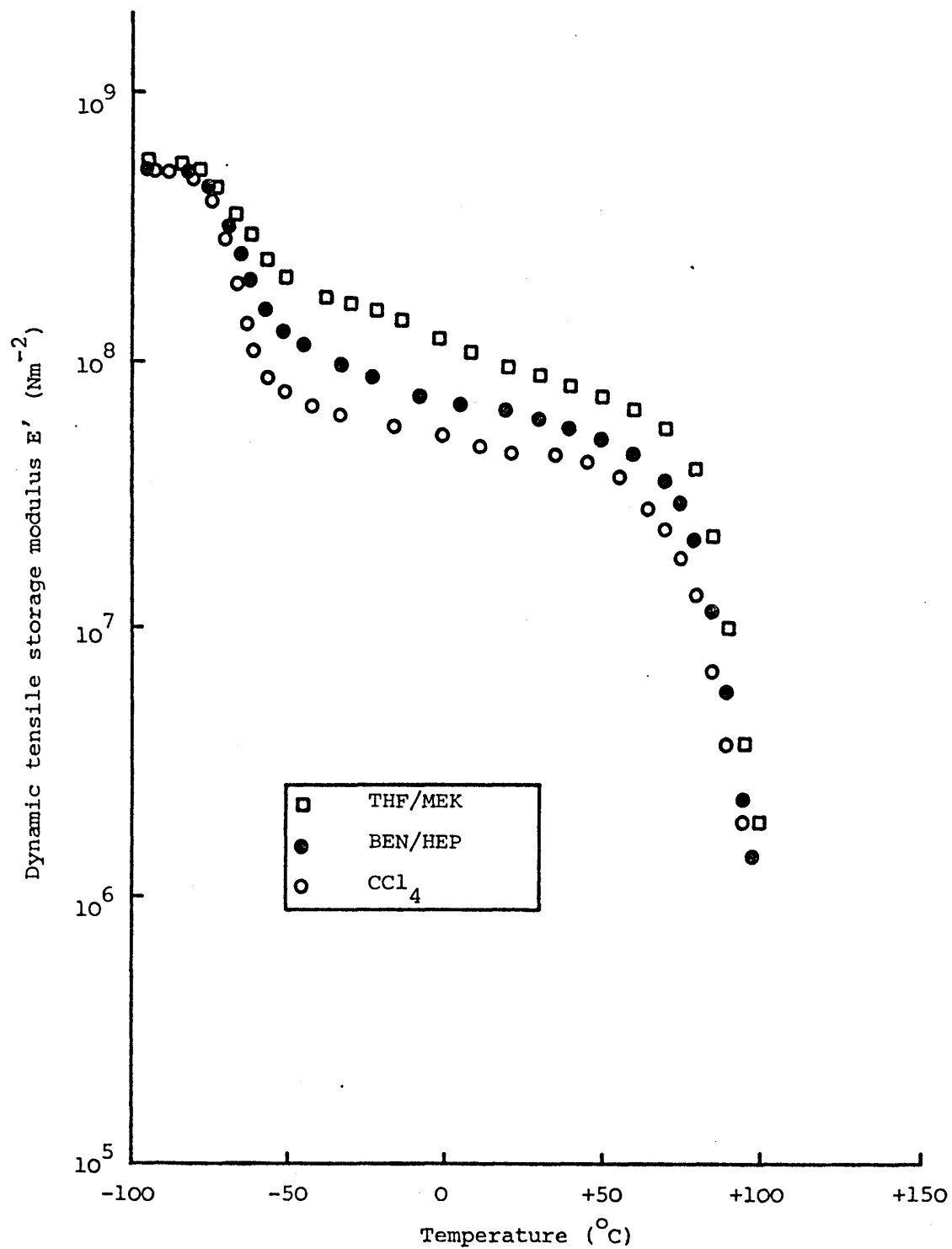


Figure 5.14 Dynamic storage modulus in tension as a function of temperature for TR 4122 cast from several solvent systems ( 11Hz ).

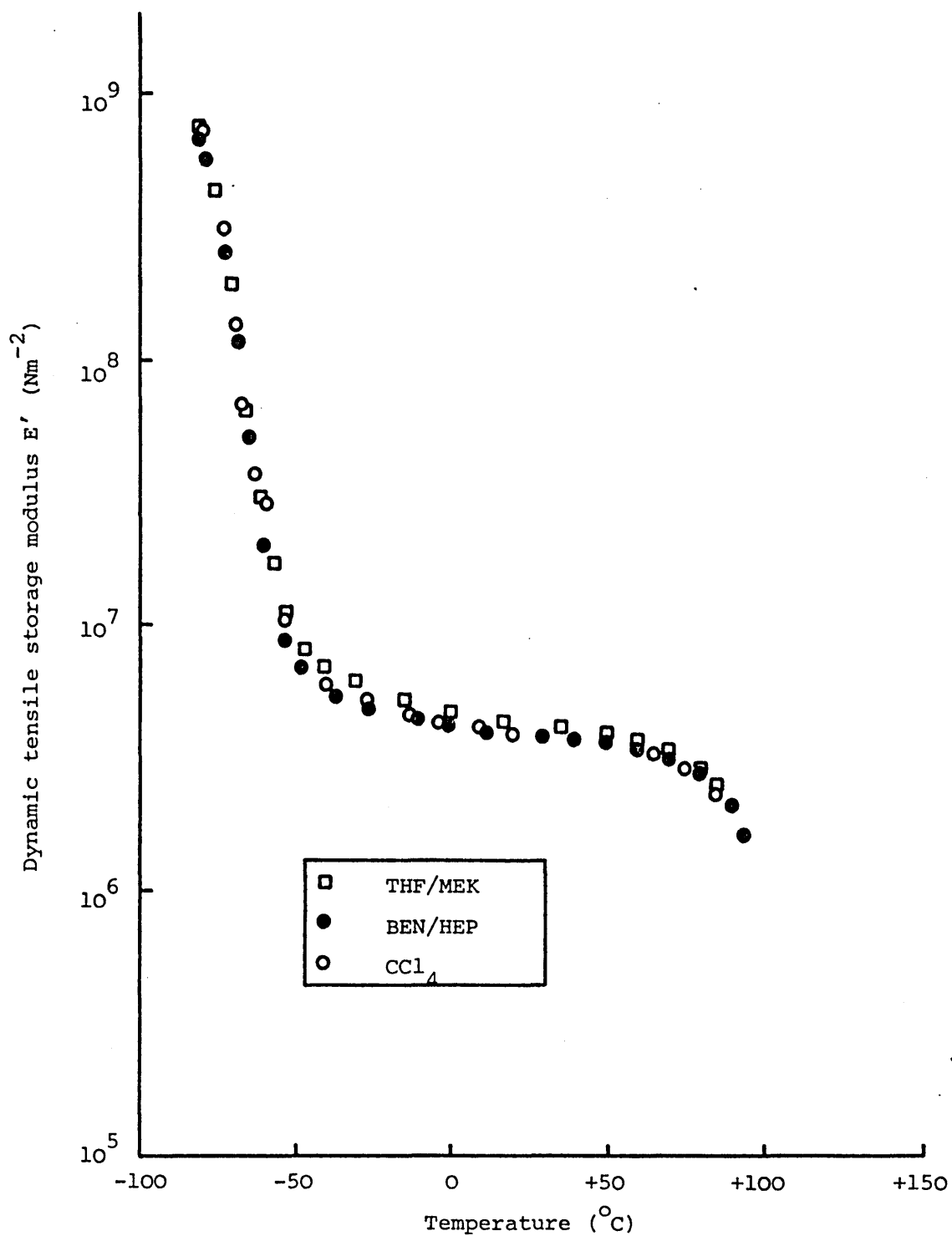


Figure 5.15 Dynamic storage modulus in tension as a function of temperature for TR 4113 cast from several solvent systems ( 11Hz ).

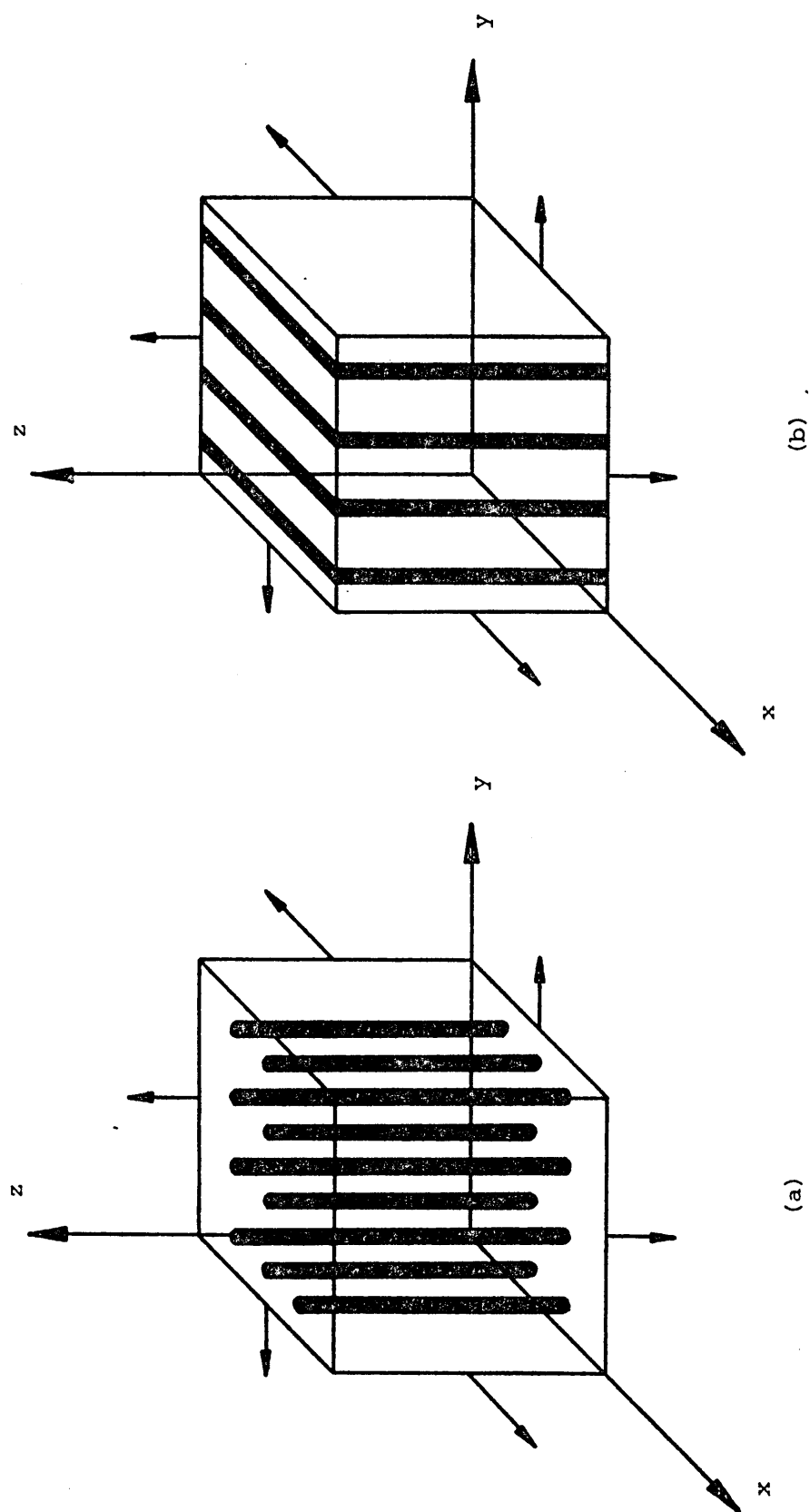


Figure 5.16 Schematic diagrams of (a) cylindrical, and (b) lamellar structures in SBS block copolymers.

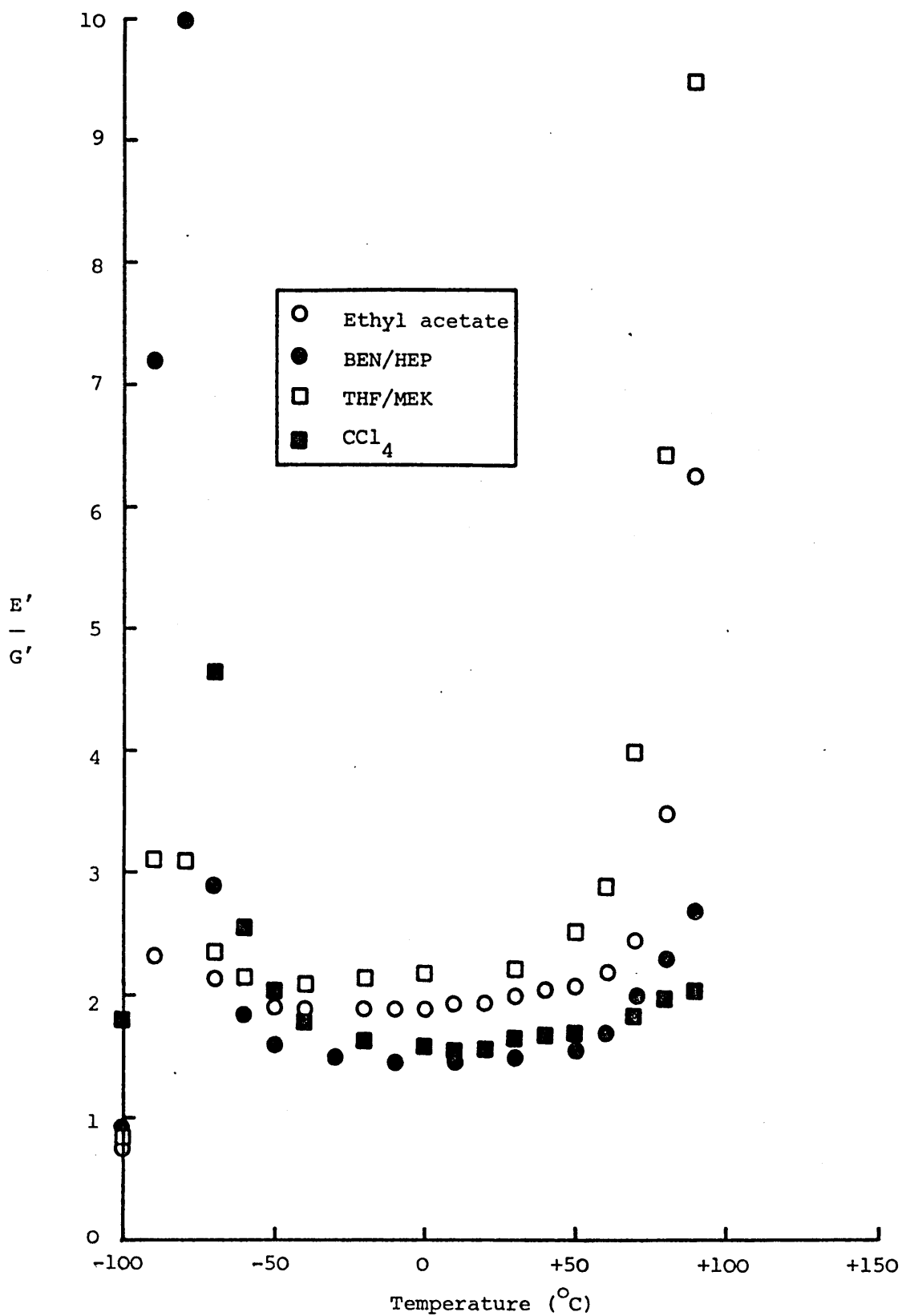


Figure 5.17  $E'/G'$  as a function of temperature for TR 1101 cast from several solvent systems.

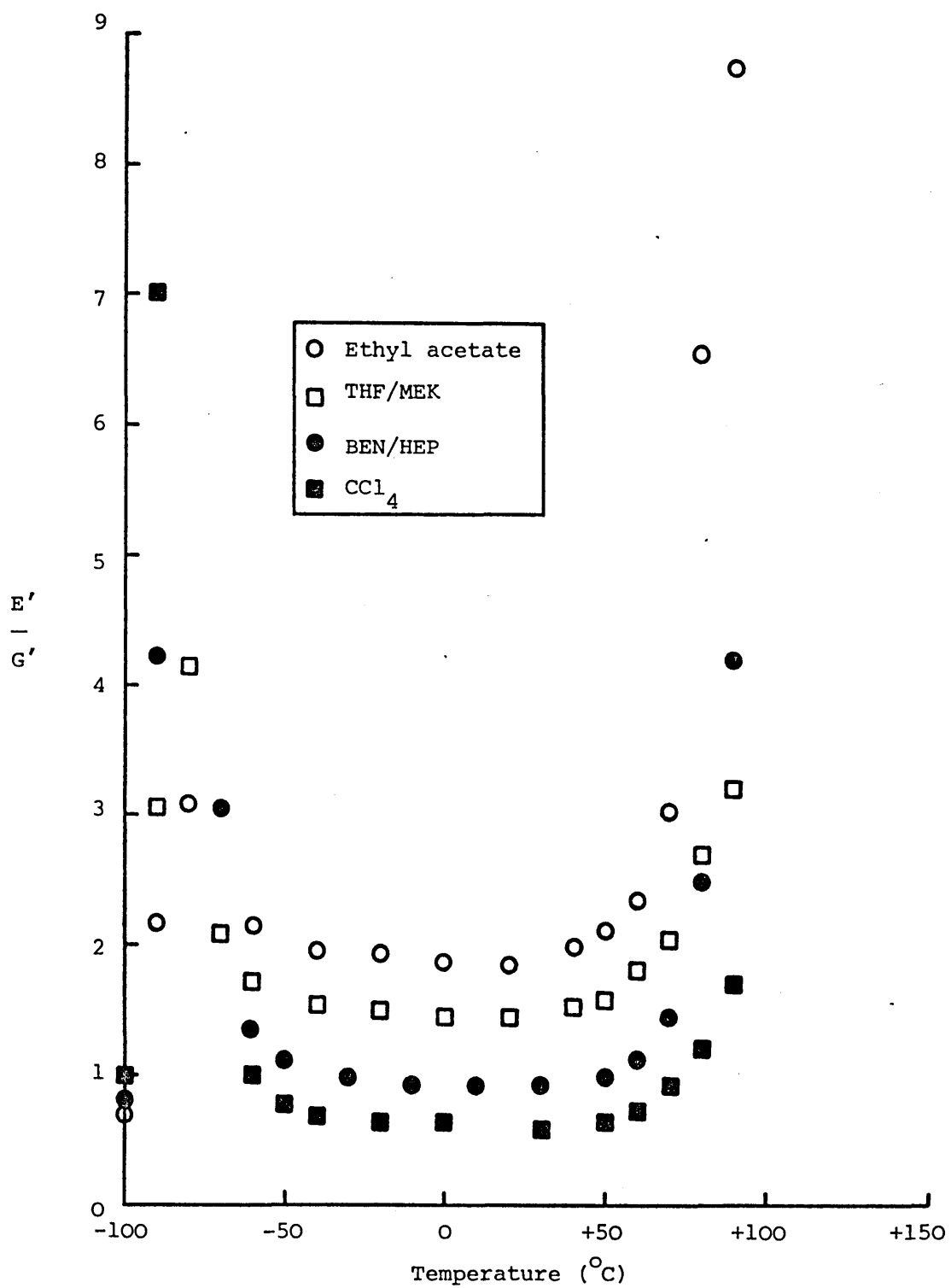


Figure 5.18  $E'/G'$  as a function of temperature for TR1102 cast from several solvent systems.



CHAPTER 6  
LARGE STRAIN TENSILE BEHAVIOUR

6.1 INTRODUCTION

The large strain tensile behaviour of block copolymers cast from different solvent systems (for the casting of sheets of material, see section 4.2) was investigated at +20°C using dumbbell-shaped specimens, as shown in Figure 6.1, and an Instron tensile testing machine. Simple tensile tests were performed at a single test speed (1 cm/min crosshead rate) in order to characterise the complete stress-strain relationship for each material from zero strain to break. No suitable extensometer was available to measure the strain in the sample during the test; it was therefore necessary to devise a method for making these measurements. Two marks were drawn in ink on the parallel section of the specimen in order to define a gauge length, as shown in Figure 6.1, and cards with marks drawn at increasing extension ratios were used as a comparator. In conjunction with a 'blipper' on the Instron chart recording the load on the specimen, this system was capable of identifying discrete strain increases and the corresponding loads.

Tensile stress-strain diagrams for TR1101 and TR1102 are shown in Figures 6.2 and 6.3; each curve is the average for five specimens. Qualitatively, the behaviour of the BEN/HEP and  $\text{CCl}_4$  cast materials was very similar, no abrupt yielding or necking of the specimens being observed. For samples cast from ethyl acetate and THF/MEK, marked yielding occurred, being associated with necking of the specimens along a line, the neck then propagating through the gauge length. This general behaviour has been described previously by Beecher et al [94], and strain levels at yield observed here were very similar to those given in the literature for similar materials and solvent systems [94,153]. Beyond 600% strain, the stress increased more rapidly, leading to fracture at between 30 MN/m<sup>2</sup> and 36 MN/m<sup>2</sup> nominal stress, and strains between 850% and 1000%.

Turning now to the plasticised materials TR4122 and TR4113, stress-strain curves are shown in Figures 6.4 and 6.5. The behaviour of TR4113 was similar for each of the solvent systems employed; no yielding was observed and stress levels throughout the tests were considerably lower than those for all other materials, fracture occurring at around 8 MN/m<sup>2</sup> and 1000% strain. The results for TR4122 were slightly surprising in that yielding was observed when BEN/HEP and  $\text{CCl}_4$  were the casting solvents, but

not with THF/MEK. In fact, when THF/MEK was the solvent, the behaviour was rather anomalous, the stress level being comparatively high up to 800% strain but, with no subsequent rapid increase in stress, fracture took place at  $6.5 \text{ MN/m}^2$  and 1000% strain. BEN/HEP and  $\text{CCl}_4$  cast materials were more conventional, fracturing at  $12 \text{ MN/m}^2$  and 1200% strain. Stress levels in the early part of the tests using TR4122 were of the same order as the TR1101/TR1102 series polymers, but fracture stresses were much lower.

The important parameters for these tests, such as initial modulus and breaking stress and strain, for each of the materials are presented in Table 6.1.

TABLE 6.1

Tensile Parameters from Gaussian and Langevin Theories

Material	Solvent	$E^{(exp)}$ ( $\text{N/m}^2 \times 10^8$ )	$E^{(Gauss)}$ ( $\text{N/m}^2 \times 10^8$ )	$\lambda_b^{(exp)}$	$\lambda_m$	$E_L$ ( $\text{N/m}^2 \times 10^6$ )	$\sigma_b^{(exp)}$ ( $\text{N/m}^2 \times 10^6$ )
TR1101	Ethyl Acetate	1.15	1.14	9.94	10.8	4.9	30.16
	THF/MEK	1.10	1.17	9.65	9.6	3.3	31.33
	BEN/HEP	0.196	0.192	9.73	9.1	2.8	31.52
	$\text{CCl}_4$	0.122	0.12	10.3	9.6	2.6	28.89
TR1102	Ethyl Acetate	0.585	0.583	10.6	9.3	2.6	33.74
	THF/MEK	0.49	0.485	10.6	9.0	2.1	31.43
	BEN/HEP	0.098	0.096	10.4	9.3	2.9	29.13
	$\text{CCl}_4$	0.101	0.099	10.3	9.2	2.6	30.31
TR4122	THF/MEK	0.361	0.363	11.0	16.52	4.4	6.99
	BEN/HEP	0.368	0.361	12.4	11.75	2.6	12.19
	$\text{CCl}_4$	0.321	0.333	12.8	11.11	2.1	11.85
	THF/MEK	0.047	0.046	11.0	11.49	2.1	7.42
TR4113	BEN/HEP	0.040	0.040	11.6	11.45	2.1	8.79
	$\text{CCl}_4$	0.037	0.037	11.4	11.27	2.0	8.17

## 6.2 ANALYSIS

### 6.2.1 The Simple Kinetic Theory

The simple kinetic (or Gaussian) theory of rubber elasticity assumes random orientation of molecules, and predicts that the engineering stress,  $\sigma$  ( $= P/A_0$ ), is related to the extension ratio,  $\lambda$  ( $= \Delta L/L$ ), by:

$$\sigma = \frac{E}{3} \left( \lambda - \frac{1}{\lambda^2} \right) \quad (6.1)$$

where  $E$  is the tensile modulus.

Plotting the stress  $\sigma$  versus the function  $(\lambda - (1/\lambda^2))$ , as shown in Figure 6.6, allows the calculation of the modulus  $E$  at low strains. The value of  $E$  obtained in this way is compared with that from the direct stress-strain plots in Table 6.1. Good agreement for this initial modulus is found for all materials.

Unfortunately, this theory breaks down at higher extension ratios owing to orientation of molecules in the direction of extension, so that their distribution is no longer random, and Gaussian statistics do not apply.

### 6.2.2 The Inverse Langevin Function

A more refined, non-Gaussian, theory [213] predicts that:

$$\sigma = \frac{G}{3} \lambda_m \left\{ L^{-1}(\lambda/\lambda_m) - \lambda^{-3/2} L^{-1}(1/(\lambda^{1/2} \lambda_m)) \right\} \quad (6.2)$$

where  $\lambda_m$  is the extension ratio when  $\sigma = \infty$  and approximates to the breaking extension ratio,  $\lambda_B$ . Here,  $\lambda_m = n^{1/2}$ , where  $n$  is the number of links in the statistical chain.

$L^{-1}(\ )$  is the inverse Langevin function, which is the series:

$$L^{-1}(x) = \left[ 3x + \frac{9}{5} x^3 + \frac{297}{175} x^5 + \frac{1539}{875} x^7 + \dots \right]$$

This expression is rather complex to deal with and an approximation for it is given by Kaelble et al [153] such that:

$$\sigma \left( \frac{\lambda}{\lambda - 1} \right) = \frac{E_L}{1 - (\lambda/\lambda_m)^2}$$

or:

$$\sigma = E_L \frac{(1 - 1/\lambda)}{1 - (\lambda/\lambda_m)^2}$$

and rearranging:

$$\frac{(1 - 1/\lambda)}{\sigma} = \frac{1}{E_L} - (1/(E_L \lambda_m^2)) \lambda^2 \quad (6.3)$$

By plotting  $(1 - 1/\lambda)/\sigma$  as a function of  $\lambda^2$ , as in Figure 6.7 for TR1101 cast from THF/MEK, it is possible to determine values of  $\lambda_m$ , and  $E_L$  which represents the terminal modulus. Data for  $\lambda_m$ ,  $E_L$ ,  $\lambda_b$  (the measured extension ratio at break), and  $\sigma_b$  (the measured stress at break) are presented in Table 6.1.

Taken together, these two theories describe reasonably accurately the pertinent features of the stress-strain behaviour of rubbery materials. The Gaussian theory being limited to quite low strains and being capable of describing the initial modulus of the material prior to any orientation. The use of the inverse Langevin function allows a characterisation of stress-strain details at high extension ratios.

It is not surprising, therefore, that a single expression has been developed to describe the full stress-strain behaviour of thermoplastic elastomers [153]. This expression incorporates a contribution describing the low extension region where Gaussian statistics apply, and the approximation to the inverse Langevin function describing the affine extension of cross-linked chains to the fully extended state.

### 6.2.3 Mathematical Model for Tensile Response

Kaelble et al [153] presented the model which gives a full description of the tensile stress-strain response of this class of materials. They show that the true stress-strain curve, plotted on bi-logarithmic axes (for schematic, see Figure 6.8), displays a smooth transition between the two analytical functions:

$$\frac{\sigma}{\epsilon} = E_0 \quad (6.4)$$

and:

$$\frac{\sigma}{\epsilon} = \frac{E_m}{1 - (\lambda/\lambda_m)^2} \quad (6.5)$$

where  $\sigma$  and  $\epsilon$  represent the stress and strain on the sample,  $E_o$  is the initial tensile modulus, and  $E_m$  the terminal modulus. Equation (6.4) describes the initial stress-strain properties prior to elastic yielding, where  $0 < \epsilon < 0.02$ ; equation (6.5) describes the stress-strain function from  $\epsilon = 2.0$  to break, and represents a first approximation to the inverse Langevin function.

The general stress-strain relation which describes the complete behaviour of the material, and includes equations (6.4) and (6.5) as special cases, has the form:

$$\frac{\sigma}{\epsilon} = E_I B_d + \frac{E_m}{1 - (\lambda/\lambda_m)^2} \quad (6.6)$$

Here,  $E_I = E_o - E_m$  and is designated the modulus of an interfacial phase,  $B_d$  is the degree of bonding for this interface.  $B_d$  is an empirically determined parameter which has an initial value of 1.0, but decreases with increasing strain to zero. It follows that  $E_I$  is the rigidity contribution of the continuous rigid phase, and that  $B_d$  may be considered as an indicator of the integrity of this rigid phase. So that  $E_I B_d$  represents the response of the polystyrene, and  $E_m/(1 - (\lambda/\lambda_m)^2)$  that of the rubbery polybutadiene phase.

The true stress-strain curve on double logarithmic axes for TR1102 cast from THF/MEK is shown in Figure 6.9, and the tensile parameters for all the materials and solvent system combinations used in this work are given in Table 6.2. It is seen from this table that, except for TR4113,  $E_m$  is at least an order of magnitude smaller than  $E_o$ ,  $E_o$  being governed primarily by the geometry and volume fraction of the rigid phase, and  $E_m$  relating to the rubbery modulus.

By rearranging equation (6.6):

$$B_d = \frac{1}{E_I} \left[ \frac{\sigma}{\epsilon} - \frac{E_m}{1 - (\lambda/\lambda_m)^2} \right] \quad (6.7)$$

which expresses the strain dependence of stress in terms of the bonding parameter,  $B_d$ . A plot of  $B_d$  as a function of log strain is shown in Figure

TABLE 6.2

Tensile Parameters for the Kaible et al Mathematical Model

Material	Solvent	$E_o$ ( $\text{N/m}^2 \times 10^8$ )	$E_m$ ( $\text{N/m}^2 \times 10^8$ )	$E_I$ ( $\text{N/m}^2 \times 10^8$ )	$\lambda_m$	$b_2$	Strain Intercept Of $b_1$ With $b_2$
TR1101	Ethyl Acetate	1.15	0.050	1.100	10.8	0.61	0.073
	THF/MEK	1.10	0.032	1.068	9.6	0.61	0.073
	BEN/HEP	0.196	0.028	0.168	9.1	0.78	0.150
	$\text{CCl}_4$	0.122	0.026	0.096	9.6	0.90	0.200
TR1102	Ethyl Acetate	0.585	0.026	0.559	9.3	0.48	0.104
	THF/MEK	0.490	0.021	0.469	9.0	0.48	0.104
	BEN/HEP	0.098	0.030	0.068	9.3	1.00	0.160
	$\text{CCl}_4$	0.101	0.026	0.075	9.2	1.00	0.160
TR4122	THF/MEK	0.361	0.043	0.318	16.5	0.59	0.056
	BEN/HEP	0.368	0.025	0.343	11.8	0.74	0.100
	$\text{CCl}_4$	0.321	0.019	0.302	11.1	0.59	0.087
	THF/MEK	0.047	0.019	0.028	11.5	1.48	0.173
TR4113	BEN/HEP	0.040	0.019	0.021	11.5	1.54	0.133
	$\text{CCl}_4$	0.037	0.018	0.019	11.3	1.54	0.110

6.10; this is typical for all the materials used with  $B_d$  beginning to decrease from its value of unity at between 2% and 5% strain, levelling off at its minimum value close to zero at about 200% strain.

In order to obtain a physical interpretation of the debonding function  $B_d$ , Kaelble makes use of the statistical model proposed by Halpin & Polley [214] for micro-defect growth in a viscoelastic body (SBR). Using constant load and unloading-reloading sequences on large numbers of specimens, Halpin & Polley showed that a cumulative damage concept is useful in describing the statistical nature of specimen rupture behaviour.

For unidimensional defect growth, the instantaneous crack length  $c(t)$  in the  $x$ -axis of growth at time  $t$ , is given by the expression [214]:

$$c(t) \approx v_d(t) = f[G_x L_y L_z(t)]$$

where  $v_d$  is the defect volume,  $G_x$  is the growth rate in the  $x$ -axis, while  $L_y$  and  $L_z$  represent the fixed crack dimensions in the  $y$  and  $z$  directions where no crack growth occurs. The corresponding expression for uniform three-dimensional crack growth:

$$v_d(t) = f[G_x G_y G_z(t)^3]$$

describes the instantaneous defect volume, where growth rates  $G_x$ ,  $G_y$  and  $G_z$  apply in the  $x$ ,  $y$  and  $z$  directions.

The Halpin-Polley model generalises the dimensionality of slow micro-flaw growth to provide an expression which describes the cumulative survival distribution,  $F(s)$ , of the material for a large number of specimens, so that:

$$F(s) = \frac{n(t_2)}{n(t_1)} = \exp \left[ -K_2 G_r (t_2 - t_1)^{b_t} \right] \quad (6.8)$$

where  $n(t_2)$  and  $n(t_1)$  represent the fractions of specimens which remain intact at times  $t_2$  and  $t_1$ ,  $K_2$  is a material constant,  $G_r$  is the generalised flaw growth rate, and  $b_t$  is an exponent which relates to the dimensionality of the crack growth process.  $b_t$  may normally take values of 1, 2 or 3, dependent upon whether flaw growth is in one, two or three dimensions. Fractional values of  $b_t$  indicate mixed modes of flaw growth involving



differing dimensionalities [155].

For the purposes of this work, it is necessary to make the assumption that the debonding parameter,  $B_d$ , is identified with the specimen survival function  $F(s)$  so that:

$$F(s) = B_d \quad (6.9)$$

Substituting equation (6.9) into equation (6.8) and taking logarithms results in the relation:

$$\log [-\log B_d] = b_t \log (t_2 - t_1) + \log K_2 G_r - 0.3622 \quad (6.10)$$

This expression suggests a plot of  $\log [-\log B_d]$  versus  $\log (t_2 - t_1)$  as a means of defining the exponent  $b_t$  of the cavitation process.

Figure 6.11 shows this plot (using strain instead of time) for TR1101 cast from different solvents, and reveals two linear curves of slopes  $b_1$  and  $b_2$ , corresponding to two stages of cavitation. The function  $b_1$  varies only slightly with solvent and indicates a three-dimensional process, whereas  $b_2$  varies somewhat more radically, although data for ethyl acetate and THF/MEK cast material are identical. The point of intersection of the lines describing this two-stage process, when referred to the strain axis, is also seen to vary with solvent system. Similar plots for the other materials are shown in Figures 6.12 to 6.14. TR1102 (Figure 6.12) cast from ethyl acetate and THF/MEK shows identical data as does the same material cast from BEN/HEP and  $\text{CCl}_4$ . The case of TR4113 (Figure 6.14) is particularly interesting in that the values of the exponent  $b_2$  are identical for each solvent system.

The data related to this analysis is summarised in Table 6.2, revealing that materials exhibiting a relatively high initial modulus,  $E_o$ , generally have a relatively low exponent,  $b_2$ . In Figure 6.15,  $E_o$  is plotted as a function of  $b_2$ , and the relationship indicates that for the high initial modulus materials a limiting  $b_2$  is achieved of value 0.5. This value of  $b_2$  was also indicated for a high modulus material investigated by Kaible et al [155]. A graph of  $E_m$  versus  $b_2$  in Figure 6.16 shows a similar relationship to that between  $E_o$  and  $b_2$ .

The  $b_1$  exponent takes values of about 3, indicating that this initial cavitation stage is a three-dimensional process.

Considering the point at which  $b_1$  and  $b_2$  intersect, Kaelble et al [155] discovered that by lowering the temperature (i.e. increasing the initial modulus  $E_0$ ), intersection occurred at a lower strain, indicating that the cavitation process initiated and propagated earlier in the stress-strain cycle. In the present study, a similar effect was found when material changes effected changes in modulus,  $E_0$ . Plotting  $E_0$  as a function of the strain intersection point of  $b_1$  and  $b_2$ , as in Figure 6.17, revealed for these materials at +20°C a limiting strain intercept of 5%.

### 6.3 DISCUSSION

The stress-strain curves of Figures 6.2 to 6.5 reveal a marked influence of casting solvent on the initial tensile modulus, ethyl acetate and THF/MEK casting, resulting in an enhanced modulus leading to yielding and drawing of the polymer. BEN/HEP and  $\text{CCl}_4$  casting results in samples which show a relatively low modulus and no yielding.

Ultimate tensile behaviour has been shown to be more or less independent of casting solvent; however, the plasticiser of TR4113 and TR4122 resulted in low tensile strength and high extensibility, compared with unplasticised TR1101 and TR1102.

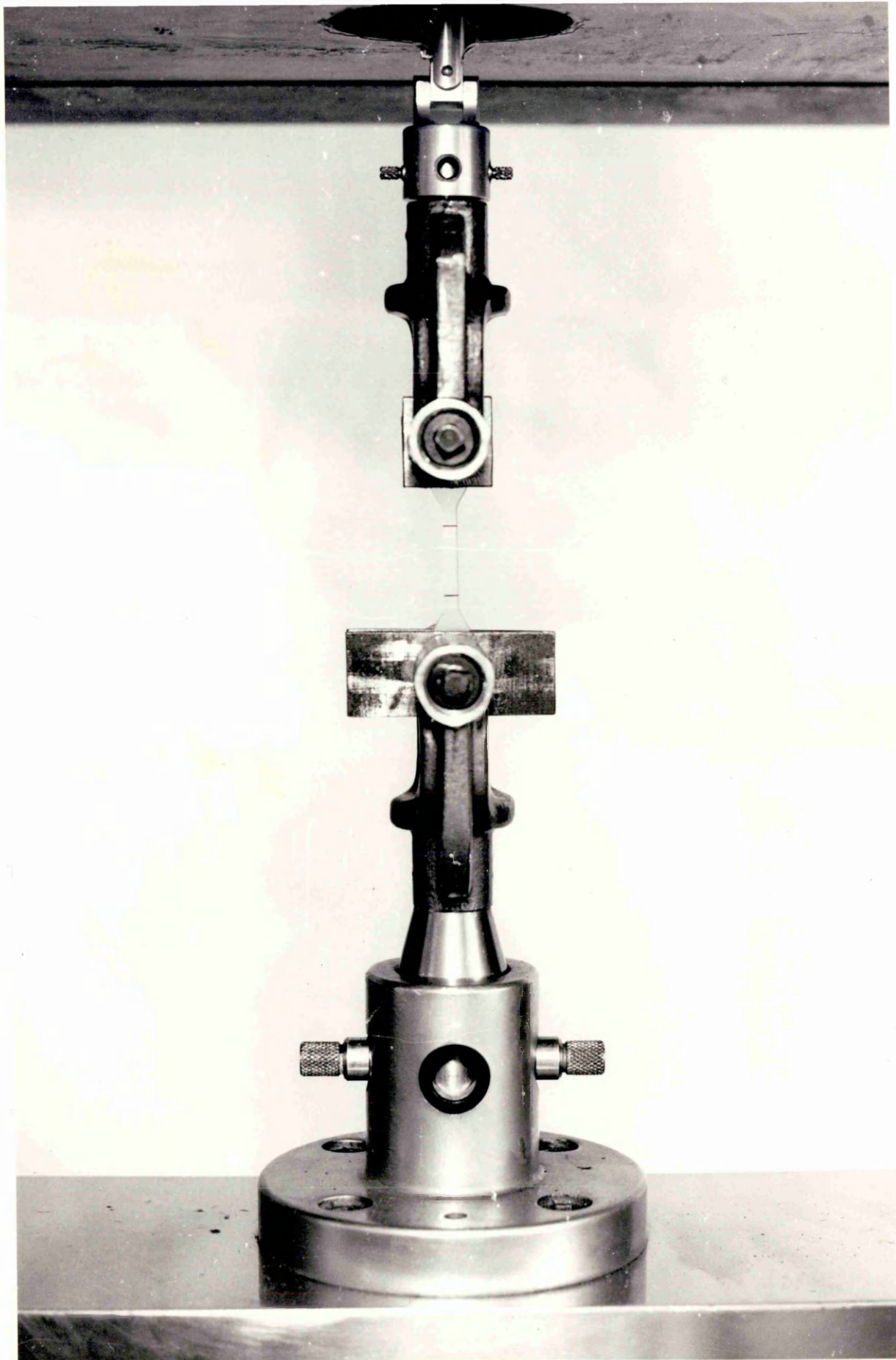
The model proposed by Kaelble and co-workers for the interfacial debonding of block copolymers has been found to describe extremely well the tensile behaviour of the materials used in this study. The model incorporates two modulus functions, one describing the low strain behaviour and the other high strain response. By use of an empirically determined debonding function,  $B_d$ , the two modulus terms are seen in equation (6.6) to describe the full stress-strain curve.

Making use of the Halpin-Polley model for the kinetics of micro-defect growth, two stages of cavitation may be defined. An initial nucleation stage where  $1.0 > B_d > 0.6$  is followed by a propagation and cavity coalescence stage where  $0.4 > B_d > 0$ .

Referring to the dimensionality factor,  $b_t$ , described by equations (6.8) and (6.10), in all cases initial low strain flaw growth is shown to be a three-dimensional process. However, a transition occurs at strains above 0.05, dependent upon the material, when this flaw growth dimensionality decreases. It is interesting to note that as the initial modulus of the material increases, the dimensionality of this second flaw growth process decreases (Figure 6.15), indicating different effects for lamellar and rod-like structures. This point is also borne out by the fact that the strain at which this transition in flaw growth dimensionality occurs is also dependent upon initial modulus, and in turn upon the microstructure of the material (Figure 6.17). Materials with a lamellar structure have a lower strain transition point of approximately 0.06, whereas rod-like structures result in a strain transition for the dimensionality factor of  $> 0.11$ .

Correlations between tensile behaviour and the swelling results of Chapter 3 have been sought and Figures 6.18 to 6.22 present the results of this investigation. From the results of the swelling experiments, it is possible to plot the equilibrium swelling strain as a function of styrene content (this is shown in Figure 6.18), and shows that as the styrene

content increases, the equilibrium swelling strain decreases. This is quite reasonable since the network at high styrene contents would be unlikely to allow much swelling of the butadiene phase. Figure 6.19 shows the styrene content plotted as a function of  $M_c$ , the entanglement molecular weight of the network. Here,  $M_c$  is seen to increase with decreasing styrene content. A similar plot is achieved when the predicted maximum extension ratio is plotted as a function of  $M_c$ , as in Figure 6.20. It follows that a plot of styrene content as a function of predicted extension ratio should produce a linear relationship within the limits of the styrene contents used in this work. This relationship is shown in Figure 6.21. One further plot worth recording is that shown in Figure 6.22, where the equilibrium swelling strain is plotted as a function of the predicted maximum tensile strain. Here, the equilibrium swelling strain is seen to decrease with increasing maximum tensile strain.



# STRESS/STRAIN CURVES FOR TR1101 AND TR1102

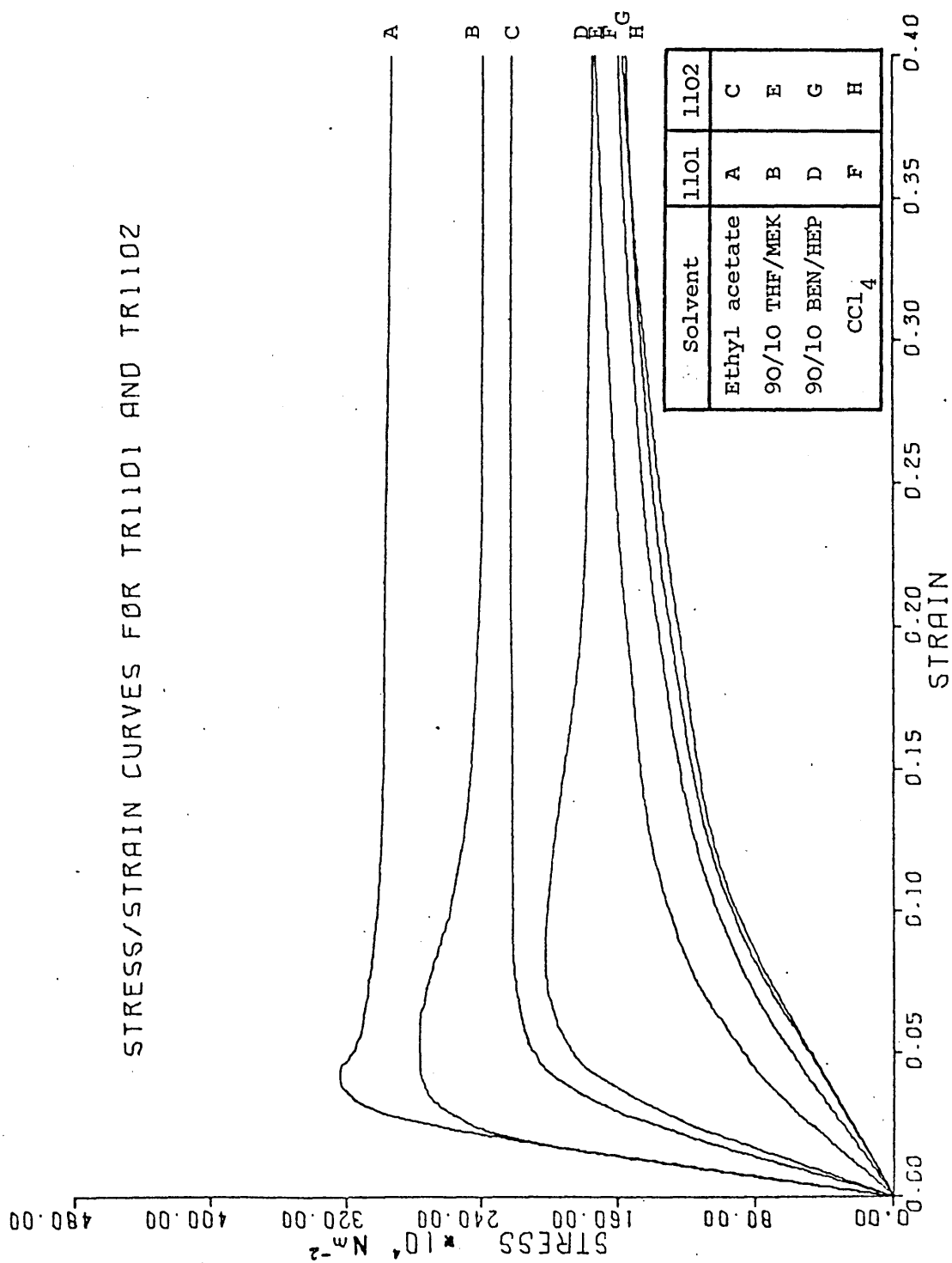


Figure 6.2 Tensile stress-strain curves for TR1101 and TR1102 cast from different solvent systems.

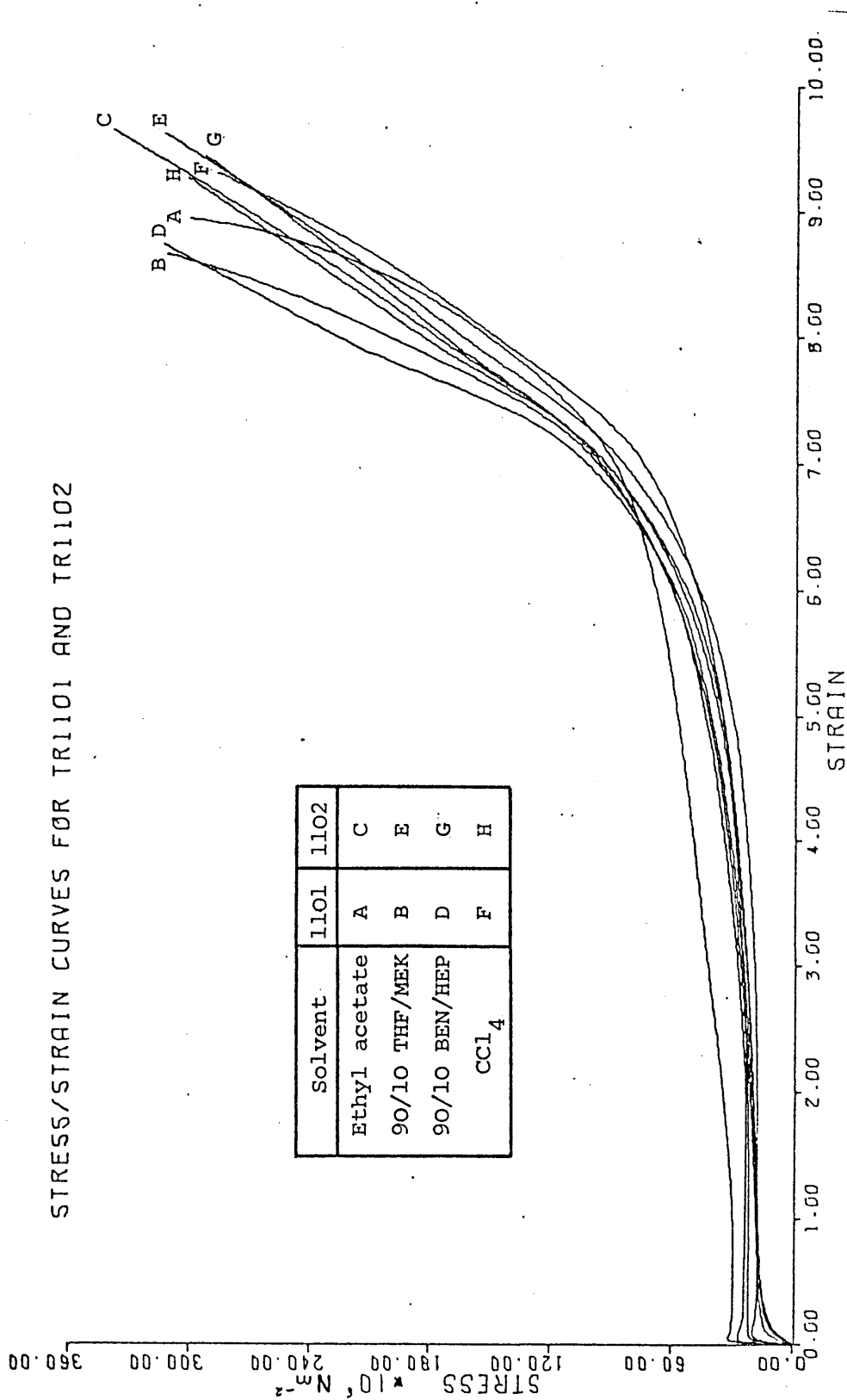


Figure 6.3 Tensile stress-strain curves for TR1101 and TR1102 cast from different solvent systems.

# STRESS/STRAIN CURVES FOR TR4122 AND TR4113

Solvent	4122	4113
90/10 THF/MEK	1	4
90/10 BEN/HEP	2	5
CCl <sub>4</sub>	3	6

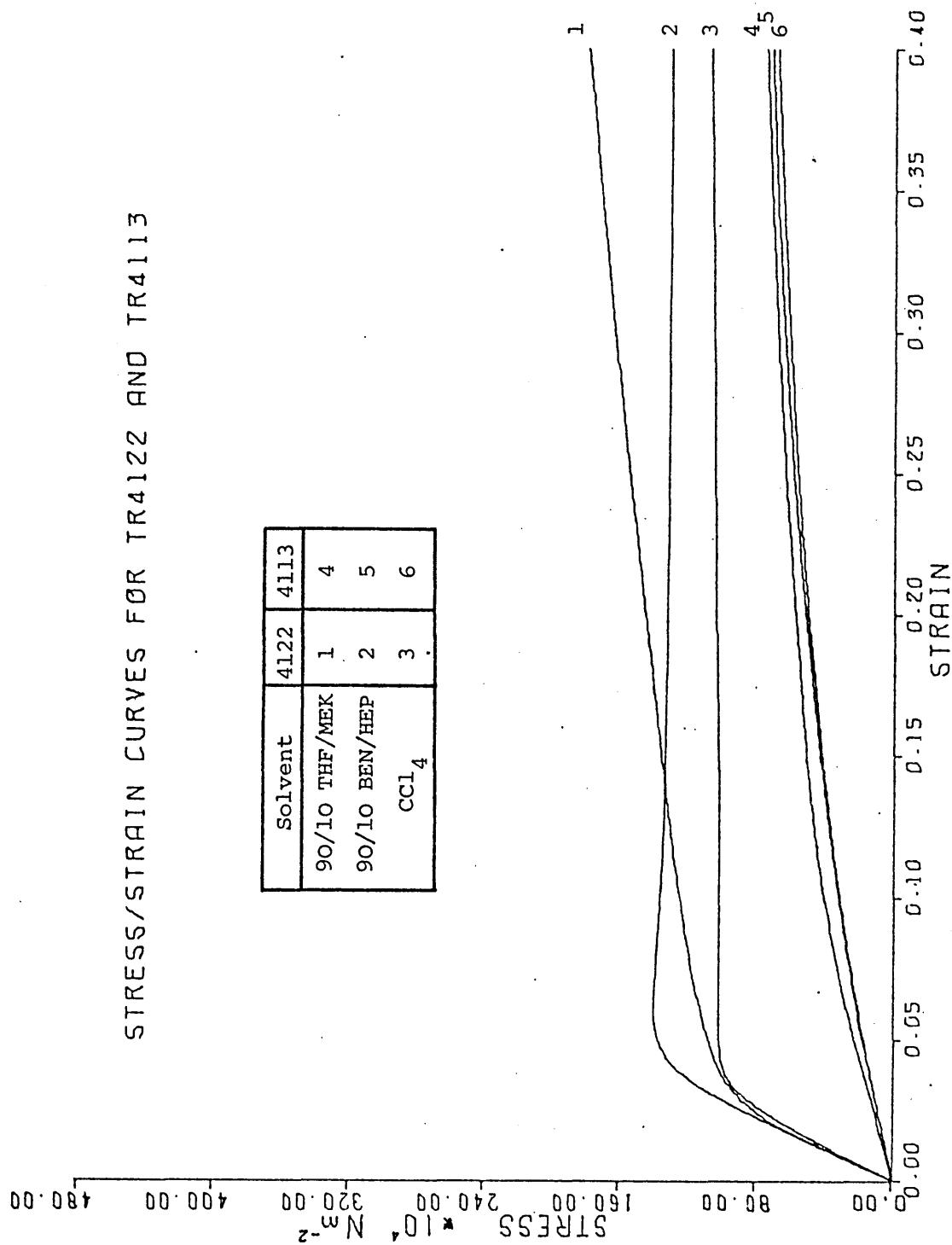


Figure 6.4 Tensile stress-strain curves for TR4122 and TR4113 cast from different solvent systems.



# STRESS/STRAIN CURVES FOR TR4122 AND TR4113

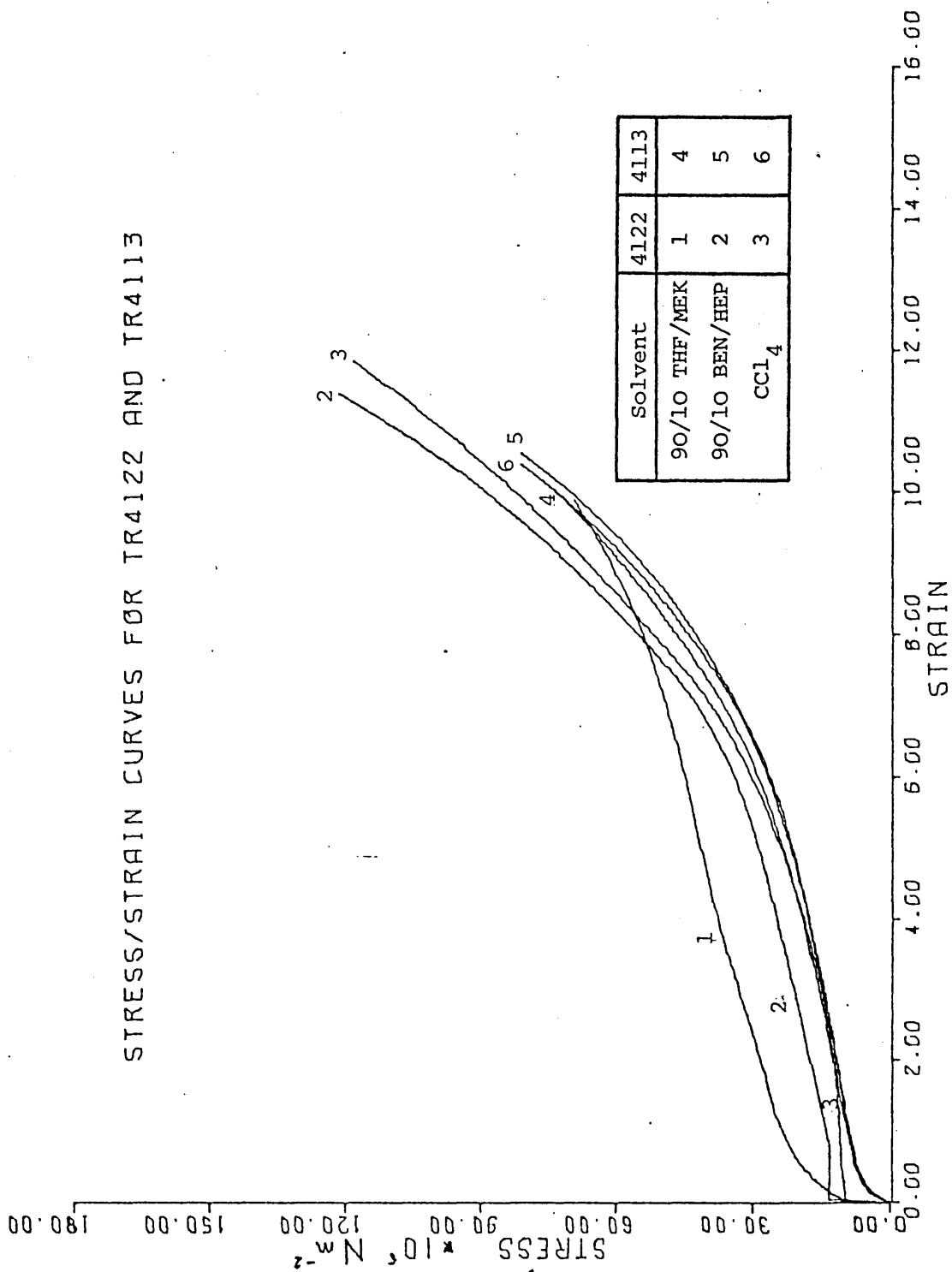


Figure 6.5 Tensile stress-strain curves for TR4122 and TR4113 cast from different solvent systems.

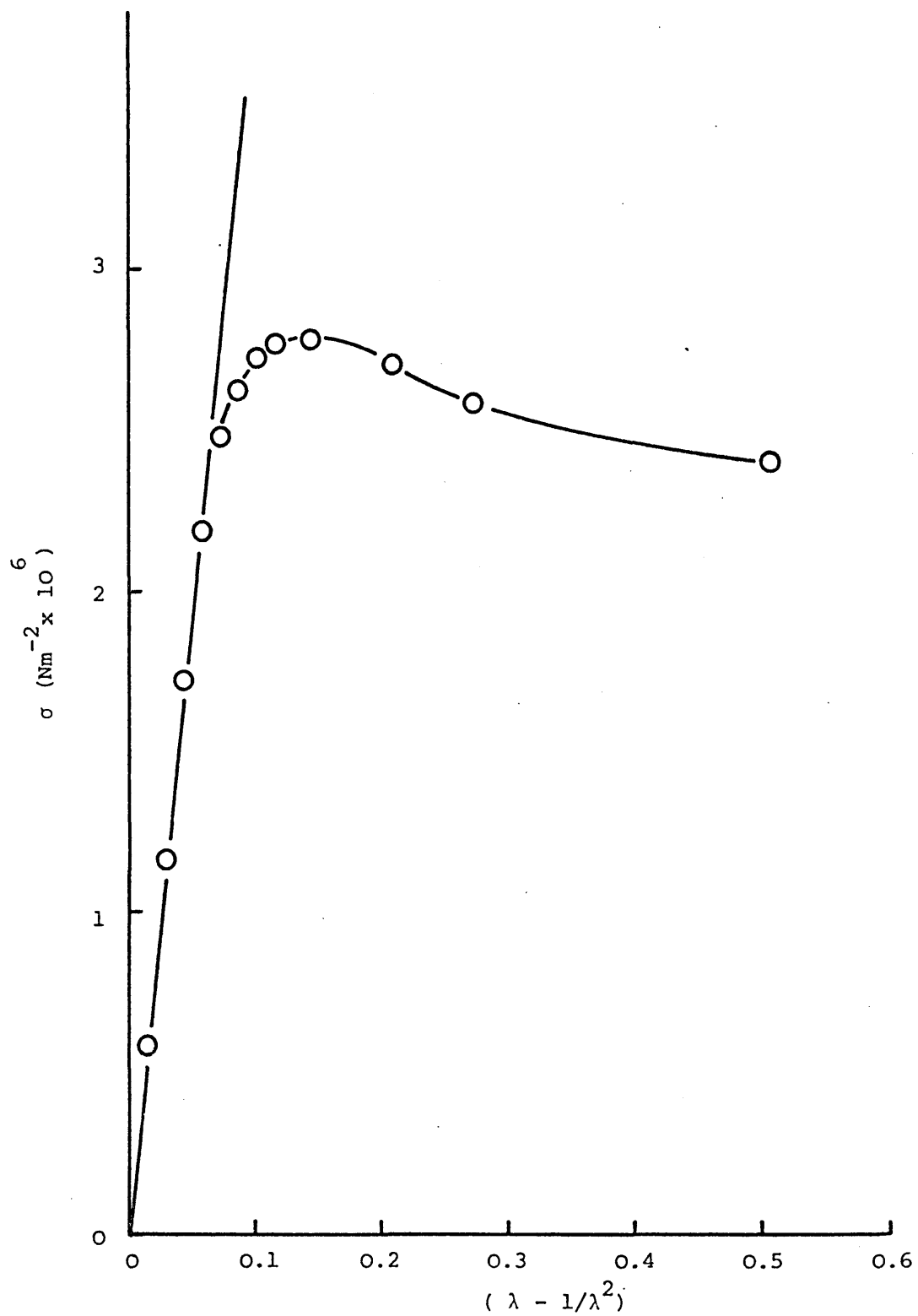


Figure 6.6 Stress as a function of strain (simple kinetic theory).

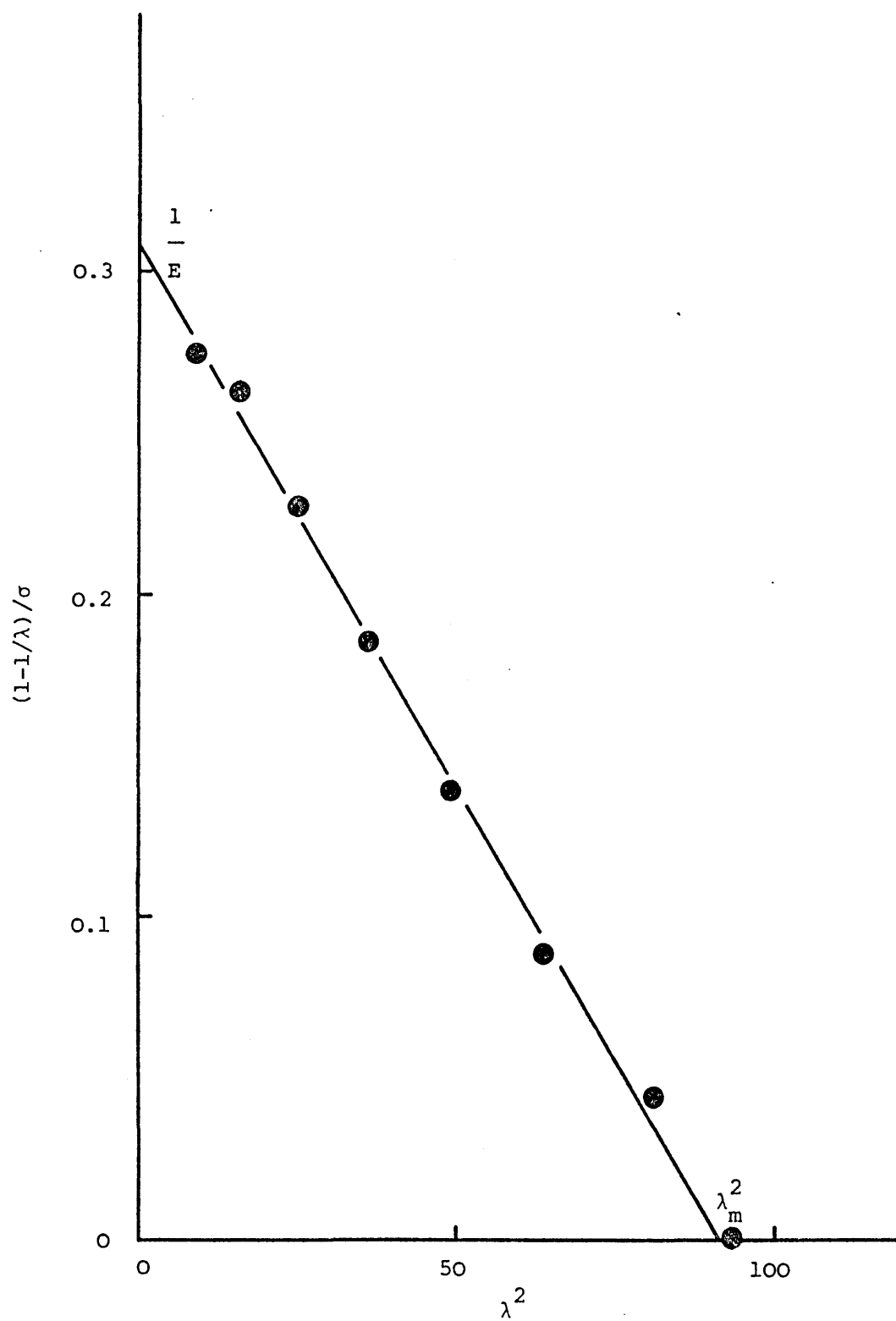


Figure 6.7 Stress as a function of strain using the inverse Langevin function.

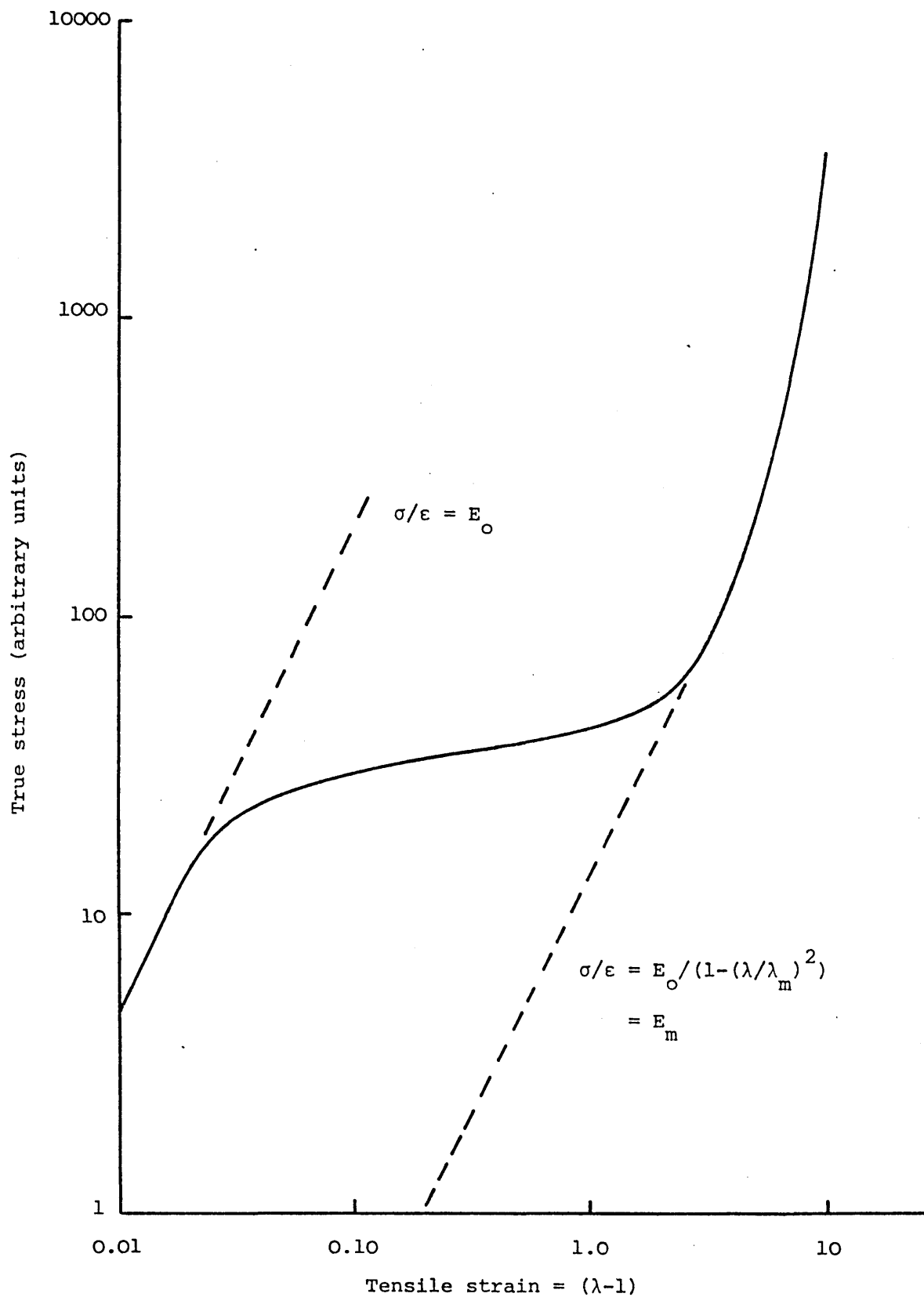


Figure 6.8 True stress as a function of strain (schematic).

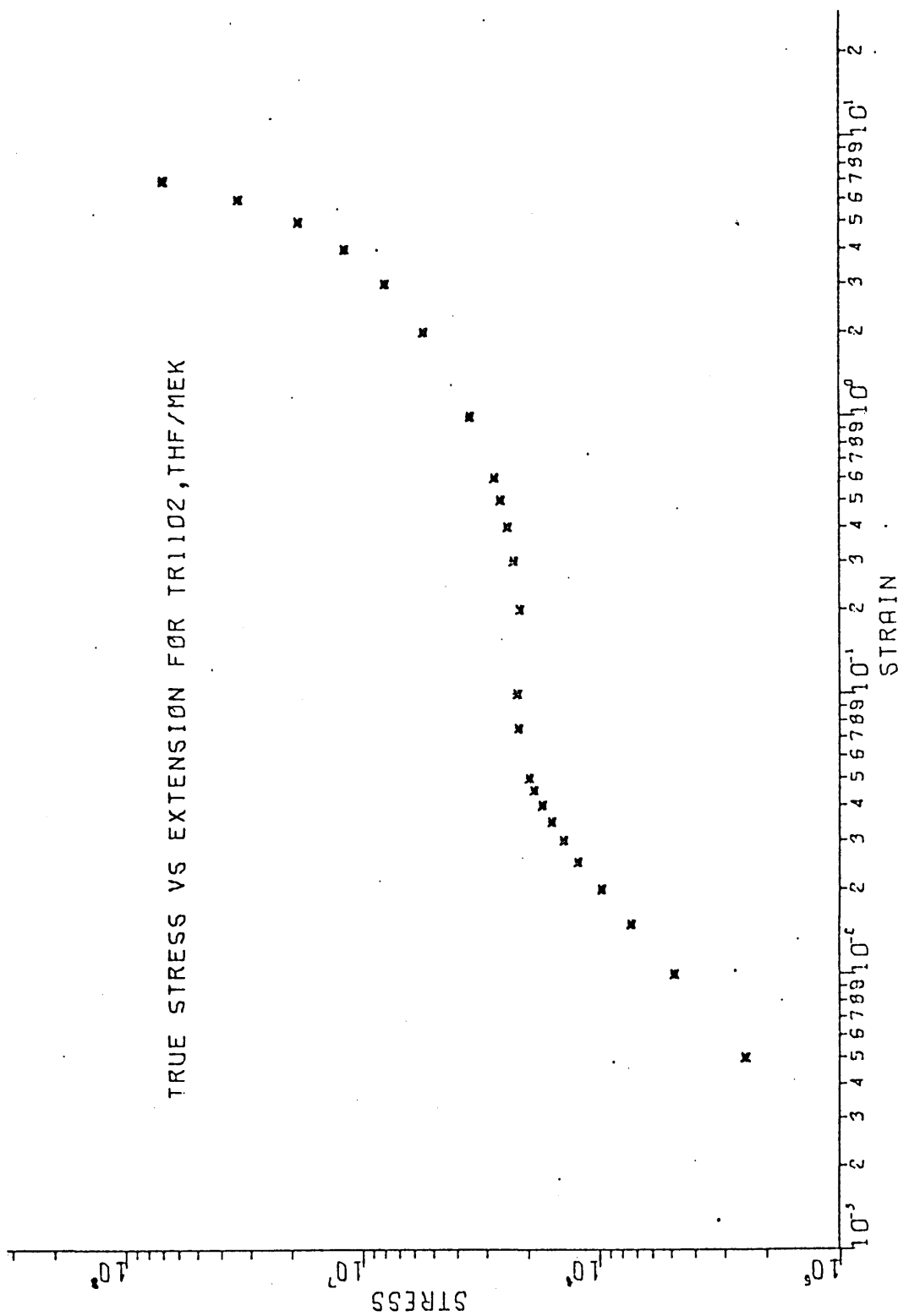


Figure 6.9 The true stress-strain curve for TR1102 cast from THF/MEK.

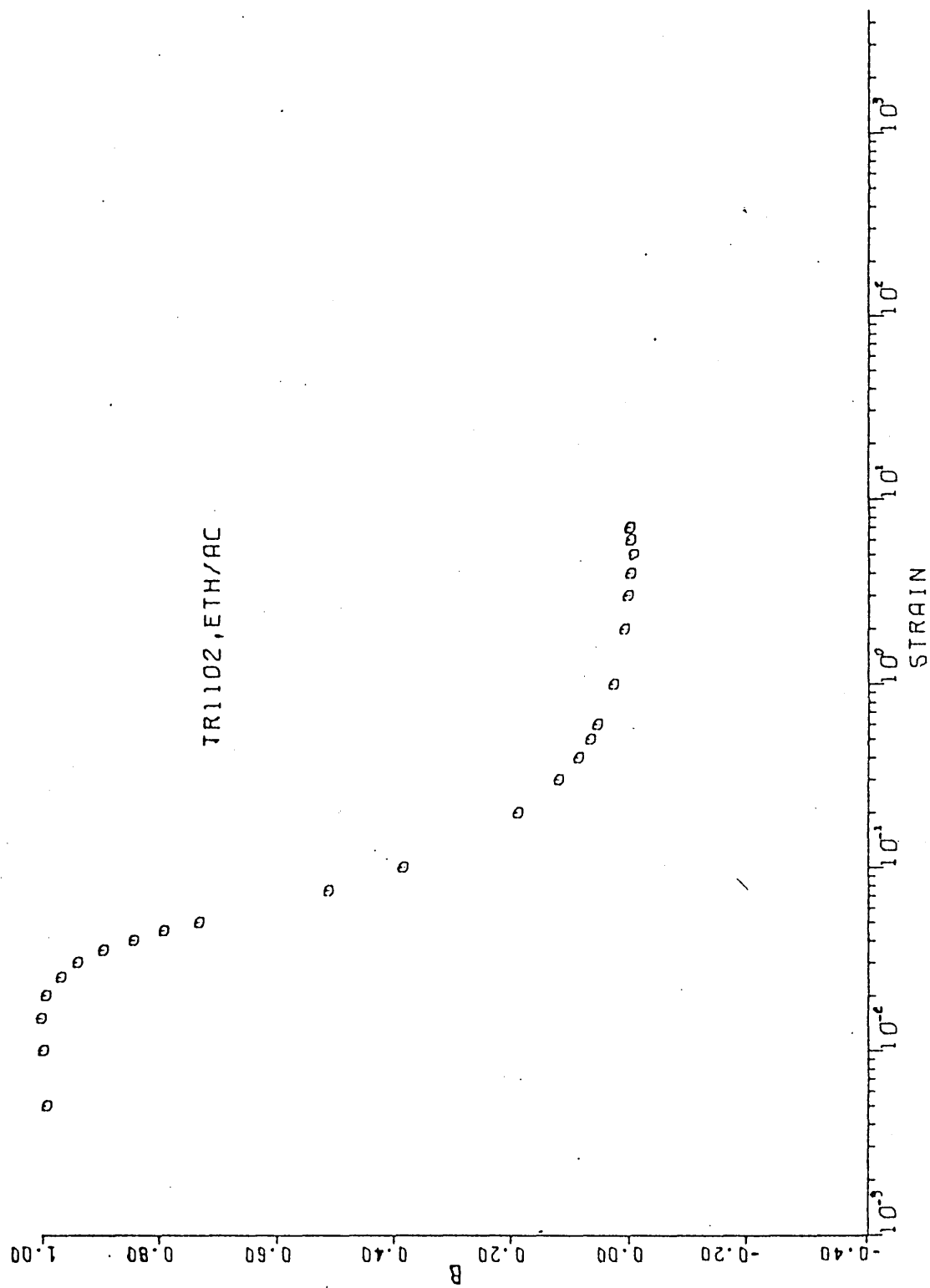


Figure 6.10 The debonding parameter  $B_d$  as a function of strain for TR1102 cast from ethyl acetate.

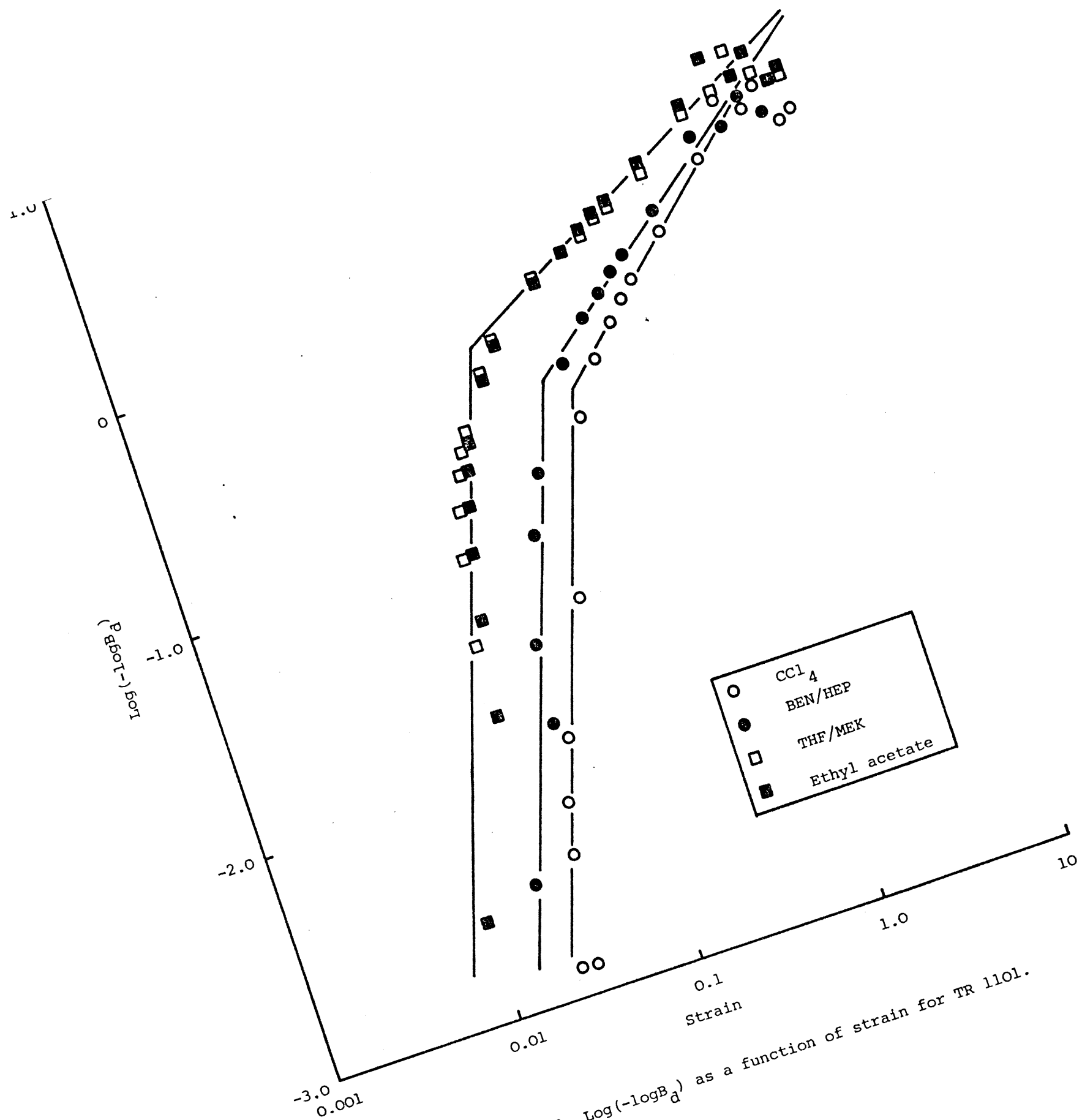


Figure 6.11  $\text{Log}(-\log B_d)$  as a function of strain for TR 1101.

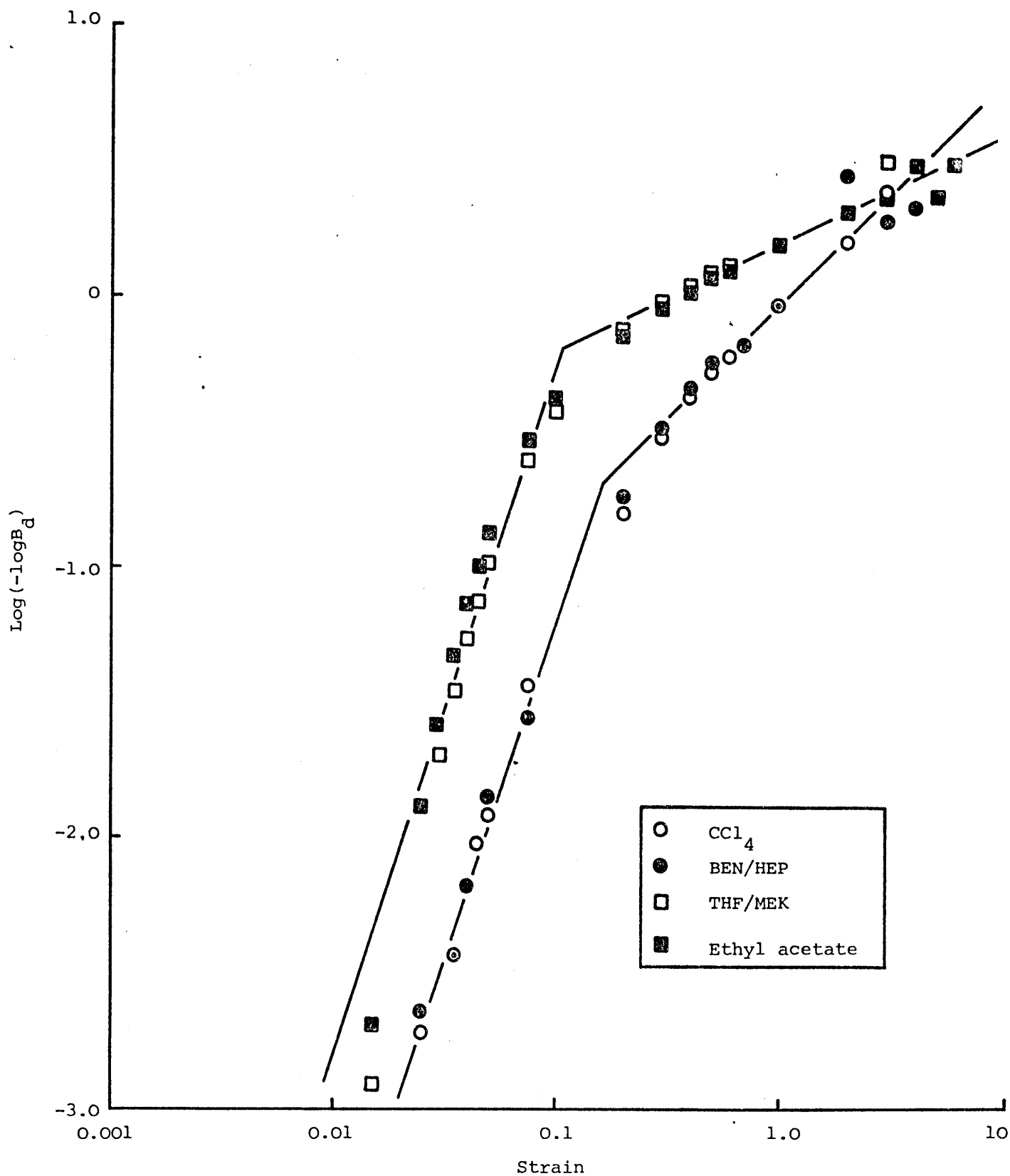


Figure 6.12 Log(-logB<sub>d</sub>) as a function of strain for TR 1102.



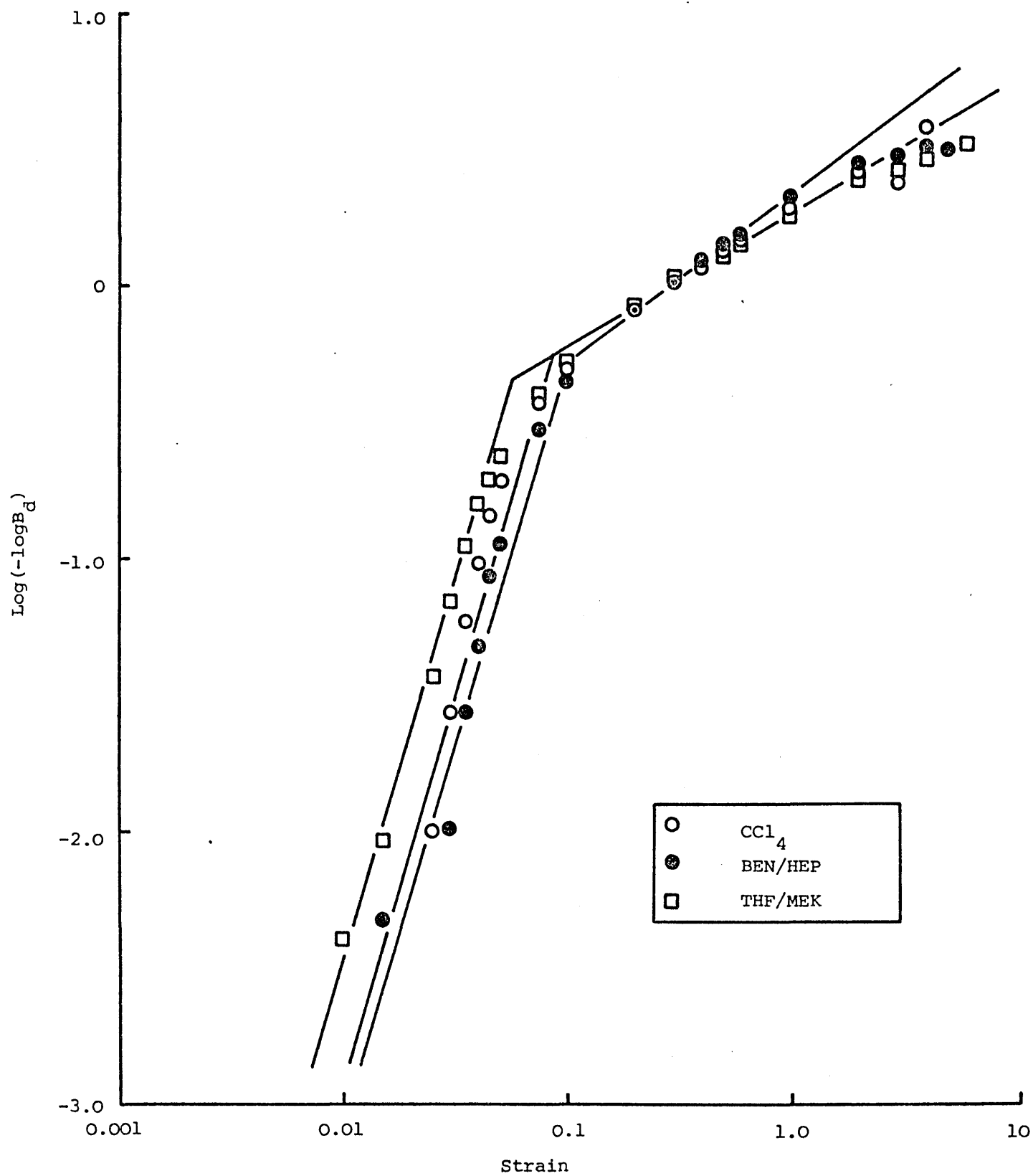


Figure 6.13 Log(-logB<sub>d</sub>) as a function of strain for TR 4122.

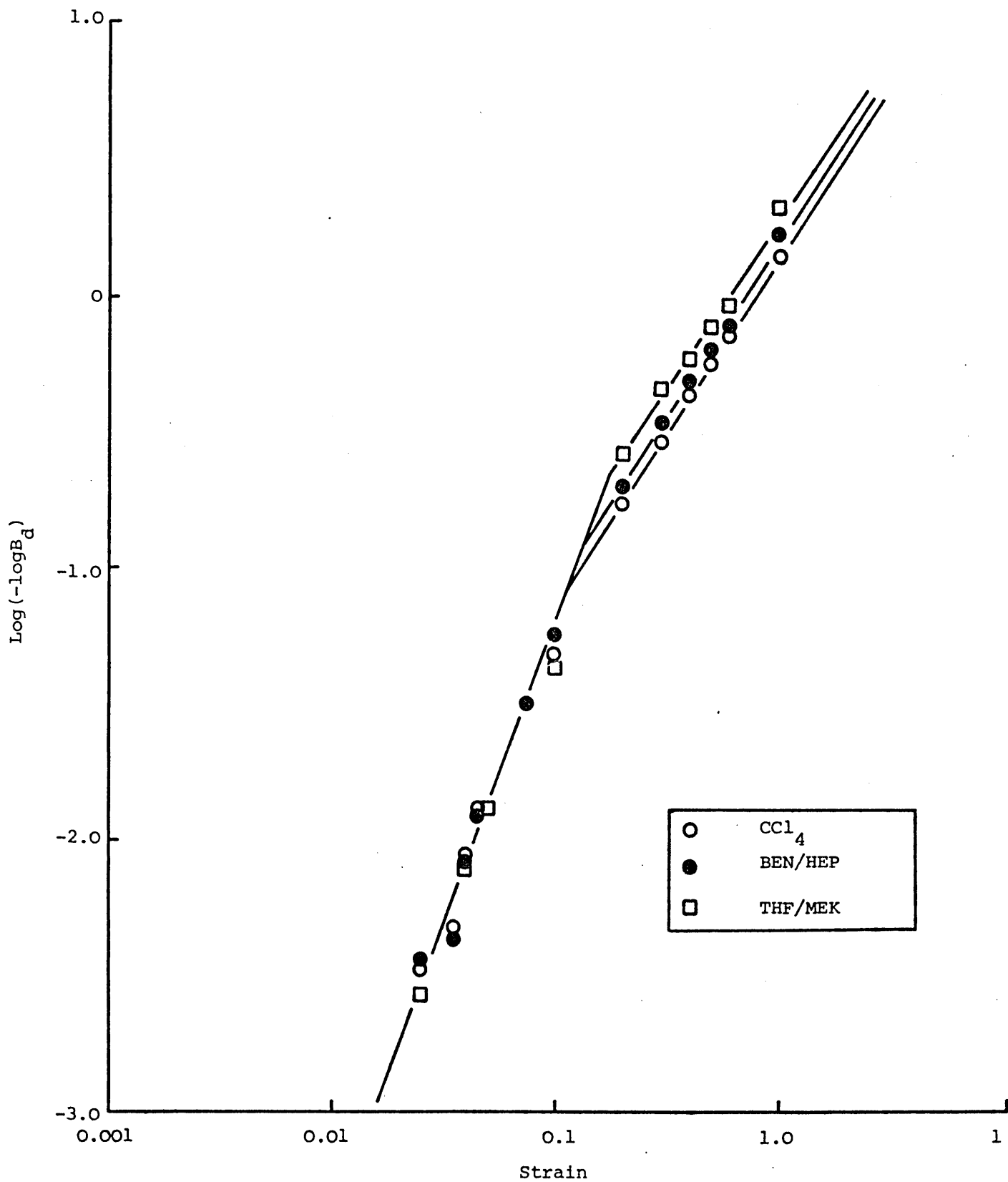


Figure 6.14 Log(-logB<sub>d</sub>) as a function of strain for TR 4113.

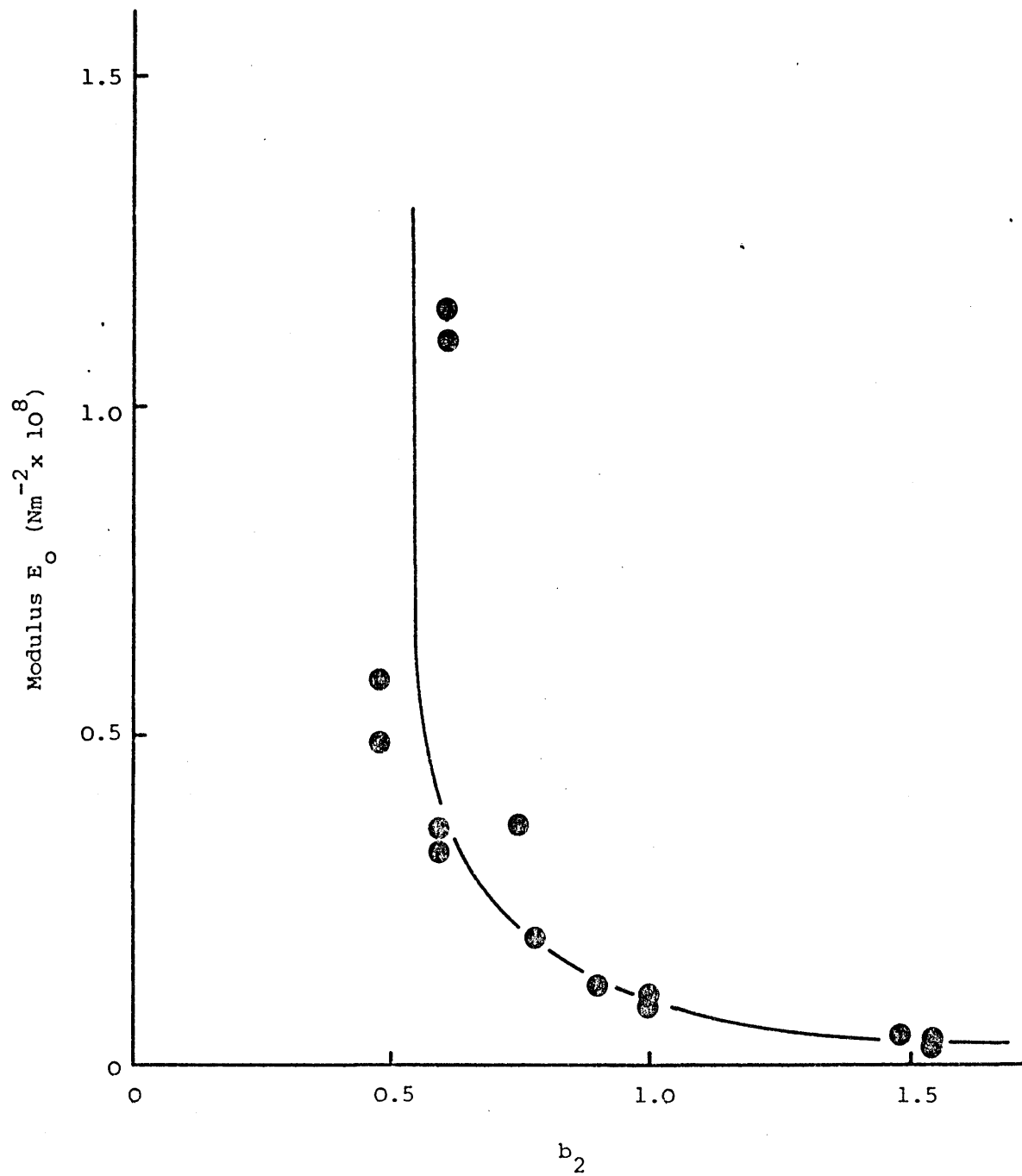


Figure 6.15 Initial modulus  $E_0$  as a function of exponent  $b_2$   
for the debonding parameter  $B_d$ .

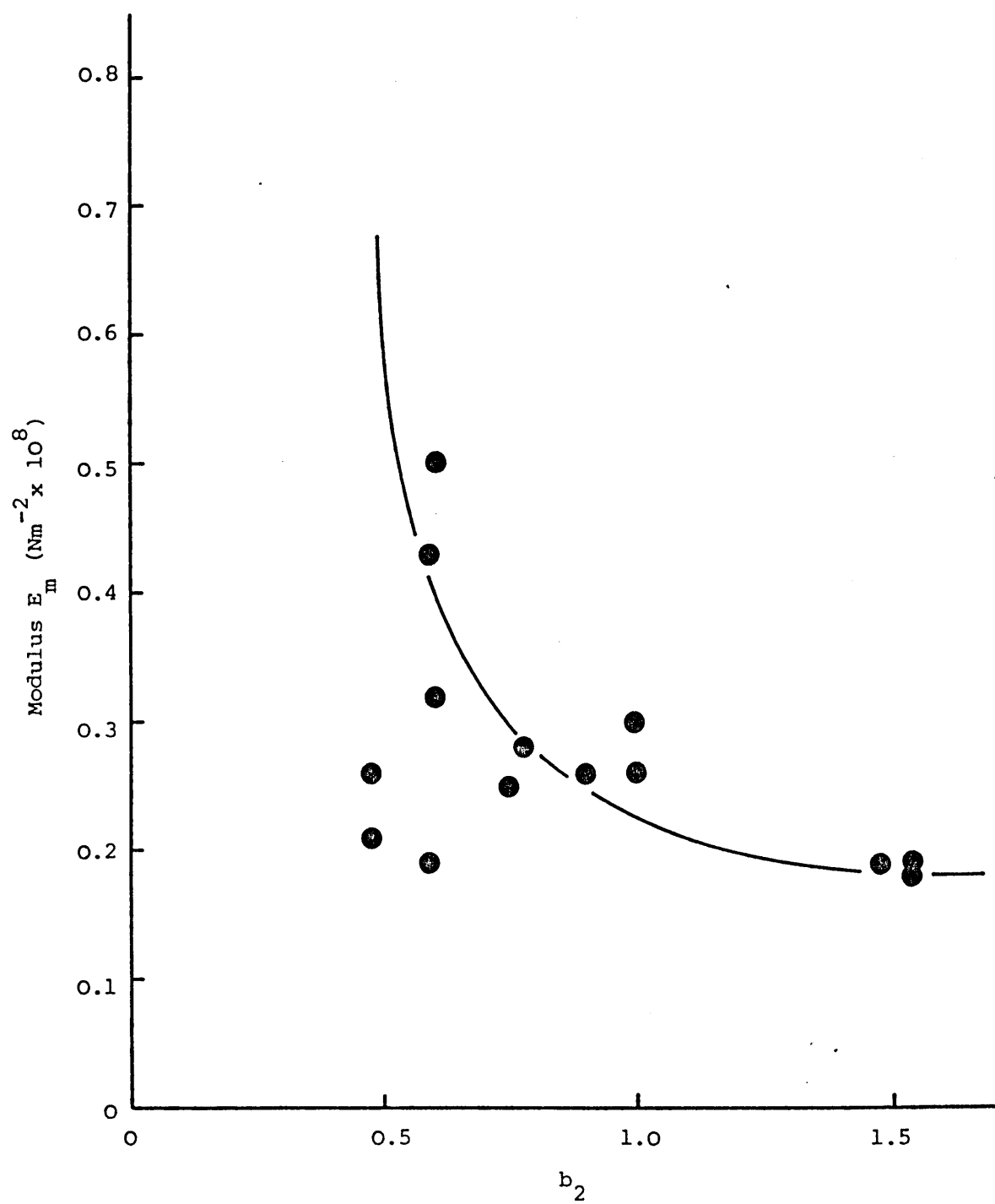


Figure 6.16 Terminal modulus  $E_m$  as a function of exponent  $b_2$   
for the debonding parameter  $B_d$ .

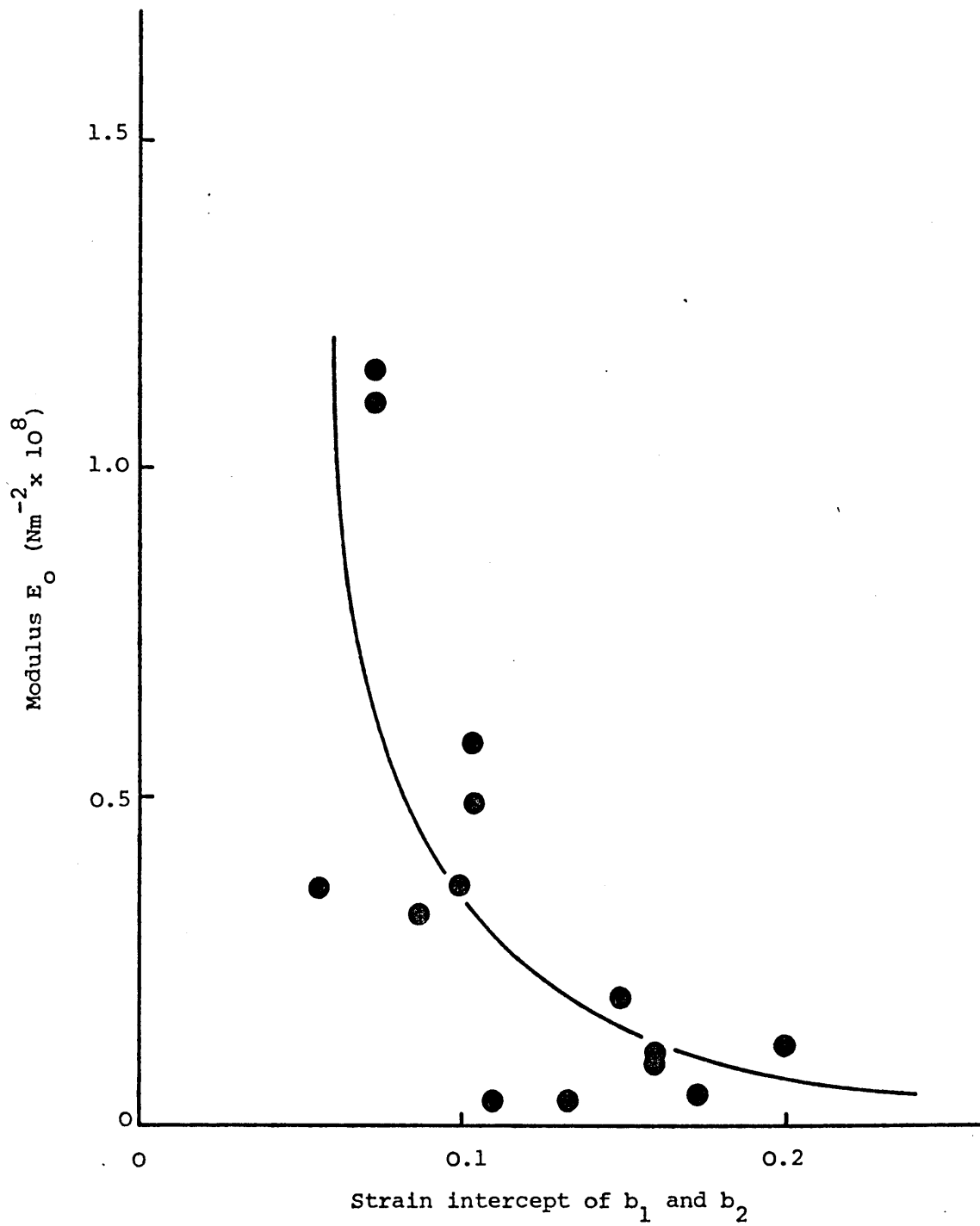


Figure 6.17 Initial modulus  $E_0$  as a function of the strain intercept for the exponents  $b_1$  and  $b_2$  of the debonding parameter  $B_d$ .

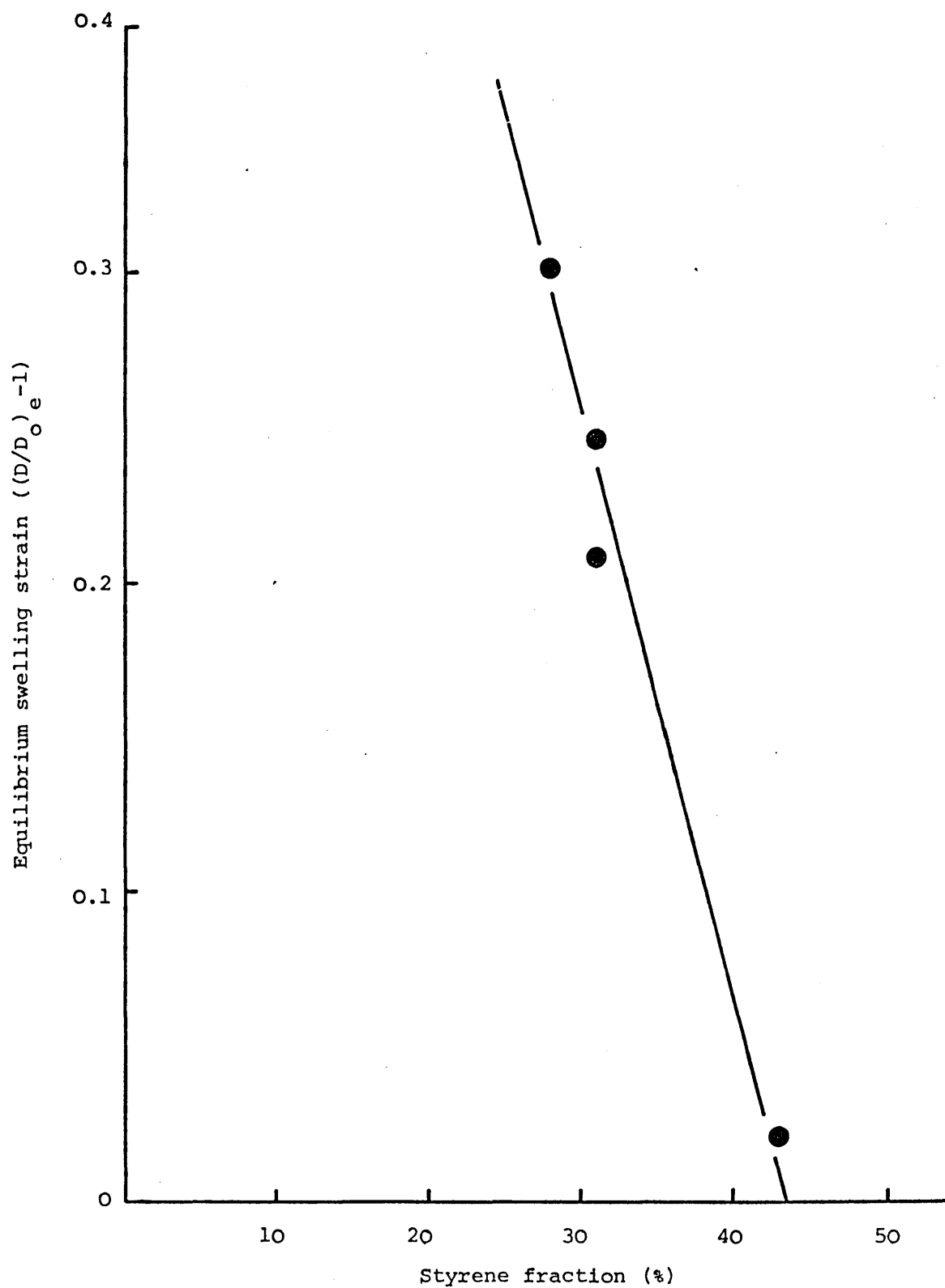


Figure 6.18 Equilibrium swelling strain as a function of styrene fraction.

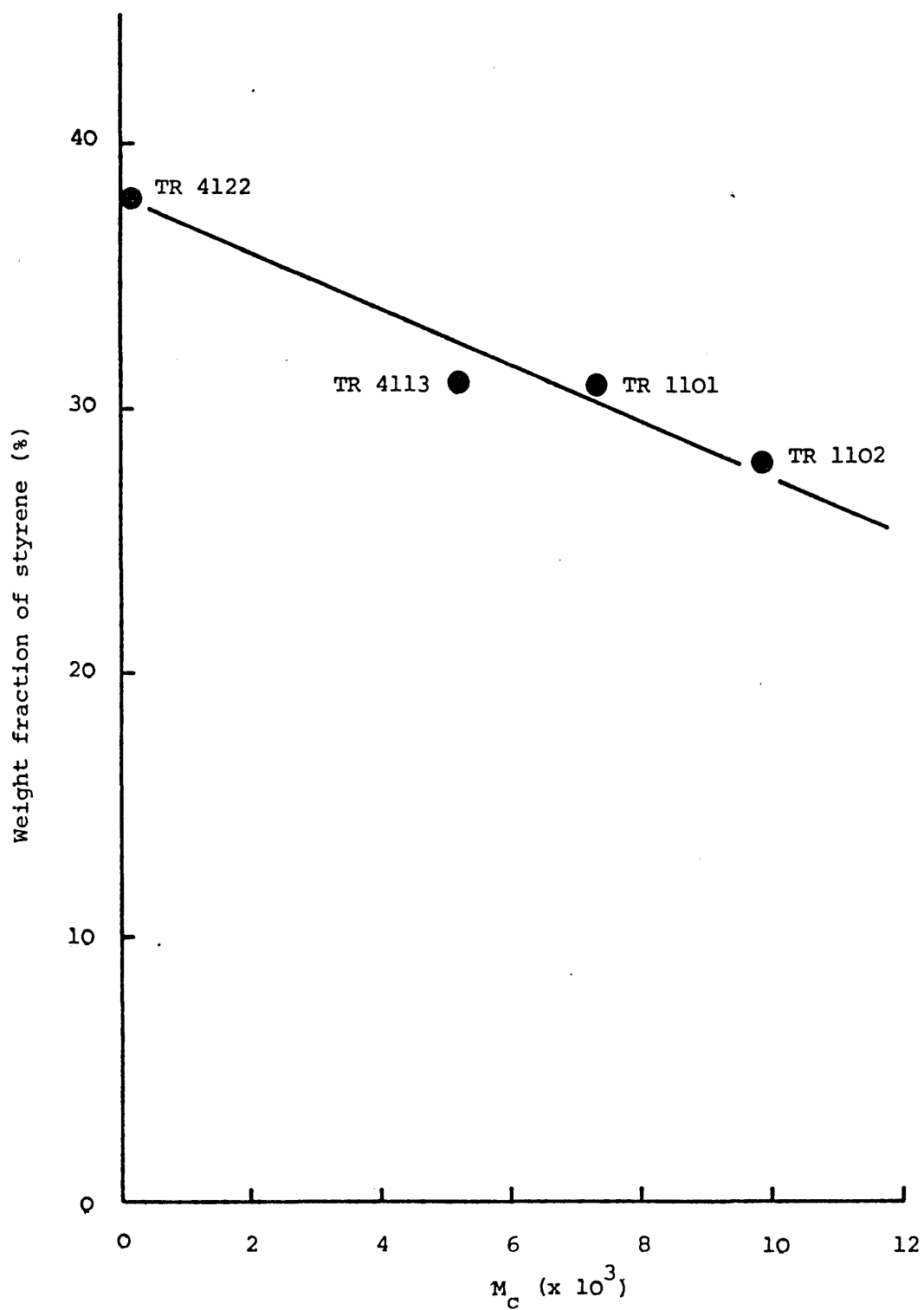


Figure 6.19 The molecular weight between entanglements  $M_c$  as a function of styrene fraction.

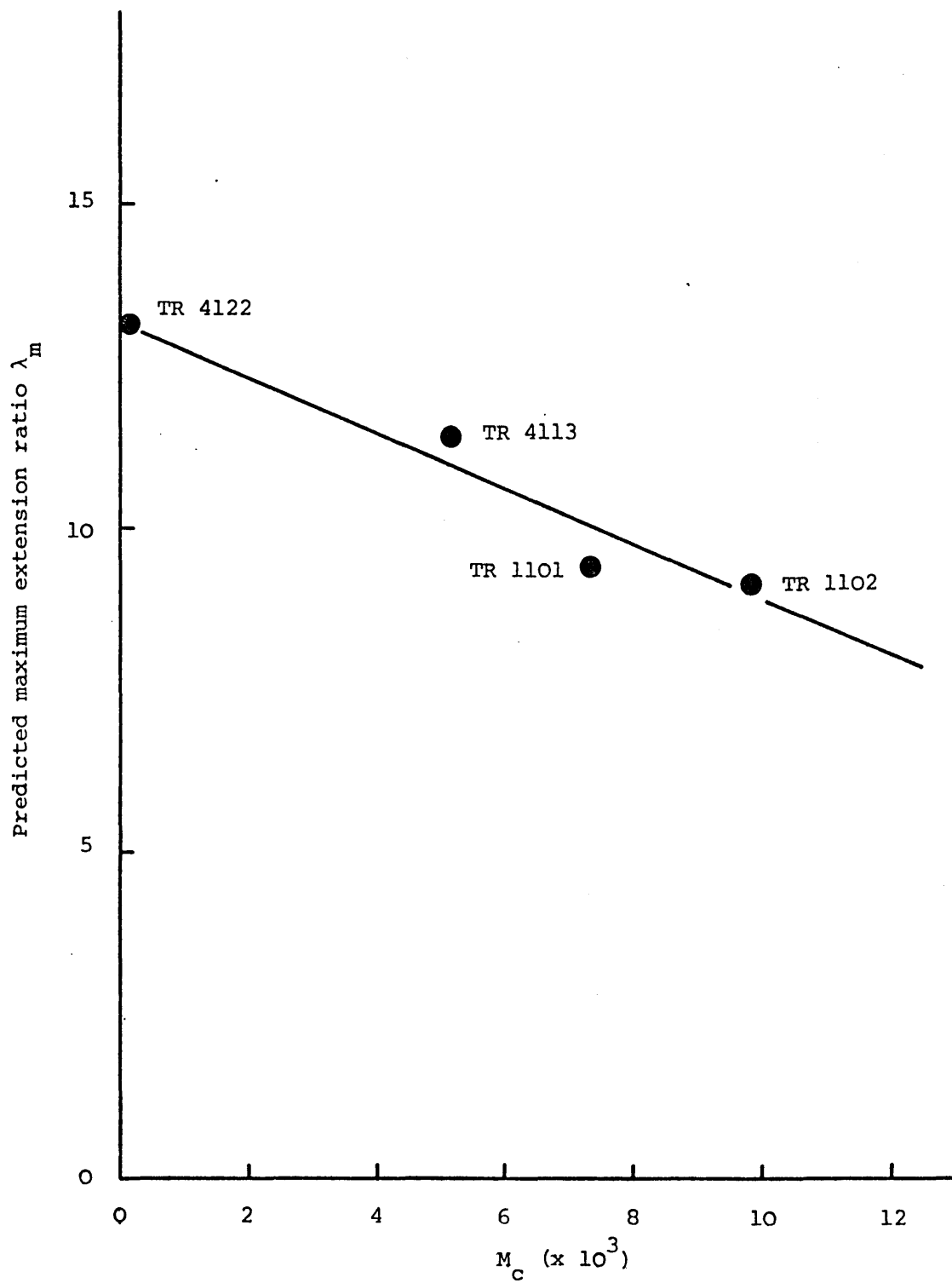


Figure 6.20 Predicted maximum extension ratio  $\lambda_m$  as a function of the molecular weight between entanglements  $M_c$ .



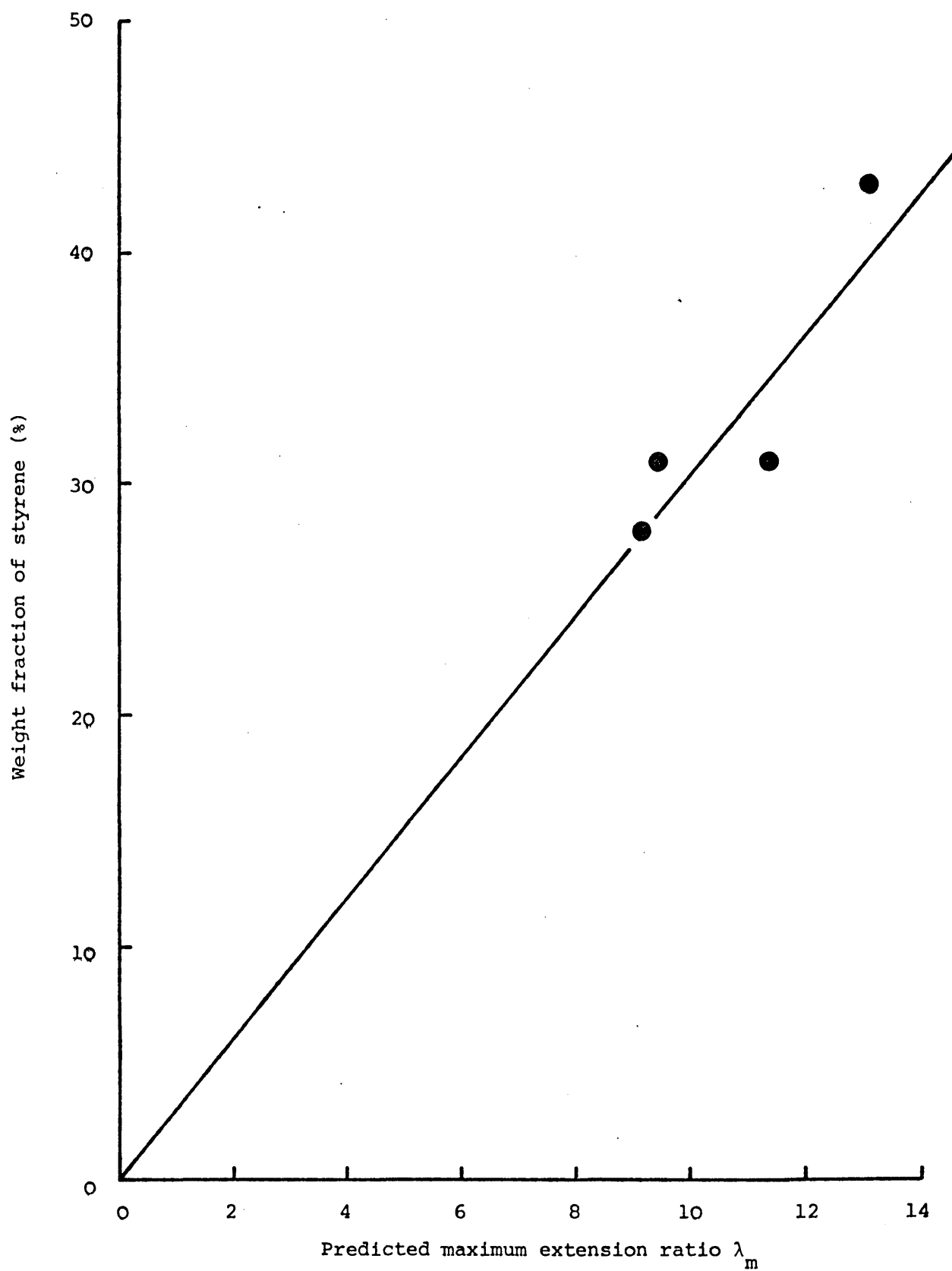


Figure 6.21 Styrene fraction as a function of the predicted maximum extension ratio  $\lambda_m$ .

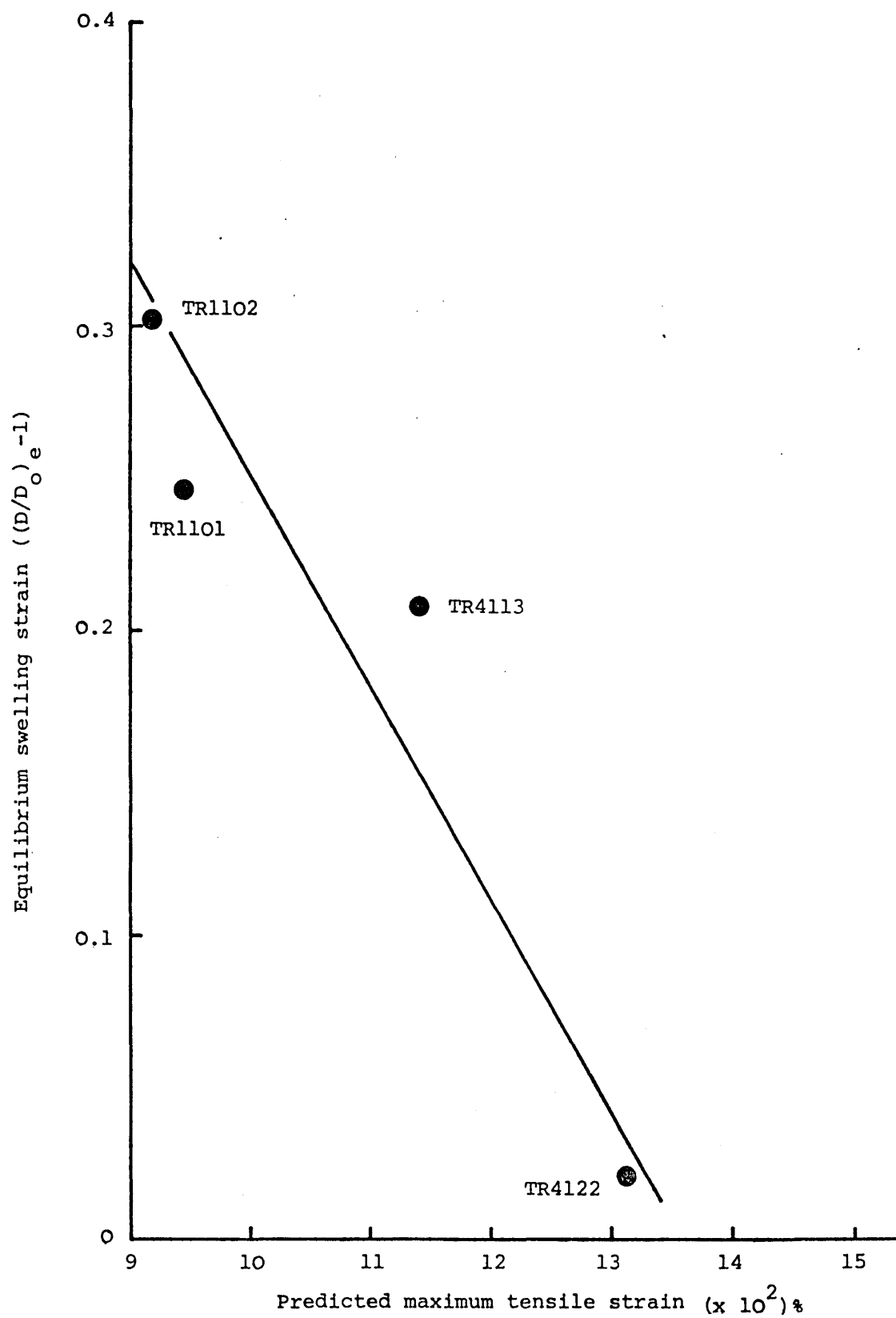


Figure 6.22 Equilibrium swelling strain as a function of the predicted maximum tensile strain.

7.1 INTRODUCTION

The prediction of the elastic modulus of block copolymer systems from a knowledge of their compositional and morphological conformation has been the subject of extensive discussion in the literature. Kaelble [154] showed that the relationships describing the effects of rigid filler on the modulus of elastomeric systems cannot be used for an accurate description of the properties of block copolymer elastomers. Using the micromechanics model of Takayanagi [55], Kaelble was able to explain the effects of compositional variations on the modulus. The Takayanagi model introduces the concept of parallel and series elements to represent the two-phase nature of a material. This arrangement, shown in Figures 7.1(a) and (b), is widely used to describe continuous filament composite materials.

For the parallel element model, assuming the strain is common to each element, it can be shown that the modulus,  $M$ , of the composite system is given by the linear law of mixtures:

$$M = M_1 \phi_1 + M_2 \phi_2 \quad (7.1)$$

where  $M_1$  and  $M_2$  are the moduli of the two phases, and  $\phi_1$  and  $\phi_2$  are the respective volume fractions, so that:

$$\phi_1 + \phi_2 = 1$$

In the series model, for which the stress is assumed to be common to each element:

$$\frac{1}{M} = \frac{\phi_1}{M_1} + \frac{\phi_2}{M_2} \quad (7.2)$$

Equations (7.1) and (7.2) define the upper and lower bounds to the modulus of the composite system, and have been used by Keller [218] to explain the properties of extruded block copolymer systems.

The polyaggregate model of Kerner [132] was employed by Faucher [215] in an analysis of data supplied by Holden et al [49] on several block

copolymer elastomers varying in styrene content. Nielsen [216] comments that it is difficult to relate the Takayanagi model to the morphology of real block copolymer systems; the same observation is true of the Kerner model used by Faucher because in many cases both phases are continuous and it is necessary to postulate a phase inversion.

Nielsen [216] used the Halpin-Tsai equations [141,142,217] which are capable of incorporating the detailed morphology of a system in a more precise fashion. Halpin & Tsai have shown that the rigorous solutions of the theory of fibre and ribbon reinforced composite materials may be reduced to the approximate form:

$$\left. \begin{aligned} E_{11} &\approx E_1 \phi_1 + E_2 \phi_2 \\ \nu_{12} &\approx \nu_1 \phi_1 + \nu_2 \phi_2 \end{aligned} \right\} \quad (7.3)$$

$$\frac{M}{M_1} = \frac{1 + A B \phi_2}{1 - B \phi_2} \quad (7.4)$$

where:

$$B = \frac{M_2/M_1 - 1}{M_2/M_1 + A} \quad (7.5)$$

The subscripts 1 and 2 refer to the continuous and disperse phases, respectively.  $E_{11}$  is the tensile modulus in the direction of orientation of the reinforcement;  $M$  is the modulus of the composite  $E_{22}$ ,  $G_{12}$  or  $G_{23}$ ;  $M_1$  is the modulus of the matrix  $E_1$ ,  $G_1$  or  $\nu_1$ ; and  $M_2$  is the modulus of the reinforcement  $E_2$ ,  $G_2$  or  $\nu_2$ . The physical arrangement of the reinforced system is shown in Figure 7.2(a) and the directions of the moduli in Figure 7.2(b).  $A$  is a measure of the reinforcement and is determined by the geometry of the system. By considering in detail systems reinforced with fibres and ribbons with rectangular cross-section, Halpin & Tsai [141,142,217] were able to show that for the transverse tensile modulus:

$$A_E = 2 \left( \frac{a_r}{b_r} \right) \quad (7.6)$$

and for the transverse shear modulus:

$$\log A_G = \sqrt{3} \log \left( \frac{a_r}{b_r} \right) \quad (7.7)$$

where  $(a_r/b_r)$  is the width/thickness ratio of the reinforcement. These dimensions are defined in Figure 7.3. The  $a_r/b_r$  ratio may take values from zero to infinity. When  $a_r/b_r$  is large, as in Figure 7.3(a), the reinforcement is almost continuous in the direction of the applied stress. Introducing  $A \rightarrow \infty$  into equation (7.5) gives:

$$B_{\infty} = \frac{M_2/M_1 - 1}{A}$$

Substituting into equation (7.4) and rearranging gives the modulus of the composite:

$$M = M_1 \phi_1 + M_2 \phi_2$$

which is identical to the parallel element model and equation (7.3).

When  $(a_r/b_r)$  is small, as in Figure 7.3(b),  $A \rightarrow 0$ ; substituting into equations (7.5) and (7.4) gives the modulus of the composite as:

$$\frac{1}{M} = \frac{\phi_1}{M_1} + \frac{\phi_2}{M_2}$$

which is equivalent to the series model, equation (7.2).

The Halpin-Tsai equations, therefore, place narrower limits on the upper and lower bounds of the composite modulus in the range where the morphology is not well defined. They are, however, sufficiently general to account for the two extremes of morphology as defined by the series/parallel systems. Nielsen [216] extended the Halpin-Tsai equations to other morphologies by introducing the generalised Einstein coefficient,  $k$ , in place of the reinforcement parameter,  $A$ .

## 7.2 THE NIELSEN EQUATIONS

According to Nielsen, the modulus,  $M$ , of a block copolymer system consisting of a rigid disperse phase with modulus  $M_2$  embedded in a rubbery continuous phase, modulus  $M_1$ , is given by:

$$\frac{M}{M_1} = \frac{1 + A B \phi_2}{1 - B \psi \phi_2} \quad (7.8)$$

where:

$$B = \frac{M_2/M_1 - 1}{M_2/M_1 + A} \quad (7.9)$$

$$A = k - 1 \quad (7.10)$$

and:

$$\psi = 1 + \left[ \frac{1 - \phi_m}{\phi_m^2} \right] \phi_2 \quad (7.11)$$

Here, the subscripts 1 and 2 refer to the continuous and disperse phases, respectively. The function  $\psi$  takes into account the maximum volumetric packing function,  $\phi_m$ , which is related to the morphology of the system and usually takes values between 0.5 and 0.9. For a random packing of spheres,  $\phi_m = 0.64$  (Nielsen [216]); for rods with simple cubic packing,  $\phi_m = 0.79$ , and close packing,  $\phi_m = 0.9$ . For rectangular strips,  $\phi_m = 1.0$ , which is the value used in the Halpin-Tsai equations.

For the inverted system consisting of a rubbery disperse phase in a rigid continuous matrix, the modulus  $M$  may be written:

$$\frac{M_2}{M} = \frac{1 + A_i B_i \phi_1}{1 - B_i \psi_i \phi_1} \quad (7.12)$$

where:

$$B_i = \frac{M_2/M_1 - 1}{M_2/M_1 + A_i} \quad (7.13)$$

and:

$$\psi_i = 1 + \left[ \frac{1 - \phi_m}{\phi_m^2} \right] \phi_1 \quad (7.14)$$

Here, the subscripts 1 and 2 again refer to the rubbery and rigid phases, respectively. Account must also be taken of the effect of Poisson's ratio. For a rigid matrix of  $\nu = 0.35$  (polystyrene) with a rubbery disperse phase of  $\nu = 0.5$ ,  $A_i$  may be determined (Nielsen [150]) and is expressed in the form:

$$A_i = \frac{1}{(0.54 k - 1)}$$

where  $k$  is the Einstein coefficient ( $A = k - 1$ ).

Equations (7.8) to (7.11) give the lower bound,  $M_L$ , to the modulus of the block copolymer and equations (7.12) to (7.14) the upper bound,  $M_U$ . These two cases may be compared with the physical arrangements shown in Figures 7.3(a) and (b), where:

$$\left[ \frac{a_r}{b} \right]_a > 1$$

and:

$$\left[ \frac{a_r}{b} \right]_b = \frac{1}{\left[ \frac{a_r}{b} \right]_a} < 1$$

The electron microscopical studies have shown that both phases may be continuous and that the material may be a polyaggregate of ordered regions. In general, the orientation of these regions is random, so that, although the regions are mechanically anisotropic, the bulk material is in fact isotropic. If, however, preferred orientation of regions exists, the material will be anisotropic (Folkes & Keller [218]). There may also be a phase inversion as the composition or method of sample preparation is altered (for instance, changing the casting solvent system). In such circumstances, Nielsen [216] has argued that provided the 'connectivity' (that is, the orientation) is random, the modulus of the composite is given by the logarithmic rule of mixtures:

$$\log M = \phi_U \log M_U + \phi_L \log M_L \quad (7.15)$$

where  $M_L$  and  $M_U$  are the lower and upper bounds to the modulus given by equations (7.8) to (7.11) and (7.12) to (7.14), respectively.  $\phi_U$  is the proportion of high modulus material in the continuous phase that is actually continuous, and  $\phi_L$  is the proportion of low modulus material in the continuous phase that is actually continuous.

The logarithmic rule of mixtures, which gives a weighted average of the property, placing greater emphasis on the lower bound, has been used by Nielsen [216] to predict the modulus of block copolymer elastomers and polyblends, and by Gray & McCrum [210] for crystalline-amorphous mixtures

of polyethylene.

For a two-phase system, with overall composition  $\phi_2$ ,  $\phi_U$  is given by:

$$\phi_U = \frac{\phi_2 - (1 - \phi'_m)}{\phi_m - (1 - \phi'_m)} \quad (7.16)$$

and:  $\phi_L = 1 - \phi_U \quad (7.17)$

where  $\phi_m$  is the maximum packing fraction in the normal system, and  $\phi'_m$  is the maximum packing fraction in the inverted system.



### 7.3 THE INITIAL STATIC TENSILE MODULI: RESULTS AND DISCUSSION

#### 7.3.1 Series-Parallel Model

Electron microscopical and X-ray studies of the morphologies (Chapter 4) revealed that these cast materials consist of arrangements of ordered regions oriented randomly within the sample. Since the material should be reasonably isotropic in the plane of the cast sheet, it is useful to apply the series/parallel model to discover what agreement, if any, is achieved between the predicted value of modulus and that measured during the simple tension tests described in Chapter 6.

In the first case, the input moduli are those for pure polybutadiene and polystyrene (taken from Keller [218] so that  $M_1$  (butadiene) =  $1 \times 10^6$  N/m<sup>2</sup>, and  $M_2$  (styrene) =  $2 \times 10^9$  N/m<sup>2</sup>). It is clear from the use of these constant values that it is not possible for the model to predict the changes in composite modulus due to structural changes resulting from the use of different casting solvents.

Here, the parallel model gives the upper bound modulus,  $M_U$ , in effect for stresses applied in the direction of orientation, and the series model gives the lower bound,  $M_L$ , for stresses normal to the direction of orientation. The composite modulus is calculated from the upper and lower bounds using the logarithmic rule of mixtures (equation (7.15)), with  $\phi_L = \phi_U = 0.5$ . Since equation (7.15) may be expressed:

$$M = M_U^{\phi_U} M_L^{\phi_L}$$

so that, here,  $M = (M_U M_L)^{\frac{1}{2}}$ , it follows that a geometric average value is achieved, rather than an arithmetic average. The values of parameters used in these calculations and the results are given in Table 7.1.

$\phi_1$  and  $\phi_2$  are the volume fractions of butadiene and styrene, respectively, calculated using the method described in Section 3.4.4.

From Table 7.1, the limitations of this analysis are immediately observed. Since the input moduli for butadiene and styrene are always the same, a single value of the composite modulus is achieved, whatever the casting solvent. For the materials TR1101 and TR1102, the predicted modulus value falls well short of the experimentally determined modulus using ethyl acetate and THF/MEK as casting solvents, and is somewhat higher than the experimental value achieved using BEN/HEP and CCl<sub>4</sub>.

For the plasticised material TR4113, the predicted value is

### Comparison of Moduli Predicted by Series/Parallel Model, Using $M_1 = 1.0 \text{ MN/m}^2$ ,

Material	Solvent	$\phi_1$	$M_1$ (MN/m <sup>2</sup> )	$\phi_2$	$M_2$ (GN/m <sup>2</sup> )	$M_L$ (MN/m <sup>2</sup> )	$M_U$ (MN/m <sup>2</sup> )	$M$ (model) (MN/m <sup>2</sup> )	$M$ (exp) (MN/m <sup>2</sup> )
TR1101	Ethyl Acetate THF/MEK BEN/HEP CCl <sub>4</sub>	0.72	1.0	0.28	2.0	1.39	561	27.9	115 110 19.6 12.2
TR1102	Ethyl Acetate THF/MEK BEN/HEP CCl <sub>4</sub>	0.75	1.0	0.25	2.0	1.33	501	25.8	58.5 49.0 9.8 10.1
TR4122	THF/MEK BEN/HEP CCl <sub>4</sub>	0.61	1.0	0.39	2.0	1.64	781	35.8	36.1 36.8 32.1
TR4113	THF/MEK BEN/HEP CCl <sub>4</sub>	0.72	1.0	0.28	2.0	1.39	561	27.9	4.7 4.0 3.7

considerably higher than that determined in practice. This was to be expected since the effect of the plasticiser is to reduce the rigidity of the styrene phase, so that in this case it would be necessary to use a lower value of  $M_2$  in the calculations in order to achieve a reasonable predicted value of composite modulus.

The fact that for TR4122 the predicted modulus value of the composite system is identical to the measured value is seen as somewhat fortuitous since the same argument applies here as with TR4113. Where a reduced  $M_2$  styrene modulus should really be introduced in the calculations, this would have the effect of reducing the predicted composite modulus.

The approach used in the series-parallel model places great emphasis on the proportions of each phase in the composite system and this is reflected in the predicted moduli achieved here. In an attempt to give the model a structure discriminating factor, the calculations were repeated using a variable polybutadiene  $M_1$  input modulus. The values used for  $M_1$  were the terminal moduli determined during the analysis of tensile stress/strain curves in Chapter 6, and indicated in Table 6.2. The results of this recalculation are shown in Table 7.2, and reveal that whilst there is now some degree of discrimination between samples cast from different solvent systems, and comparisons between predicted and experimentally determined moduli for samples cast from TR1101 and TR1102 ethyl acetate and THF/MEK are somewhat improved, no improvement is achieved for samples cast from BEN/HEP and  $\text{CCl}_4$ . For TR4113, the predicted moduli are now even greater than the previous analysis suggested, and the values achieved for TR4122 are approximately double the experimental moduli; this, however, as suggested previously, would not be such a great problem if a lower styrene modulus,  $M_1$ , were to be introduced into the calculations. If the input styrene modulus,  $M_2$ , for TR4122 and TR4113 cast from THF/MEK is reduced by a factor of 10 (from 2 GN/m<sup>2</sup> to 0.2 GN/m<sup>2</sup>), the predicted moduli are 23.7 MN/m<sup>2</sup> and 12.3 MN/m<sup>2</sup>, respectively. These values, whilst not satisfying fully the experimentally determined moduli, do show that this approach could yield a good correlation if full account were taken of the difference in structure between TR4122 and TR4113 (TR4122 is primarily lamellar in structure, whilst TR4113 has a cylindrical styrene structure in a butadiene matrix).

### 7.3.2 Use of the Structure Parameter

It follows from the results presented in Section 7.3.1 that some structure sensitive parameter must be introduced into the calculations

TABLE 7.2

Comparison of Moduli Predicted by Series/Parallel Model, Using Varying  $M_1$ ,  
With Experimentally Determined Modulus Values

Material	Solvent	$\phi_1$	$M_1$ (MN/m <sup>2</sup> )	$\phi_2$	$M_2$ (GN/m <sup>2</sup> )	$M_L$ (MN/m <sup>2</sup> )	$M_U$ (MN/m <sup>2</sup> )	$M$ (model) (MN/m <sup>2</sup> )	$M$ (exp) (MN/m <sup>2</sup> )
TR1101	Ethyl Acetate THF/MEK BEN/HEP CCl <sub>4</sub>	0.72	5.0	0.28	2.0	6.9	558	62.1	115
		0.72	3.2	0.28	2.0	4.4	557	49.6	110
		0.72	2.8	0.28	2.0	3.9	556	46.4	19.6
		0.72	2.6	0.28	2.0	3.6	556	44.7	12.2
TR1102	Ethyl Acetate THF/MEK BEN/HEP CCl <sub>4</sub>	0.75	2.6	0.25	2.0	3.5	500	41.6	58.5
		0.75	2.1	0.25	2.0	2.8	500	37.4	49.0
		0.75	3.0	0.25	2.0	4.0	500	44.7	9.8
		0.75	2.6	0.25	2.0	3.5	500	41.6	10.1
TR4122	THF/MEK BEN/HEP CCl <sub>4</sub>	0.61	4.3	0.39	2.0	7.1	786	74.5	36.1
		0.61	2.5	0.39	2.0	4.1	785	56.8	36.8
		0.61	1.9	0.39	2.0	3.1	784	49.5	32.1
TR4113	THF/MEK BEN/HEP CCl <sub>4</sub>	0.72	1.9	0.28	2.0	2.6	556	38.2	4.7
		0.72	1.9	0.28	2.0	2.6	556	38.2	4.0
		0.72	1.8	0.28	2.0	2.5	555	37.2	3.7

and this is provided for in the theory of Nielsen by the use of the Einstein coefficient,  $k$ . Although  $k$  is very sensitive to morphology, it may take the same value for different morphologies, so that it does not give an unequivocal description of the structure of the system.

Electron microscopical studies have shown that at low volume fraction,  $\phi_2$ , of the rigid phase, the polystyrene is dispersed as spheres in the rubbery butadiene matrix. At high volume fractions of styrene, a phase inversion occurs, the rubbery phase being dispersed in a rigid matrix. In the intermediate region, both phases may be continuous and the modulus is given by the logarithmic rule of mixtures (equation (7.15)), with the upper and lower bounds being given by equations (7.8) and (7.12), respectively. This averaging procedure is shown graphically in Figure 7.4. The parameter  $\phi'_m$  is related to the volume fraction of rigid material at which both phases are continuous. According to Nielsen, and also microscopical studies [51,66], this occurs when  $\phi_2$ , the volume fraction of polystyrene, is about 15%, that is  $(1 - \phi'_m) = 0.15$ . The value of  $\phi_m$  is the maximum packing fraction for the rigid phase, which depends upon the particular geometry of the domain. Some typical values are given in Table 7.3.

TABLE 7.3  
Values of  $\phi_m$  for Several Domain Morphologies

Morphology	$\phi_m$
Rectangular rods, strips or plates	1.000
HCP circular cross-section rods	0.907
HCP spheres	0.740
Random spheres	0.650

For the polymers used in this study, the volume fraction of the rigid phase,  $\phi_2$ , is such that both phases are continuous, and since  $\phi_2$  remains constant for each material, it is necessary to explain the variation in modulus with casting solvent system in terms of domain geometry or the value of the Einstein coefficient,  $k$ .

In order to determine the effect of different microstructures on predicted moduli, an analysis of TR1101 and TR1102 was carried out using

$\phi_m$  values which were consistent with those indicated in Table 7.3. The results of this analysis are shown in Figure 7.5 for TR1101 cast from ethyl acetate; the predicted static tensile modulus is plotted as a function of Einstein coefficient for several  $\phi_m$  values. The experimentally determined static tensile modulus for this particular material is also plotted with the corresponding  $k$  values being indicated for each  $\phi_m$  level. The results using the parallel and series models are also shown. Similar results were achieved for the other material/solvent combinations, and these are shown in Figures 7.6 and 7.7 for TR1101 and TR1102, but here  $\phi_m$  is chosen for each material according to evidence from the microstructural studies of Chapter 4, so that for casting from ethyl acetate and THF/MEK,  $\phi_m$  is taken as 1.0, and for BEN/HEP and  $\text{CCl}_4$ ,  $\phi_m$  is 0.907. From these graphs, it is possible to designate the appropriate Einstein coefficient for the particular material/solvent system, on the basis of the experimentally determined static tensile moduli. This data is tabulated in Table 7.4.

TABLE 7.4  
Einstein Coefficients for TR1101 and TR1102

Material	Solvent	Einstein Coefficient, $k$
TR1101	Ethyl acetate	33
	THF/MEK	53
	BEN/HEP	5.3
	$\text{CCl}_4$	3.2
TR1102	Ethyl acetate	33
	THF/MEK	31
	BEN/HEP	2.8
	$\text{CCl}_4$	3.1

#### 7.4 A THEORETICAL ANALYSIS FOR THE DYNAMIC MODULI

A rigorous theoretical analysis has not yet been developed to describe the viscoelastic behaviour of multiphase polymeric systems. It has been pointed out by Gray & McCrum [210] that the difference between an elastic and a viscoelastic solid decreases as the modulus  $M''$  decreases. Using the theory for the elastic modulus of composite systems, they propose that viscoelastic behaviour may be predicted by replacing moduli  $M_1$  and  $M_2$  for the constituents by the complex moduli  $M_1^*$  and  $M_2^*$ . Adopting this procedure, Dickie [139] studied the influence of composition on the storage modulus and loss tangent of rigid/rubbery composites. Using similar arguments, the Nielsen equations [216] may be extended in the same way.

For the non-inverted system described by equation (7.8), the complex shear modulus,  $G^*$ , of the composite may be expressed by:

$$\frac{G^*}{G_1^*} = \frac{1 + A B^* \phi_2}{1 - B^* \psi \phi_2} \quad (7.18)$$

where the subscript 1 refers to the continuous, rubbery phase, and the subscript 2 refers to the disperse rigid phase. The parameter  $B^*$  is given by:

$$B^* = B' + j B'' = \frac{G_2^*/G_1^* - 1}{G_2^*/G_1^* + A}$$

where:

$$G^* = G' + j G''$$

$$G_1^* = G_1' + j G_1''$$

$$G_2^* = G_2' + j G_2''$$

Considering the complex  $B^*$  parameter:

$$B^* = \frac{G_2^* - G_1^*}{G_2^* + A G_1^*} = \frac{(G_2' - G_1') + j (G_2'' - G_1'')}{(G_2' + A G_1') + j (G_2'' + A G_1'')}$$

Rationalising and comparing real and imaginary parts:

$$B' = \frac{(G_2' - G_1')(G_2' + A G_1') + (G_2'' - G_1'')(G_2'' + A G_1'')}{(G_2' + A G_1')^2 + (G_2'' + A G_1'')^2} \quad (7.19)$$

$$B'' = - \left[ \frac{(G_2' - G_1')(G_2'' + A G_1'') - (G_2'' - G_1'')(G_2' + A G_1')}{(G_2' + A G_1')^2 + (G_2'' + A G_1'')^2} \right] \quad (7.20)$$

The complex modulus of the composite is given by:

$$\begin{aligned} \frac{G^*}{G_1^*} &= \frac{1 + A \phi_2 (B' + j B'')}{1 - (B' + j B'') \phi_2 \psi} \\ &= \frac{(1 + A \phi_2 B') + j A \phi_2 B''}{(1 - B' \phi_2 \psi) - j (B'' \phi_2 \psi)} \end{aligned}$$

Again, rationalising and equating real and imaginary parts:

$$G' = (X/Z) G_1' - (Y/Z) G_1'' \quad (7.21)$$

$$G'' = (X/Z) G_1'' - (Y/Z) G_1' \quad (7.22)$$

$$\text{where: } X = 1 + \phi_2 B' (A + \psi) - A \phi_2^2 \psi (B'^2 + B''^2)$$

$$Y = \phi_2 B'' (A + \psi) \quad \left. \vphantom{\begin{matrix} X \\ Y \\ Z \end{matrix}} \right\} \quad (7.23)$$

$$Z = (1 - \phi_2 B' \psi)^2 + (B'' \psi \phi_2)^2$$

The loss tangent of the composite, defined as  $G''/G'$ , is given by:

$$\tan \delta = \frac{\tan \delta_1 - (Y/X)}{1 - (Y/X) \tan \delta_1} \quad (7.24)$$

where  $\tan \delta_1$  is the loss tangent for the rubbery continuous phase.

Equations (7.21), (7.22) and (7.24) are identical in form to those derived by Dickie [139].

For the inverted form, starting from equation (7.13):



$$B'_i = \frac{(G'_1 - G'_2)(G'_1 + A_i G'_2) + (G''_1 - G''_2)(G''_1 + A_i G''_2)}{(G'_1 + A_i G'_2)^2 + (G''_1 + A_i G''_2)^2} \quad (7.25)$$

$$B''_i = - \left[ \frac{(G'_1 - G'_2)(G''_1 + A_i G''_2) - (G''_1 - G''_2)(G'_1 + A_i G'_2)}{(G'_1 + A_i G'_2)^2 + (G''_1 + A_i G''_2)^2} \right] \quad (7.26)$$

where the subscript 1 refers to the rigid continuous phase and the subscript 2 refers to the rubbery disperse phase. Writing equation (7.12) in the form:

$$\frac{G^*}{G'_1} = \frac{1 - B_i^* \psi \phi_2}{1 + A_i B_i^* \phi_2}$$

it can be shown that:

$$\left. \begin{aligned} G' &= (X_i/Z_i) G'_1 + (Y_i/Z_i) G''_1 \\ G'' &= (X_i/Z_i) G''_1 - (Y_i/Z_i) G'_1 \end{aligned} \right\} \quad (7.27)$$

and: 
$$\tan \delta = \frac{\tan \delta_1 - (Y_i/X_i)}{1 + (Y_i/X_i) \tan \delta_1} \quad (7.28)$$

where  $\tan \delta_1$  is the loss tangent for the continuous phase, and:

$$\left. \begin{aligned} X_i &= 1 + \phi_2 B'_i (A_i - \psi) - \phi_2^2 \psi A_i (B_i'^2 + B_i''^2) \\ Y_i &= \phi_2 B''_i (A_i + \psi) \\ Z_i &= (1 + A_i \phi_2 B'_i)^2 + (A_i \phi_2 B''_i)^2 \end{aligned} \right\} \quad (7.29)$$

Applying the logarithmic rule of mixtures to account for the coexistence of two continuous phases, the complex modulus of the composite is given by (Gray & McCrum [210]):

$$\log G^* = \phi_U \log G_U^* + \phi_L \log G_L^* \quad (7.30)$$

with:

$$G_U^* = G_U' + j G_U''$$

$$G_L^* = G_L' + j G_L''$$

The lower and upper bounds for the moduli are given by equations (7.19) to (7.23) and (7.25) to (7.29), respectively.

Equation (7.30) may be written in the form:

$$G^* = G' + j G'' = (G_U' + j G_U'')^{\phi_U} (G_L' + j G_L'')^{\phi_L}$$

By using the binomial expansion and ignoring second and higher order terms in  $G_U''/G_U'$  and  $G_L''/G_L'$ , Gray & McCrum [210] show that:

$$\left. \begin{aligned} G' &= (G_U')^{\phi_U} (G_L')^{\phi_L} \\ G'' &= (G_U')^{\phi_U} (G_L')^{\phi_L} [\phi_U (G_U''/G_U') + \phi_L (G_L''/G_L')] \end{aligned} \right\} \quad (7.31)$$

$$\tan \delta = \phi_U \tan \delta_U + \phi_L \tan \delta_L \quad (7.32)$$

Thus, the storage modulus of the composite is given by the logarithmic rule of mixtures:

$$\log G' = \phi_U \log G_U' + \phi_L \log G_L' \quad (7.33)$$

and the loss tangent of the composite is given by the linear rule of mixtures. The effectively continuous volume fractions of the continuous phases  $\phi_U$  and  $\phi_L$  are given by equations (7.16) and (7.17).

## 7.5 THE PREDICTION OF DYNAMIC MODULI: RESULTS AND DISCUSSION

Having determined the Einstein coefficient appropriate to each material/solvent system (Section 7.3.2) and using the analysis of Section 7.4 to generate theoretical curves of dynamic modulus and  $\tan \delta$  as a function of  $k$ , experimentally determined moduli may then be inserted at the particular  $k$  value for the system.

An interesting temperature for this investigation is the low temperature polybutadiene transition, and the input data for shear and tensile dynamic modes for polystyrene and polybutadiene at this temperature are given in Table 7.5.

TABLE 7.5  
Input Data for Dynamic Modulus Prediction

Material	$E'$ (GN/m <sup>2</sup> )	$E''$ (GN/m <sup>2</sup> )	$G'$ (GN/m <sup>2</sup> )	$G''$ (GN/m <sup>2</sup> )
Polystyrene -90°C	3.0	0.09	1.0	0.03
+20°C	3.0	0.042	1.0	0.014
Polybutadiene -90°C	0.06	0.12	0.02	0.04
+20°C	0.006	0.0003	0.002	0.0001

The results of this analysis are shown in Figures 7.8 and 7.9 for TR1101 and TR1102, respectively. Here, the predicted dynamic tensile storage and shear storage moduli and  $\tan \delta$  are plotted as a function of the Einstein coefficient, and experimentally determined modulus values (Chapter 5) for the appropriate Einstein coefficient are inserted. For the shear modulus, experimental values fit the theoretical curve very well, except for TR1101 cast from CCl<sub>4</sub>. However, the experimental values for the tensile storage modulus for materials cast from BEN/HEP and CCl<sub>4</sub> do not fit the curve at all well. In both TR1101 and TR1102, the theoretical  $\tan \delta$  curve is high compared with the experimental data, although the shape of the curve appears to be correct in that  $\tan \delta$  falls with increased Einstein coefficient.

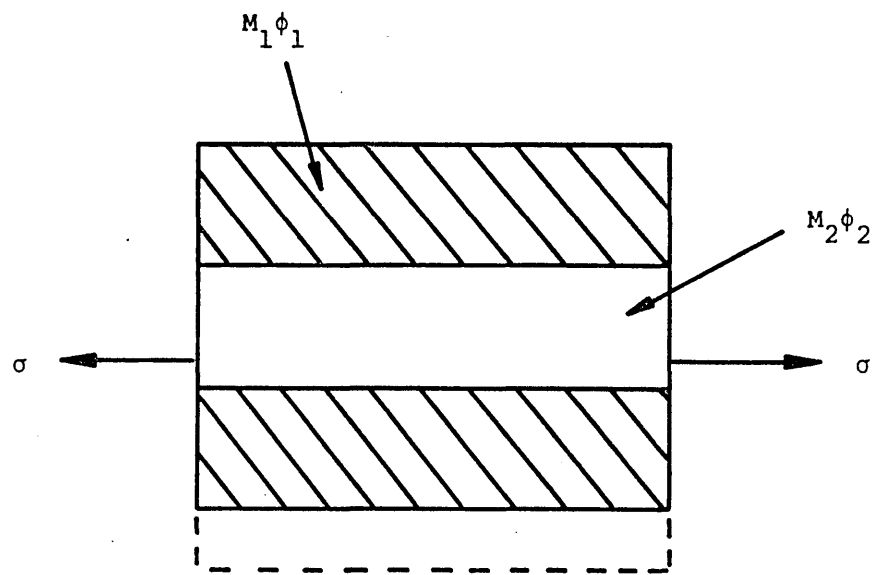
At the temperature investigated here, the experimentally determined dynamic tensile modulus appears to be unaffected by changes in the microstructure of the polystyrene phase caused by changing the casting solvent. The dynamic shear modulus, however, appears to be more sensitive to morphological change at this temperature.

A further temperature of interest is +20°C. Since this was the temperature at which the static tensile tests were carried out, and from which the  $k$  values used here were determined, one might intuitively expect improved correlation between predicted and experimental dynamic data. The input data are shown in Table 7.5. Figures 7.10 and 7.11 show the predicted modulus and  $\tan \delta$  curves as a function of Einstein coefficient for TR1101 and TR1102, respectively, at +20°C. It is felt that at this temperature, some improvement in the correlation is achieved. For TR1101 in Figure 7.10, the shear storage modulus curve fits the experimental data fairly accurately, as does the tensile storage modulus curve for ethyl acetate and THF/MEK cast materials. However, the dynamic tensile modulus results for BEN/HEP and  $\text{CCl}_4$  cast samples fall well below the predicted curve.

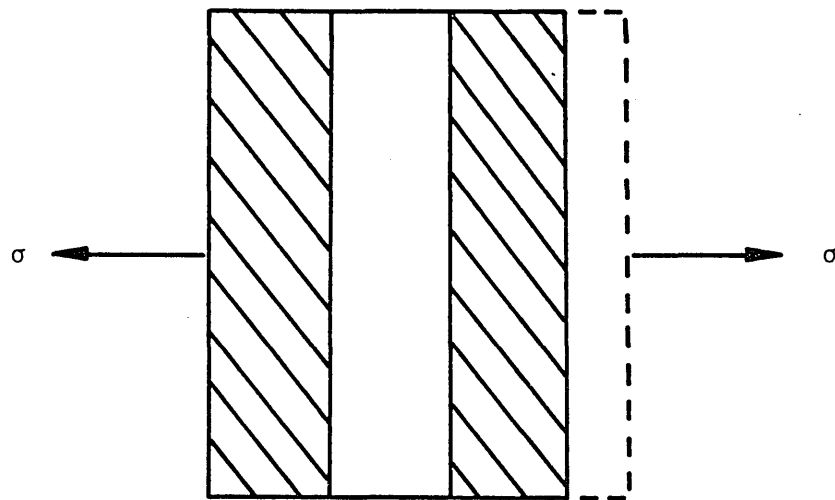
The results for TR1102 in Figure 7.11 are, if anything, slightly less scattered than for TR1101, but a definite discrepancy exists between predicted and experimental data for the tensile storage modulus, the predicted curve being well above all the experimental data. The shear results are somewhat better, good agreement being found for ethyl acetate, THF/MEK and BEN/HEP samples, a rather poorer result being found for  $\text{CCl}_4$  cast material.

The predicted curves and experimental points for  $\tan \delta$  show good agreement for both TR1101 and TR1102 in Figures 7.10 and 7.11, respectively, particularly when one considers the very low values under consideration (the loss tangent at +20°C is in the trough between the two major peaks).

Thus far, in order to simplify the computation and presentation, the predicted modulus curves have all been calculated using  $\phi_m = 1.00$  (that is, a largely lamellar structure has been considered). If, however, other microstructural possibilities are investigated, the predicted moduli at +20°C are shown to fit the experimental data somewhat better. The broken lines in Figures 7.10 and 7.11 indicate the predicted modulus curves assuming  $\phi_m = 0.74$  for the BEN/HEP and  $\text{CCl}_4$  cast samples, and  $\phi_m = 1.00$  for the THF/MEK and ethyl acetate cast materials. Whilst this approach improves agreement for the tensile dynamic mode in both TR1101 and TR1102 and the shear mode in TR1101, the correlation is in fact made worse for the shear mode in TR1102. Even so, the analysis does show some promise, and with further refinement, could have a useful rôle to play in the prediction of elastic and viscoelastic properties of block copolymer materials.



(a)

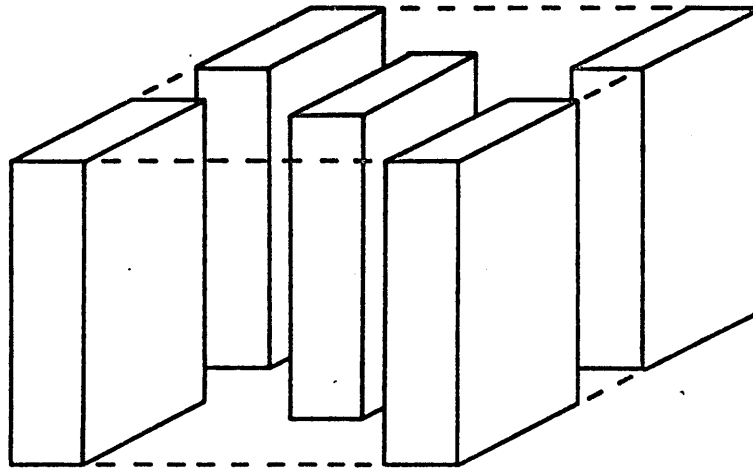


(b)

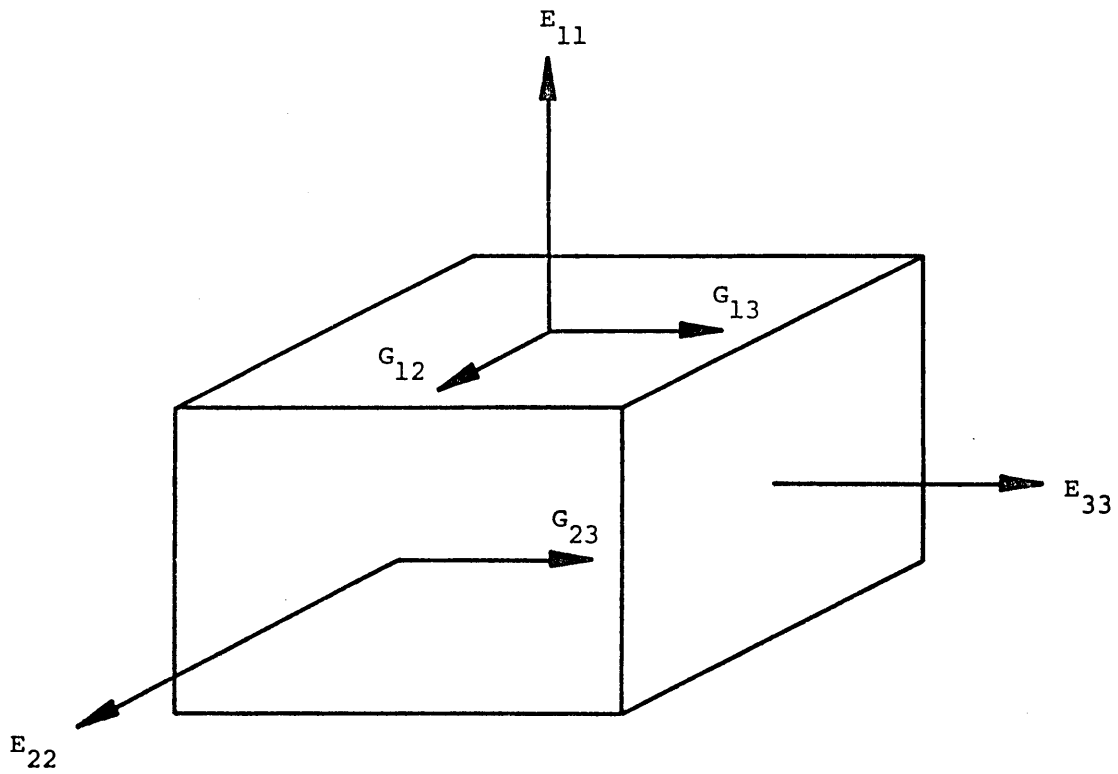
Figure 7.1 Mechanics model for composite materials

(a) parallel element model

(b) series element model



(a)



(b)

Figure 7.2 (a) the physical arrangement of the reinforced system considered by the Halpin-Tsai theory.

(b) the moduli.

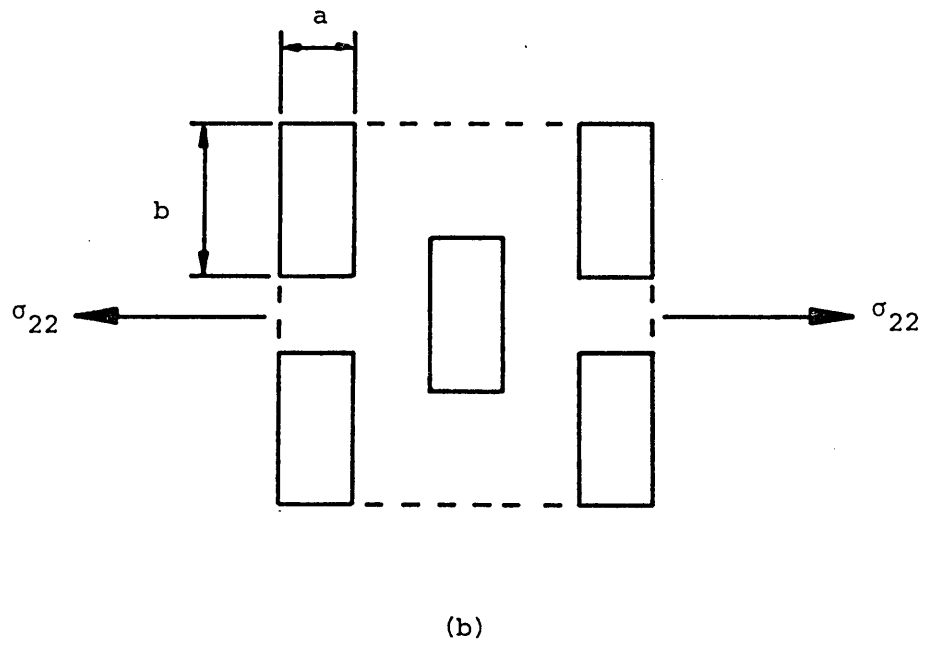
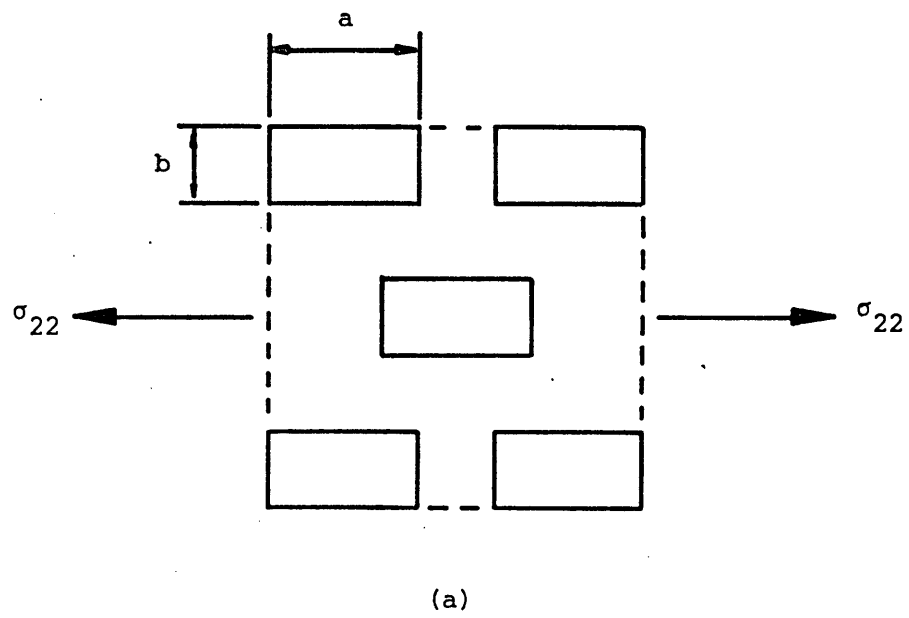


Figure 7.3 Reinforcing ribbon dimensions in composite considered in Halpin-Tsai theory.

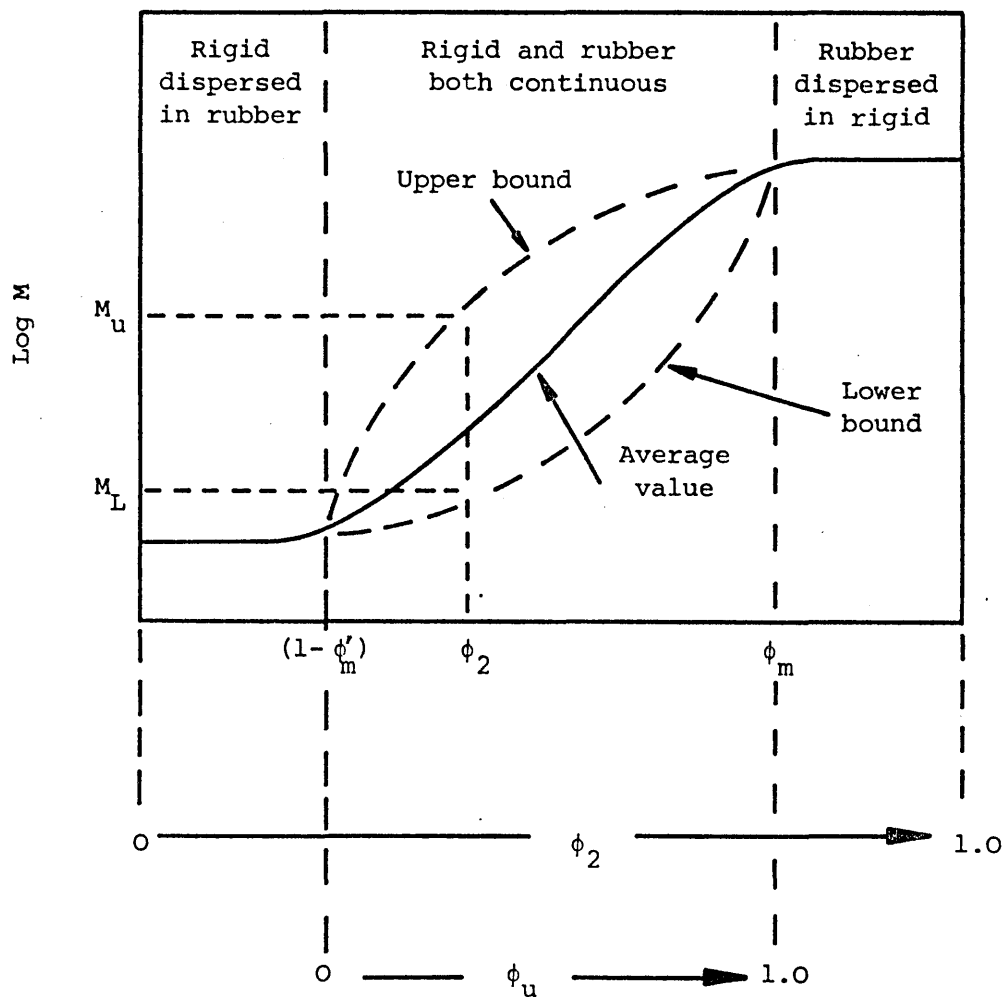


Figure 7.4 Effect of composition on modulus (schematic).



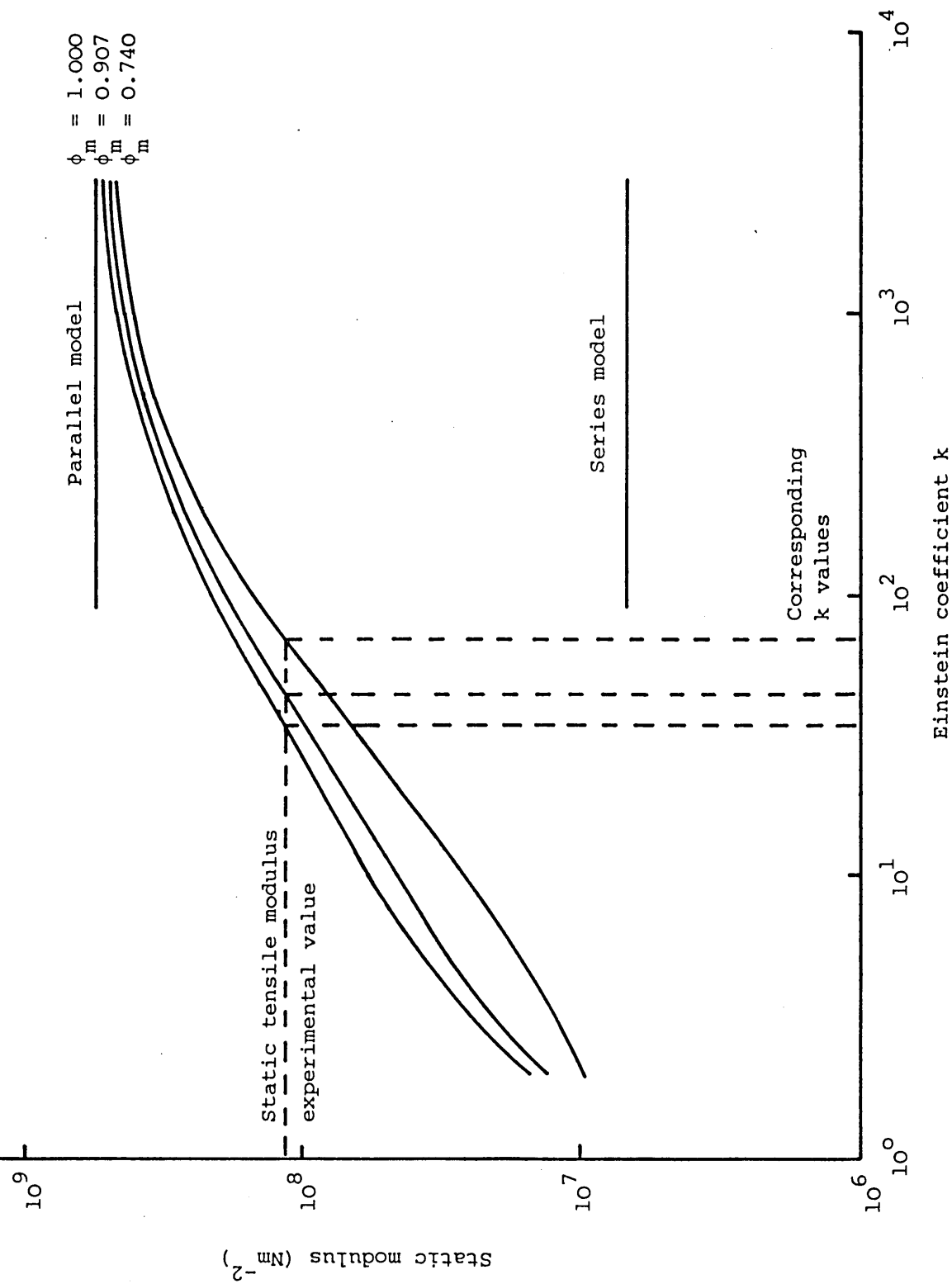


Figure 7.5 Predicted curves for the static tensile modulus as a function of Einstein coefficient  $k$ , using several packing fractions  $\phi_m$  for TR1101 ethyl acetate.

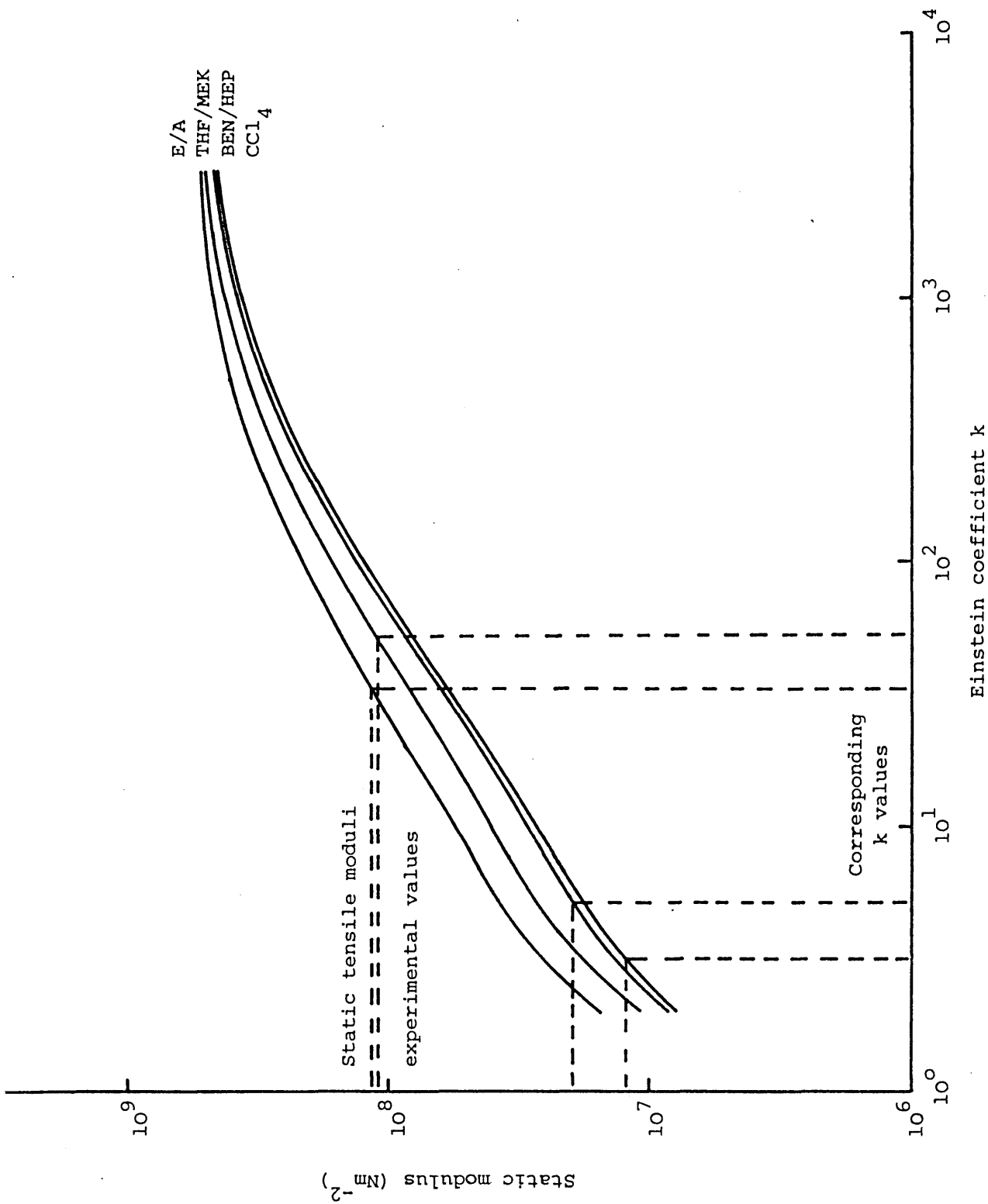


Figure 7.6 Predicted curves for static tensile modulus as a function of k, using TR1101 and several solvent systems for the most likely packing fraction.

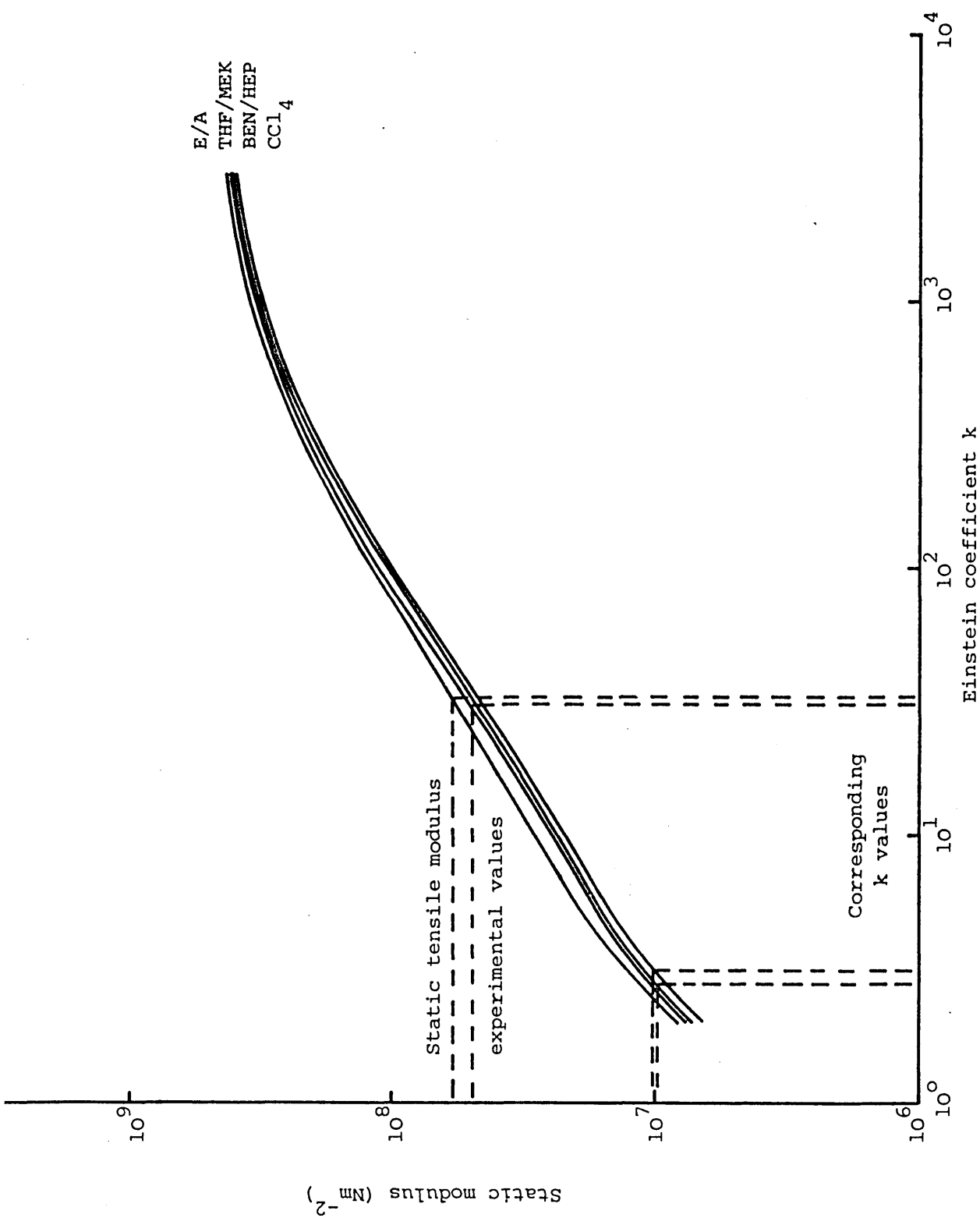


Figure 7.7 Predicted curves for static tensile modulus as a function of  $k$ , using TR1101 and several solvent systems for the most likely packing fraction.

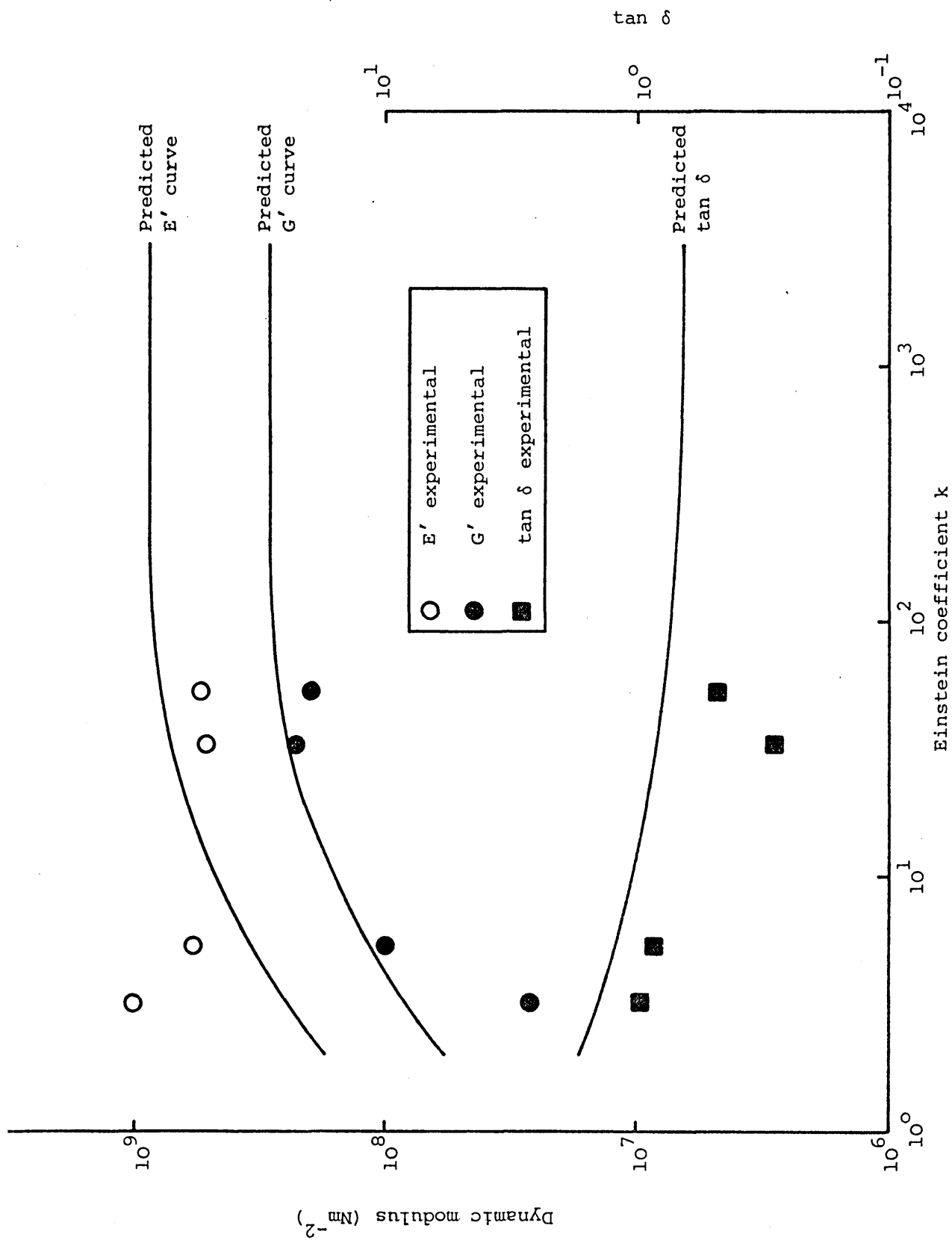


Figure 7.8 Predicted  $E'$ ,  $G'$ , and loss tangent curves at  $-90^\circ\text{C}$  compared with experimental values at that temperature (TR 1101).

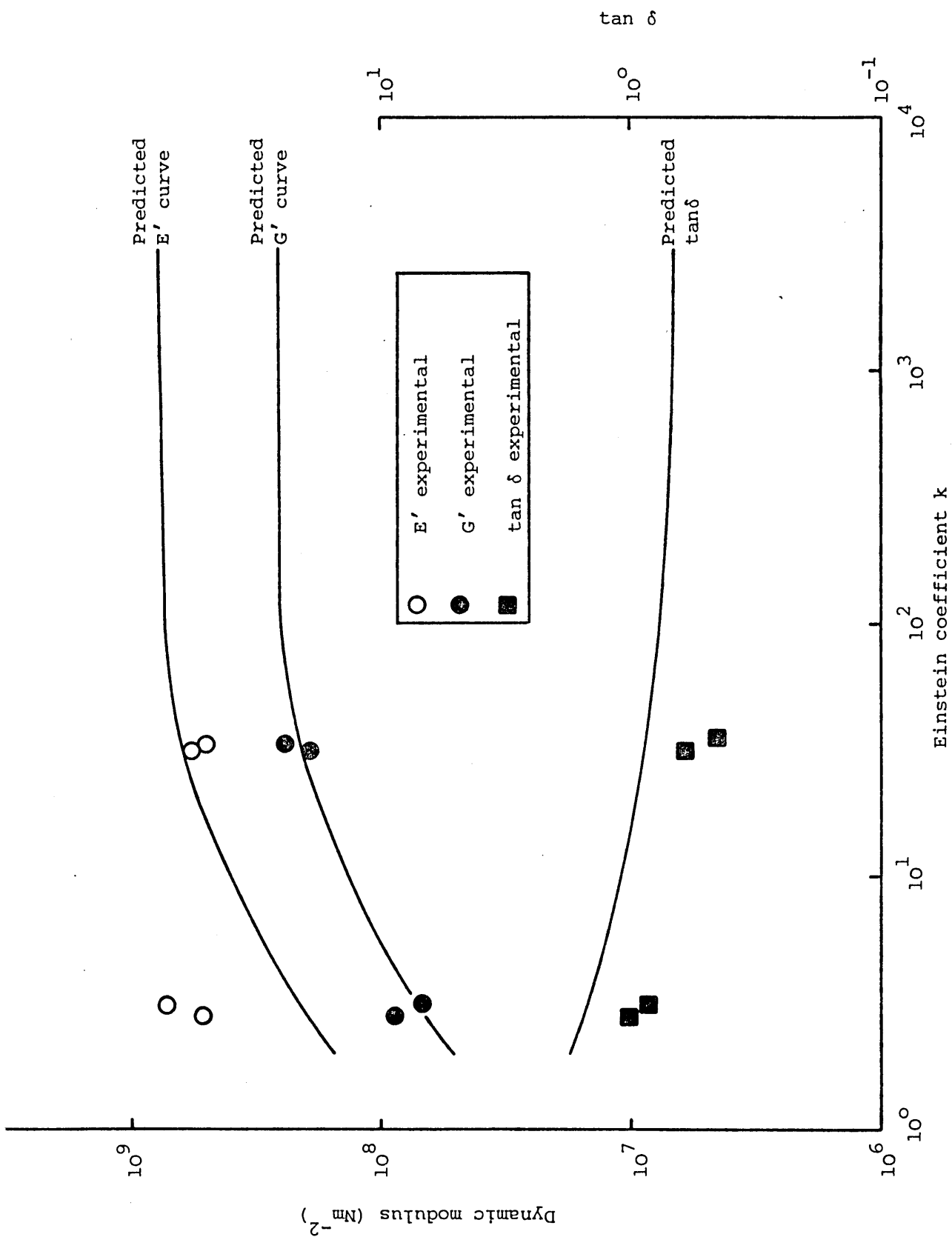


Figure 7.9 Predicted E', G', and loss tangent curves at -90°C compared with experimental values at that temperature (TR 1102).

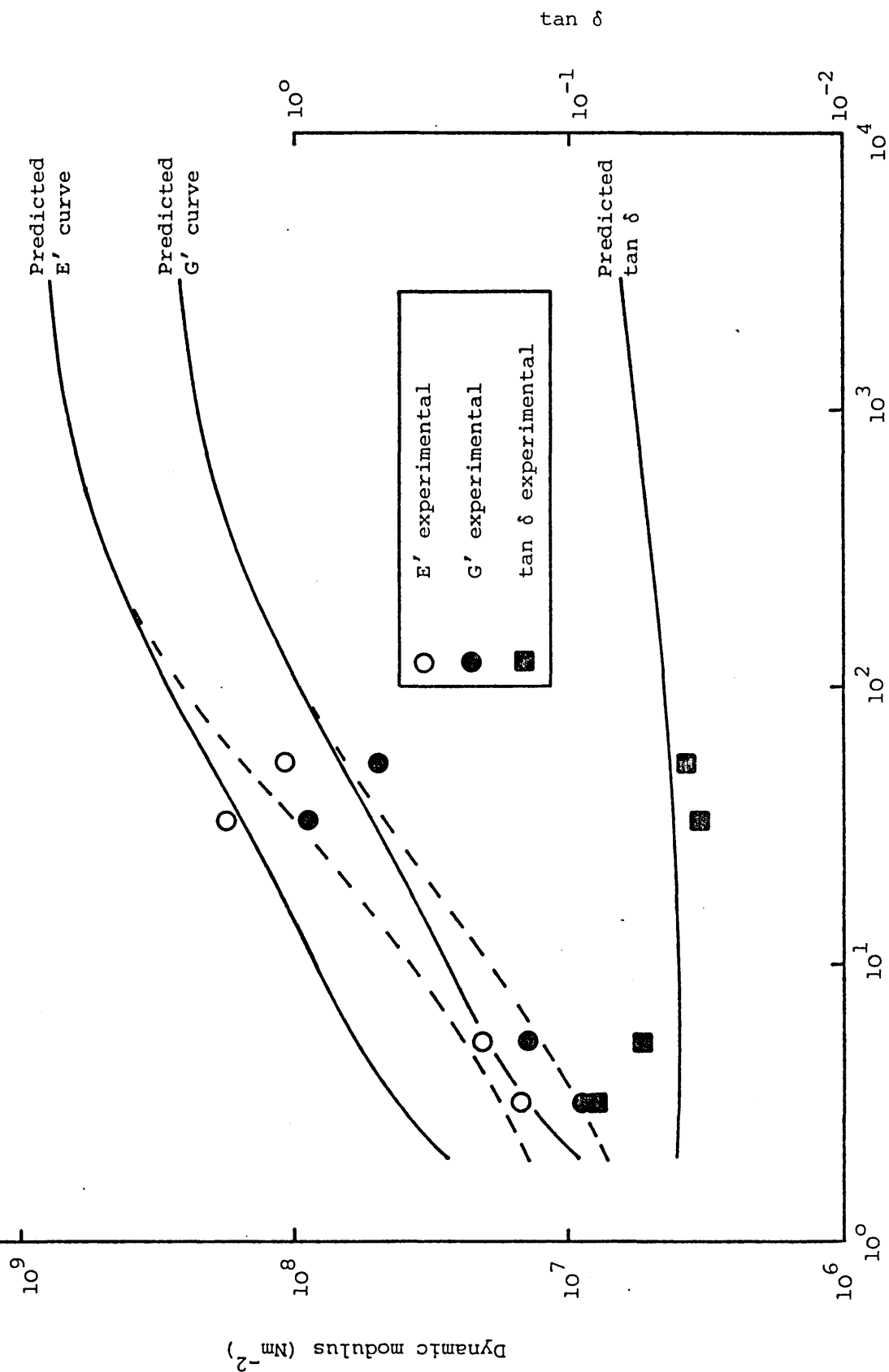


Figure 7.10 Predicted  $E'$ ,  $G'$ , and loss tangent curves at  $+20^\circ\text{C}$  compared with experimental values at that temperature (TR1101).

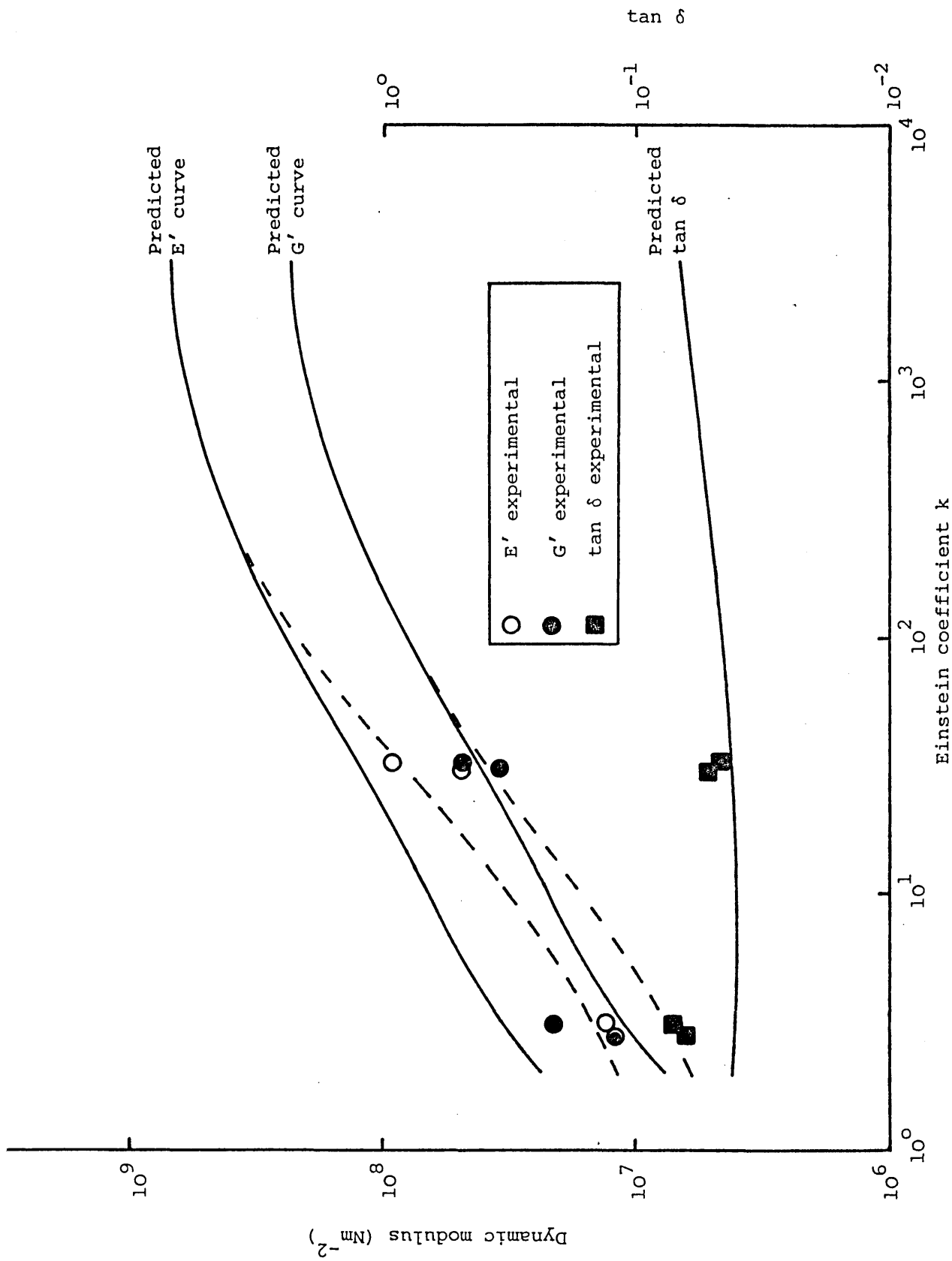


Figure 7.11 Predicted  $E'$ ,  $G'$ , and loss tangent curves at  $+20^\circ\text{C}$  compared with experimental values at that temperature (TR1102).

8.1 THE CLASSICAL ANALYSIS AND RELATED EXPERIMENTATION8.1.1 Introduction

In section 2.4, much of the background work relevant to the tearing of rubbery materials has been reviewed. For flat sheet test specimen, a tearing energy or strength,  $T$ , has been defined that is independent of the geometry of the specimen, provided the stored energy density of the specimen can be measured. The relation for the tearing energy of the "trouser" tear specimen is:

$$T_c = 2\lambda F t^{-1} - 2b W \quad (8.1)$$

where  $T_c$  = tear strength

$\lambda$  = extension ratio in the legs of the testpiece

$F$  = force applied to testpiece ends

$2b$  = total width of specimen

$t$  = thickness of material

$W$  = strain density in legs of specimen

For some rubbers, provided  $2b$  is large enough, elongation of the legs is essentially zero ( $\lambda \approx 1$ ); it follows that  $W$  reduces to zero, and that:

$$T_c = \frac{2F}{t} \quad (8.2)$$

Many published reports by NRPA workers imply that for the materials they have worked on, equation (8.2) may be used satisfactorily for routine tear measurements. However, preliminary tear tests on S-B-S copolymers indicated that two serious problems existed:

- (a) Leg extension was often appreciable ( $\lambda \neq 1$ ), even when  $2b$ , the specimen width, was large.
- (b) At some point knotty tearing developed, the tear growing laterally through one leg of the specimen.

Leg extension could be allowed for if the strain energy density,  $W$ , was known, but a separate stress-strain curve would be required. If



one leg of the specimen was torn through, further testing would be precluded with that testpiece, and in any case development of equations (8.1) and (8.2) is based on tear propagation down the central axis of the specimen. It was also intended in this present work to measure a quantity which might be taken as the intrinsic tear strength, a material property, not some value arbitrarily increased by tear tip deviation. A study of the tearing behaviour of various vulcanizates (Gent & Henry [173]) shows that when tear tip deviations are restricted, knotty tearing does not develop, and consequently the recorded loads, and hence  $T_c$ , were much reduced.

Since leg extension and knotty tearing behaviour mitigated against any rapid and meaningful routine measurement of this intrinsic tear strength with the simple trousers testpiece, it was decided to modify the trousers specimen to avoid these two specific problems.

#### 8.1.2 The Modified Trousers Tear Specimen

An obvious method of ensuring that the tear develops down the centre of the specimen and to limit extension is to reinforce the legs to prevent their elongation, and to provide a path of least resistance for tear propagation. Gent & Henry [173] adhered shim steel to the legs of the specimen, whilst Veith [172] formed specimen with a reduced section along the centre-line and reinforced the legs with fabric moulded into the material.

In this work, it was decided to simply reduce the tearing thickness along the specimen centre-line. This was achieved using the flat cast sheet (section 4.2) and the jig shown in Figure 8.1, a sharp scalpel blade cutting the specimen to a uniform depth. The jig consisted of a mild steel base with dowels to locate the centrally slotted upper mild steel plate. The specimen, cut to overall size and placed in position on the base could be cut to any required depth, using a scalpel, by interposing the appropriate number of shim steel spacers between the specimen and the upper plate. The slot in the upper plate being just wide enough to allow the insertion of the scalpel blade with its handle acting as a stop. The reduction in thickness of the material constrained the tear along the specimen centre-line and is in keeping with many other instances in the fracture field where it has been found necessary to use control grooves to promote crack propagation in a particular direction. For example, double cantilever and double torsion specimens [219,220]. The strain in the legs of the specimen was reduced to negligible proportions, and it was possible to take measurements of the tearing force at several different strain rates on the same specimen.

### 8.1.3 Environmental Chamber and Temperature Control Equipment

In order to carry out tear tests at temperatures other than ambient, an environmental chamber was constructed, shown in Figure 8.2; it consisted of a cubic framework of 1" x 1" steel box section. The walls of the chamber were lined with an insulating sandwich of inner 1" thick fibre glass/hard board/outer 1" thick polystyrene foam. A hinged door with double glazed window being incorporated in the front face, and the rear wall supported an electric fan. The box structure was rigidly attached to the floor model Instron by means of a cradle slung from the upper crosshead.

The chamber was used in conjunction with an Ellen spray system and low temperature control unit supplied by the British Oxygen Company Limited. This consisted of a temperature sensing platinum resistance thermometer, related switching equipment, liquid nitrogen pump and dewar, and lengths of spray tube which were plumbed into the cabinet. The Instron and ancillary equipment are shown in Figure 8.3.

Above ambient temperatures were achieved using a continuously blowing industrial hair dryer unit inserted into the rear of the chamber. Temperature was sensed using a thermocouple; related equipment varied the current in the hair dryer coils in order to achieve and maintain a set temperature. Both heating and cooling had relatively inaccurate temperature setting dials; it was therefore necessary to incorporate a separate temperature measuring device. A copper/constantan thermocouple with one junction at 0°C, the other fitted inside the chamber in close proximity to the test specimen, and a digital voltmeter (DVM) were included in the rig.

The true temperature inside the cabinet, a measure of which was displayed on the DVM, could be altered rapidly to any required temperature in the range -100°C to +100°C. Below ambient temperatures being controlled to within  $\pm 1^\circ\text{C}$ ; above ambient control was better than  $\pm 0.5^\circ\text{C}$ , the temperature variation along a tear specimen being no more than  $2^\circ\text{C}$ .

### 8.1.4 The Testing Programme

The polymers used in this study were Cariflex TR1101, TR1102, TR4113 and TR4122 supplied by the Shell Chemical Company UK Limited. To determine the performance of these materials when subjected to the tear test, an extensive programme was conducted.

Each polymer was cast from three solvent systems into flat

sheet form of some 1 mm thickness (see section 4.2). Specimens for tear testing were cut from these sheets using a sharp scalpel, together with a template. The centre-line thickness was reduced as outlined previously (section 8.2). The precise dimensions of the specimens are shown in Figure 8.4.

Four crosshead speeds were used (50, 10, 0.5 and 0.1 cm/min) for testing at temperatures between  $-80^{\circ}\text{C}$  and  $+80^{\circ}\text{C}$  with  $20^{\circ}\text{C}$  increments.

#### 8.1.5 Test Procedure

The legs of the specimen were formed by making a cut of 6 cm down the centre-line of the specimen, the final cut being made with a sharp razor blade. The legs of the specimen were attached to the upper and lower crossheads of the Instron testing machine as shown in Figure 8.5. The remainder of the specimen was torn at a selected rate and temperature.

The thickness of the torn rubber was measured by examining the fracture surface under a travelling microscope, and averaging a number of readings over the length of a test run.

Two distinct types of tear curves (tearing load as a function of time) were obtained, dependent upon testing speed and temperature. Typical examples of these curves are shown in Figure 8.6. Curve (a) was produced by smooth tearing at a jaw separation rate of 0.1 cm/min, the tear load fluctuating only slightly and the rate of tear propagation being essentially constant and roughly equal to one-half the rate of jaw separation. Curve (b) was obtained at a jaw separation rate of 50 cm/min and is typical of stick-slip knotty tearing, consisting of a series of peak loads, each corresponding to a catastrophic tear. In this case, the mechanism consists of a build-up of strain energy in the tearing zone as the load is applied; a critical load is exceeded at some point and catastrophic rupture occurs. The rate of tear propagation after this rupture is rapid and the tear continues to advance until the high strain gradient is removed; the rate then drops to zero. The jaws continue to separate, however, and the process repeats several times during a test, resulting in a saw-tooth load-time curve.

For the purposes of analysis, the tear strength is defined here by equation (8.2), where  $F$  is the median peak load value. The median peak load is selected because it is relatively easy to obtain and identify, and also it gives no undue weight to excessively high peak loads (Veith [172]). For tear curves with an even number of peaks, the median is assumed to be the average of the two middle peaks. When the tear curve is smooth, the

general level of the tearing load can usually be established without difficulty.

#### 8.1.6 Testing the Tear Criterion

According to the theory of Rivlin and co-workers referred to earlier, a linear relationship should exist between the tearing force and the torn thickness of the trouser leg specimen. In order to demonstrate that this is true for thermoplastic elastomers, a number of specimens varying in thickness were tested. TR1101 cast from  $\text{CCl}_4$  was selected as the test material and the experiments were carried out at  $+20^\circ\text{C}$ . The results of this series of tests are shown in Figure 8.7, and, as predicted within the bounds of the specimen thicknesses tested, the linear correlation is a reasonable one.

#### 8.1.7 Tearing Energy/Rate/Temperature Surfaces

A common method of presentation for tearing data [169], when both temperature and rate are varied, is to construct graphs such as those drawn in Figures 8.8 to 8.10. Here, TR1101 cast from several solvent systems is the material presented.  $\log T_c$  is plotted as a function of temperature and  $\log R$ , the jaw separation rate. This type of plot generates surfaces which give a good general indication of the effects of the two variables on tearing energy. Similarly plotted surfaces for all the other materials and solvent systems are contained in Appendix A.

Although these plots are not easily used for either detailed analysis or comparison of material behaviour, the immediate visual effect cannot be equalled by the usual two-dimensional graphs which could not contain a comparable degree of detail without becoming incomprehensible.

At high temperatures and low tearing rates, the tear strength is at its lowest level in all cases, although the effect is less marked in TR1101 than it is with TR1102 and the plasticised materials TR4122 and TR4113. At these temperatures and higher rates, tear strength increases rapidly to approach what appears to be a maximum at the fastest rate. As the temperature decreases,  $T_c$  increases rapidly at the lower rates until  $+40^\circ\text{C}$  ( $+60^\circ\text{C}$  in the case of TR1101), at which point a maximum frequently occurs. At this stage, as the temperature increases further, although  $T_c$  continues to increase gradually, a plateau region tends to form covering the whole rate spectrum. The occasional hump does deform the general pattern at this stage, but can probably be attributed to experimental error.

In some cases, for example, TR4122 cast from THF/MEK and TR4113 cast from  $\text{CCl}_4$ , the plateau region extends as far as the lowest test temperature of  $-80^\circ\text{C}$ . In other samples, there is a roll-off at temperatures below  $-60^\circ\text{C}$  (TR1102 cast from THF/MEK and BEN/HEP). However, the sample of TR4113 cast from BEN/HEP shows a rapid rise in tear strength between  $-60^\circ\text{C}$  and  $-80^\circ\text{C}$ .

#### 8.1.8 Detailed Analysis of Tear Data

In order to carry out a more detailed investigation of the tearing data, it was necessary to draw conventional two-dimensional graphs of tearing energy,  $T_c$ , as a function of temperature and rate. Examples of these relationships for TR1101 are plotted in Figures 8.11 to 8.17. Similar graphs for the other materials and comparisons between TR1101 and TR1102 are presented in Appendices B and C.

#### 8.1.9 The Effect of Temperature and Rate

In Figures 8.11 to 8.13, tearing energy is plotted as a function of rate for TR1101 at each test temperature, and separately for each solvent system. Although at first sight these graphs are perhaps a little intimidating, careful examination does reveal both the temperature and rate dependence of the tearing energy for the material/solvent system.

For TR1101 cast from THF/MEK (Figure 8.11), the catastrophic fall in tear strength can be seen at  $+80^\circ\text{C}$ , being particularly noticeable at the lower rates. At  $+60^\circ\text{C}$ , tear strength has increased across the whole rate spectrum, and almost identical data are achieved at  $+40^\circ\text{C}$ . Data at  $+20^\circ\text{C}$  show a further slight increase, but at lower temperatures the tear energy increases more rapidly through  $0^\circ\text{C}$ ,  $-20^\circ\text{C}$ , peaking at  $-40^\circ\text{C}$ , then falling quickly to approximate  $+20^\circ\text{C}$  data at  $-80^\circ\text{C}$ . A feature of all the data for TR1101 cast from THF/MEK is that at the lowest and highest rates, the tear energy tends to fall when compared with the mid-rate values, except at  $-80^\circ\text{C}$  where a constant value of tear strength occurs at all rates.

When the casting solvent is  $\text{CCl}_4$ , a similar pattern emerges, except that a large peak occurs at  $+60^\circ\text{C}$  and a crosshead rate of  $10^{-4}$  m/s. Most of the data has a tendency to fall off at high and low rates, and again a peak occurs at  $-40^\circ\text{C}$  after which, as the temperature is lowered, the tear energy decreases, but not as rapidly as when THF/MEK was the casting solvent. The effect of using  $\text{CCl}_4$  as casting solvent is to lower

quite appreciably the tear energy over the whole temperature and rate range.

Turning to the BEN/HEP cast material at +80°C, the level of tear energy at the high rates is almost identical to the THF/MEK cast samples, but the decrease in tear energy at the lower rates is not as rapid. Tear energy increases with decreasing temperature but instead of peaking at -40°C, it levels off through -60°C to -80°C. The level of the tearing energy is higher than for CCl<sub>4</sub> cast samples at +40°C and +20°C, but lower at 0°C and -20°C, and again higher at -60°C and -80°C.

In Appendix B is shown similar data for TR1102. For all solvent systems, the +80°C data is lower than for TR1101, but again BEN/HEP proves to have the greatest resistance to tearing at this temperature. A feature of the TR1102 samples is that the fall off in tear strength at lower rates is still noticeable in the +60°C data, and at this temperature none of the solvents has a distinct advantage. At +40°C, THF/MEK and CCl<sub>4</sub> cast materials have approximately the same tear strength, but BEN/HEP is inferior. A similar situation exists at +20°C and 0°C, but at -20°C it is CCl<sub>4</sub> which gives the lowest value, and at -40°C THF/MEK is higher than both CCl<sub>4</sub> and BEN/HEP which are at about the same level. A peak occurs in THF/MEK and BEN/HEP at -60°C, but in CCl<sub>4</sub> it is at a temperature between -40°C and -60°C. The level of the -80°C data is approximately the same for all casting solvent systems.

Also shown in Appendix B are the tearing energy/rate graphs for TR4122 and TR4113. These show that at a high temperature, TR4122 is superior to TR4113, but as the temperature decreases the tear strength of TR4113 increases to become more or less equivalent to the TR4122 material, temperature for temperature.

Decrease in tear strength at the highest rate is not as noticeable with these plasticised materials as it was with TR1101 and TR1102, although at the low rate tear strength is normally inferior to the higher rates.

Tear strength in TR4113 increases down to the lowest test temperature with all casting solvent systems, whereas with TR4122 this only occurs with the THF/MEK cast material.

#### 8.1.10 The Effect of Casting Solvent

In order to ascertain whether the casting solvent had any systematic effect on tear strength, plots were drawn of tearing energy as

a function of crosshead rate at each individual temperature. These graphs are shown in Figures 8.14 to 8.17 for TR1101 and for TR1102 in Appendix C.

Considering TR1101 in Figures 8.14 to 8.17, at  $-80^{\circ}\text{C}$  it is reasonable to suggest that there is no solvent effect of any consequence. At  $-60^{\circ}\text{C}$ , an effect is, however, noticed with the order being  $\text{THF/MEK} > \text{BEN/HEP} > \text{CCl}_4$ . At  $-40^{\circ}\text{C}$ , THF/MEK is still the strongest material, but BEN/HEP is now more or less equivalent to  $\text{CCl}_4$ . Moving to  $0^{\circ}\text{C}$ , again THF/MEK is the stronger of the three, but now  $\text{CCl}_4$  is stronger than BEN/HEP cast material. At  $+20^{\circ}\text{C}$ , the positions of BEN/HEP and  $\text{CCl}_4$  are again reversed with BEN/HEP being the stronger; the same is true at  $+40^{\circ}\text{C}$ , but another reversal has occurred at  $+60^{\circ}\text{C}$ , and at  $+80^{\circ}\text{C}$  the order is  $\text{BEN/HEP} > \text{THF/MEK} > \text{CCl}_4$ , although at this temperature all materials are fairly weak.

For TR1102 (Appendix C), again at  $+80^{\circ}\text{C}$ , there is virtually no solvent effect, but at  $-60^{\circ}\text{C}$  a large effect is noticed with  $\text{THF/MEK} > \text{BEN/HEP} > \text{CCl}_4$ . The situation is similar at  $-40^{\circ}\text{C}$ , but the differences are not as marked. At  $0^{\circ}\text{C}$ , THF/MEK still produces the strongest material, but the positions of BEN/HEP and  $\text{CCl}_4$  are reversed; the same is true at  $+20^{\circ}\text{C}$  and  $+40^{\circ}\text{C}$ .  $+60^{\circ}\text{C}$  and  $+80^{\circ}\text{C}$  give data which are a little inconclusive since at  $+60^{\circ}\text{C}$  THF/MEK is marginally the stronger material and BEN/HEP and  $\text{CCl}_4$  about equivalent, but at  $+80^{\circ}\text{C}$  THF/MEK is the weakest material, with BEN/HEP the strongest.

The effect of casting solvent on tear strength is better presented in tabular form and this is shown in Table 8.1 for all the materials used in this study.

Although it was noted that in TR1101 and TR1102, THF/MEK casting invariably produced materials more resistant to tearing than other solvent systems, this was not the case for TR4122 and TR4113. As shown in Table 8.1, casting TR4122 from  $\text{CCl}_4$  gives the strongest material at high and low temperatures, whereas at and around room temperature BEN/HEP casting gives the highest values. THF/MEK tends to produce the weakest material over the whole temperature range, except at  $-40^{\circ}\text{C}$ , where rather anomalously it gives the highest value.

For TR4113 at all temperatures above and including  $0^{\circ}\text{C}$ , THF/MEK produces the strongest material; this also occurs at  $-60^{\circ}\text{C}$ . However,  $\text{CCl}_4$  casting gives the strongest material at  $-20^{\circ}\text{C}$  and  $-40^{\circ}\text{C}$ , and BEN/HEP cast materials are the stronger at  $-80^{\circ}\text{C}$ . At  $-80^{\circ}\text{C}$  and all temperatures above  $0^{\circ}\text{C}$ , except  $+80^{\circ}\text{C}$ ,  $\text{CCl}_4$  gives the weakest material.

TABLE 8.1

Summary of the Effect of Casting Solvent on Tear Strength

Temperature (°C)	TR1101	TR1102
-80	THF/MEK = BEN/HEP = $CCl_4$	THF/MEK = BEN/HEP = $CCl_4$
-60	THF/MEK > BEN/HEP > $CCl_4$	THF/MEK > BEN/HEP > $CCl_4$
-40	THF/MEK > BEN/HEP = $CCl_4$	THF/MEK > BEN/HEP > $CCl_4$
-20	THF/MEK > $CCl_4$ > BEN/HEP	THF/MEK = BEN/HEP > $CCl_4$
0	THF/MEK > $CCl_4$ > BEN/HEP	THF/MEK > $CCl_4$ > BEN/HEP
+20	THF/MEK > BEN/HEP > $CCl_4$	THF/MEK > $CCl_4$ > BEN/HEP
+40	THF/MEK > BEN/HEP > $CCl_4$	THF/MEK > $CCl_4$ > BEN/HEP
+60	THF/MEK > $CCl_4$ > BEN/HEP	THF/MEK > BEN/HEP > $CCl_4$
+80	BEN/HEP > THF/MEK > $CCl_4$	BEN/HEP > $CCl_4$ > THF/MEK
Temperature (°C)	TR4122	TR4113
-80	$CCl_4$ > BEN/HEP > THF/MEK	BEN/HEP = THF/MEK = $CCl_4$
-60	$CCl_4$ > BEN/HEP > THF/MEK	THF/MEK = $CCl_4$ > BEN/HEP
-40	THF/MEK = BEN/HEP > $CCl_4$	$CCl_4$ > THF/MEK > BEN/HEP
-20	BEN/HEP > THF/MEK > $CCl_4$	$CCl_4$ > THF/MEK > BEN/HEP
0	BEN/HEP > $CCl_4$ > THF/MEK	THF/MEK > BEN/HEP > $CCl_4$
+20	BEN/HEP > $CCl_4$ > THF/MEK	THF/MEK = BEN/HEP > $CCl_4$
+40	BEN/HEP > $CCl_4$ > THF/MEK	THF/MEK = BEN/HEP > $CCl_4$
+60	$CCl_4$ > BEN/HEP > THF/MEK	THF/MEK = BEN/HEP = $CCl_4$
+80	$CCl_4$ > THF/MEK > BEN/HEP	THF/MEK = $CCl_4$ > BEN/HEP

8.1.11 Comparing TR1101 and TR1102

Further plots which are of some interest are those which compare directly the materials TR1101 and TR1102 when cast from different solvents. Graphs of tearing energy as a function of rate to demonstrate any differences between the two materials when cast from THF/MEK are shown in Figures 8.18 to 8.21. Graphs for other solvent systems are in Appendix D. For each casting solvent, the effect is found to be remarkably similar. At -80°C, -60°C and -40°C, TR1102 has a higher tearing energy; conversely, at +40°C, +60°C and +80°C, TR1101 is the stronger material. Tests at the intermediate temperatures (-20°C, 0°C and +20°C) reveal that on the whole neither material has any distinct advantage.



### 8.1.12 A Comparison of the Tear Behaviour of Thermoplastic Elastomers with Other Rubbery Materials

Since a large amount of tear data on natural rubber and both filled and unfilled synthetic vulcanizates is available in published work by researchers at NRPPA, it is useful to carry out a comparison of the performance of these materials with the thermoplastic elastomers used in the present study.

In Figures 8.22 to 8.24 are data at three temperatures for TR1101 and TR1102, both cast from  $\text{CCl}_4$ ; these materials are compared with natural rubber [159], unfilled GRS Polysar, a synthetic SBR [159], and the same GRS filled with HAF carbon black reinforcement [160]. Unfortunately, no data is available for the NRPPA work at temperatures below  $-20^\circ\text{C}$ , so that the range of tests available for comparison does not cover the region in which thermoplastic rubbers have their highest tear energy. The temperatures used for comparison purposes are  $-20^\circ\text{C}$ ,  $0^\circ\text{C}$  and  $+80^\circ\text{C}$ .

At  $-20^\circ\text{C}$  in Figure 8.22, the thermoplastic elastomers compare favourably with the other materials throughout the entire rate range studied; at this temperature, the tear strength of natural rubber suffers a precipitous decline at intermediate rates, but at the extremes of the rate range has a strength similar to that of the thermoplastic elastomers. Unfilled GRS is weak at low rates but increases in strength through the range to become almost equivalent to TR1102 at the highest rate; conversely, filled GRS has a high strength at low rates which falls off at the high rates to approximate that of the thermoplastic materials.

The situation at  $0^\circ\text{C}$  in Figure 8.23 is rather different. The strengths of the triblocks at this temperature are similar to those at  $-20^\circ\text{C}$ , but here natural rubber has an identical tear strength throughout the rate range. Unfilled GRS is weaker in tearing than at  $-20^\circ\text{C}$  throughout the range, and although at the highest rates the filled material has the same strength as natural rubber and the triblocks, at low rates it is rather weak.

At the maximum test temperature (Figure 8.24), the thermoplastic elastomers suffer from softening of the polystyrene domains and both materials show little resistance to tearing, particularly at low rates; TR1101 is the stronger of the two materials at this temperature. At  $+80^\circ\text{C}$ , unfilled GRS is extremely weak but filled GRS and natural rubber remain strong in tearing.

To sum up, filled GRS has a high tear strength at all the temperatures considered here, whereas the unfilled material is invariably

the weakest, except at  $-20^{\circ}\text{C}$  where natural rubber appears to lose its strain crystallising properties over the intermediate rate range. At higher temperatures, natural rubber proves to be a material with a high tear resistance equivalent to that of the thermoplastic elastomers which suffer from a decline in tear strength at about  $+60^{\circ}\text{C}$ . However, even at  $+80^{\circ}\text{C}$ , the triblocks perform as well as unfilled GRS at  $0^{\circ}\text{C}$ .

A point which should be emphasised at this stage is that the tearing experiments of this work are likely to produce a value for the tear energy which is near to the intrinsic tear strength of the material. Since the effects of tear tip deviation have been suppressed by the use of a reduction in the thickness of the specimen along the line of the tear, and that the effect of this suppression must be to lower the measured tear strength, since tip deviation and notch blunting would increase tear strength. It follows that comparisons with data on other materials where this suppression has not been used are a little unfair; even so, SBS block copolymers do come out of the comparison quite favourably.

#### 8.1.13 Discussion

Analysis of the tearing behaviour of the block copolymer elastomers studied in this work has been carried out in two distinct sections. In this first part, deference has been paid to the classical analysis developed by researchers at NRPPRA who specialised in the tear testing of a variety of gums and vulcanised rubber materials. Results here have been presented in terms of the tear strength,  $T$ , as a function of temperature and tearing rate in order to generate tear energy surfaces (Figures 8.8 to 8.10 and Appendix A ).

The initial impressions created from a study of these graphs were that:

- (a) Tear energy gradually decreases as the test temperature increases, with a rapid decrease in tear strength above  $+40^{\circ}\text{C}$  to  $+60^{\circ}\text{C}$ .
- (b) The effect of jaw separation rate is not all that great, except at high temperatures when tearing energy decreases rapidly at low rates. There is, however, a tendency for tear strength to decrease at the highest and lowest rates at other test temperatures.
- (c) The effect of casting solvent appeared marginal with no marked trends, except at the higher temperatures.

Although these tearing energy surfaces are a good means of presenting a large amount of information in a minimum of space, they do not allow the extraction of accurate comparisons. Several other graphs were therefore necessary to convey the detailed information required.

Plots of tearing energy as a function of jaw separation rate were made to show the effects of temperature and casting solvent (Figures 8.11 to 8.17 and Appendices B and C) and to compare in detail TR1101 and TR1102 (Appendix D). Over the range of temperatures and rates studied, the effects of changing material, casting solvent system and tearing rate were not in fact as large as expected, considering the different microstructures involved and also the fact that two of the materials were plasticised.

One consistent trend noted with TR1101 and TR1102 was that THF/MEK casting invariably produced a stronger material than the other two solvent systems. However, this was not found to be the case for the plasticised materials TR4122 and TR4113.

Attempts to correlate tear strength with the damping parameter  $\tan \delta$  were unsuccessful, but a fair degree of success was achieved when tear strength was plotted as a function of dynamic modulus,  $E'$ , as shown in Figures 8.25 to 8.27. Figure 8.25 shows the relationship for materials which had no sharp yield point in their stress-strain curve (see Chapter 6), and for each material a sensibly linear relationship is obtained. The same is shown to be true for materials which did display sharp yield points in their stress-strain curves (Figures 8.26 and 8.27); these were materials cast from THF/MEK and all the TR4122 cast samples. (TR4122 cast from THF/MEK did not, in fact, have a sharp yield point in its stress-strain curve, but its initial modulus was high, of the order of the TR1101 and TR1102 series polymers.)

The slope of this linear relationship between tear strength and modulus varies depending upon the material, but also depending upon the solvent used for casting; this in turn determines the microstructure of the material. All of the polymers of Figure 8.25 showed no sharp yield point and had a microstructure which consisted of polystyrene rods in a butadiene matrix. The data plotted in Figures 8.26 and 8.27 is for microstructures containing a lamellar component (the microstructure for TR1102 cast from THF/MEK was actually designated as styrene rods in a butadiene matrix, but although rods were observed on the micrographs, this material/solvent combination may be a borderline case between the two microstructures).

It appears then that a relationship exists between some

tearing parameter and the tensile properties of these materials. This relationship is explored further in the second part of this chapter.

## 8.2 AN ALTERNATIVE CORRELATION

### 8.2.1 Introduction

Analysis of the tearing behaviour of elastomers used in this study has so far followed the classical approach proposed by workers at NRPRA, whose analysis depends upon a linear relationship between the tearing force and material thickness. It is, however, of considerable interest to note that other workers [221,222] have demonstrated for a wide range of thin materials, both metallic and polymeric, that the tearing force is proportional to the square of material thickness. Furthermore, they go on to propose that the tearing force is also related to the modulus of elasticity and the energy to break in simple tension. The NRPRA workers linked the tear strength of vulcanised rubbers to the energy to break, hysteresis and damping properties [158,162,165,169,230]. Earlier in this chapter, it was shown that for the materials of the present study, some relationship exists between tearing properties and tensile behaviour.

In the light of the available evidence and since the materials dealt with here are a new generation of elastomers with a very different chemical background to the vulcanised rubbers investigated previously, it was decided to see how well tearing properties related to tensile properties for the block copolymers of this work, using the approach suggested by Isherwood & Williams [222].

### 8.2.2 Theoretical

An early investigation [223] into the fracture behaviour of materials subject to the notched tension test led to the following relationship between fracture toughness,  $G_c$ , and tensile properties:

$$G_c = W_p^* \cdot l \quad (8.3)$$

where  $W_p^*$  is the area under the tensile stress-strain curve, and  $l$  is the width of the plastic zone developed at the crack tip. It was also found that the plastic zone width was very nearly equal to the sheet thickness,  $t$ ; using this equivalence gave good agreement for a wide range of materials. It has also been shown [221] that the same form of thickness-controlled plastic zone width is exhibited in tearing test specimens of PVC.

Taking the failure load,  $P$ , crack length,  $2c$ , and sheet width,  $w$ , in a wide sheet, Isherwood & Williams [222] were able to express equation (8.3) as:

$$P^2 = \frac{E W^* t^3 w^2}{p c} \quad (8.4)$$

where  $E$  is the tensile modulus of elasticity.

Examination of equation (8.4) to determine to what extent it could be used to describe the tearing mode of failure leads to the conclusion that the tearing force is proportional to the modulus of elasticity, the energy to failure in simple tension and a function of specimen thickness. Since it is known that the tearing force is independent of specimen width and crack length, the introduction of a constant,  $m_l$ , having dimensions of length, gives:

$$F^2 = E \frac{W^*}{p} t^3 m_l \quad (8.5)$$

where  $F$  is the tearing force. However, by geometrical considerations,  $m_l$  must be proportional to thickness, since no other length term has any effect, so that:

$$F^2 \propto E \frac{W^*}{p} t^4$$

or:

$$F \propto \left( E \frac{W^*}{p} \right)^{\frac{1}{2}} t^2 \quad (8.6)$$

This expression relating tearing force to tensile modulus, energy to break and specimen thickness was also arrived at by consideration of a model for tearing [221] which was developed from a model initially used to describe the fracture of notched sheet tensile specimens.

### 8.2.3 Energy Density at Break, $\frac{W^*}{p}$

The energy density at break in simple tension for all the materials cast from different solvents was determined at +20°C from the areas under the stress-strain curves, the data for which are presented in Table 8.2. Since data are required for the full temperature range of the tear tests, it was necessary to extrapolate to high and low temperature, as shown in Figure 8.28 for TR1101, assuming zero energy density to break at +100°C. From the evidence of Goh [224], this appears to be a reasonable extrapolation. The values of energy density at particular temperatures obtained from these graphs for each material are given in Table 8.2.

TABLE 8.2  
Energy Density  $\frac{W}{p}$  \* (MN/m<sup>2</sup>) at Different Temperatures

Material and Solvent	Temperature (°C)								
	-80	-60	-40	-20	0	+20	+40	+60	+80
TR1101 Ethyl Acetate	146.5	130.4	114.0	97.9	81.5	66.3	49.0	32.6	16.4
TR1101 THF/MEK	131.5	117.0	102.4	87.8	73.0	58.6	43.8	29.0	14.4
TR1101 BEN/HEP	137.6	122.5	107.1	92.0	76.7	61.0	46.0	30.8	15.4
TR1101 CCl <sub>4</sub>	136.0	120.9	105.8	90.7	75.6	60.7	45.3	30.2	15.0
TR1102 Ethyl Acetate	177.9	158.0	138.4	118.5	98.8	79.3	59.2	39.4	19.6
TR1102 THF/MEK	159.4	141.8	124.0	106.4	88.6	71.0	53.2	35.4	17.5
TR1102 BEN/HEP	162.3	144.5	126.5	108.4	90.4	72.1	54.3	36.0	18.0
TR1102 CCl <sub>4</sub>	151.8	135.0	118.1	101.2	84.4	67.7	50.6	33.8	16.9
TR4122 THF/MEK	94.2	83.7	73.3	62.8	52.3	41.8	31.3	20.8	10.3
TR4122 BEN/HEP	115.2	102.3	89.5	76.7	63.8	51.2	38.2	25.4	12.6
TR4122 CCl <sub>4</sub>	115.2	102.3	89.5	76.7	63.8	51.2	38.2	25.4	12.6
TR4113 THF/MEK	65.9	58.5	51.2	43.9	36.6	29.3	22.0	14.7	7.3
TR4113 BEN/HEP	75.5	67.1	58.8	50.3	42.0	33.6	25.2	16.8	8.5
TR4113 CCl <sub>4</sub>	69.1	61.4	53.7	46.1	38.4	30.8	23.0	15.4	7.7

#### 8.2.4 Elasticity Modulus, $E$

In addition to energy density at break, the elasticity modulus is also required over the same temperature range. Since the relationship between modulus and temperature is by no means linear, the data available from simple tension tests at +20°C was of no real value. However, a tensile dynamic modulus was determined over the full temperature range for each material; the experimental details are discussed in Chapter 5, and the values of moduli obtained are presented in Table 8.3.

#### 8.2.5 The Relationship Between Tearing Force and Thickness

Evidence was presented earlier in Figure 8.7 which showed that

TABLE 8.3  
Dynamic Modulus  $E'$  ( $\text{N/m}^2 \times 10^8$ ) at Different Temperatures

Material and Solvent	Temperature ( $^{\circ}\text{C}$ )								
	-80	-60	-40	-20	0	+20	+40	+60	+80
TR1101 Ethyl Acetate	3.82	2.53	2.18	2.04	1.94	1.77	1.69	1.52	1.15
TR1101 THF/MEK	2.80	1.75	1.47	1.35	1.24	1.07	0.97	0.84	0.58
TR1101 BEN/HEP	3.20	0.36	0.27	0.24	0.22	0.21	0.19	0.17	0.13
TR1101 $\text{CCl}_4$	3.32	0.32	0.21	0.19	0.17	0.15	0.14	0.12	0.09
TR1102 Ethyl Acetate	3.32	1.55	1.25	1.12	1.03	0.92	0.83	0.67	0.37
TR1102 THF/MEK	3.03	0.89	0.71	0.63	0.57	0.49	0.46	0.34	0.16
TR1102 BEN/HEP	2.41	0.20	0.15	0.13	0.12	0.12	0.11	0.10	0.08
TR1102 $\text{CCl}_4$	4.71	0.26	0.17	0.15	0.14	0.13	0.12	0.10	0.07
TR4122 THF/MEK	5.28	2.69	1.79	1.53	1.24	0.93	0.81	0.66	0.40
TR4122 BEN/HEP	4.93	1.92	1.06	0.85	0.72	0.67	0.56	0.44	0.21
TR4122 $\text{CCl}_4$	4.81	1.07	0.69	0.58	0.52	0.46	0.44	0.33	0.13
TR4113 THF/MEK	6.49	0.25	0.07	0.05	0.05	0.04	0.04	0.04	0.03
TR4113 BEN/HEP	7.43	0.18	0.06	0.05	0.04	0.04	0.04	0.03	0.03
TR4113 $\text{CCl}_4$	5.67	0.20	0.06	0.05	0.04	0.04	0.04	0.03	0.03

for TR1101 cast from  $\text{CCl}_4$  and tested at  $+20^{\circ}\text{C}$ , the tearing force was proportional to the material thickness. This graph is now reproduced in Figure 8.29 but added to it is the tearing force as a function of  $t^2$ . There is in fact very little to choose between the two correlations so that these results are rather inconclusive. A limited number of examples are available of other materials and conditions which have a sufficiently wide variation in specimen thickness to draw sensible graphs of tearing force as a function of thickness and thickness squared. In these cases, a more convincing trend is noted. As shown in Figures 8.30 to 8.33 for a number of materials at a variety of test rates and temperatures, the dependence of tearing force,  $F$ , on  $t^2$  is consistently one of proportionality.



### 8.2.6 The Relationship Between Tearing Force and Tensile Data

Figures 8.34 to 8.37 show the tearing force,  $F$ , plotted as a function of  $(E W_p^*)^{\frac{1}{2}} t^2$  for TR1101. Similar graphs for the other materials are in Appendix E. Data for each jaw separation rate are plotted on different graphs, but each plot comprises the results for one material with each of its solvent derivatives over the whole temperature range of the tear tests. Some plots have more scatter than others, and it is reasonable comment to say that in the worst cases a fair degree of scatter exists; however, taken as a whole, and considering the wide variation in material properties over this temperature range, there is good evidence of a linear relationship between tearing force and tensile properties.

The histogram in Figure 8.38 summarises the quality of the relationship between tearing force and tensile data. Over 70% of the total number of tests carried out are within  $\pm 40\%$  of the predicted value.

Taking the results for a number of metallic and polymeric materials from reference [221] and plotting the log of tearing force as a function of  $\log (E W_p^*)^{\frac{1}{2}} t^2$ , gives the good correlation shown in Figure 8.39. The correlation holds over a very extensive range of material tensile properties. When averaged results at each strain rate for the thermoplastic elastomers are inserted, they correlate reasonably well with the remainder of the data. Also included in this figure are results for SBR and natural rubber (NR) taken from references [163,169,174,225-228]; these two materials also fit the relationship fairly well.

More detailed plots of  $\log F$  versus  $\log (E W_p^*)^{\frac{1}{2}} t^2$  are shown in Figures 8.40 to 8.43 for TR1101. Each graph shows the material with its solvent derivatives tested at a particular jaw separation rate. The correlation is seen to be quite good throughout the rate and temperature range used, and results for the other materials were very similar.

### 8.2.7 Discussion

Whilst the analysis proposed by the NRPRA workers predicts a linear relationship between tearing force and specimen thickness, and the data here have been analysed accordingly, an alternative approach suggests that for many materials the tearing force is in fact proportional to the thickness squared. Supporting evidence for this proposal has been found from tests on the materials of this study. In addition, this second theory for tearing suggests that tearing data are also related to the modulus of elasticity and the energy to break in simple tension. So that the relationship between tearing force and tensile data forms the basis of

the second section of this chapter.

Using values of energy density at break,  $W_p^*$ , determined in simple tension, and modulus values,  $E$ , from tensile mode dynamic experiments, tearing forces for all the materials and test conditions are shown to correlate linearly with  $(E W_p^*)^{\frac{1}{2}} t^2$  as predicted by the theory. A log/log plot used in order to embrace a wide range of material properties shows that SBS block polymers fit this relationship well when compared with a diverse selection of materials. It is noted that two other elastomers, SBR and NR, also fit this relationship, although the data for these materials were collected from a number of sources and may not be very reliable.

In conclusion, from the evidence presented here, it appears that a relationship does exist between tearing behaviour and tensile properties for SBS elastomers and that the classical theory for tearing behaviour may not be the most appropriate for this class of materials. As indeed it is not for a wide variety of other materials.

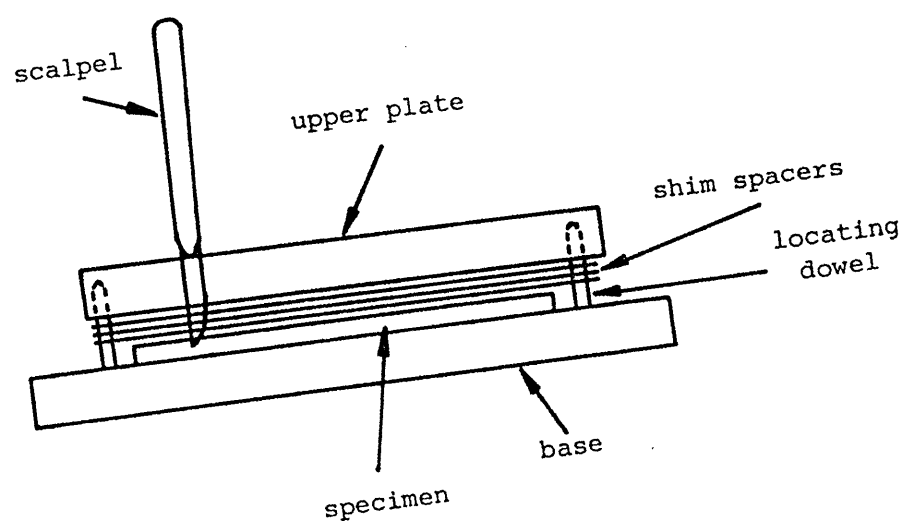
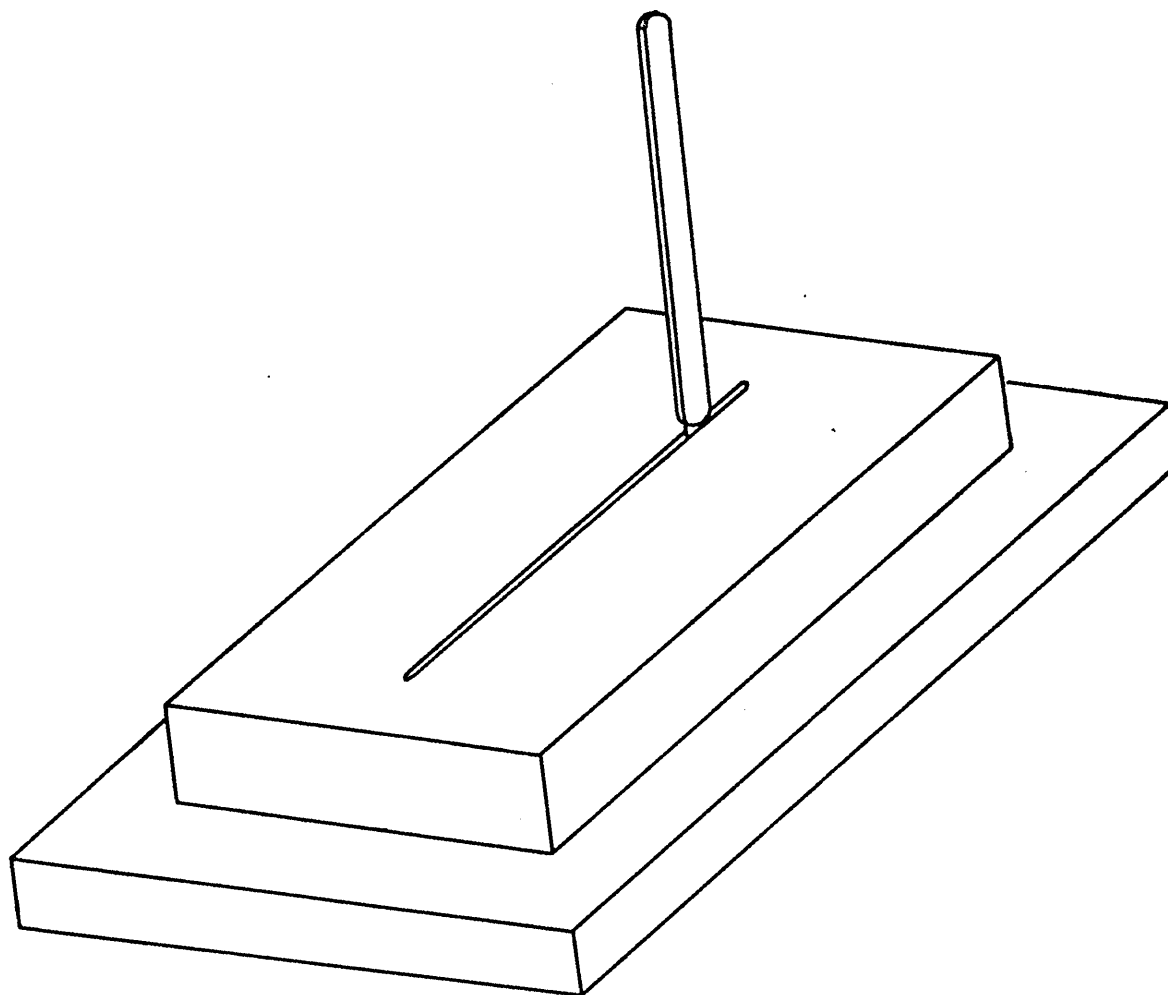
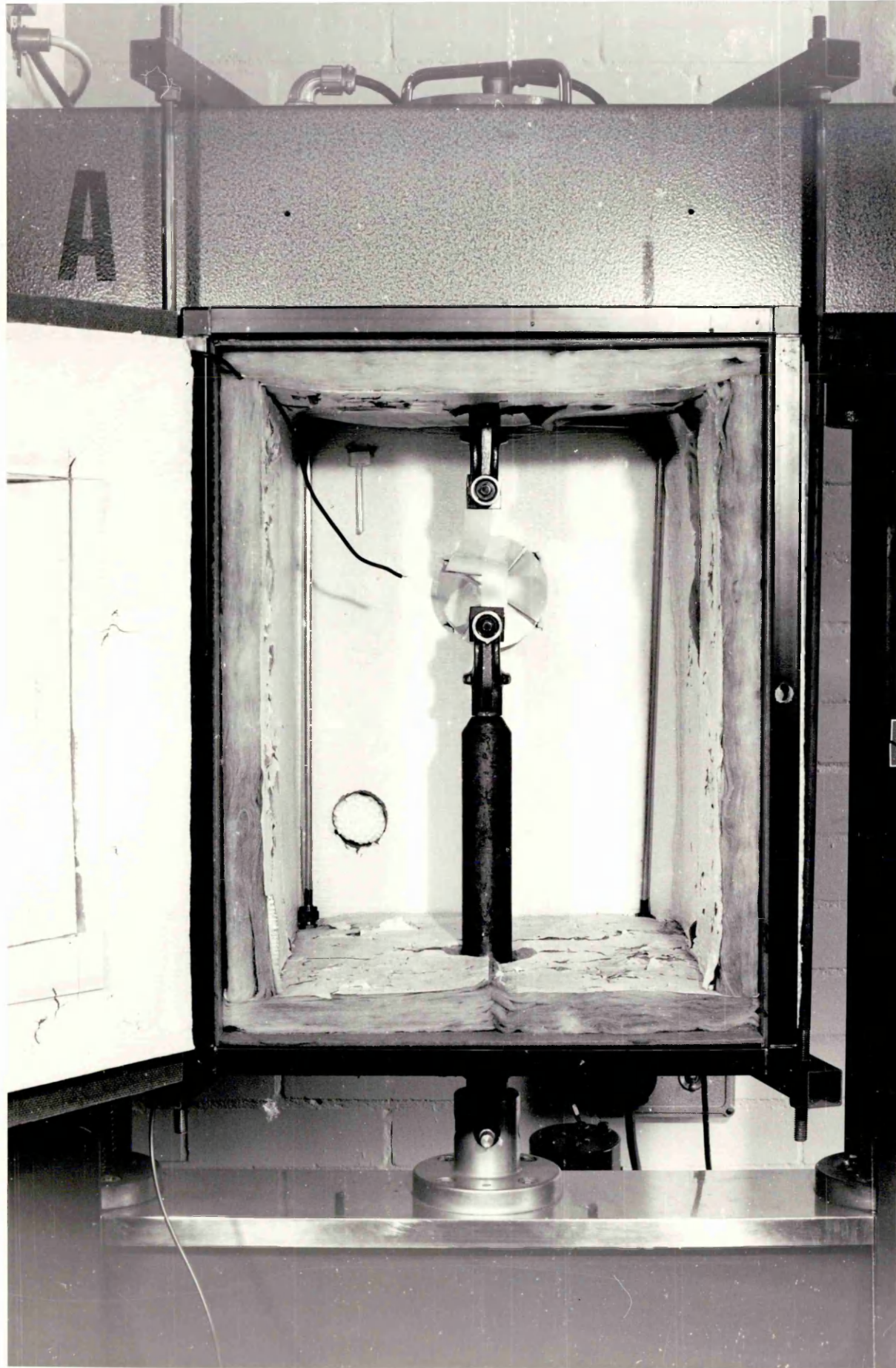


Figure 8.1 The cutting jig.







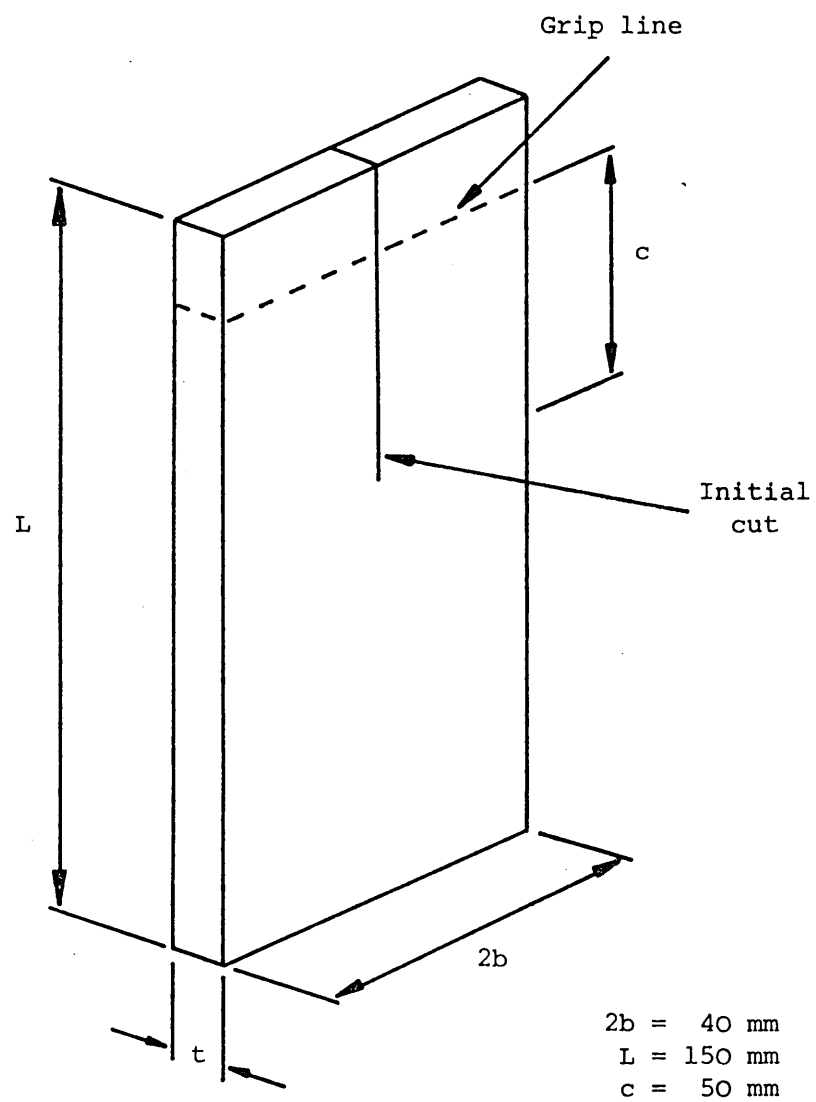
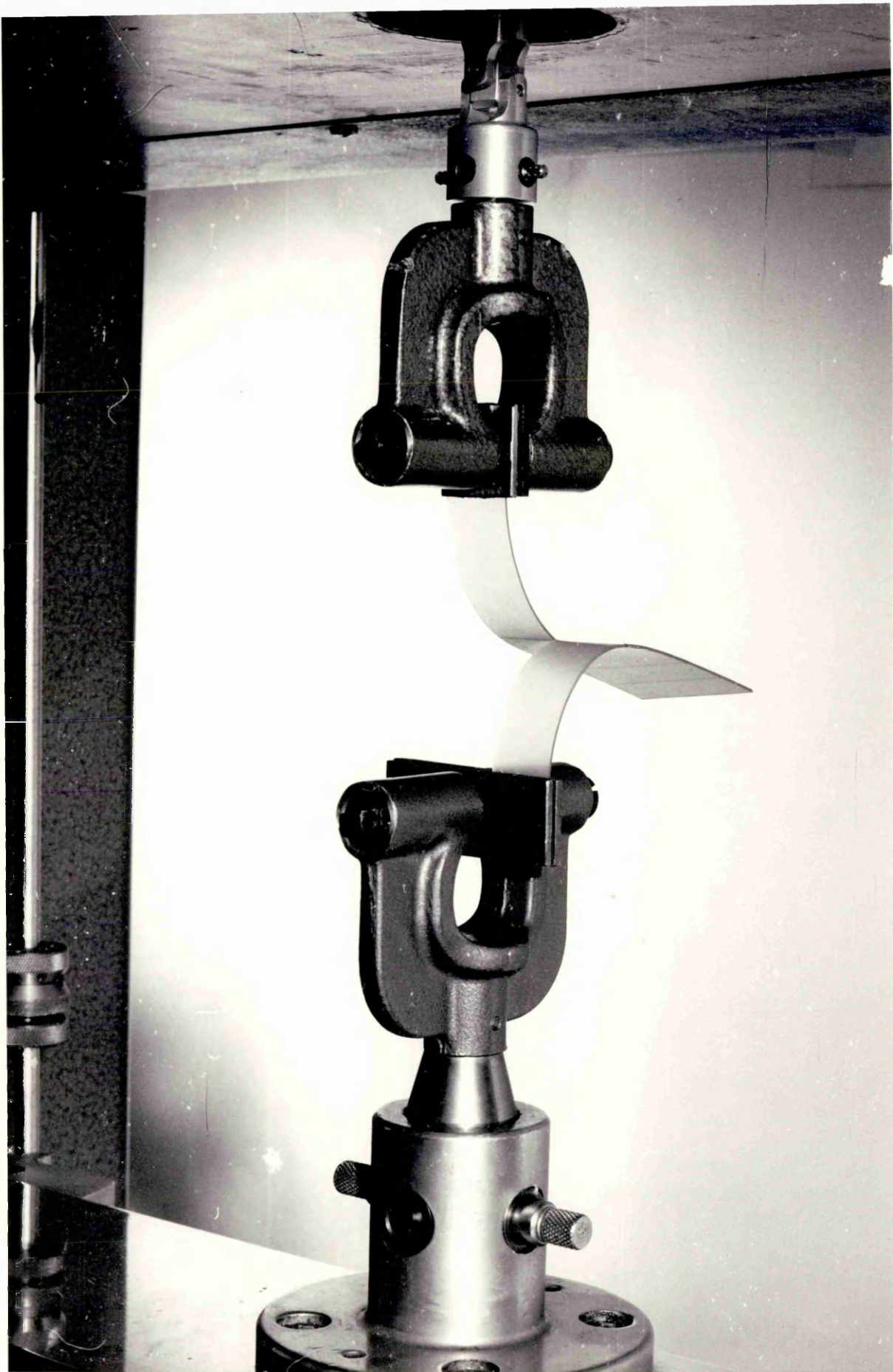


Figure 8.4 The trousers tear specimen.





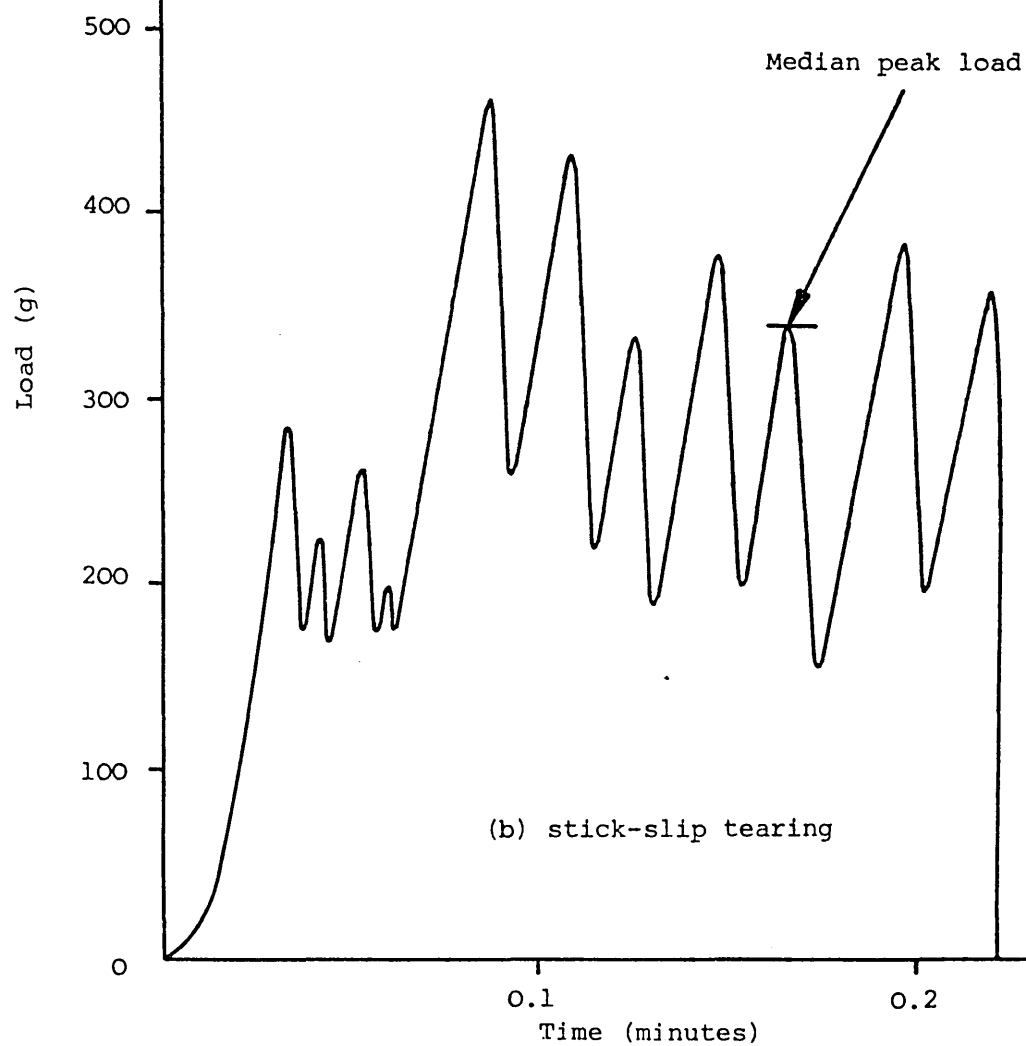
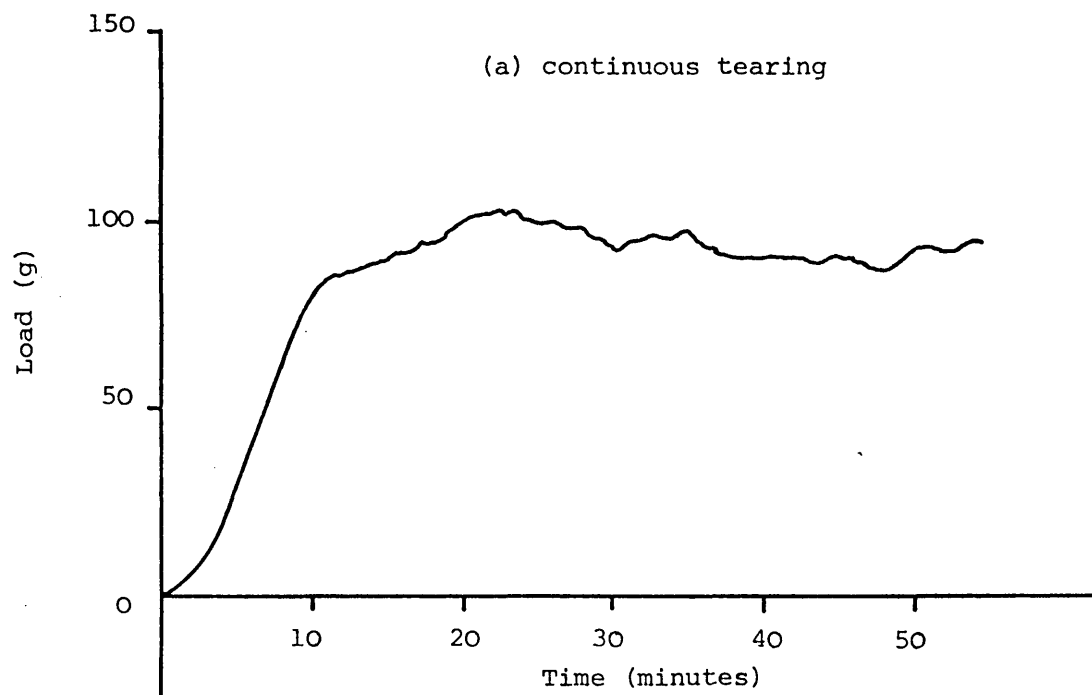


Figure 8.6 Tearing force as a function of time.  
(a) Continuous tearing.  
(b) Stick-slip tearing.



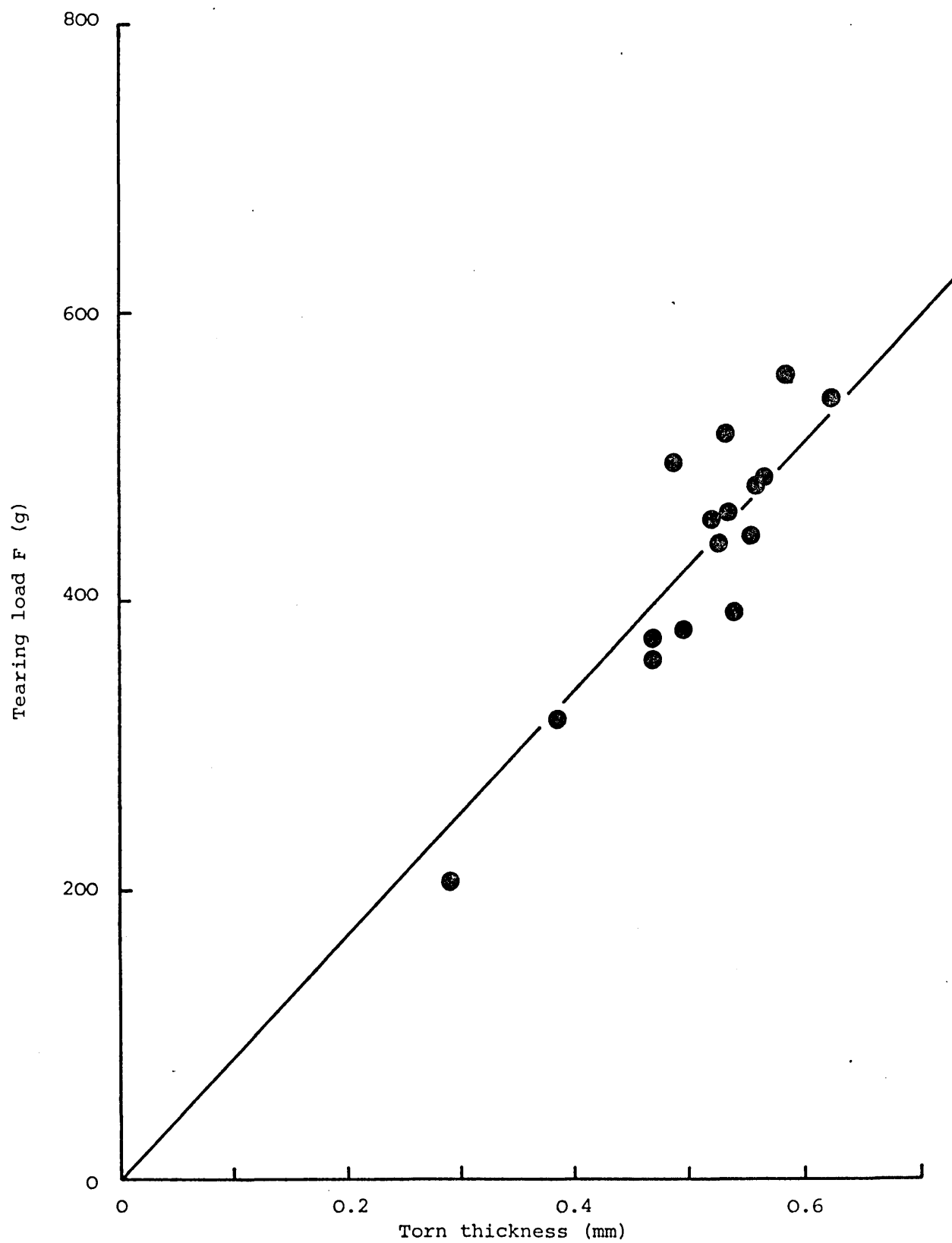


Figure 8.7 Tearing load as a function of specimen thickness for TR1101 cast from  $\text{CCl}_4$ , at  $+20^\circ\text{C}$  and  $10 \text{ cm.min}^{-1}$ .

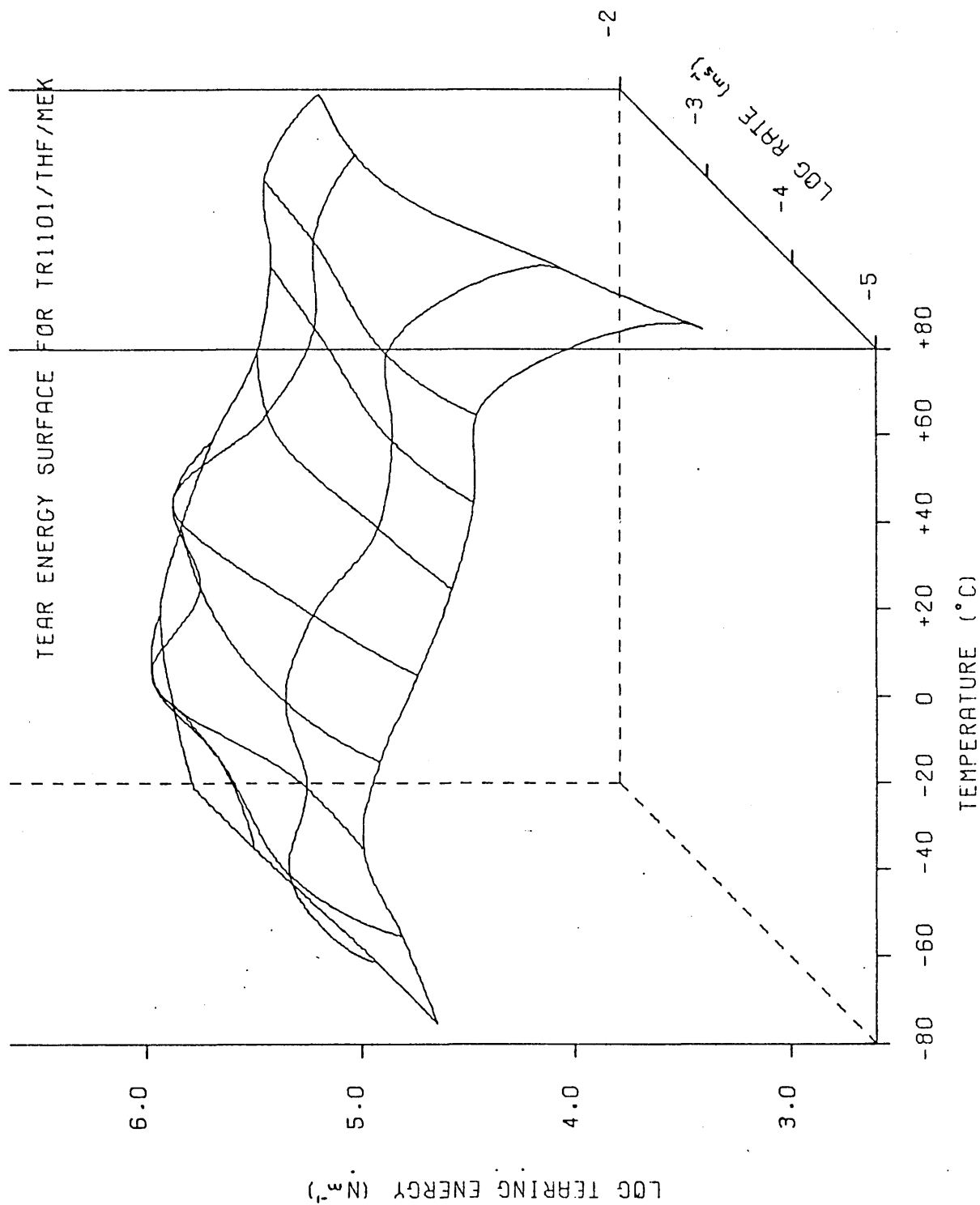


Figure 8.8 Tearing energy as a function of temperature and rate.

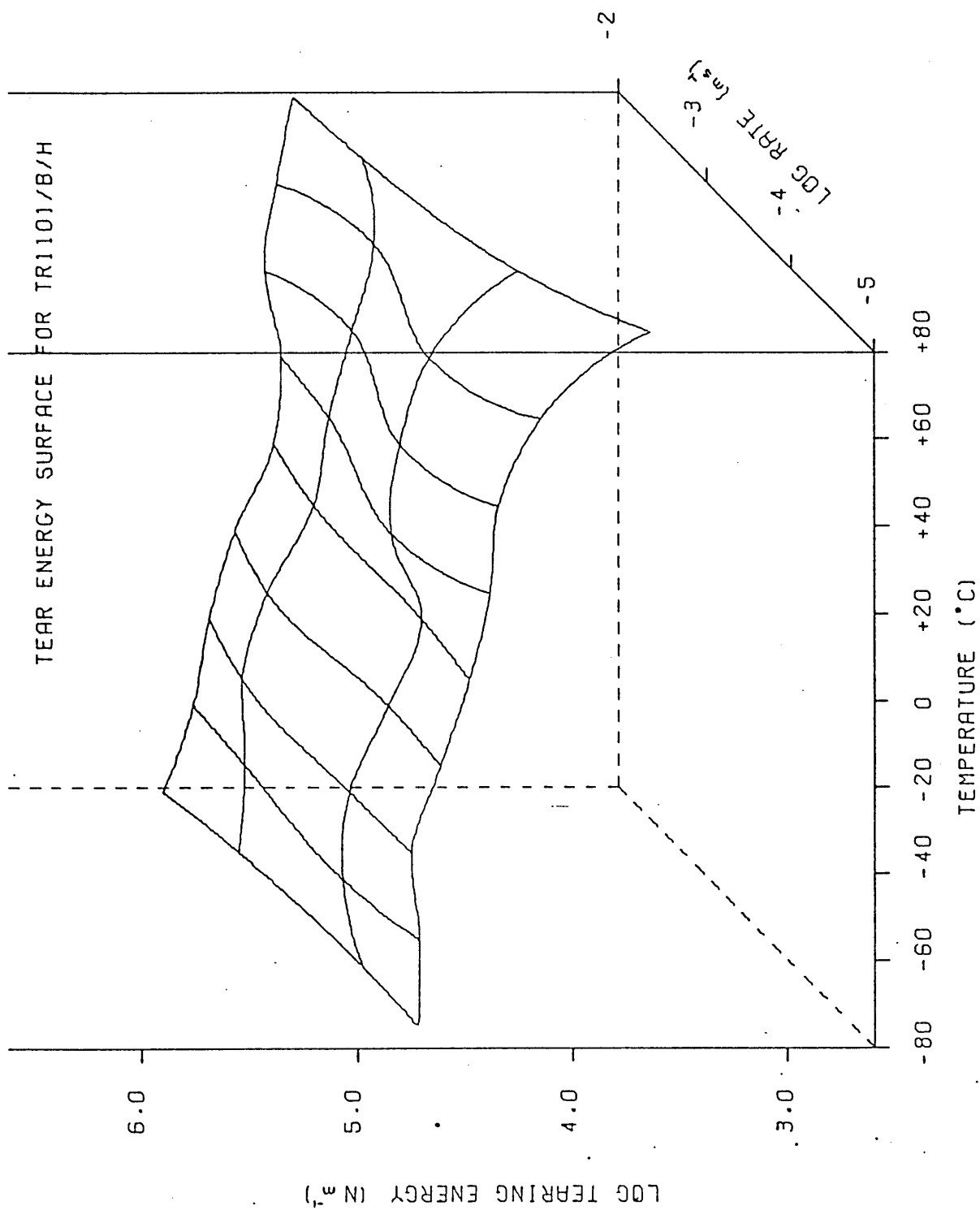


Figure 8.9 Tearing energy as a function of test temperature and rate for TR1101 B/H

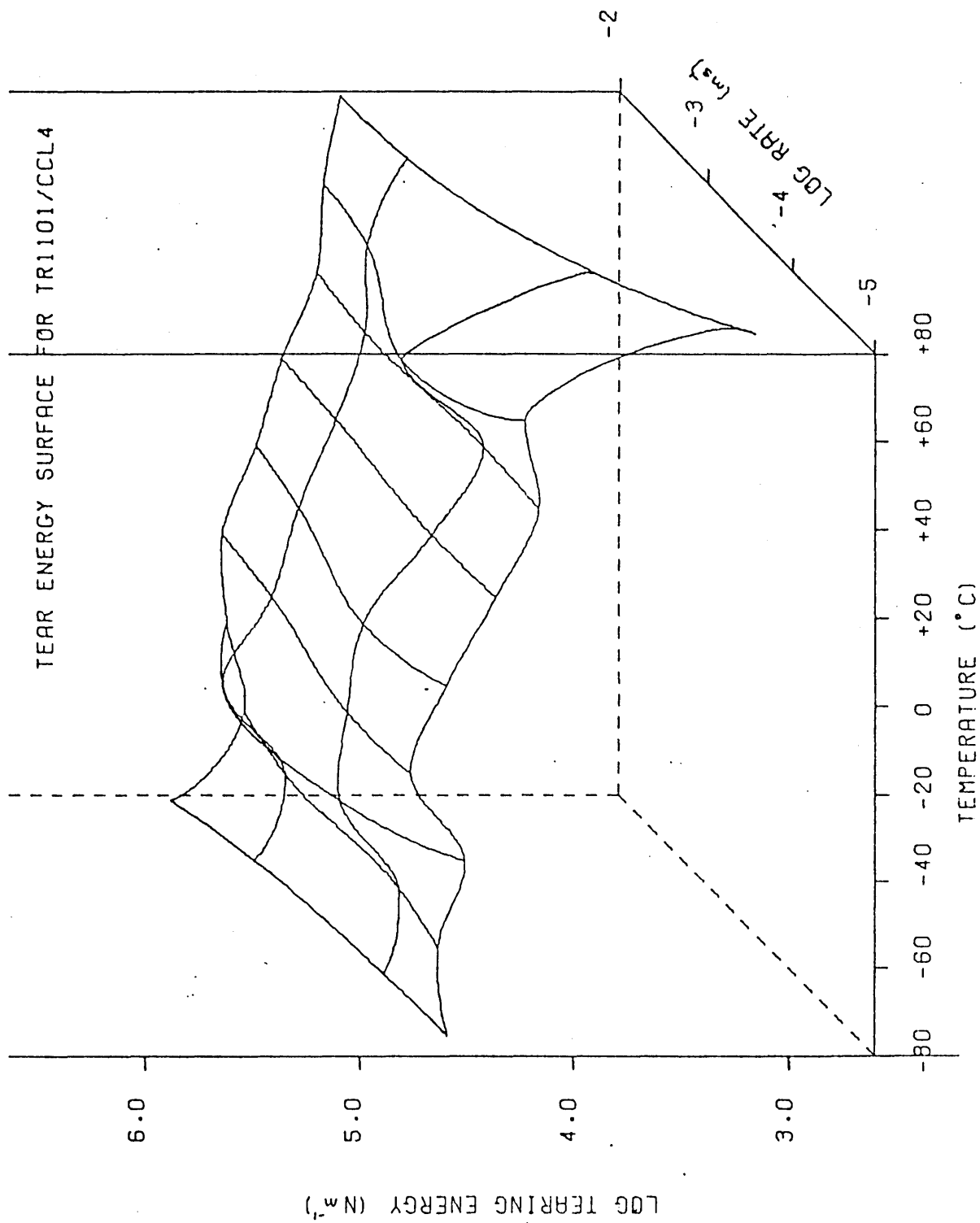


Figure 8.10 Tearing energy as a function of test temperature and rate for TR1101 CCl<sub>4</sub>.

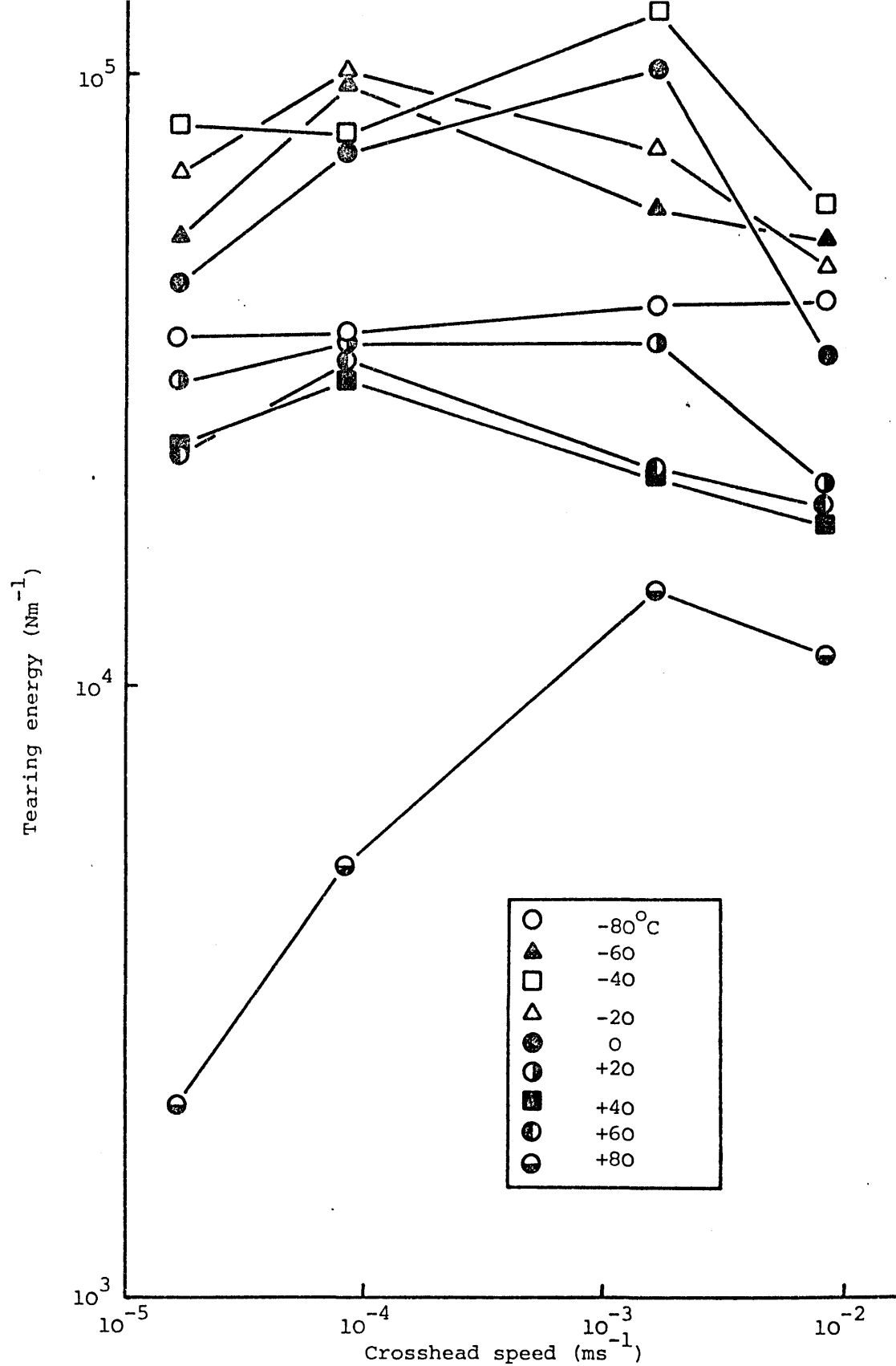


Figure 8.11 Tearing energy as a function of rate for different test temperatures (TR1101 THF/MEK).

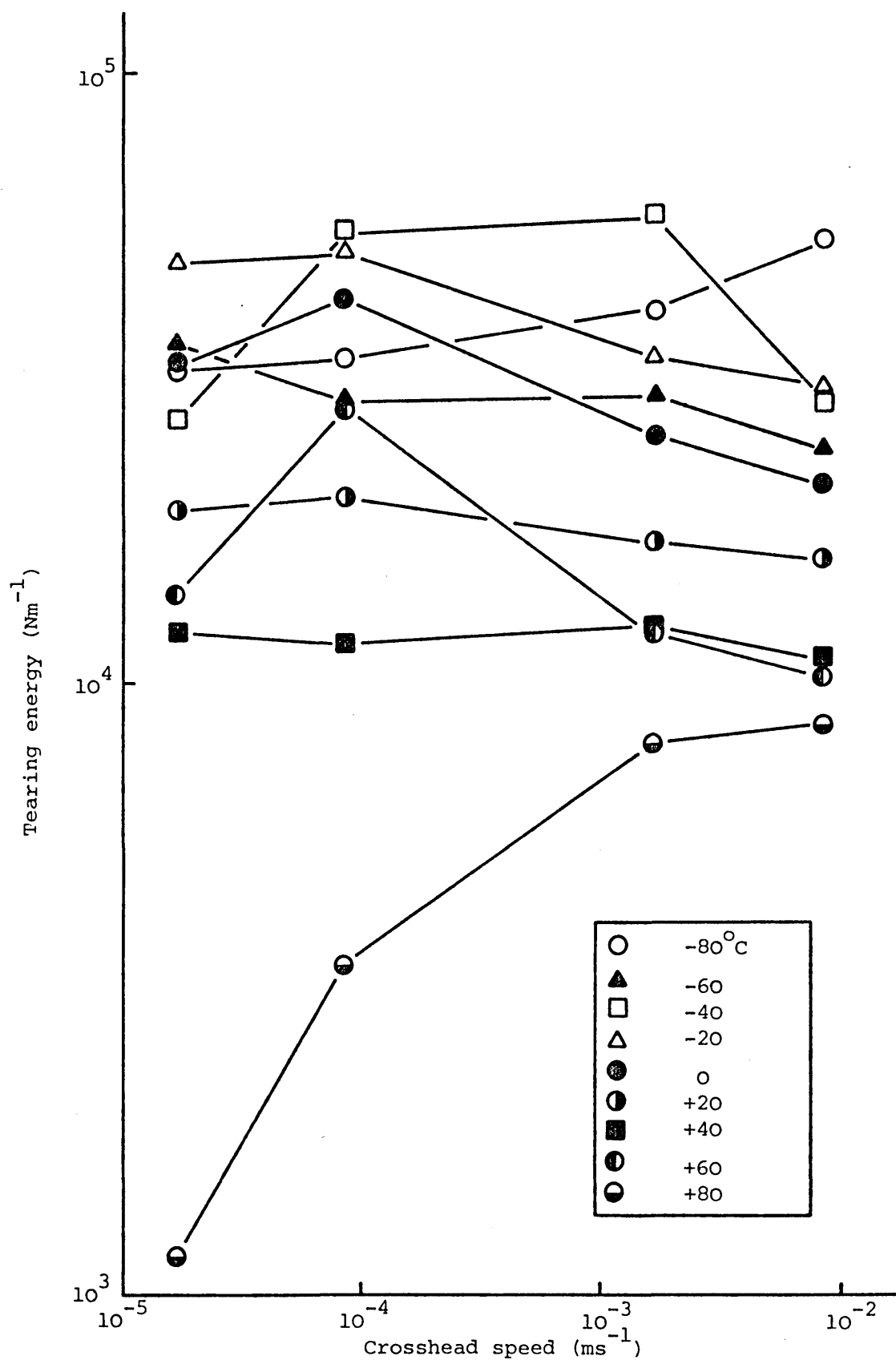


Figure 8.12 Tearing energy as a function of rate for different test temperatures (TR1101  $\text{CCl}_4$ ).

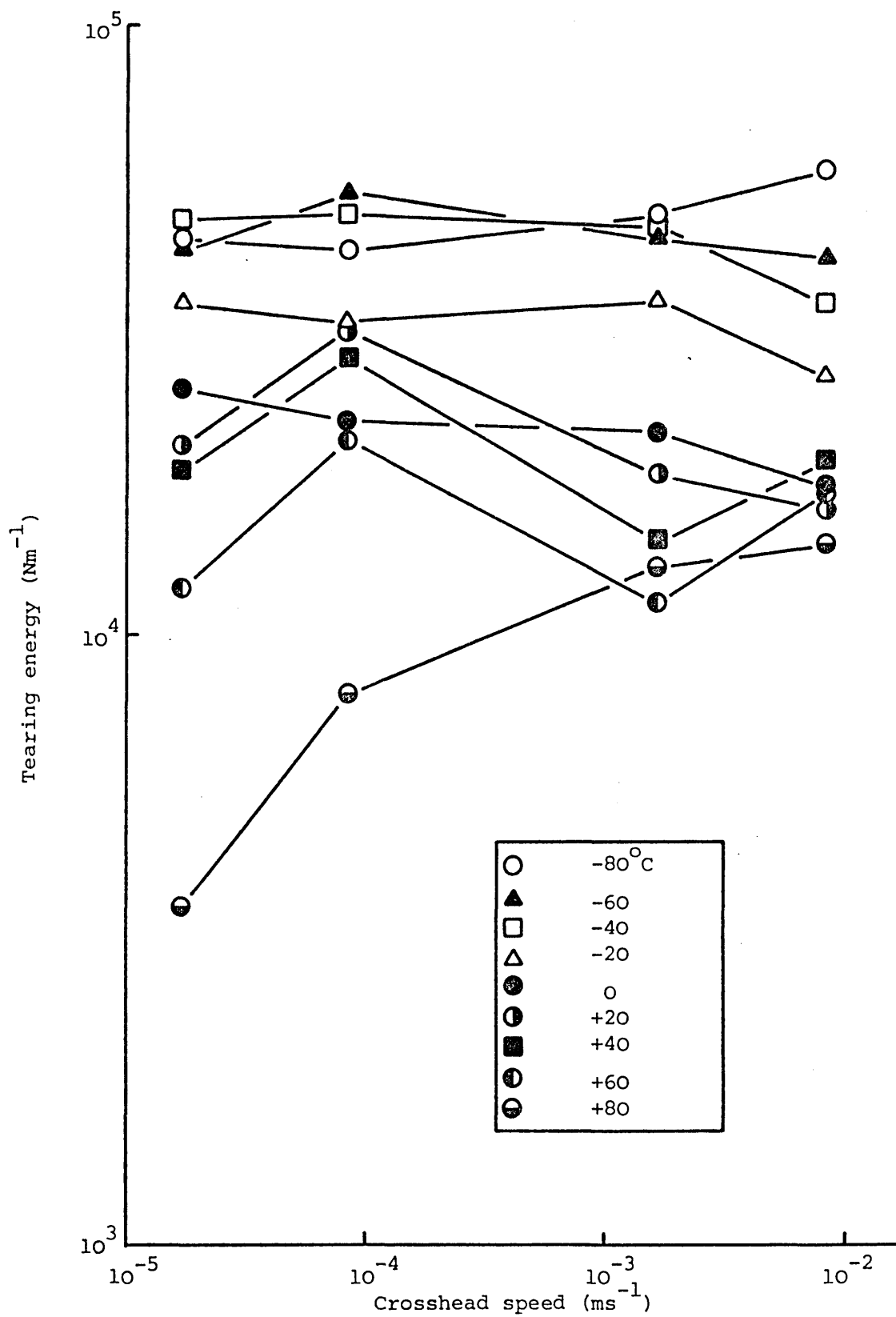


Figure 8.13 Tearing energy as a function of rate for different test temperatures (TR1101 B/H).

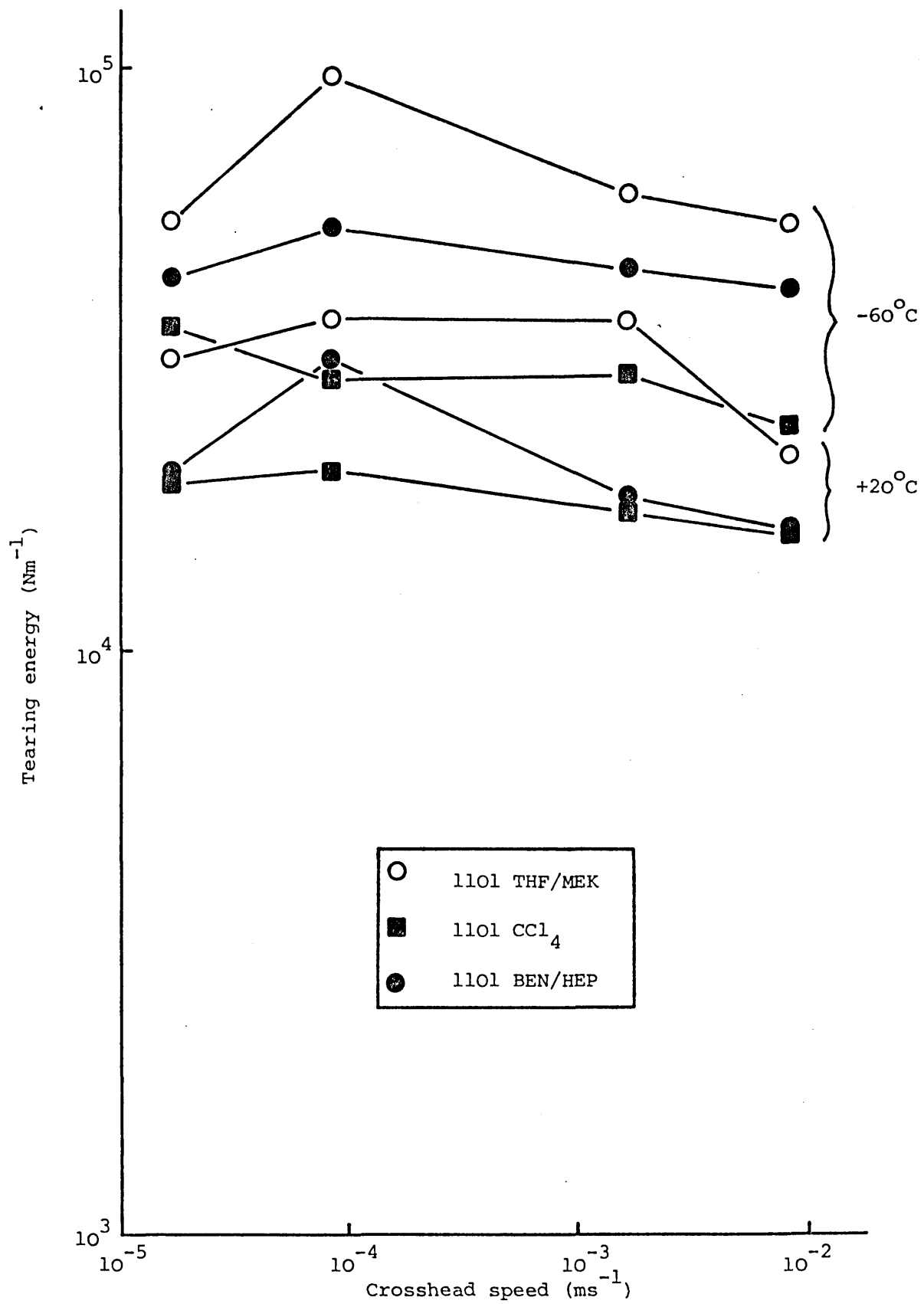


Figure 8.14 Tearing energy as a function of rate for TR1101 cast from different solvent systems.



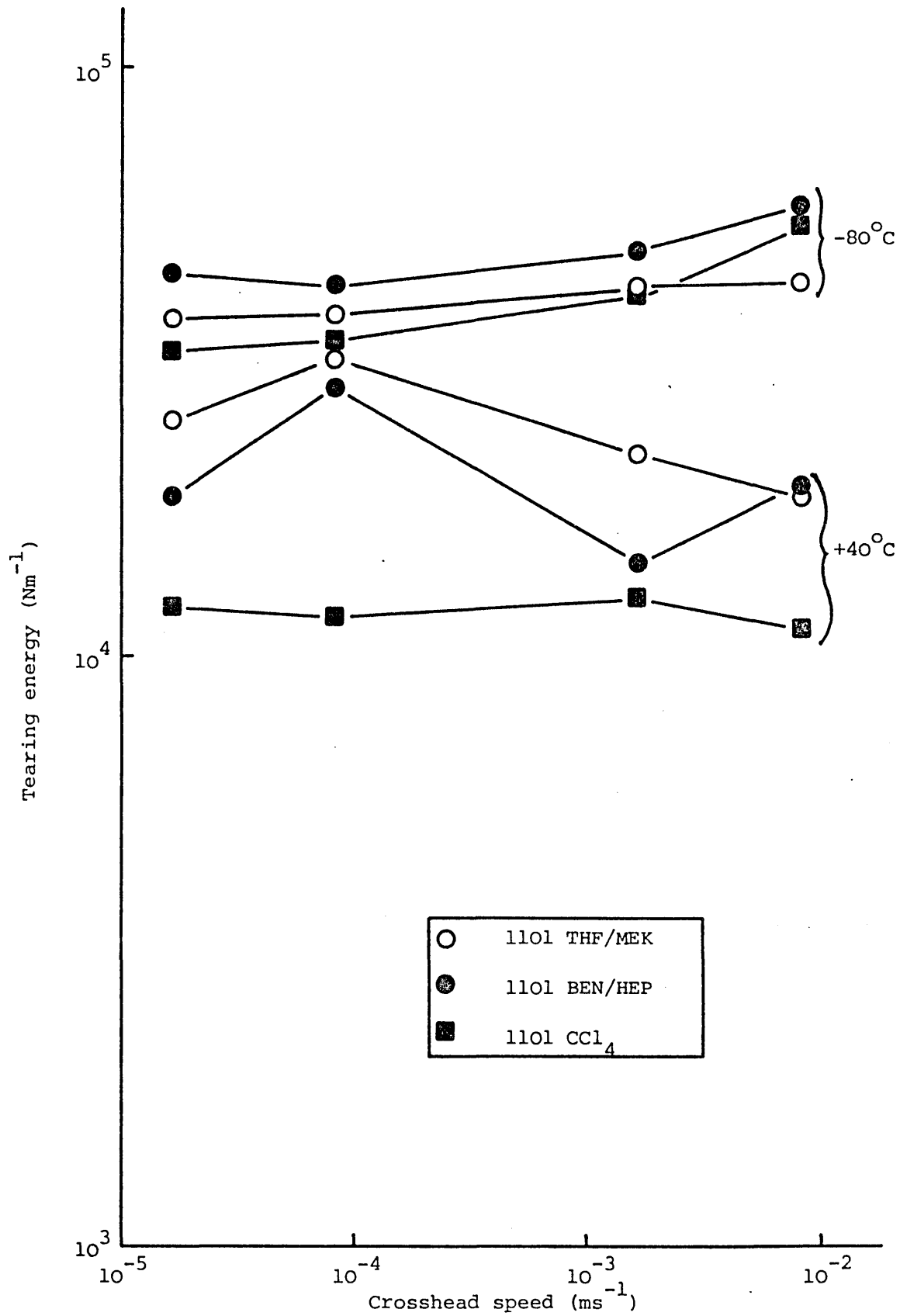


Figure 8.15 Tearing energy as a function of rate for TR1101 cast from different solvent systems.

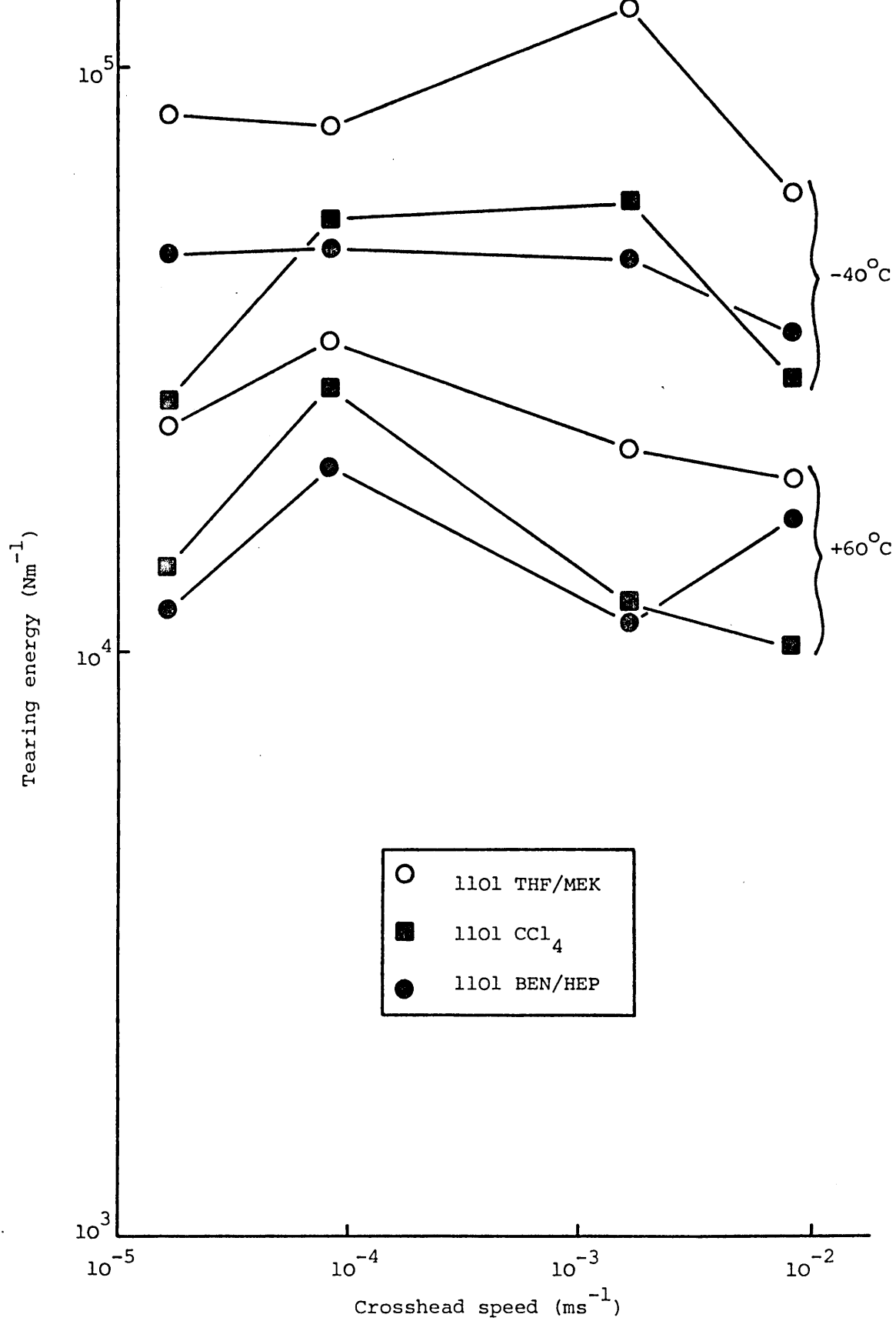


Figure 8.16 Tearing energy as a function of rate for TR1101 cast from different solvent systems.

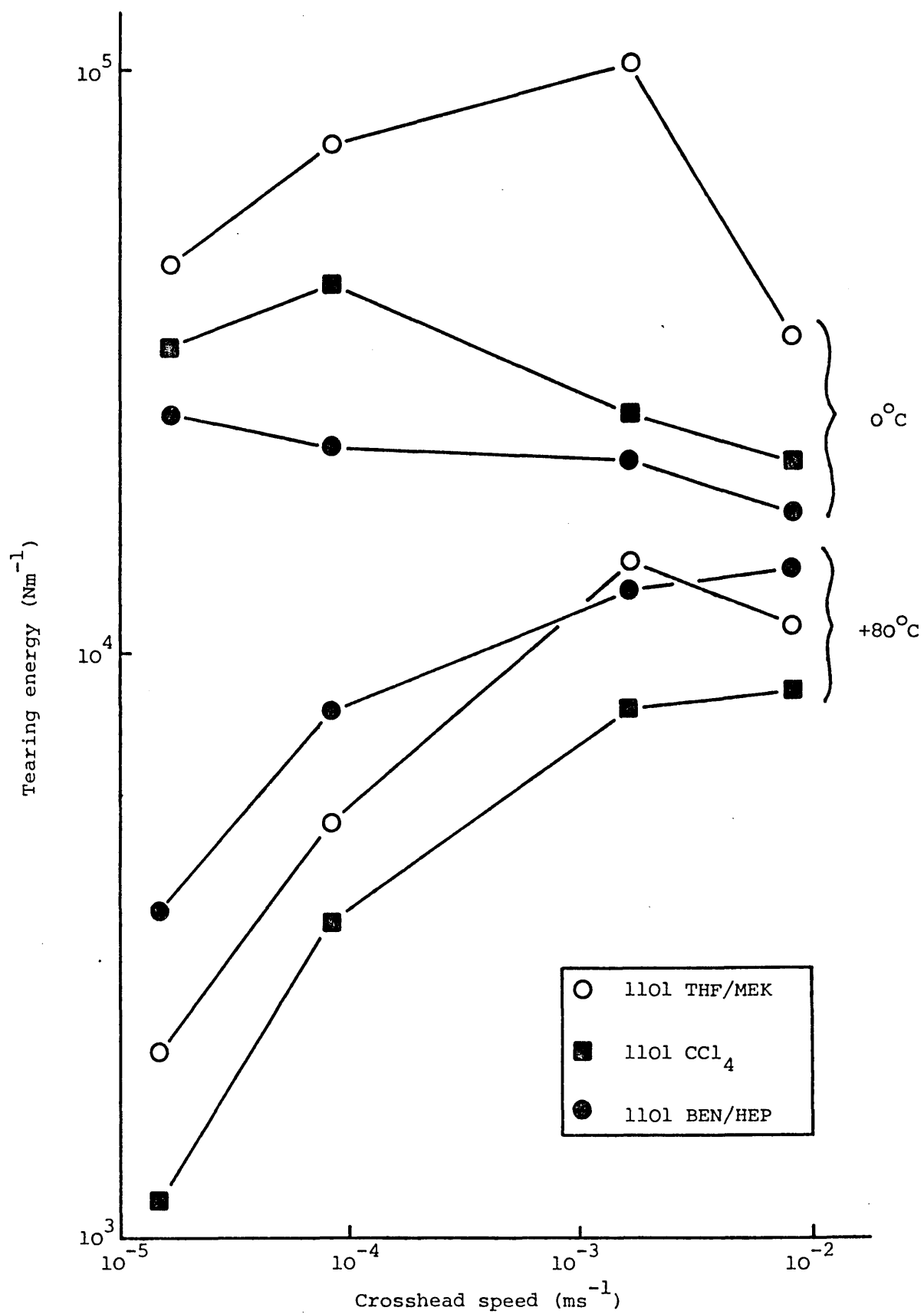


Figure 8.17 Tearing energy as a function of rate for TR1101 cast from different solvent systems.

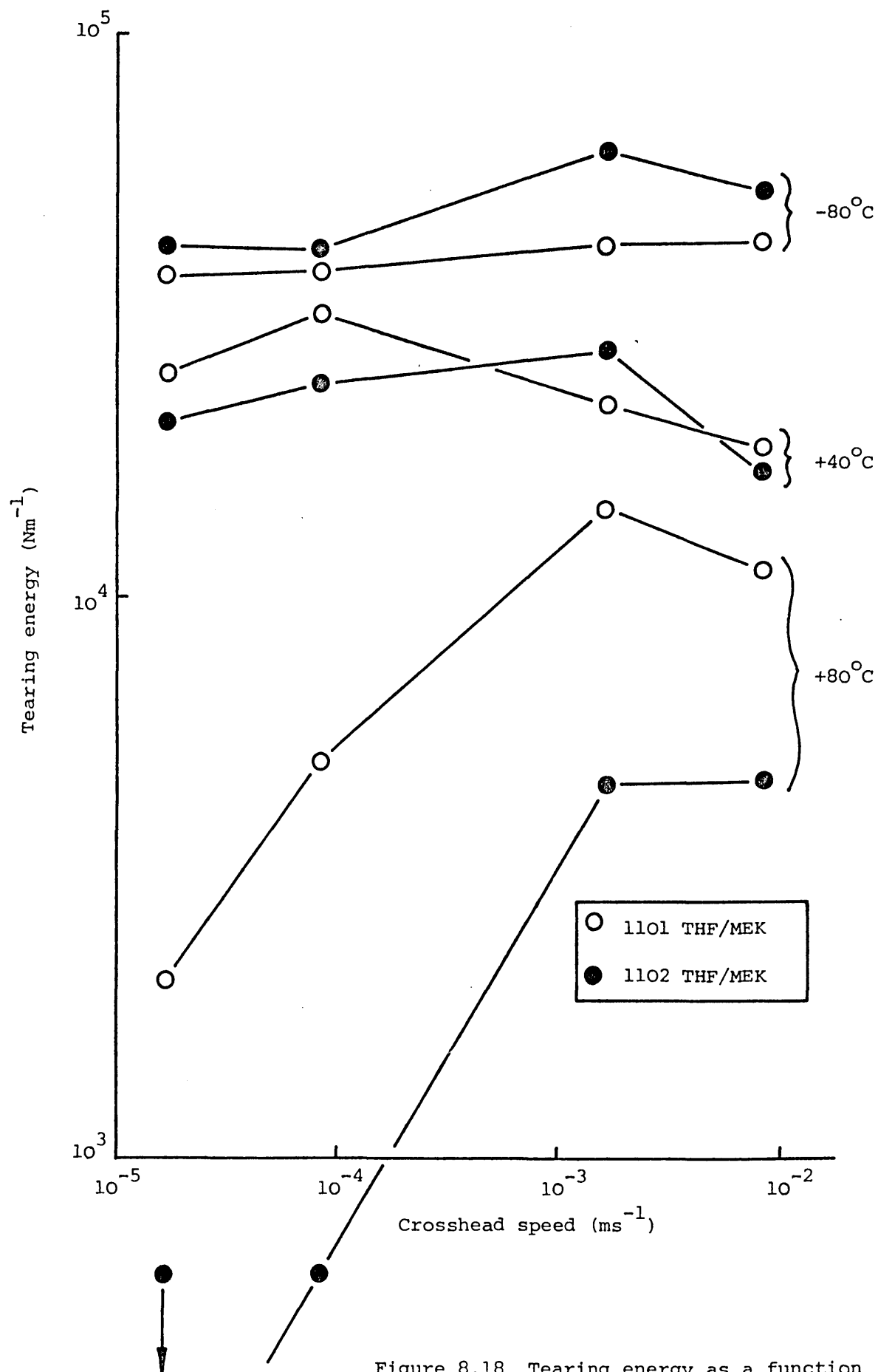


Figure 8.18 Tearing energy as a function of rate comparing TR1101 and TR1102 cast from THF/MEK.

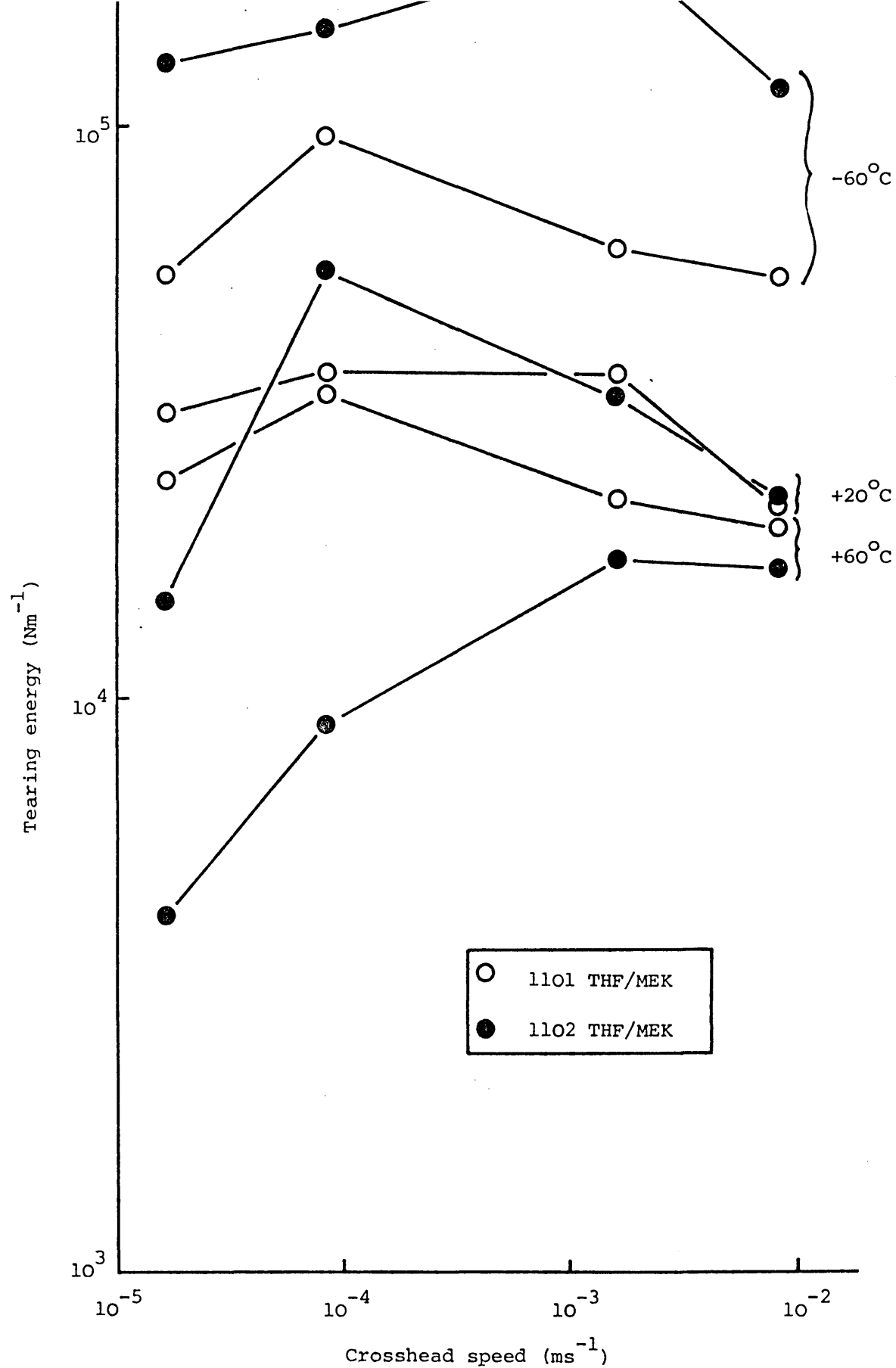


Figure 8.19 Tearing energy as a function of rate comparing TR1101 and TR1102 cast from THF/MEK.

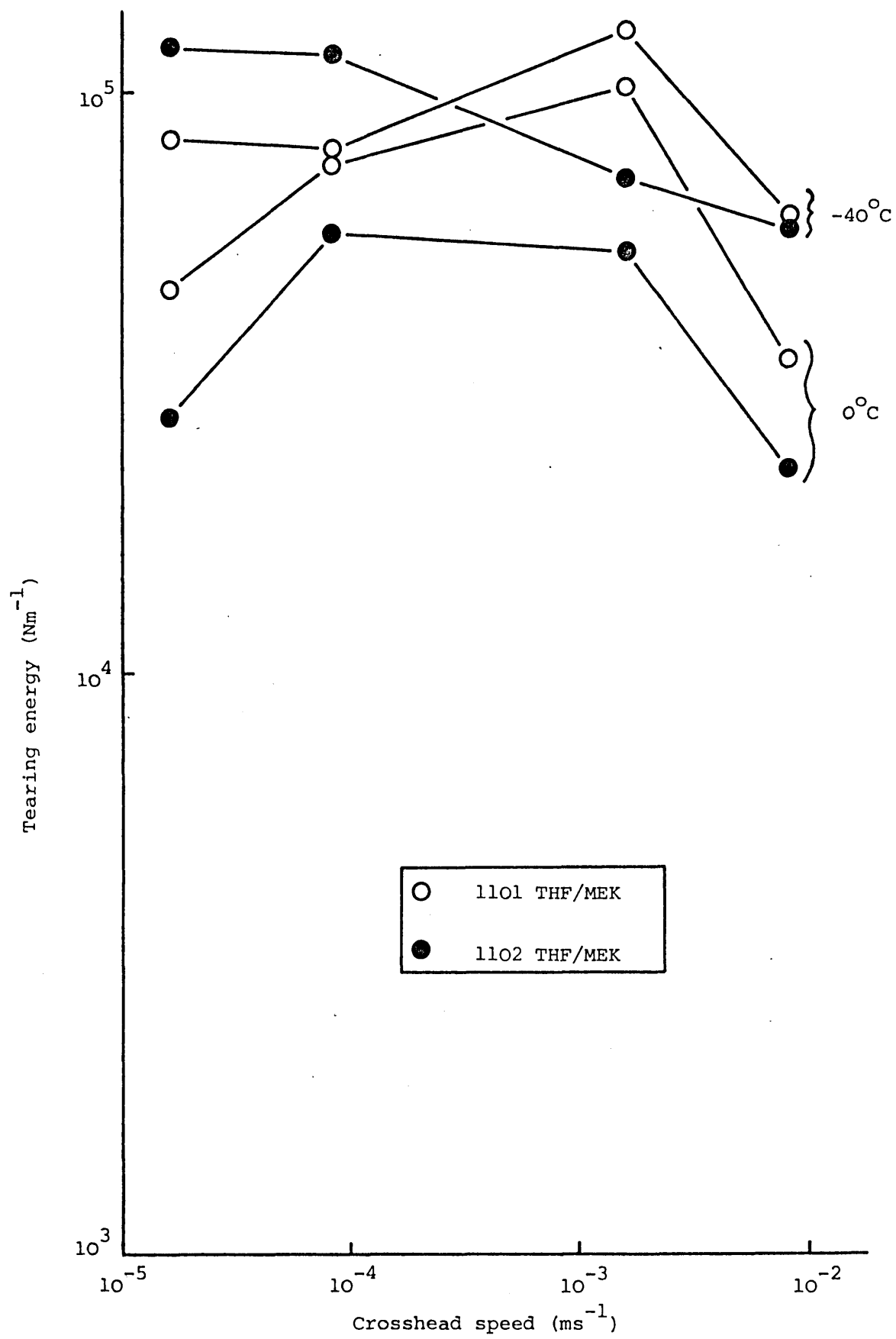


Figure 8.20 Tearing energy as a function of rate comparing TR1101 and TR1102 cast from THF/MEK.

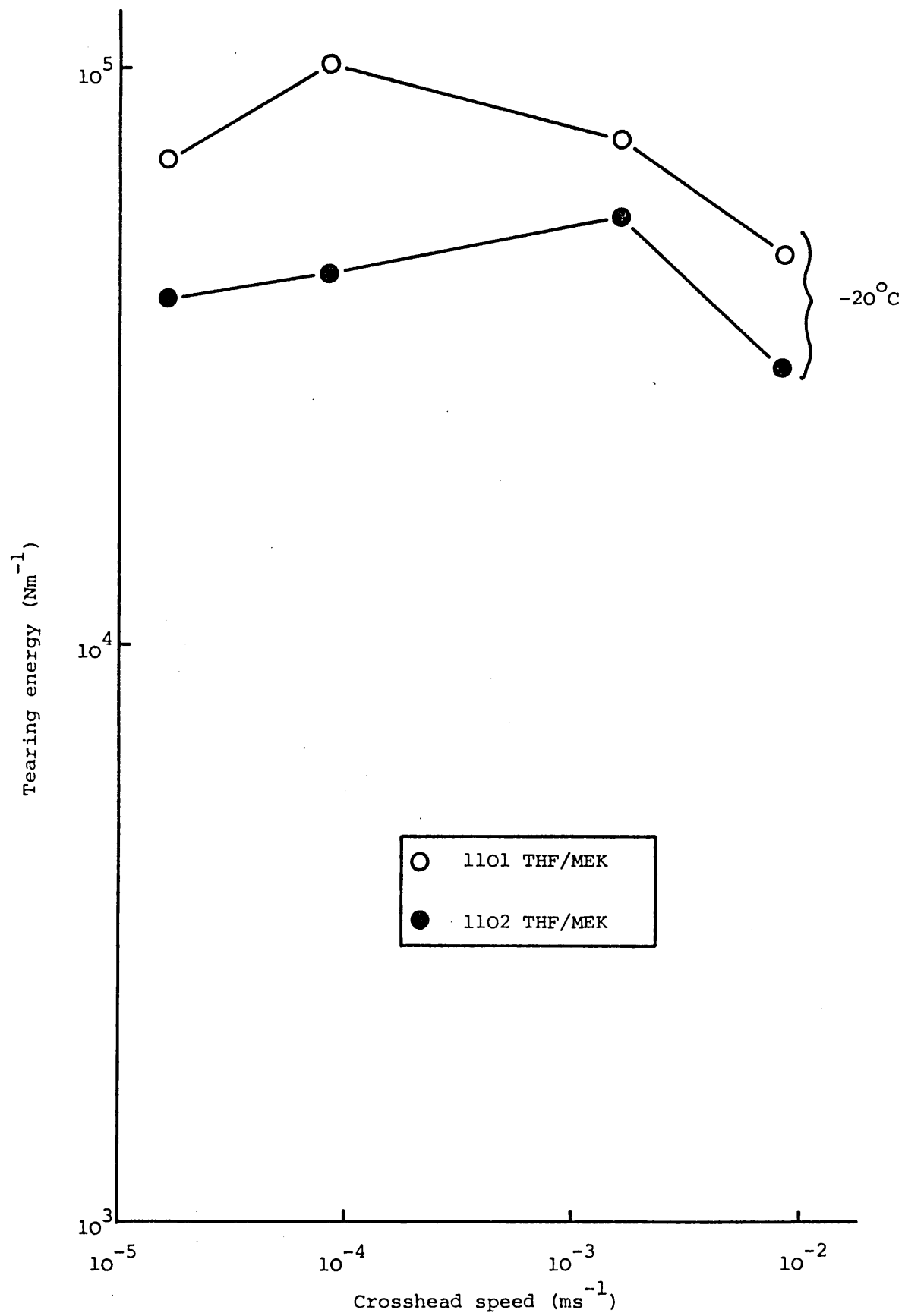


Figure 8.21 Tearing energy as a function of rate comparing TR1101 and TR1102 cast from THF/MEK.

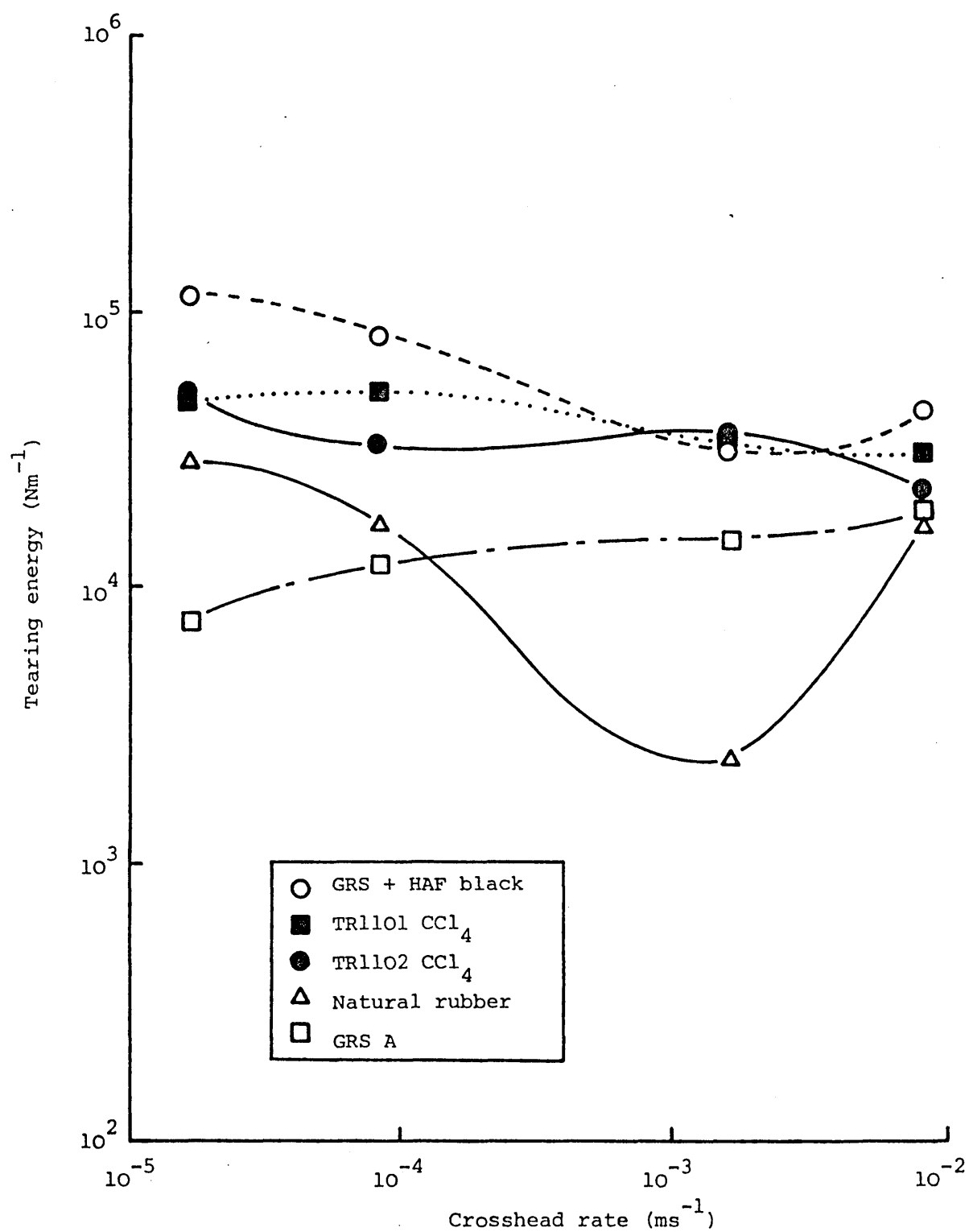


Figure 8.22 Comparison of the tear strength of thermoplastic elastomers with that of other rubbery materials at  $+20^\circ\text{C}$ .



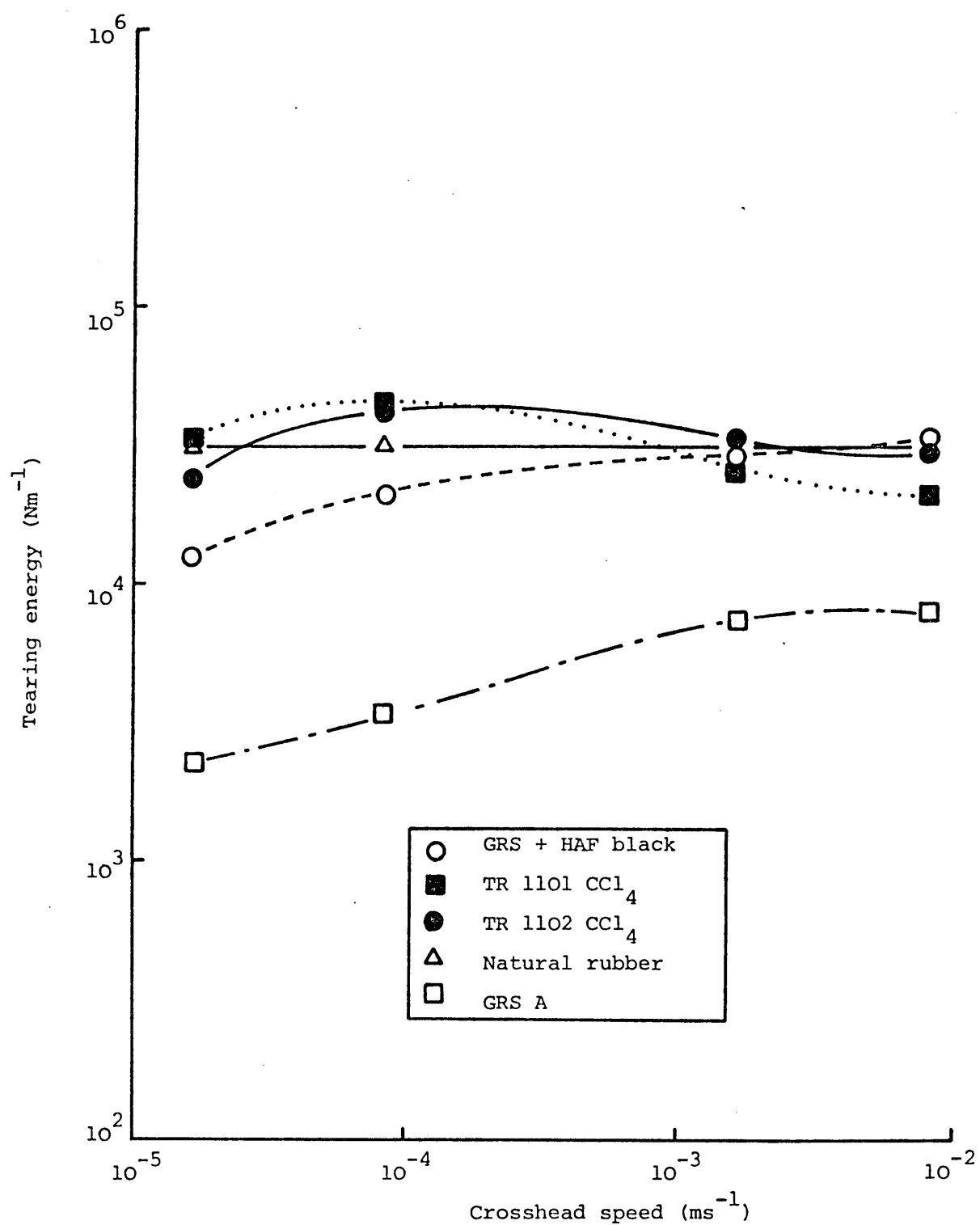


Figure 8.23 Comparison of the tear strength of thermoplastic elastomers with that of other rubbery materials at  $0^\circ\text{C}$ .

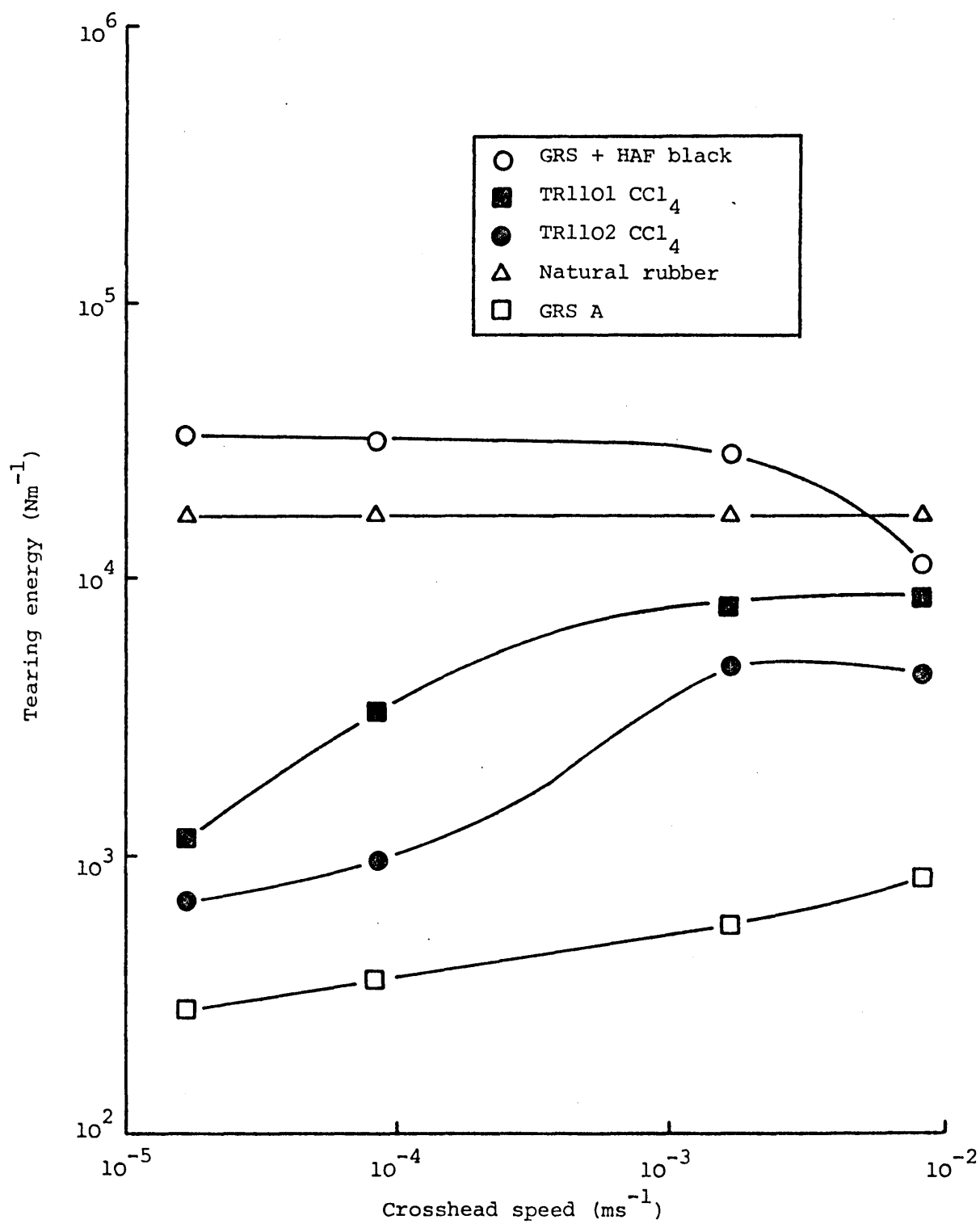


Figure 8.24 Comparison of the tear strength of thermoplastic elastomers with that of other rubbery materials at  $+80^\circ\text{C}$ .

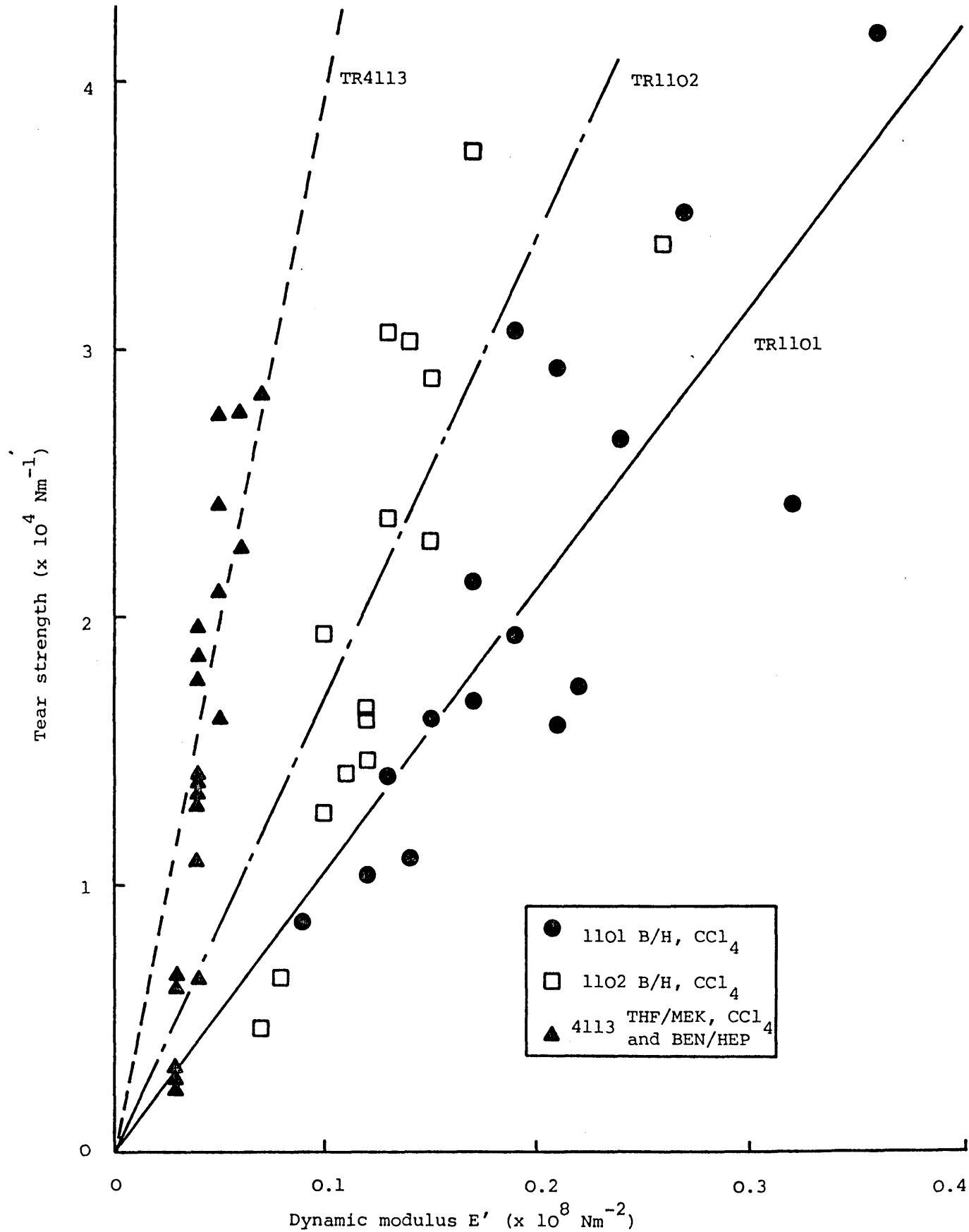


Figure 8.25 Tear strength as a function of dynamic modulus for the non-yielding SBS thermoplastic elastomers.

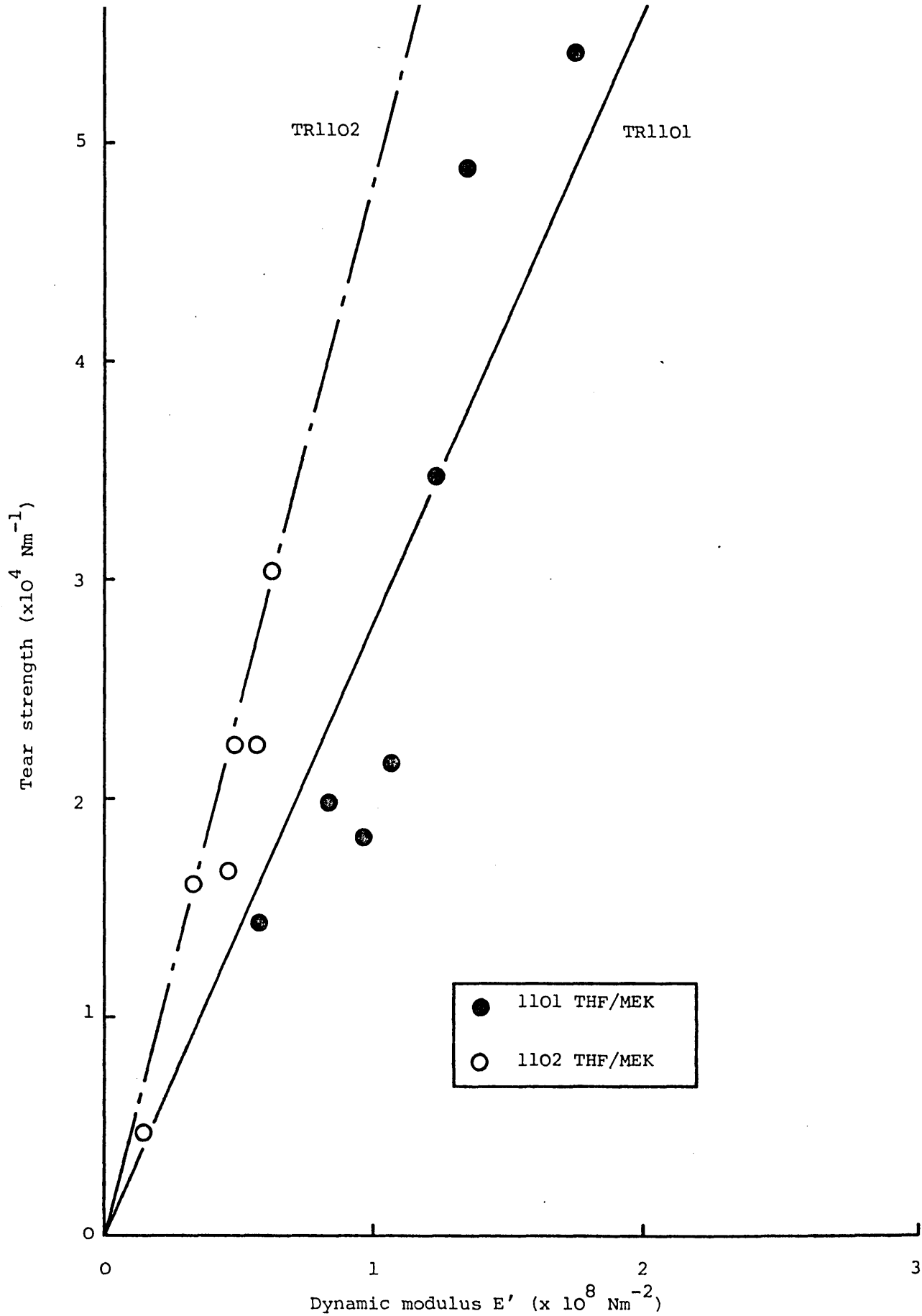


Figure 8.26 Tear strength as a function of dynamic modulus for yielding SBS thermoplastic elastomers cast from THF/MEK.

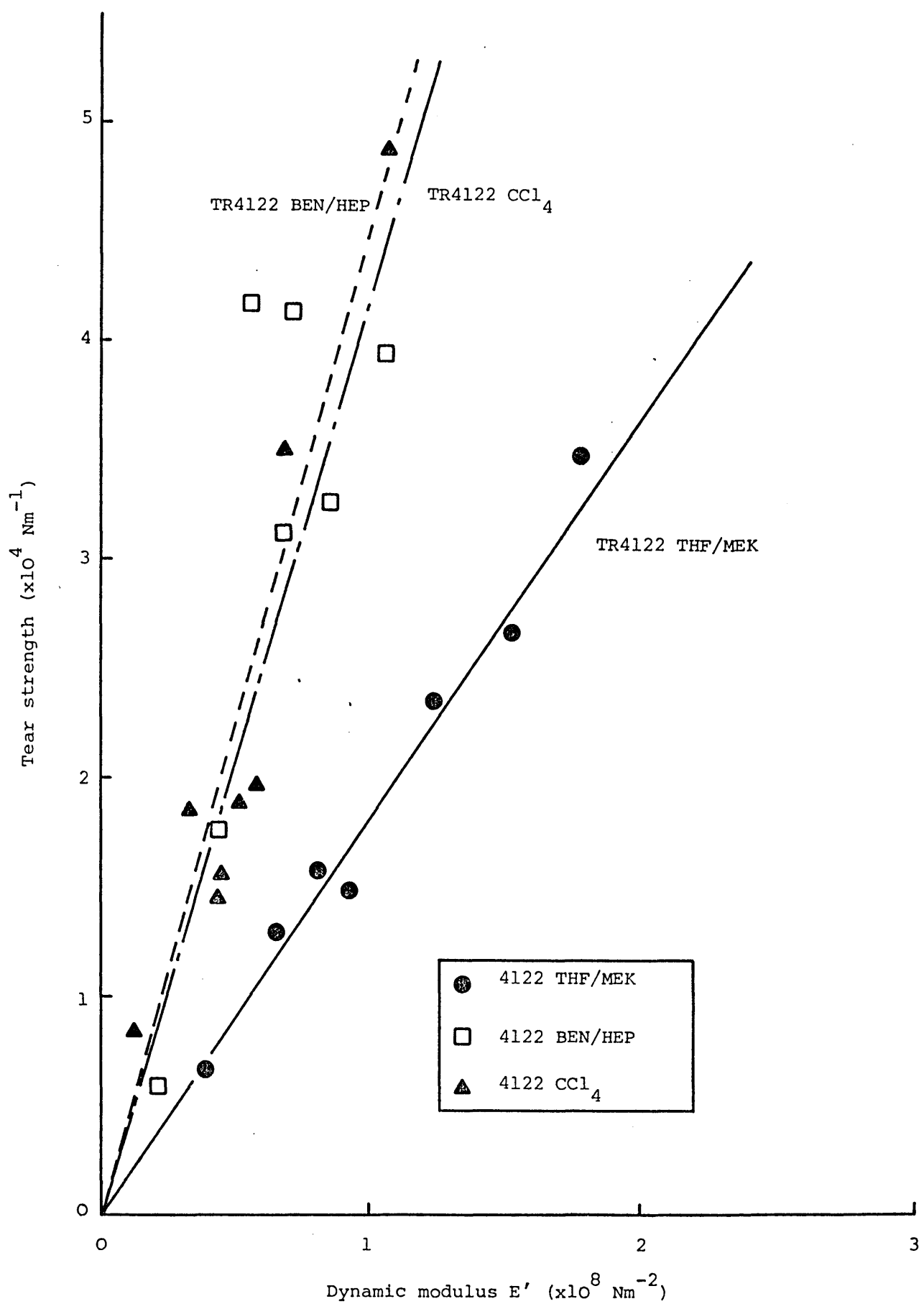


Figure 8.27 Tear strength as a function of dynamic modulus for yielding SBS TR4122 cast from several solvent systems.

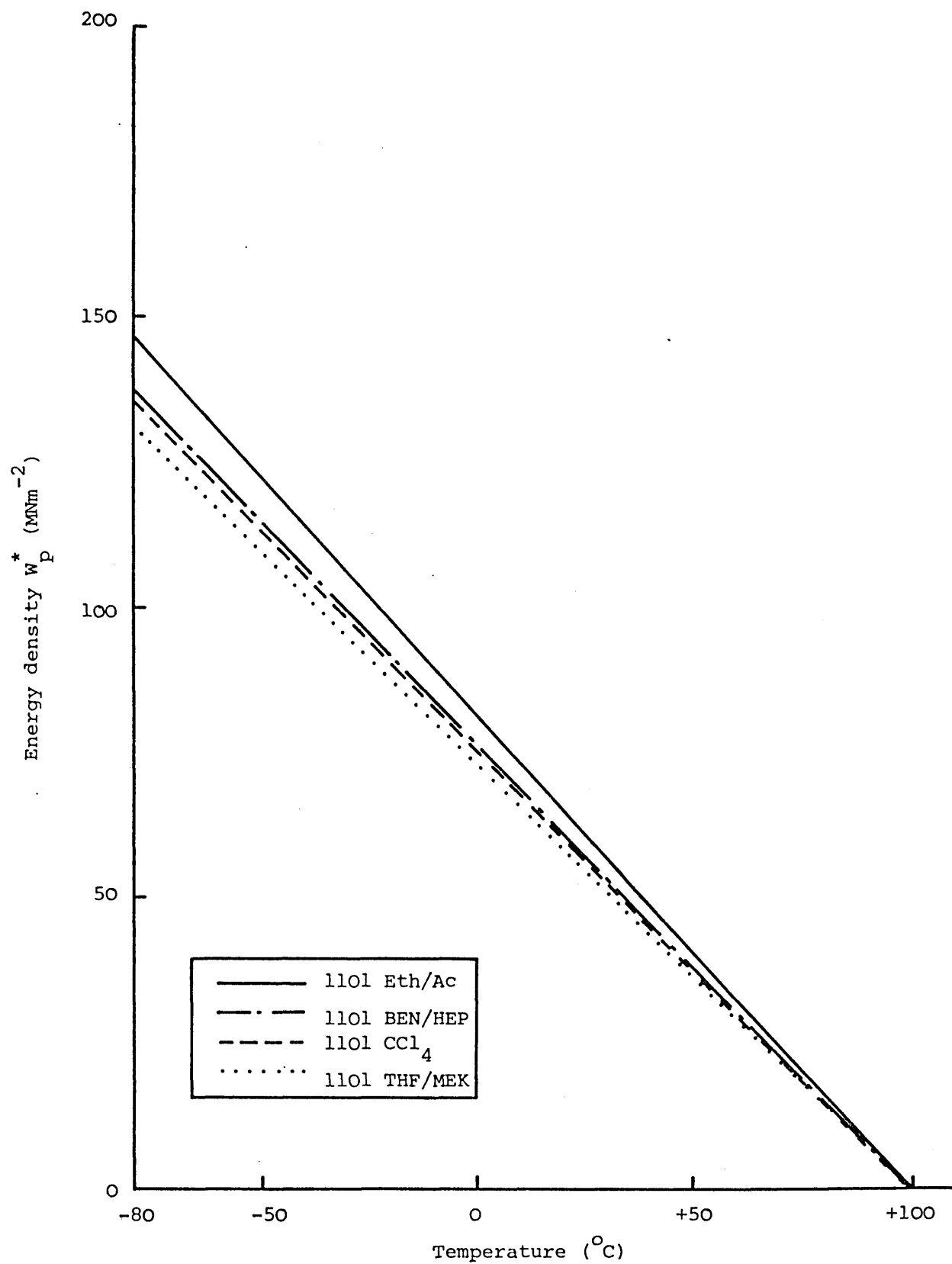


Figure 8.28 Energy density in tensile test as a function of temperature for TR1101 cast from several solvents.

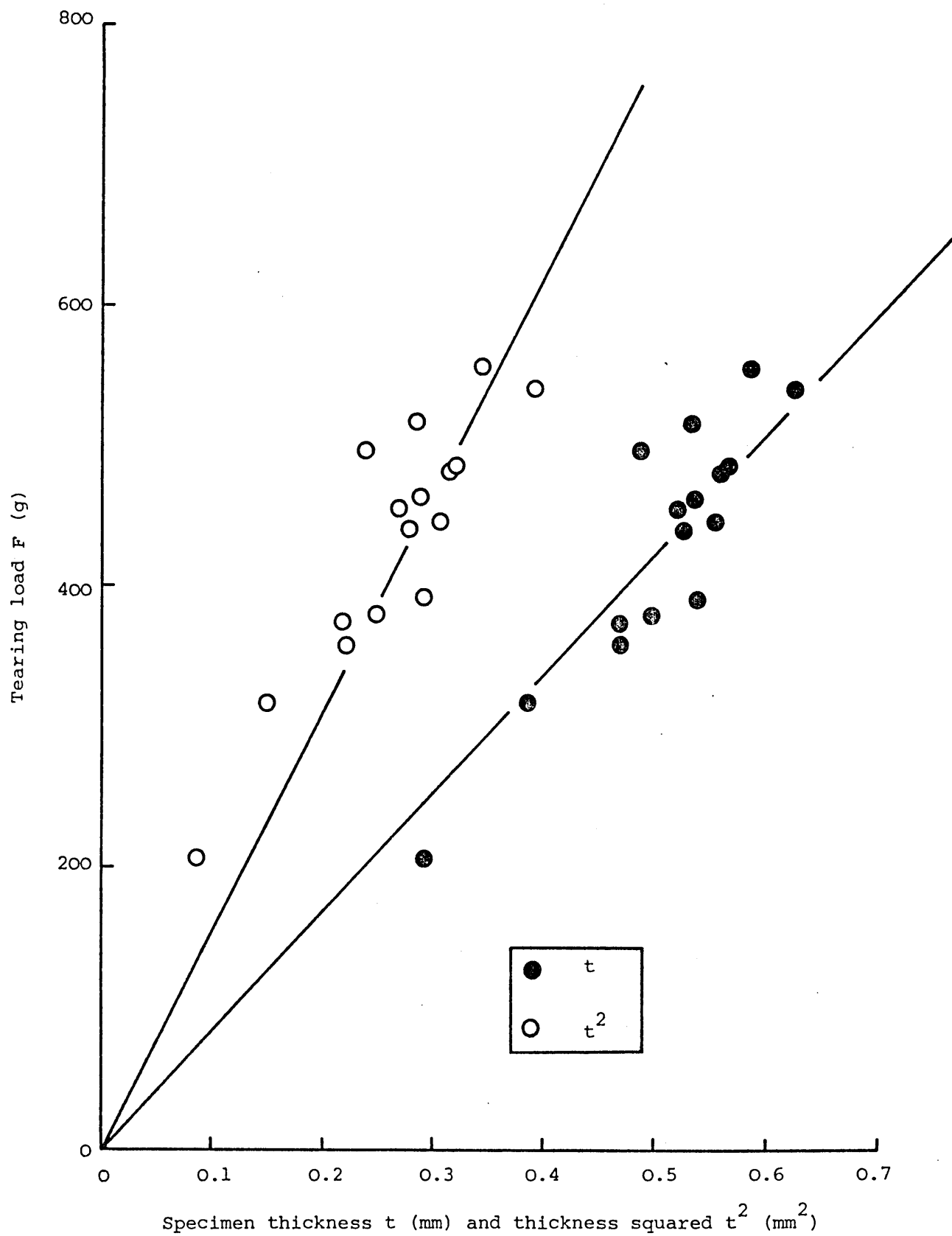


Figure 8.29 Tearing force as a function of  $t$  and  $t^2$  for TR1101  $\text{CCl}_4$ .

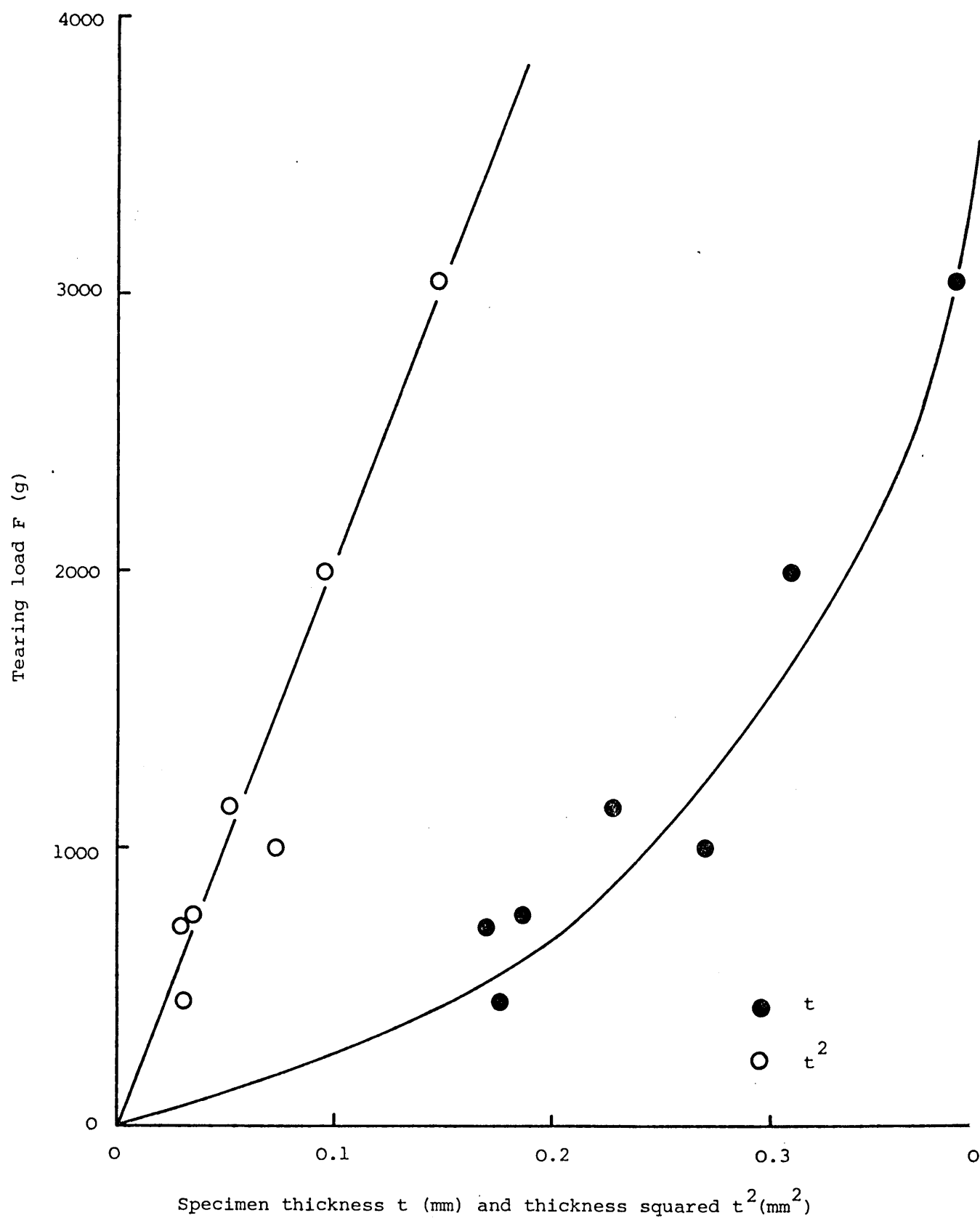


Figure 8.30 Tearing load as a function of  $t$  and  $t^2$  for TR1101 THF/MEK at  $-40^{\circ}\text{C}$ .



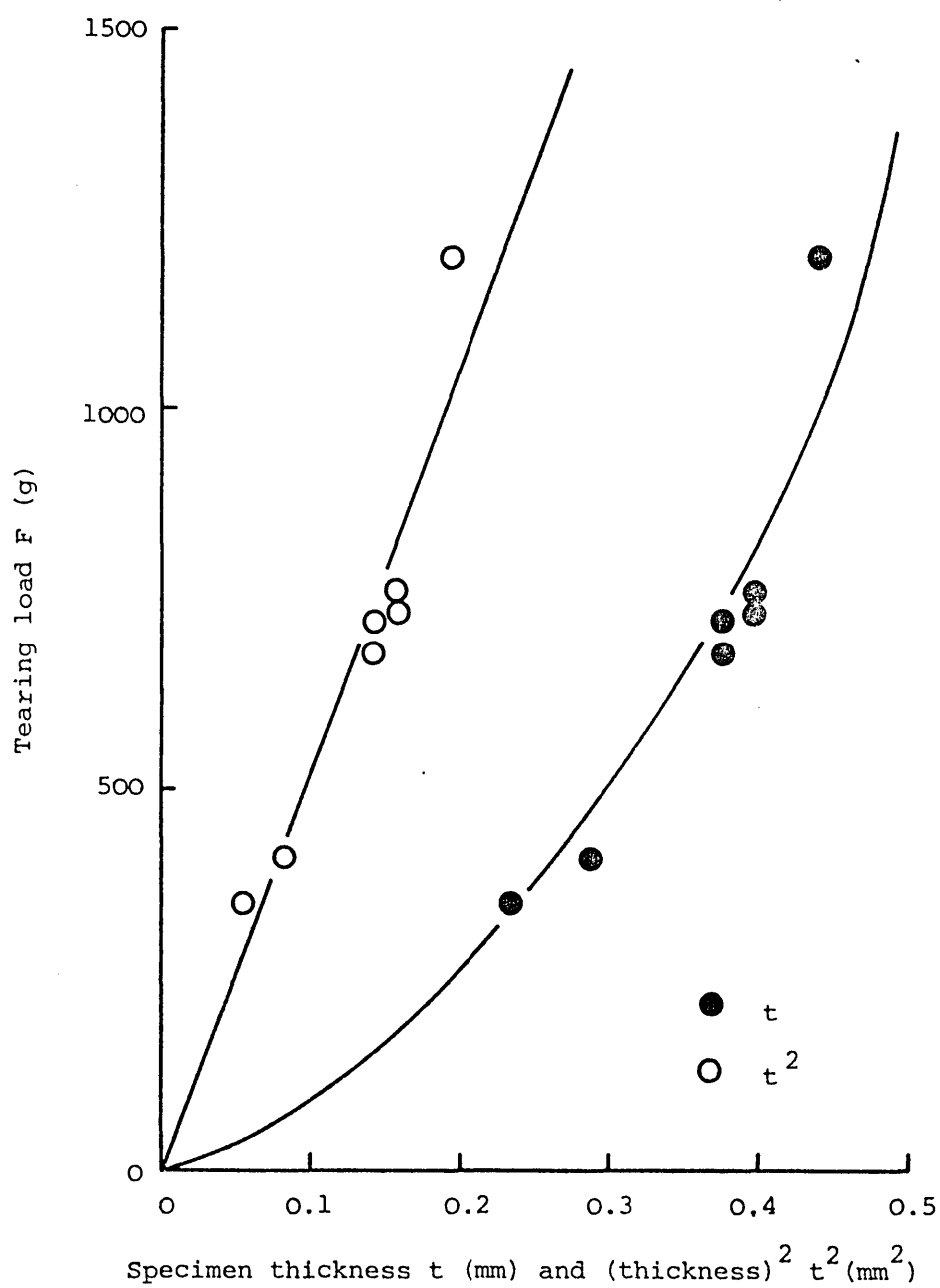


Figure 8.31 Tearing load as a function of  $t$  and  $t^2$  for TR4122 BEN/HEP at +40°C.

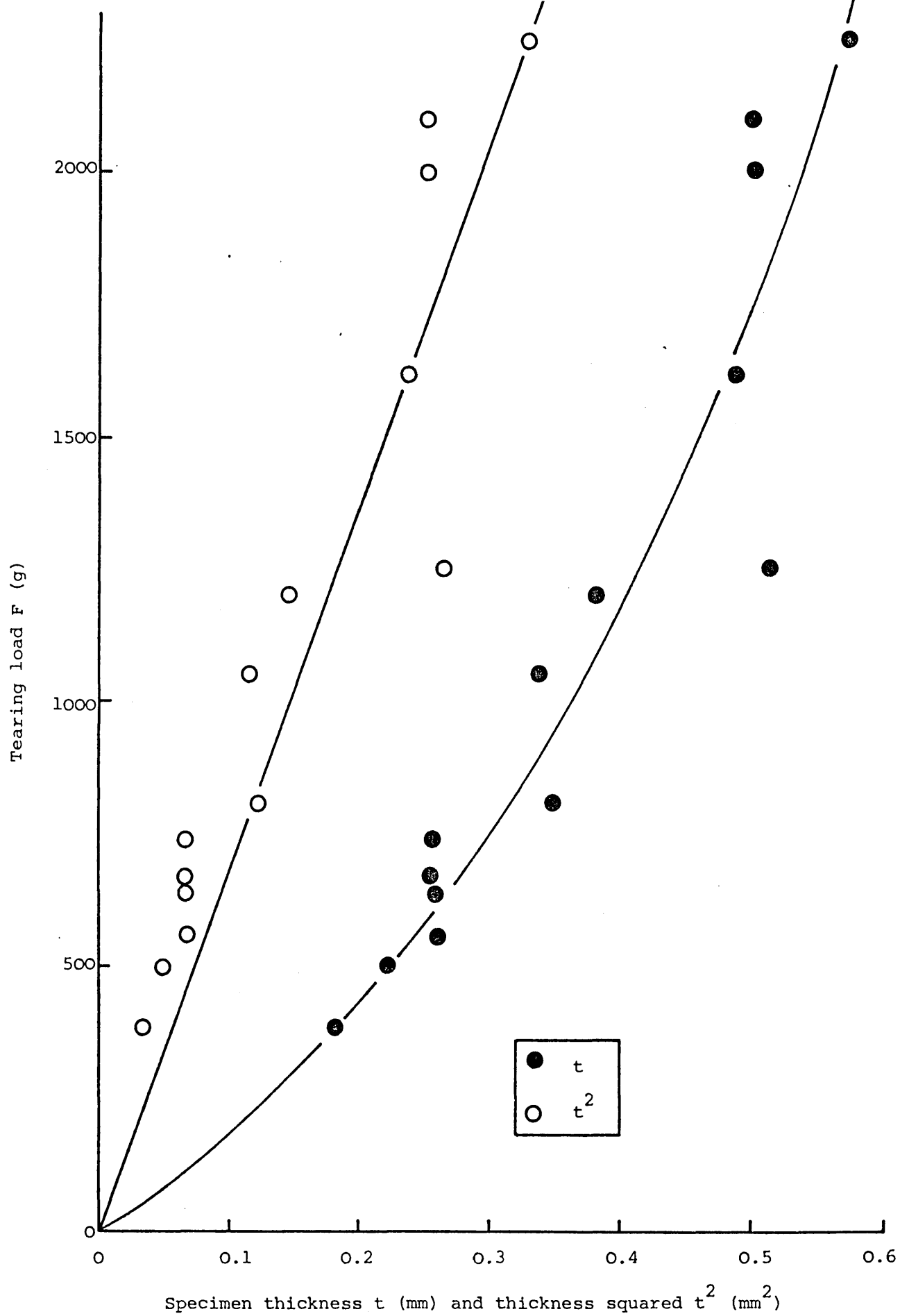


Figure 8.32 Tearing load as a function of  $t$  and  $t^2$  for all materials at  $-80^{\circ}\text{C}$ .

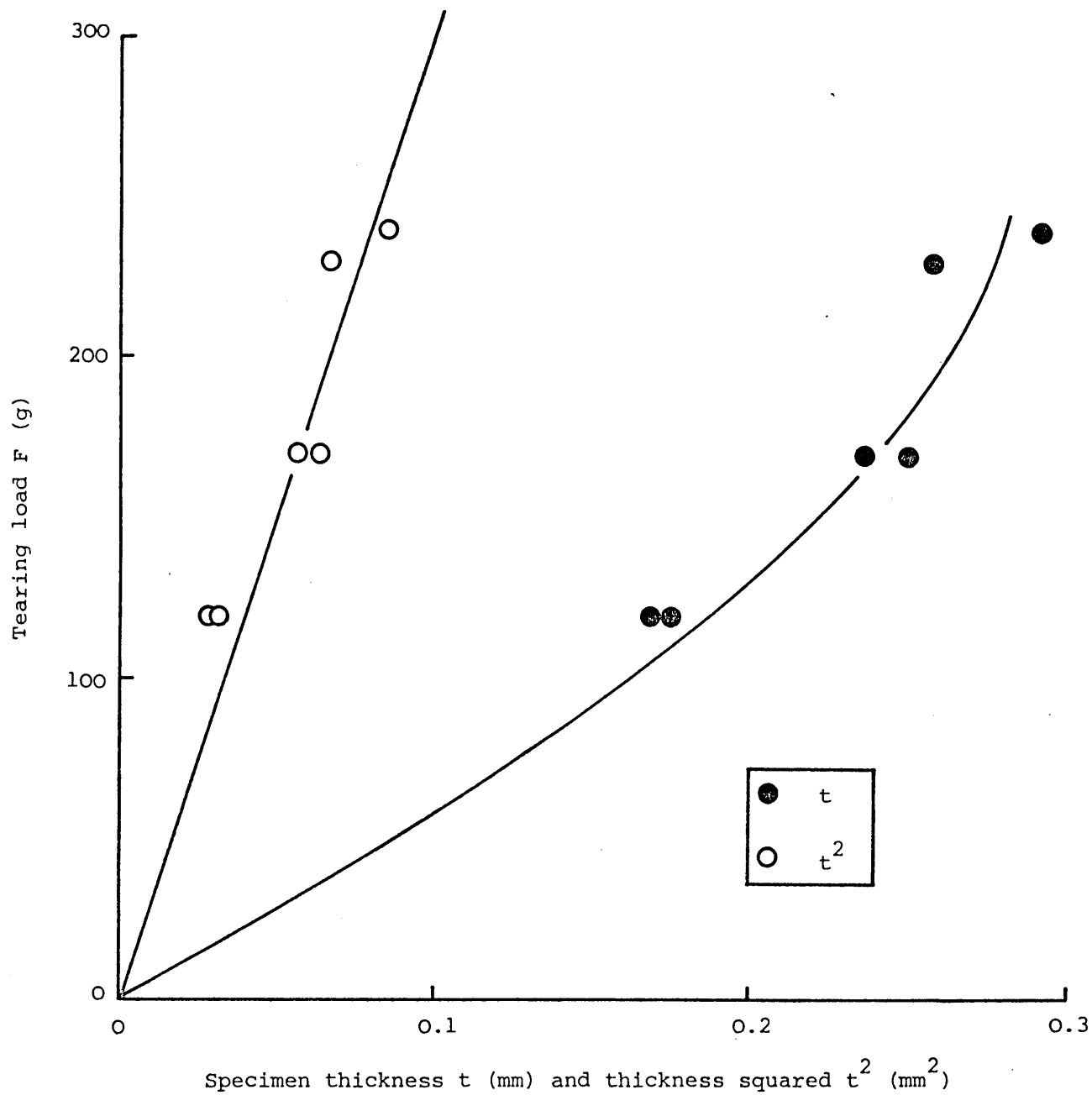


Figure 8.33 Tearing load as a function of  $t$  and  $t^2$  for TR4122 THF/MEK at +20°C.

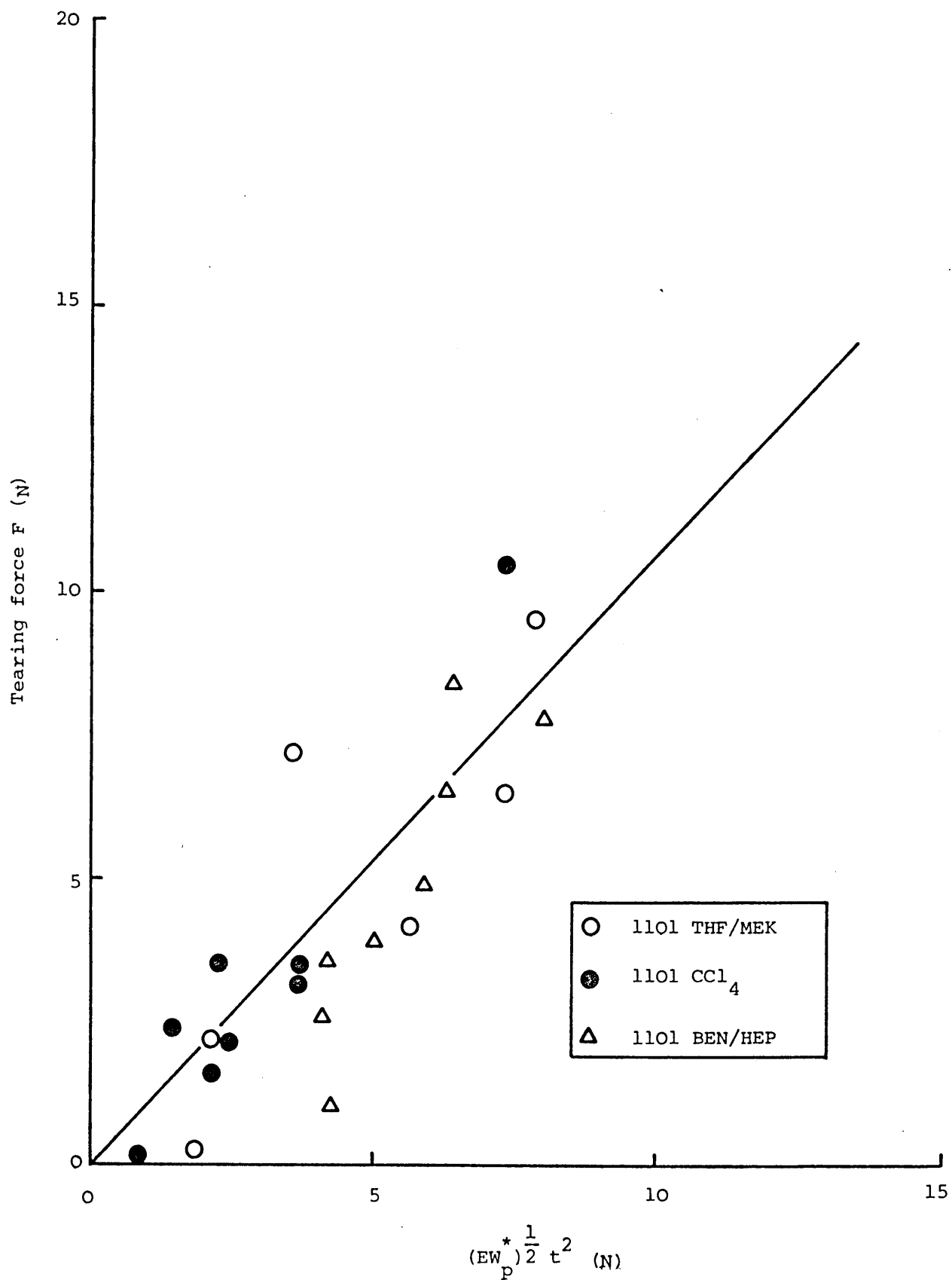


Figure 8.34 Tearing force as a function of the tensile parameter for TR1101 cast from several solvent systems. At a tearing rate of  $0.1 \text{ cm.min}^{-1}$  and all temperatures.

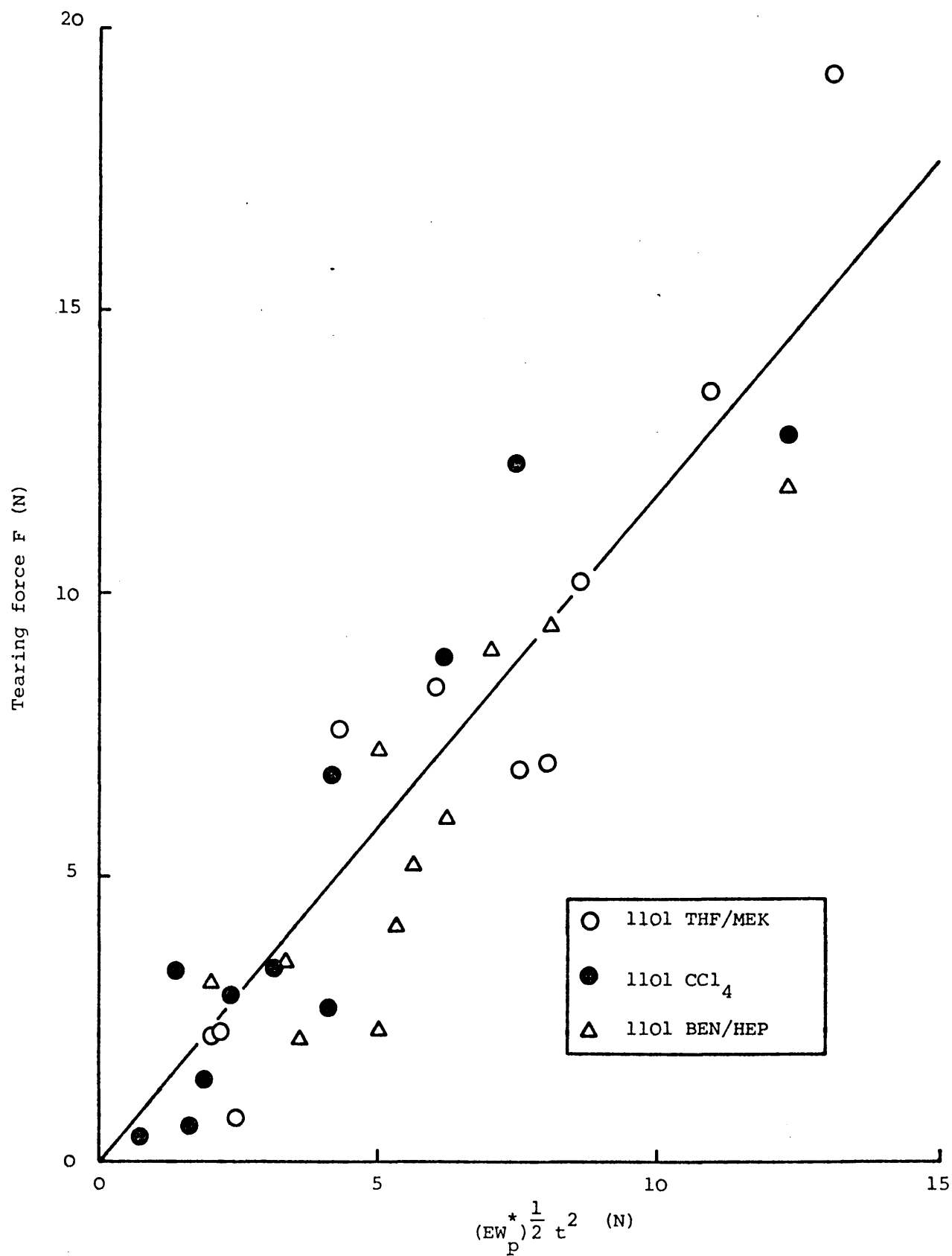


Figure 8.35 Tearing force as a function of the tensile parameter for TR1101 cast from several solvent systems. At a tearing rate of  $0.5 \text{ cm} \cdot \text{min}^{-1}$  and all temperatures.

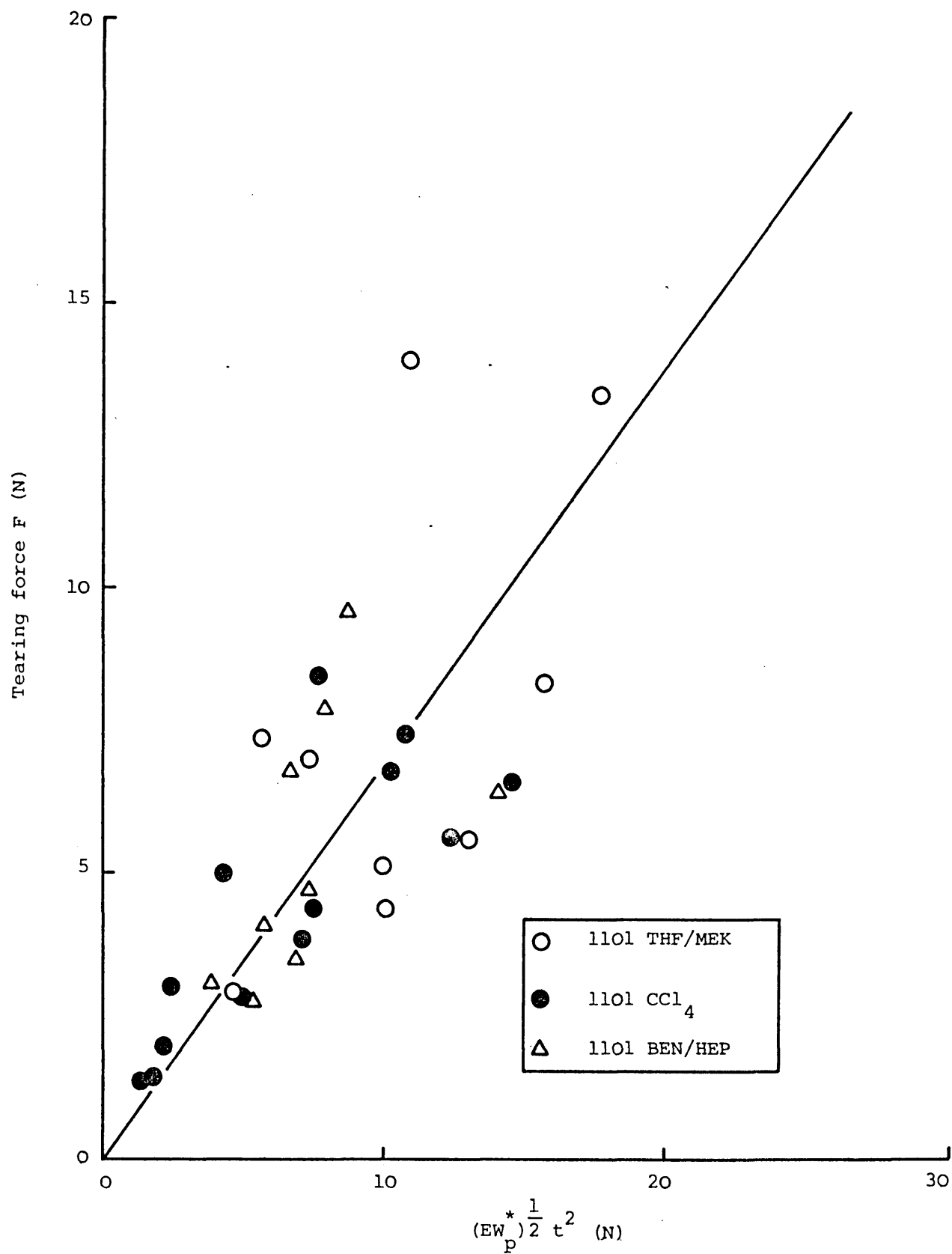


Figure 8.36 Tearing force as a function of the tensile parameter for TR1101 cast from several solvent systems. At a tearing rate of  $10 \text{ cm.min}^{-1}$  and all temperatures.

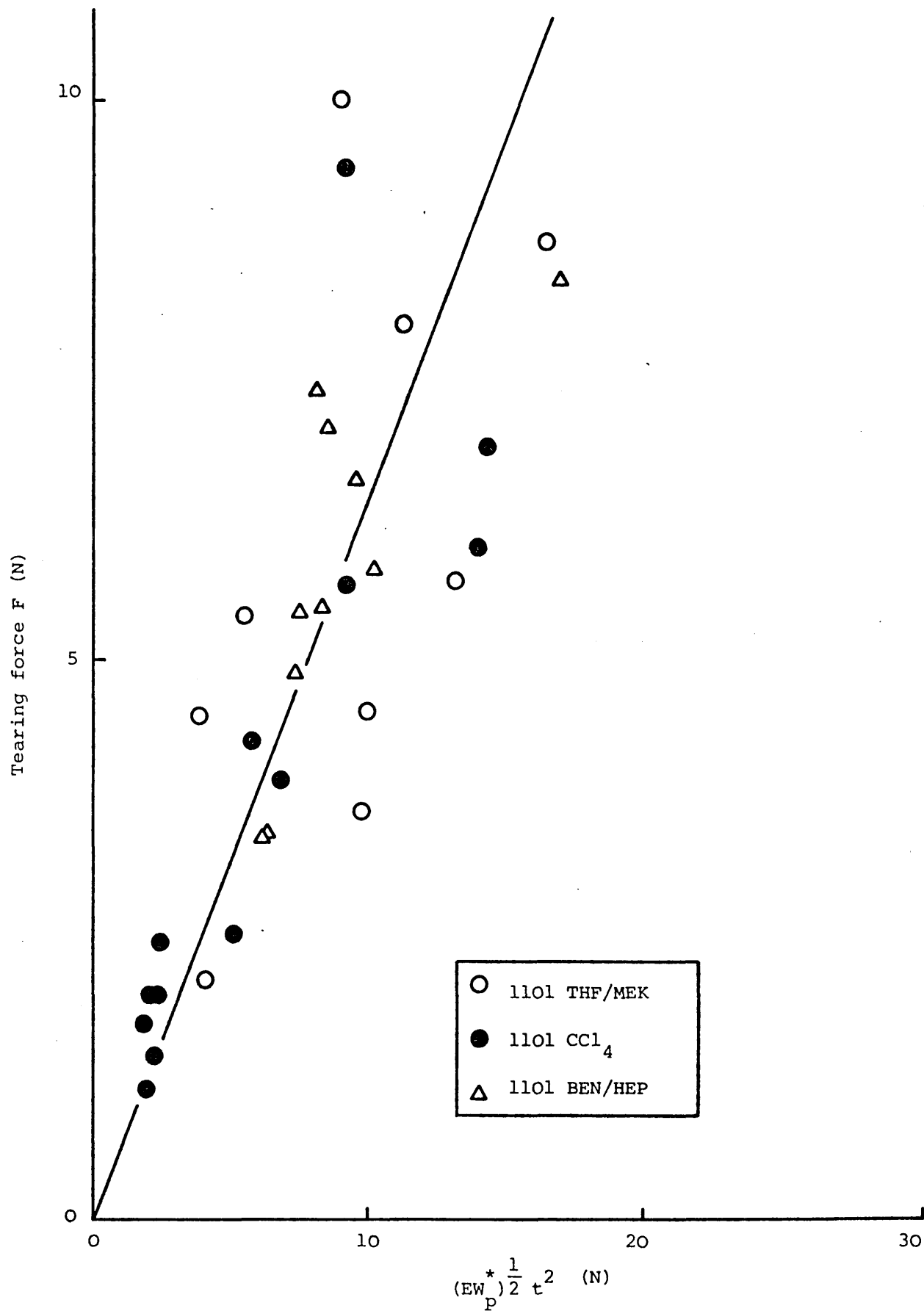


Figure 8.37 Tearing force as a function of the tensile parameter for TR1101 cast from several solvent systems. At a tearing rate of  $50 \text{ cm.min}^{-1}$  and all temperatures.

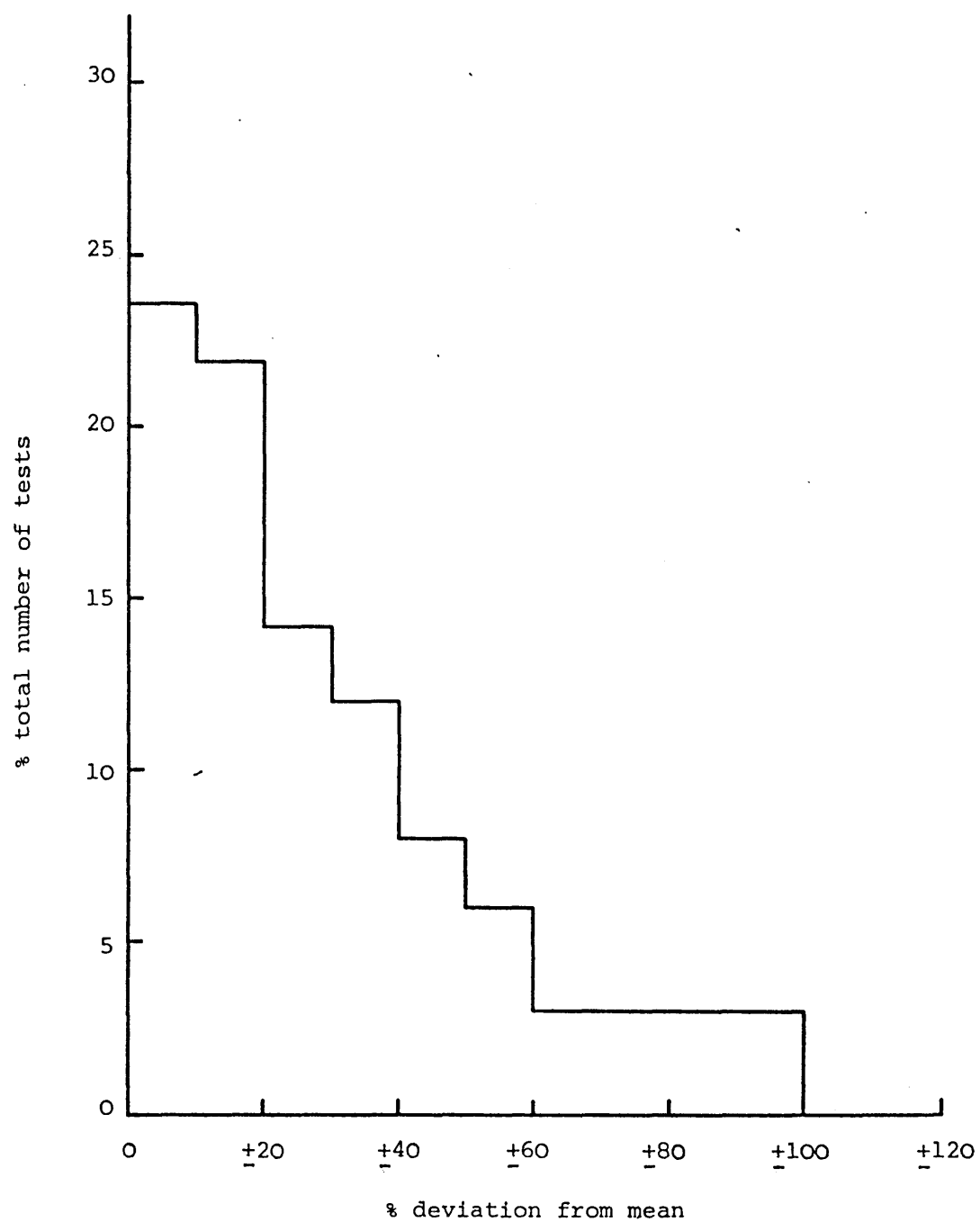


Figure 8.38 Histogram showing the distribution of the measured force about the predicted force.



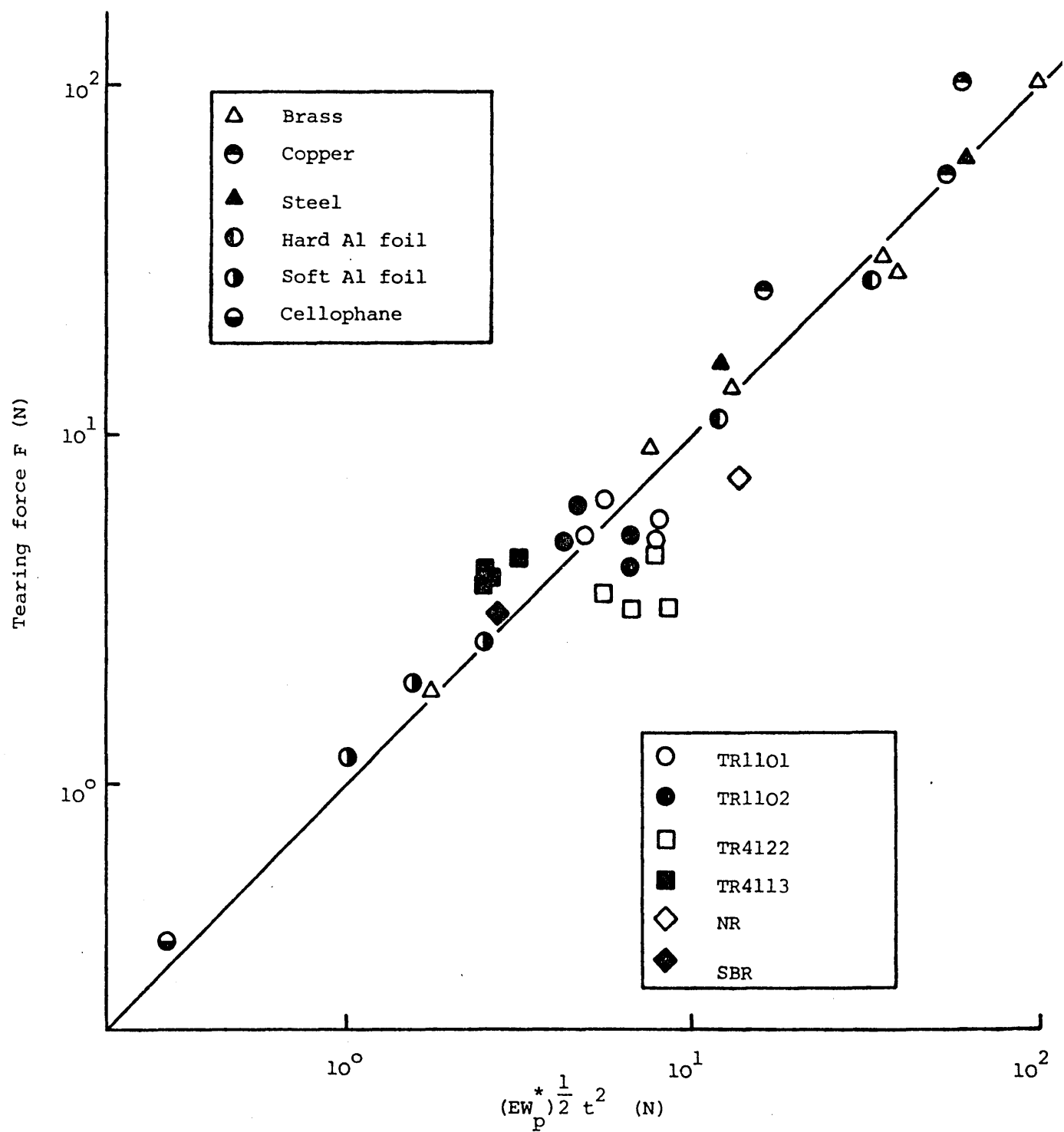


Figure 8.39 Tearing force as a function of the tensile parameter showing data from ref. 294, results for block copolymers, natural rubber and SBR.

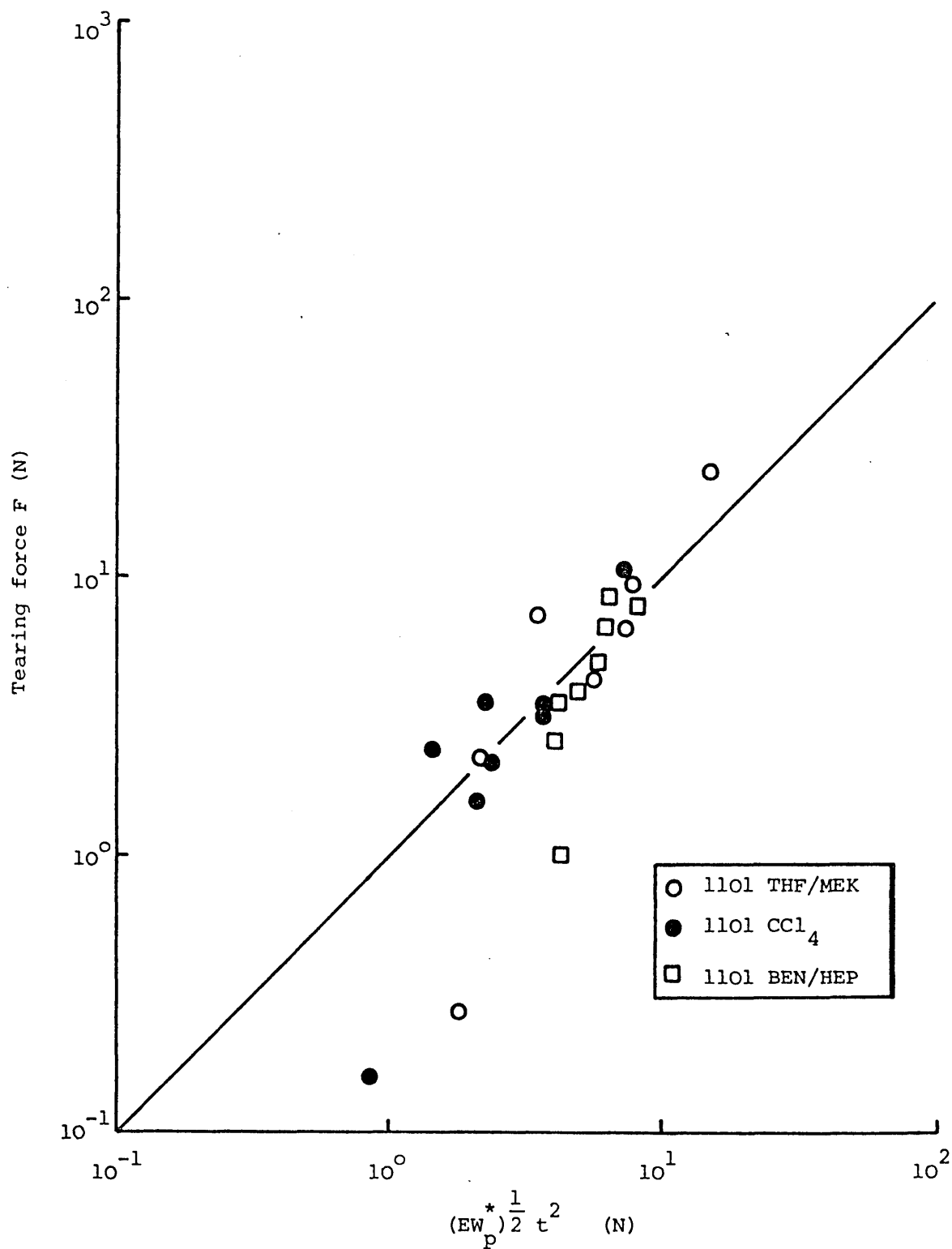


Figure 8.40 Tearing force as a function of the tensile parameter for TR1101, including all temperatures and solvents at  $0.1 \text{ cm.min}^{-1}$ .

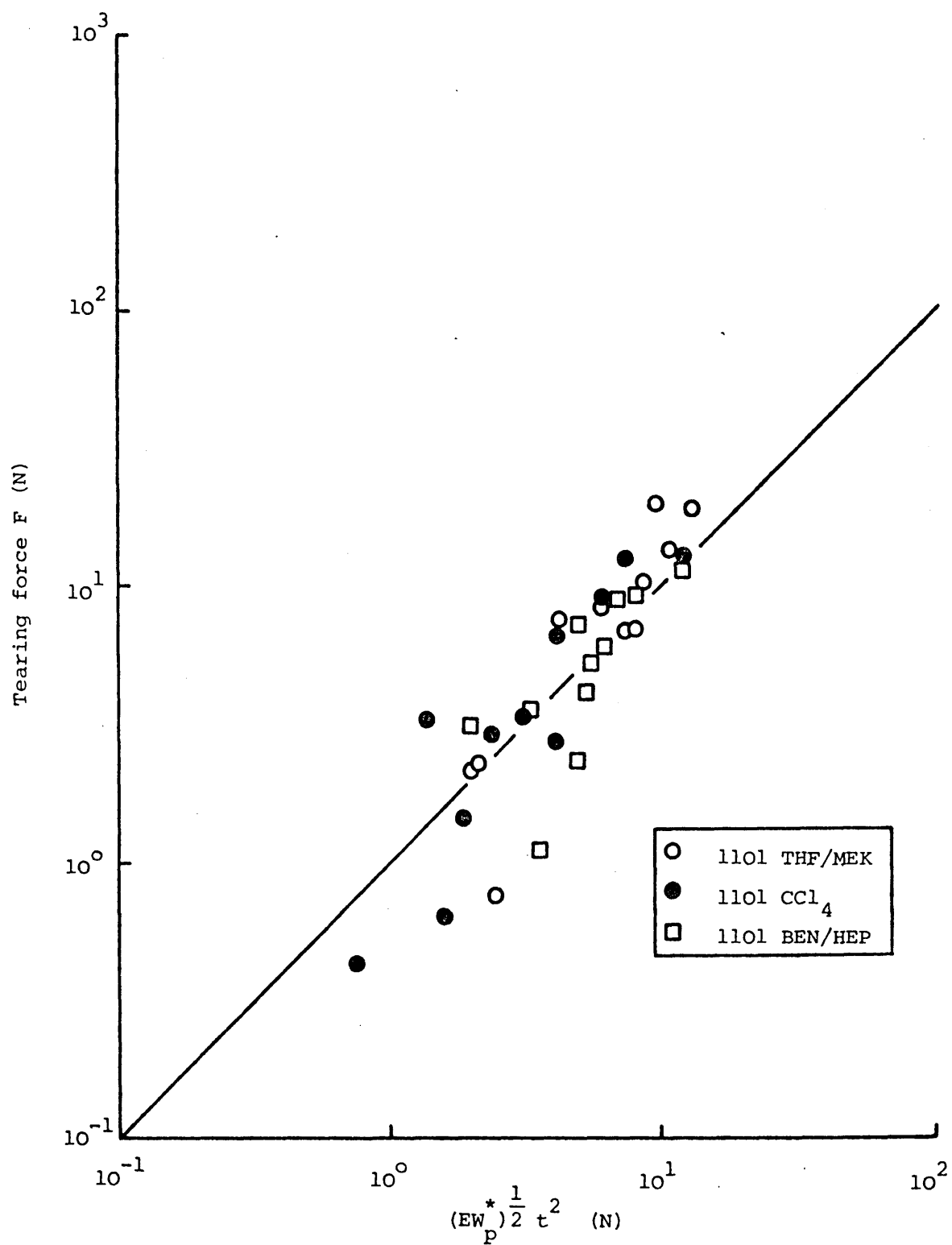


Figure 8.41 Tearing force as a function of the tensile parameter for TR1101, including all temperatures and solvents at  $0.5 \text{ cm} \cdot \text{min}^{-1}$ .

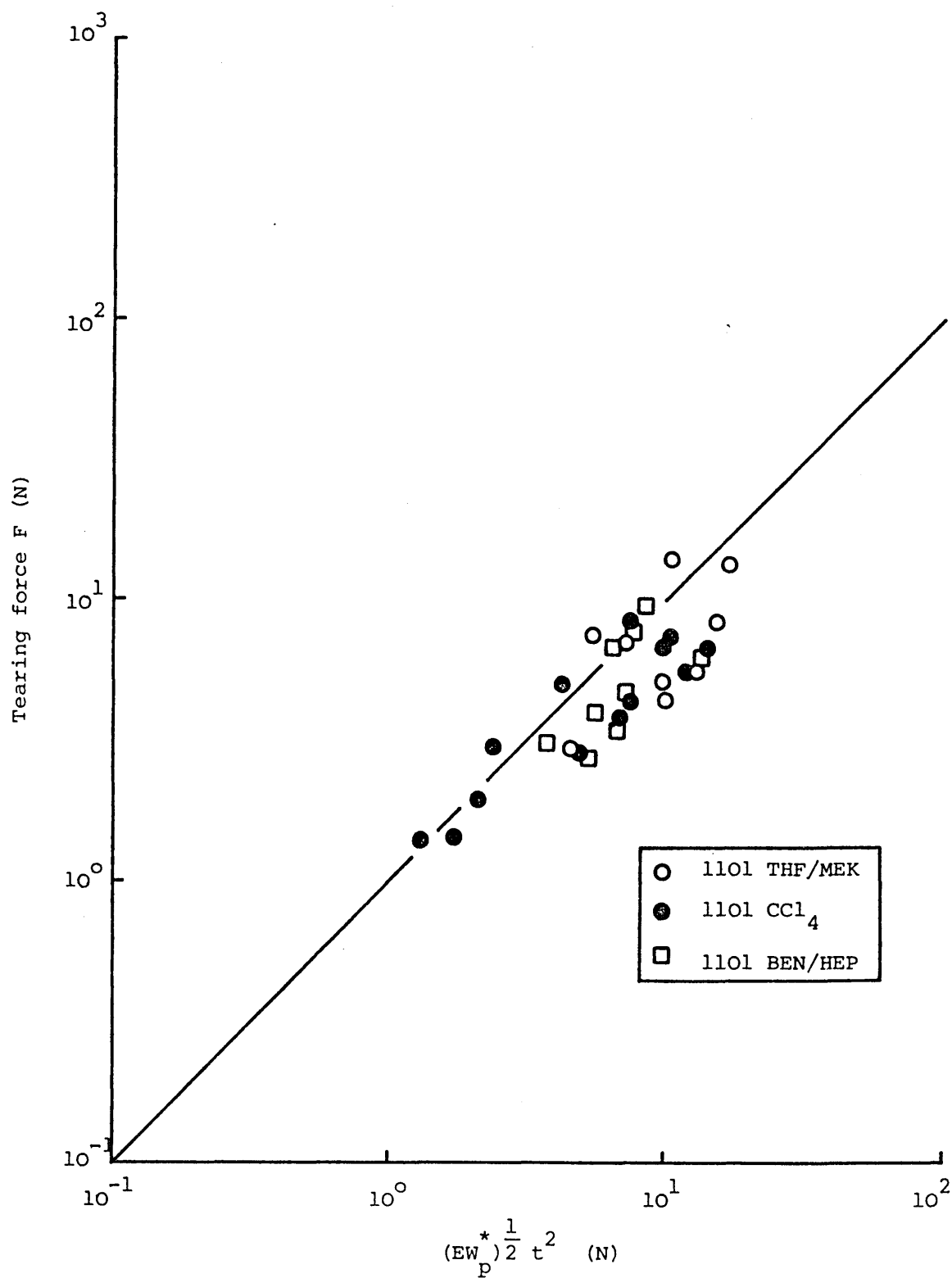


Figure 8.42 Tearing force as a function of the tensile parameter for TR1101, including all temperatures and solvents at  $10 \text{ cm.min}^{-1}$ .

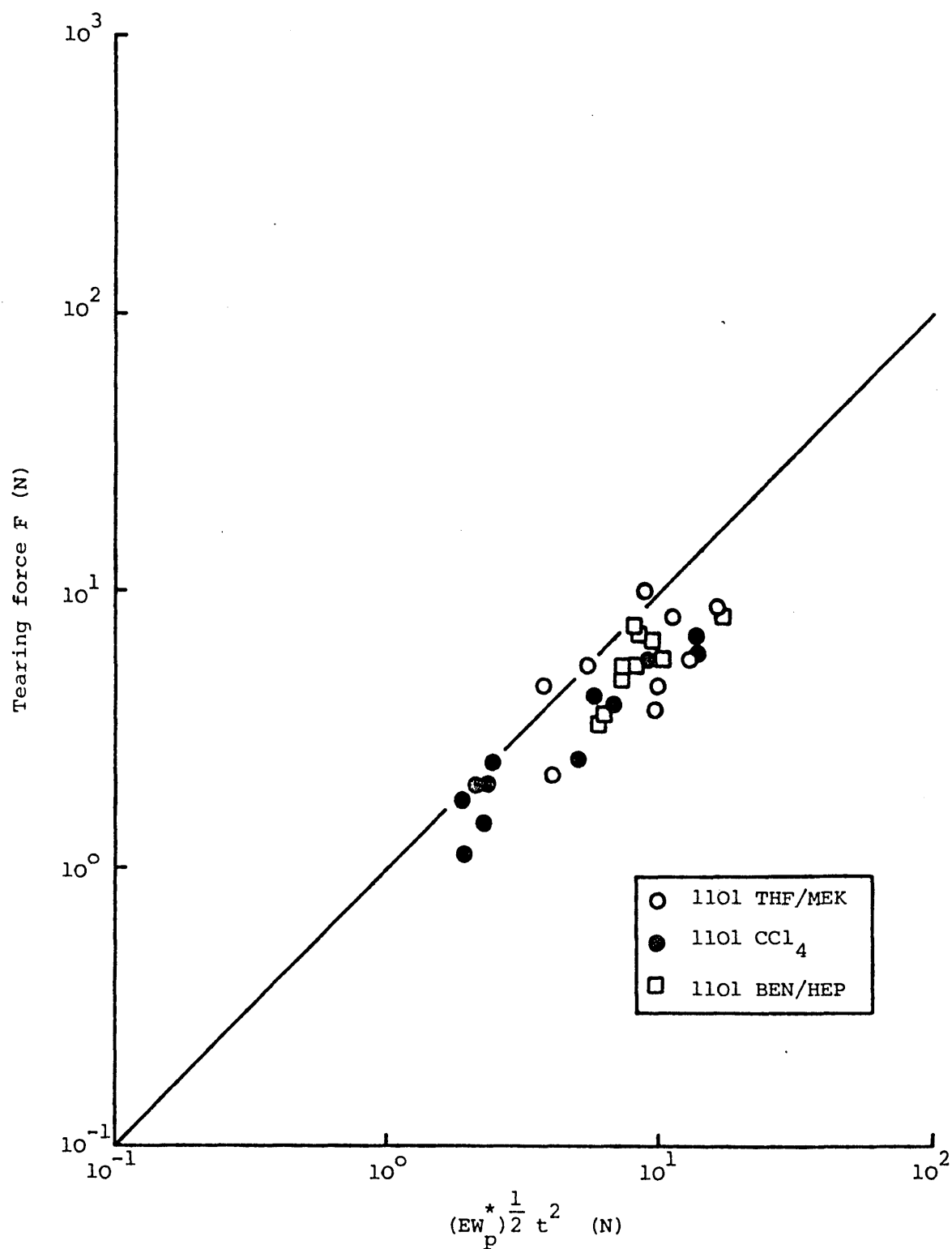


Figure 8.43 Tearing force as a function of the tensile parameter for TR1101, including all temperatures and solvents at  $50 \text{ cm.min}^{-1}$ .

The use of a variety of instruments for the measurement of molecular weights, styrene content and butadiene microstructure has proved to be an interesting exercise. Some of the instruments employed were clearly not adequate for the purpose intended for this class of materials, although in other circumstances their performance would be quite satisfactory. For the measurement of block molecular weight by gel permeation chromatography, the instrument must be designed with the specific type of polymer to be tested in mind. The set of columns used by the group at Akron would appear to be close to the ideal for these materials. Again, although all the nuclear magnetic resonance spectrometers used were capable of measuring the proportion of styrene in the samples, only the 300 MHz instrument was able to resolve the diene centre block in order that the microstructure could be analysed. The final results of the chemical characterisation are thought to be highly satisfactory and, where comparisons with other published data can be made, good agreement is achieved.

The swelling experiment, whilst being fairly simple in concept and technique, does require a number of major assumptions in the analysis and, although the absolute values of molecular weight between entanglements,  $M_c$ , cannot be relied upon too greatly, they do compare well with data published elsewhere. The main difficulty with these materials is that the morphologies are not the same, whereas the theory assumes a single morphology, and in fact was originally developed for vulcanised rubbers rather than block copolymers. This does not, however, invalidate the results completely, and the technique does probably class the materials correctly according to their molecular weight between cross-links or entanglements.

Transmission electron microscopy and small angle X-ray scattering do not individually produce sufficient evidence to designate categorically the microstructures involved. However, the results taken together do allow fairly firm proposals to be made for the morphologies of these materials. Not surprisingly, considering the styrene contents involved, the polymers appear to contain a mixture of morphologies, lamellar, cylindrical and spherical formations being noted often in the same sample. The size of the domains, that is the diameters of cylinders and spheres and the thickness of lamellae, and their spacing, is shown to be dependent

upon both the styrene fraction and the molecular weight of the individual blocks making up the polymer.

Dynamic tests in both shear and tension reveal the complex nature of these materials, with separate viscoelastic transitions indicated by loss tangent peaks corresponding to the styrene and butadiene phases. As the temperature is increased from  $-100^{\circ}\text{C}$ , the modulus decreases catastrophically as the sample passes through the butadiene glass transition. A plateau region spanning some  $140^{\circ}\text{C}$  is then experienced, during which the modulus falls quite slowly. Finally, as the styrene glass transition is approached, the modulus again falls dramatically. The level of modulus at any temperature is determined largely by the styrene fraction and casting solvent, that is by the morphology of the system. The effect of the plasticiser, on those systems containing it, is to reduce the modulus in the plateau region, although no effect is noted at low temperature. The high styrene polymer containing plasticiser (TR4122) does not suffer as greatly from this reduced modulus effect in the plateau region as does the lower styrene polymer (TR4113), which in effect is equivalent to TR1101 but with the added plasticiser. This could be expected since the lamellar structure of the high styrene material is bound to increase the modulus. The effect of the plasticiser is obviously to plasticise the styrene phase since high strain properties are affected far less radically than low strain properties, which are largely a function of the styrene phase. \*

Tensile tests at  $+20^{\circ}\text{C}$  revealed the full extent of changes in microstructure and styrene content. The initial modulus being a function of the structure of the styrene phase, with the modulus of the lower styrene TR1102 cast from THF/MEK being considerably higher than that for TR1101 cast from BEN/HEP or  $\text{CCl}_4$ . Ethyl acetate and THF/MEK cast polymers exhibited a necking phenomenon, whilst those cast from BEN/HEP and  $\text{CCl}_4$  did not. At high strains, the materials behave as conventional rubbers, but differences between materials are still evident. TR1101 fracturing at lower strains than TR1102, and the ultimate modulus being dependent upon microstructure. The tensile data was analysed using the theory developed by Kaelble et al, in which the complete stress-strain curve is described by a function including a debonding parameter, allowing the postulation of a cavitation process which effectively defines the dimensionality of the void growth in the material over the drawing region. This analysis has shown that initially the defects grow three-dimensionally in all the materials, but at a later stage the dimensionality changes. This second stage of void growth and its dimensionality depend not only on the material under test but also on the solvent system from which the material was cast,

\* Although  $T_g$  data does not strongly support large proportions of plasticiser in the styrene phase.

that is the microstructure. The strain at which the change-over from three-dimensional void growth to the lower dimensionality occurs is also found to be a function of microstructure.

Although the treatment of these materials as composites is reasonable in view of their two-phase structure, owing to their complex microstructure, the analysis required to predict elastic properties becomes very complicated. The relatively simple parallel and series models do not describe or take account of these microstructural variations. However, it has been shown that an extension of this approach, including a structure factor (the Einstein coefficient) to take account of morphological variations caused by changes in block size and casting solvent, is a viable proposition in the description of the elastic and viscoelastic properties of this class of materials. The correlations between predicted and experimental data, whilst far from perfect, do suggest that with further refinement of both the theory and its application far better agreement could be reached between predictions and measured quantities.

The tear testing of SBS block copolymers was found to be a difficult experiment under most of the conditions used in this work. The recorded data has essentially been treated in two distinct fashions; firstly, following the conventional approach initiated by researchers in the rubber industry, and secondly, an attempt has been made to relate the tearing data to the tensile properties of the material. The conventional theory for the tearing of rubbery materials relies on the tearing force being linearly dependent upon the torn thickness. This does not, however, appear to be the case with SBS block copolymers, since in all cases where a sufficiently wide variety of specimen thicknesses were tested, the relation was found to be more nearly (thickness)<sup>2</sup>. So that, although the data have been analysed thoroughly according to conventional wisdom, one of the basic tenets of the theory has not in fact been satisfied, and it would appear that this approach is perhaps not the most appropriate. However, it is worth recording that comparisons with other rubbery materials, which have been subjected to the same theoretical approach, have favoured SBS block copolymers as being equivalent to the best available vulcanised elastomers over a wide range of temperature and tearing rate.

Apart from the considerably reduced degree of presentation difficulties, the alternative treatment of the tearing data demonstrates a very interesting relationship between tearing force and tensile properties. The correlation between tearing force and the product of elastic modulus, energy to break and thickness squared holds over wide



temperature and tearing rate ranges for both raw and plasticised materials, whatever the microstructure. Not only that, but it is shown to place SBS block copolymers within the general scheme of things by placing them, with a reasonable degree of precision, on the hierarchical ladder formed by a large number of very dissimilar materials subjected to a similar analysis.

## REFERENCES

- [1] BURLANT, W.J., & HOFFMAN, A.S.  
Block and graft copolymers  
Reinhold, New York, 1960.
- [2] CERESA, R.J.  
*Polymer*, 1, 477, 1960.
- [3] CERESA, R.J.  
Block and graft copolymers  
Butterworth, London, 1962.
- [4] KOLESNIKOV, G.S., & YARALOV, L.K.  
*Russian Chem. Rev. (Eng. Trans.)*, 34 (3), 195, 1965.
- [5] GREBER, G.  
*Makromol. Chem.*, 101, 104, 1967.
- [6] ZELINSKI, R., & CHILDERS, C.W.  
*Rubb. Chem. Tech.*, 41 (1), 161, 1968.
- [7] SCHLICK, S., & LEVY, M.  
*J. Am. Chem. Soc.*, 64, 883, 1960.
- [8] REMBAUM, A., ELLIS, F.R., MORROW, R.C., & TOBOLSKY, A.V.  
*J. Poly. Sci.*, 61, 155, 1962.
- [9] BAER, M.  
*J. Poly. Sci.*, A-2, 417, 1964.
- [10] FREYSS, D., REMPP, P., & BENOIT, H.  
*J. Poly. Sci., Poly. Lett.*, 2, 271, 1964.
- [11] REMBAUM, A., MOACANIN, J., & CUDDIHY, E.  
*J. Poly. Sci.*, C-4, 529, 1964.
- [12] ANGELO, R.J., IKEDA, R.M., & WALLACH, M.L.  
*Polymer*, 6, 141, 1965.
- [13] CRAMMOND, D.N., LAWRY, P.S., & URWIN, J.R.  
*Eur. Poly. J.*, 2, 107, 1966.
- [14] MORTON, M., McGRATH, J.E., & JULIANO, P.C.  
*Div. Rubb. Chem., Am. Chem. Soc.*, Montreal, May 1967, Preprints.
- [15] YAMAZAKI, N., SHIRAKAWA, H., & KAMBARA, S.  
*J. Poly. Sci.*, C-16, 1685, 1967.

- [16] BRADFORD, E.B., & VANZO, E.  
*J. Poly. Sci.*, A-1 (6), 1661, 1968.
- [17] CRAMMOND, D.N., & URWIN, J.R.  
*Australian J. Chem.*, 21, 1835, 1968.
- [18] CUNNINGHAM, R.E., & TREIBER, M.R.  
*J. Appl. Poly. Sci.*, 12, 23, 1968.
- [19] BRADFORD, E.B., & VANZO, E.  
*J. Poly. Sci.*, C-26, 161, 1969.
- [20] CRAMMOND, D.N., & URWIN, J.R.  
*Eur. Poly. J.*, 5, 35, 1969.
- [21] CRAMMOND, D.N., & URWIN, J.R.  
*Eur. Poly. J.*, 5, 45, 1969.
- [22] FETTERS, L.J.  
*J. Poly. Sci.*, C-26, 1, 1969.
- [23] MORTON, M.  
*Polymer Preprints*, 10, 512, 1969.
- [24] WORSFOLD, D.J., & BYWATER, S.  
*Can. J. Chem.*, 42, 2884, 1964.
- [25] KUNTZ, I., & GERBER, A.  
*J. Poly. Sci.*, 42, 299, 1960.
- [26] WAGNER, R.H., & MOORE, L.D., Jr.  
"Physical methods of organic chemistry" in Determination of particle size and molecular weight  
(ed. Weissberger, A.), Part I, 816-894, Interscience, 1959.
- [27] BONNAR, R.U., DIMBAT, M., & STROSS, F.H.  
"Number-average molecular weights",  
288-293, Interscience, 1958.
- [28] DOTY, P.M., & SPURLIN, H.M.  
"Determination of molecular weight and molecular weight distribution" in Cellulose and cellulose derivatives  
(ed. Lott, E., et al), Part III, 1173-1188, Interscience, 1955.
- [29] REMPP, P., & BENOIT, H.  
*Rubb. Chem. Tech.*, 41, 245, 1968.
- [30] GRUBISIC, Z., REMPP, P., & BENOIT, H.  
*J. Poly. Sci.*, B-5, 735, 1967.

- [31] MORTON, M., McGRATH, J.E., & JULIANO, P.C.  
*J. Poly. Sci.*, C-26, 99, 1969.
- [32] DOUY, A., & GALLOT, B.  
*Die Makro. Chemie*, 156, 81, 1972.
- [33] MAYER, R.  
*Polymer*, 15, 137, 1974.
- [34] DOUY, A., & GALLOT, B.  
*Die Makro. Chemie*, 165, 297, 1973.
- [35] CAMPOS-LOPEZ, E., McINTYRE, D., & FETTERS, L.J. .  
*Macromolecules*, 6 (3), 415, 1973.
- [36] FETTERS, L.J., MEYER, B.H., & McINTYRE, D.  
*J. Appl. Poly. Sci.*, 16, 2079, 1972.
- [37] BOVEY, F.A., TIERS, G.V.D., & FILIPOVICH, G.  
*J. Poly. Sci.*, 38, 73, 1959.
- [38] SANTEE, E.R., Jr., MALOTKY, L.O., & MORTON, M.  
*Rubb. Chem. Tech.*, 46, 5, 1973.
- [39] SANTEE, E.R., Jr., CHANG, R., & MORTON, M.  
*J. Poly. Sci., Poly. Lett.*, 7, 449, 1973.
- [40] SANTEE, E.R., Jr., MOCHEL, V.D., & MORTON, M.  
*J. Poly. Sci., Poly. Lett.*, 7, 453, 1973.
- [41] MOCHEL, V.D.  
*Rubb. Chem. Tech.*, 4, 1200, 1967.
- [42] TANAKA, Y., TAKEUCHI, Y., KOBAYASHI, M., & TADOKORO, H.  
*J. Poly. Sci.*, A-2 (9), 43, 1971.
- [43] MORTON, M., FETTERS, L.J., SCHWAB, F.C., STRAUSS, C.R., & KAMMERECK, R.F.  
*Int. Rubb. Symp.*, London, 3, 70, 1969.
- [44] ROSEN, S.L.  
*Poly. Eng. Sci.*, 7 (2), 115, 1967.
- [45] FEDERS, R.F.  
*J. Poly. Sci.*, C-26, 189, 1969.
- [46] MEIER, D.J.  
*J. Poly. Sci.*, C-26, 81, 1969.
- [47] KRAUSE, S.  
*J. Poly. Sci.*, A-2 (7), 249, 1969.

- [48] KRAUSE, S.  
*Macromolecules*, 3, 84, 1970.
- [49] HOLDEN, G., BISHOP, E.T., & LEGGE, N.R.  
*J. Poly. Sci.*, C-26, 37, 1969.
- [50] INOUE, T., SOEN, T., KAWAI, H., FUKATSU, M., & KURATA, M.  
*J. Poly. Sci., Poly. Lett.*, 6, 75, 1968.
- [51] MATSUO, M.  
*Japan Plastics*, 6, July 1968.
- [52] SOEN, T., INOUE, T., MIYOSHI, K., & KAWAI, H.  
*J. Poly. Sci.*, A-2 (10), 1757, 1972.
- [53] CORISH, P.J.  
*Rubb. Chem. Tech.*, 40 (2), 324, 1967.
- [54] CLOUGH, S.B., & SCHNEIDER, N.S.  
US Army Tech. Rept. No. 67-77-CM, Natick Laboratories, Natick, Massachusetts, 1967.
- [55] TAKAYANAGI, M.  
*Mem. Fac. Eng. Kyushu Univ.*, 23 (1), 1, 1963.
- [56] "Some processing and end-use properties of Shell thermoplastic rubber",  
Shell Chemicals Tech. Bull., RB/68/9.
- [57] HOLDEN, G.  
*J. Elastoplastics*, 2, 234, October 1970.
- [58] KATO, K.  
*J. Poly. Sci., Poly. Lett.*, 4, 35, 1966.
- [59] KATO, K.  
*Poly. Eng. Sci.*, 7 (1), 38, 1967.
- [60] KATO, K.  
*Polymer*, 9, 225, 1968.
- [61] KATO, K.  
*Polymer*, 9, 419, 1968.
- [62] BEECHER, J.F., MARKER, L., BRADFORD, R.D., & AGGARWAL, S.L.  
*Polymer Preprints*, 8, 1532, 1967.
- [63] INOUE, T., SOEN, T., HASHIMOTO, T., & KWAI, H.  
Block copolymers  
(ed. Aggarwal, S.L.), 53-78, Plenum Press, 1970.

- [64] INOUE, T., SOEN, T., HASHIMOTO, T., KWAI, H.  
*J. Poly. Sci.*, A-2 (7), 1283, 1969.
- [65] MATSUO, M., UENO, T., HORINO, H., CHUJYO, S., & ASAI, H.  
*Polymer*, 9, 425, 1968.
- [66] MATSUO, M., SAGAE, S., & ASAI, H.  
*Polymer*, 10, 79, 1969.
- [67] MOLAU, G.E.  
*J. Poly. Sci., Poly. Lett.*, 3, 1007, 1965.
- [68] MOLAU, G.E., & WITTBRODT, W.M.  
*Macromolecules*, 1 (3), 260, 1968.
- [69] BLOKLAND, R., & PRINS, W.  
*J. Poly. Sci.*, A-2 (7), 1595, 1969.
- [70] LEWIS, P.R., & PRICE, C.  
*Polymer*, 12, 258, 1971.
- [71] LEWIS, P.R., & PRICE, C.  
*Polymer*, 13, 20, 1972.
- [72] BI, L.K., & FETTERS, L.J.  
*Macromolecules*, 8 (1), 90, 1975.
- [73] PEDEMONTE, E., & ALFONSO, G.C.  
*Macromolecules*, 8 (1), 85, 1975.
- [74] KELLER, A., PEDEMONTE, E., & WILLMOUTH, F.M.  
*K-Zuz Polymere*, 238, 25, 1970.
- [75] FOLKES, M.J., KELLER, A., & SCALISI, F.P.  
*Polymer*, 12 (12), 793, 1971.
- [76] DLUGOSZ, J., FOLKES, M.J., & KELLER, A.  
*J. Poly. Sci., Poly. Phys.*, 11, 929, 1973.
- [77] ODELL, J.A., & KELLER, A.  
*Poly. Eng. Sci.*, 17 (8), 544, 1977.
- [78] PEDEMONTE, E., TURTURRO, A., BIANCHI, U., & DEVETTA, P.  
*Polymer*, 14, 145, 1973.
- [79] PEDEMONTE, E., TURTURRO, A., & DONDERO, G.  
*Bri. Poly. J.*, 6, 277, 1974.
- [80] PEDEMONTE, E., DONDERO, G., & ALFONSO, G.C.  
*Polymer*, 16, 531, 1975.

- [81] HENDUS, H., ILLERS, K.H., & ROPTE, E.  
*Kolloid-Z.*, 216, 110, 1967.
- [82] FISCHER, E.  
*J. Macromol. Sci.-Chem.*, A-2 (6), 1285, 1968.
- [83] LEWIS, P.R., & PRICE, C.  
*Nature*, 223, 494, 1969.
- [84] BROWN, D.S., FULCHER, K.U., & WETTON, R.E.  
*J. Poly. Sci., Poly. Lett.*, 8, 659, 1970.
- [85] MCINTYRE, D., & CAMPOS-LOPEZ, E.  
*Macromolecules*, 3 (3), 322, 1970.
- [86] KIM, H.  
*Macromolecules*, 5, 594, 1972.
- [87] INOUE, T., MORITANI, M., HASHIMOTO, T., & KAWAI, H.  
*Macromolecules*, 4 (4), 500, 1971.
- [88] MONTIEL, R., KUO, C., & MCINTYRE, D.  
*Polymer Preprints*, 15 (2), 169, 1974.
- [89] PILLAI, P.S., LIVINGSTON, D.I., & STRANG, J.D.  
*Rubb. Chem. Tech.*, 241, 1972.
- [90] HASHIMOTO, T., NAGATOSHI, K., TODO, A., HASEGAWA, H., & KAWAI, H.  
*Macromolecules*, 7 (3), 364, 1974.
- [91] SADRON, C., & GALLOT, B.  
*Die Makromol. Chemie*, 164, 801, 1973.
- [92] CHILDERS, C.W., & KRAUS, G.  
*Rubb. Chem. Tech.*, 40, 1183, 1967.
- [93] KRAUS, G., CHILDERS, C.W., & GRUVER, J.T.  
*J. Appl. Poly. Sci.*, 11, 1581, 1967.
- [94] BEECHER, J.F., MARKER, L., BRADFORD, R.D., & AGGARWAL, S.L.  
*J. Poly. Sci.*, C-26, 117, 1969.
- [95] ROBINSON, R.A., & WHITE, E.F.T.  
Proc. Symp. Block Polym., ACS, New York, September 1969,  
Block copolymers  
(ed. Aggarwal, S.L.), 123-136, Plenum Press, 1970.
- [96] MIYAMOTO, T., KODAMA, K., & SHIBAYAMA, K.  
*J. Poly. Sci.*, A-2 (8), 2095, 1970.

- [97] KRAUS, G., ROLLMAN, K.W., & GARDNER, J.O.  
*J. Poly. Sci., Poly. Phys.*, 10, 2061, 1972.
- [98] COHEN, R.E., & TSCHOEGL, N.W.  
*Int. J. Poly. Mat.*, 2, 49, 1972.
- [99] COHEN, R.E., & TSCHOEGL, N.W.  
*Int. J. Poly. Mat.*, 3, 3, 1974.
- [100] FLORY, P.J., & REHNER, J.  
*J. Chem. Phys.*, 18, 108, 1943.
- [101] KRAUS, G.  
*J. Appl. Poly. Sci.*, 7, 861, 1963.
- [102] BISHOP, E.T., & DAVISON, S.  
*J. Poly. Sci.*, C-26, 59, 1969.
- [103] MEIER, D.J.  
*Appl. Poly. Symp.*, 24, 67, 1974.
- [104] GUTH, E.  
*J. Appl. Phys.*, 16, 20, 1945.
- [105] BONOTTO, S.  
*Rubber Age*, 98 (11), 79, 1966.
- [106] COOPER, S.L., HUH, D.S., & MORRIS, W.J.  
*Ind. Eng. Chem., Prod. Res. Develop.*, 7 (4), 248, 1968.
- [107] FIELDING-RUSSELL, G.S.  
*Rubb. Chem. Tech.*, 45 (1), 252, 1972.
- [108] SMITH, T.L., & DICKIE, R.A.  
*J. Poly. Sci.*, C-26, 163, 1969.
- [109] SMITH, T.L.  
*Polymer Preprints*, 10 (2), 670, 1969.
- [110] SMITH, T.L.  
Proc. Symp. Block Polym., ACS, New York, September 1969,  
Block copolymers  
(ed. Aggarwal, S.L.), 137, Plenum Press, 1970.
- [111] SMITH, T.L.  
*J. Poly. Sci., Poly. Phys.*, 12, 1825, 1974.
- [112] UCHIDA, T., SOEN, T., INOUE, T., & KAWAI, H.  
*J. Poly. Sci.*, A-2 (10), 101, 1972.
- [113] BRUNWIN, D.M., FISCHER, E., & HENDERSON, J.F.  
*J. Poly. Sci.*, C-26, 135, 1969.



- [114] FISCHER, E., & HENDERSON, J.F.  
*Rubb. Chem. Tech.*, 40 (5), 1373, 1967.
- [115] FISCHER, E., & HENDERSON, J.F..  
*J. Poly. Sci.*, C-26, 149, 1969.
- [116] HENDERSON, J.F., GRUNDY, K.H., & FISCHER, E.  
*J. Poly. Sci.*, C-16, 3121, 1968.
- [117] BAILEY, J.T., BISHOP, E.T., HENDRICKS, W.R., HOLDEN, G., &  
LEGGE, N.R.  
*Rubber Age*, 98, 69, 1966.
- [118] WILKES, G.L., & STEIN, R.S.  
*J. Poly. Sci.*, A-2 (7), 1525, 1969.
- [119] WILLIAMS, M.L., LANDEL, R.F., & FERRY, J.D.  
*J. Phys. Chem.*, 77, 3701, 1955.
- [120] NAGAMATSU, N., TADEMURA, T., YOSHITOMI, T., & TADEMOTO, T.  
*J. Poly. Sci.*, 33, 515, 1958.
- [121] VANZO, E.  
*J. Poly. Sci.*, A-1 (4), 1727, 1966.
- [122] SHEN, M., & KAELEBLE, D.H.  
*J. Poly. Sci., Poly. Lett.*, 8, 149, 1970.
- [123] FIELDING-RUSSELL, G.S., & FITZHUGH, R.L.  
*J. Poly. Sci.*, A-2, 1625, 1972.
- [124] FESKO, D.G., & TSCHOEGL, N.W.  
*Int. J. Poly. Mat.*, 3, 51, 1974.
- [125] LIM, C.K., COHEN, R.E., & TSCHOEGL, N.W.  
"Time-temperature superposition in block copolymers",  
ACS, Washington, 397-417, 1971.
- [126] KRAUS, G.  
*Rubb. Chem. Tech.*, 38 (5), 1070, 1965.
- [127] NIELSEN, L.E., & STOCKTON, F.D.  
*J. Poly. Sci.*, A-1, 1995, 1963.
- [128] SMALLWOOD, H.M.  
*J. Appl. Phys.*, 15, 758, 1944.
- [129] SCHWARZL, F.R., BREE, H.W., NEDERVEEN, C.J., STRUIK, L.C.E., &  
VANDERWAL, C.W.  
*Tno Nieuws*, 21, 74, 1966.

- [130] EINSTEIN, A.  
*Ann. Physik.*, 19, 289, 1906.
- [131] EINSTEIN, A.  
*Ann. Physik.*, 34, 591, 1911.
- [132] KERNER, E.H.  
*Proc. Phys. Soc. (London)*, B69, 808, 1956.
- [133] NIELSEN, L.E.  
*J. Appl. Poly. Sci.*, 10, 97, 1966.
- [134] TOBOLSKY, A.V.  
*J. Chem. Phys.*, 37, 1139, 1962.
- [135] UEMURA, S., & TAKAYANAGI, M.  
*J. Appl. Poly. Sci.*, 10, 113, 1966.
- [136] COOPER, S.L., & TOBOLSKY, A.V.  
*J. Appl. Poly. Sci.*, 10, 1837, 1966.
- [137] ZITEK, R., & ZELINGER, J.  
*J. Poly. Sci.*, A-1 (6), 467, 1968.
- [138] FUJINO, K., OGAWA, Y., & KWAI, H.  
*J. Appl. Poly. Sci.*, 8, 2147, 1964.
- [139] DICKIE, R.A.  
*J. Appl. Poly. Sci.*, 17, 45, 1973.
- [140] HASHIN, Z., & SHTRIKMAN, S.  
*J. Mech. Phys. Solids*, 11, 127, 1963.
- [141] TSAI, S.W.  
"Formulae for the elastic properties of fibre reinforced composites",  
AD 834851, National Tech. Inf. Service, Springfield, Virginia,  
June 1968.
- [142] ASHTON, J.E., HALPIN, J.C., & PETIT, P.H.  
Primer on composite materials: Analysis,  
Technomic Publishing Company, Stamford, Connecticut, Chapter 5, 1969.
- [143] HILL, R.  
*J. Mech. Phys. Solids*, 11, 357, 1963.
- [144] HILL, R.  
*J. Mech. Phys. Solids*, 12, 199, 1964.
- [145] HERMANS, J.J.  
*Koninkl. Nederl. Akademie Van Wetenschappen - Amsterdam, Proceedings*  
Series B, 70, 1, 1967.

- [146] HALPIN, J.C., & KARDOS, J.L.  
*Poly. Eng. Sci.*, 16 (5), 344, 1976.
- [147] NICOLAIS, L.  
*Poly. Eng. Sci.*, 15 (3), 137, 1975.
- [148] KARDOS, J.L., & RAISONI, J.  
*Poly. Eng. Sci.*, 15 (3), 183, 1975.
- [149] SMITH, J.C.  
*Poly. Eng. Sci.*, 16 (6), 394, 1976.
- [150] NIELSEN, L.E.  
*J. Appl. Phys.*, 41, 4626, 1970.
- [151] NIELSEN, L.E.  
*Rheol. Acta*, 13, 86, 1974.
- [152] SHEN, M., CIRLIN, E.H., & KAEUBLE, D.H.  
Colloidal and morphological behaviour of block and graft copolymers,  
(ed. Molau, G.E.), Plenum Press, New York, 307, 1971.
- [153] KAEUBLE, D.H., & CIRLIN, E.H.  
*ibid*, 295.
- [154] KAEUBLE, D.H.  
*Trans. Soc. Rheol.*, 15 (2), 235, 1971.
- [155] KAEUBLE, D.H., & CIRLIN, E.H.  
*J. Poly. Sci.*, Symp. No. 43, 131, 1973.
- [156] KAINRADL, P., & HANDLER, F.  
*Rubb. Chem. Tech.*, 23 (5), 1438, 1960.
- [157] RIVLIN, R.S., & THOMAS, A.G.  
*J. Poly. Sci.*, 10 (3), 291, 1953.
- [158] THOMAS, A.G.  
*J. Poly. Sci.*, 18, 177, 1955.
- [159] GREENSMITH, H.W., & THOMAS, A.G.  
*J. Poly. Sci.*, 18, 189, 1955.
- [160] GREENSMITH, H.W.  
*J. Poly. Sci.*, 21, 175, 1956.
- [161] THOMAS, A.G.  
*J. Poly. Sci.*, 31, 467, 1958.
- [162] THOMAS, A.G.  
*J. Appl. Poly. Sci.*, 3 (8), 168, 1960.

- [163] GREENSMITH, H.W.  
*J. Appl. Poly. Sci.*, 3 (8), 175, 1960.
- [164] GREENSMITH, H.W.  
*J. Appl. Poly. Sci.*, 3 (8), 183, 1960.
- [165] MULLINS, L.  
*Trans. Inst. Rubb. Ind.*, 35, 213, 1959.
- [166] GREENSMITH, H.W.  
*J. Appl. Poly. Sci.*, 7, 993, 1963.
- [167] ANDREWS, E.H.  
*J. Mech. Phys. Solids*, 11, 231, 1963.
- [168] ANDREWS, E.H.  
*Rubb. Chem. Tech.*, 36, 325, 1963.
- [169] GREENSMITH, H.W., MULLINS, L., & THOMAS, A.G.  
*Trans. Soc. Rheol.*, 4, 179, 1960.
- [170] GRIFFITH, A.A.  
*Phil. Trans.*, A221, 163, 1920.
- [171] GREENSMITH, H.W.  
*J. Appl. Poly. Sci.*, 8, 1113, 1964.
- [172] VEITH, A.G.  
*Rubb. Chem. Tech.*, 38, 700, 1965.
- [173] GENT, A.N., & HENRY, A.W.  
Proc. 5th Int. Rubber Conf., 193, 1967 (published 1968).
- [174] ANDREWS, E.H.  
*J. Appl. Phys.*, 32, 542, 1961.
- [175] GREENSMITH, H.W.  
Rheology of elastomers,  
(ed. Mason, P., & Wookey, N.), Pergamon Press, London, 113, 1958.
- [176] GREENSMITH, H.W., MULLINS, L., & THOMAS, A.G.  
The chemistry and physics of rubber-like substances,  
(ed. Bateman, L.), John Wiley, New York, 249, 1963.
- [177] BUSSE, W.F.  
*Rubb. Chem. Tech.*, 8, 122, 1935.
- [178] MULLINS, L.  
*Rubb. Chem. Tech.*, 33, 315, 1960.

- [179] MULLINS, L.  
The chemistry and physics of rubber-like structures,  
(ed. Bateman, L.), John Wiley, New York, 301, 1963.
- [180] HALPIN, J.C.  
*J. Appl. Phys.*, 35, 3133, 1964.
- [181] GUL, V.E.  
*Rubb. Chem. Tech.*, 34, 101, 1961.
- [182] PURDON, J.R., Jr., & MATE, R.D.  
*J. Poly. Sci.*, A-1 (6), 243, 1968.
- [183] FRANK, F.C., WARD, I.M., & WILLIAMS, T.  
*J. Poly. Sci.*, A-2 (6), 1357, 1968.
- [184] DAWKINS, J.V.  
*Br. Poly. J.*, 4, 87, 1972.
- [185] URWIN, J.R., & CRAMMOND, D.N.  
*Aust. J. Chem.*, 22, 543, 1969.
- [186] BENOIT, H., GRUBISIC, Z., REMPP, P., DECKER, D., & ZILLIOX, J.G.  
*J. Chim. Phys.*, 63, 1507, 1966.
- [187] COOPER, A.R., & JOHNSON, J.F.  
*J. Appl. Poly. Sci.*, 15, 2293, 1971.
- [188] COOPER, A.R., & KISS, I., Jr.  
*Br. Poly. J.*, 5, 433, 1973.
- [189] YAU, W.W., SUCHAN, H.L., & MALONE, C.P.  
*J. Poly. Sci.*, A-2 (6), 1349, 1968.
- [190] COOPER, A.R., JOHNSON, J.F., & BRUZZONE, A.R.  
ACS Div. Poly. Chem. Preprints, 10, 1455, 1969.
- [191] SMITH, W.V., & FELDMAN, G.A.  
*J. Poly. Sci.*, A-2 (7), 163, 1969.
- [192] CHEN, H.Y.  
*Anal. Chem.*, 34, 1134, 1962.
- [193] CHEN, H.Y.  
*Anal. Chem.*, 34, 1793, 1962.
- [194] SENN, W.L., Jr.  
*Anal. Chim. Acta*, 29, 505, 1963.
- [195] KRAUS, G., & MOCZVIGEMBA, G.A.  
*J. Poly. Sci.*, A-2, 277, 1964.

- [196] HASSAN, A.M., & RAY, L.N., Jr.  
*J. Appl. Poly. Sci.*, 15, 1837, 1971.
- [197] GENT, A.N., & KUAN, T.H.  
*J. Poly. Sci., Poly. Phys.*, 11, 1723, 1973.
- [198] FLORY, P.J., & TATARA, Y.  
*J. Poly. Sci., Poly. Phys.*, 13, 683, 1975.
- [199] PICO, E.R., & WILLIAMS, M.C.  
*J. Appl. Poly. Sci.*, 22, 445, 1978.
- [200] KRAUS, G.  
*Rubb. Plast. Age*, 38, 880, 1957.
- [201] PRICE, C., LALLY, T.P., WATSON, A.G., WOODS, D., & CHOW, M.T.  
*Br. Poly. J.*, 4, 413, 1972.
- [202] KRIGBAUM, W.R., YAZGAN, S., & TOLBERT, W.R.  
*J. Poly. Sci., Poly. Phys.*, 11, 511, 1973.
- [203] PRICE, C., SINGLETON, R., & WOODS, D.  
*Polymer*, 15, 117, 1974.
- [204] BEAMISH, A., GOLDBERG, R.A., & HOURSTON, D.J.  
*Polymer*, 18, 49, 1977.
- [205] KOPPLEMAN, J.  
*Kolloid-Zeits*, 144, 12, 1955.
- [206] NIELSEN, L.E.  
*ASTM Bull.*, 165, 48, April 1950.
- [207] NEDERVEEN, C.J., & VAN DER WAAL, C.W.  
*Rheol. Acta*, 6 (4), 316, 1967.
- [208] STRUIK, L.C.E.  
*Rheol. Acta*, 6 (2), 119, 1967.
- [209] MARKOVITZ, H.  
*J. Appl. Phys.*, 34, 21, 1963.
- [210] GRAY, R.W., & McCURUM, N.G.  
*J. Poly. Sci.*, A-2 (7), 1329, 1969.
- [211] RHEOVIBRON  
Toyo Measuring Instruments Company Limited, 104, 1-Chome,  
Chofuminemachi, Ota-ku, Tokyo, Japan.
- [212] NAKAJIMA, N., BOWERMAN, H.H., & COLLINS, E.A.  
*Rubb. Chem. Tech.*, 46 (2), 417, 1973.

- [213] TRELOAR, L.R.G.  
The physics of rubber elasticity,  
Oxford University Press, 1958.
- [214] HALPIN, J.C., & POLLEY, H.W.  
*J. Composite Mat.*, 1, 64, 1967.
- [215] FAUCHER, J.A.  
*J. Poly. Sci., Poly. Phys.*, 12, 2153, 1974.
- [216] NIELSEN, L.E.  
*Rheol. Acta*, 13, 86, 1974.
- [217] HALPIN, J.C.  
*J. Composite Mat.*, 3, 732, 1969.
- [218] FOLKES, M.J., & KELLER, A.  
*Polymer*, 12, 222, 1971.
- [219] BERRY, J.P.  
Fracture processes in polymeric solids,  
(ed. Rosen), Wiley Interscience, 221, 1964.
- [220] MARSHALL, G.P., CULVER, L.E., & WILLIAMS, J.G.  
*Plast. Polym.*, 2, 75, 1969.
- [221] ISHERWOOD, D.P.  
PhD Thesis, Imperial College University of London, 1968.
- [222] ISHERWOOD, D.P., & WILLIAMS, J.G.  
*Eng. Fract. Mech.*, 10, 887, 1978.
- [223] HAHN, G.T., DAI, P.K., & ROSENFELD, A.R.  
Proc. 1st Int. Conf. Fracture, 1, 229, 1965.
- [224] GOH, S.H.  
PhD Thesis, University of Akron, Ohio, USA, 1971.
- [225] HARWOOD, J.A.C., PAYNE, A.R., & WHITTAKER, R.E.  
*Rubb. Chem. Tech.*, 690, 1971.
- [226] HARWOOD, J.A.C., & PAYNE, A.R.  
*J. Appl. Poly. Sci.*, 7, 1825, 1967.
- [227] MORRIS, R.E., & BONNAR, R.U.  
*Anal. Chem.*, 19, 436, 1947.
- [228] GREENE, H.E., & LOUGHBOROUGH, D.L.  
*J. Appl. Phys.*, 16, 3, 1945.

- [229] ARRIDGE, R.G.C., & FOLKES, M.J.  
*J. Phys. D. Appl. Phys.*, D5, 344, 1972.
- [230] GROSCH, K.A., HARWOOD, J.A.C., & PAYNE, A.R.  
*Inst. Phys. Phys. Soc.*, Conf. Series No. 1, 144, 1966.
- [231] ILLERS, K.H.  
*Z. Elektrochem.*, 65, 679, 1961.



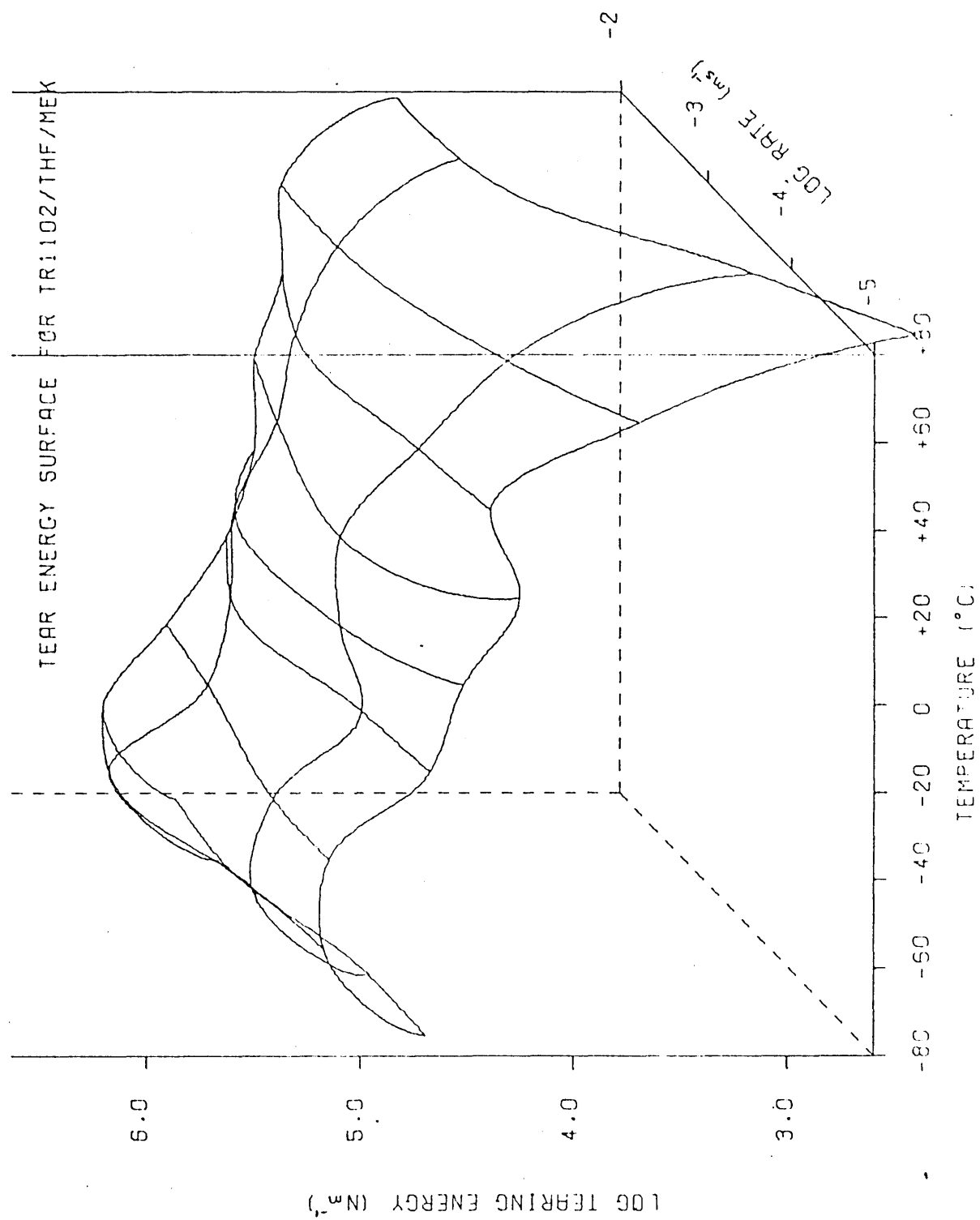


Figure A.1 Tearing energy as a function of temperature and rate.

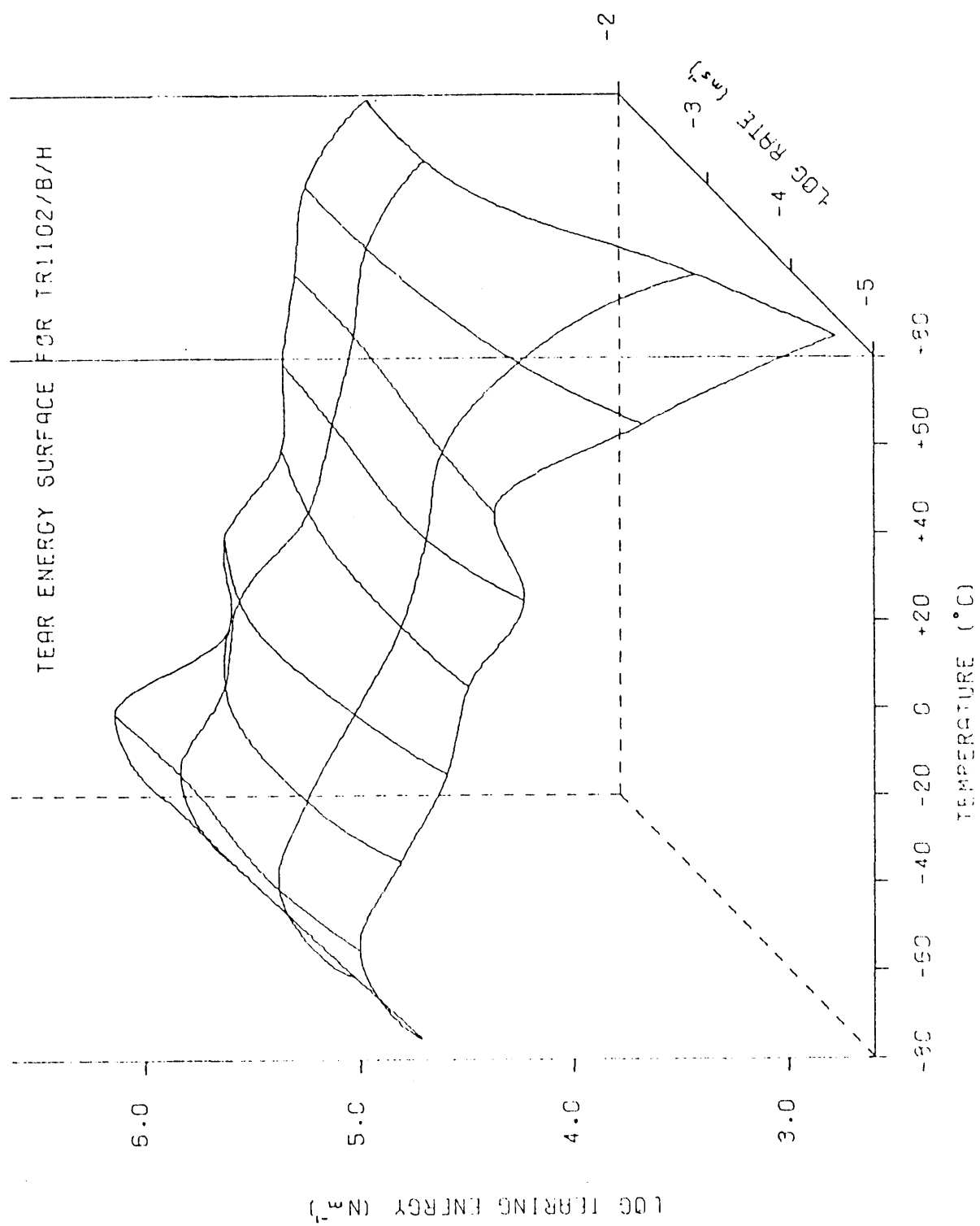


Figure A.2 Tearing energy as a function of temperature and rate.

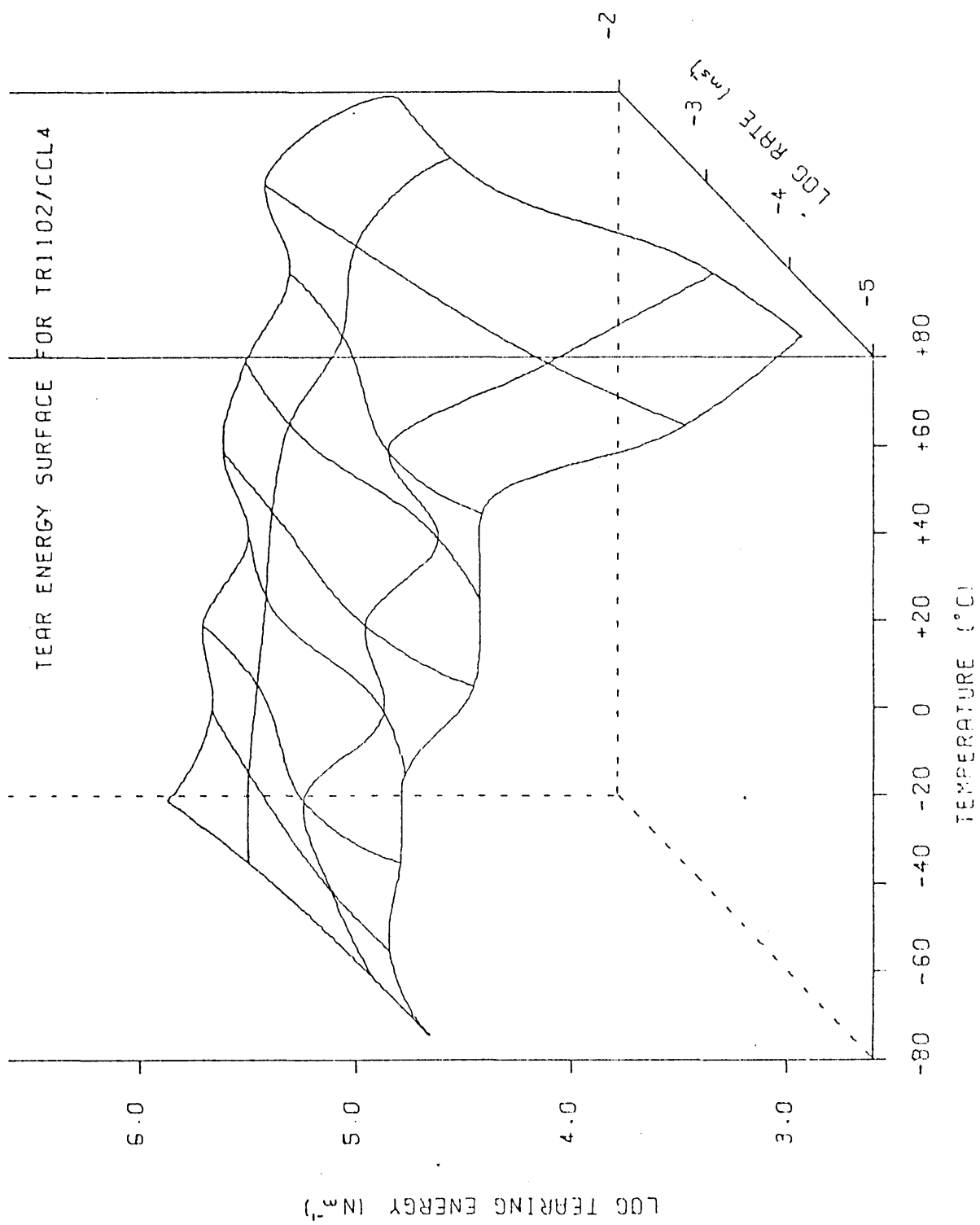


Figure A.3 Tearing energy as a function of temperature and rate.

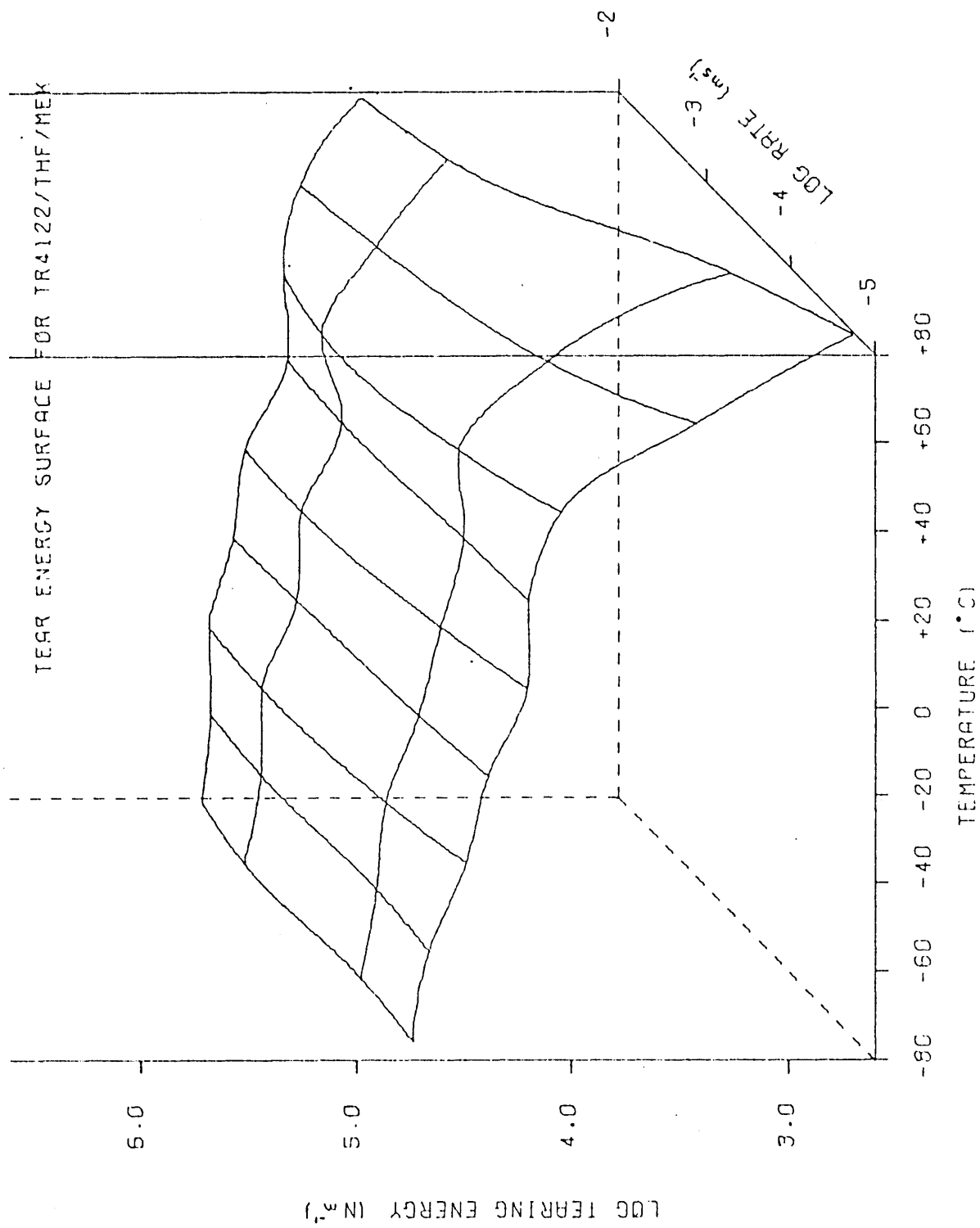


Figure A.4 Tearing energy as a function of temperature and rate.

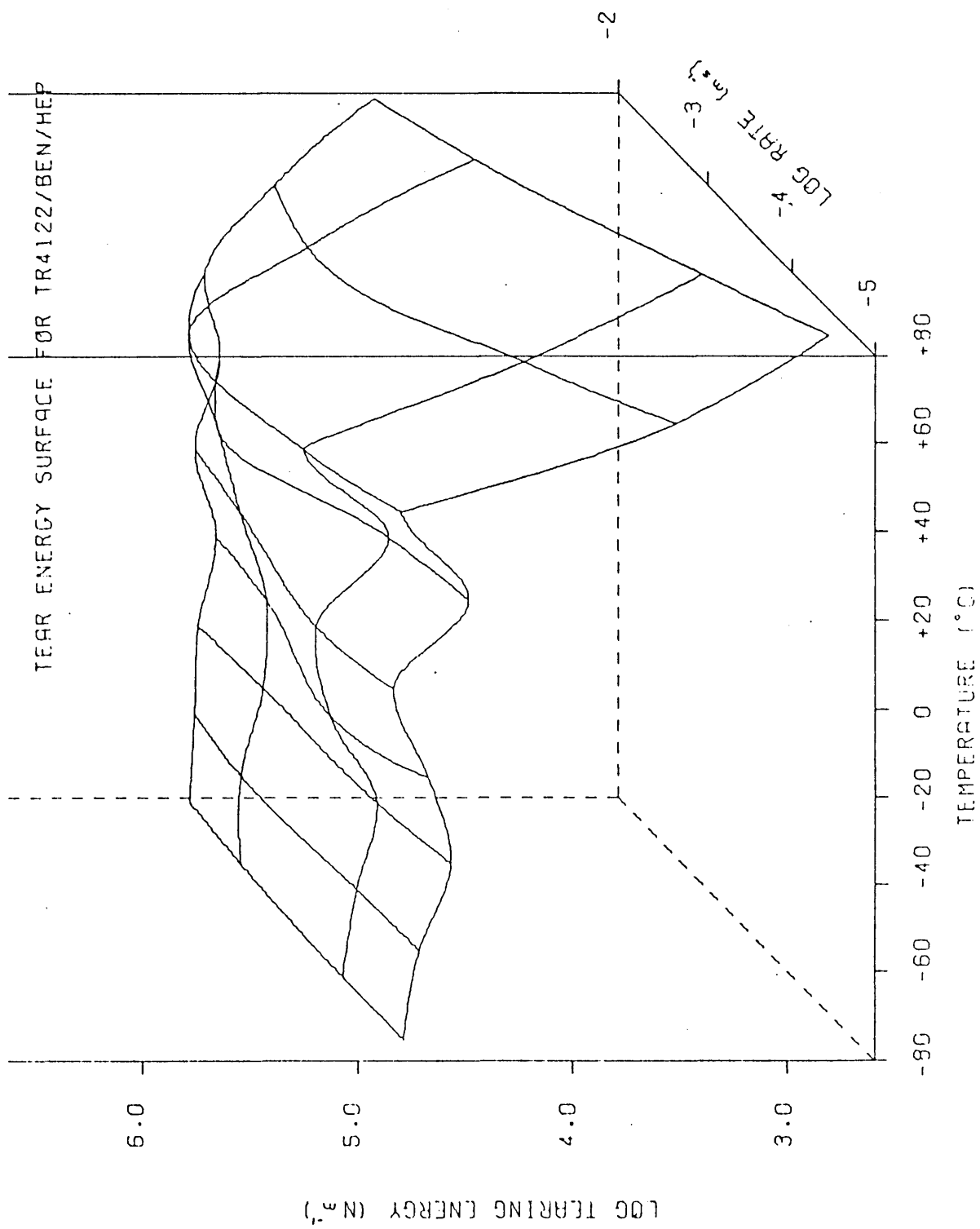


Figure A.5 Tearing energy as a function of temperature and rate.

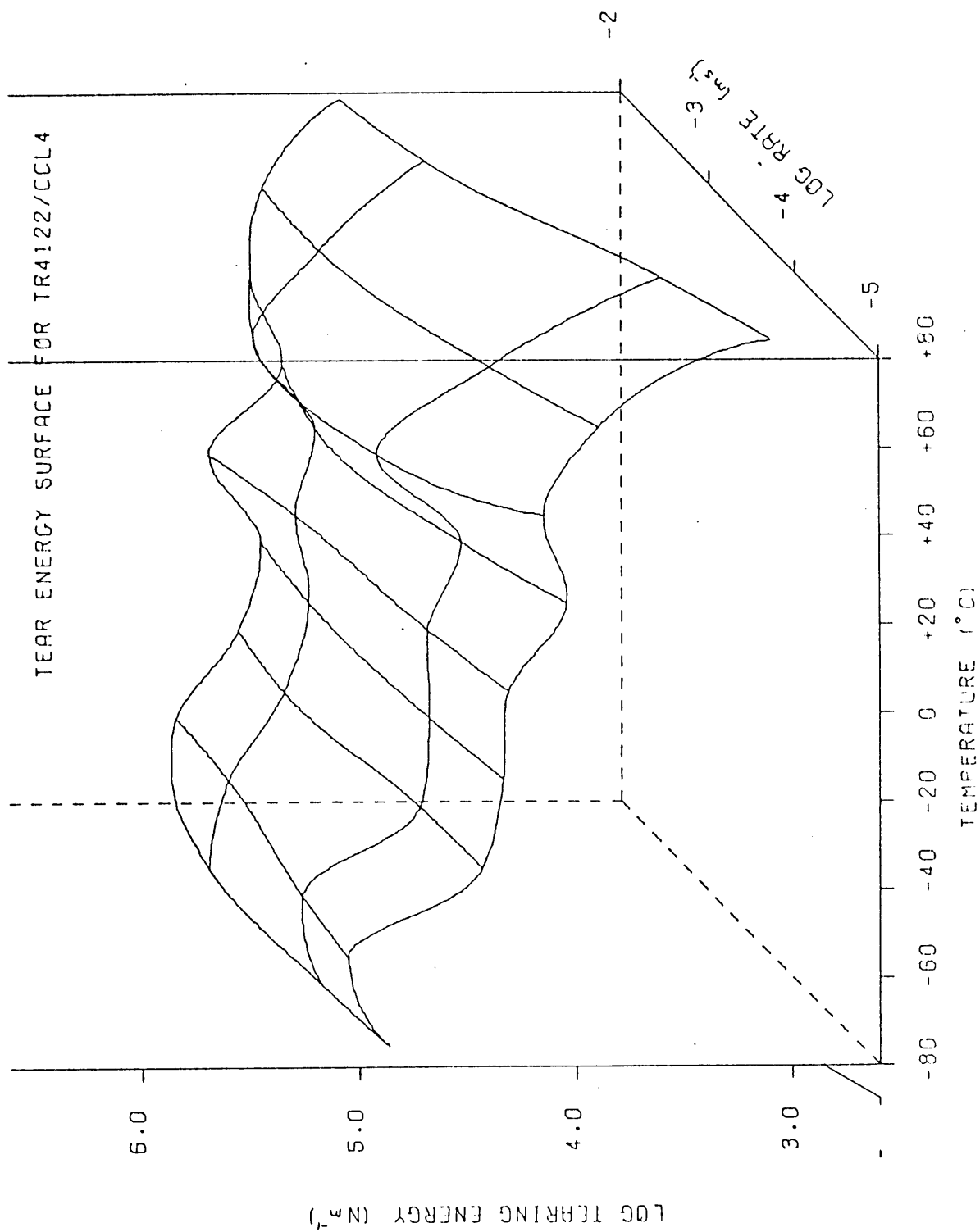


Figure A.6 Tearing energy as a function of temperature and rate.

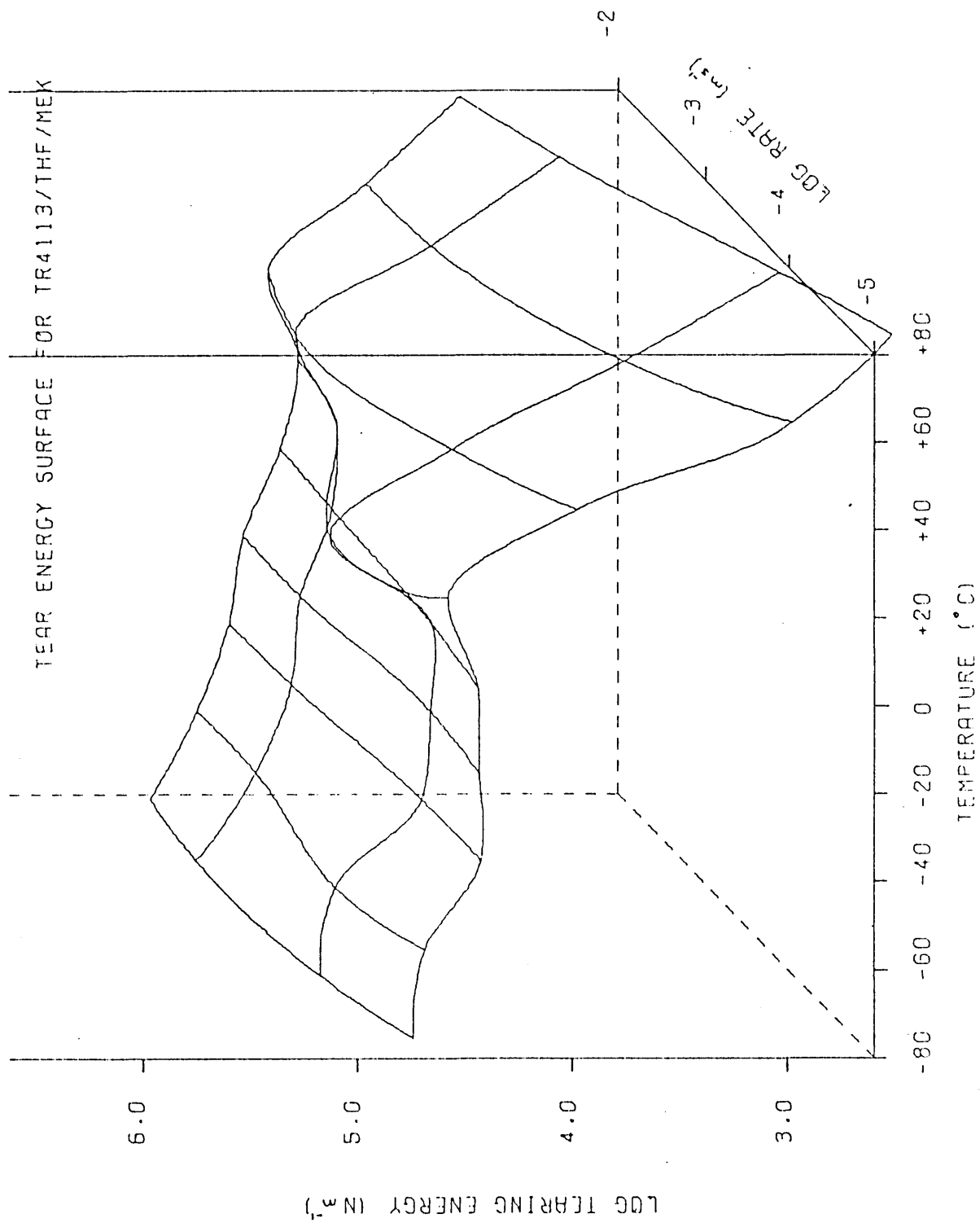


Figure A.7 Tearing energy as a function of temperature and rate.

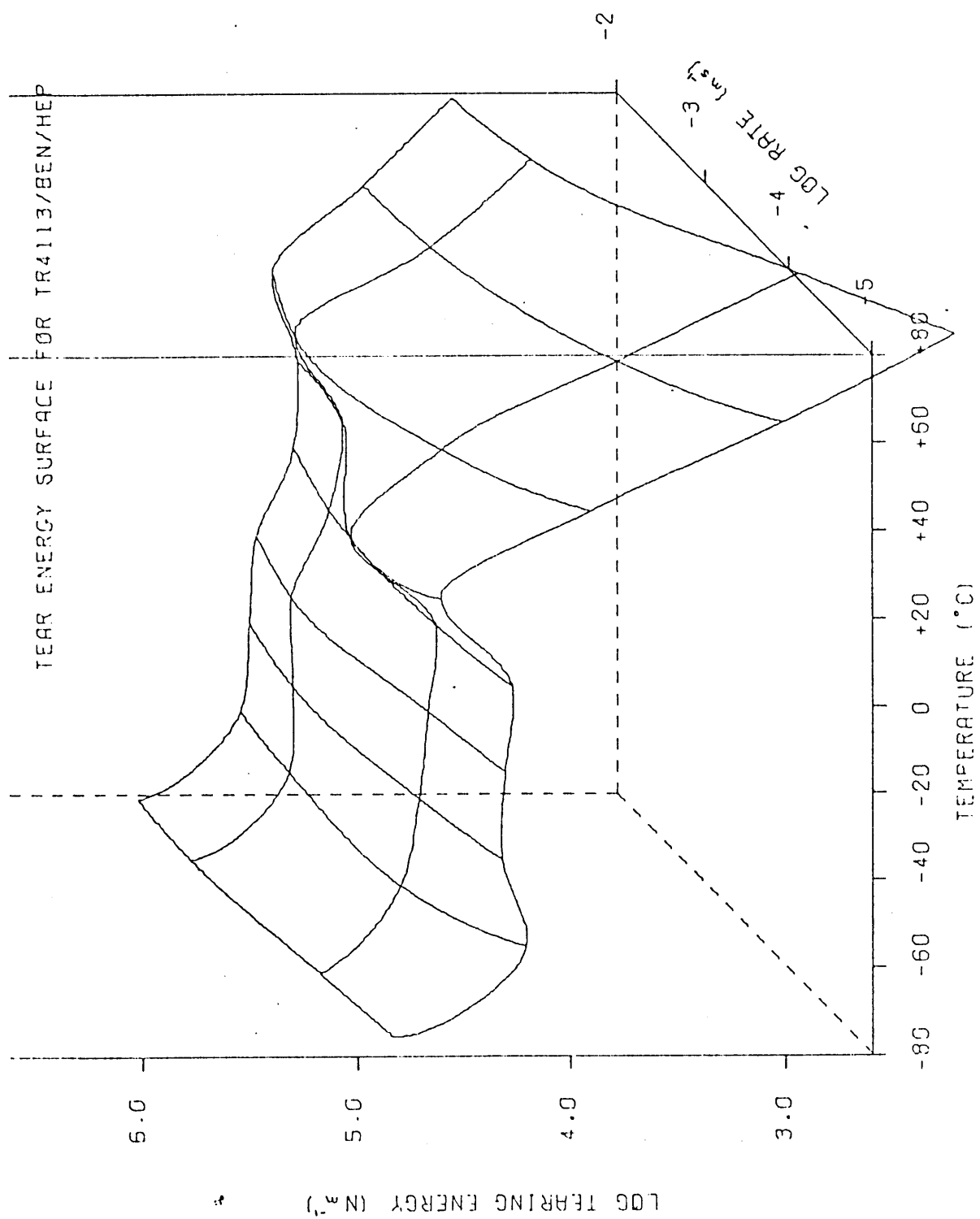


Figure A.8 Tearing energy as a function of temperature and rate.



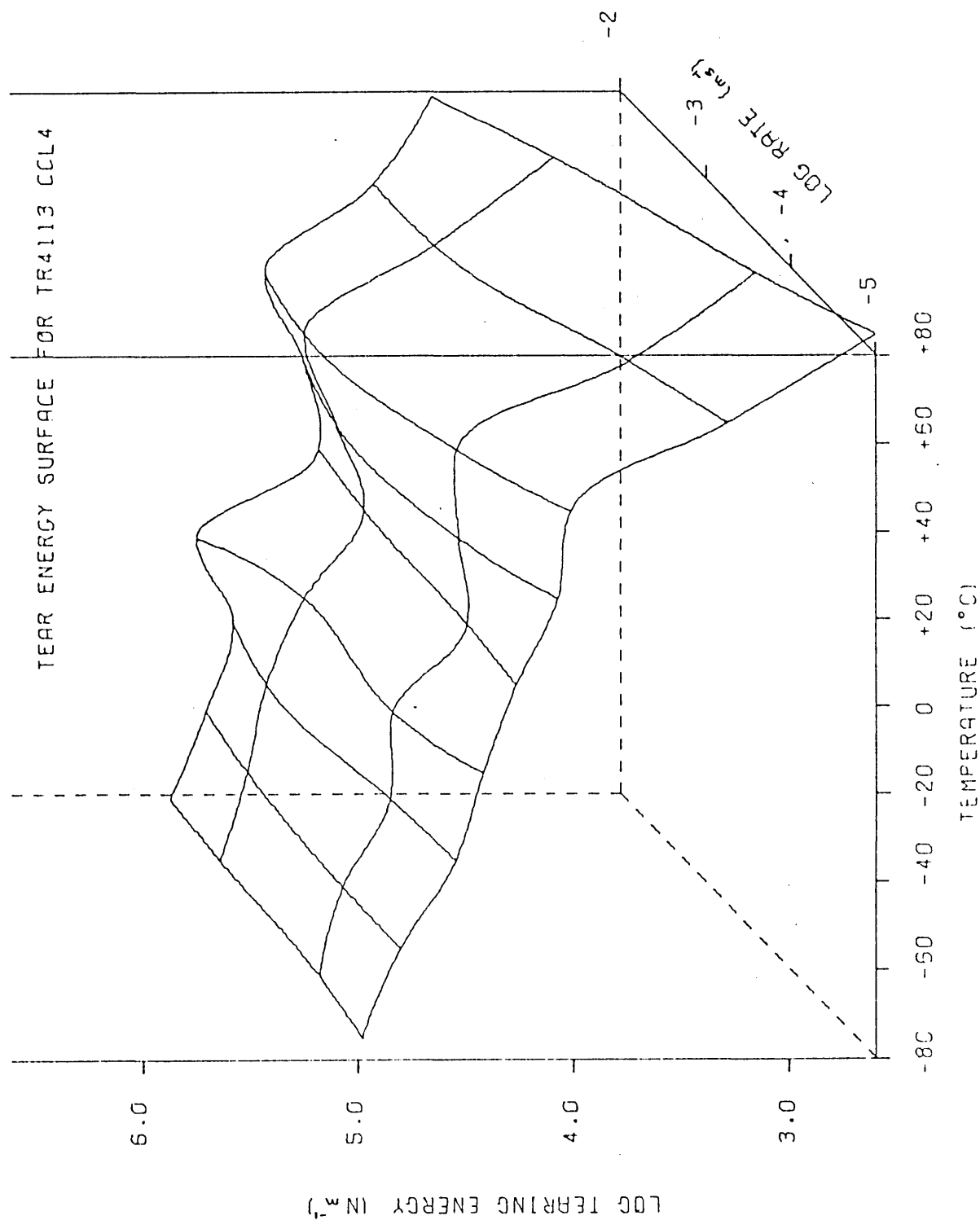


Figure A.9 Tearing energy as a function of temperature and rate.

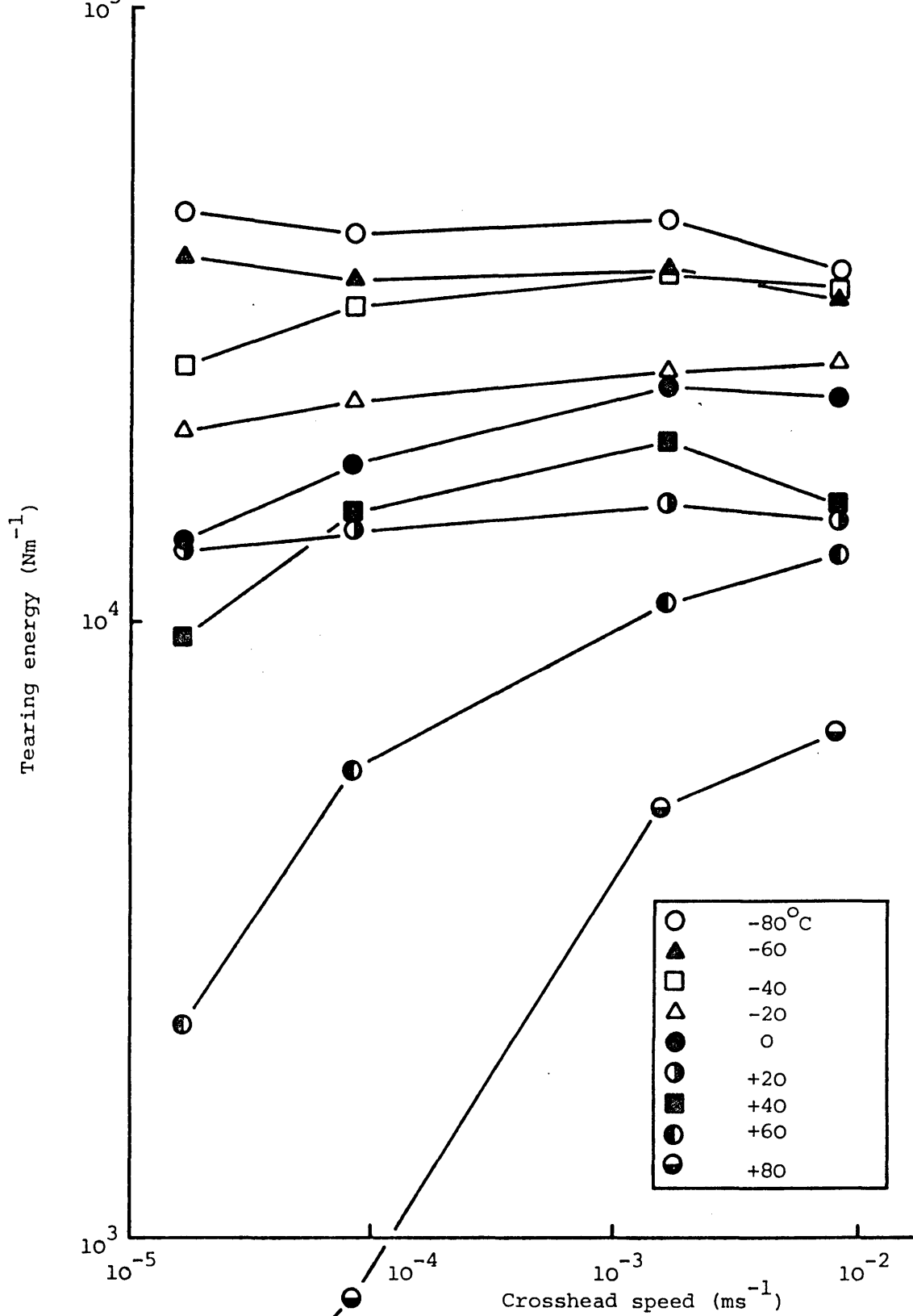


Figure B.1 Tearing energy as a function of rate for different test temperatures (TR4122 THF/MEK)

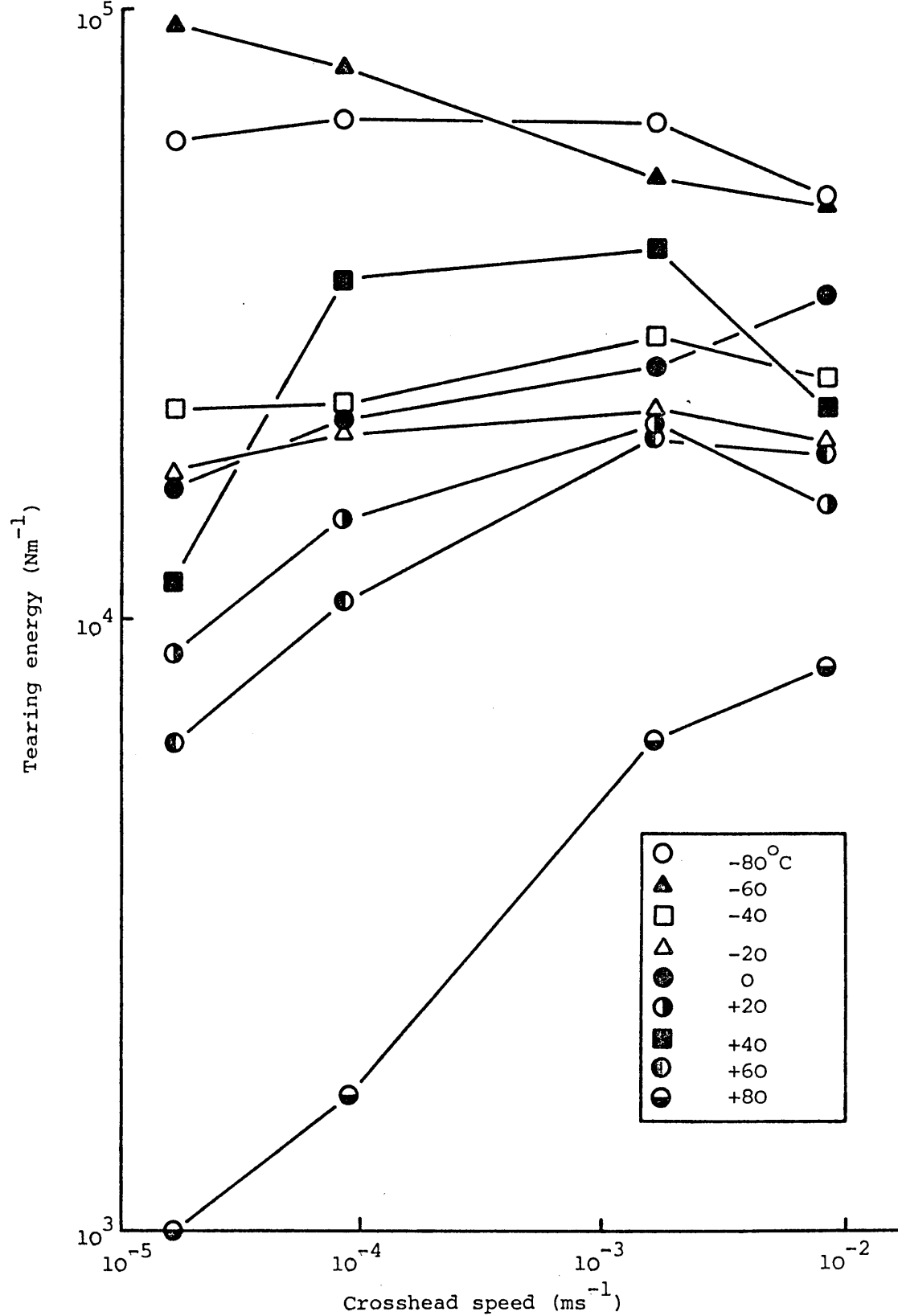


Figure B.2 Tearing energy as a function of rate for different test temperatures (TR4122  $\text{CCl}_4$ )

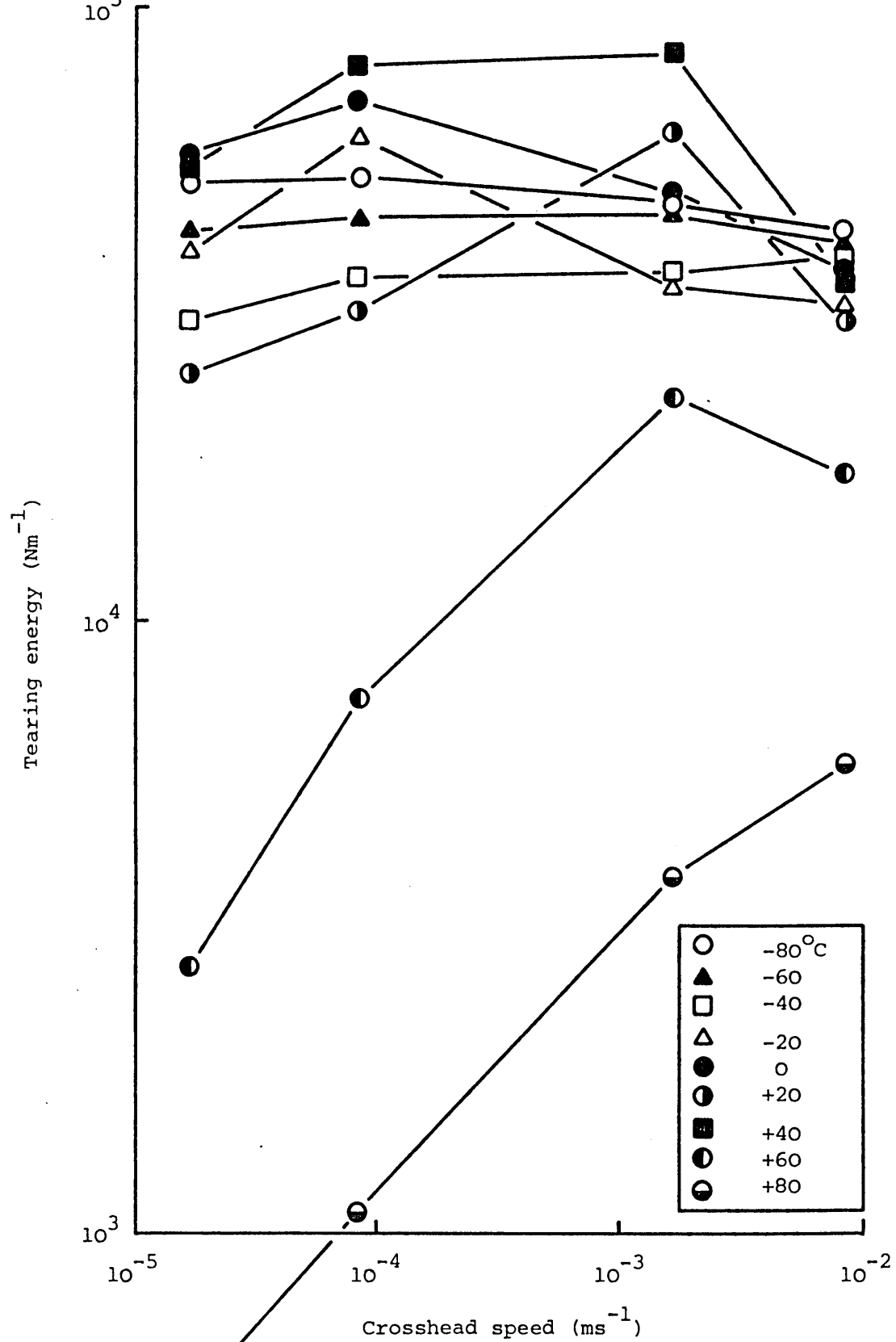


Figure B.3 Tearing energy as a function of rate for different test temperatures (TR4122 BEN/HEP).

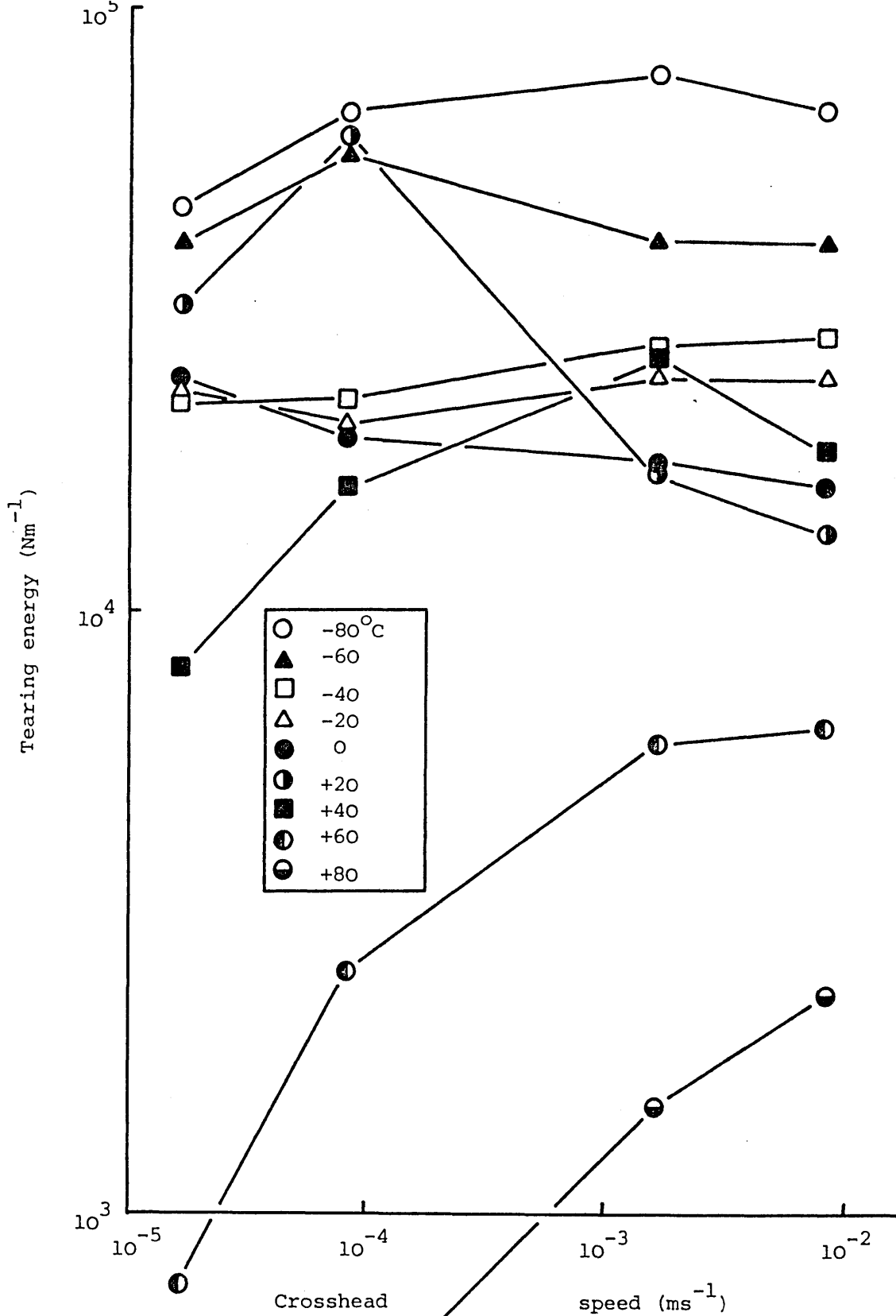


Figure B.4 Tearing energy as a function of rate for different test temperatures (TR4113 THF/MEK)

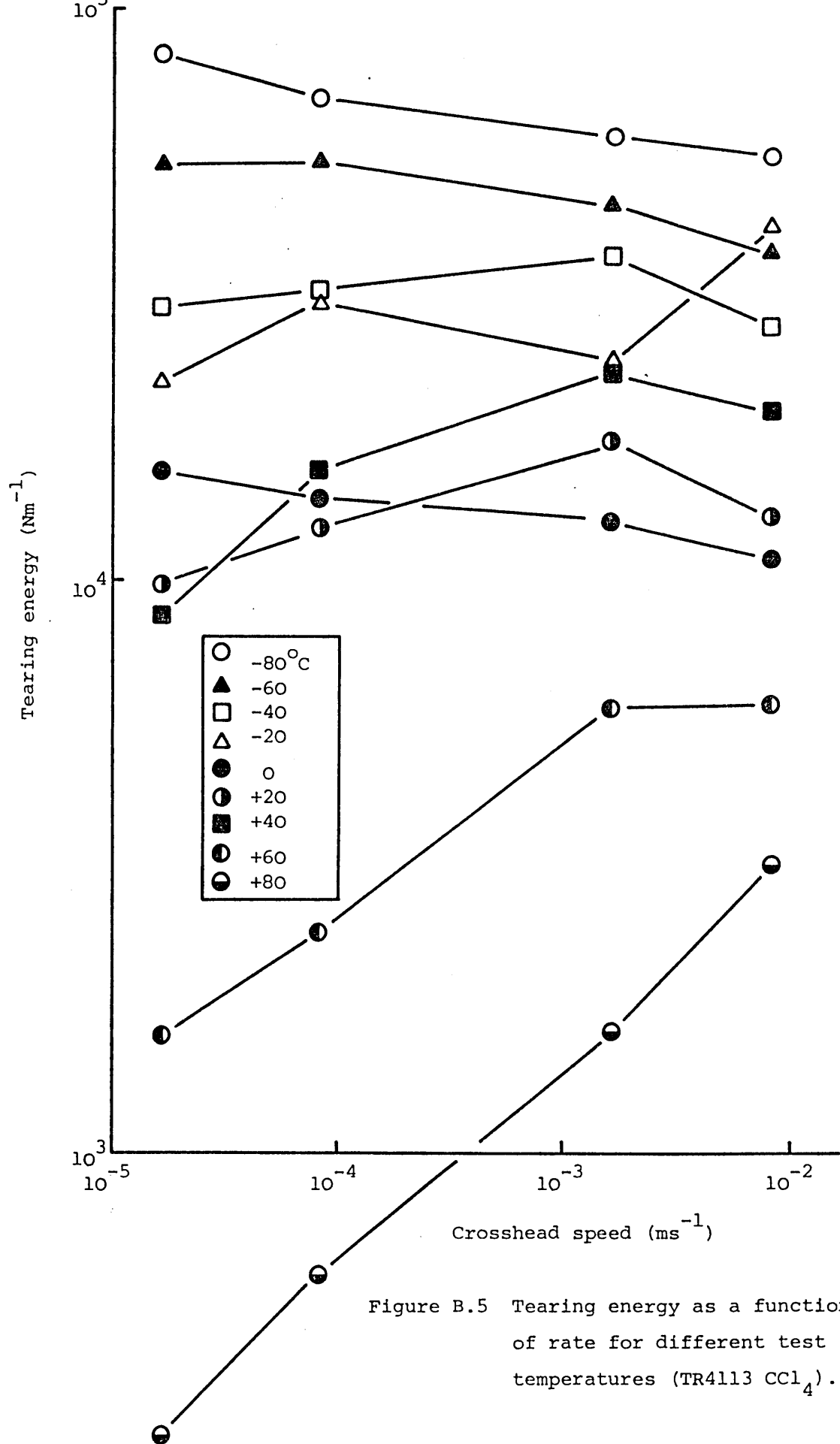


Figure B.5 Tearing energy as a function of rate for different test temperatures (TR4113  $\text{CCl}_4$ ).

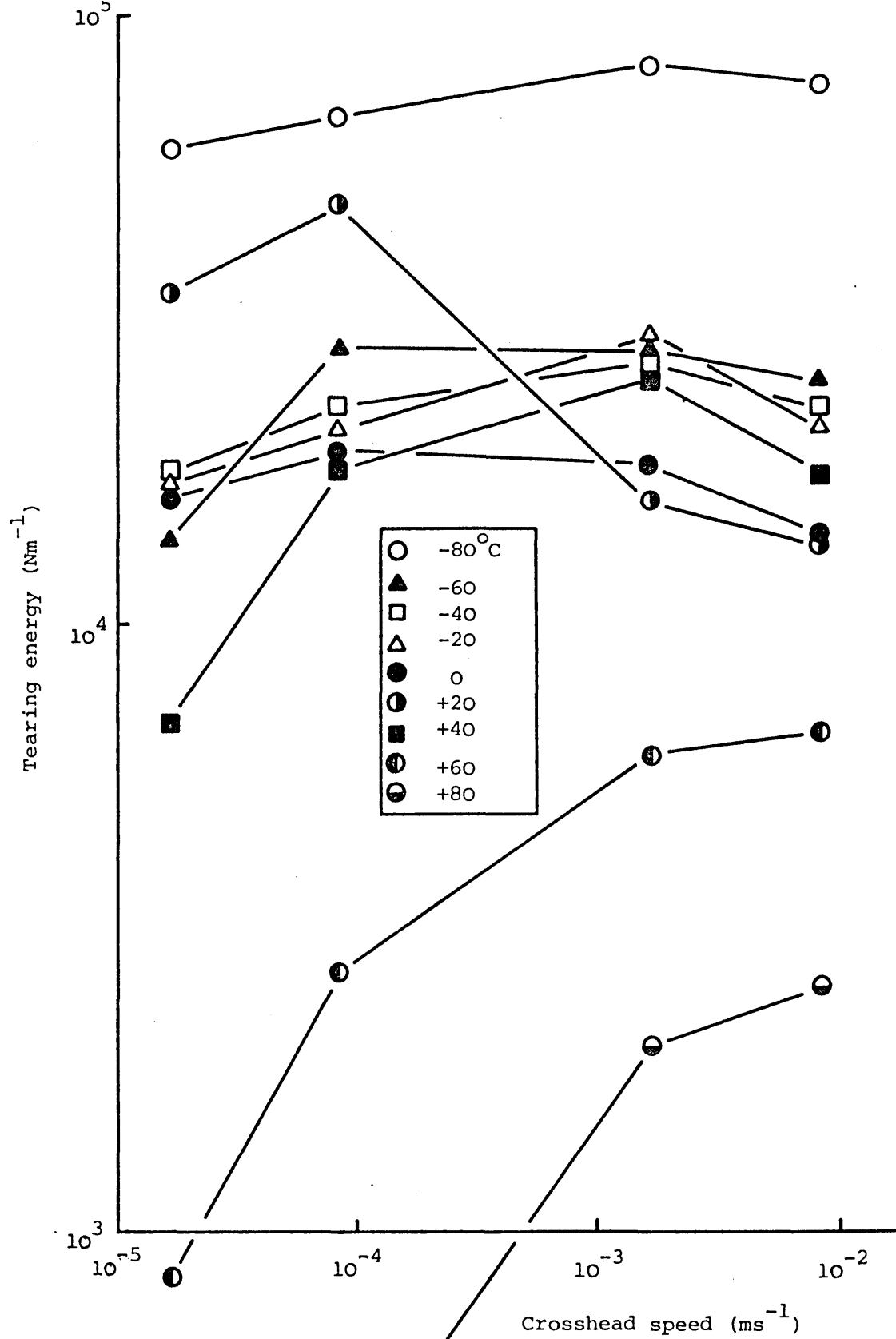


Figure B.6 Tearing energy as a function of rate for different test temperatures (TR4113 BEN/HEP)

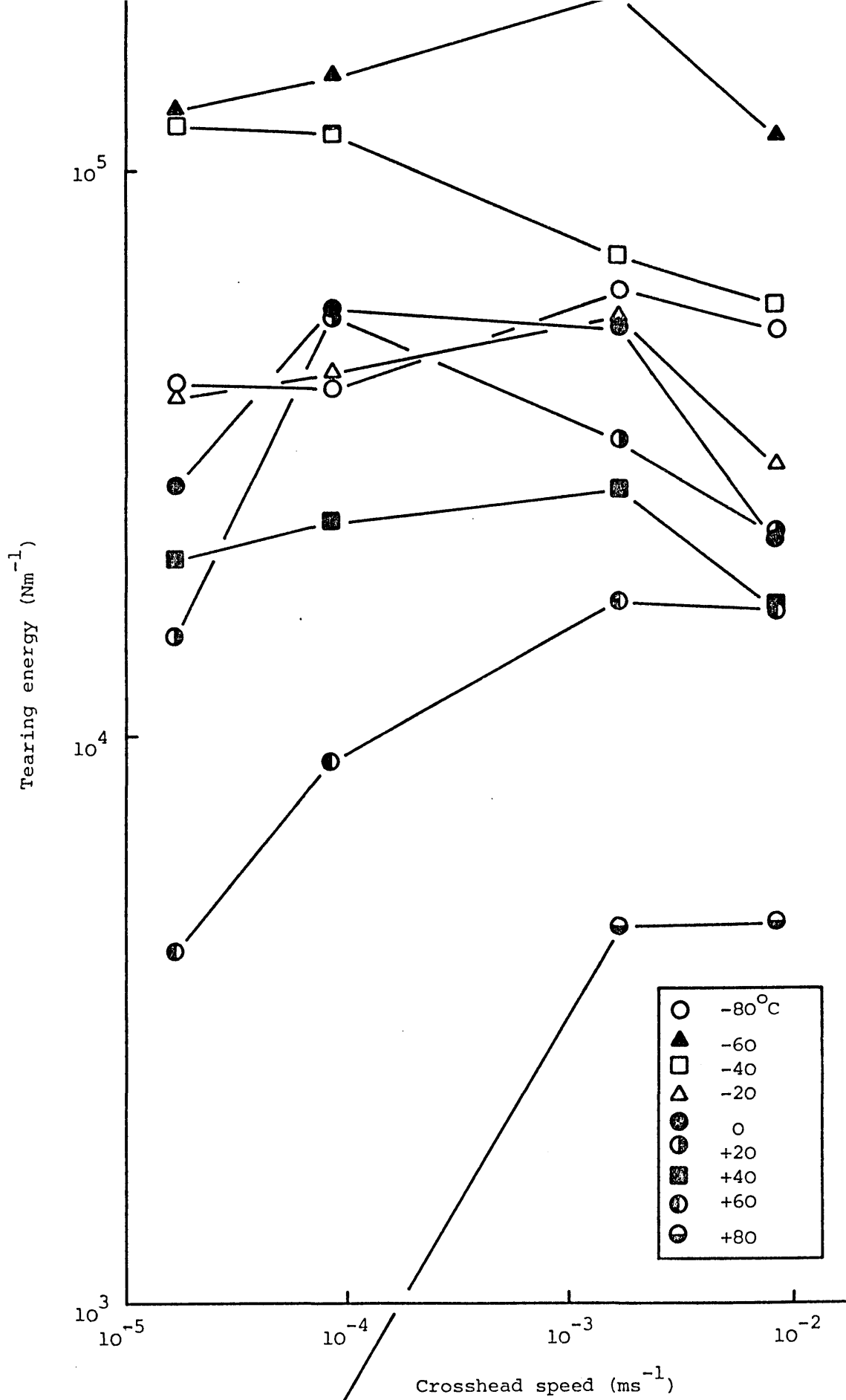


Figure B.7 Tearing energy as a function of rate for different test temperatures (TR1102 THF/MEK)



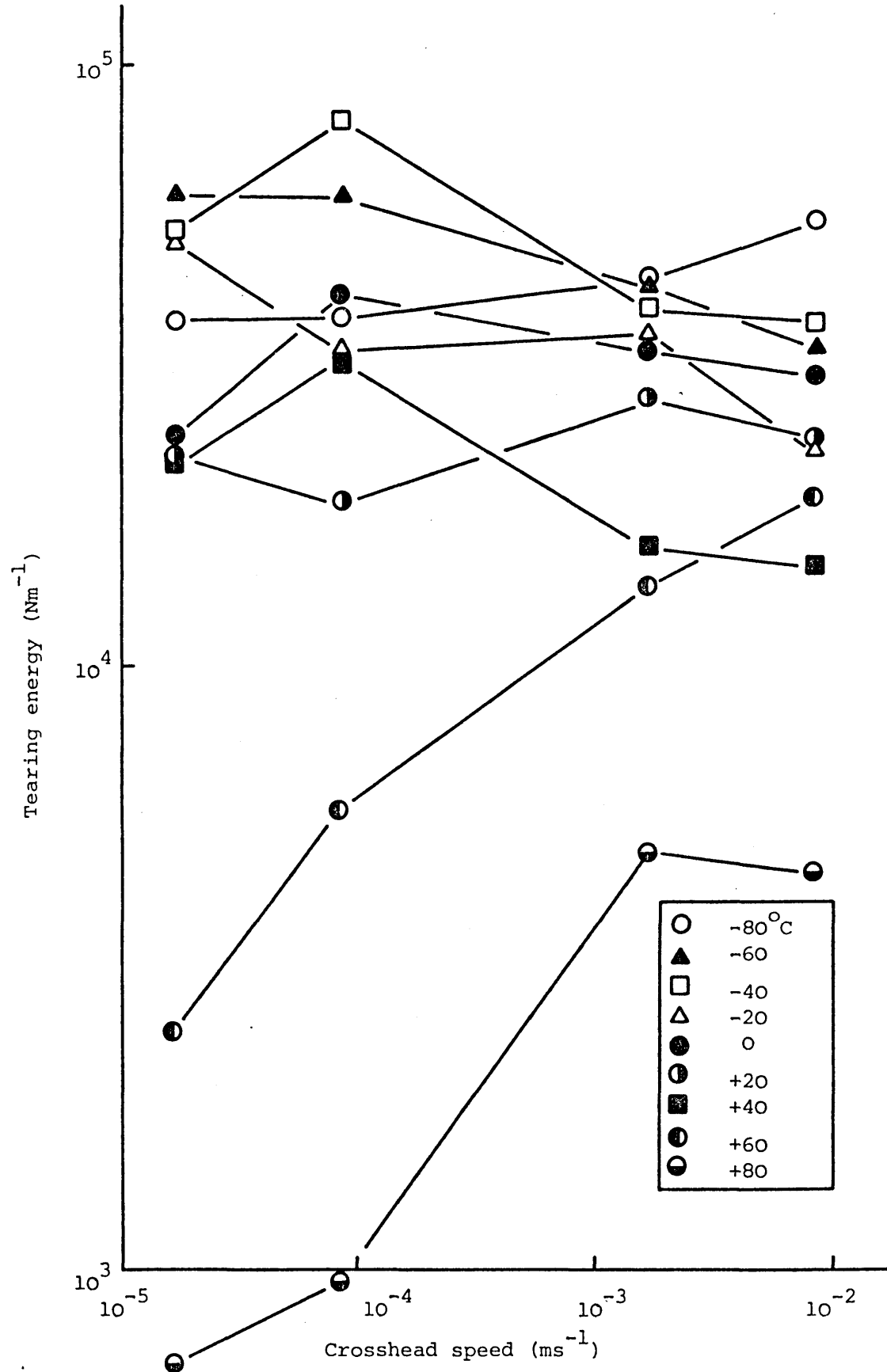


Figure B.8 Tearing energy as a function of rate for different test temperatures (TR1102  $\text{CCl}_4$ ).

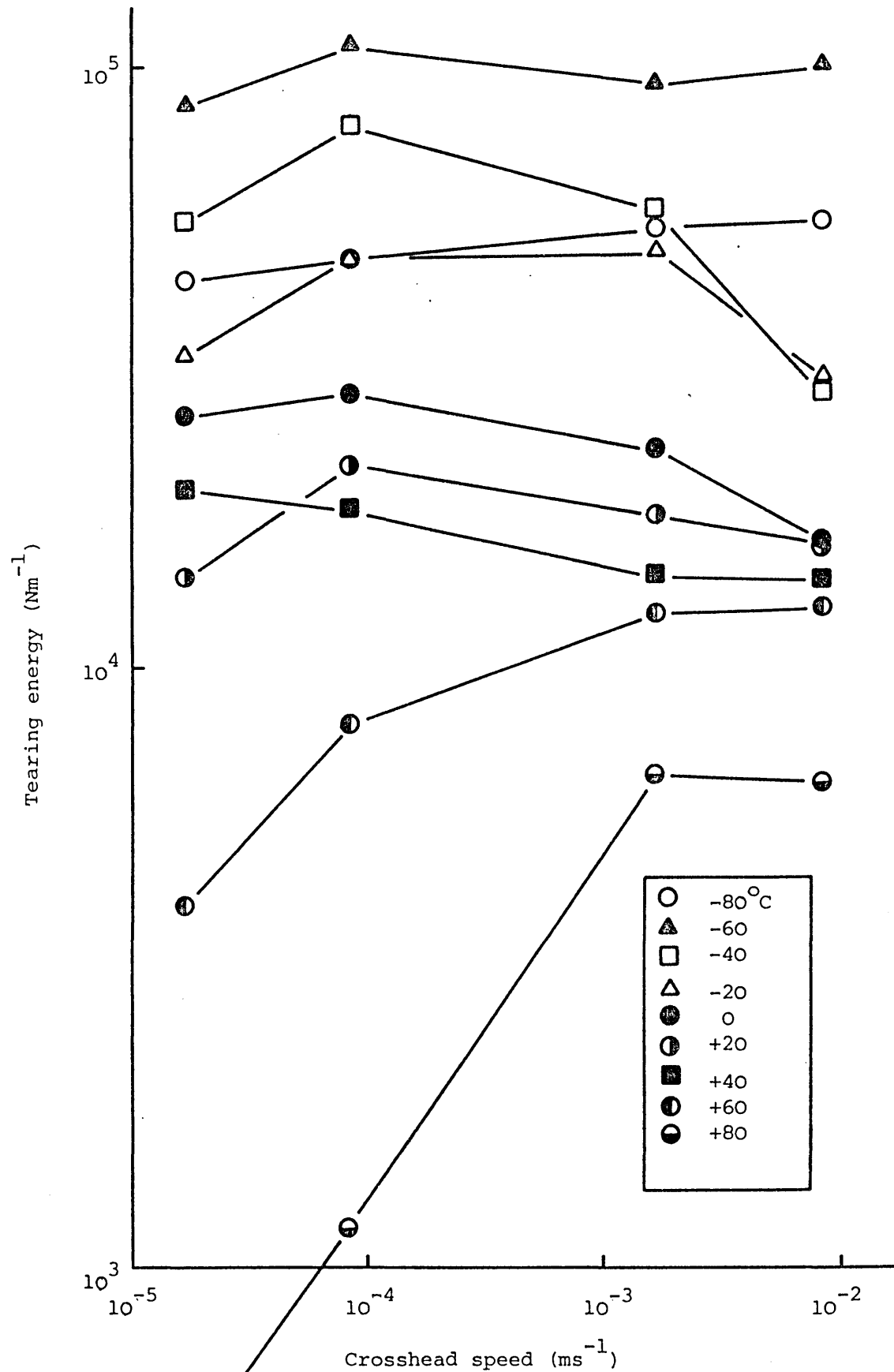


Figure B.9 Tearing energy as a function of rate for different test temperatures (TR1102 BEN/HEP).

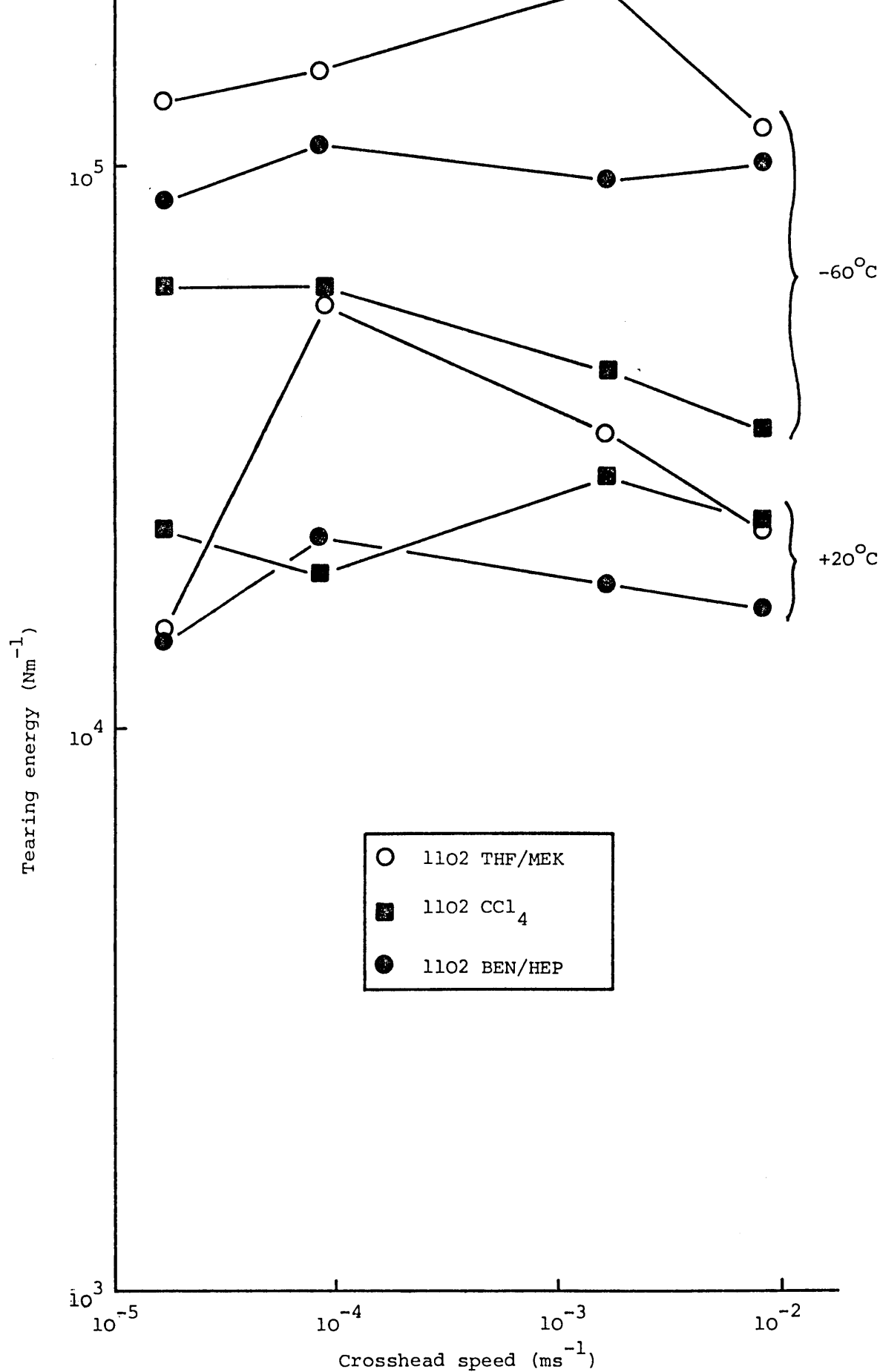


Figure C.1 Tearing energy as a function of rate for TR1102 cast from different solvents.

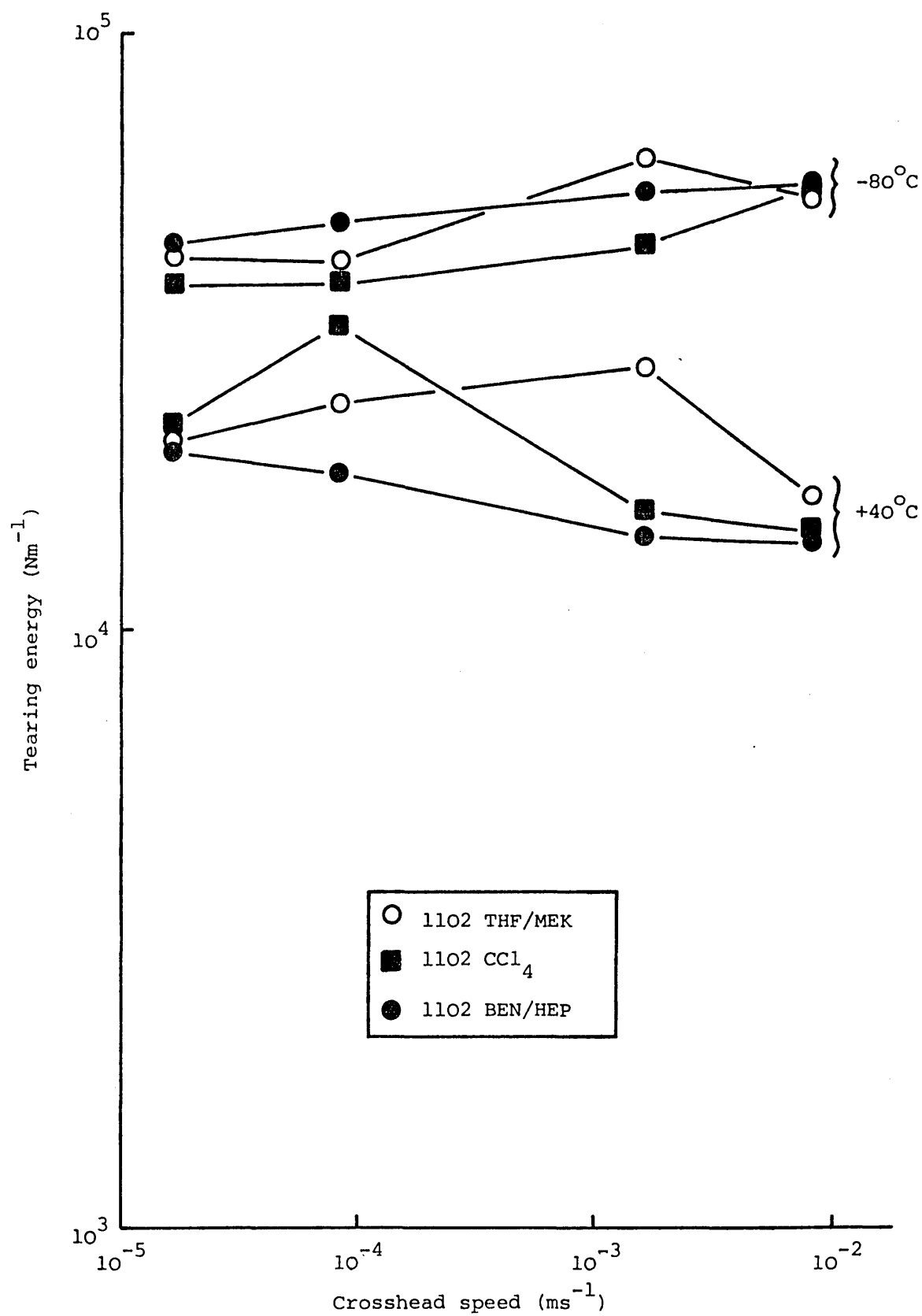


Figure C.2 Tearing energy as a function of rate for TR1102 cast from different solvent systems.

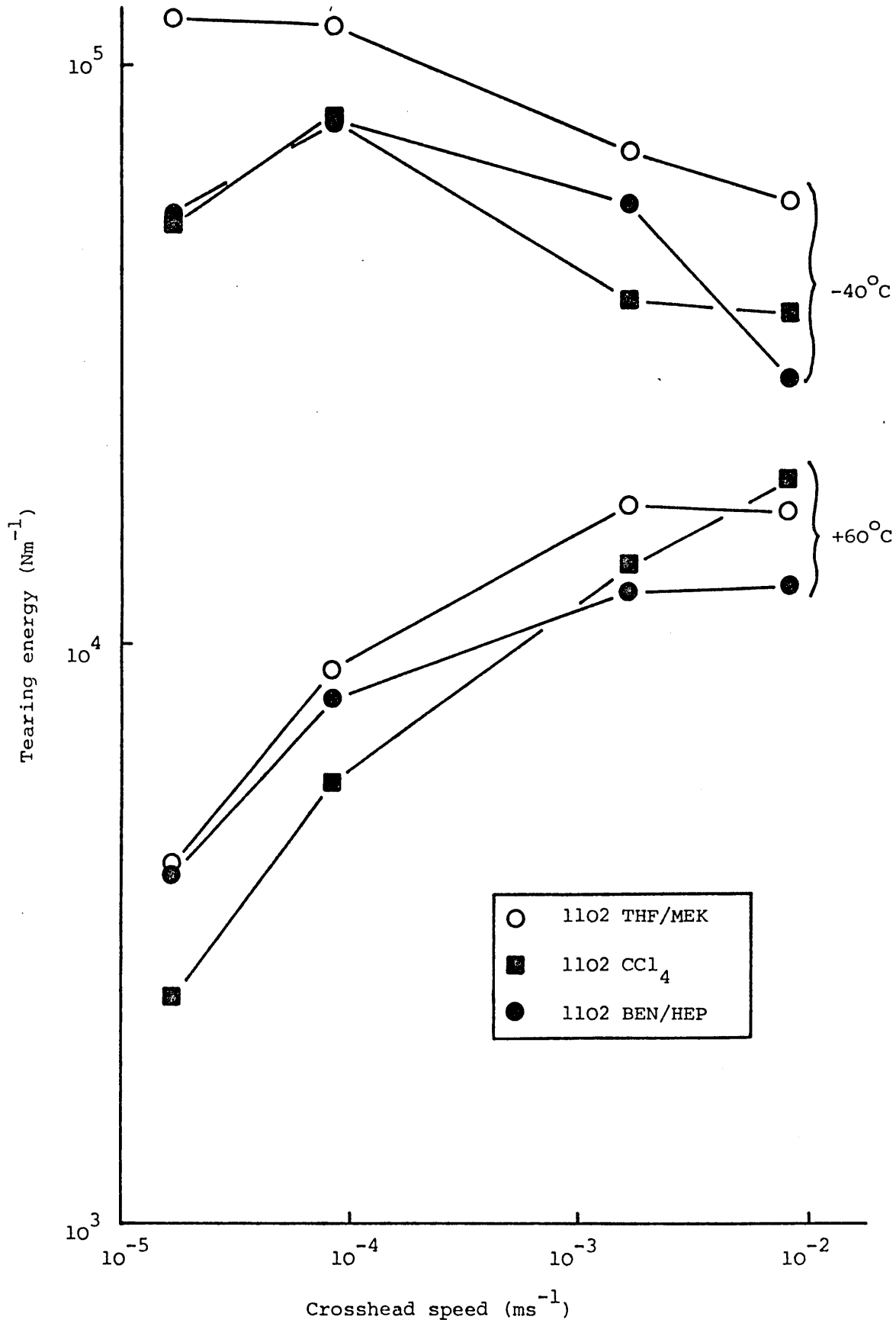


Figure C.3 Tearing energy as a function of rate for TR1102 cast from different solvent systems.

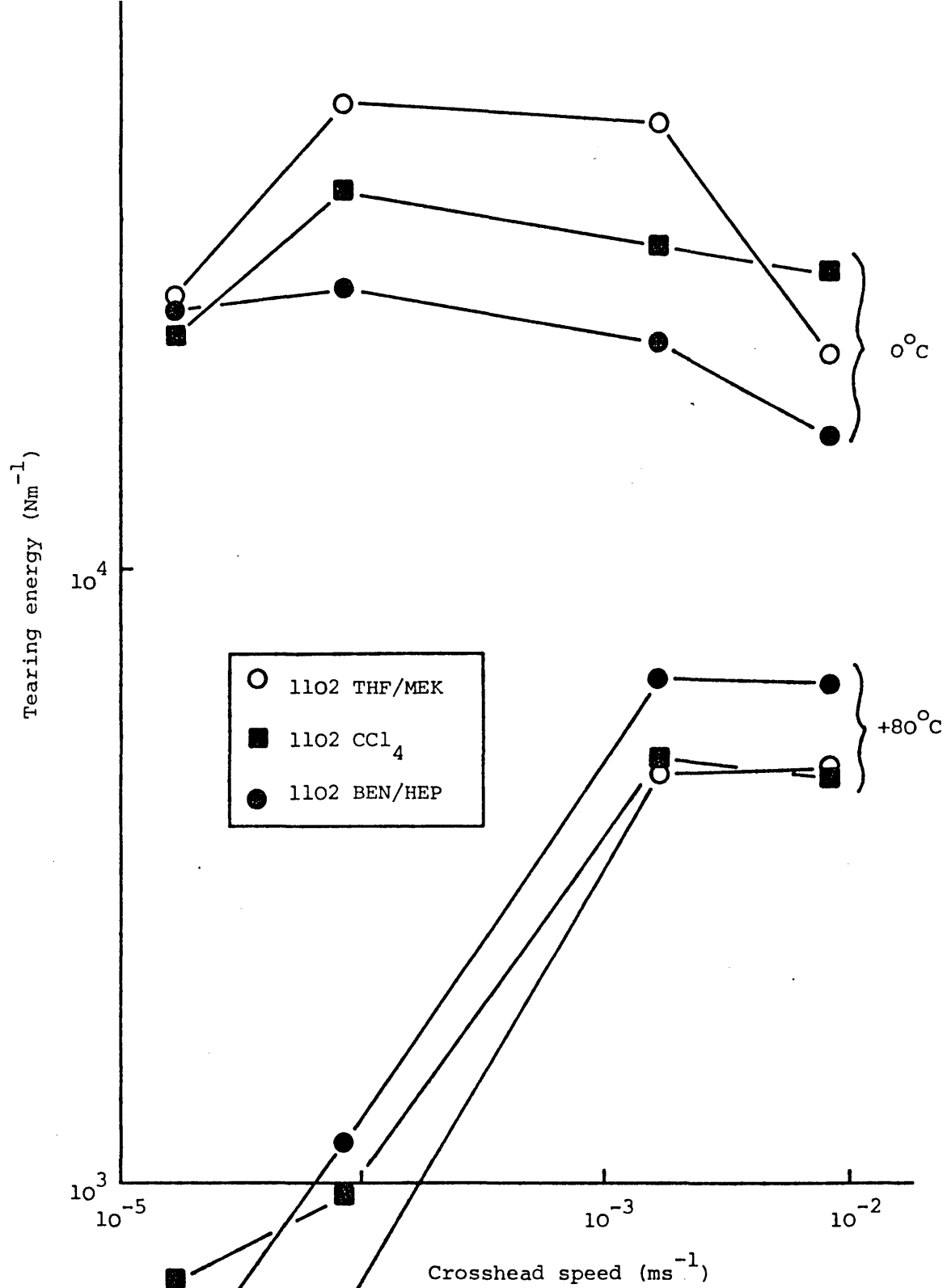


Figure C.4 Tearing energy as a function of rate for TR1102 cast from different solvent systems.

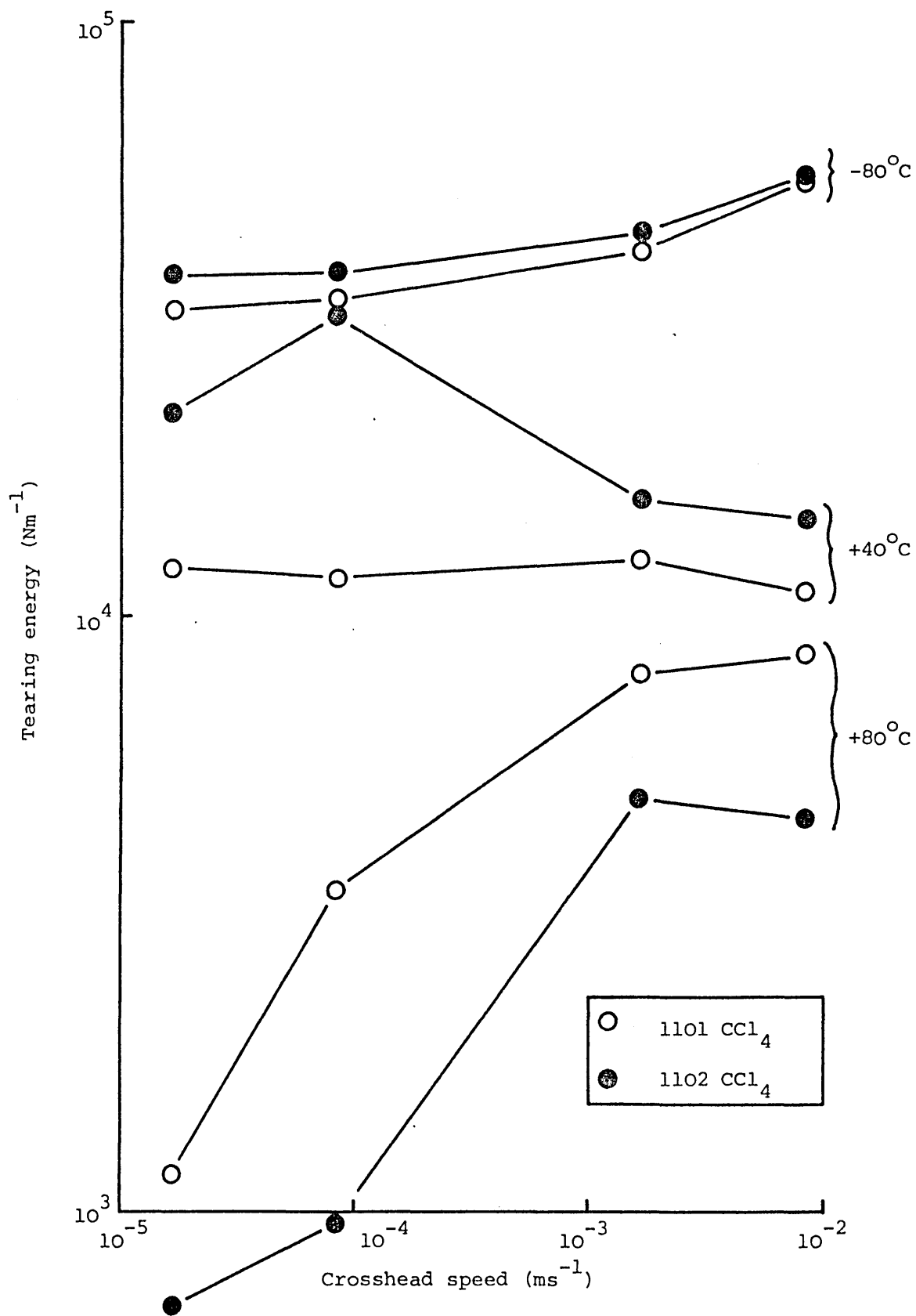


Figure D.1 Tearing energy as a function of rate comparing TR1101 and TR1102 cast from  $\text{CCl}_4$ .

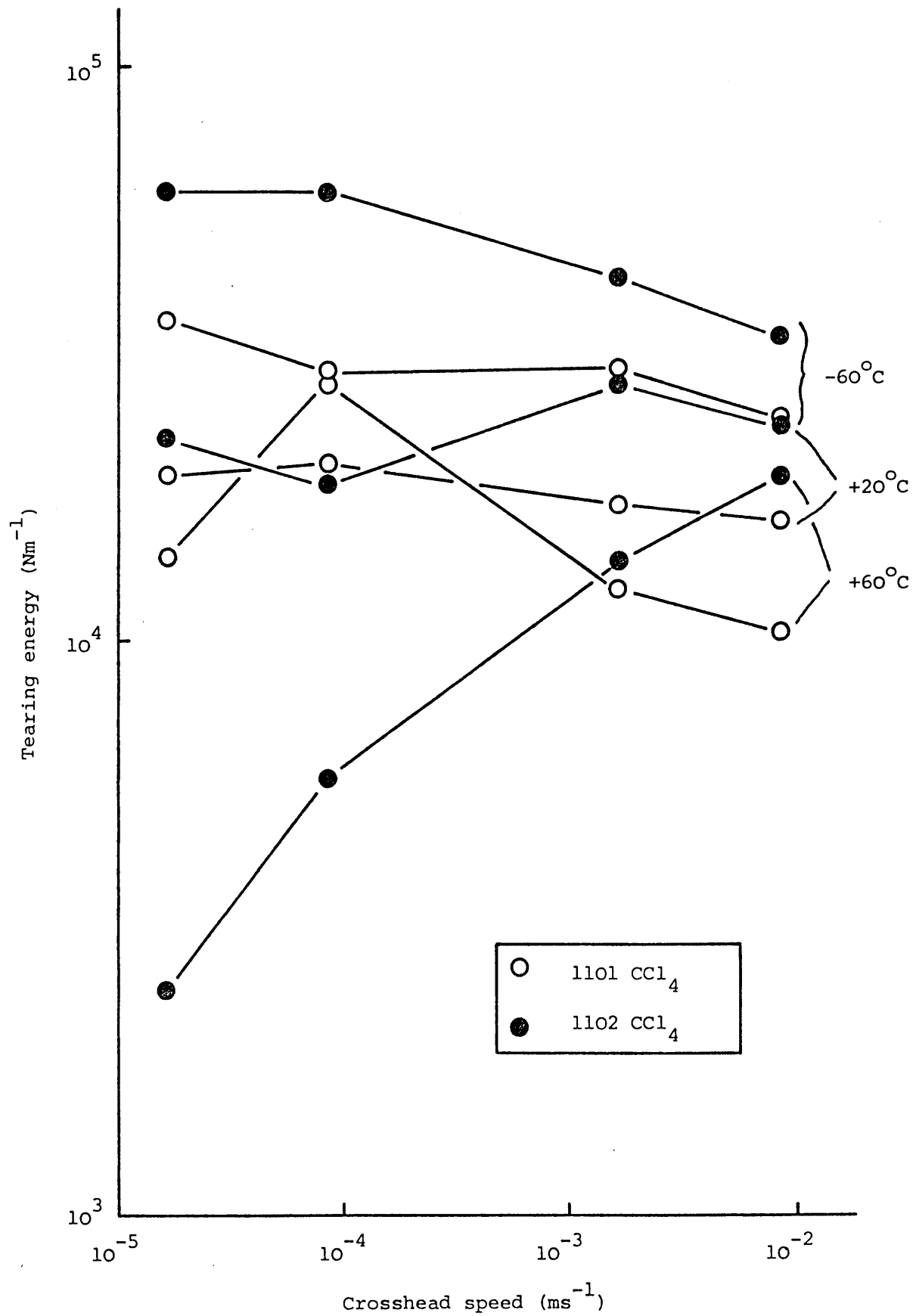


Figure D.2 Tearing energy as a function of rate comparing TR1101 and TR1102 cast from  $\text{CCl}_4$ .



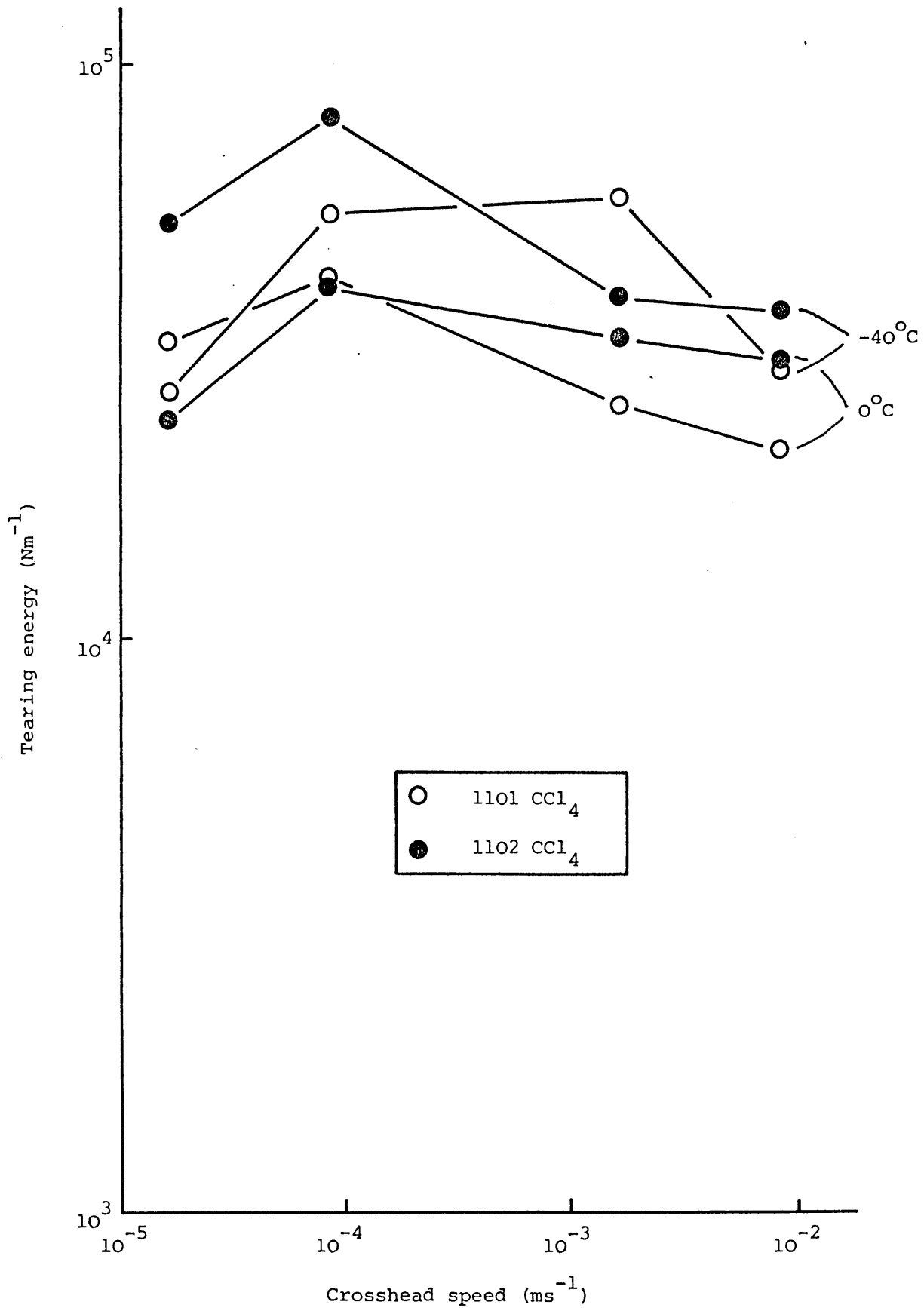


Figure D.3 Tearing energy as a function of rate comparing TR1101 and TR1102 cast from  $\text{CCl}_4$ .

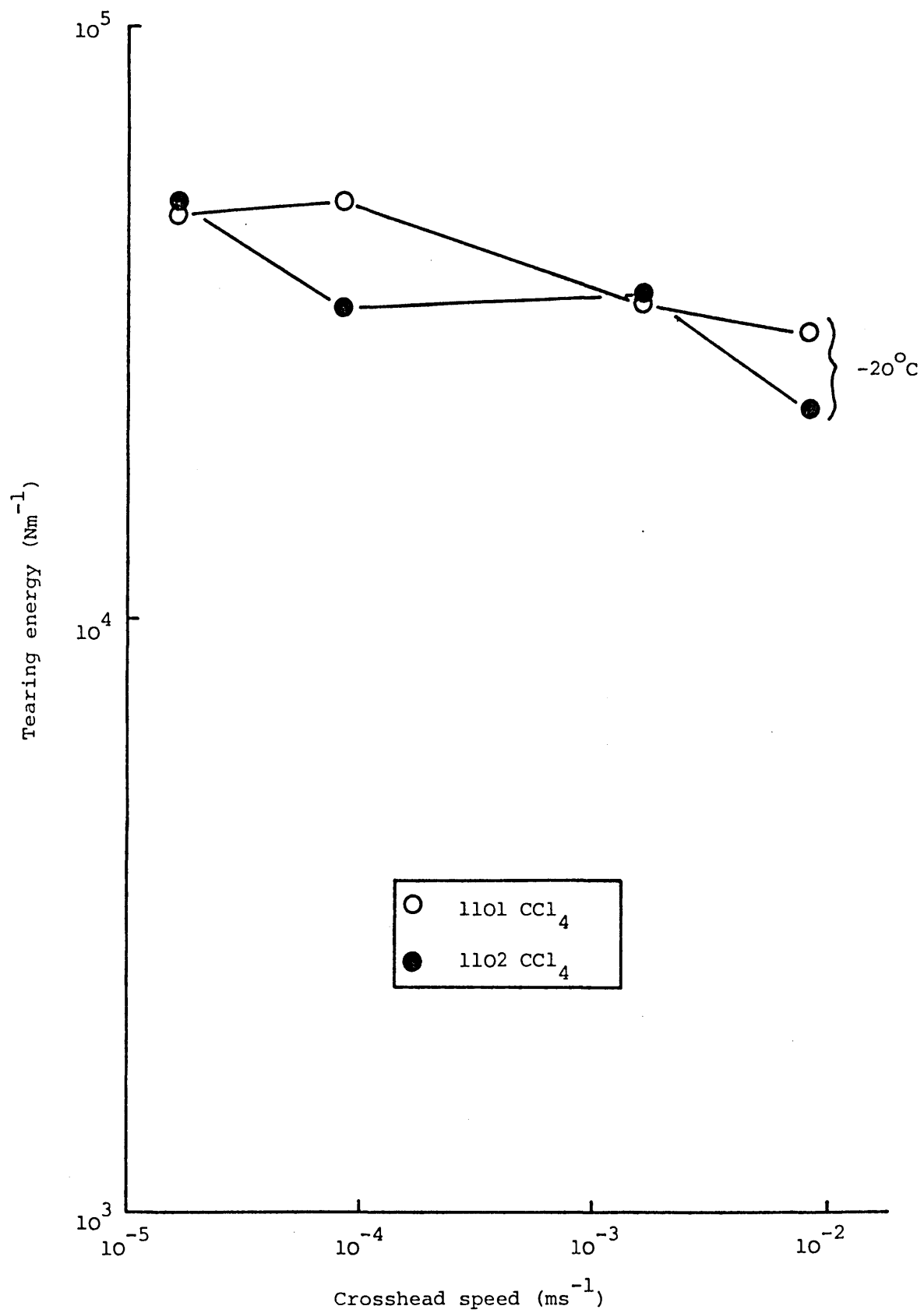


Figure D.4 Tearing energy as a function of rate comparing TR1101 and TR1102 cast from  $\text{CCl}_4$ .

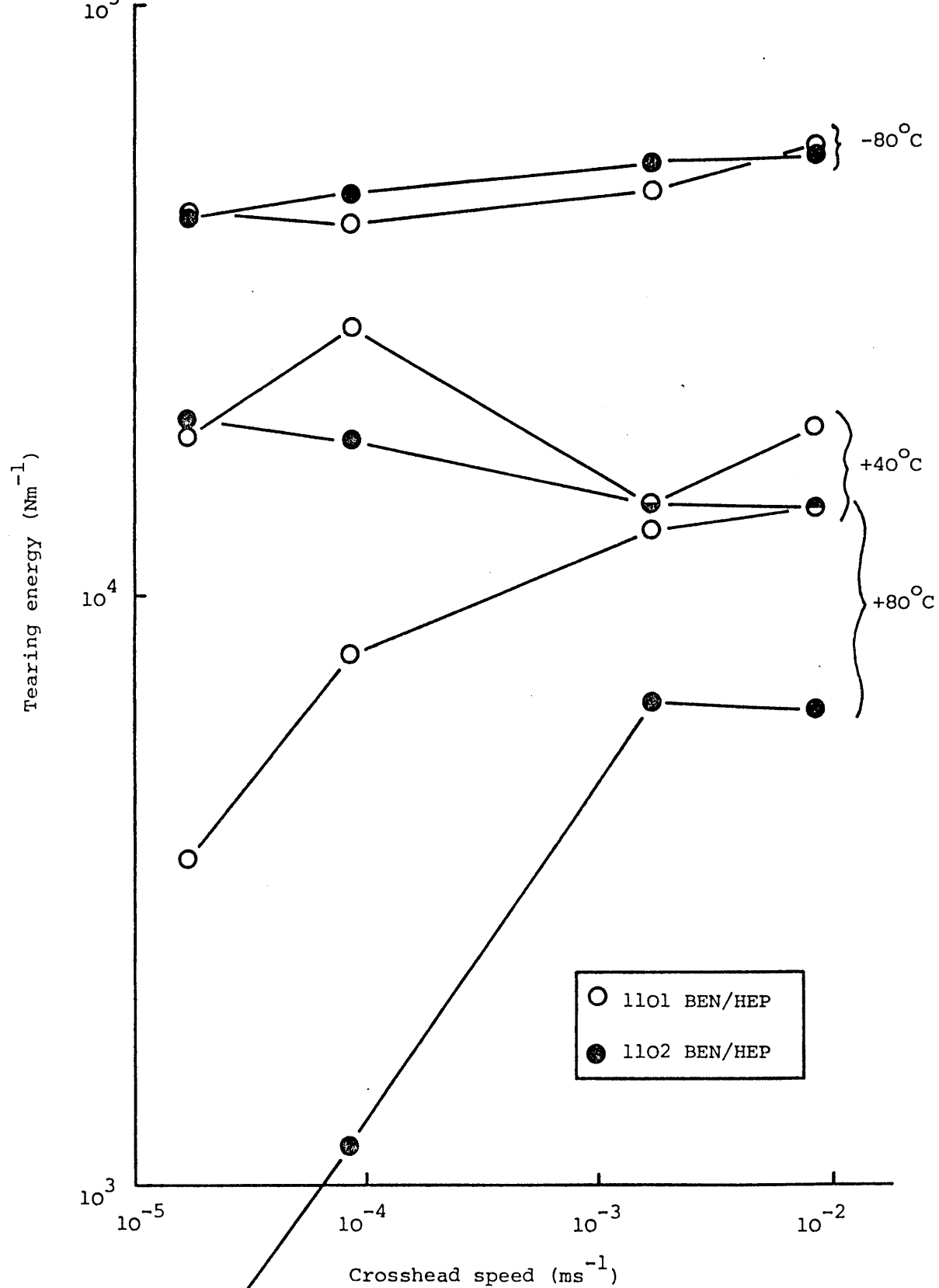


Figure D.5 Tearing energy as a function of rate comparing TR1101 and TR1102 cast from BEN/HEP.

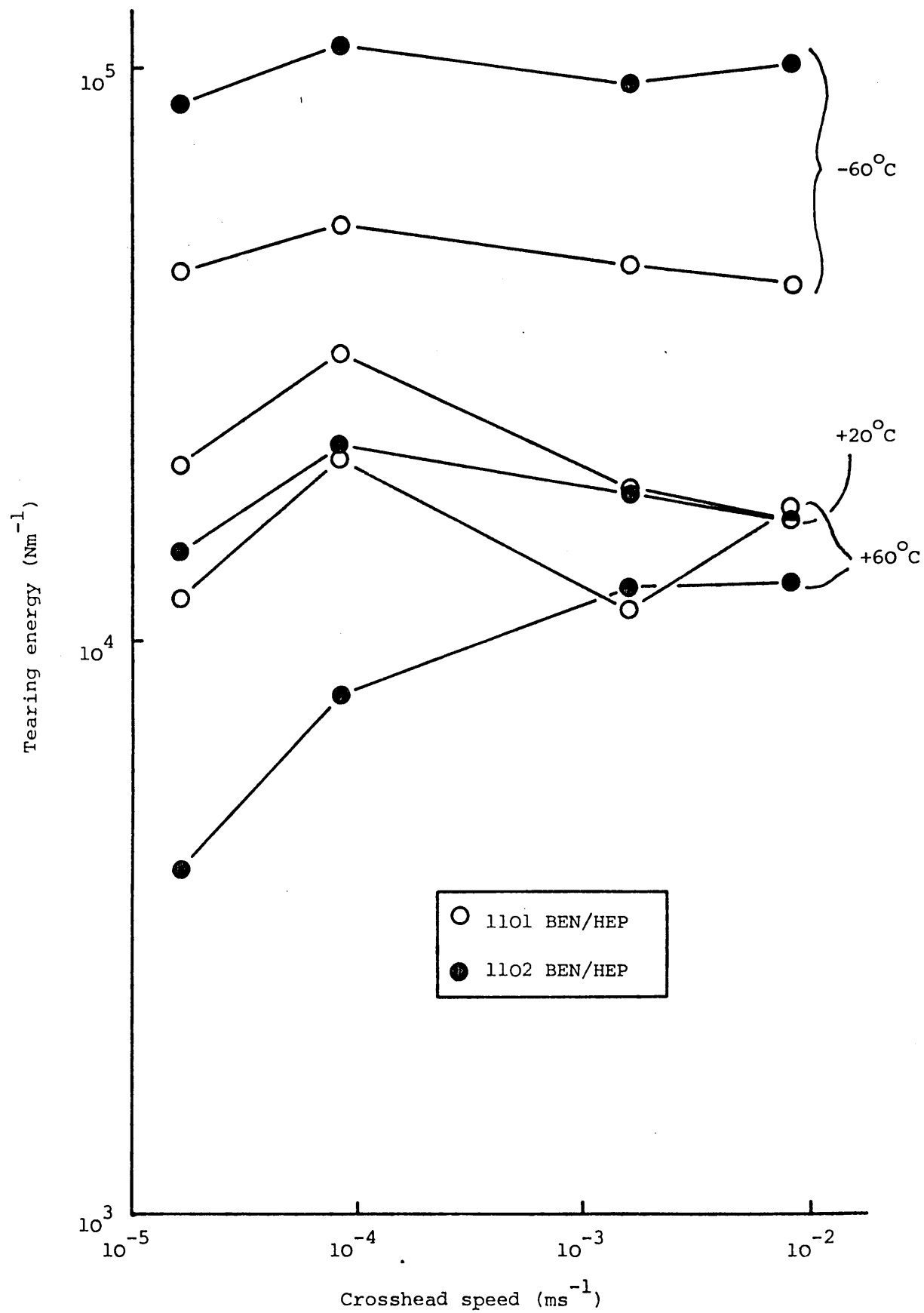


Figure D.6 Tearing energy as a function of rate comparing TR1101 and TR1102 cast from BEN/HEP.

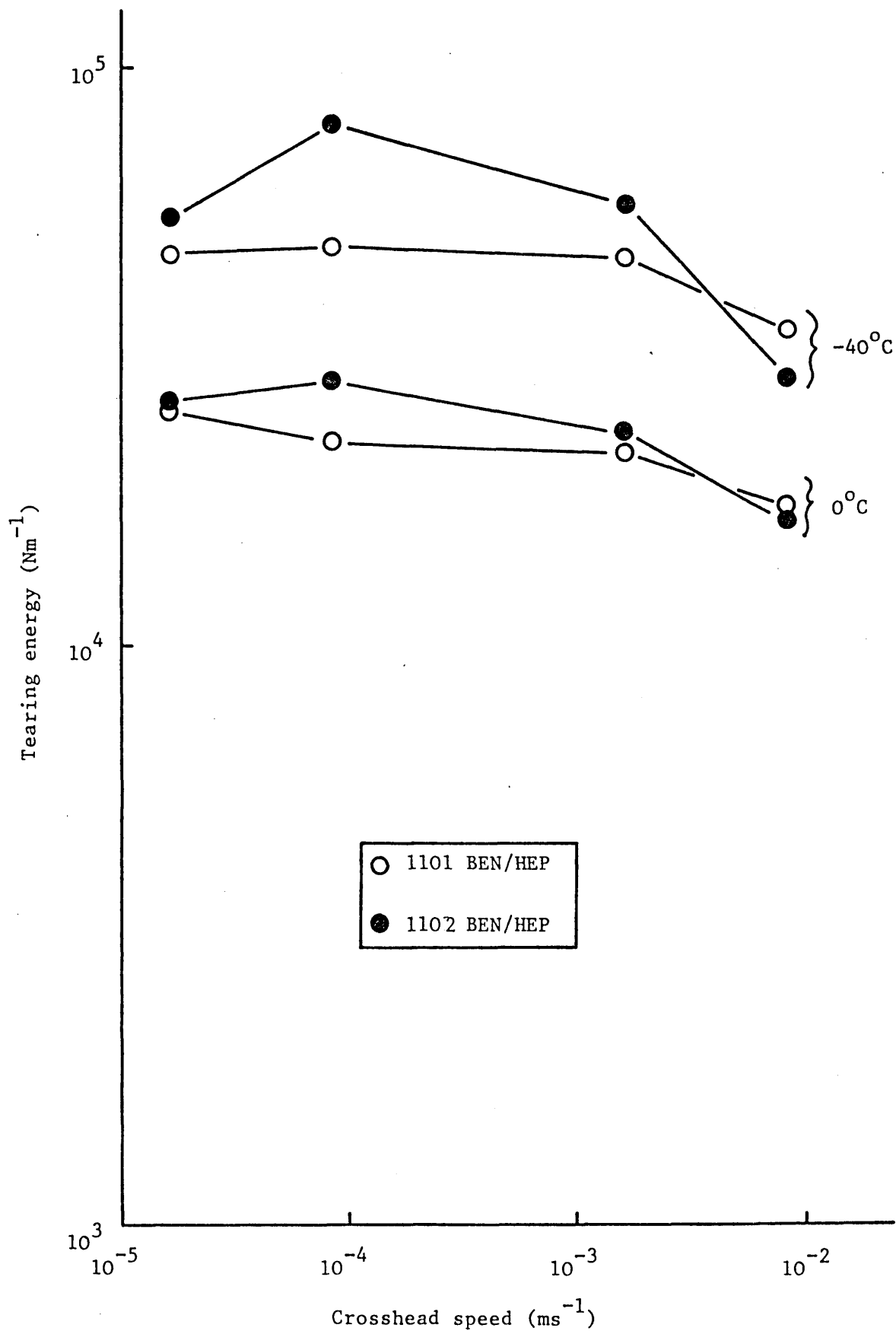


Figure D.7 Tearing energy as a function of rate comparing TR1101 and TR1102 cast from BEN/HEP.

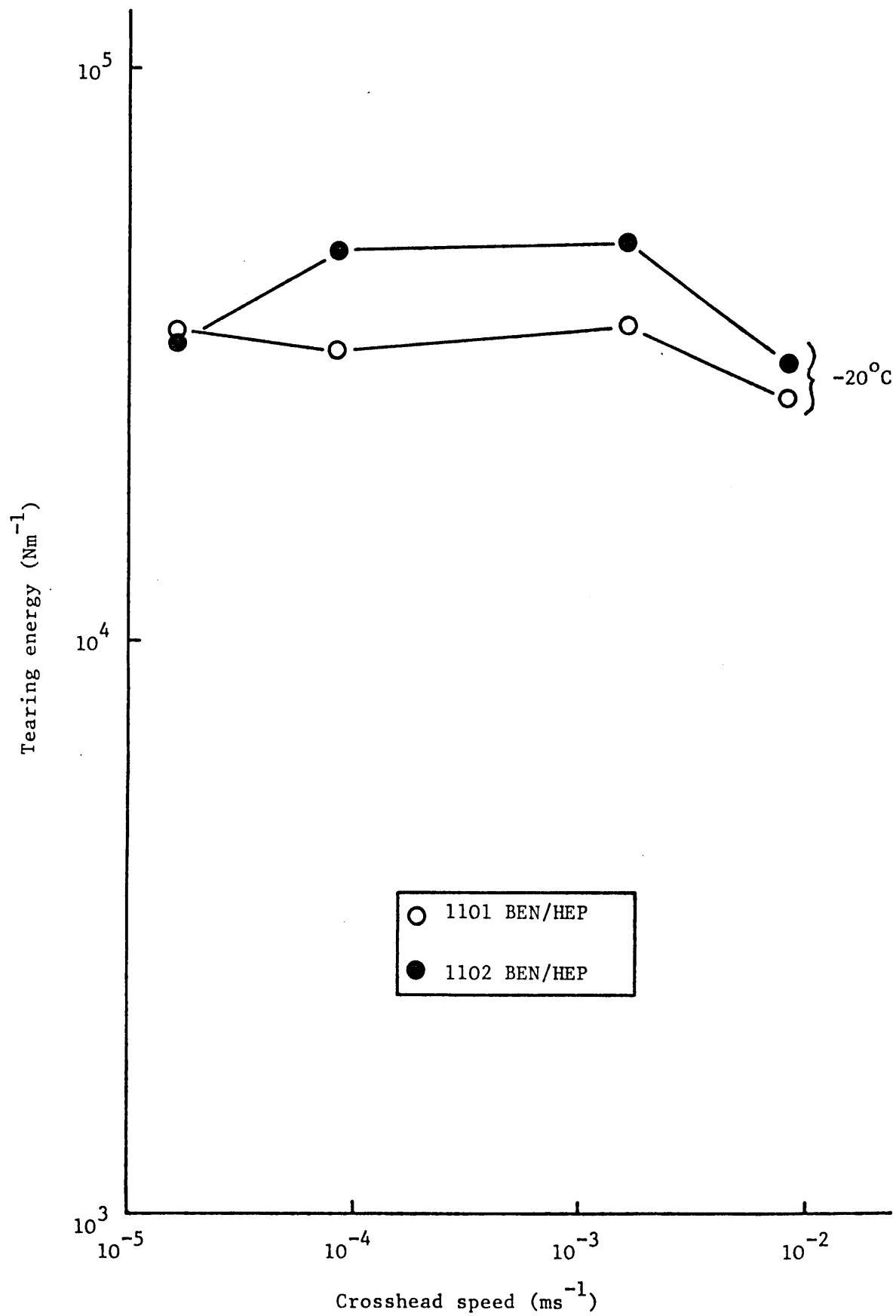


Figure D.8 Tearing energy as a function of rate comparing TR1101 and TR1102 cast from BEN/HEP.

## Appendix E

Tearing force as a function of the tensile  
parameter for TR1102, 4122 and 4113

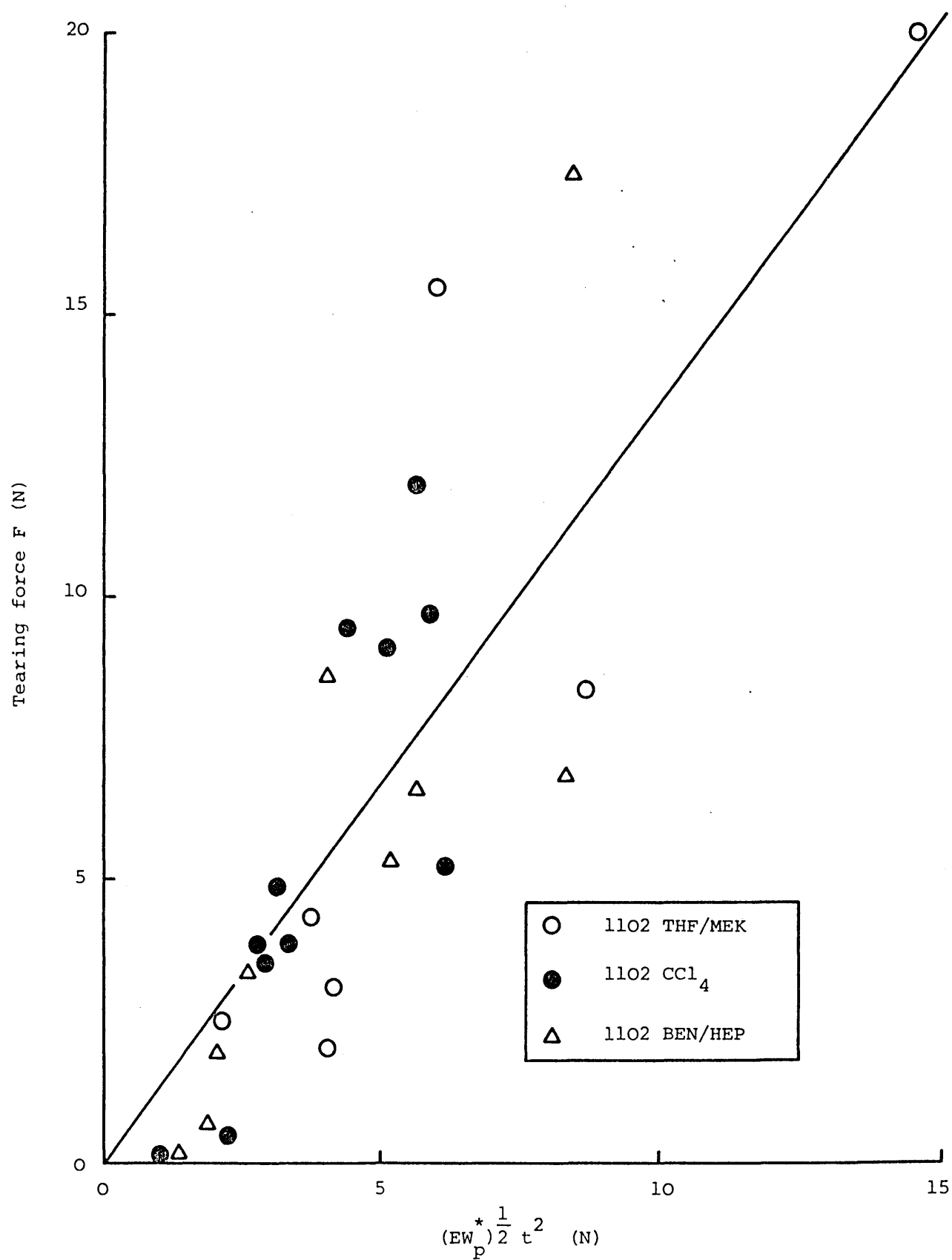


Figure E.1 Tearing force as a function of the tensile parameter for TR1102 cast from several solvent systems. At a rate of  $0.1 \text{ cm} \cdot \text{min}^{-1}$  and all temperatures.



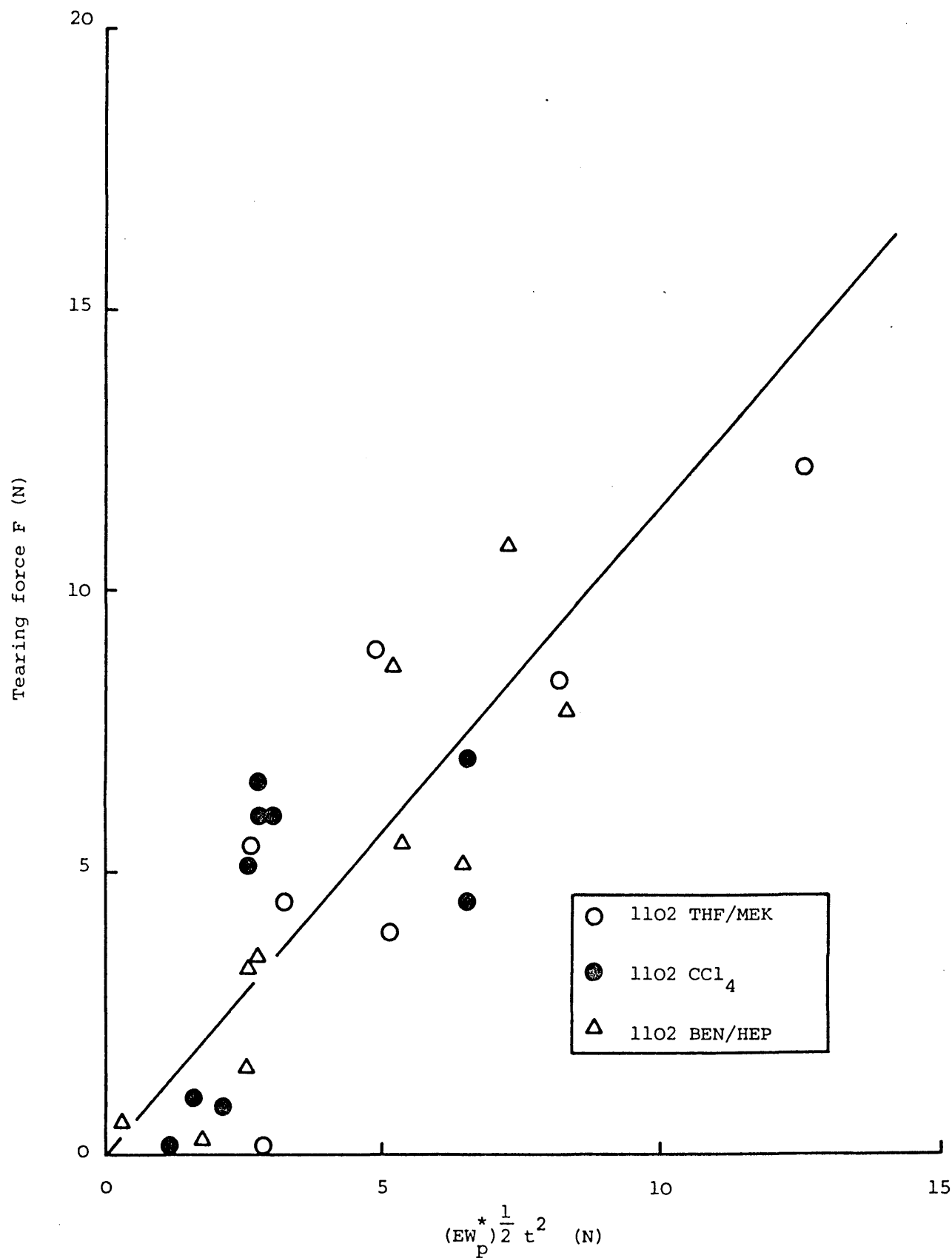


Figure E.2 Tearing force as a function of the tensile parameter for TR1102 cast from several solvents. At a tearing rate of  $0.5 \text{ cm} \cdot \text{min}^{-1}$  and all temperatures.

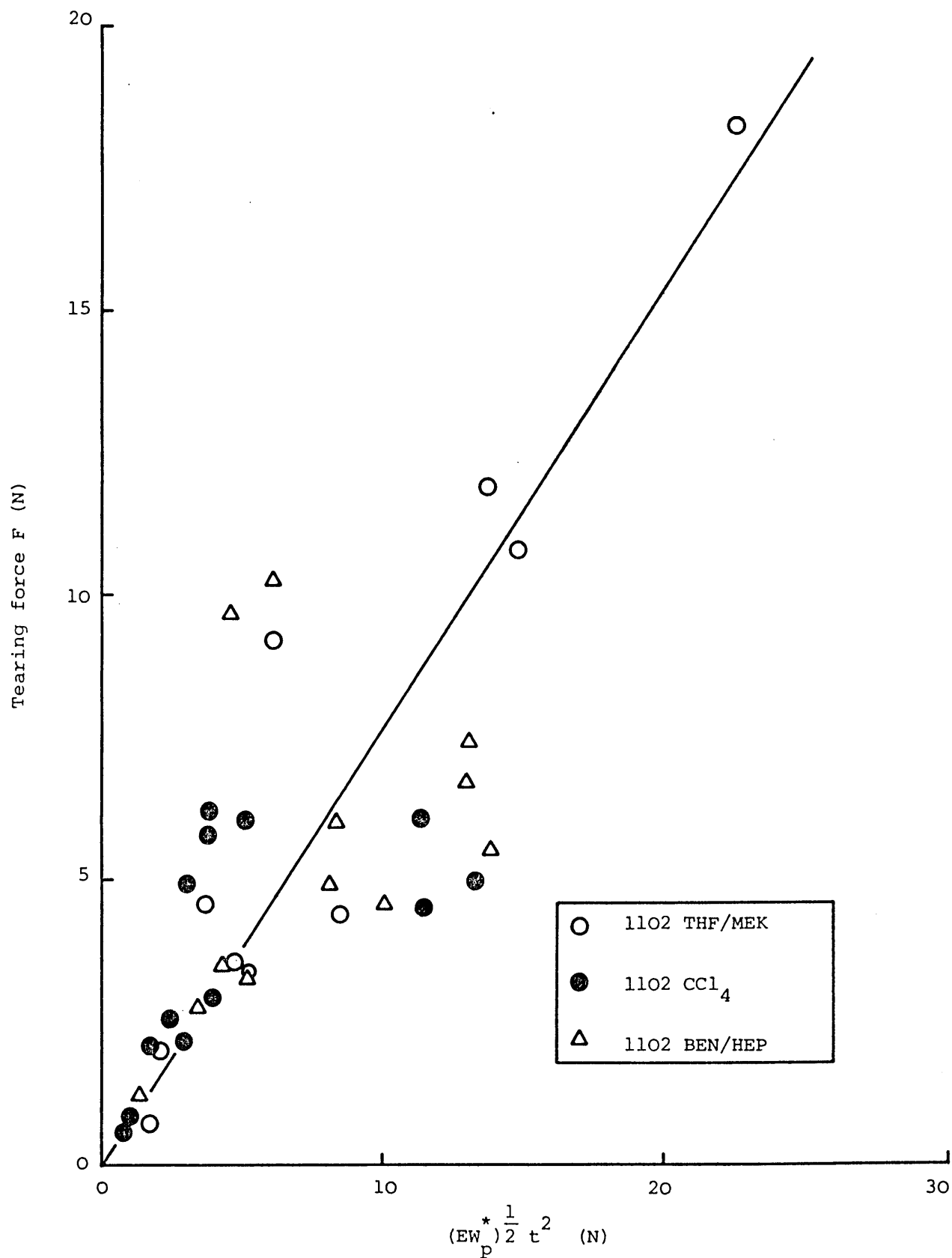


Figure E.3 Tearing force as a function of the tensile parameter for TR1102 cast from several solvents. At a tearing rate of  $10 \text{ cm} \cdot \text{min}^{-1}$  and all temperatures.

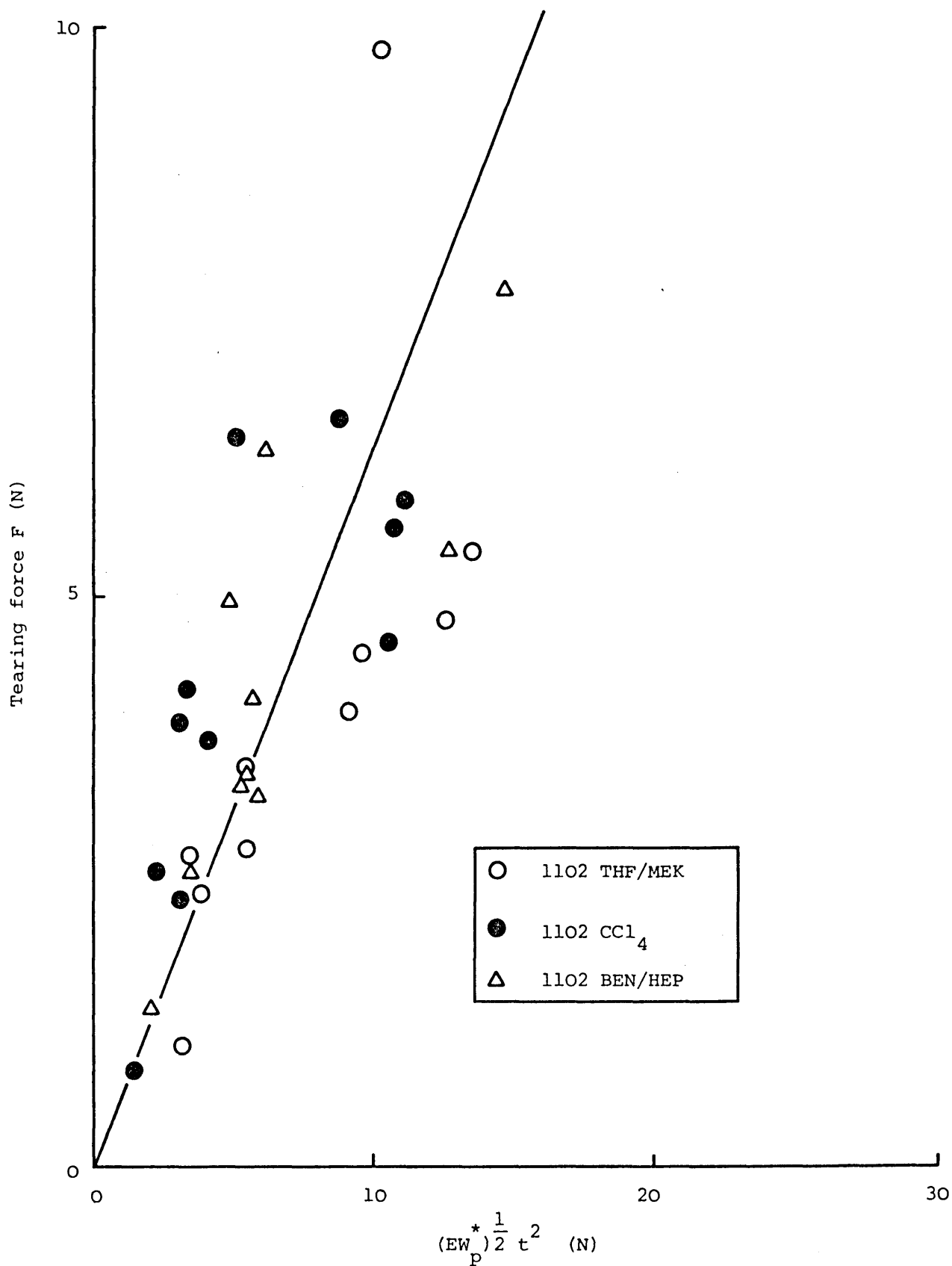


Figure E.4 Tearing force as a function of the tensile parameter for TR1102 cast from several solvents. At a tearing rate of  $50\text{cm}\cdot\text{min}^{-1}$  and all temperatures.

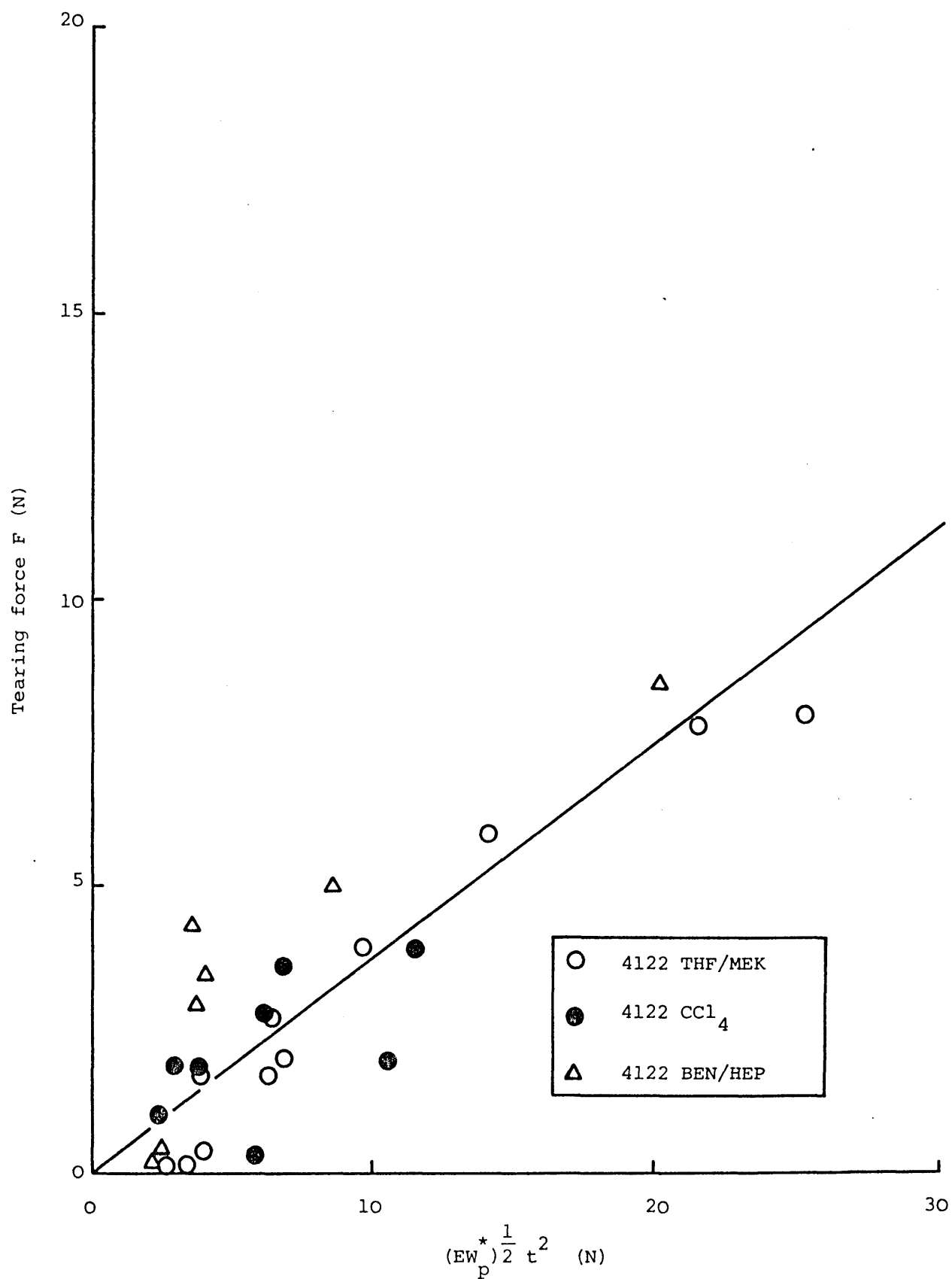


Figure E.5 Tearing force as a function of the tensile parameter for TR4122 cast from several solvents. At  $0.1 \text{ cm.min}^{-1}$  and all temperatures.

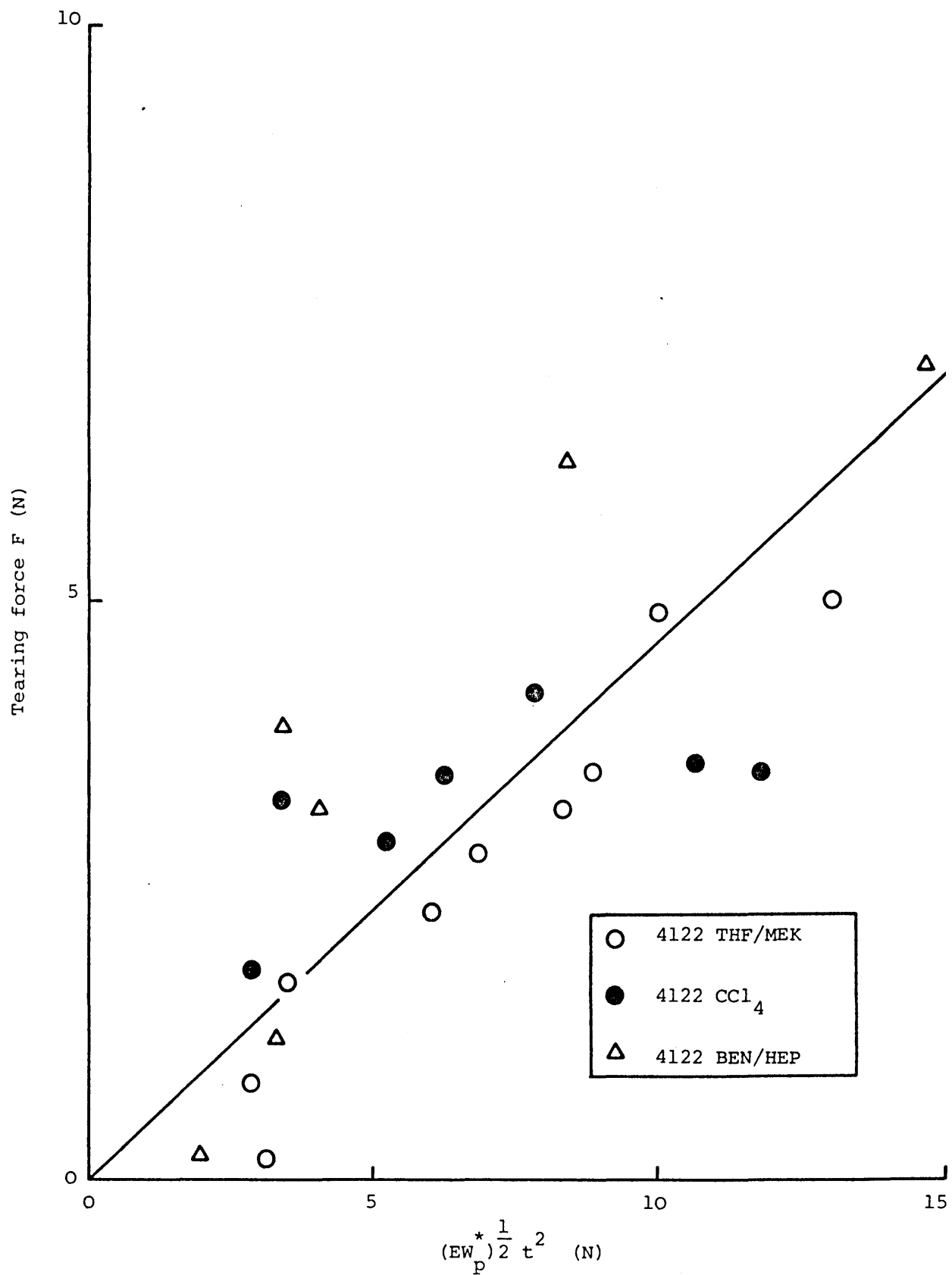


Figure E.6 Tearing force as a function of the tensile parameter for TR4122 cast from several solvent systems. At  $0.5 \text{ cm.min}^{-1}$  and all temperatures.

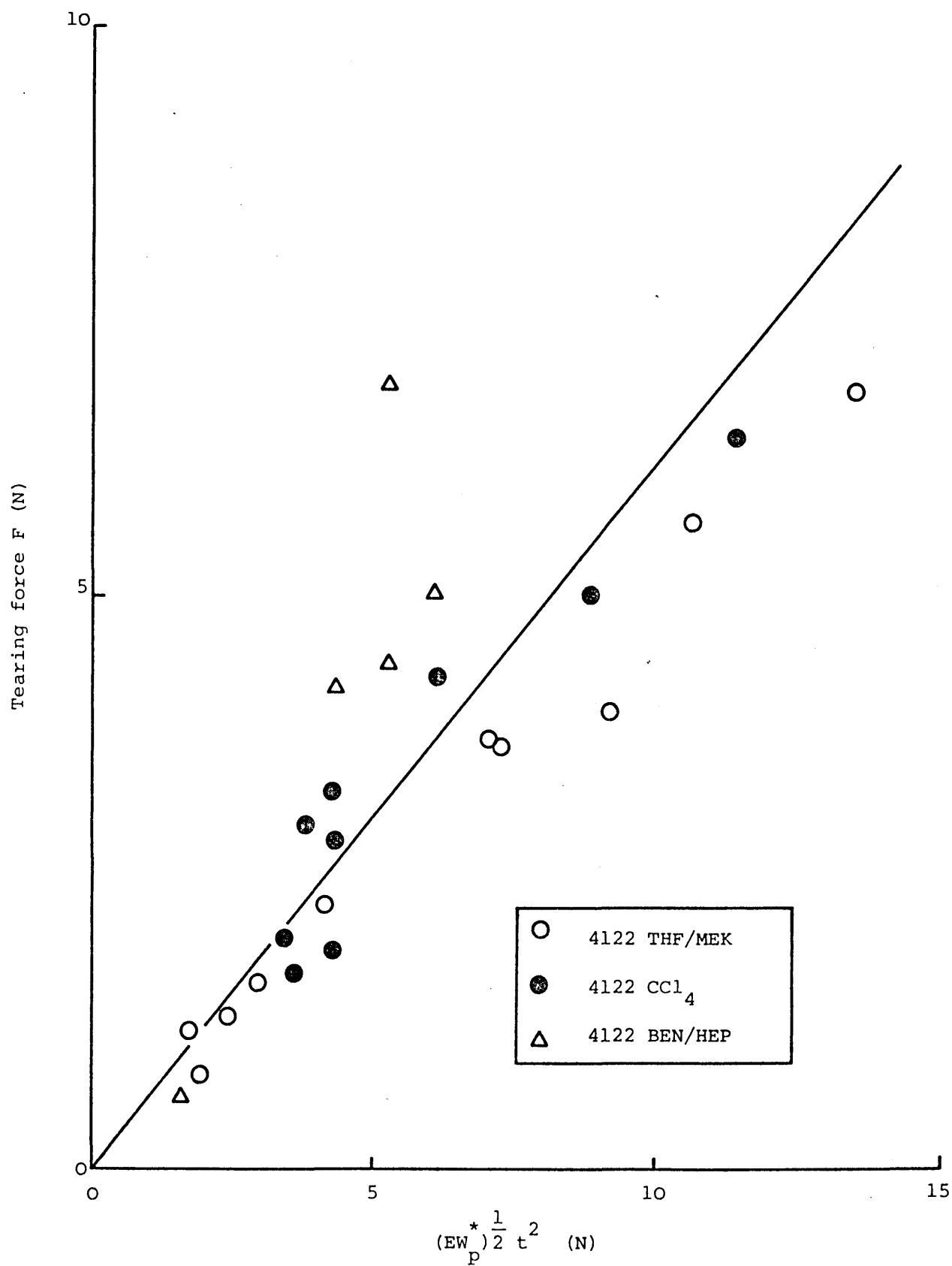


Figure E.7 Tearing force as a function of the tensile parameter for TR4122 cast from several solvents. At  $10 \text{ cm.min}^{-1}$  and all temperatures.

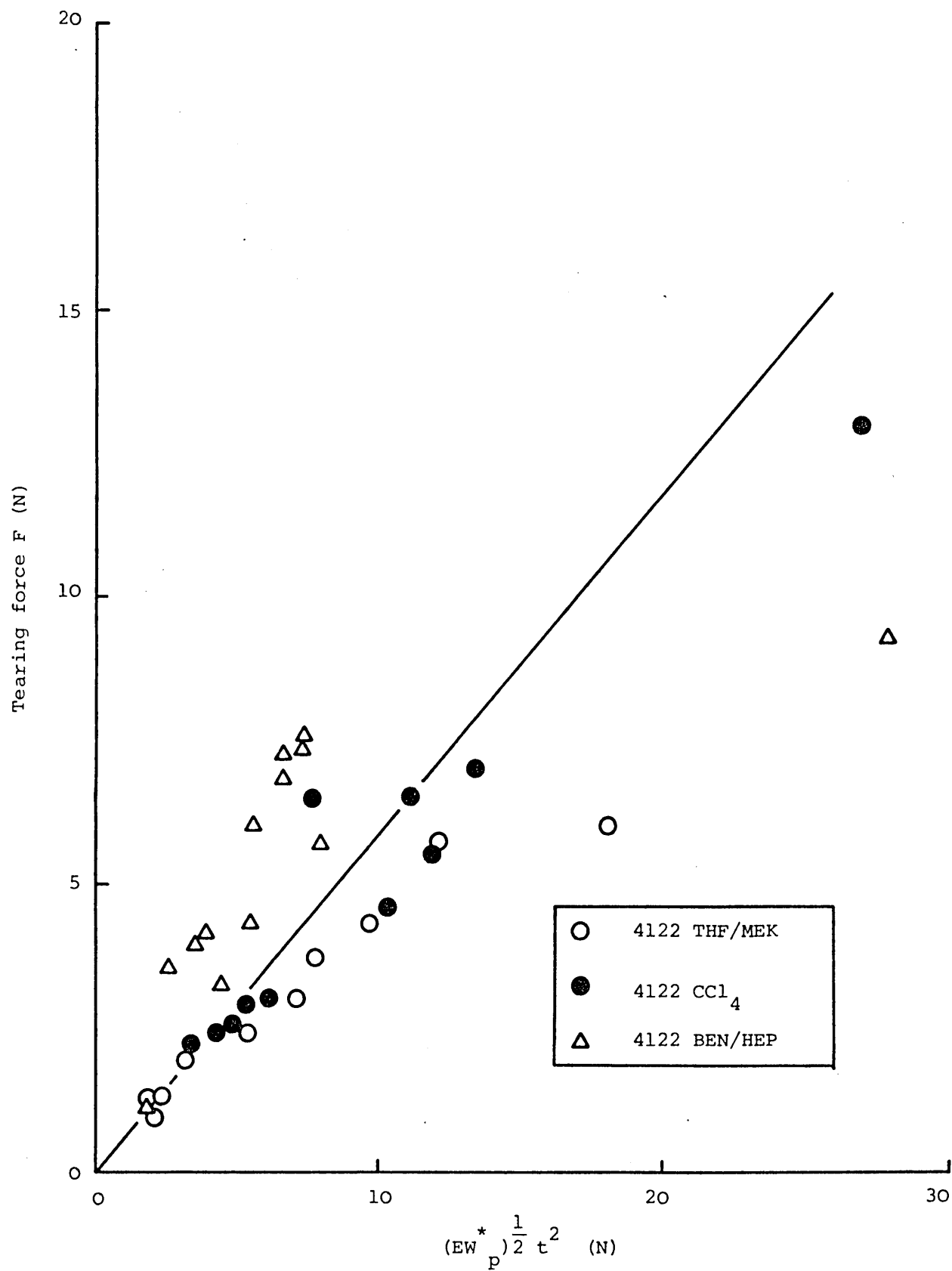


Figure E.8 Tearing force as a function of the tensile parameter for TR4122 cast from several solvents. At  $50 \text{ cm.min}^{-1}$  and all temperatures.

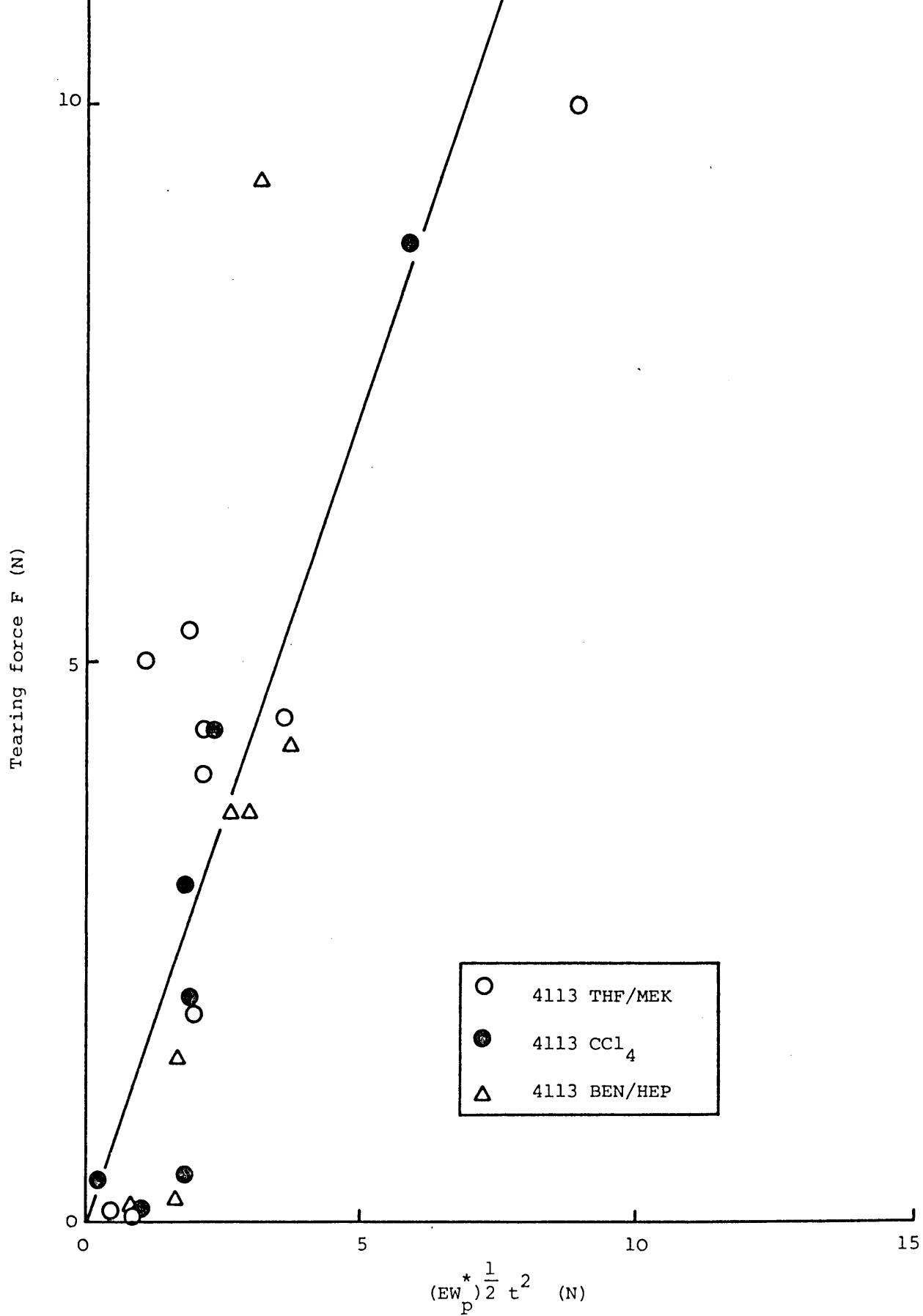


Figure E.9 Tearing force as a function of the tensile parameter for TR4113 cast from several solvents. At  $0.1 \text{ cm.min}^{-1}$  and all temperatures.



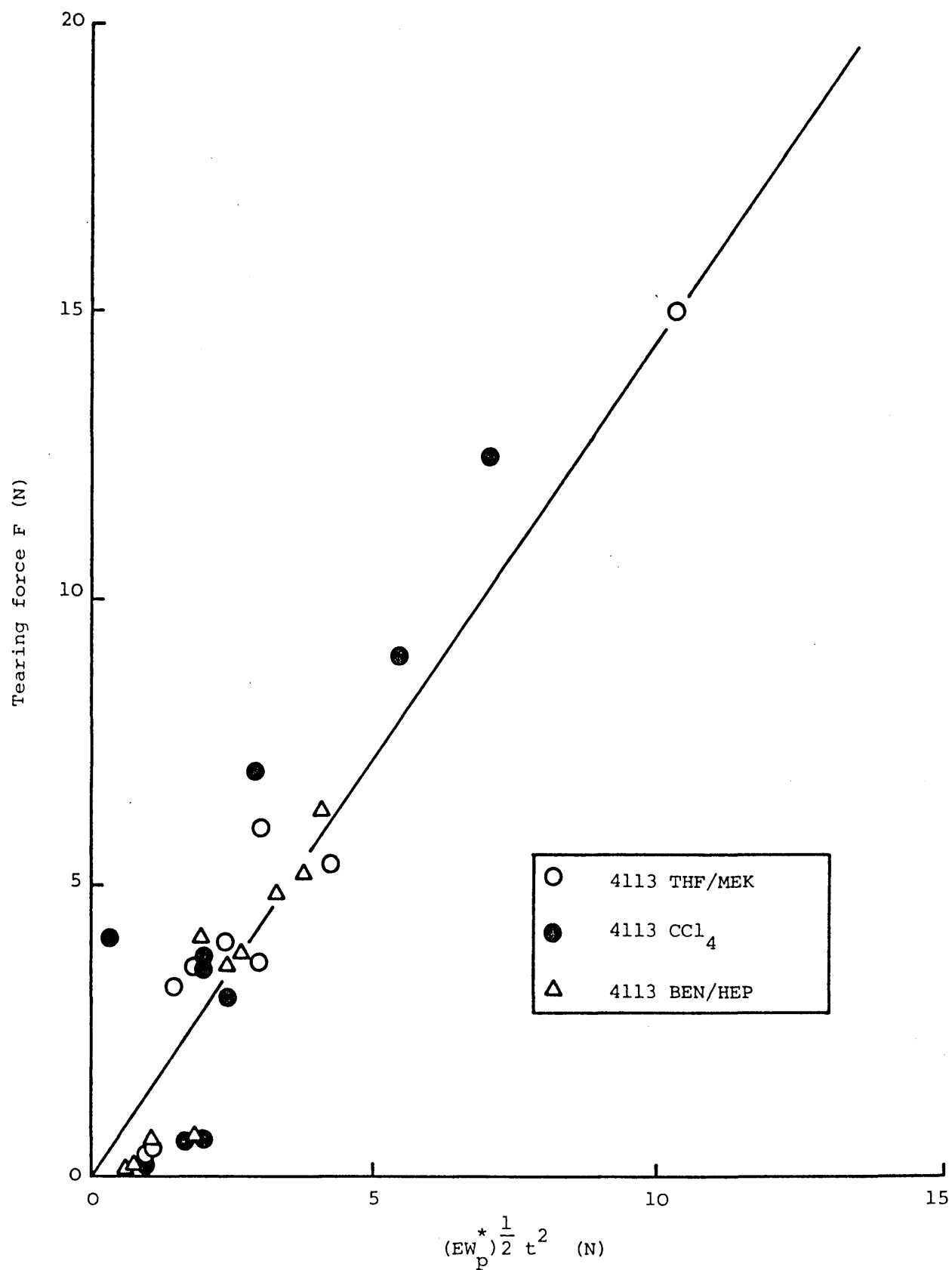


Figure E.10 Tearing force as a function of the tensile parameter for TR4113 cast from several solvents. At  $0.5 \text{ cm} \cdot \text{min}^{-1}$  and all temperatures.

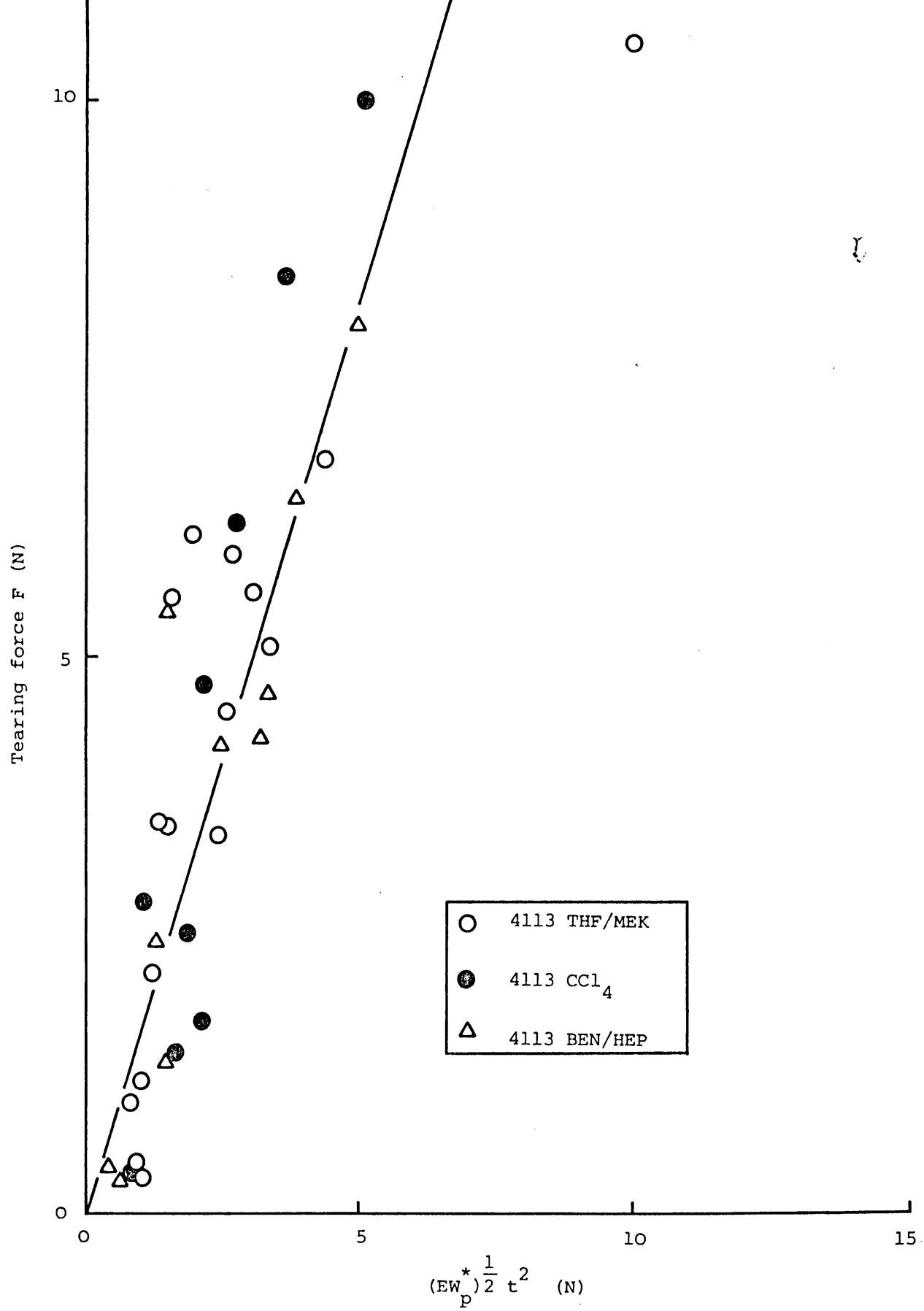


Figure E.11 Tearing force as a function of the tensile parameter for TR4113 cast from several solvents. At  $10\text{cm}\cdot\text{min}^{-1}$  and all temperatures.

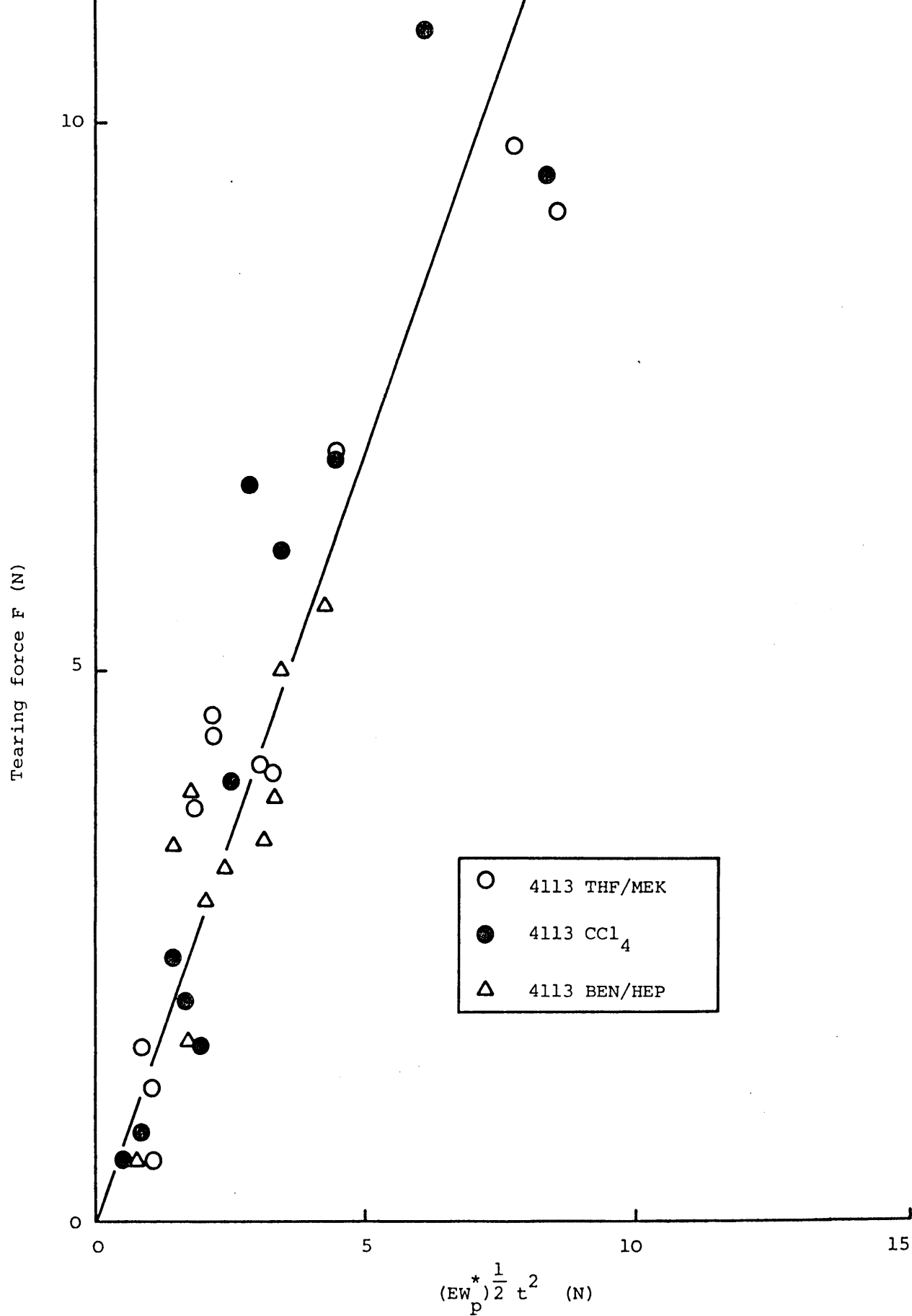


Figure E.12 Tearing force as a function of the tensile parameter for TR4113 cast from several solvents. At 50 cm.min<sup>-1</sup> and all temperatures.